Transactions of the ASME®

Transactions of the ASME, Journal of Fluids Engineering (ISSN 0098-2202) is published quarterly (Mar., June, Sept., Dec.) by The American Society of Mechanical Engineers, Three Park Avenue, New York, NY 10016. Periodicals postage paid at New York, NY and additional mailing offices.
POSTMASTER: Send address changes to Transactions of the ASME, Journal of Fluids Engineering, c/o THE AMERICAN SOCIETY OF MECHANICAL ENGINEERS, 22 Law Drive, Box 2300, Fairfield, NJ 07007-2300.
CHANGES OF ADDRESS must be received at Society headquarters seven weeks before they are to be effective. Please send old label and new address.
STATEMENT from By-Laws. The Society shall not be responsible for statements or opinions advanced in papers or ... printed in its publications (B7.1, Par. 3).

INDEXED by Applied Mechanics Reviews and Engineering Information, Inc. Canadian Goods & Services Tax Registration #126148048.

Journal of Fluids Engineering

Published Quarterly by The American Society of Mechanical Engineers

VOLUME 124 • NUMBER 4 • DECEMBER 2002

Special Section on Alternative LES and Hybrid RANS/LES for Turbulent Flows

(Contents continued on inside back cover)

This journal is printed on acid-free paper, which exceeds the ANSI Z39.48-1992 specification for permanence of paper and library materials. ♾™
♻ 85% recycled content, including 10% post-consumer fibers.

Journal of Fluids Engineering Volume 124, Number 4 DECEMBER 2002

TECHNICAL BRIEF

ANNOUNCEMENTS

Journal of Fluids Engineering

Guest Editorial

Alternative LES and Hybrid RANS/LES for Turbulent Flows

After more than 30 years of intense research on large-eddy simulations (LES) of turbulent flows based on eddy-viscosity subfilter models, [1], there is now consensus that such an approach is subject to fundamental limitations. It has been demonstrated for a number of different flows that the shear stress and strain tensors involved in subfilter eddy-viscosity models have different topological features rendering scalar eddy-viscosity models inaccurate. There have been other proposals that do not employ the assumption of colinearity of strain and stress embedded in the eddy-viscosity models, e.g., the scale-similarity model of Bardina [2]. However, such models are numerically unstable, and more recent efforts have focused on developing mixed models, combining in essence the dissipative eddy-viscosity models with the more accurate but unstable scale-similarity models. The results from such mixed models have been mostly satisfactory but the implementation and computational complexity of the combined approach have limited its popularity.

Recognizing the aforementioned difficulties but also motivated by new ideas pioneered at the Naval Research Laboratory by Jay Boris, several researchers have abandoned the classical formulation and started employing the original, unfiltered, Navier-Stokes equations (NSE) instead of the filtered ones. In this case, one could use *ab initio* scale separation with additional assumptions for stabilization, or invoke monotonicity via nonlinear limiters that implicitly act as a filtering mechanism for the small scales. The latter was the original proposal of Boris et al. [3] in the early 1990s, although as a concept it goes back to von Neumann and Richtmyer, who were working on explicit artificial dissipation schemes. It was actually this concept that also motivated Smagorinsky [4] in developing his model. An intriguing feature of the monotonically integrated LES (or MILES) approach, [3], is the activation of the limiter on the convective fluxes and its role in generating *implicitly* a tensorial form of eddy-viscosity that acts to stabilize the flow and suppress oscillations.

Today development of more sophisticated subgrid scale (SGS) models is actively pursued, and *alternative* nonclassical formulations are being developed. The features of the new LES models can be investigated based on the partial differential equations satisfied by the numerical solution—the modified LES equations, which reveal the competing effects of discretization and explicit SGS modeling. From this perspective, *all* numerical schemes provide a built-in *implicit* SGS model effectively enforced by the leading order discretization errors. The modified LES equations' analysis can likewise be used to address the extent to which a specific *implicit* SGS model might be adequate by itself when suitable algorithms are used, or when additional filtering and/or approximate deconvolution procedures are included as part of the overall LES approach.

For turbulent flows of industrial complexity the Reynolds-averaged Navier-Stokes (RANS) equations, with averaging typically carried out over time, homogeneous directions, or across an ensemble of equivalent flows has been employed. Additional semi-empirical information on the turbulence structure and its relation to the mean flow may also be required depending on the variant of the RANS model. A new trend, which had a fair amount of success, is to combine RANS with LES in order to exploit the best features of both approaches in a complementary manner. LES is capable of simulating flow features which cannot be handled with RANS, such as significant flow unsteadiness and strong vortex-acoustic couplings. However, this added capability carries a high computational cost—at least an order of magnitude more expensive than RANS, and it is a particularly important problem when LES is applied to the entire flow domain. As a consequence, *hybrid* RANS/LES approaches have been developed restricting the use of LES to flow regions where it is crucially needed while using RANS elsewhere. Such developments are thought to be particularly effective for practical flow configurations.

These new advances both on the LES as well as the RANS fronts have attracted a lot of interest recently and have comprised a special focus of several workshops and conferences. Four well attended invited sessions on ''Alternative LES and Hybrid RANS/LES'' addressing this timely subject were organized by one of us (F.F.G.) at the 40th AIAA Aerospace Sciences Meeting at Reno, NV, Jan. 14–15, 2002. Thirteen selected papers from those sessions are included in this special issue of JFE: The first nine are devoted to alternative LES formulations, and the following four to hybrid RANS/LES.

In the *first paper*, Domaradzki and Radhakrishnan use concepts from their SGS estimation modeling approach to develop an LES procedure which employs the NSE truncated to an available mesh resolution. Operationally, the procedure consists of numerically solving the truncated NSE and a periodic processing of the small-scale component of its solution. The use of this approach is exemplified by simulations of Raleigh-Bénard convection. In the *second paper* Von Kaenel et al. describe their approximate deconvolution model for LES based on a second-order finite volume scheme, in which an approximation of the unfiltered solution is obtained by repeated filtering, and given a good approximation of the unfiltered solution, the nonlinear terms of the NSE are computed directly. The effect of scales not represented on the grid is modeled by a relaxation regularization involving a secondary filter operation. Simulations of a supersonic turbulent channel flow with this approach are presented. In the *third paper*, Visbal and Rizzetta describe an LES approach on curvilinear grids combining the use of 4th and 6th-order compact differencing and 10th-order low-pass Padé-type filtering schemes. The performance of their approach is illustrated in the simulation of decaying compressible isotropic turbulence and turbulent channel flow.

In the *fourth paper*, in the monotonically integrated LES (MILES) approach, Grinstein and Fureby focus on the unfiltered NSE and on emulating (near the LES cutoff), the high-wave-number end of the inertial subrange region—characterized by thin filaments of intense vorticity embedded in a background of weak vorticity. This motivates using numerical (flux-limiting) schemes incorporating a sharp velocity-gradient capturing capability operating at the smallest resolved scales. A formal analysis of MILES

is carried out based on the modified equations and applications discussed include both free and wall-bounded flows. In the *fifth paper*, Margolin et al. demonstrate the effectiveness of monotonicity (sign) preserving formulations by arguing that the leading order truncation error introduced by nonoscillatory finite volume schemes represents a physical flow regularization term, providing necessary modifications to the governing equations that arise when the motion of *observables*—finite volumes of fluid convected over finite intervals of time—is considered. Their analysis is based on Burgers' equations and the modified equations, and illustrated with simulations of fully developed turbulence. In the *sixth paper*, Yan et al. report the first LES predictions of heat transfer in adiabatic and isothermal supersonic flat-plate boundary layers using the MILES technique.

In the *seventh paper*, the basic modeling idea in the simulation method presented by Fan et al. is similar to that used in shock capturing, where intrinsically discrete equations are satisfied in thin modeled regions. Their vorticity confinement method does not attempt to accurately discretize the flow equations, but, rather, serves as an implicit nonlinear model of the vortical structures directly on the grid, where structures at the smallest scales ($\sim$2 grid cells) are captured and treated effectively as solitary waves. Applications presented include simulations of flows over round and square cylinders and a realistic helicopter landing ship. In the *eighth paper*, Kirby and Karniadakis present an overview of their spectral vanishing viscosity (SVV) method and its proper use in achieving monotonicity without changing the formal (spectral) accuracy of their discretizations. Some new enhancements of the technique presented here include a new SVV filtering for the continuous Galerkin method in which filtering is accomplished on a fully orthogonal set of modes, and a proposed new method to compute adaptively the viscosity amplitude according to the local strain. Results for turbulent incompressible channel flow are presented to illustrate the application of the method. In the *ninth paper*, Persson et al. consider the homogenization method as alternative to the filtering approach fundamental to conventional LES; it consists of finding a so-called homogenized problem—i.e., finding an homogeneous ''material'' whose overall response is close to that of the heterogeneous ''material'' when the size of the inhomogeneity is small. The authors develop an homogenization-based LES model using a multiple-scales expansion technique and taking advantage of the scaling properties of the NSE. This method is used to simulate forced homogeneous isotropic turbulence and turbulent channel flow, and results are compared with available DNS results and laboratory data.

In the area of hybrid RANS-LES, in the *tenth paper*, Constantinescu et al. present prediction of the flow over a prolate spheroid using the detached-eddy Simulation (DES), in addition to solutions obtained from of the unsteady RANS equations. The study offers the opportunity to gain some insight into application of DES to a complex flow experiencing smooth-surface separation and to also assess corrections for streamline curvature and a nonlinear constitutive relation applied to the underlying RANS model. In the *eleventh paper*, Forsythe et al. computed the supersonic flow around a missile base using DES along with several RANS models. This work offers an opportunity to compare DES and RANS predictions against experimental measurements in a compressible flow, allowing assessment of corrections to the RANS models for compressibility. Predictions of the base pressure and structure of the wake are among the results that are presented.

In the *twelfth paper*, Morton et al. use DES to predict the flow over a delta wing at 27 deg angle of attack, contrasting the calculations against unsteady RANS predictions that include corrections for streamline curvature. A key feature of the configuration and a challenge to models is prediction of vortex burst over the wing. Results of the flow structure are presented along with quantitative comparison to experimental measurements of kinetic energy levels in the vortex core. In the *thirteenth and final paper*, Fasel et al. apply a hybrid RANS-LES approach coined as ''Flow Simulation Methodology'' in which a contribution function is introduced to delineate the level of predicted stress that is modeled and resolved. Application of the method to wall-bounded and open flows is presented.

We would like to thank Prof. Kyle Squires for summarizing the highlights of the RANS/LES papers. On behalf of all authors contributing to this special issue, we are grateful to JFE Technical Editor, Prof. Joe Katz, for recognizing the timeliness and importance of this subject, and we offer sincere thanks to Ms. Laurel Murphy for her patience and skill in coordinating various aspects of the review and processing of the papers.

References

[1] Deardorff, J. W., 1970, ''A Numerical Study of Three-Dimensional Turbulent Channel Flow at Large Reynolds Numbers,'' J. Fluid Mech., **41**(2), p. 453.
[2] Bardina, J., 1983, ''Improved Turbulence Models Based on Large Eddy Simulation of Homogeneous Incompressible Turbulent Flows,'' Ph.D. thesis, Stanford University, Stanford, CA.
[3] Boris, J. P., Grinstein, F. F., Oran, E. S., and Kolbe, R. J., 1992, ''New Insights in Large Eddy Simulations,'' Fluid Dyn. Res., **10**, p. 199.
[4] Smagorinsky, J., 1983, ''The Beginnings of Numerical Weather Prediction and General Circulation Modeling: Early Recollections,'' Adv. Geophys., **25**, p. 3.

Fernando F. Grinstein
Naval Research Laboratory

George Em Karniadakis
Brown University

Subgrid-Scale Modeling of Turbulent Convection Using Truncated Navier-Stokes Dynamics

J. A. Domaradzki

S. Radhakrishnan

Aerospace and Mechanical Engineering,
University of Southern California,
Los Angeles, CA 90089-1191

Using concepts from the subgrid-scale estimation modeling we develop a procedure for large-eddy simulations which employs Navier-Stokes equations truncated to an available mesh resolution. Operationally the procedure consists of numerically solving the truncated Navier-Stokes equation and a periodic processing of the small scale component of its solution. The modeling procedure is applied to simulate turbulent Rayleigh-Bénard convection. [DOI: 10.1115/1.1514206]

1 Introduction

The large-eddy simulation (LES) equations for an incompressible flow are formally obtained by filtering, signified by an overbar, of the full Navier-Stokes equations

$$\frac{\partial}{\partial t}\overline{u_i}+\frac{\partial}{\partial x_j}\overline{u_i}\,\overline{u_j}=-\frac{1}{\rho}\frac{\partial}{\partial x_i}\overline{p}+\nu\frac{\partial^2}{\partial x_j\partial x_j}\overline{u_i}-\frac{\partial}{\partial x_j}\tau_{ij} \tag{1}$$

$$\frac{\partial}{\partial x_i}\overline{u_i}=0, \tag{2}$$

where $u_i=(u_1,u_2,u_3)=(u,v,w)$, p, and ν are the velocity, pressure, and the kinematic viscosity, respectively. In deriving (1) and (2) it is assumed that the filtering and differentiation commute and the filtered product $\overline{u_iu_j}$ is rewritten in the form of the subgrid scale (SGS) stress tensor

$$\tau_{ij}=\overline{u_iu_j}-\overline{u_i}\,\overline{u_j}, \tag{3}$$

such that the remaining terms form the Navier-Stokes equation for the filtered velocity $\overline{u_i}$. The SGS stress tensor is the quantity that requires modeling in LES. The averaging for a quantity $f(\mathbf{x})$ is a linear operation, denoted by L_G, and usually is defined as a convolution integral with a given smoothing kernel G

$$\overline{f}(\mathbf{x})=L_Gf(\mathbf{x})=\int G(\mathbf{x}-\mathbf{x}')f(\mathbf{x}')d\mathbf{x}'. \tag{4}$$

In actual LES in addition to a spatial filtering the "bar" operation involves an implicit projection on a numerical mesh that has an effect of discarding information about subgrid scales smaller than twice the mesh size. The part $u_i^{\mathcal{L}}$ of the total velocity field with the spectral support determined by the mesh resolution can be recovered by various deconvolution procedures (e.g., [1–3]). The effects of the remaining subgrid scales $u_i^{\mathcal{S}}$ must be modeled. Most frequently they are modeled using eddy viscosity concepts. Another approach is to introduce explicit physical models for the subgrid scales and then compute the SGS stress tensor from the definition (3). For instance, Scotti and Meneveau [4] construct subgrid scales using the fractal interpolation technique and Hylin et al. [5] use chaotic maps. Kerr et al. [6] model unresolved subgrid-scale vorticity by calculating the vorticity production by the resolved scales in a limited range of wave numbers outside the resolved range. The approximate inertial manifolds theory of Foias et al. [7] provides an approximate expression for the unknown, subgrid modes. Concepts from the approximate inertial manifolds theory are also employed in the dynamic multilevel method of Dubois et al. [8] where a separate dynamic equation is used to determine subgrid scales. Similarly, Zhou et al. [9] solve the additional dynamic equation for a range of subgrid scales using the Smagorinsky model.

The subgrid-scale estimation model of Domaradzki et al. [10,11] provides the estimate of the unfiltered velocity field appearing in the definition of the subgrid-scale stress tensor. It consists of two steps. In the kinematic step an approximate inversion of the filtering operation is performed on an LES mesh as in the deconvolution approaches. Subsequently, the nonlinear step is used to model a range of subgrid-scales on a mesh two times finer than the LES mesh. The SGS estimation model was applied to LES of low Reynolds number incompressible turbulence in channel flow, [10–12]; to spatially evolving compressible turbulence, [13,14]; to isotropic turbulence in a rotating frame, [15]; and to Rayleigh-Bénard convection, [16], providing generally very good results. A simple modification to increase the nonlinear couplings was developed in [17] to address the inertial range dynamics in high Reynolds number turbulence. That approach as well as the original estimation model can be viewed as special cases of a more general LES procedure which evolves the estimation velocity using the truncated Navier-Stokes equations and which was investigated recently in [18] and [19]. In the procedure the large eddy simulation equations are advanced in time with the subgrid-scale stress tensor calculated from the parallel solution of the truncated Navier-Stokes equations on a mesh two times smaller in each Cartesian direction than the mesh employed for a discretization of the resolved quantities. The truncated Navier-Stokes equations are solved through a sequence of runs, each initialized using the subgrid-scale estimation model. The modeling procedure was evaluated in [20] by comparing results of large-eddy simulations for isotropic turbulence and turbulent channel flow with the corresponding results of experiments, theory, direct numerical simulations, and other large-eddy simulations.

It was further proposed in [20] that this approach can be simplified by dispensing entirely with the LES equations and associated SGS quantities and retaining only the truncated Navier-Stokes (TNS) part of the method. Here, we investigate such a simplification that does not invoke the concept of the subgrid-scale stress tensor at all. The procedure is formulated solely in terms of the truncated Navier-Stokes equation and a periodic processing of the small scale component of its solution. The method shares some similarities with various methods that replace the physical models of the subgrid scale tensor by the mathematical

Contributed by the Fluids Engineering Division for publication in the JOURNAL OF FLUIDS ENGINEERING. Manuscript received by the Fluids Engineering Division March 12, 2002; revised manuscript received June 24, 2002. Associate Editor: F. F. Grinstein.

regularization procedures, see e.g. [21–24], some of them known as the monotonically integrated large-eddy simulations (MILES).

In the next section we describe rationale for the proposed approach provided by the previous work on the SGS estimation model. That section concludes with a description of specific steps that are used to implement the method. The results of simulations for turbulent Rayleigh-Bénard convection are described in following section.

2 Truncated Navier-Stokes Equations Applied to Subgrid Scale Modeling

In order to discuss how the unresolved part of the modeled velocity can be constructed let us consider an idealized large-eddy simulation coupled to a fully resolved direct numerical simulation (DNS). At each time-step in DNS the full velocity field u_i is known on a mesh with the mesh size Δ_{DNS} and the subgrid-scale (SGS) stress τ_{ij} can be computed and used to advance the large-eddy simulation (LES) equations on a coarser mesh with $\Delta_{\mathrm{LES}} \gg \Delta_{\mathrm{DNS}}$. In practice there is no guarantee that the solution $\overline{u_i}$ of the LES equations will follow the filtered and truncated solution of the Navier-Stokes equations for all times. If both systems are chaotic even small numerical errors in computing τ_{ij} may cause both solutions to decorrelate in time. According to the statistical predictability theory the decorrelation time is on the order of several large-eddy turnover periods (Lesieur [25]). In order to prevent decorrelation one may periodically replace the large scales $u_i^{\mathcal{L}}$ in DNS by the corresponding large scales from LES, i.e., the result of deconvolving $\overline{u_i}$. In such a procedure the continuous in time LES evolution is coupled to a sequence of periodically reinitialized DNS. Of course, in actual LES information from a fully resolved DNS will never be available. Consider then truncated Navier-Stokes (TNS) equations with the truncation wave number, K_c, intermediate between the truncation wavenumber in LES, k_c, and the Kolmogoroff wave number in DNS, k_η, i.e., $k_c < K_c \ll k_\eta$. If the same initial condition is used to numerically solve all three equations, i.e., DNS, LES, and TNS, the following qualitative picture is expected. First, after some fraction of the large-eddy turnover time the TNS solution will begin to deviate from the DNS solution, initially for the largest wave numbers, which have the fastest time scale, and the error will propagate progressively toward large scales. However, by the predictability argument, there will be a finite time, say T, over which TNS and DNS solutions will remain close to each other for wave numbers less than the LES cutoff k_c. Second, for these times and K_c sufficiently larger than k_c the SGS stress tensor in LES computed using TNS solution will be a good approximation to the actual SGS stress computed from DNS data. If these expectations are correct then the SGS stress could be computed from a solution of a parallel TNS simulation that is much less expensive than the full DNS. Similarly to the idealized LES discussed above the TNS would need to be re-initialized with a period on the order of T to conform to the actual DNS solution at large wave numbers and to the LES solution in the resolved range. To be successful as a modeling tool such a procedure requires a method for the periodic re-initialization of TNS and the determination of the time period T and the truncation wave number K_c. Guidelines are provided by previous work in this area (Domaradzki et al. [10–12]) that has established that it is sufficient to take the intermediate wave number K_c twice as large as the LES cutoff k_c and the time period T on the order of the eddy turnover time of the smallest resolved scales.

Accordingly, we will consider the LES Eqs. (1)–(2) for the velocity $\overline{u_i}$ together with the truncated Navier-Stokes equations for the estimated velocity $\tilde{u}_i$

$$\frac{\partial}{\partial t}\tilde{u}_i + \frac{\partial}{\partial x_j}\tilde{u}_i\tilde{u}_j = -\frac{1}{\rho}\frac{\partial}{\partial x_i}\tilde{p} + \nu\frac{\partial^2}{\partial x_j \partial x_j}\tilde{u}_i, \tag{5}$$

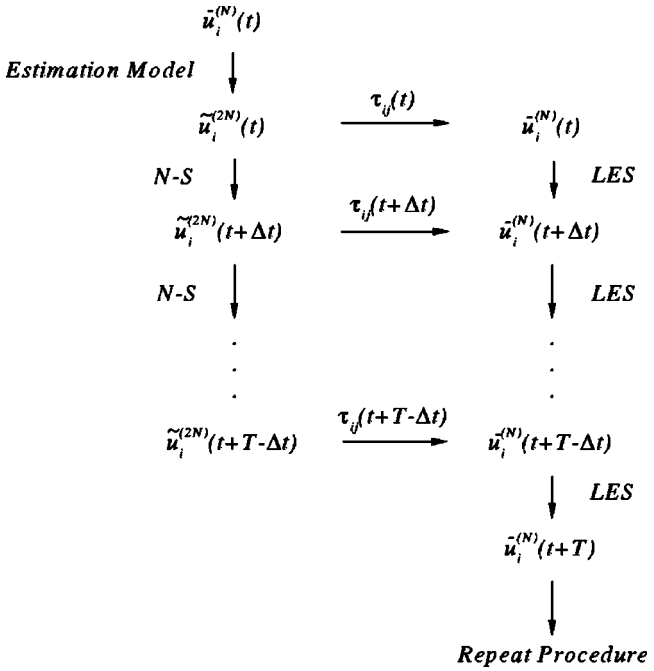

Fig. 1 The large-eddy simulation procedure. The superscripts (*N*) and (2*N*) refer to the LES and TNS resolution, respectively.

$$\frac{\partial}{\partial x_i}\tilde{u}_i = 0. \tag{6}$$

The LES velocity is the result of filtering the full Navier-Stokes velocity u_i with a top hat filter with a filter width Δ and is represented on a mesh with the mesh size Δ_{LES} (or the spectral cutoff k_c), where we choose $\Delta_{\mathrm{LES}} = \Delta/2$. The mesh size Δ_{TNS} used to represent $\tilde{u}_i$ is a factor of two smaller than the mesh size Δ_{LES}, $\Delta_{\mathrm{TNS}} = \Delta_{\mathrm{LES}}/2$, (or the spectral cutoff is $2k_c$). Initial conditions for the TNS velocity $\tilde{u}_i$ periodically required by the procedure are constructed from the corresponding LES velocity $\overline{u_i}$ using the estimation model described in detail in [11]. The complete procedure is illustrated in Fig. 1.

Also, note that the term ''truncated'' applied to Eqs. (5)–(6) refers not to the form of the equations, which is no different from the form of the full Navier-Stokes equations, but to the limited numerical resolution used to solve these equations.

The main purpose of advancing in time two sets of equations, LES and TNS, is the consistency with the traditional LES formalism and the clear definition of the large-scale quantities, e.g., $\overline{u_i}$, as a solution of the LES equation. However, in principle the information about the LES solution $\overline{u_i}$ should be contained in the TNS solution $\tilde{u}_i$. If this information could be extracted then the task of solving the LES equation could be avoided. In a case of a sharp spectral filter the large-scale component $\overline{u_i}$ is obtained trivially from $\tilde{u}_i$ by setting to zero all Fourier modes with wave numbers $k > k_c$, where k_c is the coarse LES mesh cutoff wave number. However, in a more general case of spatial filters the extraction of the large-scale component from the complete field $\tilde{u}_i^{(2N)}$ presents difficulties. Consider the initial condition for TNS, $\tilde{u}_i(t) = \tilde{u}_i^0(t) + \tilde{u}_i'(t)$, on the fine mesh. Here $\tilde{u}_i^0$ is the result of a deconvolution of $\overline{u}_i^{(N)}$ performed on the coarse LES mesh and then interpolated to the fine TNS mesh and $\tilde{u}_i'$ is the estimated subgrid scale velocity on the fine mesh. Because the physical space operations are used to construct this field both $\tilde{u}_i^0(t)$ and $\tilde{u}_i'(t)$ overlap spectrally although $\tilde{u}_i^0(t)$ is dominated by the large scales and $\tilde{u}_i'(t)$ by the small scales. If now the field $\tilde{u}_i(t)$ is filtered and sampled on the coarse LES mesh the result will contain a contribution from the

spectral content of $\tilde{u}_i'(t)$ in the large scales. This implies that the field $\tilde{u}_i^0(t)$ cannot be recovered from the complete $\tilde{u}_i(t)$ by filtering and sampling alone. It is possible to write a coupled set of equations for fields $\tilde{u}_i^0(t)$ and $\tilde{u}_i'(t)$ and follow their evolution for time T. The field $\tilde{u}_i^0(t+T)$ from such a run would be the required large-scale field at time T needed to initialize the next run in the sequence. However, if only the complete $\tilde{u}_i(t+T)$ is known the field $\tilde{u}_i^0(t+T)$ cannot be obtained by sampling and filtering in the physical space and additional approximations must be invoked. We have used the following procedure. Consider a formal inverse of the linear operator L_G in (4) as a power series expansion

$$L_G^{-1}=(I-(I-L_G))^{-1}=I+(I-L_G)+(I-L_G)^2+\ldots \quad (7)$$

where I is the identity operator. Stolz and Adams [3] note that the product of L_G and a finite term truncation of (7) produces a filter which strongly damps the smallest resolved scales and does not affect the largest scales. The further control is provided by a choice of the filter L_G which does not have to be the same as the original ''bar'' filter defined as the top hat filter with the width $\Delta=2\Delta_{\mathrm{LES}}$ and the Simpson's rule of integration. We found that the best compromise in terms of the numerical complexity and the ability to extract the large-scale component of a field was a combination employing first three terms in (7) and the top hat filter with the width $\Delta=\Delta_{\mathrm{LES}}$ and the trapezoidal rule of integration, denoted here by ''hat.'' This combination provides the following expression for the large-scale component of the field $\tilde{u}_i$

$$\tilde{u}_i^0=3\hat{\tilde{u}}_i-3\hat{\hat{\tilde{u}}}_i+\hat{\hat{\hat{\tilde{u}}}}_i. \quad (8)$$

The perturbation velocity $\tilde{u}_i'$ can be computed using the standard subgrid scale estimation method, [11,12], and the large-scale velocity (8) obtained from the TNS velocity $\tilde{u}_i$. To avoid the contamination of the mean of $\tilde{u}_i^0$ by the mean of $\tilde{u}_i'$, however small it is, it is replaced by

$$\tilde{u}_i''=\tilde{u}_i'-\hat{\tilde{u}}_i'. \quad (9)$$

With these definitions the modeling procedure that does not use LES equations at all and is formulated entirely in the physical space reads

$$\tilde{u}_i^0(t)\rightarrow\tilde{u}_i''(t)\rightarrow[\tilde{u}_i(t)=\tilde{u}_i^0(t)+\tilde{u}_i''(t)]\overset{N-S}{\rightarrow}\tilde{u}_i(t+T)\rightarrow\tilde{u}_i^0(t+T). \quad (10)$$

Between time t and $t+T$ the estimated field $\tilde{u}_i$ evolves through the truncated Navier-Stokes equation solved on the fine mesh with the cutoff $2k_c$. In some cases, especially at lower Reynolds numbers, the estimated subgrid velocity $\tilde{u}_i''$ can be simply set to zero at time intervals T. In this case the subgrid scales $\tilde{u}_i''$ at intermediate times will be generated by Navier-Stokes dynamics from the initial condition $\tilde{u}_i^0$. Such an approach met with success in LES of isotropic turbulence in a rotating frame, [15], and is also applied here.

In summary, the method is applied operationally as follows. First, a mesh with the mesh size Δ_{TNS} is constructed and the truncated Navier-Stokes Eqs. (5) and (6) are discretized on that mesh. Note that this step is just a standard DNS implementation of the Navier-Stokes equations on a given mesh; the term TNS simply signifies that the numerical resolution is insufficient to perform accurate DNS. Using a particular initial condition for the velocity field $\tilde{u}_i(t_0)$ the TNS equations are solved numerically for a prescribed time T. The time T is a free parameter in the method and is determined using the theoretical estimate of the eddy turnover time of the smallest resolved scales or can be determined by a numerical experimentation. At time t_0+T the velocity $\tilde{u}_i$ is filtered using Eq. (8). The ''hat'' denotes the top hat filter with the filter width twice the mesh size, i.e., $\Delta=2\Delta_{\mathrm{TNS}}$. Numerically it is implemented by applying the trapezoidal rule of integration over interval spanning three neighboring mesh points. The perturbation velocity $\tilde{u}_i''$ in this work is simply set to zero so that $\tilde{u}_i(t_0+T)=\tilde{u}_i^0(t_0+T)$. This becomes the initial condition for the TNS run for the next time interval T. Therefore, the complete simulation consists of a sequence of TNS runs, each initialized by applying filter (8) to the velocity field at the last time-step in the preceding TNS run.

3 Numerical Simulations

In [20] the method has been implemented for forced and decaying isotropic turbulence and for turbulent channel flow. However, in contradistinction to the present work the perturbation velocity $\tilde{u}_i''$ at time intervals T was computed using the subgrid scale (SGS) estimation model methodology and was nonzero. The simulation results were in a very good agreement with experiments and direct numerical simulations. In the application of the truncated Navier-Stokes (TNS) to simulate isotropic turbulence in a rotating frame the perturbation velocity (9) was set to zero at the beginning of each TNS subrun, [15]. A very good agreement with the corresponding direct numerical simulation (DNS) results was obtained. Here, we extend and evaluate this TNS procedure for flows affected by buoyancy effects, choosing a case of turbulent Rayleigh-Bénard convection between two parallel plates. The temperature equation for the estimated temperature $\tilde{T}$ in the Boussinesq approximation is

$$\frac{\partial}{\partial t}\tilde{T}+\frac{\partial}{\partial x_j}\tilde{u}_j\tilde{T}=\kappa\frac{\partial^2}{\partial x_j\partial x_j}\tilde{T}. \quad (11)$$

Also the truncated momentum Eq. (5) is modified by adding the buoyancy term

$$\frac{\partial}{\partial t}\tilde{u}_i+\frac{\partial}{\partial x_j}\tilde{u}_i\tilde{u}_j=-\frac{1}{\rho}\frac{\partial}{\partial x_i}\tilde{p}+\nu\frac{\partial^2}{\partial x_j\partial x_j}\tilde{u}_i+[1-\alpha(\tilde{T}-T_0]g_i. \quad (12)$$

In the equations above κ is the conductivity, α the volumetric expansion coefficient, g_i the gravitational acceleration, and T_0 is the constant reference temperature. The fluid is bounded by two square, rigid horizontal walls with a linear dimension L, and separated by a distance H. The upper wall is maintained at temperature T_0 and the lower wall at higher temperature $T_1=T_0+\Delta T$, creating unstable stratification. The strength of convection is determined by the Rayleigh number

$$\mathrm{Ra}=\frac{\alpha g H^3\Delta T}{\kappa\nu}. \quad (13)$$

All simulations were performed in a box with the aspect ratio $L/H=6$. The details of the numerics are described by Domaradzki et al. [10,11] and Loh and Domaradzki [12]. We employ a numerical Navier-Stokes code developed by Chan [26] which uses a pseudo-spectral numerical method for spatial discretization with Fourier expansions in the streamwise and spanwise directions, and Legendre polynomials in the wall normal direction. As for all spectral codes the numerical dissipation is negligible. Three-dimensional filters were obtained as a tensor product of one-dimensional filters. The simulation parameters are reported in Table 1. In particular, the TNS are re-initialized every $N_T=20$ time steps using Eq. (8) applied to velocity and temperature fields. The values of the Rayleigh number were chosen to be the same as in the classical experiments of Deardorff and Willis [27]. Among quantities of interest is the Nusselt number which is the measure of the heat flux across the layer

$$\mathrm{Nu}=\frac{-\kappa d\langle T\rangle/dz+\langle w'T'\rangle}{\kappa\Delta T/H}, \quad (14)$$

where the fluctuating temperature T' and vertical velocity w' are variations from the mean

Table 1 Parameters for simulations of Rayleigh-Bénard convection. Experimental values of the Nusselt number Nu_{exp} from [27].

Case	Grid	Ra	Δt	N_T	Nu	Nu_{exp}
UDNS	$64^2 \times 33$	6.3×10^5	10^{-5}	⋯	7.8	5.8
CTNS1	$64^2 \times 33$	6.3×10^5	10^{-5}	20	6.8	5.8
CTNS2	$32^2 \times 33$	6.3×10^5	10^{-5}	20	6.1	5.8
CTNS3	$64^2 \times 33$	2.5×10^6	10^{-5}	20	9.5	9.0
CTNS4	$32^2 \times 33$	2.5×10^6	10^{-5}	20	8.1	9.0
CTNS5	$32^2 \times 33$	1.0×10^7	10^{-5}	20	11.5	12.5

$$T' = T - \langle T \rangle,$$

$$w' = w - \langle w \rangle,$$

where $\langle \ldots \rangle$ denotes a horizontally averaged quantity.

The case UDNS is an under-resolved direct numerical simulation. The grid size $64^2 \times 33$ was the smallest that allowed at this Rayleigh number stable time integration by the numerical scheme used. For a fully resolved DNS the grid requirement is $128^2 \times 65$ according to Christie and Domaradzki [28]. The TNS at this Rayleigh number were performed with two different resolutions, cases CTNS1 and CTNS2. The same resolutions were used for cases CTNS3 and CTNS4 at $Ra = 2.5 \times 10^6$ while the lower resolution of $32^2 \times 33$ mesh points was used in the remaining high Rayleigh number case CTNS5. For a fully resolved DNS at $Ra = 1.0 \times 10^7$ the resolution requirements given by Kerr [29] are $288^2 \times 96$ mesh points. The Nusselt number averaged over the layer fluctuates in time as shown in Fig. 2. Superimposed on the long-time fluctuations are short-time variations caused by the periodic filtering (8). These variations can be removed by defining Nu in terms of large-scale quantities $\tilde{u}_i^0$ and $\tilde{T}^0$ rather than the complete estimated quantities $\tilde{u}_i$ and $\tilde{T}$ which contain subgrid scales that are periodically filtered out.

The Nusselt number across the convective layer averaged over several time instants is shown in Fig. 3 for all cases at $Ra = 6.3 \times 10^5$. The under resolved DNS shows the largest departure from the experimental data which is improved by applying the model at the same resolution (case CTNS1). Surprisingly the best agreement with the experiment is obtained in the lower resolution TNS simulation CTNS2. For $Ra = 2.5 \times 10^6$ the Nusselt number was around 9.5 and 8.1 for the cases CTNS3 and CTNS4, respectively, while the experimental value is close to 9.0. For the case CTNS5 the value of Nu is 11.5 and compares well with the experimental value around 12.5. Therefore the TNS approach predicts the averaged heat flux quite well even at these low resolutions.

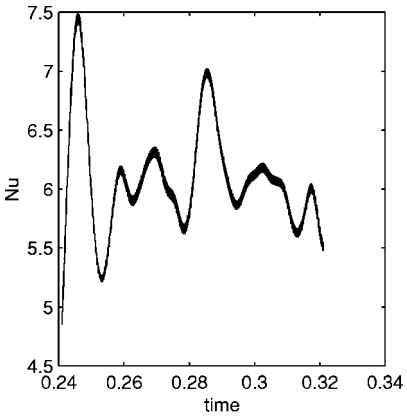

Fig. 2 Time variation of Nu for the case CTNS2

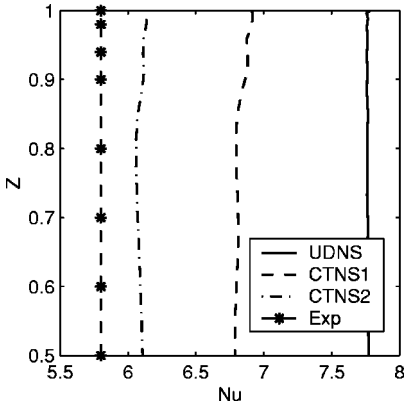

Fig. 3 Nu across the convective half-layer at $Ra = 6.3 \times 10^5$. Solid line: case UDNS; dashed line: case CTNS1; dashed-dotted line: case CTNS2; dashed-asterisk line: averaged Nu from experiments of Deardorff and Willis [27].

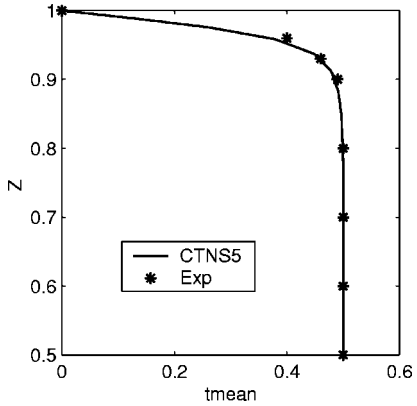

Fig. 4 Mean temperature $\langle T \rangle(z)$ for the case CTNS5. Solid line: model; asterisks: experiment.

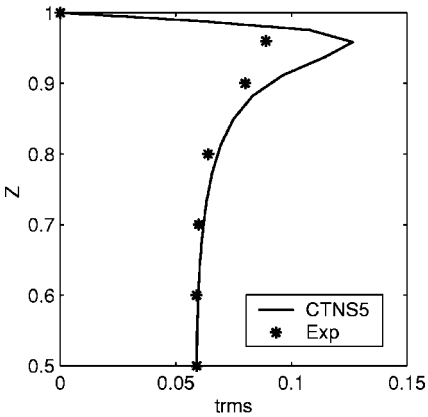

Fig. 5 Rms temperature fluctuation for the case CTNS5. Solid line: model; asterisks: experiment.

Further assesment of the modeling precedure is made for the highest Rayleigh number case CTNS5. The mean temperature $\langle T \rangle(z)$ is reproduced by the TNS very well (Fig. 4). The observed good agreement in the vicinity of the wall explains why the heat flux predictions are in a good agreement with the experimental results. Indeed, according to Eq. (14) the heat flux at the wall is determined solely by the mean temperature gradient because the fluctuating quantities w' and T' vanish. The rms values of the temperature (Fig. 5) and horizontal and vertical components of the

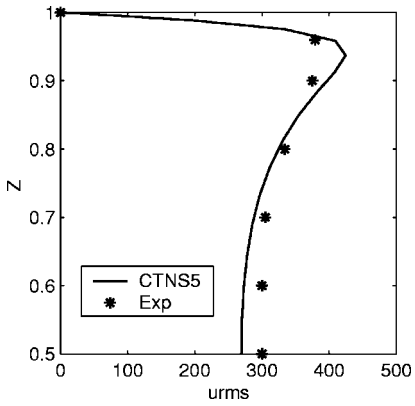

Fig. 6 Rms horizontal velocity fluctuation for the case CTNS5. Solid line: model; asterisks: experiment.

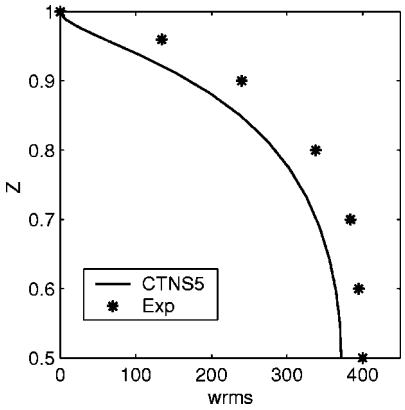

Fig. 7 Rms vertical velocity fluctuation for the case CTNS5. Solid line: model; asterisks: experiment.

velocity (Figs. 6 and 7, respectively) are in a good qualitative agreement with the experimental values though the peak values do not match exactly. We conclude that the TNS procedure is capable to properly model turbulent convection flows at numerical resolutions on the order of only 1 percent of the resolution required for DNS.

4 Conclusions

In closing, the method (10) relies on the dynamics of the truncated Navier-Stokes equations and a periodic replacement of the small-scale component by the modeled field obtained using the subgrid scale estimation procedure. If the energy of the new modeled field, $\tilde{u}_i^{ini}(t+T)$, is less than the energy of the field that is being replaced, $\tilde{u}_i^{end}(t+T)$, then the method can be seen as a dissipative model with the entire dissipation occuring at discrete times rather than continuously. It is thus possible that for such situations the described approach is equivalent to traditional dissipative subgrid scale (SGS) models. Nevertheless, updating the small scales at discrete times rather than continuously may be preferred. For an imperfect model of the subgrid scales which is applied continuously the modeling error will propagate and contaminate the large scales in predictability time. This raises the possibility that the long-time energy balance between the resolved and the modeled subgrid scales will be incorrect, for instance different from that implied by the Kolmogoroff theory for high Reynolds number turbulence. In the truncated Navier-Stokes (TNS) model the subgrid scales are generated and affected only by the Navier-Stokes dynamics. Consequently, such a method should better capture energy transfer properties of actual turbulence. There are additional advantages of the proposed approach. The method can be easily implemented for an arbitrary Navier-Stokes solver without changing its internal structure but merely processing a solution at discrete times. New physical phenomena such as related to temperature effects in convection and stratified turbulence, compressibility, rotation, etc., can be treated in the same framework without a need for new closure assumptions and concepts such as the turbulent Prandtl number. The procedure is fairly robust. The only major parameter in the method is the reinitialization period T and the large-eddy simulation (LES) results were found to be quite insensitive to variations in T even by a factor of two. Because the explicit filter is used its width can be tailored to the available numerical resolution. Since the modeling procedure does not invoke assumptions of local isotropy and the inertial range it may be expected to be applicable to strongly anisotropic flows. Therefore, it may be a good candidate for VLES where only the energy peak is assumed to be resolved and the unresolved subgrid scales are neither in the inertial range nor isotropic.

However, there are physical phenomena that this approach will not be able to address. The primary assumption in the method is that the small scales of turbulence originate from the larger scales, consistent with the Kolmogoroff picture of the turbulent cascade process. If the assumption of this unidirectional coupling, from large to small scales, is violated the method will break down. The typical example is combustion, where the chemical processes on the molecular scale affect the larger, hydrodynamic scales. The additional concerns in using this approach is its numerical cost, application to engineering flows in complex geometries and at high Reynolds numbers, and implementation in finite difference or finite element codes. If resolved quantities of interest are represented on N mesh points in each Cartesian direction the modeled TNS quantities require $2N$ points. Therefore, formally in three dimensions the TNS resolution is almost an order of magnitude greater than that required to discretize the underlying resolved fields. However, this may not be a more serious drawback that encountered by traditional LES where only the largest scales are represented accurately while the small scales from the vicinity of a mesh cutoff are affected by the modeling and truncation errors. For instance, Lund and Kaltenbach [30] suggest that those errors should in general be removed by an explicit filtering of the smallest scales at each time-step. Therefore, the effective resolution in such a LES will be less than the nominal mesh resolution, similarly to the TNS approach. The TNS method can be applied to flows in complex geometries if the underlying Navier-Stokes solver can handle such flows. Indeed, the method only adds periodic processing of a solution without a need to change the Navier-Stokes solver. The TNS approach has been previously applied to high Reynolds number isotropic turbulence correctly reproducing the $k^{-5/3}$ spectrum and the Kolmogoroff constant, [20]. The application of the method to high Reynolds number wall bounded flows and in the context of finite difference codes is currently in progress.

Acknowledgments

This work was supported by the NSF Grant CTS-0000572 and partially by the ONR Contract No. N00014-00-1-0756.

References

[1] Leonard, A., 1997, "Large-Eddy Simulation of Chaotic Convection and Beyond," AIAA Paper No. 97-0204.
[2] Geurts, B. J., 1997, "Inverse Modeling for Large-Eddy Simulation," Phys. Fluids, **9**, p. 3585.
[3] Stolz, S., and Adams, N. A., 1999, "An Approximate Deconvolution Procedure for Large-Eddy Simulations," Phys. Fluids, **11**, p. 1699.
[4] Scotti, A., and Meneveau, C., 1999, "A Fractal Model for Large Eddy Simulation of Turbulent Flow," Physica D, **127**, pp. 198–232.
[5] Hylin, E. C., and McDonough, J. M., 1999, "Chaotic Small-Scale Velocity Fields as Prospective Models for Unresolved Turbulence in an Additive Decomposition of the Navier-Stokes Equations," Int. J. Fluid Mech. Res., **26**, p. 164.
[6] Kerr, R. M., Domaradzki, J. A., and Barbier, G., 1996, "Small-Scale Properties

of Nonlinear Interactions and Subgrid-Scale Energy Transfer in Isotropic Turbulence,'' Phys. Fluids, **8**, p. 197.
[7] Foias, C., Manley, O. P., and Temam, R., 1991, ''Approximate Inertial Manifolds and Effective Eddy Viscosity in Turbulent Flows,'' Phys. Fluids A, **3**, p. 898.
[8] Dubois, T., Jauberteau, F., and Temam, R., 1999, *Dynamic Multilevel Methods and the Numerical Simulation of Turbulence*, Cambridge University Press, Cambridge, UK.
[9] Zhou, Y., Brasseur, J. G., Juneja, A., and Wyngaard, J. C., 2001, ''A Resolvable Subfilter-Scale Model Specific to Large-Eddy Simulation of Near-Wall Turbulence,'' Phys. Fluids, **13**, p. 2602.
[10] Domaradzki, J. A., and Saiki, E. M., 1997, ''A Subgrid-Scale Model Based on the Estimation of Unresolved Scales of Turbulence,'' Phys. Fluids, **9**, p. 2148.
[11] Domaradzki, J. A., and Loh, K. C., 1999, ''The Subgrid-Scale Estimation Model in the Physical Space,'' Phys. Fluids, **11**, p. 2330.
[12] Loh, K. C., and Domaradzki, J. A., 1999, ''The Subgrid-Scale Estimation Model on Non-uniform Grids,'' Phys. Fluids, **11**, p. 3786.
[13] Domaradzki, J. A., Dubois, T., and Honein, A., 1998, ''The Subgrid-Scale Estimation Model Applied to Large Eddy Simulations of Compressible Turbulence,'' *Proceedings of the 1998 Summer Program*, Center for Turbulence Research, NASA Ames, Stanford, p. 351.
[14] Dubois, T., Domaradzki, J. A., and Honein, A., 2002, ''The Subgrid-Scale Estimation Model Applied to Large Eddy Simulations of Compressible Turbulence,'' Phys. Fluids, **14**, p. 1781.
[15] Domaradzki, J. A., and Horiuti, K., 2001, ''Similarity Modeling on an Expanded Mesh Applied to Rotating Turbulence,'' Phys. Fluids, **13**, p. 3510.
[16] Kimmel, S. J., and Domaradzki, J. A., 2000, ''Large Eddy Simulations of Rayleigh-Bénard Convection Using Subgrid Scale Estimation Model,'' Phys. Fluids, **12**, p. 169.
[17] Domaradzki, J. A., and Yee, P. P., 2000, ''The Subgrid-Scale Estimation Model for High Reynolds Number Turbulence,'' Phys. Fluids, **12**, p. 193.
[18] Yee, P. P., 2000, ''A Velocity Estimation Model for Large Eddy Simulations of High Reynolds Number Homogeneous, Isotropic Turbulence,'' Ph.D. thesis, University of Southern California.
[19] Loh, K.-C., 2000, ''The Subgrid-Scale Estimation Procedure in the Physical Space Representation,'' Ph.D. thesis, University of Southern California.
[20] Domaradzki, J. A., Loh, K. C., and Yee, P. P., 2002, ''Large Eddy Simulations Using the Subgrid-Scale Estimation Model and Truncated Navier-Stokes Dynamics,'' Theor. Comput. Fluid Dyn., **15**, pp. 421–450.
[21] Boris, J. P., Grinstein, F. F., Oran, E. S., and Kolbe, R. L., 1992, ''New Insights Into Large Eddy Simulation,'' Fluid Dyn. Res., **10**, pp. 199–228.
[22] Karamanos, G.-S., and Karniadakis, G. E., 2000, ''A Spectral Vanishing Viscosity Method for Large-Eddy Simulations,'' J. Comput. Phys., **163**, pp. 22–50.
[23] Margolin, L. G., and Rider, W. J., 2003, ''A Rationale for Implicit Turbulence Modeling,'' Int. J. Numer. Math. Fluids, **39**, p. 821.
[24] Adams, N. A., 2001, ''The Use of LES Subgrid-Scale Models for Shock-Capturing,'' Int. J. Numer. Math. Fluids, **39**, p. 783.
[25] Lesieur, M., *Turbulence in Fluids*, 2nd Ed., Kluwer Academic Publishers, Dordrecht.
[26] Chan, D. C., 1996, ''Effects of Rotation on Turbulent Convection: Direct Numerical Simulation Using Parallel Computers,'' Ph.D. thesis, University of Southern California.
[27] Deardorff, J. W., and Willis, G. E., 1967, ''Investigation of Turbulent Thermal Convection Between Horizontal Plates,'' J. Fluid Mech., **28**, p. 675.
[28] Christie, S., and Domaradzki, J. A., 1993, ''Numerical Evidence for Nonuniversality of the Soft/Hard Turbulence Classification for Thermal Convection,'' Phys. Fluids, **5**, p. 412.
[29] Kerr, R., 1996, ''Rayleigh Number Scaling in Numerical Convection,'' J. Fluid Mech., **310**, p. 139.
[30] Lund, T. S., and Kaltenbach, H.-J., 1995, ''Experiments With Explicit Filtering for LES Using a Finite-Difference Method,'' Annual Research Briefs, Center for Turbulence Research, Stanford University, pp. 91–105.

R. von Kaenel
Ph.D. Student
e-mail: vonkaenel@ifd.mavt.ethz.ch

N. A. Adams[1]

L. Kleiser
Professor

ETH Zurich,
Institute of Fluid Dynamics,
CH-8092 Zurich, Switzerland

J. B. Vos
Senior Research Scientist,
CFS Engineering SA,
PSE-B,
CH-1015 Lausanne, Switzerland

The Approximate Deconvolution Model for Large-Eddy Simulation of Compressible Flows With Finite Volume Schemes

The approximate deconvolution model for large-eddy simulation is formulated for a second-order finite volume scheme. With the approximate deconvolution model, an approximation of the unfiltered solution is obtained by repeated filtering, and given a good approximation of the unfiltered solution, the nonlinear terms of the Navier-Stokes equations are computed directly. The effect of scales not represented on the numerical grid is modeled by a relaxation regularization involving a secondary filter operation. A turbulent channel flow at a Mach number of $M=1.5$ and a Reynolds number based on bulk quantities of $Re=3000$ is selected for validation of the approximate deconvolution model implementation in a finite volume code. A direct numerical simulation of this configuration has been computed by Coleman et al. Overall, our large-eddy simulation results show good agreement with our filtered direct numerical simulation data. For this rather simple configuration and the low-order spatial discretization, differences between approximate deconvolution model and a no-model computation are found to be small.
[DOI: 10.1115/1.1511167]

Introduction

Most flows of practical interest are turbulent, and for industrial applications it is important that these flows can be computed by numerical simulation with sufficient accuracy. However, numerical solutions of the Reynolds-averaged Navier-Stokes equations often fail to predict the proper flow behavior, in particular in cases where the flow exhibits large-scale unsteadiness, separation, or shock-turbulence interaction ([1]).

In large-eddy simulations (LES), the solution of the Navier-Stokes equations is convolved with a smoothing filter which reduces the numerical-resolution requirements for the filtered solution at the expense of a model for the resolved-scale/nonrepresented-scale interaction. Stolz and Adams [2] have developed a subgrid-scale model based on approximate deconvolution (ADM) and have demonstrated excellent performance of the model for a number of canonical flow configurations ([3,4]), including shock-turbulence interaction in a boundary layer. For flows at higher Reynolds numbers, a relaxation regularization is employed to represent the resolved-scale/nonrepresented-scale interaction. So far computations were performed with high-order (fourth-order, sixth-order) finite difference schemes and spectral schemes. Test computations with second-order finite difference schemes for isotropic turbulence have shown that the filter-cutoff wave number should be adjusted to the maximum wave number which can be considered to be well resolved by the underlying discretization scheme, employing the modified wave number concept [5]. In this paper we address the formulation of ADM for a given second-order finite volume scheme without further consideration of the resolution properties of this scheme. The objective is to test ADM for a numerical method which is being used in standard CFD design tasks of the aerospace industry.

We first introduce the governing equations and then briefly present the filtering, deconvolution and relaxation procedure. Next, we summarize the numerical method and introduce the parameters of our test case. Finally, the results of four different data sets, DNS, filtered DNS, LES with ADM, and underresolved DNS, are compared and analyzed.

Governing Equations

A flow in a plane channel with periodic boundary conditions in the streamwise ($x_1=x$) and spanwise ($x_2=y$) directions is considered. The computational domain with volume V is spanned by a Cartesian coordinate system. The flow is described by the compressible Navier-Stokes equations for an ideal gas with ratio of specific heats $\gamma=1.4$. Nondimensionalized with the wall temperature T_w, the channel half-width H, the bulk velocity $u_b=\int_V \rho u dV/(V\rho_b)$, and density $\rho_b=\int_V \rho dV/V$, the continuity, momentum and energy equations read (summation rule applies):

$$\frac{\partial \rho}{\partial t}+\frac{\partial}{\partial x_j}(\rho u_j)=0 \tag{1}$$

$$\frac{\partial}{\partial t}(\rho u_i)+\frac{\partial}{\partial x_j}(\rho u_i u_j)+\frac{\partial p}{\partial x_i}-\frac{\partial \sigma_{ij}}{\partial x_j}=-f_1\delta_{i1} \tag{2}$$

$$\frac{\partial E}{\partial t}+\frac{\partial}{\partial x_j}(E+p)u_j-\frac{\partial}{\partial x_j}(\sigma_{ij}u_i)+\frac{\partial}{\partial x_j}q_j=-f_1u_1, \tag{3}$$

with the total energy

$$E=p/(\gamma-1)+\frac{1}{2}\rho u_i u_i, \tag{4}$$

the temperature

$$T=\gamma M_0^2(p/\rho), \tag{5}$$

and the nondimensional dynamic viscosity

$$\mu(T)=T^{0.7}. \tag{6}$$

The heat fluxes and the viscous stresses are defined as

$$q_j=-\frac{\mu(T)}{(\gamma-1)\mathrm{Re}\,\mathrm{Pr}M_0^2}\frac{\partial T}{\partial x_j}, \tag{7}$$

[1]Presently Professor, Technical University Dresden, Dresden, Germany.

Contributed by the Fluids Engineering Division for publication in the JOURNAL OF FLUIDS ENGINEERING. Manuscript received by the Fluids Engineering Division March 12, 2002; revised manuscript received May 31, 2002. Associate Editor: F. F. Grinstein.

$$\sigma_{ij}=\frac{\mu(T)}{\mathrm{Re}}\left(\frac{\partial u_i}{\partial x_j}+\frac{\partial u_j}{\partial x_i}-\frac{2}{3}\,\delta_{ij}\frac{\partial u_k}{\partial x_k}\right), \tag{8}$$

with the Reynolds number $\mathrm{Re}=\rho_b u_b H/\mu(T_w)$, the Mach number $M_0=u_b/\sqrt{\gamma R T_w}$, and the Prandtl number $\mathrm{Pr}=0.7$. The Kronecker symbol is used, $\delta_{ij}=1$ for $i=j$ and $\delta_{ij}=0$ otherwise. For a periodic wall-bounded flow, the addition of a driving force to the Navier-Stokes equations is necessary to compensate the wall-friction forces and to maintain a stationary flow. Following Deschamps [6], the flow is driven in the streamwise direction with a body force $f_1(t)$ adjusted to the instantaneous solution such that the total mass flow rate remains stationary. The wall boundary conditions are no-slip for the velocity and isothermal for the temperature.

Filtering Approach and Approximate Deconvolution

In most large-eddy simulation (LES) methods, filtering is performed implicitly by the projection of the equations onto the computational grid, formally including all wave numbers up to the Nyquist wave number ω_n in the solution. Since for finite difference or finite volume schemes the wave number up to which scales can be considered to be resolved is often significantly smaller than ω_n, it is desirable to suppress nonresolved solution components by application of an explicit filter operation ([5]). Even for spectral schemes the relative error at the Nyquist wave number is of order $\mathcal{O}(1)$. In the following we will distinguish between *resolved wave numbers* $|\omega|\leqslant\omega_c$, where ω_c is the primary-filter cutoff wave number, *represented wave numbers* $|\omega|\leqslant\omega_n$ which can be represented on the given mesh, and nonrepresented wave numbers $|\omega|>\omega_n$.

The governing equations of LES are obtained by applying the primary-filter operation to the Navier-Stokes equations. Any flow variable u can be decomposed as $u=\overline{u}+u'+u''$ where $\overline{u}$ represents the resolved scales, u' the represented nonresolved scales, and u'' the nonrepresented scales. The filtering operation on a domain $[\alpha\Delta,\beta\Delta]$ is defined by a convolution of the filter kernel G and the variable. We define a one-dimensional primary filter operation with compact support by

$$\overline{u}(x)=G*u=\int_{x-\beta\Delta}^{x-\alpha\Delta}G\left(\frac{x-x'}{\Delta},x\right)u(x')\,\frac{dx'}{\Delta}$$

$$=\int_{\alpha}^{\beta}G(z,x)u(x-\Delta z)dz, \tag{9}$$

where $z=(x-x')/\Delta$ and $\Delta=\pi h/\omega_c$ is the filter width in physical space. h is the uniform grid spacing in an equidistantly spaced computational space ξ. The mapping of x onto ξ does not need to be known explicitly. ω_c is the cutoff wave number of the primary filter, nondimensionalized with h, and $G(z,x)$ is the primary filter kernel which may depend explicitly on the location x. The extension of this one-dimensional filter to three space dimensions is obtained by applying the filter in each coordinate direction successively

$$\overline{u}(x_1,x_2,x_3)=G_1*G_2*G_3*u$$

$$=\int_{\alpha_3}^{\beta_3}\int_{\alpha_2}^{\beta_2}\int_{\alpha_1}^{\beta_1}G_1(z_1,x_1)G_2(z_2,x_2)G_3(z_3,x_3)$$

$$\times u(x_1-\Delta_1 z_1,x_2-\Delta_2 z_2,x_3-\Delta_3 z_3)dz_1dz_2dz_3. \tag{10}$$

The integration in this definition is discretized by an explicit quadrature, defined in one space dimension as

$$\overline{u}_i:=\sum_{j=-\nu_l}^{\nu_r}\alpha_j u_{i+j} \tag{11}$$

for the grid function u_i, where $u_i=u(x_i)$. The cell centers in the finite-volume formulation are denoted as x_i. We consider discrete filters on a five-point stencil with $\nu_l+\nu_r=4$ for interior cells. A complete derivation of the coefficients α_j can be found in Refs. [3], [7]. The definition of the cutoff wave number ω_c is somewhat arbitrary for filters with smooth Fourier transform $\hat{G}(\omega)$. Here we choose the criterion $|\hat{G}(\omega_c)|=1/2$, leading to $\omega_c\approx 2/3\pi$. The represented but nonresolved scales $\omega_c<|\omega|\leqslant\omega_n$ are used to model the effect of the nonresolved scales $|\omega|>\omega_c$ on the resolved scales $|\omega|\leqslant\omega_c$. Resolved scales can be recovered by an approximate inversion of the filter (9) resulting in an approximation $u^\star$ of the unfiltered solution u. The approximate deconvolution $u^\star$ is given by applying the approximate deconvolution operator Q_N to $\overline{u}$,

$$u^\star=Q_N*\overline{u}. \tag{12}$$

Assuming that the filter G has an inverse, the inverse operator can be expanded as an infinite series of filter operators. Filters with compact transfer functions are noninvertible, but a regularized inverse operator Q_N can be obtained by truncating the series at some N, obtaining a regularized approximation ([2]) of G^{-1},

$$Q_N=\sum_{\nu=0}^{N}(I-G)^\nu\approx G^{-1} \tag{13}$$

where I is the identity operator.

Stolz et al. [3,4] found that $N=5$ was giving best results for a wide range of test cases. We therefore set $N=5$ in the following. Using (13), $u^\star$ can be computed by repeated filtering of $\overline{u}$ from

$$u^\star=Q_N*\overline{u}=\overline{u}+(\overline{u}-\bar{\bar{u}})+(\overline{u}-2\bar{\bar{u}}+\overline{\overline{\overline{u}}})+\ \ldots$$

$$=3\overline{u}-3\bar{\bar{u}}+\overline{\overline{\overline{u}}}+\ \ldots\ . \tag{14}$$

The adaptation of the approximate deconvolution model (ADM) for a finite volume scheme is straightforward. Note that a finite volume scheme itself comprises a deconvolution when cell-face values are reconstructed from the cell averages, see, e.g., Ref. [8]. This approach which can be exploited to construct an approximate deconvolution method directly by adapting the finite volume method accordingly, is presently under investigation. Here, we treat numerical discretization and subgrid-scale modeling as separate entities and introduce ADM into the finite volume framework. For simplicity we first consider a scalar transport equation and return to the full Navier-Stokes equations later. Starting from the generic transport equation for the variable Ψ with flux function $F(\Psi)$, integrated over the computational cell V_j

$$\int_{V_j}\frac{\partial\Psi}{\partial t}dV_j+\int_{V_j}\nabla\cdot F(\Psi)dV_j=0, \tag{15}$$

where $F(\Psi)$ is the flux, we can apply the divergence theorem so that Eq. (15) can be rewritten as

$$\int_{V_j}\frac{\partial\Psi}{\partial t}dV_j+\int_{S_j}F(\Psi)ndS_j=0, \tag{16}$$

with n being the outward normal vector of the cell surface. On applying the filter operation to Eq. (15) and exchanging the filter operation and the volume integration one obtains, under the assumption that divergence operator and filter operator commute,

$$\int_{V_j}\frac{\partial\overline{\Psi}}{\partial t}dV_j+\int_{S_j}\overline{F(\Psi)}ndS_j=0. \tag{17}$$

Using the approximately deconvolved solution $\Psi^\star$ of Ψ, the filtered flux term $\overline{F(\Psi)}$ can be approximated directly by replacing the unfiltered quantity Ψ by $\Psi^\star$,

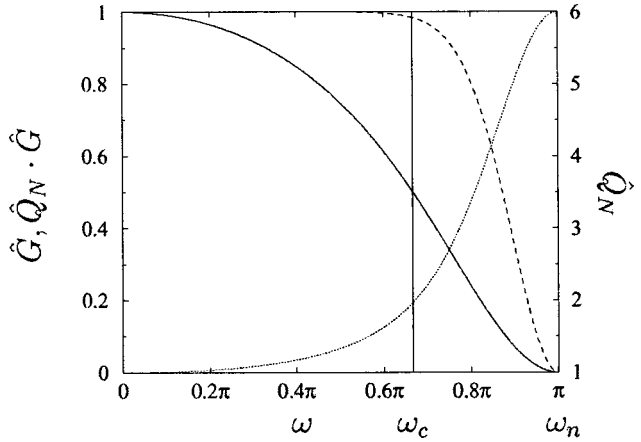

Fig. 1 Transfer functions, —— explicit primary filter for an equidistant mesh, e.g., *x* or *y* direction, · · · · approximate inverse $\hat{Q}_N$, – – – secondary filter $\hat{Q}_N \cdot \hat{G}$, for $N=5$

$$\int_{V_j} \frac{\partial \overline{\Psi}}{\partial t} dV_j + \int_{S_j} \overline{F(\Psi^\star)} n dS_j = \int_{S_j} (\overline{F(\Psi^\star)} - \overline{F(\Psi)}) n dS_j , \tag{18}$$

thus avoiding at that point the need of computing extra subgrid-scale terms.

The energy transfer to nonrepresented scales $|\omega| > \omega_n$ is modeled only partially by using $\Psi^\star$. Note that it would not be modeled at all if $\overline{\Psi}$ would be deconvolved by singular value decomposition, since the resulting Eq. (18) with $\Psi^\star$ replaced by Ψ restricted to represented scales is energy conserving. This situation corresponds to the truncated Navier-Stokes approach of Domaradzki et al. [9] without energy removal. Stolz et al. [3,4] have proposed a relaxation regularization derived from the requirement that the solution remains well-resolved within the range $|\omega| \leqslant \omega_c$. For this purpose, the integral energy of nonresolved represented scales should not increase, although energy redistribution among these scales is permitted. In order to model the energy transfer from scales $|\omega| \leqslant \omega_n$ to scales $|\omega| > \omega_n$ energy is drained from the range $\omega_c < |\omega| \leqslant \omega_n$ by subtracting a term $\chi_\Psi (I - Q_N * G)\overline{\Psi}$ from the left-hand side of the filtered differential conservation law (18). This expression, which models the nonclosed terms $\overline{F(\Psi^\star)} - \overline{F(\Psi)}$ of the right-hand side of Eq. (18), has the form of a relaxation term with a relaxation parameter $\chi_\Psi > 0$ corresponding to an inverse relaxation-time scale. Applying the finite volume discretization to the resulting equation one obtains

$$\int_{V_j} \frac{\partial \overline{\Psi}}{\partial t} dV_j + \int_{S_j} \overline{F(\Psi^\star)} n dS_j = -\int_{V_j} \chi_\Psi (I - Q_N * G) * \overline{\Psi} dV_j = -\int_{V_j} \chi_\Psi (\overline{\Psi} - \overline{\Psi}^\star) dV_j . \tag{19}$$

Since $(I - Q_N * G)$ is constructed being positive semidefinite, the relaxation term is purely dissipative. The use of the relaxation term can also be interpreted as applying a secondary filter to $\overline{\Psi}$ every $1/(\chi_\Psi \Delta t)$ time-step, Δt being the time-step of the numerical integration, which poses the approach in a relation to the truncated Navier-Stokes approach with energy removal of Domaradzki et al. [9]. The transfer function of the secondary filter $\hat{Q}_N \hat{G}$ for interior points on the equidistant mesh used in the present work is shown in Fig. 1.

To close the model without requiring an a priori parameter choice, χ_Ψ is estimated dynamically as a function of space and time. The underlying argument for determining χ_Ψ is that in order to obtain a well-resolved representation of the filtered solution no energy should accumulate during time advancement in the wave-number range $\omega_c < |\omega| \leqslant \omega_n$. The kinetic energy content of the considered wave number range can be estimated by the second-order structure function ([10,11]) applied to $\phi_\Psi = (I - Q_N * G) * \overline{\Psi}$. The discrete form of the local second-order structure function in three dimensions, which requires the value of ϕ_Ψ at the considered grid point in the computational space $\xi = (\xi_1, \xi_2, \xi_3)$ and its six next neighbors in the three computational-space coordinate directions, is given by

$$F_2(\xi, t) = \| \phi_\Psi(\xi + \mathbf{r}, t) - \phi_\Psi(\xi, t) \|^2_{||\mathbf{r}||=h} \tag{20}$$

where h is the computational-space grid spacing. Note again that the mapping of the physical space onto the computational space does not need to be known explicitly.

For an estimate of the relaxation parameter χ_Ψ we advance Eq. (19) by one Euler-forward time-step with size Δt, once using $\chi_\Psi = \chi_{\Psi 0}$ and once using $\chi_\Psi = 0$. $\chi_{\Psi 0}$ is some positive nonvanishing estimate of the parameter χ_Ψ, the value from the previous time integration step or some positive constant at time $t = 0$ for instance. The difference of the structure function $F_2(\xi, t + \Delta t)|_{\chi_\Psi = 0} - F_2(\xi, t)$ is an estimate for the integral energy generated within the time increment Δt in the range of scales with wave numbers $\omega_c < |\omega| \leqslant \omega_n$. The difference $F_2(\xi, t + \Delta t)|_{\chi_\Psi = 0} - F_2(\xi, t + \Delta t)|_{\chi_\Psi = \chi_{\Psi 0}}$ estimates how much energy would be dissipated by the relaxation term using $\chi_\Psi = \chi_{\Psi 0}$. Accordingly, χ_Ψ can be determined from

$$\chi_\Psi = \chi_{\Psi 0} \frac{F_2(\xi, t + \Delta t)|_{\chi_\Psi = 0} - F_2(\xi, t)}{F_2(\xi, t + \Delta t)|_{\chi_\Psi = 0} - F_2(\xi, t + \Delta t)|_{\chi_\Psi = \chi_{\Psi 0}}} . \tag{21}$$

In Ref. [4] this procedure is related to the requirement of no-energy accumulation in $\omega_c < |\omega| \leqslant \omega_n$. By construction, the dynamic parameter χ_Ψ is now a function of space and time. To avoid the generation of nonresolved scales due to the nonlinear product of χ_Ψ and $(I - Q_N * G) * \overline{\Psi}$, χ_Ψ is smoothed with a second-order Padé filter ([12]) whose cutoff wave number ω_c' is set to $\pi/8$. Given a time-step size Δt, an upper and a lower bound $1/100 \Delta t \leqslant \chi_\Psi \leqslant 1/\Delta t$ is imposed for numerical stability. According to previous experience, it is sufficient to update χ_Ψ every ten time-steps since it exhibits only small time variation.

Applying now the above operators to Eqs. (1), (2), and (3) we obtain the differential form of the underlying modeled conservation laws to be solved

$$\frac{\partial \overline{\rho}}{\partial t} + \overline{\frac{\partial (\rho u_j)^\star}{\partial x_j}} = -\chi_\rho (\overline{\rho} - \overline{\rho}^\star) \tag{22}$$

$$\frac{\partial \overline{\rho u_i}}{\partial t} + \overline{\frac{\partial}{\partial x_j}(\rho u_i u_j)^\star} + \overline{\frac{\partial \check{p}^\star}{\partial x_i} - \frac{\partial \check{\sigma}^\star_{ij}}{\partial x_j}} = -f_1(\overline{u})\, \delta_{i1} - \chi_{\rho u} (\overline{\rho u_i} - \overline{\rho u_i}^\star), \tag{23}$$

$$\frac{\partial \overline{E}}{\partial t} + \overline{\frac{\partial}{\partial x_j}(E^\star + \check{p}^\star) u_j^\star - \frac{\partial}{\partial x_j}(\check{\sigma}^\star_{ij} u_i^\star) + \frac{\partial}{\partial x_j} \check{q}_j^\star} = -f_1(\overline{u})\, \overline{u}_1 - \chi_E (\overline{E} - \overline{E}^\star), \tag{24}$$

for $i, j = 1,2,3$. The superscript $\check{\bullet}^\star$ indicates that the quantities are computed from the deconvolved solution, e.g., $\check{p}^\star = (\gamma - 1)(E^\star - \rho^\star u_i^\star u_i^\star / 2)$.

$f_1(\overline{u})$ means that the forcing term is computed with the filtered velocity. Note that we use the same relaxation parameter for the three momentum equations. To this set of equations the finite volume method is applied as discretization scheme as in Eq. (19).

Numerical Method

The approximate deconvolution model (ADM) was implemented in a CFD code using a cell centered second-order finite volume method ([13–15]). The particular form of the convective terms influences the stability of the numerical scheme. We use the

Table 1 Parameters of the numerical simulation

	Coleman et al. [18]	DNS	DNS Filtered	ADM	No-Model
L_x/H	4π	4π	4π	4π	4π
L_y/H	$4\pi/3$	$4\pi/3$	$4\pi/3$	$4\pi/3$	$4\pi/3$
L_z/H	2	2	2	2	2
n_x	144	288	72	72	72
n_y	80	160	40	40	40
n_z	119	237	60	60	60
M_0	1.5	1.5	-	1.5	1.5
Re	3000	3000	-	3000	3000
u_b	1	1	-	1	1
ρ_b	1	1	-	1	1

skew-symmetric form of the convective term ([16]) instead of the divergence form. In this case the nonlinear flux term is decomposed as

$$F_l^{\text{nonlin}} = \frac{1}{2}\left(\frac{\partial u_l u_m}{\partial x_m} + u_m \frac{\partial u_l}{\partial x_m}\right). \tag{25}$$

Viscous terms are integrated with a second-order centered scheme on a shifted control volume, see Ref. [17].

Time integration is performed by an explicit four-stage Runge-Kutta scheme which is formally fourth-order accurate for linear equations but drops to second-order accuracy for a general nonlinear equation. The Courant-Friedrichs-Lewy (CFL) number is set constant and an adaptive time-stepping procedure based on a linear stability analysis computes the maximum time-step ([14]).

Application to Channel Flow

As a test case the compressible channel flow as computed by Coleman et al. [18] was considered for two reasons. First, the test case requires a correct near-wall subgrid-scale treatment. Second, reference data are available in the literature, see Ref. [19]. Three different simulations have been performed: a direct numerical simulation (DNS), a no-model computation or underresolved DNS on the same mesh as the large-eddy simulation (LES), and a LES with the approximate deconvolution model (ADM). In contrast to traditional LES where filtering is the result of the projection of the solution onto the discrete mesh, the filter operator in ADM is known explicitly and allows for filtering of the DNS data with the same filter for validation of the LES. The main parameters of the simulation are summarized in Table 1. L_x, L_y, L_z are the extents of the integration domain in the streamwise, spanwise, and the wall-normal coordinate directions, respectively, and n_x, n_y, n_z are the corresponding numbers of grid points. All four simulations have the same Reynolds number Re and Mach number M_0. The forcing term is adjusted to maintain a constant mass flow. The grid spacing is constant in the streamwise and spanwise directions and is stretched with a hyperbolic tangent function in the wall-normal direction. Except for the DNS, all simulations were initialized with a laminar profile with a random velocity disturbance superimposed in each of the three coordinate directions. The initial density was $\rho(t=0)=1$ and the initial temperature was computed according to the laminar distribution $T(t=0)=1+1/3(\gamma-1)\text{Pr}M_0^2 u_{1\,\max}(1-(z-1)^4)$ where $u_{1\,\max}$ is the maximum nondimensional laminar velocity which is equal to 1.5. To save computational time, the DNS simulation was started from a turbulent profile obtained with the coarse-grid no-model computation, interpolated to the fine DNS mesh. The boundary conditions are periodic in the two homogeneous directions. Isothermal conditions with wall temperature $T_w=1$ and no-slip conditions are prescribed at the walls.

Results

Starting from the disturbed laminar solution, the computation is advanced for all large-eddy simulation (LES) cases for 380 time units $t_b = tu_b/H$. Transition from laminar to turbulent flow is observed between time $t_b=50$ and $t_b=120$. Because certain quantities, such as the temperature, attain a stationary state only rather slowly, the statistics presented here are sampled between time $t_b=300$ to $t_b=380$ with a sampling interval of 0.2. The statistics of the direct numerical simulation (DNS) were obtained after an initial transient of $t_b=160$ during 140 time units with a sampling interval of 1. The filtered DNS data were computed from 29 DNS samples of the DNS evenly spaced between time $t_b=160$ and $t_b=300$. The number of samples was found to be sufficient for the computed statistics to be symmetric across the channel halves. The filtered DNS data are generated by interpolating the DNS to the LES mesh and subsequent filtering. All statistics presented here are averaged over wall-parallel planes and over both channel halves.

Figure 2 gives a qualitative impression of the instantaneous flow close to the wall. Shown are iso-contours of the wall-normal vorticity in a near-wall plane. Clearly visible are the near-wall streak structures. Each simulation represents another realization of this flow, so that the agreement of these flow snapshots can only be qualitative.

In Table 2 averaged flow quantities measured at the wall and at the channel center are given. There are slight differences between the DNS of Coleman et al. and our DNS results. In our case the friction-velocity Reynolds number $\text{Re}_\tau = \text{Re}\, u_\tau \rho_w/(u_b\rho_b)$ is smaller and the centerline velocity u_c is larger. Also, a larger centerline temperature T_c and a smaller centerline density ρ_c are observed. These differences may be due to the different numerical method, but may also be related to differences in the implementation of the forcing f_1. For the mean flow variables the agreement between filtered DNS and DNS is good which confirms that the constructed filter leaves the mean flow essentially unchanged even on a distorted mesh. This requirement leads to moment conditions in real space on the filter as shown in Ref. [3]. A comparison of

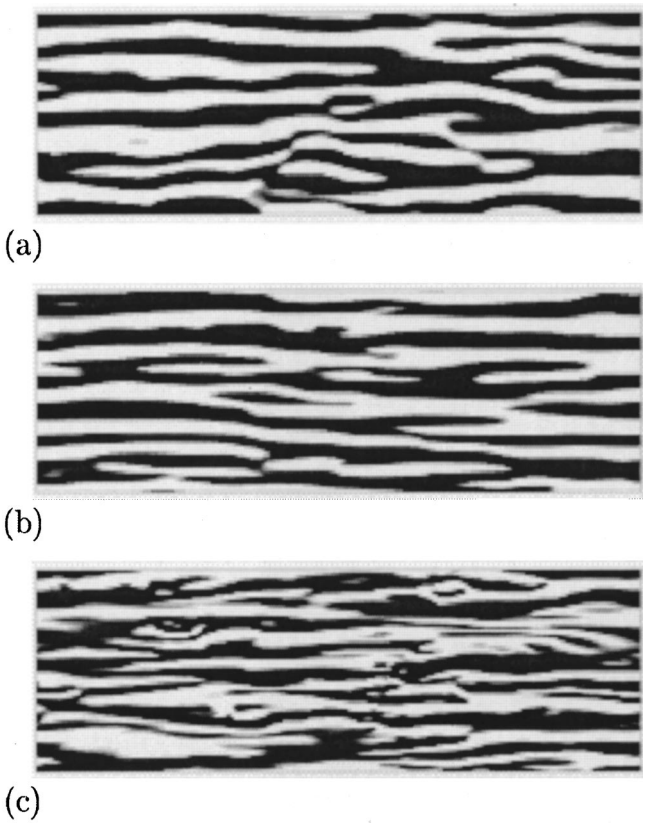

Fig. 2 Contours of instantaneous wall-normal vorticity ω_z in (x,y)-plane at $z^+\approx 10$, (*a*) ADM, (*b*) no-model, (*c*) DNS; $\omega_z \geqslant 0$ in light regions, $\omega_z < 0$ in dark regions

Table 2 Mean flow variables

	Coleman et al. [18]	DNS	DNS Filtered	ADM	No-Model
Re_τ	222	216	214	224	217
τ_w	12.12	11.41	11.35	12.44	11.61
u_τ	0.0545	0.0529	0.0530	0.0554	0.0534
Δ_x^+	19	9.4	37	39	38
Δ_y^+	12	5.6	22	23	23
$\Delta_z^+\|_w$	0.1	0.38	1	1	1
u_c	1.16	1.18	1.18	1.18	1.19
T_c	1.378	1.39	1.39	1.40	1.41
ρ_c	0.980	0.977	0.977	0.979	0.977
ρ_w	1.355	1.359	1.359	1.353	1.360

approximate deconvolution model (ADM) results with filtered DNS shows that all quantities of Table 2 are within a reasonable error margin, e.g., the Reynolds number Re_τ differs by 4.7% from the filtered DNS.

We find that the near-wall velocity gradient is slightly overpredicted by the LES, resulting in a larger Reynolds number Re_τ. The centerline velocity u_c is not affected by the near-wall velocity gradient since the forcing f_1 is adjusted such that the initial mass-flux is kept constant throughout the simulation. We find that probably due to the different initial conditions for the DNS and the LES, the stationary value of the mass flux differs by about 0.5%. As shown in Figs. 3 and 4, the mean velocity, density and temperature are predicted accurately. The temperature profile computed with the ADM shows a better agreement with the filtered DNS than the no-model computation with the DNS. For the velocity profile, a steeper slope near the wall can be seen which is responsible for the larger Reynolds number Re_τ with ADM. A similar overprediction of u_τ is responsible for the difference of the mean streamwise velocity profile in wall units between ADM and filtered DNS in the outer layer as can be seen from the van Driest transformed profiles $\langle u_{VD}\rangle^+$ (Fig. 4(*b*)) which are computed as

$$\langle u_{VD}\rangle^+ = \int_0^{\langle u\rangle^+} \sqrt{\frac{\overline{\rho}}{\rho_w}}\, d\langle u\rangle^+. \tag{26}$$

The von Karman constant is, however, predicted accurately. Interesting are the comparably good results obtained with the no-model computations. For the velocity fluctuations and Reynolds stress (Fig. 5 and 6) trends are somewhat more difficult to determine. Generally, ADM results show a similarly good agreement with the filtered DNS data as the no-model computation does with the DNS.

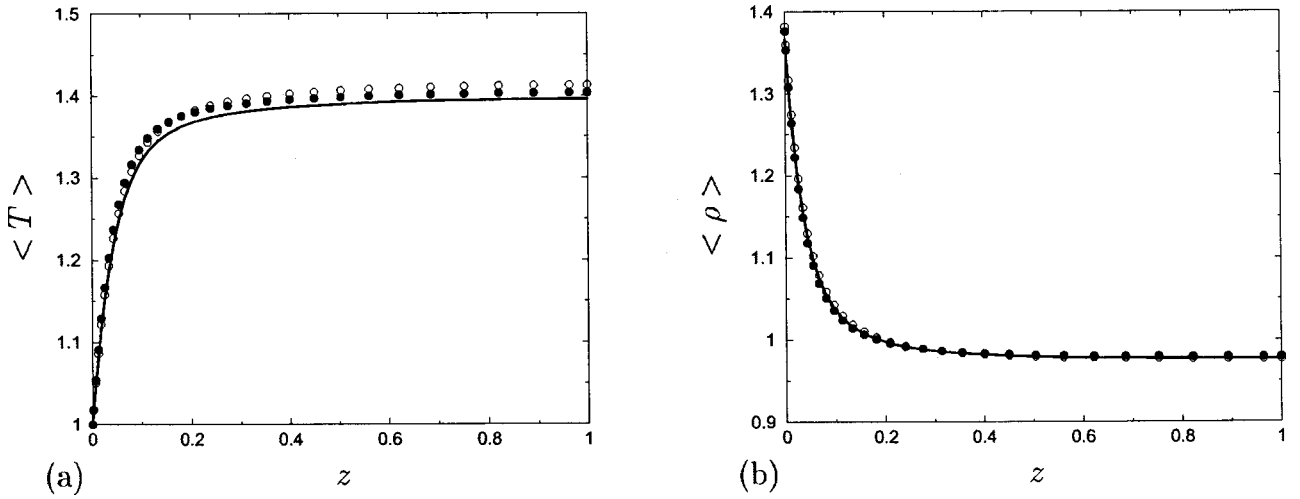

Fig. 3 (*a*) Mean temperature profile, (*b*) mean density profile, ——DNS, ● ADM, —— filtered DNS, ○ no-model

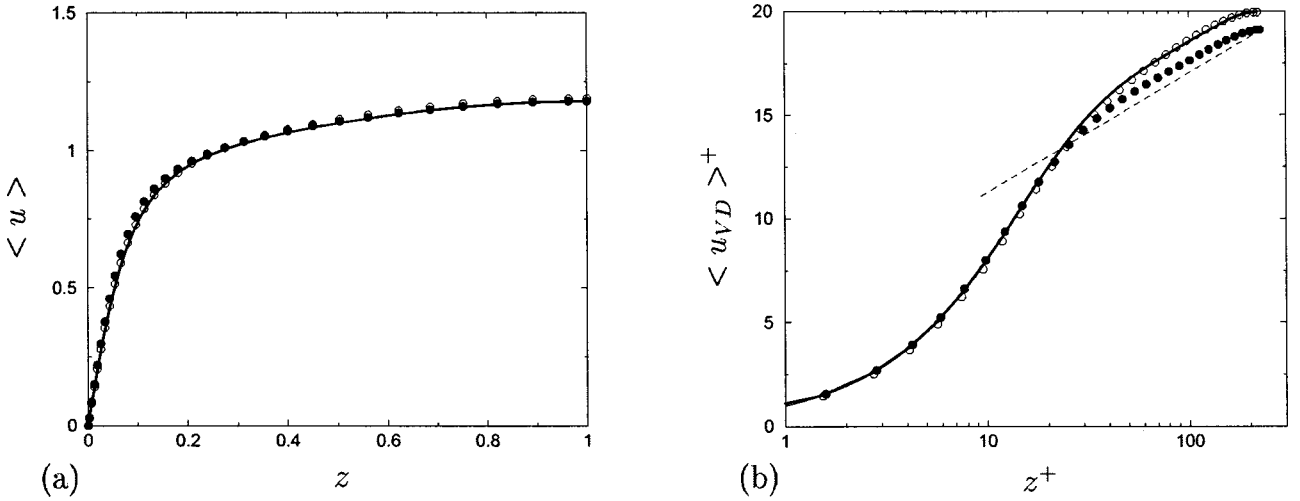

Fig. 4 Mean velocity profile, (*a*) linear plot, (*b*) van Driest transformed logarithmic plot, —— DNS, ● ADM, —— filtered DNS, ○ no-model, – – – 2.5 ln z^++5.5

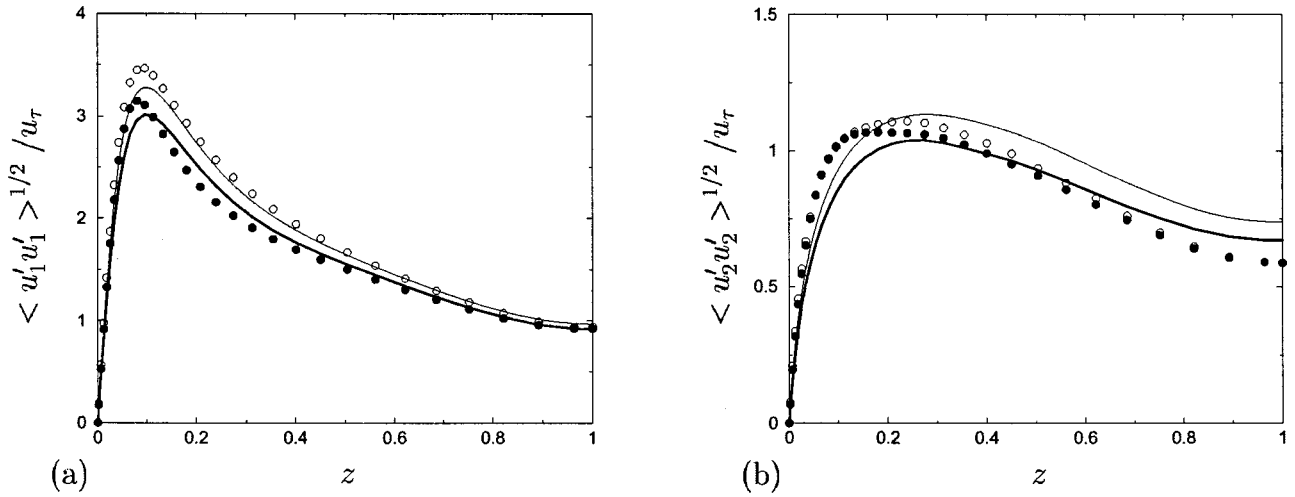

Fig. 5 Velocity fluctuations, (*a*) streamwise velocity, (*b*) spanwise velocity, —— DNS, ● ADM, —— filtered DNS, ○ no-model

Lenormand et al. [19] recently have evaluated several subgrid-scale (SGS) models for the same channel flow configuration. They discretized the convective terms in skew-symmetric form with a fourth-order finite difference scheme whereas the diffusive terms were discretized with a second-order scheme. Six different subgrid-scale models were tested on a coarse and a fine mesh (only these latter results will be considered here). Different from our computations, the streamwise extent of the computational domain was only of 2π. The number of grid points in the wall-normal direction was two times larger ($n_z = 119$) than in our case and the spanwise number of grid points was 3/2 times larger. Two of the tested SGS models are based on the Smagorinsky model, whereas the four others are based on a newly proposed mixed scale model, which estimates the subgrid-scale kinetic energy by means of a test filter and scale-similarity arguments. Linear hybridization with a Bardina-type model ([20,21]) is also considered, together with the use of a turbulent scale selection function. A priori tests suggest the use of the hybrid models, and a comparison of these models with the DNS data (nonfiltered) of Coleman et al. [18] shows results of similar quality as ours. The mean quantities are predicted accurately except for the temperature where, as in our case, the LES slightly overpredicts the temperature in the channel center. Clear trends for the velocity fluctuations and the Reynolds stress are also difficult to determine, but differences in the peak magnitude and location are visible. We can conclude that even with a lower order numerical scheme and on a coarser mesh, ADM gives results of similar quality as other SGS models on finer meshes with higher-order schemes.

Conclusions

The approximate deconvolution model was formulated to be used with a second-order finite volume method. The convective terms are discretized in their skew-symmetric form using a second-order centered scheme while the viscous terms are computed using a second-order scheme on a shifted control volume. Time integration is performed with a four-stage Runge-Kutta method. Compared to other channel flow large-eddy simulation (LES) with similar numerical discretizations, the mesh used here is coarser up to a factor of two in the wall-normal direction and of 2/3 in the spanwise direction. The model is based on an approximate deconvolution of the filtered quantities by a truncated series expansion of the inverse filter. This approximation is used to compute the nonlinear terms in the Navier-Stokes equations avoiding the need to compute subgrid-scale terms explicitly, except for a relaxation term. A relaxation term models the resolved-scale/nonrepresented-scale interaction by draining energy from the range of nonresolved represented scales $\omega_c < |\omega| \leq \omega_n$. The ap-

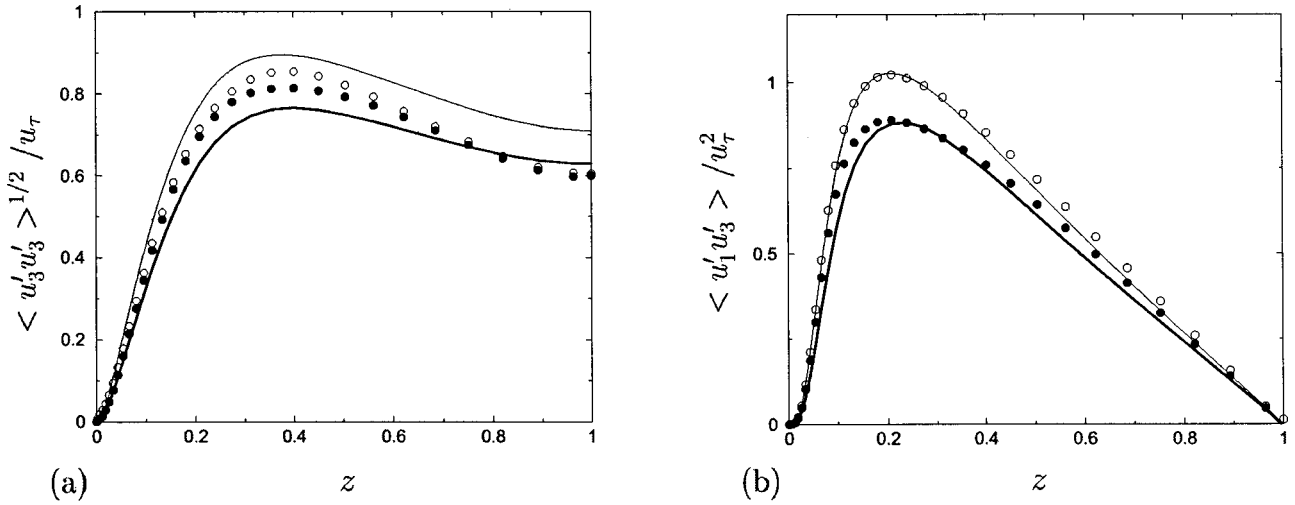

Fig. 6 (*a*) Velocity fluctuations in wall-normal direction, (*b*) Reynolds-stress, —— DNS, ● ADM, —— filtered DNS, ○ no-model

proximate deconvolution part alone of the approximate deconvolution model (ADM) is a generalized scale-similarity or tensor diffusivity model which can both be cast as special cases of ADM ([2,3]). It shares the advantages and disadvantages of these models: on the one hand a good prediction of inhomogeneous turbulent flows, on the other hand an insufficient modeling of nonrepresented scales. To cope with the latter, the relaxation term has been formulated.

Validation of the implemented model was performed for the case of a supersonic isothermal-wall channel flow. A good agreement between filtered direct numerical simulation (DNS) and LES was found for the mean flow. For the turbulence statistics, the no-model results are of the same quality as the ones with ADM. Since our observations were quite different when comparing no-model coarse-grid computations and LES with ADM for incompressible channel flow using a spectral method ([3]), we believe that the main source of error in the ADM simulations with the present primary-filter choice does not come from the subgrid-scale model but rather from the numerical discretization. Similar observations were made by Mossi [22] and Garnier et al. [23] who also found that the effect of different subgrid-scale models employed with the present numerical method was rather small. Filtering of the no-model computation would probably give results very close to ADM which suggests a small influence of the model in this particular case. Considering, however, the already good quality of the no-model computation, the ADM results can be seen positively compared to other subgrid-scale models which proved even to deteriorate results ([22]). The interplay between the numerical discretization and the subgrid-scale model has not been investigated further in the frame of this work and we refer to Ref. [16] for an analysis of the skew-symmetric form of the convective fluxes and to Stolz et al. [24] for an analysis of the effect of the discretization order on ADM.

The good results of the no-model computations can be attributed to the particular form of the truncation error induced by the skew-symmetric formulation ([16]) of the convective fluxes and to the relatively simple channel flow configuration considered here. No-model coarse-grid computations with the divergence form of the convective terms were found to be unstable for the channel flow—ADM remained stable but the results were slightly less accurate. No-model computations of more complex flows such as shock-turbulence interaction were found to be unstable. In this case the regularizing effect of the skew-symmetric form is insufficient and the benefit of ADM, providing a unified modeling of turbulent and nonturbulent subgrid scales (shocks) ([4]), should be more clearly visible.

Acknowledgments

The authors would like to acknowledge Benjamin Rembold (ETH), Dr. Steffen Stolz (ETH), and Prof. Michel Deville (EPFL) for stimulating discussions. Computations were performed on the NEC-SX5 of the Swiss Center of Scientific Computing.

References

[1] Dolling, D. S., 2001, ''Fifty Years of Shock-Wave/Boundary-Layer Interaction Research: What Next?'' AIAA J., **39**, p. 1517.
[2] Stolz, S., and Adams, N. A., 1999, ''An Approximate Deconvolution Procedure for Large-Eddy Simulation,'' Phys. Fluids, **11**, pp. 1699–1701.
[3] Stolz, S., Adams, N. A., and Kleiser, L., 2001, ''An Approximate Deconvolution Model for Large-Eddy Simulation With Application to Incompressible Wall-Bounded Flows,'' Phys. Fluids, **13**, pp. 997–1015.
[4] Stolz, S., Adams, N. A., and Kleiser, L., 2001, ''An Approximate Deconvolution Model for Large-Eddy Simulations of Compressible Flows and Its Application to Shock-Turbulent-Boundary-Layer Interaction,'' Phys. Fluids, **13**, pp. 2985–3001.
[5] Stolz, S., Adams, N. A., and Kleiser, L., 2000, ''LES of Shock-Boundary Layer Interaction With the Approximate Deconvolution Model,'' *Advances in Turbulence, Proceedings of the 8th European Turbulence Conference*, C. Dopazo et al., eds., CIMNE, Barcelona, pp. 715–718.
[6] Deschamps, V., 1988, ''Simulation Numérique de la Turbulence Inhomogène Incompressible dans un Ecoulement de Canal Plan,'' ONERA, TR 1988-5, Châtillon, France.
[7] Stolz, S., 2000, ''Large-Eddy Simulation of Complex Shear Flows Using an Approximate Deconvolution Model,'' Diss. ETH No. 13861.
[8] Adams, N. A., 2001, ''The Role of Deconvolution and Numerical Discretization in Subgrid-Scale Modeling,'' *Direct and Large-Eddy Simulation IV*, B. Geurts, R. Friedrich, and O. Métais, eds., Kluwer, Dordrecht, The Netherlands.
[9] Domaradzki, J. A., Loh, K. C., and Yee, P. P., 2001, ''Large Eddy Simulations Using the Subgrid-Scale Estimation Model and Truncated Navier-Stokes Dynamics,'' submitted for publication.
[10] Lesieur, M., and Métais, O., 1996, ''New Trends in Large-Eddy Simulations of Turbulence,'' Annu. Rev. Fluid Mech., **28**, p. 45.
[11] Batchelor, G. K., 1953, *The Theory of Homogeneous Turbulence*, Cambridge University Press, Cambridge, UK.
[12] Lele, S. K., 1992, ''Compact Finite-Difference Schemes With Spectral-Like Resolution,'' J. Comput. Phys., **103**, p. 16.
[13] Jameson, A., Schmidt, W., and Turkel, E., ''Numerical Solution of the Euler Equations by Finite-Volume Methods Using Runge-Kutta Time Stepping Schemes,'' AIAA Paper No. 81-1259, July.
[14] Vos, J. B., Leyland, P., Lindberg, P. A., van Kemenade, V., Gacherieu, C., Duquesne, N., Lotstedt, P., Weber, C., Ytterström, A., and Saint Requier, C., 2000, ''NSMB Handbook,'' Technical Report 4.5, EPF Lausanne, KTH, CERFACS, Aérospatiale, SAAB, EPF Lausanne, Switzerland.
[15] Vos, J. B., Rizzi, A. W., Corjon, A., Chaput, E., and Soinne, E., 1988, ''Recent Advances in Aerodynamics Inside the NSMB (Navier-Stokes Multi-Block) Consortium,'' AIAA Paper No. AIAA-98-0225.
[16] Ducros, F., Laporte, F., Soulères, T., Guinot, V., Moinat, P., and Caruelle, B., 2000, ''High-Order Fluxes for Conservative Skew-Symmetric-Like Schemes in Structured Meshes: Application to Compressible Flows,'' J. Comput. Phys., **161**, pp. 114–139.
[17] Peyret, R., and Taylor, T. D., 1983, *Computational Methods for Fluid Flows*, Springer-Verlag, New York.
[18] Coleman, G. N., Kim, J., and Moser, R. D., 1995, ''A Numerical Study of Turbulent Supersonic Isothermal-Wall Channel Flow,'' J. Fluid Mech., **305**, pp. 159–183.
[19] Lenormand, E., Sagaut, P., Ta Phuoc, L., and Comte, P., 2000, ''Subgrid-Scale Models for Large-Eddy Simulations of Compressible Wall Bounded Flows,'' AIAA J., **38**, pp. 1340–1350.
[20] Bardina, J., Ferziger, J. H., and Reynolds, W. C., 1983, ''Improved Turbulence Models Based on Large-Eddy Simulation of Homogeneous, Incompressible, Turbulent Flows,'' Thermosciences Div., Rept. TF-19, Department of Mechanical Engineering, Stanford University, Stanford, CA.
[21] Bardina, J., Ferziger, J. H., and Reynolds, W. C., 1980, ''Improved Subgrid Scale Models for Large-Eddy Simulation,'' AIAA J., **80**, p. 1357.
[22] Mossi, M., 1999, ''Simulation of Benchmark and Industrial Unsteady Compressible Turbulent Fluid Flows,'' Thèse EPFL No. 1958.
[23] Garnier, E., Mossi, M., Sagaut, P., Comte, P., and Deville, M., 1999, ''On the Use of Shock-Capturing Schemes for Large-Eddy Simulation,'' J. Comput. Phys., **153**, pp. 273–311.
[24] Stolz, S., Adams, N. A., and Kleiser, L., 2002, ''The Approximate Deconvolution Model for Compressible Flows: Isotropic Turbulence and Shock-Boundary-Layer Interaction,'' R. Friedrich and W. Rodi, eds., *Advances in LES of Complex Flows*, Kluwer, Dordrecht, The Netherlands.

Large-Eddy Simulation on Curvilinear Grids Using Compact Differencing and Filtering Schemes

M. R. Visbal
Technical Area Leader,

D. P. Rizzetta
Senior Research Aerospace Engineer,

Computational Sciences Branch,
Aeronautical Sciences Division,
Air Force Research Laboratory,
Wright-Patterson AFB, OH 45433

This work investigates the application of a high-order finite difference method for compressible large-eddy simulations on stretched, curvilinear and dynamic meshes. The solver utilizes 4th and 6th-order compact-differencing schemes for the spatial discretization, coupled with both explicit and implicit time-marching methods. Up to 10th order, Pade-type low-pass spatial filter operators are also incorporated to eliminate the spurious high-frequency modes which inevitably arise due to the lack of inherent dissipation in the spatial scheme. The solution procedure is evaluated for the case of decaying compressible isotropic turbulence and turbulent channel flow. The compact/filtering approach is found to be superior to standard second and fourth-order centered, as well as third-order upwind-biased approximations. For the case of isotropic turbulence, better results are obtained with the compact/filtering method (without an added subgrid-scale model) than with the constant-coefficient and dynamic Smagorinsky models. This is attributed to the fact that the SGS models, unlike the optimized low-pass filter, exert dissipation over a wide range of wave numbers including on some of the resolved scales. For channel flow simulations on coarse meshes, the compact/filtering and dynamic models provide similar results, with no clear advantage achieved by incorporating the SGS model. However, additional computations at higher Reynolds numbers must be considered in order to further evaluate this issue. The accuracy and efficiency of the implicit time-marching method relative to the explicit approach are also evaluated. It is shown that a second-order iterative implicit scheme represents an effective choice for large-eddy simulation of compressible wall-bounded flows. [DOI: 10.1115/1.1517564]

1 Introduction

Extension of large-eddy simulation (LES) to increasingly complex flows of engineering interest is currently the focus of significant research effort, [1–3]. This trend is motivated in part by the need to provide a more realistic characterization of the complex unsteady and separated flows encountered in areas such as flow control, aeroacoustics and fluid/structure interaction. Several conceptual difficulties still remain unresolved in the formulation and application of LES to nonhomogeneous flows (see, for instance, Ghosal [4] and references therein). Nonetheless, significant progress has been achieved in recent years due to advances in computational power, numerical algorithms and subgrid-scale (SGS) models. The uncertainties associated with subgrid modeling, numerical discretization errors and their interaction constitute, among others, important issues that are not fully understood. Analysis of the impact of spatial discretization errors on LES, [4,5], combined with the impetus to tackle more relevant configurations, establishes the need to develop high-order algorithms applicable to general geometries.

Due to their ''spectral-like'' resolution and ease of extension to multiple disciplines, high-order compact schemes, [6], represent an attractive choice for reducing dispersion, anisotropy and dissipation errors associated with low-order spatial discretizations. Until recently, these schemes have mostly been used in conjunction with explicit time-integration methods to address complex flow physics on Cartesian-type grids. Recent work, [7–12], has extended the use of compact algorithms to more practical applications. Particular attention has been focused on enhanced high-order (up to 10th order) low-pass spatial filtering techniques which are required to enforce numerical stability on nonuniform grids, [8]. Another important aspect is the coupling of the high-order discretization with a subiterative implicit time-advancement method which overcomes the severe time-step restriction of explicit schemes for wall-bounded flows. These new techniques have been incorporated into an existing finite difference code, [10], which solves the three-dimensional compressible Navier-Stokes equations in curvilinear grids. Extensive evaluation of the high-order approach has been previously presented for unsteady flows, [7], dynamic meshes, [11], and acoustic benchmark cases, [12].

The main objective of the present work is to evaluate the high-order compact/filtering methodology in the context of large-eddy simulation. To this end, canonical LES test cases are considered including the decay of compressible isotropic turbulence and turbulent channel flow. Particular emphasis is placed on the following aspects:

1. comparison of the high-order scheme with standard lower-order spatial discretizations,
2. evaluation of the accuracy and efficiency of the implicit iterative time-integration scheme relative to a Runge-Kutta explicit procedure,
3. effect of the required low-pass filter on turbulence dissipation,
4. proper treatment of coordinate transformation metric expressions to maintain high fidelity on general three-dimensional curvilinear and deforming meshes, and
5. comparison of solutions obtained with the compact/filtering method for the unfiltered Navier-Stokes equations (i.e., with-

Contributed by the Fluids Engineering Division for publication in the JOURNAL OF FLUIDS ENGINEERING. Manuscript received by the Fluids Engineering Division March 25, 2002, revised manuscript received May 29, 2002. Associate Editor: F. F. Grinstein.

out an explicitly added SGS model) with results based on the standard LES approach with Smagorinsky-type models.

2 Governing Equations

In order to develop a procedure suitable for nonlinear fluid dynamic, aeroacoustic, and aeroelastic applications over complex geometries, the unfiltered Navier-Stokes equations are selected and are cast in strong conservative form after introducing a time-dependent curvilinear coordinate transformation $(x,y,z,t) \rightarrow (\xi,\eta,\zeta,\tau)$, [13,14]. In vector notation, and in terms of nondimensional variables, these equations are

$$\frac{\partial}{\partial \tau}\left(\frac{\mathbf{U}}{J}\right)+\frac{\partial \hat{F}}{\partial \xi}+\frac{\partial \hat{G}}{\partial \eta}+\frac{\partial \hat{H}}{\partial \zeta}=\frac{1}{\mathrm{Re}}\left[\frac{\partial \hat{F}_v}{\partial \xi}+\frac{\partial \hat{G}_v}{\partial \eta}+\frac{\partial \hat{G}_v}{\partial \zeta}\right]. \quad (1)$$

Here $\mathbf{U}=\{\rho,\rho u,\rho v,\rho w,\rho E\}$ denotes the solution vector and $J=\partial(\xi,\eta,\zeta,\tau)/\partial(x,y,z,t)$ is the transformation Jacobian. The inviscid fluxes $\hat{F}$, $\hat{G}$, and $\hat{H}$ are

$$\hat{F}=\begin{bmatrix}\rho\hat{U}\\ \rho u\hat{U}+\hat{\xi}_x p\\ \rho v\hat{U}+\hat{\xi}_y p\\ \rho w\hat{U}+\hat{\xi}_z p\\ (\rho E+p)\hat{U}-\hat{\xi}_t p\end{bmatrix} \quad (2)$$

$$\hat{G}=\begin{bmatrix}\rho\hat{V}\\ \rho u\hat{V}+\hat{\eta}_x p\\ \rho v\hat{V}+\hat{\eta}_y p\\ \rho w\hat{V}+\hat{\eta}_z p\\ (\rho E+p)\hat{V}-\hat{\eta}_t p\end{bmatrix} \quad (3)$$

$$\hat{H}=\begin{bmatrix}\rho\hat{W}\\ \rho u\hat{W}+\hat{\zeta}_x p\\ \rho v\hat{W}+\hat{\zeta}_y p\\ \rho w\hat{W}+\hat{\zeta}_z p\\ (\rho E+p)\hat{W}-\hat{\zeta}_t p\end{bmatrix} \quad (4)$$

where

$$\hat{U}=\hat{\xi}_t+\hat{\xi}_x u+\hat{\xi}_y v+\hat{\xi}_z w \quad (5)$$

$$\hat{V}=\hat{\eta}_t+\hat{\eta}_x u+\hat{\eta}_y v+\hat{\eta}_z w \quad (6)$$

$$\hat{W}=\hat{\zeta}_t+\hat{\zeta}_x u+\hat{\zeta}_y v+\hat{\zeta}_z w \quad (7)$$

$$E=\frac{T}{(\gamma-1)M_r^2}+\frac{1}{2}(u^2+v^2+w^2). \quad (8)$$

Here, $\hat{\xi}_x=J^{-1}\partial\xi/\partial x$ with similar definitions for the other metric quantities. The viscous fluxes, $\hat{F}_v$, $\hat{G}_v$, and $\hat{H}_v$ can be found, for instance, in Ref. [15]. In the expressions above, u, v, w are the Cartesian velocity components, ρ the density, p the pressure, and T the temperature. The perfect gas relationship $p=\rho T/\gamma M_r^2$ is also assumed. All flow variables have been normalized by their respective reference values except for pressure which has been nondimensionalized by $\rho_r u_r^2$.

In the standard compressible LES approach, the above equations are filtered employing a grid filter function and introducing Favre-averaged variables, [16]. The resulting equations are similar to those above but include additional subgrid-scale stress and heat flux terms which must be modeled. For standard LES, the Smagorinsky [17] and Dynamic Smagorinsky [18,19] models have been incorporated into the solver as previously described in Ref. [20].

3 Numerical Methodology

3.1 Spatial Discretization. A finite difference approach is employed to discretize the governing equations, and all discrete quantities are therefore assumed to be pointwise in nature. This choice is motivated by the relative ease of formal extension to higher-order accuracy.

For any scalar quantity, ϕ, such as a metric, flux component, or flow variable, the spatial derivative ϕ' is obtained along a coordinate line in the transformed plane by solving the tridiagonal system:

$$\alpha\phi'_{i-1}+\phi'_i+\alpha\phi'_{i+1}=b\frac{\phi_{i+2}-\phi_{i-2}}{4}+a\frac{\phi_{i+1}-\phi_{i-1}}{2} \quad (9)$$

where α, a, and b determine the spatial properties of the algorithm. The formula yields the compact five-point, sixth-order $C6$, and three-point fourth-order $C4$ schemes with $\alpha=\frac{1}{3}$, $a=\frac{14}{9}$, $b=\frac{1}{9}$, and $\alpha=\frac{1}{4}$, $a=\frac{3}{2}$, $b=0$, respectively. Equation (9) also incorporates the standard explicit fourth-order $E4$ ($\alpha=0$, $a=4/3$ and $b=-1/3$) and second-order $E2$ ($\alpha=0, a=1, b=0$) schemes. At boundary points 1, 2, $IL-1$ and IL, higher-order one-sided formulas are utilized which retain the tridiagonal form of the equation set. These are described in more detail in Refs. [7] and [10].

The derivatives of the inviscid fluxes are obtained by forming the fluxes at the nodes and differentiating each component with the above formulas. Viscous terms are obtained by first computing derivatives of the primitive variables. Subsequently, the components of the viscous flux are then constructed at each node and differentiated by a second application of the same scheme. Although this approach is not as accurate as that in which a Padé-type scheme is employed directly for the second derivative, it is significantly cheaper to implement in curvilinear coordinates. As previously demonstrated in Ref. [7], successive differentiation yields an accurate and stable method in conjunction with the added low-pass filter procedure described in Section 3.2.

In Fig. 1, the dispersion-error characteristics for several schemes are shown in the context of the one-dimensional linear advection equation. Here $w(=2\pi k\Delta x/L)$ and w' denote the scaled and modified scaled wave numbers, respectively. The $C6$ method exhibits the least dispersion error whereas the $E2$ scheme has significant phase-speed errors over a wide range of wave numbers. Note that the three-point $C4$ scheme is superior to the five-point $E4$ and even to the seven-point explicit sixth-order scheme ($E6$). Although not shown, the third-order upwind-biased MUSCL scheme, [21], exhibits similar dispersion properties as $E4$, but has a dominant dissipation error. Based on the resolving power of the various schemes displayed in Fig. 1, it is expected that the chosen numerical procedure will have a significant impact on LES as the grid is coarsened relative to a DNS. For instance, in

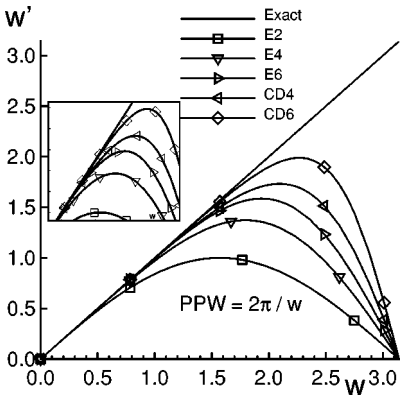

Fig. 1 Dispersion-error characteristics of various spatial discretizations for one-dimensional advection equation

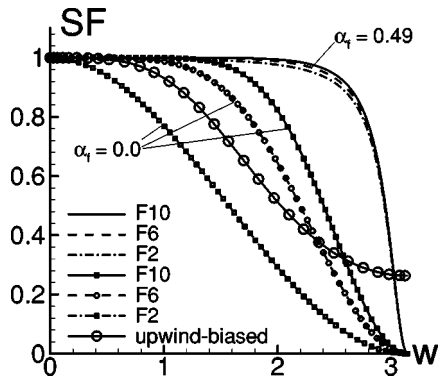

Fig. 2 Spectral response of interior low-pass spatial filters

finite difference LES employing a dynamic SGS model, a test filter operation is typically performed with a test-filter width corresponding to $w=\pi/2$ where significant errors are present for the low-order approaches.

3.2 Low-Pass Spatial Filtering Scheme. Compact difference discretizations, like other centered schemes, are nondissipative and therefore susceptible to numerical instabilities due to the unrestricted growth of high-frequency modes. These difficulties originate from several sources including mesh nonuniformity, approximate boundary conditions and nonlinear flow features. In LES (where the physical viscous dissipation at the Kolmogorov scale is not represented), the use of a nondissipative spatial scheme typically leads to the pileup of energy at the high-wave numbers of the mesh and ultimately to numerical instability.

In order to extend the compact discretization approach to practical applications, a high-order low-pass spatial filtering technique, [7,9], is incorporated. This low-pass filter provides dissipation at the high modified wave numbers *only* where the spatial discretization already exhibits significant dispersion errors. If a typical component of the solution vector is denoted by ϕ, filtered values at interior points $\hat{\phi}$ in transformed space satisfy

$$\alpha_f\hat{\phi}_{i-1}+\hat{\phi}_i+\alpha_f\hat{\phi}_{i+1}=\sum_{n=0}^{N}\frac{a_n}{2}(\phi_{i+n}+\phi_{i-n}). \tag{10}$$

Equation (10) is based on templates proposed in Refs. [6] and [22] and with proper choice of coefficients, provides a $2N$th-order formula on a $2N+1$ point stencil. The $N+1$ coefficients, $a_0, a_1, \ldots a_N$, are derived in terms of α_f with Taylor and Fourier-series analyses and are given in Refs. [8] and [10].

The dissipation characteristics of the filter operator as function of scaled wave number are given by the corresponding spectral function (denoted as *SF*). It can be shown [8] that

$$SF(w)=\frac{\sum_{n=0}^{N}a_n\cos(nw)}{1+2\alpha_f\cos(w)} \tag{11}$$

For proper behavior of *SF*, the adjustable parameter α_f must be in the range $-0.5<\alpha_f<0.5$, with higher values of α_f corresponding to a less dissipative filter. Also, for $\alpha_f=0.0$ (spatially) explicit filter formulas, [23], are obtained. On uniform meshes, these symmetric filters are nondispersive (i.e., *SF* is real), do not amplify any waves ($SF\leqslant 1$), preserve constant functions ($SF(0)=1.0$), and completely eliminate the odd-even mode ($SF(\pi)=0.0$).

The spectral response of the second, sixth, and tenth-order implicit ($\alpha_f=0.49$) and explicit ($\alpha_f=0$) filters are shown in Fig. 2. The optimized filters exhibit fairly sharp cutoff characteristics for various orders of accuracy. By contrast, the explicit filters display significant degradation of the spectral response as the order of accuracy is reduced. The dissipation error inherent in a third-order upwind-biased, [21], approximation of the first derivative is also shown in Fig. 2 for the purpose of comparison. Unlike the high-order low-pass filter, the dissipation of the upwind-biased scheme does not exhibit a sharp cutoff but instead applies over a wide range of wave numbers. This is also the case for standard numerical damping approaches (e.g., Refs. [24] and [25]), unless the damping term is derived based on spectral considerations as described in Ref. [26].

In this work, the filter operator is applied to the conserved variables along each transformed coordinate direction and after each time step. For the near-boundary points, the filtering strategies described in Refs. [7], [8] are employed. The impact of filtering on the accuracy and stability of the high-order approach has been investigated in Refs. [7], [8], and [12] for several applications including nonuniform grids, approximate boundary treatments and nonlinear governing equations.

3.3 Evaluation of Spatial and Temporal Coordinate Transformation Metrics. The extension of high-order schemes to curvilinear and deforming meshes requires a careful evaluation of the spatial and temporal metric expressions arising from the coordinate transformation. Failure to enforce metric cancellation and freestream preservation in the finite-difference discretization of the strong-conservation form of the governing equations can catastrophically degrade the fidelity of higher-order approaches, [7,8,12].

In deriving the strong-conservation flow equations, the following metric identities have been implicitly invoked:

$$I_1=(\hat{\xi}_x)_\xi+(\hat{\eta}_x)_\eta+(\hat{\zeta}_x)_\zeta=0 \tag{12}$$

$$I_2=(\hat{\xi}_y)_\xi+(\hat{\eta}_y)_\eta+(\hat{\zeta}_y)_\zeta=0 \tag{13}$$

$$I_3=(\hat{\xi}_z)_\xi+(\hat{\eta}_z)_\eta+(\hat{\zeta}_z)_\zeta=0 \tag{14}$$

$$I_4=(1/J)_\tau+(\hat{\xi}_t)_\xi+(\hat{\eta}_t)_\eta+(\hat{\zeta}_t)_\zeta=0 \tag{15}$$

where subscripts denote partial derivatives. The first three identities constitute a differential statement of surface conservation for a closed cell. The last metric identity (I_4) is referred to in the literature as the geometric conservation law (GCL), [27], and becomes important in the case of dynamic meshes. In a finite-difference discretization, these identities must be also satisfied numerically in order to ensure freestream preservation.

To numerically enforce identities I_1, I_2, and I_3 (Eqs. (12)–(14)), the transformation metrics are evaluated in the manner described in Refs. [8], [12]. This approach adopts the formulation developed in the context of lower-order methods, [27], in which the metric relation, for example,

$$\hat{\xi}_x=y_\eta z_\zeta-y_\zeta z_\eta \tag{16}$$

is evaluated by considering its analytically equivalent ''conservative'' form:

$$\hat{\xi}_x=(y_\eta z)_\zeta-(y_\zeta z)_\eta. \tag{17}$$

Similar expressions are employed for the remaining metric terms. As demonstrated in Refs. [8] and [12], freestream preservation and improved accuracy is achieved on general three-dimensional meshes when the transformation metrics are cast in the form of Eq. (17), and the derivatives are evaluated with the same high-order formulas employed for the fluxes.

In order to satisfy the GCL identity of Eq. (15), the time-derivative term in Eq. (1) is split using chain-rule differentiation as follows:

$$(\mathbf{U}/J)_\tau=(1/J)\mathbf{U}_\tau+\mathbf{U}(1/J)_\tau. \tag{18}$$

The first term involves the inverse Jacobian J^{-1}, which is evaluated in a standard fashion using the instantaneous values of the grid coordinates. The second term, which includes the time-derivative of the Jacobian, requires special treatment. Rather than

attempting to compute the time-derivative of J^{-1} directly from the grid coordinates at various time levels (either analytically or numerically), we simply invoke Eq. (15) to evaluate $(1/J)_\tau$, i.e.,

$$(1/J)_\tau = -[(\xi_t/J)_\xi + (\eta_t/J)_\eta + (\zeta_t/J)_\zeta] \tag{19}$$

where

$$\begin{aligned}
\xi_t/J &= -[x_\tau(\xi_x/J) + y_\tau(\xi_y/J) + z_\tau(\xi_z/J)] \\
\eta_t/J &= -[x_\tau(\eta_x/J) + y_\tau(\eta_y/J) + z_\tau(\eta_z/J)] \\
\zeta_t/J &= -[x_\tau(\zeta_x/J) + y_\tau(\zeta_y/J) + z_\tau(\zeta_z/J)].
\end{aligned} \tag{20}$$

As shown in Ref. [11], this strategy ensures freestream preservation and high fidelity on rapidly deforming meshes for either analytic or numerically evaluated grid speed terms.

3.4 Time Integration. The compact differencing scheme has been coupled with both explicit and implicit time-integration methods. The classical fourth-order four-stage Runge-Kutta scheme ($RK4$), implemented in low-storage form, is utilized primarily for wave propagation problems. For the highly stretched meshes employed in LES of wall-bounded flows, the stability constraint of explicit time-marching methods is too restrictive and the use of an implicit approach becomes necessary. For this purpose, an implicit approximately factored scheme, [28], is incorporated and augmented through the use of Newton-like subiterations. In delta form, and for second-order temporal accuracy (denoted as $BW2$), the scheme may be written as

$$\begin{aligned}
&\left[J^{-1^{p+1}} + \phi^i \Delta\tau \delta_\xi^{(2)}\left(\frac{\partial \hat{F}^p}{\partial U} - \frac{1}{\mathrm{Re}}\frac{\partial \hat{F}_v^p}{\partial U}\right)\right] J^{p+1} \\
&\quad \times \left[J^{-1^{p+1}} + \phi^i \Delta\tau \delta_\eta^{(2)}\left(\frac{\partial \hat{G}^p}{\partial U} - \frac{1}{\mathrm{Re}}\frac{\partial \hat{G}_v^p}{\partial U}\right)\right] J^{p+1} \\
&\quad \times \left[J^{-1^{p+1}} + \phi^i \Delta\tau \delta_\zeta^{(2)}\left(\frac{\partial \hat{H}^p}{\partial U} - \frac{1}{\mathrm{Re}}\frac{\partial \hat{H}_v^p}{\partial U}\right)\right] \Delta U \\
&= -\phi^i \Delta\tau \left[J^{-1^{p+1}} \frac{(1+\phi)U^p - (1+2\phi)U^n + \phi U^{n-1}}{\Delta\tau}\right. \\
&\quad + U^p (1/J)_\tau^p + \delta_\xi\left(\hat{F}^p - \frac{1}{\mathrm{Re}}\hat{F}_v^p\right) + \delta_\eta\left(\hat{G}^p - \frac{1}{\mathrm{Re}}\hat{G}_v^p\right) \\
&\quad \left. + \delta_\zeta\left(\hat{H}^p - \frac{1}{\mathrm{Re}}\hat{H}_v^p\right)\right].
\end{aligned} \tag{21}$$

where $\partial\hat{F}/\partial U$, etc, are flux Jacobians, δ represents the spatial difference operator, and $\Delta U = U^{p+1} - U^p$. The method combines the approximate factorization procedure of Ref. [28] with the diagonalized simplification of Ref. [29]. Note that while the derivatives of the flux Jacobians have been obtained to second-order accuracy (denoted with the superscript (2)), those on the right-hand side, i.e., in the residual, are evaluated with the compact-difference based higher-order method. Nonlinear artificial dissipation terms, [24,25], not explicitly shown in Eq. (21), are also appended to the implicit operator to enhance stability. In order to reduce errors associated with these simplifications, a subiteration strategy is employed. Thus, for the first subiteration, $p=1$, $U^p = U^n$ and as $p \to \infty$, $U^p \to U^{n+1}$. Typically, three subiterations are applied per time-step. By changing the number of time levels employed to evaluate the time-derivative term appearing in the RHS of Eq. (21), first ($BW1$) and third-order ($BW3$) accurate forms of the implicit algorithm can be constructed. As demonstrated in Refs. [11] and [30], as well as in the examples below, second-order temporal accuracy provides adequate accuracy.

4 Results

The previous computational methodology has been demonstrated for a number of DNS/LES applications. These include: unsteady vortical flows, [7], forced transitional plane walljet, [31], synthetic jet actuators, [32], boundary layer transition over a flexible panel, [33], decay of compressible isotropic turbulence, turbulent channel flow, three-dimensional flow past a circular cylinder, [20], supersonic turbulent flat-plate boundary layer, [34], and shock/turbulent boundary layer interactions, [35,36]. In this paper, only the case of decaying isotropic turbulence and turbulent channel flow are presented.

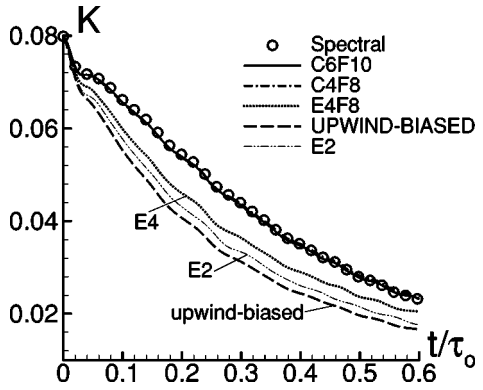

Fig. 3 Effect of spatial discretization on time history of TKE for decaying isotropic turbulence on 32^3 mesh

The computational results to be described below have been obtained employing several numerical approaches. The centered spatial schemes ($E2$,$E4$,$C4$,$C6$) have been defined in Section 3.1. The low-pass filters employed (Section 3.2) are designated by appending the filter order to the scheme. For instance, $C4F8$ denotes the fourth-order compact scheme combined with an 8th-order filter. The second-order algorithm ($E2$) incorporates, instead of a low-pass filter, the standard fourth-order (Jameson-type) scalar dissipation, [24,25]. For the purpose of comparison, a third-order MUSCL-based upwind-biased Roe scheme, [21,37], is also considered. Unless otherwise noted, results are obtained by solving the unfiltered Navier-Stokes equations (i.e., without a subgrid-scale model). In this situation, for an LES grid, dissipation is mainly provided by the properties of the numerical scheme (i.e., damping terms, low-pass filter or the inherent dissipation of the upwind-biased approach). It should be noted that the compact/filtering scheme without an SGS model bears some similarities with other regularization approaches, including MILES, [38], "Truncated Navier-Stokes Dynamics," [39], and the approximate deconvolution method, [40].

4.1 Decay of Compressible Isotropic Turbulence. The first test case considered is the decay of compressible isotropic turbulence. This flow has been used to investigate compressible formulations of SGS models for large-eddy simulations by Moin et al. [19] and Spyropoulos and Blaisdell [41], among others. Although this case represents a very simple example of turbulent flow, it allows for an evaluation of the dissipation characteristics of the numerical schemes in the absence of mean flow inhomogeneity.

The isotropic turbulence simulations correspond to the compressible low-Reynolds number conditions denoted as Case 6 in Spyropoulos and Blaisdell [41]. The initial three-dimensional turbulence spectrum is defined as

$$E_{3D} \propto k^4 \exp[-2(k/k_p)^2], \tag{22}$$

where k is the magnitude of the wave number vector, and $k_p = 4$ is the wave number at the peak in the spectrum. Root-mean-square (RMS) levels of the velocity, density, and temperature are established by adjusting the proportionality constant in the spectra. The velocity fluctuations are specified so that the initial turbulent Mach number $M_t = 0.4$, defined as the ratio of the RMS magnitude of the fluctuating velocity to the mean speed of sound. In addition

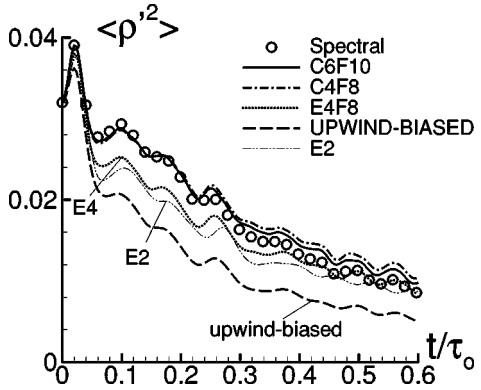

Fig. 4 Effect of spatial discretization on time history of density fluctuations for decaying isotropic turbulence on 32^3 mesh

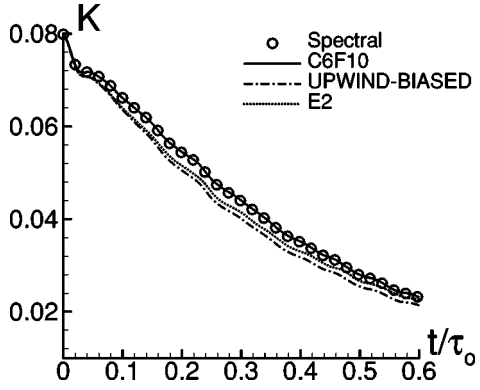

Fig. 6 Effect of spatial discretization on time history of TKE for decaying isotropic turbulence on 64^3 mesh

to the turbulent Mach number, the velocity field is parametrized by the fraction of energy in the dilatational part of the velocity, χ (see Ref. [41]). In the current simulations, initial values are given by $\chi=0.2$, ${\rho'_{\rm rms}}^2/\langle\rho\rangle^2=0.032$, and ${T'_{\rm rms}}^2/\langle T\rangle^2=0.005$. The turbulent Reynolds number is equal to 2157.0.

The computational domain of size $(2\pi\times2\pi\times2\pi)$ in physical space is discretized with a mesh of uniformly distributed grid points. Periodic conditions are enforced at all domain boundaries, and are implemented numerically employing an overlap of five grid points in each coordinate direction in order to facilitate the application of the implicit time-marching procedure. Three levels of numerical resolution (32^3, 64^3, and 128^3) are used in the simulations. Unless noted otherwise, the solutions are obtained employing the explicit ($RK4$) time-marching algorithm and the sixth-order compact scheme ($C6$) combined with a 10th-order low-pass filter ($F10,\alpha_f=0.49$). The time-step for the 32^3 and 64^3 grid computations is specified as $\Delta t=0.05$ which yields an initial maximum CFL number of approximately 0.8 on the coarse mesh. This Δt corresponds to approximately 250 time-steps per eddy turnover time τ_o, which is defined as the ratio of K to the dissipation rate based on the initial field. On the 128^3 mesh, a $\Delta t=0.01$ is specified.

4.1.1 Effect of Spatial Discretization. The time history of the resolved (volume-averaged) turbulent kinetic energy $K=\langle\rho(u'^2+v'^2+w'^2)\rangle$ is shown in Fig. 3 for the 32^3 mesh and for several spatial discretizations without the inclusion of any SGS model. Spectral DNS results from Spyropoulos and Blaisdell [41] are also shown for the purpose of comparison. The Pade-type schemes ($C6F10$,$C4F8$) are observed to be in good agreement with the DNS data. Reducing the fidelity of the spatial discretization just to a fourth-order explicit method ($E4$) combined with and explicit (i.e., $\alpha_f=0.0$) eighth-order filter produces excessive dissipation of turbulent kinetic energy. This error becomes more pronounced for the second-order and third-order upwind-biased algorithms. The superior behavior of the compact schemes relative to the lower order or explicit approaches is also demonstrated in Fig. 4 which displays the time history of the density fluctuations.

The origin of the excessive dissipation encountered with the lower-order approximations can be clarified by examining the instantaneous three-dimensional energy spectra, shown in Fig. 5, at $t/\tau_o=0.2985$. The highest wave number represented on this 32^3 mesh corresponds to $k_c=16$. It is observed that the lower-fidelity schemes damp the high wave number content of the energy. For the upwind-biased and $E2$ schemes, this occurs for $k>4.5$ ($w>0.28\pi$) which corresponds approximately to PPW<7. Since significant energy is still present above this wave number, a more rapid decay of turbulent kinetic energy ensues (Fig. 3). The spectra for the compact/filtering schemes display good agreement with the DNS results up to $k\approx12$ ($w\approx0.75\pi$). Also, the spectra for the DNS and compact schemes display a limited inertial subrange ($E(k)\propto k^{-5/3}$), not apparent in the low-order spatial discretizations.

Figures 6 through 9 show a comparison of the $C6F10$, $E2$, and upwind-biased schemes for the 64^3 and 128^3 grids. Differences are still observed between the high-order and low-order discretizations on the 64^3 mesh (Fig. 6). The corresponding spectra for the $E2$ and upwind schemes (Fig. 8) begin to depart noticeably from the DNS data for $k>8$ ($w\approx0.25$, PPW≈8). On the finest mesh (Fig. 9), all schemes generate essentially the same results.

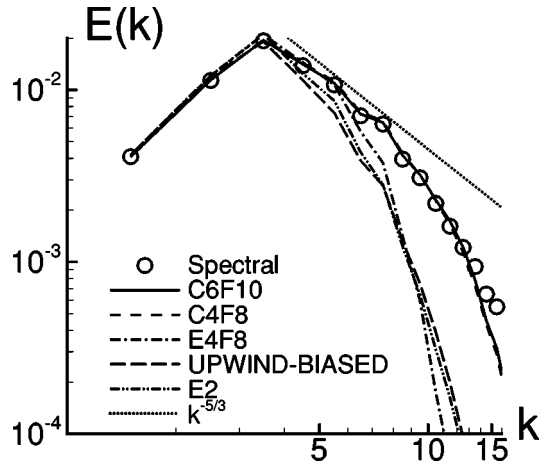

Fig. 5 Effect of spatial discretization on instantaneous three-dimensional energy spectra at $t/\tau_o=0.2985$ (32^3 mesh)

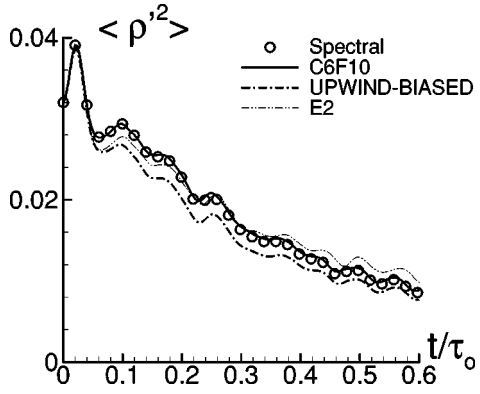

Fig. 7 Effect of spatial discretization on time history of density fluctuations for decaying isotropic turbulence on 64^3 mesh

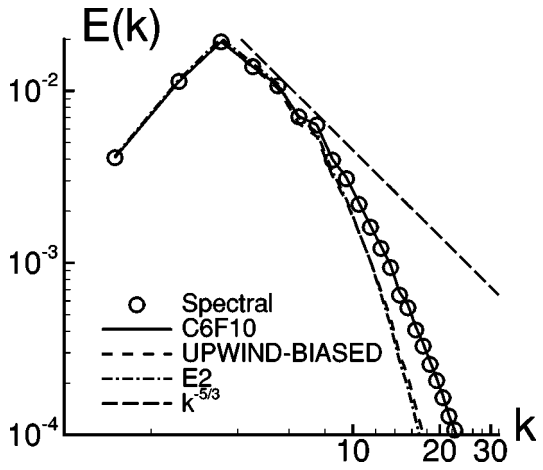

Fig. 8 Effect of spatial discretization on instantaneous three-dimensional energy spectra at $t/\tau_o = 0.2985$ (64^3 mesh)

Based on the above characteristics of the spatial discretizations for this turbulence decay problem, it is clear that the high-order differencing approach has an advantage over standard low-order schemes. In order for the low-order method to reach the same level of accuracy as the compact/filtering scheme, a grid between two to four times finer must be used. This translates in an increase in the total number of grid points by a factor of 8 to 64. In terms of CPU time required per grid point per time-step, the high-order solver is more expensive than the second-order and upwind procedures by a factor of only 2.0 and 1.6, respectively. Therefore, a significant net gain in efficiency is achieved with the high-fidelity formulation.

An investigation of the effect of the low-pass filter order on the decay of isotropic turbulence was also performed. This was done in order to provide some guidance in the selection of the filter operator needed to maintain acceptable accuracy. In principle, for proper resolution of the low wave numbers, the filter order should be equal or greater than the corresponding order of accuracy of the spatial discretization. Computations were performed using the 6th-order compact scheme in combination with various filter operators ranging from second to tenth-order accuracy. The corresponding decay of turbulent kinetic energy obtained on the 32^3 mesh is shown in Fig. 10. The results for $F6$, $F8$, and $F10$ are in good agreement with each other and with the DNS solution. Excessive dissipation starts to become apparent for $F4$, and is quite significant for $F2$ at which point the compact/filtering solution provides no improved accuracy relative to the second-order approach (Fig. 3).

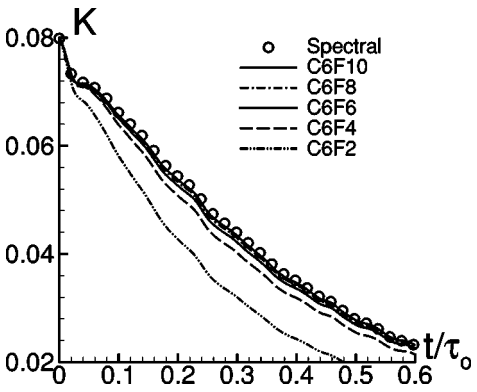

Fig. 10 Effect of low-pass filter order on time history of TKE for decaying isotropic turbulence (32^3 mesh)

4.1.2 Effect of Time-Marching Scheme. Although the implicit time-integration method is not needed for the efficient computation of isotropic turbulence decay on a uniform mesh, this test case was selected for validation and examination of accuracy issues of the implicit subiterative approach. For this purpose, computations of isotropic turbulence were performed on the 32^3 mesh using both the first and second-order versions of the implicit algorithm (denoted as $BW1$ and $BW2$, respectively). The number of subiterations was set equal to two for both implicit schemes, and the time step previously employed with the explicit ($RK4$) solver was retained. The corresponding time histories of the turbulent kinetic energy and density fluctuations are shown in Figs. 11 and 12, respectively. Results obtained with the first-order implicit method ($BW1$) are found to be extremely dissipative which renders the scheme unsuitable for LES. On the other hand, going to the second-order method ($BW2$) produces results which are in good agreement with the previous explicit calculation. Reasonable agreement was also found between the $BW2$ and $RK4$ results in terms of the energy spectra (not shown) for wavenumbers up to $k \approx 10$. This value of k is very close to the wave number beyond which the spatial discretization itself ceases to be sufficiently accurate (Section 4.1.1). Although the isotropic turbulence decay was not computed employing the third-order implicit method ($BW3$), preliminary calculations of benchmark acoustic problems, [30], indicate only a marginal gain in accuracy relative to the second-order scheme (accompanied also by a loss of robustness). The second-order subiterative approach therefore appears to be a good compromise in terms of accuracy and stability.

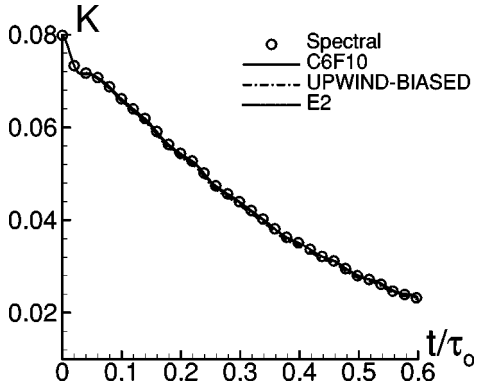

Fig. 9 Effect of spatial discretization on time history of TKE for decaying isotropic turbulence on 128^3 mesh

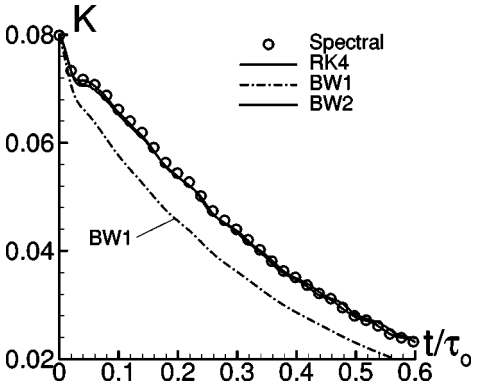

Fig. 11 Effect of time-integration scheme on TKE for decaying isotropic turbulence (32^3 mesh, $C6F10$)

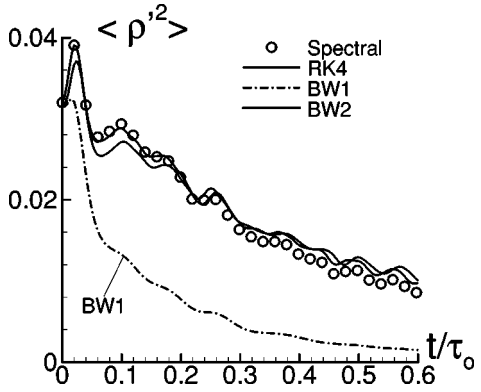

Fig. 12 Effect of time-integration scheme on density fluctuations for decaying isotropic turbulence (32^3 mesh, *C6F10*)

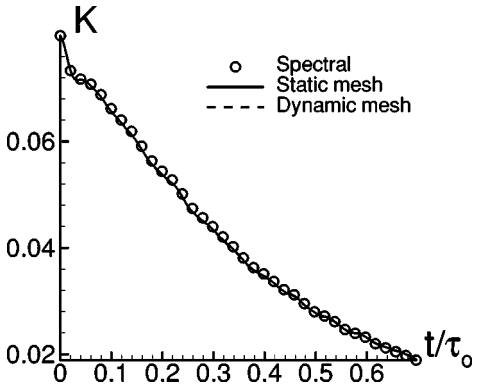

Fig. 14 Time history of TKE for decaying isotropic turbulence on deforming 32^3 mesh (*C6F10–RK4* scheme)

4.1.3 Turbulence Decay on a Deforming Curvilinear Mesh Since one of the objectives of this work is to develop a high-order computational approach suitable for DNS and LES on three-dimensional curvilinear and dynamic meshes, the decay of isotropic turbulence was also computed on a deforming curvilinear grid (Fig. 13). This arbitrary dynamic mesh was generated analytically by deforming the (x, y) coordinates of the original Cartesian 32^3 grid according to the expressions

$$x_{i,j,k}(\tau)=x_{\min}+\Delta x_o\Big[(i-1)+A_x f\sin(2\pi\omega\tau)\times\sin\frac{n_{xy}\pi(j-1)\Delta y_o}{L_y}\sin\frac{n_{xz}\pi(k-1)\Delta z_o}{L_z}\Big] \quad (23)$$

$$y_{i,j,k}(\tau)=y_{\min}+\Delta y_o\Big[(j-1)+A_y f\sin(2\pi\omega\tau)\times\sin\frac{n_{yx}\pi(i-1)\Delta x_o}{L_x}\sin\frac{n_{yz}\pi(k-1)\Delta z_o}{L_z}\Big]$$

$$i=1\ldots IL;\ \ j=1\ldots JL;\ \ k=1\ldots KL$$

$$\Delta x_o=\frac{L_x}{IL-1};\ \ \Delta y_o=\frac{L_y}{JL-1};\ \ \Delta z_o=\frac{L_z}{KL-1}$$

with the specified parameters $IL=JL=KL=33$, $A_x=A_y=1.5$, $L_x=L_y=L_z=2\pi$ and $n_{xy}=n_{yz}=\ldots=6$. A blending factor f (defined in terms of the product of three squared-sine functions) is chosen to limit the deformation to the interior of the domain. In addition, at $\tau=0$, the grid is undeformed and the previous initial turbulent flow conditions are specified. The frequency of oscillation was set to $\omega=0.266$ which gave approximately two cycles of the grid oscillation during the time of the computation. At the phase of maximum distortion (shown in Fig. 13) significant skewing of the grid is apparent. The grid speeds (x_τ, y_τ) were obtained analytically by direct differentiation of Eq. (23). The maximum value of the grid speed was approximately $0.2a_\infty$. The spatial and temporal transformation metric expressions were evaluated according to the procedure described in Section 3.3. The time history of the turbulent kinetic energy computed with the $C6F10$ scheme on the dynamic mesh is displayed in Fig. 14. The high-order compact/filtering procedure is shown to retain its fidelity despite the significant imposed mesh distortions.

4.1.4 Comparison of Compact/Filtering Approach With Standard SGS Models. In this section, we compare the accuracy of the present high-order low-pass filtering approach for the unfiltered Navier-Stokes equations with the standard LES method employing the Smagorinsky (with $C_s=0.092$) and the dynamic Smagorinsky subgrid-scale models. In the dynamic approach, both a trapezoidal and a seven-point least-square, [41] test filters with filter width $w=\pi/2$ were implemented. However, only results with the least-square filter are included since it provided slightly improved turbulence dissipation characteristics.

The time histories of turbulent kinetic energy obtained with the various SGS approaches on the 32^3 grid are shown in Fig. 15. First, it should be noted that all models were found to be numerically unstable without the inclusion of the low-pass filter operator. Therefore, in all computations, the 10th-order Pade-type filter was used in conjunction with the baseline $C6$ scheme. The decay of K is seen to be quite similar for the Smagorinsky and dynamic models, and both display excessive dissipation relative to the DNS. It is also apparent that for this case better results are obtained with the compact/filtering approach for the unfiltered equations (i.e., without the inclusion of an SGS model). A partial explanation of

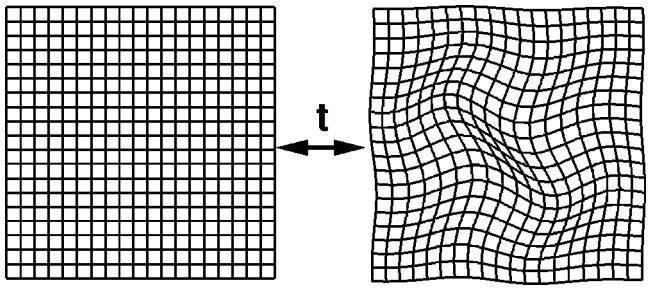

Fig. 13 Deforming curvilinear mesh for isotropic turbulence simulation

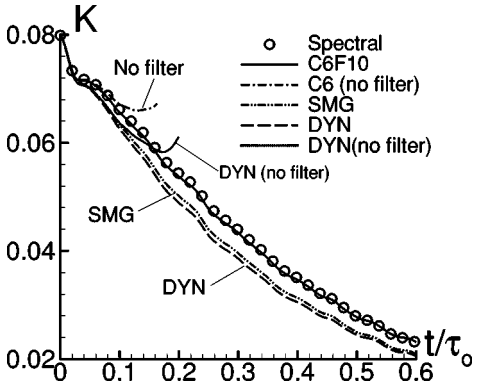

Fig. 15 Time history of TKE for decaying isotropic turbulence using several SGS models (32^3 mesh, *C6F10–RK4* scheme)

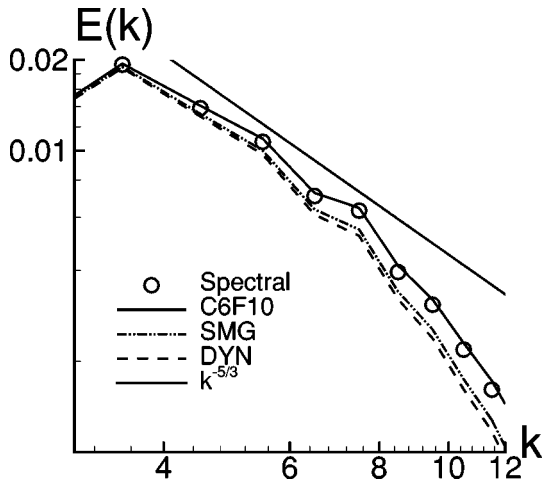

Fig. 16 Instantaneous three-dimensional energy spectra at $t/\tau_o = 0.2985$ for several SGS models (32^3 mesh, *C6F10–RK4* scheme)

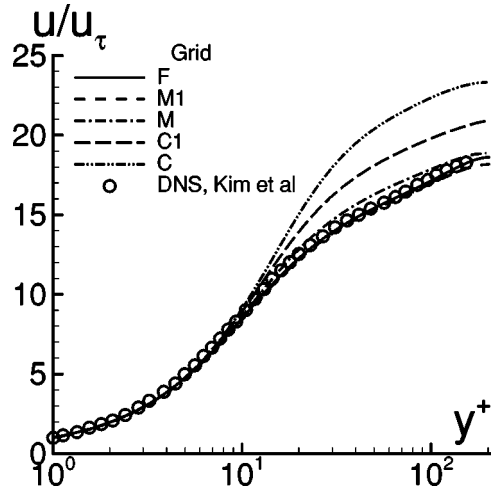

Fig. 17 Effect of spatial resolution on computed mean streamwise velocity profile for turbulent channel flow (*C6F10–BW2* scheme)

this behavior can be offered from the comparison of the energy spectra, shown in Fig. 16. Unlike the high-order filter (which acts only at high wave number), the standard eddy-viscosity SGS models dissipate energy over a wide range of wavenumbers including the resolved scales. This problem emanates from the inability of the model to effectively discriminate between resolved and unresolved scales (see, for instance, Ref. [42]), and cannot be corrected by simply adjusting the constant in the model.

4.2 Turbulent Channel Flow. The next case considered is that of turbulent channel flow which has been commonly employed in LES studies of wall-bounded flows (e.g., Refs. [43], [44]). The Reynolds number based on channel height, $\mathrm{Re}_h = 6600$ ($\mathrm{Re}_\tau \approx 180$), corresponds to the incompressible DNS of Kim et al. [45]. Since the present code solves the compressible form of the Navier-Stokes equations, a low Mach number, $M_\infty = 0.1$, is specified.

A summary of the computational grids employed is provided in Table 1. In all case the streamwise extent of the computational domain is set to $L_x/h = 2\pi$, whereas two different spanwise lengths $L_z/h = \pi$, $2\pi/3$ are considered. The mesh spacing is constant in the x and z directions, and geometrically stretched in y. For Grid M in Table 1, $\Delta x^+ = 47.1$, $\Delta y^+_{\mathrm{wall}} = 0.45$, $\Delta y^+_{\mathrm{max}} = 25.8$ and $\Delta z^+ = 23.4$. The grid stretching factor in the normal direction is equal to 1.15.

Periodic boundary conditions are applied for all variables in the streamwise and spanwise directions. At the channel walls, the no slip condition is satisfied, along with a constant surface temperature, and a vanishing normal pressure gradient. Due to the periodic streamwise boundary condition, the flow cannot sustain a streamwise pressure gradient. Therefore, an artificial source term is introduced, [20], in order to provide a driving mechanism which mimics an imposed constant pressure gradient.

Channel flow computations were performed using the following spatial discretizations: $C6F10$ scheme with $\alpha_f = 0.49$, the standard second-order $E2$ scheme with damping, as well as a third-order upwind-biased approach. No SGS model was incorporated, unless otherwise noted. The iterative implicit second-order solver ($BW2$) was employed with a baseline nondimensional time-step $\Delta t = 0.001$ and three subiterations. In terms of wall units, this time-step corresponds to $\Delta t^+ = \Delta t u_\tau^2/\nu = 0.025$ which should be sufficiently accurate based on the study of Choi and Moin [46].

Table 1 Grid designation for turbulent channel flow simulations

Grid	Size	L_z/h
C	31×61×31	π
C1	31×61×31	$2\pi/3$
M	61×61×61	π
M1	61×61×61	$2\pi/3$
F	91×91×91	π

4.2.1 Effect of Grid Resolution and Spatial Discretization The mean streamwise velocity profiles obtained on various levels of resolution with the compact/filtering $C6F10$ scheme are display in Fig. 17, and compared with the DNS data of Ref. [45]. The computed results are observed to approach the DNS solution as the mesh is refined. In particular, good agreement is observed for the medium and fine meshes (Grids M, M1, and F, Table 1). The effect of grid resolution on the velocity fluctuations is shown in Fig. 18. Again, a consistent trend is observed with grid refinement. However, even on the finest mesh considered, some discrepancies relative to the DNS are apparent towards the channel centerline. In retrospect, a smaller value of $\Delta y^+_{\mathrm{max}}$ should have been specified through an improved grid-point distribution in the normal direction. Nonetheless, based on the comparison with the DNS data, the present compact/filtering approach without the inclusion of an SGS model seems to provide encouraging results. A representative computed instantaneous flow structure corresponding to the fine mesh is shown in Fig. 19 in terms of contours of streamwise velocity on both a transverse and a longitudinal plane close to the surface ($y^+ = 8.3$). The low-speed streaks typical of wall-bounded turbulent flows are clearly observed.

A comparison of the channel flow solutions computed on Grid M1 using several spatial discretizations is given in Figs. 20 and 21. On this level of resolution, the prediction of the mean velocity profile deteriorates significantly when switching to the lower-order second and upwind-biased schemes. Unlike the $C6F10$, which is in good agreement with the log-law, the $E2$ and upwind methods display a profile which resembles more a laminar flow. Indeed, examination of the spanwise velocity fluctuations (Fig. 21) shows a significant suppression of the turbulence fluctuations with the lower-fidelity algorithms. Significant improvements are therefore achieved when employing the high-order compact/filtering approach. It should be noted, however, that the poor behavior of the standard schemes may be attributable in part to the low Mach number ($M_\infty = 0.1$) specified for these test cases, and could become less severe as the Mach number is increased.

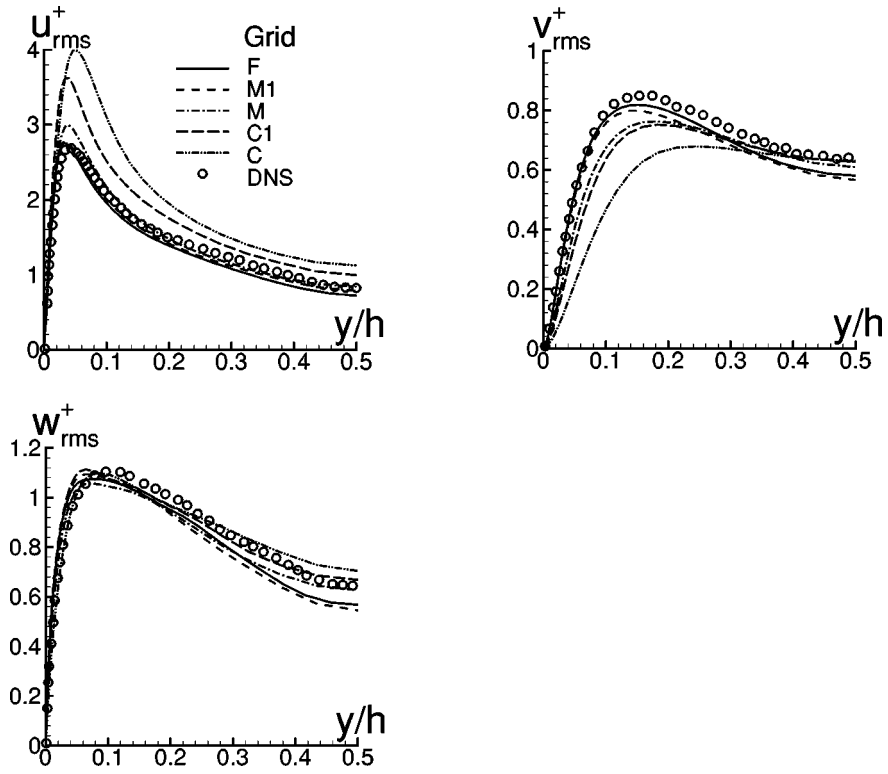

Fig. 18 Effect of spatial resolution on velocity fluctuations for turbulent channel flow (*C6F10–BW2* scheme)

4.2.2 Comparison of Compact/Filtering Approach With Standard SGS Models. The question of whether or not the inclusion of a standard SGS model could improve the computed channel flow results on an LES grid with limited resolution was also addressed. To this end, computations were performed, [20], for a slightly higher Reynolds number ($Re_h = 7700$) on Grid M employing the constant-coefficient and dynamic Smagorinsky models, as well as the (no-model) compact/filtering approach. Calculations with the SGS models were obtained using the same spatial discretization ($C6F10$), and the inclusion of the low-pass filter was required in order to maintain numerical stability. Figure 22 displays a comparison of the mean velocity profiles. Although the dynamic model provides a small improvement over the Smagorinsky model, the compact/filtering results are still in slightly better agreement with the DNS data. A plot of the normal velocity fluctuations (Fig. 23), indicates that the Smagorinsky model is too dissipative. Implementing the dynamic model, improves the results but still does not provide a better answer than the one already achieved with the compact/filtering procedure alone.

4.2.3 Effect of Time-Integration Scheme. The present test case permits a comparison of the relative efficiency of explicit and implicit time-marching procedures for the simulation of turbulent wall-bounded flows. The results given above were computed with a time-step $\Delta t = 0.001$, $\Delta t^+ \approx 0.025$ which corresponds to a maximum CFL number of approximately 8.3 (on Grid M). Numerical

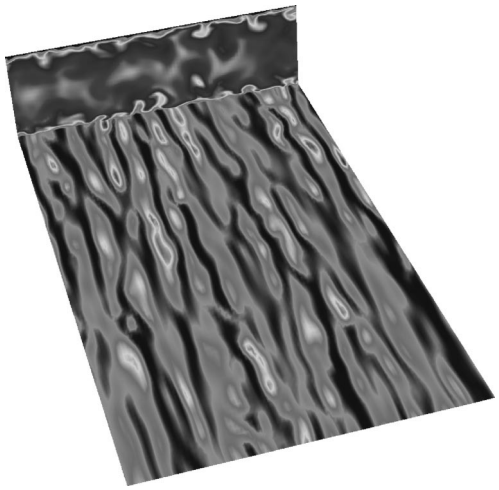

Fig. 19 Instantaneous turbulent channel flow structure computed on Grid F with *C6F10–BW2* scheme

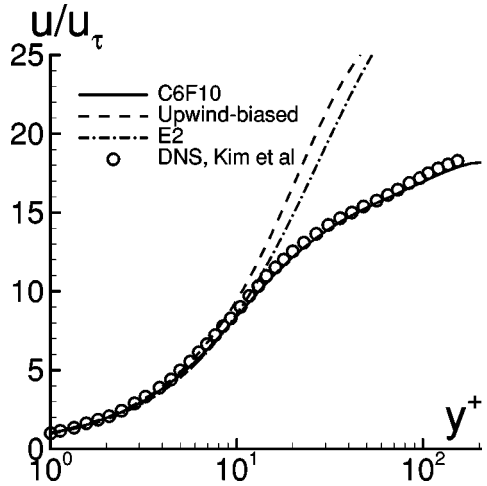

Fig. 20 Effect of spatial discretization on computed mean streamwise velocity profile for turbulent channel flow (Grid M1)

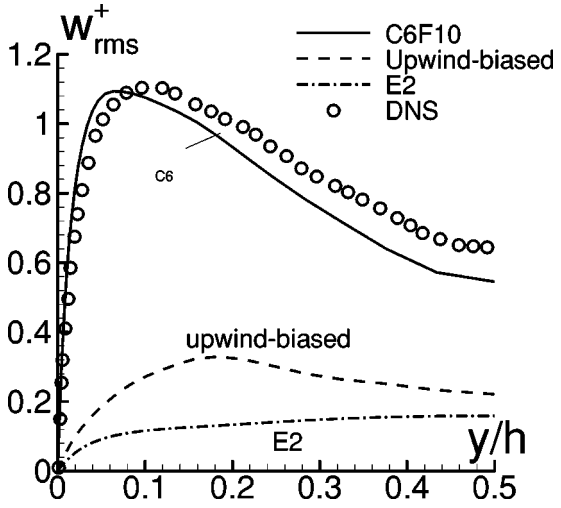

Fig. 21 Effect of spatial discretization on computed spanwise velocity fluctuations (Grid M1)

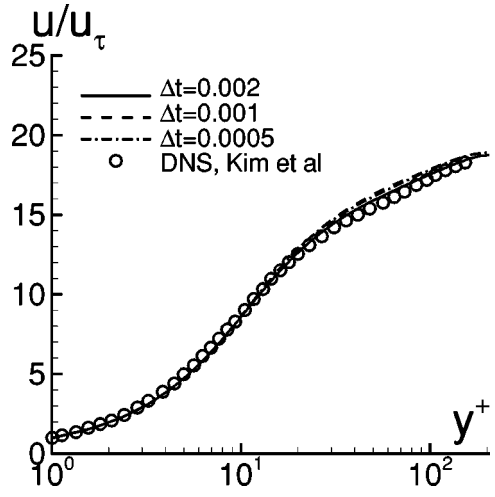

Fig. 24 Effect of computational time-step on mean streamwise velocity profile for channel flow (Grid M, *C6F10–BW2* scheme)

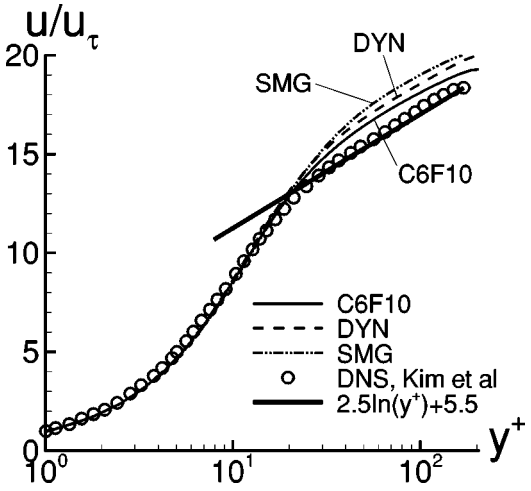

Fig. 22 Mean streamwise velocity profile for turbulent channel flow computed with different SGS models (Grid M, *C6F10–BW2* scheme)

instability was encountered with the $C6F10$-$BW2$ method for $\Delta t = 0.004$, $\Delta t^+ \approx 0.05$. It should be noted that in the present *compressible* solver, instability sets in at values of Δt^+ which are smaller than those reported in Ref. [46] for an implicit *incompressible* method. In that study, as Δt was increased, turbulence suppression occurred prior to the onset of numerical instability. The $RK4$ scheme was found to be very inefficient on this highly stretched mesh. The explicit method was unstable for a time-step as low as 0.0001 which corresponds to a CFL$\approx$0.8. Assuming that a $\Delta t = 5 \times 10^{-5}$, CFL$\approx$0.4 could be used, this value would still be a factor of 20 smaller that the corresponding time step for the implicit solver.

The effect of Δt on the solution computed with the implicit scheme was also investigated. The number of subiterations was held constant and equal to three. Over the range $0.0005 < \Delta t < 0.002$, the effect of time-step on the mean velocity profile (Fig. 24) was found to be negligible. The turbulence fluctuations were somewhat more sensitive, as shown in Fig. 25, for the spanwise velocity. Nonetheless, results obtained with the two smallest time-steps are in very close agreement. The second-order iterative im-

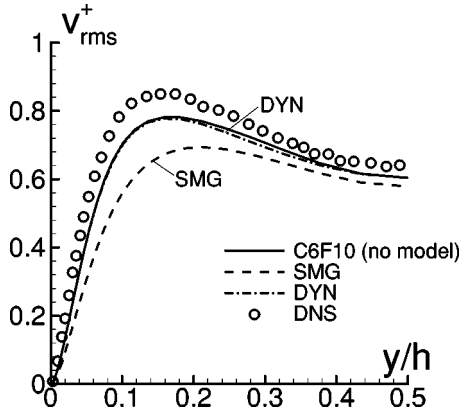

Fig. 23 Normal velocity fluctuations for turbulent channel flow computed with different SGS models (Grid M, *C6F10–BW2* scheme)

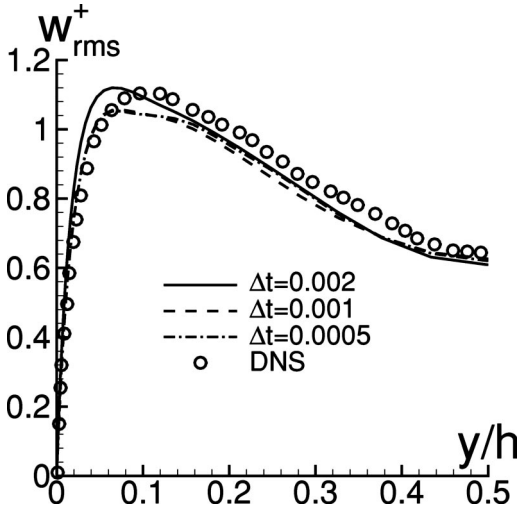

Fig. 25 Effect of computational time-step on spanwise velocity fluctuations for channel flow (Grid M, *C6F10–BW2* scheme)

plicit procedure therefore appears to be an accurate and efficient approach for the simulation of compressible wall-bounded flows.

5 Summary

The evaluation of a recently developed high-order finite-difference solver for compressible large-eddy simulation has been presented. The method employs 4th- and 6th-order compact schemes in conjunction with up to 10th-order low-pass Pade-type filter operators which are required for numerical stability on stretched and curvilinear meshes. The spatial schemes are coupled with both explicit and implicit time-integration methods.

A comparison of several spatial discretizations and SGS approaches has been presented for the decay of compressible isotropic turbulence and turbulent channel flow. The improved accuracy of the compact/filtering method relative to standard second-order, fourth-order, and upwind-biased approaches has been demonstrated. This improvement is attributed to the better dispersion-error characteristics of the compact approach, as well as to the dissipation properties of the low-pass filter which only damps high-frequency components. The accuracy and efficiency of the implicit time-marching method relative to the explicit approach has also been evaluated. It has been shown that the second-order iterative implicit scheme represents an effective choice for LES of compressible wall-bounded flows.

For the case of isotropic turbulence, better results are obtained with the compact/filtering scheme applied to the unfiltered Navier-Stokes equations (i.e., without an explicitly added SGS model) than with the constant-coefficient and dynamic Smagorinsky LES models. This is due to the fact that the SGS models, in contrast with the optimized low-pass filter, exert dissipation over a wide range of wave numbers including a portion of the resolved scales. For low-Reynolds number turbulent channel flow simulations on coarse meshes, the compact/filtering and dynamic models provide similar results, with no clear advantage achieved through incorporation of the SGS model.

Application of the high-order solver to more complex flows, including supersonic flat-plate boundary layer, [34], cylinder wake, [20], and separated shock/boundary layer interactions, [35,36], have shown encouraging results. In all of those cases, the compact/filtering and dynamic Smagorinsky approaches have yielded comparable predictions. However, additional computations, in particular at higher Reynolds numbers, must be carried out in order to further evaluate this issue. In addition, further analysis of the turbulent kinetic energy dissipation enforced by the spatial low-pass filter is also required.

Acknowledgments

The authors are grateful for AFOSR sponsorship under task 2304IW monitored by Major W. Hilbun and Dr. T. Beutner. This work was also supported in part by a grant of HPC time from the DoD HPC Shared Resource Centers at ASC, ERDC and NAVO. The authors would like to thank Dr. G. Blaisdell for providing the codes used to generate the initial isotropic turbulence conditions, and for several helpful discussions. Many fruitful conversations with Dr. D. Gaitonde regarding the numerical algorithms are also gratefully acknowledged.

References

[1] Lesieur, M., and Metais, O., 1996, ''New Trends in Large-Eddy Simulations of Turbulence,'' Annu. Rev. Fluid Mech., **28**, pp. 45–82.
[2] Liu, C., and Liu, Z., eds. 1997, *Advances in DNS/LES, Proceedings of First AFOSR International Conference on DNS/LES*, Ruston, LA, Aug., Greyden Press.
[3] Knight, D., and Sakell, L., eds., 1999, *Recent Advances in DNS and LES, Proceedings of Second AFOSR International Conference on DNS/LES*, New Brunswick, NJ, June, Kluwer, Dordrecht, The Netherlands.
[4] Ghosal, S., 1999, ''Mathematical and Physical Constraints on Large-Eddy Simulation of Turbulence,'' AIAA J., **37**(4), pp. 425–433.
[5] Kravchenko, A., and Moin, P., 1997, ''On the Effects of Numerical Errors in Large Eddy Simulation of Turbulent Flows,'' J. Comput. Phys., **131**(2), pp. 310–322.
[6] Lele, S. K., 1992, ''Compact Finite Difference Schemes With Spectral-Like Resolution,'' J. Comput. Phys., **103**, pp. 16–42.
[7] Visbal, M. R., and Gaitonde, D. V., 1999, ''High-Order Accurate Methods for Complex Unsteady Subsonic Flows,'' AIAA J., **37**(10), pp. 1231–1239.
[8] Gaitonde, D. V., and Visbal, M. R., 1999, ''Further Development of a Navier-Stokes Solution Procedure Based on Higher-Order Formulas,'' AIAA Paper No. 99-0557.
[9] Gaitonde, D. V., Shang, J. S., and Young, J. L., 1999, ''Practical Aspects of Higher-Order Numerical Schemes for Wave Propagation Phenomena,'' Int. J. Numer. Methods Eng., **45**, pp. 1849–1869.
[10] Gaitonde, D. V., and Visbal, M. R., 1998, ''High-Order Schemes for Navier-Stokes Equations: Algorithm and Implementation into FDL3DI,'' Technical Report AFRL-VA-WP-TR-1998-3060, Air Force Research Laboratory, Wright-Patterson AFB, OH.
[11] Visbal, M. R., and Gordnier, R. E., 2000, ''A High-Order Flow Solver for Deforming and Moving Meshes,'' AIAA Paper No. 2000-2619.
[12] Visbal, M., and Gaitonde, D., 2001, ''Very High-Order Spatially Implicit Schemes for Computational Acoustics on Curvilinear Meshes,'' J. Comput. Acoust., **9**(4), pp. 1259–1286.
[13] Vinokur, M., 1974, ''Conservation Equations of Gasdynamics in Curvilinear Coordinate Systems,'' J. Comput. Phys., **14**, pp. 105–125.
[14] Steger, J. L., 1976, ''Implicit Finite-Difference Simulation of Flow About Arbitrary Two-Dimensional Geometries,'' AIAA J., **16**(7), pp. 679–686.
[15] Anderson, D. A., Tannehill, J. C., and Pletcher, R. H., 1984, *Computational Fluid Mechanics and Heat Transfer*, McGraw-Hill, New York.
[16] Erlebacher, G., Hussaini, M. Y., Speziale, C. G., and Zang, T. A., 1992, ''Toward the Large-Eddy Simulation of Compressible Turbulent Flows,'' Journal of Fluid Mechanics, **238**, pp. 155–185.
[17] Smagorinsky, J. S., 1963, ''General Circulation Experiments With the Primitive Equations,'' Mon. Weather Rev., **91**(1), pp. 99–165.
[18] Germano, M., Piomelli, U., Moin, P., and Cabot, W. H., 1991, ''Dynamic Subgrid-Scale Eddy Viscosity Model,'' Phys. Fluids A, **3**(7), pp. 1760–1765.
[19] Moin, P., Squires, W., Cabot, W., and Lee, S., 1991, ''A Dynamic Subgrid-Scale Model for Compressible Turbulence and Scalar Transport,'' Phys. Fluids A, **3**(11), pp. 2746–2757.
[20] Rizzetta, D. P., Visbal, M. R., and Blaisdell, G. A., 1999, ''Application of a High-Order Compact Difference Scheme to Large-Eddy and Direct Numerical Simulation,'' AIAA Paper No. 99-3714.
[21] van Leer, B., 1979, ''Towards the Ultimate Conservative Difference Scheme. V. A Second-Order Sequel to Godunov's Method,'' J. Comput. Phys., **32**, pp. 101–136.
[22] Alpert, P., 1981, ''Implicit Filtering in Conjunction With Explicit Filtering,'' J. Comput. Phys., **44**, pp. 212–219.
[23] Vichnevetsky, R., and Bowles, J. B., 1982, *Fourier Analysis of Numerical Approximations of Hyperbolic Equations* (SIAM Studies in Applied Mathematics), SIAM, Philadelphia.
[24] Jameson, A., Schmidt, W., and Turkel, E., 1981, ''Numerical Solutions of the Euler Equations by a Finite Volume Method Using Runge-Kutta Time Stepping Schemes,'' AIAA Paper No. 81-1259.
[25] Pulliam, T., 1986, ''Artificial Dissipation models for the Euler Equations,'' AIAA J., **24**(12), pp. 1931–1940.
[26] Tam, C. K. W., 1995, ''Computational Aeroacoustics: Issues and Methods,'' AIAA J., **33**(10), pp. 1788–1796.
[27] Thomas, P. D., and Lombard, C. K., 1979, ''Geometric Conservation Law and Its Application to Flow Computations on Moving Grids,'' AIAA J., **17**(10), pp. 1030–1037.
[28] Beam, R., and Warming, R., 1978, ''An Implicit Factored Scheme for the Compressible Navier-Stokes Equations,'' AIAA J., **16**(4), pp. 393–402.
[29] Pulliam, T. H., and Chaussee, D. S., 1981, ''A Diagonal Form of an Implicit Approximate-Factorization Algorithm,'' J. Comput. Phys., **39**(2), pp. 347–363.
[30] Visbal, M., 2001, ''Advances in High-Resolution Schemes for Computational Acoustics on General Geometries,'' RTO-MP-079(A), *Proceedings From RTO Symposium on Aging Mechanisms and Control/Part A: Developments in Computational Aero- and Hydro-Acoustics*, RTO Applied Vehicle Technology Panel, Manchester, UK, Oct.
[31] Visbal, M. R., Gaitonde, D. V., and Gogineni, S. P., 1998, ''Direct Numerical Simulation of a Forced Transitional Plane Wall Jet,'' AIAA Paper No. 98-2643.
[32] Rizzetta, D. P., Visbal, M. R., and Stanek, M. J., 1999, ''Numerical Investigation of Synthetic-Jet Flow Fields,'' AIAA J., **37**(8).
[33] Visbal, M. R., and Gordnier, R. E., 2001, ''Direct Numerical Simulation of the Interaction of a Boundary Layer With a Flexible Panel,'' AIAA Paper No. 2001-2721.
[34] Rizzetta, D. P., Visbal, M. R., and Gaitonde, D. V., 2000, ''Direct Numerical and Large-Eddy Simulation of Supersonic Flows by a High-Order Method,'' AIAA Paper No. 2000-2408.
[35] Rizzetta, D. P., and Visbal, M. R., 2001, ''Large-Eddy Simulation of Supersonic Compression-Ramp Flows,'' AIAA Paper No. 2001-2858.
[36] Rizzetta, D. P., Visbal, M. R., and Gaitonde, D. V., 2001, ''Large-Eddy Simulation of Supersonic Compression-Ramp Flow by a Hihg-Order Method,'' AIAA J., **39**(12), pp. 2283–2292.
[37] Roe, P. L., 1981, ''Approximate Riemann Solvers, Parameter Vectors and Difference Schemes,'' J. Comput. Phys., **43**, pp. 357–372.
[38] Grinstein, F., and Fureby, C., 2002, ''Recent Progress on Miles for High Reynolds-Number Flows,'' AIAA Paper No. 2002-0134.
[39] Domaradzki, J., and Radhakrishnan, S., 2002, ''Subgrid-Scale Modeling Using

Truncated Navier-Stokes Dynamics,'' AIAA Paper No. 2002-0285.
[40] Stolz, S., and Adams, N., 1999, ''An Approximate Deconvolution Procedure for Large-Eddy Simulation,'' Phys. Fluids, **11**(7), pp. 1699–1701.
[41] Spyropoulos, E. T., and Blaisdell, G. A., 1996, ''Evaluation of the Dynamic Model for Simulations of Compressible Decaying Isotropic Turbulence,'' AIAA J., **34**(5), pp. 990–998.
[42] Hughes, T. J., Mazzei, L., and Jansen, K., 2000, ''Large Eddy Simulation and the Variational Multiscale Method,'' Comput. Visual. Sci., **3**, pp. 47–59.
[43] Schumann, U., 1975, ''Subgrid-Scale Model for Finite Difference Simulations of Turbulent Flows in Plane Channels and Annuli,'' J. Comput. Phys., **18**(4), pp. 376–404.
[44] Piomelli, U., 1993, ''High Reynolds Number Calculations Using the Dynamic Subgrid-Scale Stress Model,'' Phys. Fluids, **5**(6), pp. 1484–1490.
[45] Kim, J., Moin, P., and Moser, R., 1992, ''Turbulent Statistics in Fully Developed Channel Flow at Low Reynolds Number,'' ASME J. Fluids Eng., **117**, pp. 133–166.
[46] Choi, H., and Moin, P., 1994, ''Effects of the Computational Time Step on Numerical Solutions of Turbulent Flow,'' J. Comput. Phys., **113**(1), pp. 1–4.

F. F. Grinstein
Naval Research Laboratory,
Laboratory for Computational
Physics and Fluid Dynamics,
Code 6410,
Washington, DC 20375-5344

C. Fureby
The Swedish Defence Research Agency,
FOI,
Department of Weapons and Protection,
Warheads and Propulsion,
SE-172 90, Stockholm,
Sweden

Recent Progress on MILES for High Reynolds Number Flows

A promising large-eddy simulation (LES) approach is monotonically integrated LES (MILES) which involves solving the Navier-Stokes equations using high-resolution monotone algorithms. In MILES, the subgrid scale (SGS) flow physics is provided by intrinsic, nonlinear, high-frequency filters built into the discretization and implicit SGS models. Mathematical and physical aspects of implicit SGS modeling using nonlinear flux-limiters are addressed using a formalism based on the modified LES equations approach. Detailed properties of the implicit subgrid model are related to the flux limiter, which in turn depends on the specifics of the numerical scheme; we illustrate how the latter properties can directly affect their potential in the MILES framework. Major unresolved issues relevant to LES of complex practical turbulent flows are discussed in this context, including some aspects of boundary condition modeling and overall computational model validation. [DOI: 10.1115/1.1516576]

1 Introduction

Large-eddy simulation (LES) has emerged as a viable alternative to direct numerical simulation (DNS) and Reynolds average Navier-Stokes (RANS) modeling to challenge the scale-complexity problem of high Reynolds (Re) number flow. As opposed to RANS, in which the NSE are averaged over time homogeneous directions, or across ensembles of equivalent flows, LES relies on local volumetric averaging, thus preserving the dynamics of the large scales. This averaging is devised to eliminate eddies smaller than the characteristic mesh resolution Δ. As a consequence of this averaging, the LES equations are incomplete since they do not contain information about the unresolved subgrid scale (SGS) flow, and modeling is required to provide guidance about the effects of the subgrid flow on the resolved flow. In the absence of a universal theory of turbulence the development and progress of such models must include the rational use of empirical information. Present-day SGS models include algebraic and semi-algebraic models developed in physical space, [1–3], and models developed in some adjoint space, [1,4,5]. Although some of the more advanced SGS models, [1], can outperform the traditional isotropic eddy-viscosity models, their practical use is typically limited by their complexity, and it is therefore desirable to also investigate alternative nonconventional approaches.

Far from solid boundaries the SGS flow physics is ideally considered homogeneous and isotropic. However, laboratory studies, [6], and numerical simulations, [7], proved the existence of organized vortical structures—with concentration of vorticity in elongated filaments (worm-vortices) characterizing the smallest coherent structures (CS) of turbulent flows, [8,9]. The existence of worm-vortices in isotropic homogeneous turbulent flows can be traced to an anisotropic feature of the small-scale organization of turbulent flows: the fact that high-magnitude vorticity is preferentially aligned with the eigenvector corresponding to the intermediate eigenvalue of the rate-of-strain tensor with very little such preferential alignment for the lower-magnitude vorticity, [10,11]. This is a kinematic property independent of the dynamics involved in the vorticity generation, [8,11], and it suggests that characteristic small-scale CS in turbulent flows can be locally regarded as two-dimensional structures stretched by strain weaker than the small-scale vorticity—a concept that has been used when developing vortex-based SGS models, [12]. Close to the wall, the length scales of the most energetic eddies decrease, and if the computational grid in LES is unable to resolve these length scales then anisotropy in the turbulent flow will become anisotropy of the SGS motion thus necessitating SGS models capable of handling simultaneous flow and grid anisotropy. The number of nodes required in LES of wall bounded flows scales with the square of the friction-velocity-based Re number, [13], which is almost the same as for DNS, and fine grids are necessary to resolve the mechanisms responsible for self-sustaining turbulence in wall-bounded flows, [14].

Drawbacks of the conventional LES model include the possible masking of the SGS terms by the leading order truncation error, the ambiguity in using spatial filtering and the difficulty of formulating SGS models for complex high Re number wall-bounded flows. The task of formulating numerical simulation models involves tradeoffs, both numerically and from a physical standpoint and the accuracy of the computer model is not better than the weakest part of the model. With this regard it is important to consider not only physical and numerical aspects but also their combined effects. Advanced SGS models for LES as well as numerical schemes have been developed and successfully applied to different flow problems, but not very often has the computational model, i.e., the modified equations, been carefully examined. LES models taking these aspects into account may be based on solving the NSE with high-resolution schemes such as the flux corrected transport (FCT) method, [15], the piecewise parabolic method (PPM), [16,17], total variational diminishing (TVD) schemes, [18], Riemann solvers, [19], the MPDATA advection scheme [20], and the spectral vanishing viscosity method, [21].

Here we focus on the monotonically integrated LES (MILES) approach, [22,23], in which non-linear high-frequency filters built into a particular class of algorithms are used to provide implicit SGS models, in contrast to conventional LES where explicit SGS models are introduced for closure prior to discretization. Although the history of MILES draws on the development of shock-capturing schemes, e.g., [15], the concept of MILES, as developed in [23,24], attempts to embody a general computational procedure for solving the NSE for high Re number turbulent flows as accurately as possible using built-in (implicit) SGS turbulence models. Due to the anisotropic nature of the SGS modeling in MILES, simultaneously handling flow and grid anisotropies, we believe it provides an improved computational framework for inhomogeneous high Re flows.

The outline of the paper is as follows. A brief overview of LES and its analysis is presented in Section 2, which is used as reference for the formal discussion of the properties of subgrid modeling using MILES presented in Section 3; selected previous applications of MILES in the study of inhomogeneous flows are

Contributed by the Fluids Engineering Division for publication in the JOURNAL OF FLUIDS ENGINEERING. Manuscript received by the Fluids Engineering Division, March 11, 2002; revision received, April 22, 2002. Associate Editor: G. E. Karniadakis.

reviewed in Section 4. Relevant issues of near-wall flow modeling with LES and MILES are discussed in Section 5, and further illustrated by channel-flow case studies. Section 6 discusses the crucial additional aspects of LES of practical complex flows relating to overall computational model development and validation. Finally, some concluding remarks are given in Section 7.

2 The Conventional Large-Eddy Simulation Model

To simplify the discussion of the LES and MILES formalism, the focus in this and the next section is on the incompressible limit regime; a more general presentation can be found in [23] or [24]. In LES, the motion is separated into small and large eddies and equations are solved for the latter. The separation is achieved by means of a low-pass filter, for details see [1,25]. Convoluting the NSE with a pre-defined filter kernel $G=G(\mathbf{x},\Delta)$ yields the LES equations,

$$\begin{cases} \nabla\cdot\overline{\mathbf{v}}=m^{\rho}, \\ \partial_t(\overline{\mathbf{v}})+\nabla\cdot(\overline{\mathbf{v}}\otimes\overline{\mathbf{v}})=-\nabla\overline{p}+\nabla\cdot(\overline{\mathbf{S}}-\mathbf{B})+\mathbf{m}^{v}, \end{cases} \tag{1}$$

where $\mathbf{v}$ is the velocity, p the pressure, $\mathbf{S}=2\upsilon\mathbf{D}$ the viscous stress tensor, $\mathbf{D}=1/2(\mathbf{L}+\mathbf{L}^T)$ the rate-of-strain tensor, υ the viscosity, and $\mathbf{L}=\nabla\mathbf{v}$. Specific to LES is the resolved parts (denoted by an overbar), the subgrid scale stress tensor $\mathbf{B}=(\overline{\mathbf{v}\otimes\mathbf{v}}-\overline{\mathbf{v}}\otimes\overline{\mathbf{v}})$ and the commutation error terms $m^{\rho}=[G^*,\nabla]\mathbf{v}$ and $\mathbf{m}^{v}=[G^*,\nabla](\mathbf{v}\otimes\mathbf{v}+p\mathbf{I}-\mathbf{S})$, where $[G^*,\nabla]f=\overline{\nabla f}-\nabla\overline{f}$ is the commutation operator. Only the resolved scales are thus retained in LES whereas the subgrid scales are grouped in $\mathbf{B}$, which has to be modeled using an expression of the type $\mathbf{B}(\mathbf{x},t)=\mathbf{B}[\overline{\mathbf{v}}(\mathbf{x}',t');\mathbf{x},t]$. Physical arguments and mathematical analysis suggests that (i) $\mathbf{B}$ is invariant under a change of frame, [26,27]; (ii) $\mathbf{B}$ is positive definite symmetric, provided $G(\mathbf{x})$ is symmetric, [26,28]; and (iii) that the inequalities $k=1/2\,\mathrm{tr}\mathbf{B}\geqslant 0$, $k^2\geqslant\|\mathbf{B}\|^2$ and $\det\mathbf{B}\geqslant 0$ must be satisfied in order for $\mathbf{B}$ to be positive definite, [26,28]. The commutation errors, m^{ρ} and $\mathbf{m}^{v}$, reflect the fact that filtering and differentiation do not generally commute, [26,29], and the effects of these terms on the resolved flow are currently not well known, particularly for complex flows, and must be further investigated.

Two modeling strategies for $\mathbf{B}$ exist. *Functional modeling* consists in modeling the action of the subgrid scales on the resolved scales. This is basically of energetic nature so that the balance of the energy transfers between the two scale ranges is sufficient to describe the subgrid scale effects. Hence, the energy transfer mechanism from the resolved to the subgrid scales is assumed analogous to that of a Brownian motion superimposed on the large scale motion, i.e., $\mathbf{B}=-2\upsilon_k\overline{\mathbf{D}}$ where υ_k is the subgrid viscosity. A wide range of models of this type is presently being used, [30–32]. *Structural modeling* consists of modeling $\mathbf{B}$ without incorporating any knowledge of the nature of the interactions between the subgrid and the resolved scales. Such models can be based either on (i) series expansion techniques, [32,33], (ii) modeled transport equations for $\mathbf{B}$, [34], (iii) scale similarity or mixed models, [35,36], or (iv) other deterministic models, [1].

LES requires high-order numerical methods to avoid masking $\nabla\cdot\mathbf{B}$ by the leading-order truncation error. In general, Δ is related to the grid, $\Delta\propto|\mathbf{d}|$, where $|\mathbf{d}|$ is the grid size, which makes the modeled subgrid stresses $O(|\mathbf{d}|^2)$ terms. In LES, spectral and high-order finite volume, element or difference methods are used for spatial discretization, while explicit semi-implicit or predictor-corrector methods are used for time-integration. For complex geometries the finite volume (FV) method is the most convenient technique. Here, the domain D is partitioned into cells Ω_P so that $\cup_P(\Omega_P)=D\cup\delta D$ and $\cap_P(\Omega_P)=\varnothing$. The cell-average of f over the Pth cell is $f_P=1/\delta V\int_{\Omega}f dV$ so that Gauss theorem may be used to derive the semi-discretized LES equations. By integrating these over time, using, e.g., a multistep method, [37],

$$\begin{cases} \dfrac{\beta_i\Delta t}{\delta V_P}\displaystyle\sum_f\,[F_f^{C,\rho}]^{n+i}=0, \\ \displaystyle\sum_{i=0}^{m}\left(\alpha_i(\overline{\mathbf{v}})_P^{n+i}+\frac{\beta_i\Delta t}{\delta V_P}\sum_f\,[\mathbf{F}_f^{C,v}+\mathbf{F}_f^{D,v}+\mathbf{F}_f^{B,v}]^{n+i}\right)=-\beta_i(\nabla\overline{p})_P^{n+i}\Delta t+\beta_i(\overline{\mathbf{f}})_P^{n+i}\Delta t, \end{cases} \tag{2}$$

where m, α_i, and β_i are parameters of the scheme and $F_f^{C,\rho}=(\overline{\mathbf{v}}\cdot d\mathbf{A})_f$, $\mathbf{F}_f^{C,v}=(\overline{\mathbf{v}}\cdot d\mathbf{A})_f\overline{\mathbf{v}}_f$, $\mathbf{F}_f^{B,v}=(\mathbf{B})_f d\mathbf{A}$ and $\mathbf{F}_f^{D,v}=(\upsilon\nabla\overline{\mathbf{v}})_f d\mathbf{A}$ and are the convective, viscous and subgrid fluxes. To close the FV discretization the fluxes (at face f) need to be reconstructed from the variables at adjacent cells. This requires flux interpolation for the convective fluxes and difference approximations for the inner derivatives of the other fluxes. Typically, for second-order accuracy,

$$\begin{cases} \mathbf{F}_f^{D,v}=\upsilon|d\mathbf{A}|(\overline{\mathbf{v}}_N-\overline{\mathbf{v}}_P)/|\mathbf{d}|+\dfrac{1}{6}\upsilon(\mathbf{d}\otimes\mathbf{d})\nabla^3\overline{\mathbf{v}}, \\ \mathbf{F}_f^{C,v}=F_f^{C,\rho}\overline{\mathbf{v}}_f=F_f^{C,\rho}\left(\curlywedge\overline{\mathbf{v}}_P+(1-\curlywedge)\overline{\mathbf{v}}_N-\dfrac{1}{8}(\mathbf{d}\otimes\mathbf{d})\nabla^2\overline{\mathbf{v}}\right), \end{cases} \tag{3}$$

where $1/6\,\upsilon(\mathbf{d}\otimes\mathbf{d})\nabla^3\overline{\mathbf{v}}$ and $-1/8(\mathbf{d}\otimes\mathbf{d})\nabla^2\overline{\mathbf{v}}$ represent the leading-order truncation errors. The Eqs. (2) can be decoupled by combining (2_1) and (2_2) into a Poisson equation for $\overline{p}$, that is solved together with (3_2). The scalar equations are usually solved sequentially, with iteration over the explicit source terms to obtain rapid convergence.

3 Monotonically Integrated Large-Eddy Simulation

The task of formulating computational fluid dynamics models involves both numerical and physical tradeoffs and the accuracy of the model is not better than its weakest part. With this regard it is important to consider not only physical and numerical aspects but also their combined effects. Sophisticated SGS models and advanced numerical methods have been developed for LES and successfully applied to different flow problems, but not very often has the overall computational model, i.e., the modified equations, been used as basis for improved LES. Although the history of MILES draws on the development of shock-capturing schemes, [15], the concept of MILES, as developed in [22–24], attempts to embody a computational procedure for solving the NSE as accurately as possible using built-in, or implicit, SGS models. Because of the anisotropic features of the SGS modeling in MILES, [23], with possibilities of simultaneously handling flow and grid anisotropies, this may provide a better approach for inhomogeneous turbulent flows.

As compared to conventional LES, where the SGS effects are represented by explicit SGS models, MILES uses the features of particular numerical methods to construct implicit SGS models by means of the leading order truncation error, [23]. By incorporating

a sharp velocity-gradient capturing capability operating at the smallest resolved scales, with MILES we seek to emulate (near the cutoff), the high wave number end of the inertial subrange region—characterized by thin filaments of intense vorticity embedded in a background of weak vorticity, [6–11,23,38]. MILES draws on the fact that finite difference, volume and element methods filter the NSE over cells Ω_P, with typical dimension $|\mathbf{d}|$—using a top-hat shaped kernel $f_P=(1/\delta V_P)\int_{\Omega_p} f dV$. In the FV context the semi-discretized MILES equations can be obtained from the NSE using Gauss' theorem, viz.,

$$\begin{cases} \dfrac{\beta_i \Delta t}{\delta V_P}\displaystyle\sum_f [F_f^{C,\rho}]^{n+i}=0, \\ \displaystyle\sum_{i=0}^{m}\left(\alpha_i(\mathbf{v})_P^{n+i}+\frac{\beta_i\Delta t}{\delta V_P}\sum_f [\mathbf{F}_f^{C,v}+\mathbf{F}_f^{D,v}]^{n+i}\right)=-\beta_i(\nabla p)_P^{n+i}\Delta t+\beta_i(\mathbf{f})_P^{n+i}\Delta t, \end{cases} \tag{4}$$

where $F_f^{C,\rho}=(\mathbf{v}\cdot d\mathbf{A})_f$, $\mathbf{F}_f^{C,v}=(\mathbf{v}\cdot d\mathbf{A})_f\mathbf{v}_f$ and $\mathbf{F}_f^{D,v}=(v\nabla\mathbf{v})_f d\mathbf{A}$ are the convective and viscous fluxes. To complete the discretization, all fluxes at face f need to be reconstructed from the dependent variables at adjacent cells. This requires flux interpolation for the convective fluxes and difference approximations for the inner derivatives in the other fluxes. Given (4) the methods available for constructing implicit SGS models by means of the leading order truncation errors are generally restricted to nonlinear "high-resolution" methods for the convective fluxes $\mathbf{F}_f^{C,v}$ and $F_f^{C,e}$, in order to maintain second-order accuracy in smooth regions of the flow, [39]. The term high-resolution applies to methods that are at least second-order accurate on smooth solutions and yet give well-resolved, nonoscillatory discontinuities. In addition, these schemes are required to provide a leading order truncation error that vanishes as $\mathbf{d}\to\mathbf{0}$, so that it remains consistent with the NSE and the conventional LES model (1). There are a wide variety of approaches that can be taken, e.g., [37,40], but here we will focus on flux-limiting/correcting methods.

Here we introduce a flux-limiter Γ to combine a high-order convective flux-function $\mathbf{v}_f^H$ that is well behaved in smooth flow regions, with a low-order dispersion-free flux-function $\mathbf{v}_f^L$, being well behaved near sharp gradients, so that the total flux-function becomes $\mathbf{v}_f=\mathbf{v}_f^H-(1-\Gamma)[\mathbf{v}_f^H-\mathbf{v}_f^L]$. Typically, $\mathbf{v}_f^H$ is obtained from linear or cubic interpolations resulting in second or fourth-order accurate central schemes, respectively, while $\mathbf{v}_f^L$ is obtained from an upwind-biased piecewise constant approximation, i.e.,

$$\begin{cases} \mathbf{F}_f^{C,v,H}=F_f^{C,\rho}\left[\lambda\mathbf{v}_P+(1-\lambda)\mathbf{v}_N-\dfrac{1}{8}(\mathbf{d}\otimes\mathbf{d})\nabla^2\mathbf{v}+\ \ldots\right], \\ \mathbf{F}_f^{C,v,L}=F_f^{C,\rho}[\beta^+\mathbf{v}_P+\beta^-\mathbf{v}_N+(\beta^+-\beta^-)(\nabla\mathbf{v})\mathbf{d}+\ \ldots]; \end{cases}$$

$$\beta^{\pm}=\frac{1}{2}(\mathbf{v}_f\cdot d\mathbf{A}\pm|\mathbf{v}_f\cdot d\mathbf{A}|)/|\mathbf{v}_f\cdot d\mathbf{A}|, \tag{5}$$

where λ is the distance function, and $-1/8(\mathbf{d}\otimes\mathbf{d})\nabla^2\mathbf{v}$ and $(\beta^+-\beta^-)(\nabla\mathbf{v})\mathbf{d}$ are the leading order truncation errors. The flux limiter Γ is to be formulated as to allow as much as possible of the correction or anti-diffusion term $[\mathbf{v}_f^H-\mathbf{v}_f^L]$ to be included without increasing the variation of the solution—e.g., to comply with the physical principles of causality, monotonicity and positivity (when applicable), [22], and thus to preserve the properties of the NSE.

To see the effects of this convection discretization we consider the modified equations corresponding to the semi-discretized Eq. (4) with the flux-functions (5) for the viscous, diffusive, auxiliary and convective fluxes, respectively,

$$\begin{cases} \nabla\cdot\mathbf{v}=0, \\ \partial_t(\mathbf{v})+\nabla\cdot(\mathbf{v}\otimes\mathbf{v})=-\nabla p+\nabla\cdot\mathbf{S}+\mathbf{f}+\nabla \\ \cdot\left(\mathbf{C}\mathbf{L}^T+\mathbf{L}\mathbf{C}^T+\chi^2\mathbf{L}\mathbf{d}\otimes\mathbf{L}\mathbf{d}+\dfrac{1}{6}v(\mathbf{d}\otimes\mathbf{d})\nabla^3\mathbf{v}\right), \end{cases} \tag{6}$$

where $\mathbf{C}=\chi(\mathbf{v}\otimes\mathbf{d})$ and $\chi=1/2(1-\Gamma)(\beta^--\beta^+)$. As compared to the NSE the discretization has introduced additional dissipative and dispersive terms, from which we identify the implicit SGS term,

$$\mathbf{B}=\mathbf{C}\mathbf{L}^T+\mathbf{L}\mathbf{C}^T+\chi^2\mathbf{L}\mathbf{d}\otimes\mathbf{L}\mathbf{d}. \tag{7}$$

The implicit SGS stress tensor can be split into $\mathbf{B}^{(1)}=\mathbf{C}\mathbf{L}^T+\mathbf{L}\mathbf{C}^T$ and $\mathbf{B}^{(2)}=\chi^2(\mathbf{L}\mathbf{d}\otimes\mathbf{L}\mathbf{d})$, in which the former is a tensor-valued eddy-viscosity model, while the latter is of a form similar to the SSM part in the mixed model, [35]. This decomposition is also attractive considering the decomposition into rapid and slow parts, [41]. In MILES, the rapid part that cannot be captured by isotropic models relates to $\mathbf{B}^{(2)}$, while the slow part relates to $\mathbf{B}^{(1)}$. Borue and Orszag, [42], have shown that a $\mathbf{B}^{(2)}$ type term improves the correlations between the exact and modeled SGS stress tensor. A closely-related view supporting the suitability of the implicit SGS modeling thus enforced has been recently given, [43]; the suggestion is that the leading order truncation error introduced by nonoscillatory finite volume schemes represents a physical flow regularization term, providing necessary modifications to the governing equations that arise when the motion of finite volumes of fluid over finite intervals of time is considered.

The challenge is to identify features that must be built into the flux limiters, and thus into the numerical schemes, to achieve desirable physical properties in the associated implicit SGS modeling, such as frame indifference, realizability, symmetry and non-negative dissipation of SGS kinetic energy. In previous work, [22], we outlined a formalism providing mathematical and physical constraints which can be used as guideline in choosing flux-limiters—a choice similar to that of choosing an SGS model in the context of conventional LES. Detailed properties of the implicit SGS model are related to the flux limiter Γ, which in turn depends on the specifics of the numerical scheme. Seeking to characterize these features, we consider a one-dimensional continuity equation $\partial_t(\rho)+\partial_x(\rho v)=0$, with $v>0$. Discretization using the FV method and the flux-limiter formulation $\rho_f=\rho_f^H-(1-\Gamma)[\rho_f^H-\rho_f^L]$ yields

$$\begin{aligned}\rho_P^{n+1}&=\rho_P^n-v\left[\left(1-\frac{1}{2}\Gamma_{P-1/2}\right)\delta\rho_{P-1/2}^n-\frac{1}{2}\Gamma_{P+1/2}\delta\rho_{P+1/2}^n\right] \\ &=-C\,\delta\rho_{P-1/2}^n+D\,\delta\rho_{P+1/2}^n,\end{aligned} \tag{8}$$

where $\delta\rho_{P-1/2}^n=\rho_P^n-\rho_{P-1}^n$, $\delta\rho_{P+1/2}^n=\rho_{P+1}^n-\rho_P^n$ and $v=v\Delta t/\Delta x$ is the Courant number. Following Harten [44], a method of this form is total variation diminishing (TVD), i.e., $TV(\rho^{n+1})\leqslant TV(\rho^n)$, where $TV(\rho^n)=\Sigma_P|\rho_{P+1}^n-\rho_P^n|$ is the total variation, if and only if $C\geqslant 0$, $D\geqslant 0$ and $C+D\leqslant 1$. Assuming that the flux limiter can be expressed as $\Gamma=\Gamma(r)$, in which $r=\delta\rho_{P-1/2}^n/\delta\rho_{P+1/2}^n=(\rho_P^n-\rho_{P-1}^n)/(\rho_{P+1}^n-\rho_P^n)$ is the ratio of consecutive gradients, these inequalities are simultaneously satisfied if and only if,

$$0 \leqslant |\Gamma(r), \quad \Gamma(r)/r| \leqslant 2. \tag{9}$$

To reach second-order accuracy we further require that $\Gamma(1)=1$ and that Γ be Lipschitz continuous in r. It is helpful to examine the significance of the constraint (10) graphically in Fig. 1 (see also [45]), where a trace lying above another (e.g., "superbee" relative to "minmod") is associated with a less diffusive scheme. The TVD constraints are satisfied within the shaded area in Fig. 1, where we have chosen to locate the intermediate van Leer limiter and the border-line minmod and superbee limiters; also indicated in Fig. 1, are the useful r-independent limiting reference cases—the first-order upwind (UD, $\Gamma=0$) and the second-order central difference (CD, $\Gamma=1$) schemes. Unfortunately, this kind of comparative analysis cannot be readily extended to include all possible flux limiters of interest for MILES—e.g., FCT and PPM, for which the corresponding Γ's are not expressible as function only of the ratio r. Various other constraints can be imposed on the overall scheme, depending on the computational model requirements. If the scheme can be expressed as $\rho_P^{n+1} = H(\rho_{P-k}^n, \rho_{P-k+1}^n, \ldots, \rho_{P+k}^n)$, the most common constraints are

- monotonicity, $\partial H/\partial \rho_j^n \geqslant 0$ for all $P-k<j<P+k$,
- 1_1-contraction, $\|\rho_P^{n+1} - \tilde{\rho}_P^{n+1}\|_1 \leqslant \|\rho_P^n - \tilde{\rho}_P^n\|_1$, where ρ and $\tilde{\rho}$ are solutions to the same equation with different initial data, and where $\|\cdot\|_1$ denotes the 1_1-norm,
- monotonicity preservation, i.e., if $\rho_P^0 \geqslant \rho_{P+1}^0$ then $\rho_P^n \geqslant \rho_{P+1}^n$ for all P and n.

It is evident that a monotone method is also 1_1-contracting, and thus TVD, which implies that the scheme is monotonicity preserving. On the other hand, it can be verified that the first-order upwind scheme (being first-order TVD) is not necessarily monotone. In contrast with the global constraints imposed by TVD methods, weaker constraints result from requiring that a dependent variable should be instantaneously and locally monotone preserving. Because of their inherently less-diffusive nature, local monotone constraints are more attractive choices in developing MILES schemes. Based on our accumulated experience, monotone and 1_1-contracting methods are generally too diffusive, whereas some TVD methods (e.g., the superbee limiter, [46]) together with most monotonicity preserving methods (e.g., FCT, PPM, and GAMMA, [47]) work well for MILES. In order to illustrate this, we show, in Fig. 2, results from MILES of fully developed turbulent channel flow at a friction velocity based Re number of $\mathrm{Re}_t=395$. Included are also the DNS results, [48]. The computational details will be described in Section 5. From this comparison it is evident that the van Leer limiter is too diffusive, producing poor velocity profiles, while both FCT and GAMMA produce velocity profiles that agree well with the reference DNS data.

4 Inhomogeneous Free Flows

FCT-based MILES of free shear flows have been extensively compared with laboratory flows in various different shear flow configurations at moderately high Re numbers. Recent studies of forced and decaying homogeneous isotropic turbulence, [23,24], and studies of subsonic, [49,50] and supersonic, [51,52], jet flows demonstrated that MILES can be successfully used to simulate (and elucidate) the governing features of the unsteady vortex dynamics.

A representative example of the MILES jet studies is shown in Fig. 3. Figure 3(*a*) illustrates the axis-switching and bifurcation from visualizations of laboratory elliptical jets subject to strong excitation at the preferred mode, [53], compared to the results of carefully developed simulations designed to address unresolved issues of the vortex dynamics suggested by the laboratory studies. The key underlying aspects of the vortex ring bifurcation process were first demonstrated by the simulations, [49,50], including self-induced deformation, reconnection, bridging and threading—mechanisms which could not be captured by the laboratory visualizations. A path for transition to turbulence based on strong vortex interactions—partially shown on the right of Fig. 3(*b*), was also demonstrated; the cascade scenario involves "fusion" of the split rings to form a larger distorted ring followed by subsequent global self-deformation and axis-switching, additional reconnections and shedding of (predominantly axial) vorticity in its wake, and more contorted (and azimuthally unstable) split rings. There are different interesting possibilities for how the jet flow develops, depending on the particular jet initial conditions (see, e.g., Fig. 3(*c*)), the nozzle geometry and modifications introduced at the jet exit, the types of unsteady vortex interactions initiated, as well as local transitions from convectively to absolutely unstable flow. This is of interest in the context of improving the mixing of a jet (or plume) with its surroundings in many practical applications.

Jet noise generation, for example, is associated with mixing of the turbulent jet exhaust with the entrained ambient flow. The active noise producing regions in a high-speed jet are characterized by two distinct well-separated components (see [54] and references therein). The lower-k radiation component is associated with inherently inviscid mechanisms involving large-scale vortical coherent structures (CS) (e.g., [55]) and dominates in the downstream directions of the jet; the higher k component is more isotropic, it is associated with the finer-scale turbulent mechanisms, and dominates on the sidelines and upstream directions. Presently used practical hybrid approaches consider the jet aeroacoustics computation as consisting of two parts: nonlinear sound generation and linear (far-field) sound propagation, [56]. As noted in [54], the particular features of the relevant turbulent energy spectrum in the noise-producing region of high-speed jets directly supports the prospect of performing simulation of the noise-generating near and midfield regions of the jet with LES; the appropriate LES approach would use an LES cutoff wavelength suitably chosen between the peaks in the energy spectrum—so that large scales of the near and midjet flow can be simulated, and less-demanding (more universal) accounting of the small-scale flow features can be undertaken by using suitable SGS models.

The contribution of CS to jet noise can be related directly to the CS dynamics (Fig. 4). Based on the database generated with MILES, the basic features of acoustic radiation generated by vortex rollup and pairing in the shear layer could be captured, and used to demonstrate global instabilities in convectively unstable subsonic shear flow, [57]; features captured with MILES included, the quadrupole pattern associated with vortices, the significantly more intense dilatation and pressure fluctuations associated with vortex pairing, and the very low characteristic fluctuation level (e.g., three to four orders of magnitude smaller than ambient values), [52,57]. Complex mechanisms occurring when vortex ring structures break down, e.g., involved in vortex ring bifurcation discussed above, have been hypothesized, [58], to be responsible for most of the jet noise. Carefully executed simulations may be used to isolate the assumed dominant three-dimensional vortex dynamical processes in the jet regions where most of the sound generation is believed to occur. Of particular interest, is to address the sensitivity of these mechanisms to modifications in the initial conditions that can significantly affect the Kelvin-Helmholtz instabilities as well as local transitions from convectively to absolutely unstable flow.

Accurate resolution of the very small characteristic fluctuation levels associated with acoustical radiation from the jet represents a major computational challenge: dispersiveness of the numerical algorithm should be minimized to ensure good modeling of the acoustical propagation properties of the small wavelengths, [59], and because of the very small energy of the acoustic field as compared to that of flowfield, there is a potential for spurious sound sources due to numerical discretization. Conventional numerical schemes used in these kind of simulations are thus required to provide high-order accuracy—at least fourth-order in space and second-order in time, [59]. Because of the tensorial

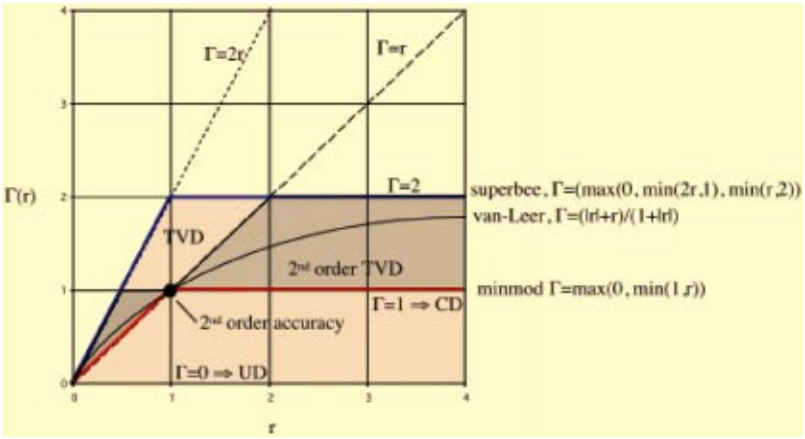

Fig. 1 TVD regions for first and second accurate TVD schemes together with selected limiters

nature of its implicit SGS model, and the inherently low numerical diffusion involved, the use of flux-limiting in MILES offers an overall effective computational alternative to conventional SGS models when seeking refined LES for inhomogeneous turbulent flows as required in this context. Flux-limiting schemes are more accurate than comparable conventional schemes; FCT as used here, for example, is second-order accurate in amplitude and fourth-order phase accurate [15], based on its formal properties in smooth regions (where the higher-order scheme is active), while the concept of accuracy based on Taylor series is actually meaningless near discontinuities (where the lower-order scheme is active).

5 Near-Wall Flow Physics and Modeling

LES of wall-bounded flows becomes prohibitively expensive at high Re numbers if one attempts to resolve the small but dynamically important eddies in the near-wall region. These structures can be captured in so-called wall-resolved LES with $\Delta y^+ < 2$, $\Delta x^+ < 200$, and $\Delta z^+ < 30$, in the wall normal, streamwise, and spanwise directions, respectively. Here, the superscript "+" denotes the inner-scale nondimensionalization utilizing the viscous length scale, $\lambda_\tau = \upsilon / u_\tau$, and the friction velocity, $u_\tau = \tau_w^{1/2}$, where the wall-shear stress is defined by $\tau_w = \upsilon (\partial v / \partial y)|_w$, so that $\mathbf{x}^+ = \mathbf{x} u_\tau / \upsilon$ and $\mathbf{v}^+ = \mathbf{v} / u_\tau$. The number of grid points required scales with the square of the friction Re number, i.e., $N \propto \mathrm{Re}_\tau^2$, which is nearly the same as for DNS; here, $\mathrm{Re}_\tau = u_\tau \delta / \upsilon$ and δ is the boundary layer thickness, which is used as outer length-scale for wall-normal nondimensionalization. To circumvent this severe resolution requirement, the subgrid models can either be modified to accommodate integration all the way to the wall, or one may try to introduce explicit wall models, or subgrid simulation models may be developed. In all these methods, LES is conducted on a relatively coarse grid designed to resolve the desired outer flow scales. When using separate wall models, the dynamic effects of the energy-containing eddies in the wall layer (viscous and buffer regions) are determined from a wall-model calculation, which provides to the outer flow LES with a set of approximate boundary conditions or parameters.

The simplest approach to circumvent the near-wall problem is

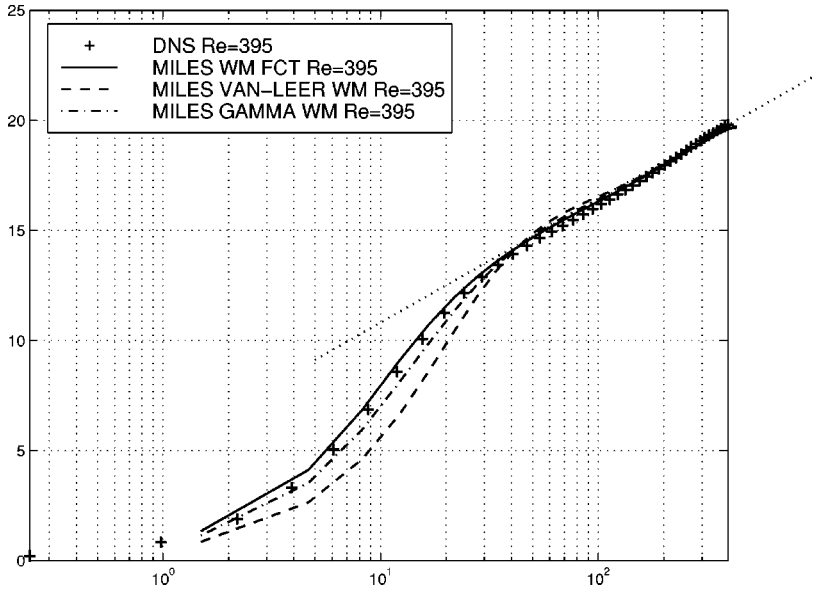

Fig. 2 Time-averaged (or mean) velocity profiles $\langle \bar{v}_1 \rangle$ normalized by the friction velocity $u_{\tau t}$ for fully developed turbulent channel flow at $\mathrm{Re}_t = 395$ from MILES using different flux-limiters

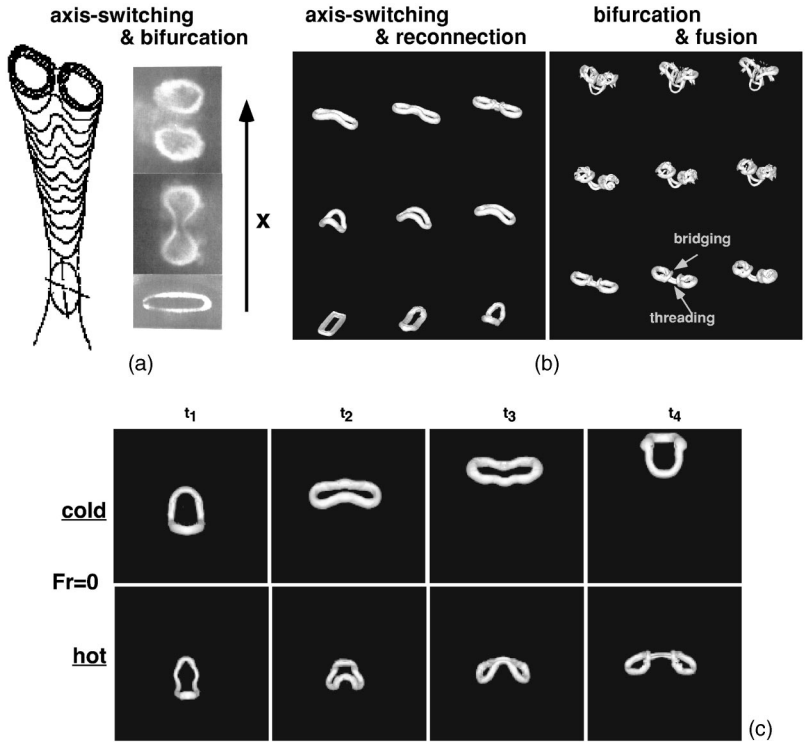

Fig. 3 Flow visualizations of vortex-ring bifurcation phenomena for AR=4 jets; (*a*) elliptic cold jets (laboratory), [53] and (*b*) rectangular cold jets (MILES), [50]. The flow direction is from bottom to top and time-sequences progress from left to right, in the numerical visualizations (based on isosurfaces of the vorticity magnitude); (*c*) sensitivity of vortex ring dynamics to jet initial conditions ($T_j/T_a=1$ in "cold" case, and $T_j/T_a=5$ in "hot" case); Re=Γ>90,000, and $M=0.6$, based on the circulation Γ of the initial vortex rings and transient jet velocity.

to modify the subgrid models using: (i) damping functions, D, so that $v_k=Dv_k$, where typically $D=(1-\exp(-(\beta y^+)^3))^{1/2}$, [1], (ii) dynamic procedures, [60], to determine the model coefficients (c_D, c_k and c_ε) in a subgrid eddy-viscosity model, (iii) models for the eddy-viscosity coefficients (c_D, c_k, and c_ε) that include viscous subrange effects, Voke, [61], or (iv) SGS models with structural sensors, Sagaut, [62]. These methods are, however, not believed useful for high Re number complex flows.

The simplest wall models are based on analytical expressions for the wall shear stress τ_w, which are analogous to the wall

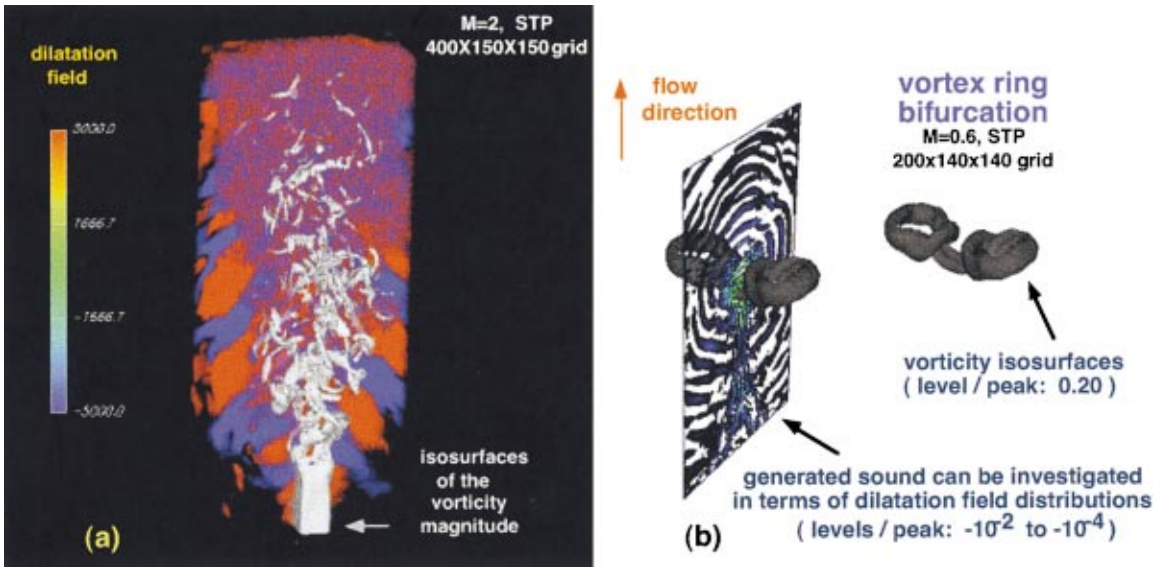

Fig. 4 Near-field MILES simulations of vortex-ring dynamics and associated sound generation in free jets emerging from rectangular nozzles, [51]; instantaneous visualizations: (*a*) unforced supersonic jet with AR=2, (*b*) axially forced subsonic jet with AR=4

Table 1 Nominal characteristic parameters for fully developed channel flow

	Grid	Re_τ	y^+	U_m/u_τ	C_f	Δx_3^+
DNS, [48]	$256^2\times160$	395	<1	17.47	$6.55e^{-03}$	100
MILES	60^3 (90^3)	390 (394)	2–10 (1–7)	17.4 (17.7)	$6.4e^{-03}$ ($6.6e^{-03}$)	110(105)
MILES+WM	60^3	391	2–10	17.5	$6.5e^{-03}$	107
OEEVM	60^3 (90^3)	391 (390)	2–10 (1–7)	17.6 (17.3)	$6.7e^{-03}$ ($6.5e^{-03}$)	106(113)
OEEVM+WM	60^3 (90^3)	393 (394)	2–10 (1–7)	17.2 (17.5)	$6.1e^{-03}$ ($6.3e^{-03}$)	107(105)
EXP, [69]		2030				
MILES	60^3 (90^3)	2048 (2036)	1–10 (1–7)	18.4 (18.8)	$4.6e^{-03}$ ($4.9e^{-03}$)	225(146)
MILES+WM	60^3	2034	1–10	18.6	$4.7e^{-03}$	231
OEEVM	60^3 (90^3)	2045 (2019)	6–14 (3–10)	18.3 (18.7)	$4.3e^{-03}$ ($4.6e^{-03}$)	249(136)
OEEVM+WM	60^3 (90^3)	2024 (2041)	6–14 (3–10)	18.4 (18.6)	$4.4e^{-03}$ ($4.8e^{-03}$)	243(138)
		10000				
MILES+WM	60^3	10098	25–40	19.4	$4.1e^{-03}$	743
OEEVM+WM	60^3	10112	25–40	19.8	$4.3e^{-03}$	678

functions commonly used in RANS calculations. They provide an algebraic relationship between the local wall stresses and the tangential velocities at the first off-wall velocity nodes, e.g., Grötzbach [63], and Piomelli et al. [64]. These algebraic models all imply the logarithmic law of the wall for the time-averaged velocity, which is not valid in many complex flows. To incorporate more physics into the model, wall models based on the boundary layer approximations have been proposed in recent years, Cabot and Moin [65]. In these models, turbulent boundary layer equations are solved on an embedded near-wall grid to compute τ_w, using a mixing length model. Reasonable success has been achieved in predicting attached flows and flows with fixed separation points, e.g., the backward-facing step flow. However, the model parameters have to be adjusted from the ordinary RANS values in order to obtain accurate results. We here propose to determine (locally) the friction velocity u_τ from

$$\begin{aligned} v_y^+ &= y^+ \quad \text{if} \quad y^+ \leqslant 11.225 \quad \text{and} \\ v_y^+ &= \kappa^{-1}\ln(y^+) + B \quad \text{if} \quad y^+ > 11.225. \end{aligned} \tag{10}$$

The approximate wall boundary condition can be implemented by adding a subgrid wall-viscosity v_{BC} to the molecular viscosity v on the wall so that the effective viscosity becomes

$$\begin{aligned} v + v_{BC} &= \tau_w/(\partial v_y/\partial y)_P = u_\tau^2 y_P/v_{y,P} = u_\tau y_P/(v_{y,P}/u_\tau) \\ &= u_\tau y_{y,P}/v_{y,P}^+, \end{aligned} \tag{11}$$

where the superscript P denotes that the quantity is to be evaluated at the first grid point away from the wall. The calculation of u_τ is performed (locally) by a Newton-Raphson algorithm.

A further, more advanced category is based on a "grid within the grid" approach, [66,67], in which simplified one-dimensional momentum equations are solved on a one-dimensional grid, aligned with the wall-normal embedded into the LES grid.

5.1 LES and MILES of Fully Developed Turbulent Channel Flows. To investigate MILES for wall-bounded flows we start by examining fully developed turbulent flows in a channel confined between two parallel plates at a distance $2h$ apart, where h is the channel half-width. The flow is driven by a constant mass flow in the streamwise ($\mathbf{e}_1$) direction defining the mean velocity $\langle\overline{\mathbf{v}}\rangle$. No-slip conditions are imposed in the cross-stream ($\mathbf{e}_2$) direction and periodic conditions are used in the spanwise ($\mathbf{e}_3$) direction. As initial conditions we use a parabolic velocity profile with 5% Gaussian white noise. After reaching a statistically steady state the simulations were continued for another $40\cdot h/u_\tau$ time units to obtain statistics. We study three cases with target Re numbers of Re_τ=395, 2030, and 10,000, for which data is available, from DNS, [48,68], and experiments, [69], respectively. The size of the channel is $6h\times2h\times3h$ in the streamwise, cross-stream, and spanwise directions. To analyze the effects of resolution two grids of 90^3 and 60^3 cells were employed, having uniform spacing in the $\mathbf{e}_1$ and $\mathbf{e}_3$-directions and geometrical progression is used in the $\mathbf{e}_2$-direction to concentrate the grid towards the walls.

In Table 1 the parameters of the channel flow simulations are presented—following standard practice $U_m = 1/2\int_{-1}^{1}(\overline{v_1})d(x_2/\delta)$ is the mean velocity, $\mathrm{Re}_\tau = u_\tau\delta/v$ the Re number and $C_f = \tau_w/1/2\overline{\rho}U_m^2$ the skin-friction coefficient. These are all in acceptable agreement with DNS and the experimental data, [70]. The influence of the subgrid model on U_m, Re_τ, and C_f is small when the grid spacing in the near-wall region is below about $y^+<5$, but this is impossible to maintain as Re increases. When increasing Re without refining the grid this results in an underprediction of τ_w and thus of u_τ and C_f, that motivates the use of wall models, which compensates for the lack of resolution by incorporating more physics and particularly a correct value of τ_w. At Re_τ=395 the mean streak spacing Δx_z^+, is properly resolved and all simulations give results within 15% of the DNS data. At Re_τ=2030 and 10,000 the mean streak spacing is not resolved, and the predicted mean streak spacing is found to be between $2.0\,\Delta x_3^+$ and $2.5\,\Delta x_3^+$, which is representative of the smallest coherent structure that can be resolved. Considerable improvement on τ_w and C_f is achieved by using the wall model.

In Fig. 5 typical flow features in the lower half of the channel are shown in terms of vortex lines, contours of the streamwise vorticity on side and bottom walls, and an isosurface of the second invariant of the velocity gradient $Q = 1/2(\|\mathbf{W}\|^2 - \|\mathbf{D}\|^2)$. The regions enclosed within these structures are thus vortical regions with $\|\mathbf{W}\| > \|\mathbf{D}\|$. The location of a vortex line is given by the equation $d\mathbf{x}/ds = \boldsymbol{\omega}/|\overline{\boldsymbol{\omega}}|$, where s is the distance along the vortex line. This equation is integrated for $\mathbf{x}$ using a third-order Runge-Kutta method, and second-order linear interpolation is used to compute the vorticity from the grid points. By correlating isosurfaces of Q with the velocity distribution close to the wall it is found that vortices located above the low-speed streaks are repeatedly ejected away from the wall—as formerly found in experiments and DNS/LES studies, which produces hairpin vortices stretched by the ambient shear. It has been conjectured that in this ejection mechanism vorticity, produced in the vicinity of the wall, is convected into the boundary layer, making it turbulent. An interesting observation, also observed in DNS, is that the hairpins are asymmetric, with one leg (often the right leg) being stronger than the other. Moreover, it is evident that the spanwise resolution is more important for the coherent structure dynamics than the streamwise resolution, whereas the wall-normal resolution is important to predict the correct wall shear stress, which, however, also can be represented by a wall model. Although models based on experiments or simulations have been proposed, [71–73], the interpretation of low and high-speed streaks and their relation with the ejection mechanism are still not fully understood.

In Fig. 6 we show the mean-velocity profiles $\langle\overline{v_1}\rangle$ for the cases reported in Table 1, where, $\langle\cdot\rangle$ denotes combined spanwise,

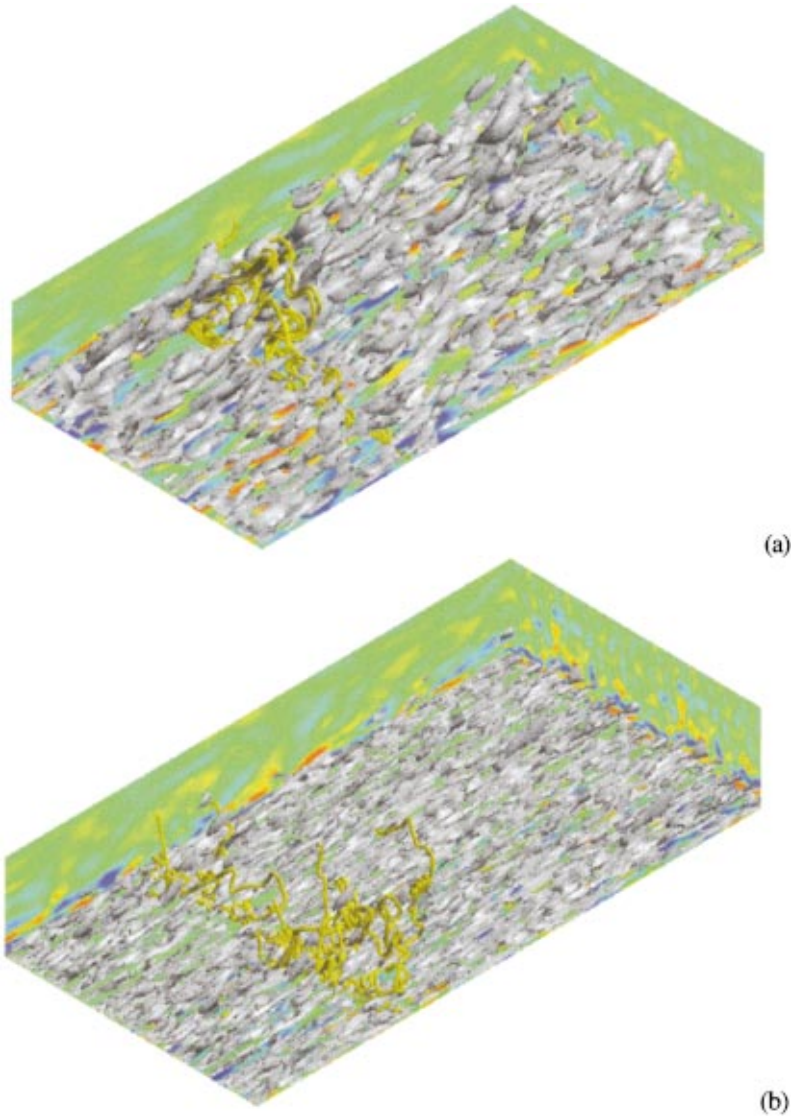

Fig. 5 Contours of streamwise vorticity projected onto the side and bottom walls, vortex lines and iso-surfaces for $Q=1$ for (*a*) MILES+WM at 60^3 resolution at $\mathrm{Re}_\tau=2030$ and (*b*) OEEVM+WM at 90^3 resolution at $\mathrm{Re}_\tau=2030$

streamwise and time averaging. For $\mathrm{Re}_\tau=395$ the $\langle\overline{v_1}\rangle$ profiles are in very good agreement with each other as well as with the DNS data, cf. [48,68], and the expressions $\langle v_1^+\rangle=x_2^+$ (for $x_2^+\leqslant 5$) and $\langle v_1^+\rangle=\kappa^{-1}\ln(x_2^+)+B$ (for $5<x_2^+<350$), where $\kappa=0.4$ and $B=5.2$, as included in Fig. 3(*b*). Differences attributed to gridding are small, and mainly limited to the buffer region ($5<x_2^+<50$), suggesting that the 60^3 grid is appropriate. For $\mathrm{Re}_\tau=2030$ the $\langle\overline{v_1}\rangle$ profiles show significant differences depending on how the wall region is handled. Good agreement with experimental data and analytical profiles is found when using a wall model (suffix WM in legends) or when the grid is sufficiently refined ($y^+<3$) towards the walls, otherwise large errors occur between $y^+=10$ and 100 as a result of the inadequate spanwise and wall-normal resolutions. Differences in $\langle\overline{v_1}\rangle$ due to explicit or implicit subgrid models are usually small, provided enough resolution or appropriate wall models are used. For $\mathrm{Re}_\tau=10{,}000$ the $\langle\overline{v_1}\rangle$ profiles using the wall model together with either OEEVM and MILES show good agreement with the analytical profiles dispite the fact that the first grid point on the 60^3 grid is at about $y^+=35$. Beyond about $y^+\approx 350$ a considerable fraction of the wake region is present in the $\mathrm{Re}_\tau=10{,}000$ profiles as expected.

In Fig. 7 we present the corresponding rms-velocity fluctuations $\overline{v_1}^{\mathrm{rms}}$ normalized by u_τ. In the core of the channel the $\overline{v_1}^{\mathrm{rms}}$ profiles are self-similar with respect to Re_τ. However, in the near-wall region, the peak values increase with increasing Re_τ as expected. For $\mathrm{Re}_\tau=395$ the agreement between LES, MILES, and DNS is satisfactory regardless of whether wall models are utilized or not. The difference between LES/MILES and DNS is below 7%, with the maximum error occuring close to the peaks (at $x_2^+\approx 15$) in $\overline{v_1}^{\mathrm{rms}}$. The difference between LES and MILES are generally small which is supported by previous studies, [24], using a wider range of subgrid models. For $\mathrm{Re}_\tau=2030$ the predicted $\overline{v_1}^{\mathrm{rms}}$ profiles are broader than the measured profile, [68], and the peaks occur at $x_2^+\approx 40$, whereas in the data they occur at $x_2^+\approx 20$. This difference is consistent with the LES results of Moin and Kim [74], at $\mathrm{Re}_\tau=640$, reporting wider $\overline{v_1}^{\mathrm{rms}}$ profiles, having peaks at $x_2^+\approx 30$. This trend is further supported by the $\mathrm{Re}_\tau=10{,}000$ case, having the highest peaks values of $\overline{v_1}^{\mathrm{rms}}$ occurring at approximately $x_2^+\approx 60$.

Figure 8 shows the resolved Reynolds stress profiles $-\langle v_1' v_2'\rangle$, where $v_i'=\overline{v_i}-\langle\overline{v_i}\rangle$ represents the resolved velocity fluctuations, for all cases in Table 1. Based on evaluations of the shear stress

$-\langle v_1' v_2' \rangle + (1/\mathrm{Re}_\tau)(\partial \langle \overline{v_2} \rangle / \partial x_2)$ it is clear that the flow is in equilibrium, with the shear stress balancing the downstream pressure gradient in the regions away from the walls. The contribution of the (explicit or implicit) subgrid model is negligible far from the walls; however, in the viscous sublayer and in the buffer layer, the model contribution is comparatively large and differences between LES and MILES are found. In general, the (explicit or implicit) subgrid models tend to increase τ_w in the wall proximity, relative to a reference, whereas the wall model fixes τ_w according to the self-similar velocity distribution, i.e., $\langle v_1^+ \rangle = x_2^+$ for $x_2^+ \leq 5$ and $\langle v_1^+ \rangle = \kappa^{-1} \ln(x_2^+) + B$ for $5 < x_2^+ < 350$. For all values of Re_τ the best agreement with experimental or DNS data is obtained with OEEVM+WM, although the differences decrease with decreasing Re_t number, so that at $\mathrm{Re}_\tau = 395$ virtually no differences can be detected. The differences in Fig. 5 may be attributed to the effects of the (explicit or implicit) model, i.e., $\langle B_{12} \rangle$ and the resolvable part $-\langle v_1' v_2' \rangle$, implicitly affected by **B**. When the resolution is inadequate to resolve the mean streak spacing much of the dynamics in the near wall region is lost, which translates into poor predictions of $-\langle v_1' v_2' \rangle$. For the same resolution, but using a wall model, the predictions are improved, suggesting that correct prediction of τ_w is important for the overall flow and statistics. Finally, it is worth noticing that the peak shear stress $\langle v_1' v_2' \rangle + \langle B_{12} \rangle$ increases in magnitude and is closer to the wall as Re_τ increase. Since the maximum of $\langle v_1' v_2' \rangle + \langle B_{12} \rangle$ is not the same for each profile, it does not scale properly with the inner variables in the Re_τ number range examined, Wei and Willmarth [75], and Comte-Bellot [76].

6 Complex Flows

The main focus of the discussion in the previous sections has been on issues of SGS modeling in relatively simple idealized flows. Furthermore, boundary layer modeling issues have been also raised in the context of near-wall flow modeling. Important additional aspects of LES of high Re flows to be also addressed relate to the issues of boundary condition (supergrid) modeling, and overall computational model validation. From a practical point of view, it is of outmost importance to consider how the non-linear combination of all—algorithmic, physics-based, subgrid, and supergrid—aspects of the computational model affect the simulation of complex systems for which detailed DNS-type approaches are not possible and for which only limited experimental data might be available at best.

6.1 Supergrid Modeling. Supergrid modeling issues to be addressed in connection with numerical simulations involves (i) establishing suitable physical boundary conditions (PBC) emulating those in the laboratory or in practical applications—which are usually not known in sufficient detail, and ensuring the well-posedness of the governing system of partial differential equations; and (ii) specifying additional numerical boundary conditions consistent with the unsteady flow equations and imposed physical boundary conditions for closure of the discretized system of equations.

Open boundary conditions are required when only a portion of the flow can be investigated—as is frequently the case in laboratory experiments, where finite dimensions of the facilities are unavoidable. We must ensure that the presence of artificial open boundaries adequately bounds the computational domain without polluting the solution in a significant way, e.g., [77–79]. From the purely mathematical point of view, so-called *nonreflective* boundary conditions of various types have been proposed for hyperbolic equations, [80]. The general idea is to use knowledge on the mathematical solution outside of the computational domain to define conditions to minimize spurious reflections at artificial boundaries. These nonreflective conditions are generally non-local and can be either totally absorbing or allow for some *natural reflections* to occur. For example, natural reflections should be built into the outflow boundary conditions in the simulation of subsonic flows if we are to have emulation of feedback effects by which events assumed to virtually occur outside of the computational domain can effectively influence the flow inside.

Prescribing and enforcing wall boundary conditions presents also practical challenges. We must deal with viscous boundary layers that typically cannot be resolved by practical computational grids, and improved wall turbulence models that will capture the dominant details of the near-wall flowfield need to be developed. An additional difficulty involves the thermal wall boundary conditions that should be enforced in the simulations. Actual wall conditions in the laboratory experiments are typically not reported with sufficient detail, they lie in between the mathematically well-defined isothermal and adiabatic conditions, and they have a crucial role in determining the heat transport in the thermal boundary layer. For example, temperature fluctuation levels in the near-wall regions of isothermal and isoflux walls are known to be very different from each other in the nonreactive case, e.g., [81], and are likely to be much more pronounced when local temperature-dependent viscous effects due to chemical exothermicity are present.

Because of discretization, derivatives can only be approximated at the boundaries, and in order to ensure the closure of the discretized system of equations additional numerical boundary conditions need to be specified (NBC). The standard procedure is to introduce these new conditions by defining the behavior of the dependent variables at one or more extra rows of guard cells surrounding the computational domain. The NBC are clearly distinct from the discretized representations of the PBC required to uniquely define the solution of the nondiscretized fluid-dynamical problem. For hyperbolic equations for example, it is well known that the nth-order internal solution of the equations requires at least $(n\text{-}1)$th-order additional NBC to preserve the formal spatial accuracy of the calculations, [82]. The goal is to ensure that the expected flow behavior outside the computational domain be properly and *consistently* imposed on the solution inside, a requirement that is frequently overlooked. The consistency requirement demands that in the continuum limit the NBC be compatible with the flow equations and PBC, in such a way that they do not generate distinctly new boundary conditions thus over-specifying the fluid dynamical problem. However, this guideline is not sufficient to uniquely determine the NBC and some degree of ambiguity appears to be unavoidable, unless additional requirements are imposed.

For hyperbolic equations, a relatively simple framework for BC implementation can be based on focusing on the terms of the flow equations containing derivatives with respect to the (local) direction perpendicular to the (solid or open) boundary, [83,84]. These terms require special numerical treatment because they partially depend on incoming information from outside of the computational domain. Other terms in the flow equations not containing these derivatives, can be treated in the neighborhood of the boundary in the same way as inside the computational domain. Although limited due to its one-dimensional characteristic-analysis basis, [77], it offers a systematic approach, [78], to the problem of imposing PBC and NBC in practical simulations.

6.2 Flow Over a Backward Facing Step. An appropriate case for overall LES model validation studies, for which experimental data is available, is the combustion tunnel of Pitz and Daily [85,86]. This rig consists of a rectilinear channel (of height $2h$) followed by a contraction into one half of its height and continued by the step expansion into the test section, see Fig. 9. To examine the LES and MILES models we have undertaken simulations at a step-height Re number of $\mathrm{Re}_h = 22{,}000$, with two different inlet velocity profiles. The first of these is the uniform profile with value u_0, whereas the second is a flattened parabolic profile with mean-value u_0. The grids employed use $220 \times 32 \times 64$ nodes in the streamwise, spanwise and cross-stream directions, respectively. The cells are clustered towards the shear layer,

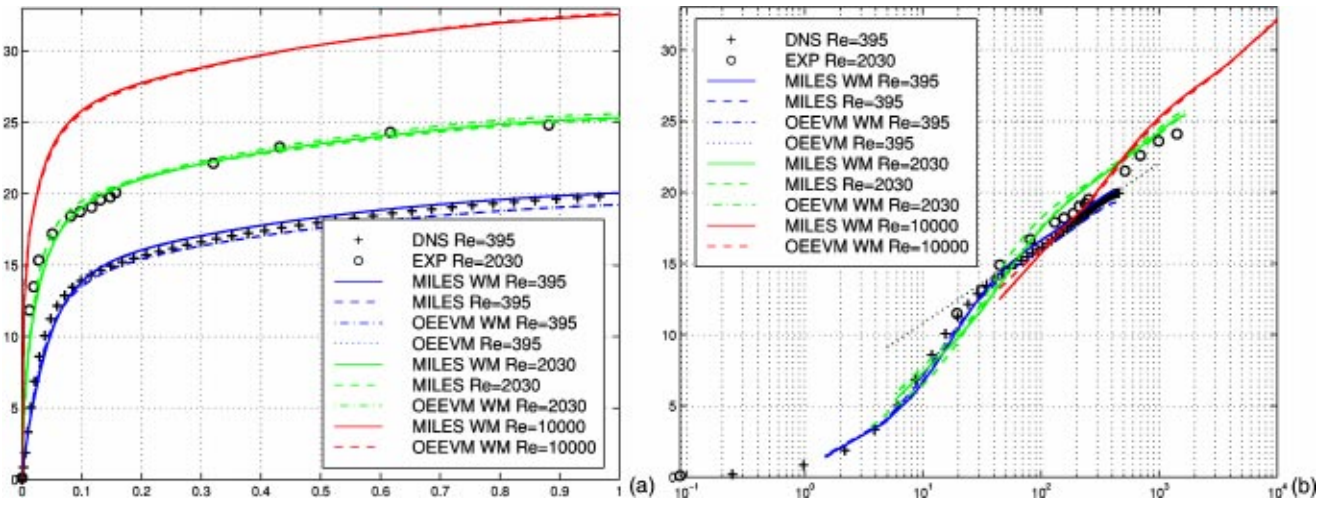

Fig. 6 Time-averaged (or mean) velocity profiles $\langle \overline{v_1} \rangle$ normalized by the friction velocity u_τ versus the wall-normal distance at Re_τ=395 (blue), Re_τ=2030 (green), and Re_τ=10,000 (red) for all channel flow cases reported in Table 1. Panel (*a*) represents outer scaling whereas panel (*b*) represents inner scaling.

developing from the step, and towards the upper and lower walls. The first node is placed either at $y^+ \approx 3$ or $y^+ \approx 15$ in order to illustrate the effects of the wall model, [87]. The simulations start from rest and the unsteady flow evolves naturally. At the inlet, $\overline{\mathbf{v}} = \overline{u}(y)\mathbf{e}_x$ and $\nabla \overline{p} \cdot \mathbf{e}_x = 0$, where $\overline{u}(y)$ is the given profile and $\mathbf{e}_x$ is the unit vector in the streamwise direction. At the outlet $(\nabla \overline{\mathbf{v}})\mathbf{e}_x = 0$ and $\overline{p} = p_0$, whereas at the upper and lower walls no-slip conditions are enforced. Periodic conditions are used in the spanwise direction. Table 2 presents the simulations and the values of some key parameters such as the recirculation length λ, and the Strouhal number $\mathrm{St} = fh/u_0$.

Figure 10 shows a perspective view of the flow in terms of isosurfaces of the second invariant of the velocity gradient tensor $Q = 1/2(\|\overline{\mathbf{W}}\| - \|\overline{\mathbf{D}}\|)$, where $\overline{\mathbf{W}} = 1/2(\nabla \overline{\mathbf{v}} - \nabla \overline{\mathbf{v}}^T)$ and $\overline{\mathbf{D}} = 1/2(\nabla \overline{\mathbf{v}} + \nabla \overline{\mathbf{v}}^T)$, at $Q = u_0/h$ in order to identify the characteristic vortical patterns and the evolution of the vortical structures. The initial laminar shear layer breaks up from Kelvin-Helmholtz, or KH, instabilities whereby the large coherent structures are formed. The quasi-two-dimensional KH vortices that shed of the step are influenced by merging, pairing and reconnection events as they are convected downstream under influence of vortex stretching due to the three-dimensional effects. Downstream of the step, for $x < 2h$, the flow consists predominantly of $\overline{\omega}_z$-vortices that are gradually transformed into longitudinal $\overline{\omega}_z$-vortices that characterize the flow in the remaining part of the flow domain. An imperious feature of this flow is the transformation of vorticity from spanwise $\overline{\omega}_z$-vortices into longitudinal $\overline{\omega}_z$-vortices. Based on animations of Q a possible scenario for the vortex dynamics can be that spanwise $\overline{\omega}_z$-vortices are shed of the step, and between about h and $3h$ downstream of the step these are exposed to helical pairing, and a mixed pattern of Ω and big Λ-vortices is formed. These vortices impinge on the lower wall and are either carried away downstream and transformed into arcs, or become trapped within the recirculation bubble. A consequence of the vortical flow is that the growth of the vortical structures with downstream dis-

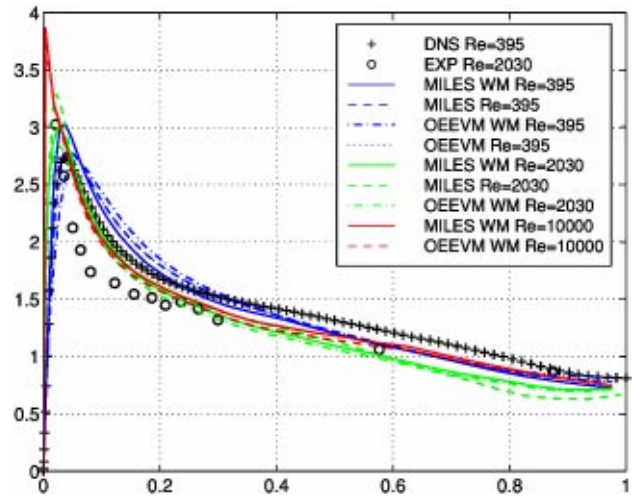

Fig. 7 Turbulent kinetic energy $\overline{v}_1^{rms}$, normalized by the friction velocity u_τ versus the wall-normal distance at Re_τ=395 (blue), Re_τ=2030 (green), and Re_τ=10,000 (red) for all cases reported in Table 1; outer scaling is used at the horizontal axis

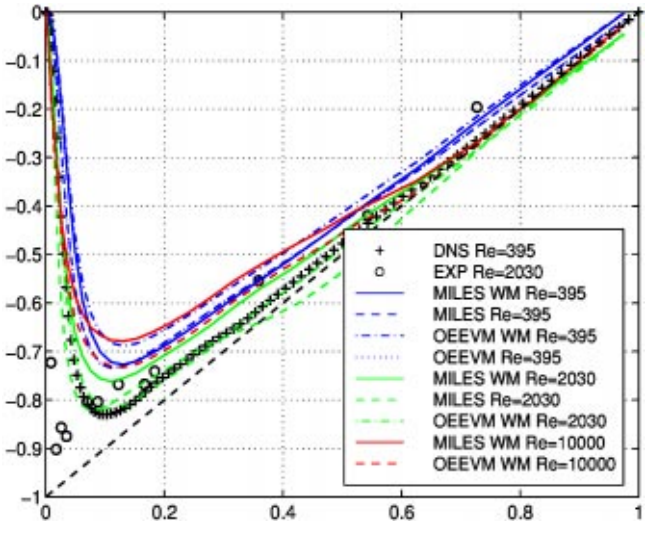

Fig. 8 Resolved Reynolds stress profiles $\langle v_1' v_2' \rangle$, normalized by the friction velocity u_τ versus the wall-normal distance at Re_τ=395 (blue), Re_τ=2030 (green), and Re_τ=10,000 (red) for all cases reported in Table 1; outer scaling is used at the horizontal axis

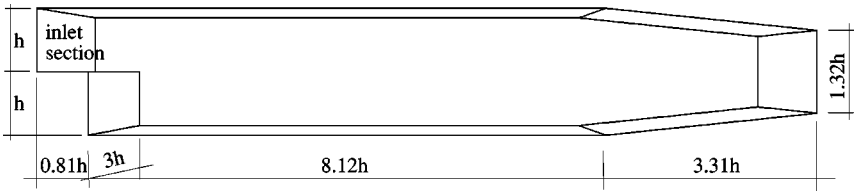

Fig. 9 Schematic of the Pitz-Daily backward-facing step configuration

tance from the step affects the recirculation region and the spreading-rate of the top boundary of the shear layer into the freestream.

Based on the statistics in Table 1, the length of the recirculation bubble, λ, and the Strouhal frequency, St, are well predicted. The differences due to choice of inlet velocity profile are somewhat larger than the differences due to subgrid model or the use of wall models. This illustrates the importance of proper supergrid modeling addressed earlier. In this specific case, no measurements were made upstream of the step—a fact that notably complicates the modeling, since proper inlet conditions have to be presumed. As illustrated in Fig. 11, this may affect the results.

Table 2 Nominal characteristic parameters for backward-facing step flow

	Grid	SGS Model	y^+	λ	St
Exp, [86]	—	—	—	7.3	0.23
Case I, $u(y)=u_0$	220×32×64	OEEVM	3	7.0	0.24
Case II, $u(y)=u_0$	220×32×64	OEEVM+WM	15	7.2	0.22
Case III, $u(y)=u_0$	220×32×64	MILES+WM	15	7.1	0.23
Case IV, $u(y)=f(y)$	220×32×64	OEEVM	3	6.8	0.25
Case V, $u(y)=f(y)$	220×32×64	OEEVM+WM	15	6.9	0.23
Case VI, $u(y)=f(y)$	220×32×64	MILES+WM	15	6.7	0.22

Figure 11 presents a comparison of the time-averaged streamwise velocity $\langle\overline{v}\rangle_x$ and its rms fluctuations $\overline{v}^x_{\rm rms}$ between LES with OEEVM, MILES and experimental data, [85]. For the $\langle\overline{v}\rangle_x$ profiles, good agreement with the experimental data is obtained only with the top-hat inflow velocity profile, with the flattened parabolic profile resulting in a too thick upper boundary layer. Furthermore, the maximum reverse velocity is somewhat underpredicted, i.e., $0.30u_0$ as compared to the experimental value of $0.33u_0$. Eaton and Johnston [88], report reverse velocities of $0.25u_0$, and the higher value observed in the predictions and in the experiments may be due to the lower aspect ratio or the effects of wall. The difference between MILES and LES predictions (using the OEEVM subgrid model) is virtually marginal. Similar results (in good agreement with experimental data) are obtained when using the high wall-normal resolution and no wall model, and when using the wall model in conjunction with the low wall-normal resolution. However, the results are less satisfactory when using the lower wall-normal resolution and no wall model (data not shown). Grid refinement, [87], gives virtually no improvement of the $\langle\overline{v}\rangle_x$ profiles, with the exception of a small increase in the peak reverse velocity. From the $\overline{v}^x_{\rm rms}$ profiles regions of intense turbulence are confined by the shear layer and spread as the shear layer widens downstream. At reattachment the turbulence decreases, and the rms profiles begin to take on the characteristics of fully developed turbulent channel flow. The position of the peak rms fluctuation initially coincides with the centerline, but drops towards the lower wall with downstream distance at the same time as the profiles broadens. The peak values of $\overline{v}^x_{\rm rms}$ increase at first due to the formation of large coherent structures, to stabilize around 20% of u_0, being in good agreement with experimental

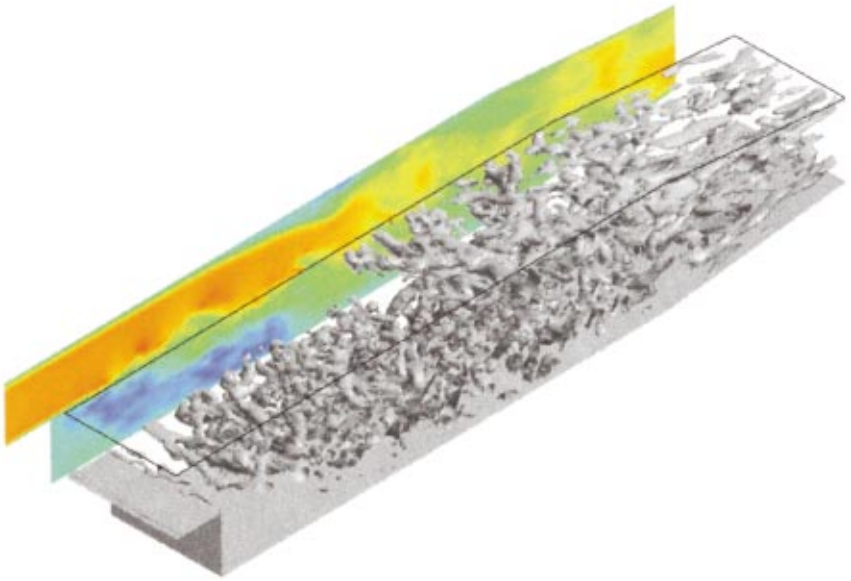

Fig. 10 Visualization of the flowfield for the nonreacting case using contours of the instantaneous streamwise velocity component at the centerplane and iso-surfaces of the second invariant, *Q*, of the velocity gradient tensor

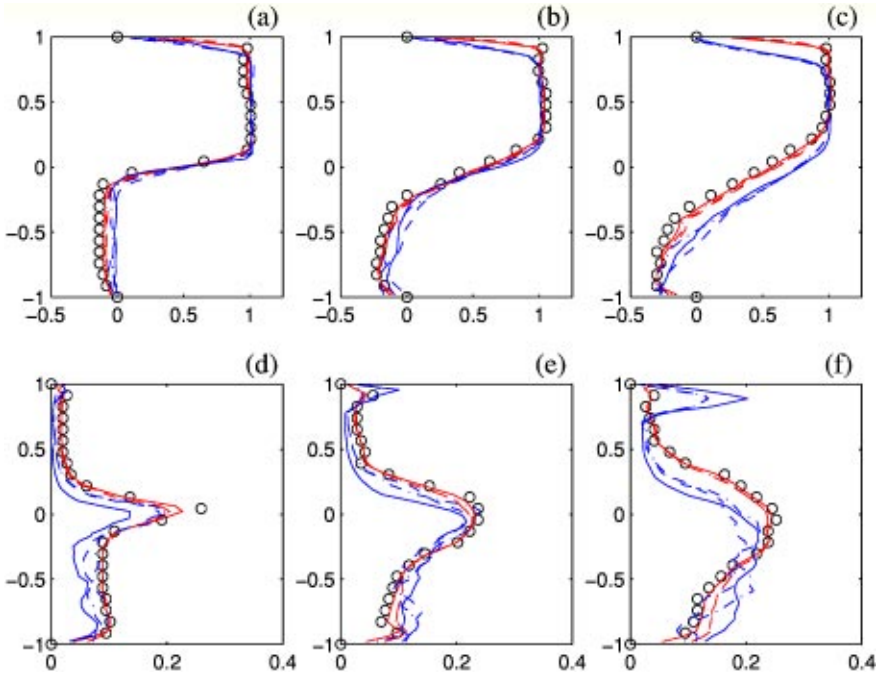

Fig. 11 First and second-order statistical moments of the streamwise velocity component, $\langle \bar{v} \rangle_x$ and $\bar{v}^x_{\rm rms}$, respectively. Panels (*a*) to (*c*) show $\langle \bar{v} \rangle_x$ at $x/h=1.0$, 2.0, and 3.0, respectively, whereas panels (*d*) to (*f*) show $\bar{v}^x_{\rm rms}$ at $x/h=1.0$, 2.0, and 3.0, respectively. Legend: (○) experiments, [86], (——) MILES+WM, (— — —) OEEVM+WM and (—·—·—·—) OEEVM. Red (darker) lines represent simulations using the top-hat inlet velocity profile, whereas blue (lighter) lines represent simulations using the flattened parabolic inlet velocity profile.

data, [85]. The agreement between measured and predicted $\bar{v}^x_{\rm rms}$ profiles drops with distance from the step, an observation that can be explained by the stretched grid used towards the end of the domain.

7 Concluding Remarks

In conventional LES, explicit SGS models are introduced for closure and to provide a mechanism by which dissipation of kinetic energy accumulated at high wavenumbers may occur. The MILES approach provides a promising practical alternative to conventional LES, involving the solution of the unfiltered NSE with high-resolution locally monotone algorithms by which the effects of the SGS flow physics on the GS flow are incorporated in the functional reconstruction of the convective fluxes. By incorporating a sharp velocity gradient capturing capability operating at the smallest resolved scales, MILES emulates (near the cutoff), the high wave number end of the inertial subrange region—characterized by thin filaments of intense vorticity embedded in a background of weak vorticity. A formal advantage of MILES is that no commutation errors are involved, since it uses no explicit filtering; this may, however, not be of practical consequence, since commutation errors can be lumped together with the explicit subgrid models. Because of the intrinsically anisotropic nature of the SGS modeling in MILES associated with the functional reconstruction, with possibilities of concurrently handling flow and grid anisotropies, we expect it may provide an optimal computational framework for inhomogeneous high Re complex flows.

Although the history of MILES draws on analogies with the development of shockcapturing schemes, the concept of MILES, as developed here and in our earlier work, [23,24], attempts to embody a general computational procedure for solving the NSE for high Re number flows as accurately as possible using built-in SGS models. We have chosen to emphasize the overall modeling aspects of LES based on the modified equations, which are rarely examined in this context. Analysis based on the modified equations can be used to study how the explicit SGS model terms compete with leading-order truncation errors resulting from the discretization. Likewise, the analysis can be used to address the extent to which the leading order truncation may provide an implicit SGS model when suitable computational methods are used. It is worth reiterating here that relying on arbitrary methods to emulate the additional required damping to achieve numerical stability will not necessarily provide the smooth transition to SGS's ensuring the correct distribution of energy on the resolved scales in general. We have used the modified-equations' analysis to show that a particular form of functional reconstruction—involving flux limiters—can be consistently regarded as an implicitly implemented LES approach, where choosing flux-limiters is effectively similar to choosing an SGS model in conventional LES.

The practical challenge is to identify features that should be built into the numerical methods, and the flux limiters in particular, to achieve desirable physical properties in the associated implicit SGS modeling. Detailed properties of the implicit SGS model are related to the flux limiter Γ, which in turn depends on the specific features of the numerical scheme—such as monotonicity, 1_1-contraction, and monotonicity preservation; we have illustrated how the latter properties can directly affect their potential in the MILES context.

Our previous results from the forced [23] and decaying [24] isotropic turbulence case show that (i) the influence of the (explicit or implicit) SGS model is important and (ii) that fairly good results can be obtained using both kinds of SGS models, provided that the numerical methods used are sufficiently accurate and only marginally affected by numerical diffusion and the Gibbs error. These trends have been also confirmed for the wall bounded (channel) flows investigated in the present and previous work, cf. [24]. Because in applications involving turbulent flows near walls much less universal properties are involved and characteristic

length scales of the most energetic eddies decrease, SGS models capable of handling simultaneous flow and grid anisotropy such as built in the MILES approach can be reasonably expected to provide an efficient computational procedure in this context. MILES can reproduce the first and second-order statistical moments of the velocity field almost as accurately as when using explicit, significantly more-complex SGS models, and better than isotropic eddy viscosity models—while being also very competitive computationally, [24]. We argue that this is due to the intrinsic nature of the MILES model, in which a nonlinear tensorial eddy-viscosity model is built into the algorithm, based on a carefully chosen functional reconstruction of the convective terms.

Acknowledgments

This research was performed with support from ONR through the NRL 6.1 Computational Physics task area. Computer time was provided by the DoD-HPC-MP program at NRL-DC.

References

[1] Sagaut, P., 2001, *Large Eddy Simulation for Incompressible Flows*, Springer-Verlag, Heidelberg.
[2] Lesieur, M., and Metais, O., 1996, ''New Trends in Large Eddy Simulations of Turbulence,'' Annu. Rev. Fluid Mech., **28**, p. 45.
[3] Fureby, C., Tabor, G., Weller, H., and Gosman, D., 1997, ''A Comparative Study of Sub Grid Scale Models in Homogeneous Isotropic Turbulence,'' Phys. Fluids, **9**, p. 1416.
[4] Metais, O., and Lesieur, M., 1992, ''Spectral Large Eddy Simulation of Isotropic and Stably Stratified Turbulence,'' J. Fluid Mech., **239**, p. 157.
[5] McComb, W. D., 1994, *The Physics of Fluid Turbulence*, Clarendon Press, Oxford.
[6] Kuo, A. Y., and Corrsin, S., 1971, ''Experiment on the Geometry of the Fine-Structure Regions in Fully Developed Turbulent Fluid,'' J. Fluid Mech., **56**, p. 447.
[7] Sigga, E. D., and Patterson, G. S., 1988, ''Intermittency Effects in a Numerical Simulation of Stationary Three Dimensional Turbulence,'' J. Fluid Mech., **86**, p. 567.
[8] Jimenez, J., Wray, A., Saffman, P., and Rogallo, R., 1993, ''The Structure of Intense Vorticity in Isotropic Turbulence,'' J. Fluid Mech., **255**, p. 65.
[9] Vincent, A., and Meneguzzi, M., 1994, ''The Spatial Structure and Statistical Properties of Homogeneous Turbulence,'' J. Fluid Mech., **225**, p. 1.
[10] Kerr, R. M., 1985, ''Higher Order Derivative Correlation and the Alignment of Small Scale Structures in Numerical Turbulence,'' J. Fluid Mech., **153**, p. 31.
[11] Ashurst, W. T., Kerstein, A. R., Kerr, R. M., and Gibson, C. H., 1987, ''Alignment of Vorticity of Scalar Gradients With Strain Rate in Simulated Navier Stokes Turbulence,'' Phys. Fluids, **30**, p. 2343.
[12] Misra, A., and Pullin, D. I., 1997, ''A Vortex Based Subgrid Stress Model for Large Eddy Simulation,'' Phys. Fluids, **9**, p. 2443.
[13] Bagget, J. S., Jiménez, J., and Kravchenko, A. G., 1997, ''Resolution Requirements in Large Eddy Simulations of Shear Flows,'' Ann. Res. Briefs, CTR, NASA Ames/Stanford University, p. 55.
[14] Jimenez, J., 1998, private communication; see also AIAA 98-2891.
[15] Boris, J. P., and Book, D. L., 1973, ''Flux Corrected Transport I, SHASTA, a Fluid Transport Algorithm That Works,'' J. Comput. Phys., **11**, p. 38.
[16] Colella, P., and Woodward, P., 1984, ''The Piecewise Parabolic Method (PPM) for Gas Dynamic Simulations,'' J. Comput. Phys., **54**, p. 174.
[17] Sytine, I. V., Porter, D. H., Woodward, P. R., and Hodson, S. W., 2000, ''Convergence Tests for the Piecewise Parabolic Method and Navier-Stokes Solutions for Homogeneous Compressible Turbulence,'' J. Comput. Phys., **158**, p. 225.
[18] Garnier, E., Mossi, M., Sagaut, P., Comte, P., and Deville, M., 2000, ''On the Use of Shock-Capturing Schemes for Large Eddy Simulation,'' J. Comput. Phys., **153**, p. 273.
[19] Okong'o, N., Knight, D. D., and Zhou, G., 2000, ''Large Eddy Simulations Using an Unstructured Grid Compressible Navier-Stokes Algorithm,'' Int. J. Comput. Fluid Dyn., **13**, p. 303.
[20] Margolin, L. G., Smolarkiewicz, P. K., and Sorbjan, Z., 1999, ''Large-Eddy Simulation of Convective Boundary Layers Using Non-Oscillatory Differencing,'' Physica D, **133**, p. 390.
[21] Karamanos, G.-S., and Karniadakis, G. E., 2000, ''A Spectral Vanishing Viscosity Method for Large-Eddy Simulations,'' J. Comput. Phys., **163**, p. 22.
[22] Boris, J. P., Grinstein, F. F., Oran, E. S., and Kolbe, R. J., 1992, ''New Insights Into Large Eddy Simulation,'' Fluid Dyn. Res., **10**, p. 199.
[23] Fureby, C., and Grinstein, F. F., 1999, ''Monotonically Integrated Large Eddy Simulation of Free Shear Flows,'' AIAA J., **37**, p. 544.
[24] Fureby, C., and Grinstein, F. F., 2002, ''Large Eddy Simulation of High Reynolds Number Free and Wall Bounded Flows,'' J. Comput. Phys., **181**, p. 68.
[25] Ferziger, J. H., and Leslie, D. C., 1979, ''Large Eddy Simulation—A Predictive Approach to Turbulent Flow Computation,'' AIAA paper 79-1441.
[26] Fureby, C., and Tabor, G., 1997, ''Mathematical and Physical Constraints on Large Eddy Simulations,'' J. Theoretical Fluid Dyn., **9**, p. 85.
[27] Speziale, C. G., 1985, ''Galilean Invariance of Sub Grid Scale Stress Models in Large Eddy Simulations of Turbulence,'' J. Fluid Mech., **156**, p. 55.
[28] Vreman, B., Geurts, B., and Kuerten, H., 1994, ''Realizability Conditions for the Turbulent Stress Tensor in Large Eddy Simulation,'' J. Fluid Mech., **278**, p. 351.
[29] Ghosal, S., and Moin, P., 1995, ''The Basic Equations for the Large Eddy Simulation of Turbulent Flows in Complex Geometry,'' J. Comput. Phys., **118**, p. 24.
[30] Lesieur, M., and Metais, O., 1996, ''New Trends in Large Eddy Simulations of Turbulence,'' Annu. Rev. Fluid Mech., **28**, p. 45.
[31] Sullivan, P. P., McWilliams, J. C., and Moeng, C. H., 1994, ''A Subgrid Scale Model for Large Eddy Simulation of Planetary Boundary-Layer Flows,'' Bound. Layer Meth., **71**, p. 247.
[32] Fureby, C., 2001, ''Towards Large Eddy Simulation of Complex Flows,'' *Direct and Large Eddy Simulation IV*, R. Friedrich and W. Rodi, eds., Kluwer, Dordrecht, The Netherlands.
[33] Lund, T. S., and Novikov, E. A., 1994, ''Parameterization of Subgrid-Scale Stress by the Velocity Gradient Tensor,'' Annual Res. Briefs, Center for Turbulence Research, p. 185.
[34] Deardorff, J. W., 1973, ''The Use of Subgrid Transport Equations in a Three-Dimensional Model of Atmospherical Turbulence,'' ASME J. Fluids Eng., **95**, p. 429.
[35] Bardina, J., Ferziger, J. H., and Reynolds, W. C., 1980, ''Improved Subgrid Scale Models for Large Eddy Simulations,'' AIAA Paper No. 80-1357.
[36] Liu, S., Meneveau, C., and Katz, J., 1994, ''On the Properties of Similarity Subgridscale Models as Deduced From Measurements in a Turbulent Jet,'' J. Fluid Mech., **275**, p. 83.
[37] Hirsch, C., 1999, *Numerical Computation of Internal and External Flows*, John Wiley and Sons, New York.
[38] Fureby, C., Tabor, G., Weller, H., and Gosman, D., 1997, ''A Comparative Study of Sub Grid Scale Models in Homogeneous Isotropic Turbulence,'' Phys. Fluids, **9**, p. 1416.
[39] Godunov, S. K., 1959, ''A Difference Method for Numerical Calculation of Discontinuous Solutions of the Equations of Hydrodynamics,'' Mat. Sb., **47**, p. 271.
[40] LeVeque, R. J., 1992, *Numerical Methods for Conservation Laws*, 2nd Ed., Birkhüser Verlag, Berlin.
[41] Shao, L., Sarkar, S., and Pantano, C., 1999, ''On the Relationship Between the Mean Flow and Subgrid Stresses in Large Eddy Simulation of Turbulent Shear Flows,'' Phys. Fluids, **11**, p. 1229.
[42] Borue, V., and Orszag, S. A., 1998, ''Local Energy Flux and Subgrid-Scale Statistics in Three Dimensional Turbulence,'' J. Fluid Mech., **366**, p. 1.
[43] Margolin, L. G., and Rider, W. J., 2002, ''A Rationale for Implicit Turbulence Modeling,'' Intl. J. Numer. Meth. Fluids, **39**, p. 821.
[44] Harten, A., 1984, ''On a Class of High Resolution Total Variation Stable Finite Difference Schemes,'' SIAM (Soc. Ind. Appl. Math.) J. Numer. Anal., **21**, p. 1.
[45] Sweby, P. K., 1984, ''High Resolution Schemes Using Flux Limiters for Hyperbolic Conservation Laws,'' SIAM (Soc. Ind. Appl. Math.) J. Numer. Anal., **21**, p. 995.
[46] Roe, P. L., 1985, *Some Contributions to the Modelling of Discontinuous Flows* (Lectures in Applied Mathematics), Springer-Verlag, Heidelberg, **22**, p. 163.
[47] Jasak, H., Weller, H. G., and Gosman, A. D., 1999, ''High Resolution NVD Differencing Scheme for Arbitrarily Unstructured Meshes,'' Int. J. Numer. Methods Fluids, **31**, p. 431.
[48] Sandham, N. D., and Howard, R. J. A., 1995, ''Statistics Databases From Direct Numerical Simulation of Fully-Developed Turbulent Channel Flow,'' private communication, QMW-EP-1106, Queen Mary and Westfield College, Department of Engineering, London.
[49] Grinstein, F. F. et al., 1996, ''Streamwise and Spanwise Vortex Interaction in an Axisymmetric Jet. A Computational and Experimental Study,'' Phys. Fluids, **8**, p. 1515.
[50] Grinstein, F. F., 2001, ''Vortex Dynamics and Entrainment in Regular Free Jets,'' J. Fluid Mech., **437**, p. 69.
[51] Grinstein, F. F., 1998, ''Vortex Dynamics and Aeroacoustics of Low Aspect Ratio Rectangular Jets,'' *Proc. AFOSR Conference on Turbulence and Internal Flows*, Annapolis, MD, Aug. 18–20, AFOSR, Washsington, DC, p. 131.
[52] Grinstein, F. F., and DeVore, C. R., 2002, ''On Global Instabilities in Countercurrent Jets,'' Phys. Fluids, **14**, p. 1095.
[53] Hussain, F., and Husain, H. S., 1989, ''Elliptic Jets. Part I. Characteristics of Unexcited and Excited Jets,'' J. Fluid Mech., **208**, p. 257.
[54] Tam, C., 1998, ''LES for Aeroacoustics,'' AIAA Paper 98-2805.
[55] Brown, G., and Roshko, A., 1974, ''On Density Effects and Large Structure in Turbulent Mixing Layers,'' J. Fluid Mech., **64**, p. 775.
[56] Mitchell, B. E., Lele, S. K., and Moin, P., 1999, ''Direct Computation of the Sound Generated by Vortex Pairing in an Axisymmetric Jet,'' J. Fluid Mech., **383**, p. 113.
[57] Grinstein, F. F., Oran, E. S., and Boris, J. P., 1991, ''Pressure Field, Feedback and Global Instabilities of Subsonic Spatially Developing Mixing Layers,'' Phys. Fluids A, **A3**, p. 2401.
[58] Bridges, J., and Hussain, F., 1992, ''Direct Evaluation of Aeroacoustic Theory in a Jet,'' J. Fluid Mech., **240**, p. 469.
[59] Tam, C. K. W., and Webb, J. C., 1993, ''Dispersion Related Preserving Finite Difference Schemes for Computational Aeroacoustics,'' J. Comput. Phys., **107**, p. 1262.
[60] Germano, M., Piomelli, U., Moin, P., and Cabot, W. H., 1994, ''A Dynamic Sub Grid Scale Eddy Viscosity Model,'' Phys. Fluids A, **A3**, p. 1760.

[61] Voke, P., 1996, ''Subgrid-Scale Modeling at Low Mesh Reynolds Number,'' J. Theoret. Fluid Dyn., **8**, p. 131.
[62] Sagaut, P., 1996, ''Numerical Simulations of Separated Flows With Subgrid Models,'' Rech. Aerosp., **1**, p. 51.
[63] Grötzbach, G., 1987, ''Direct Numerical and large Eddy Simulation of Turbulent Channel Flows,'' *Encyclopedia of Fluid Mechanics*, N. P. Cheremisinoff, ed., **34**, Gulf Publishing, Houston, p. 1337.
[64] Piomelli, U., Ferziger, J., and Moin, P., 1981, ''New Approximate Boundary Conditions for Large Eddy Simulations of Wall Bounded Flows,'' Phys. Fluids, **1**, p. 1061.
[65] Cabot, W., and Moin, P., 2000, ''Approximate Wall Boundary Conditions in the Large Eddy Simulation of High Reynolds Number Flows,'' Flow, Turbul. Combust., **63**, p. 269.
[66] Menon, S., 2001, private communication.
[67] Fureby, C., Persson, L., and Svanstedt, N., 2002, ''On Homogenization Based Methods for Large Eddy Simulation,'' AIAA Paper No 02-7462; J. Fluids Engineering, in press.
[68] Antonia, R. A., Teitel, M., Kim, J., and Browne, L. W. B., 1992, ''Low-Reynolds-Number Effects in a Fully Developed Turbulent Channel Flow,'' J. Fluid Mech., **236**, p. 579.
[69] Wei, T., and Willmarth, W. W., 1989, ''Reynolds Number Effects on the Structure of a Turbulent Channel Flow,'' J. Fluid Mech., **204**, p. 57.
[70] Dean, R. B., 1978, ''Reynolds Number Dependence of Skin Friction and Other Bulk Flow Variables in Two-Dimensional Rectangular Duct Flow,'' ASME J. Fluids Eng., **100**, p. 215.
[71] Smith, C. R., and Walker, J. D. A., 1995, ''Turbulent Wall-Layer Vortices,'' *Fluid Vortices*, S. Green ed., Kluwer, Dordrecht, The Netherlands.
[72] Blackwelder, R. F., 1979, ''Boundary Layer Transition,'' Phys. Fluids, **22**, p. 583.
[73] Jeong, J., Hussain, F., Shoppa, W., and Kim, J., 1997, ''Coherent Structures Near the Wall in a Turbulent Channel Flow,'' J. Fluid Mech., **332**, p. 185.
[74] Moin, P., and Kim, J., 1982, ''Large Eddy Simulation of Turbulent Channel Flow,'' J. Fluid Mech., **118**, p. 341.
[75] Comte-Bellot, G., 1965, ''Ecoulment Turbulent Entre Deaux Parois Paralleles,'' Publications Scientifiques et Techniques du Ministere de l'Air No. 419.
[76] Author please insert Ref. [76]
[77] Colonius, T., Lele, S. K., and Moin, P., 1993, ''Boundary Conditions for Direct Computations of Aerodynamic Sound,'' AIAA J., **31**, p. 1574.
[78] Poinsot, T. J., and Lele, S. K., 1994, ''Boundary Conditions for Direct Simulations of Compressible Viscous Flows,'' J. Comput. Phys., **101**, p. 104.
[79] Grinstein, F. F., 1994, ''Open Boundary Conditions in the Simulation of Subsonic Turbulent Shear Flows,'' J. Comput. Phys., **115**, p. 43.
[80] Turkel, E., 1998, ''Special Issue on Absorbing Boundary Conditions,'' Appl. Numer. Math., **27**, p. 327.
[81] Kong, H., Choi, H., and Lee, J. S., 2000, ''Direct Numerical Simulation of Turbulent Thermal Boundary Layers,'' Phys. Fluids, **12**, p. 2555.
[82] Strikwerda, J. C., 1977, ''Initial Value Boundary Value Problems for Incompletely Parabolic Systems,'' Commun. Pure Appl. Math., **30**, p. 797.
[83] Thompson, K., 1987, ''Time Dependent Boundary Conditions for Hyperbolic Systems,'' J. Comput. Phys., **68**, p. 1.
[84] Thompson, K., 1990, ''Time Dependent Boundary Conditions for Hyperbolic Systems, II,'' J. Comput. Phys., **89**, p. 439.
[85] Pitz, R. W., and Daily, J. W., 1983, ''Experimental Study of Combustion in a Turbulent Free Shear Layer Formed at a Rearward Facing Step,'' AIAA J., **21**, p. 1565.
[86] Pitz, R. W., and Daily, J. W., 1981, ''Experimental Study of Combustion: The Turbulent Structure of a Reacting Shear Layer Formed at a Rearward Facing Step,'' NASA Contractor Report 165427.
[87] Fureby, C., 1999, ''Large Eddy Simulation of Rearward Facing Step Flow,'' AIAA J., **37**, p. 1401.
[88] Eaton, J. K., and Johnston, J. P., 1980, ''Turbulent Flow Reattachment: An Experimental Study of the Flow and Structure Behind a Backward Facing Step,'' Stanford University, Report No. MD-39.

L. G. Margolin
Center for Nonlinear Studies,
Los Alamos National Laboratory,
MS B258,
Los Alamos, NM 87545
e-mail: len@lanl.gov

P. K. Smolarkiewicz
Microscale and Mesoscale Meteorology Division,
National Center for Atmospheric Research,
Boulder, CO 80307
e-mail: smolar@ncar.ucar.edu

A. A. Wyszogrodzki[1]
Institute for Geophysics and Plenetary Physics,
Earth and Space Sciences Division,
Los Alamos National Laboratory,
MS C305,
Los Alamos, NM 87545
e-mail: wyszog@kokopelli.lanl.gov

Implicit Turbulence Modeling for High Reynolds Number Flows

Implicit turbulence modeling is the numerical simulation of high Reynolds fluid flow using nonoscillatory finite volume (NFV) schemes without any explicit subgrid scale model. Here we investigate the ability of a particular NFV scheme, MPDATA, to simulate decaying turbulence in a triply periodic cube for a variety of viscosities, comparing our results to analogous pseudo-spectral studies. In the regime of direct numerical simulation, MPDATA is shown to agree closely with the pseudo-spectral results. As viscosity is reduced, the two model results diverge. We study the MPDATA results in the inviscid limit, using a combination of mathematical analysis and computational experiment. We validate these results as representing the turbulent flow in the limit of very high Reynolds number.
[DOI: 10.1115/1.1514210]

1 Introduction

There is a kind of magic[2] about nonoscillatory methods for numerical simulation of complex fluid flows. Beyond the obvious benefits of avoiding unphysical oscillations by preserving positivity and/or monotonicity, and of ensuring nonlinear stability, high-order upwind methods appear to correlate well with the underlying physics, leading to simulations that are more physically realizable.

As a recent and unexpected example of realizability, nonoscillatory methods have demonstrated the ability to simulate turbulent flows without need for explicit subgrid scale models, a property that we refer to as ''implicit turbulence modeling.'' This property has been validated in direct comparisons with experimental data and with high-resolution direct numerical simulation (DNS) for a variety of flows, and for a variety of nonoscillatory algorithms (see, for example, [2–5]) over the past ten years. In our own research, we have employed the nonoscillatory algorithm Multidimensional Positive Definite Advection Transport Algorithm (MPDATA) see [6] and references therein, to model all-scale meteorological flows including atmospheric boundary layers, [7], gravity-wave dynamics, [8], and global climate, [9].

More recently, the beginnings of a theoretical framework has been proposed for implicit turbulence modeling in [10]. These authors derived a finite-scale (i.e., coarse-grained) version of the pointwise Burgers' equation—a version appropriate for describing the dynamics of finite volumes of (Burgers') fluid. They compared this finite-scale equation to the MPDATA approximation of the pointwise equation, and showed that MPDATA already accounts for the finite-scale effects. Since each computational cell is a finite volume, they rationalized that the success of MPDATA in modeling turbulent flows results from its accurate representation of the coarse-grained equations of motion.

The theory in [10] and the computational examples that support it are suggestive. However, there are significant differences between Burgers' and Navier-Stokes equations. Perhaps the most important of these is that the solutions of Burgers' equation are deterministic while those of Navier-Stokes are stochastic. This difference may be readily appreciated by considering simulations at two distinct resolutions. In the case of Burgers' equation the two solutions will be close, while for Navier-Stokes equations it is only the statistics of the solutions that will be close, [11].

In this paper, we extrapolate the finite-volume theory of [10] to analyze nonoscillatory simulations of a turbulent flow governed by three-dimensional Navier-Stokes equations. We compare MPDATA simulations of decaying turbulence in a triply periodic cube with the pseudo-spectral results of Herring and Kerr [12]. For two values of physical viscosity corresponding to direct numerical simulations (DNS) where all dynamical scales are resolved, the MPDATA and the pseudo-spectral solutions compare closely in all integral measures.

We also compare simulations using zero viscosity. The pseudo-spectral simulation, in this Euler equation limit of Navier-Stokes, shows an enstrophy blowup at finite time. The MPDATA simulation tracks the pseudo-spectral results for a while, but does not show any blowup of enstrophy. The pseudo-spectral result is unphysical—all physical flows exhibit viscous dissipation at some finite length scale. In contrast, enstrophy in the MPDATA simulation remains uniformly bounded, and the solution appears physically reasonable. However, the question remains whether the MPDATA simulation is the result of a well-posed physical problem, and if so, what this problem is.

To address this question—the central issue of the paper—we analyze the zero-viscosity MPDATA results by combining theoretical arguments with computational experiments. In Section 3, we derive a relation between the numerical energy spectra at different resolutions. In Section 4, we validate this relation computationally. A theoretical consequence is the existence of an asymptotic spectrum in the continuum limit. For zero explicit viscosity, we interpret the asymptotic spectrum as the high Reynolds number (Re) limit of viscous flows, [13]. We elaborate, and then summarize our conclusions in Section 5.

2 MPDATA: Properties and Implementation

The simulations presented in this paper all employed the nonoscillatory fluid solver MPDATA. We would emphasize that implicit turbulence modeling appears to be a property of all nonoscillatory finite volume (NFV) schemes; however, MPDATA does have some unique features. MPDATA was developed originally for applications in meteorology. Since it is likely unfamiliar

[1]On leave from the Institute of Geophysics, Warsaw University, Warsaw, Poland.

Contributed by the Fluids Engineering Division for publication in the JOURNAL OF FLUIDS ENGINEERING. Manuscript received by the Fluids Engineering Division Mar. 12, 2002; revised manuscript received May 29, 2002. Associate Editor: F. F. Grinstein.

[2]''Any significantly advanced technology is indistinguishable from magic.'' Arthur C. Clarke's third law of science [1].

to the aeronautics community, we take this opportunity to summarize some of its features. The interested reader can find a comprehensive description of MPDATA in [6], including both the underlying concepts and the details of implementation.

MPDATA in its basic form is sign preserving, but not monotonicity preserving. For meteorological applications, we have found that sign preservation is often sufficient and leads to a less diffusive solution. MPDATA is fully second-order accurate and conservative. A variety of options have been documented, [6], that extend MPDATA to full monotonicity preservation, to third-order accuracy, and to fields that do not preserve sign (of which the most important is momentum).

Unlike most NFV methods, MPDATA is not based on the idea of flux limiting. Instead it is based more directly on upwinding. In practical terms, the algorithm consists of a series of donor cell steps; the first step provides a first-order accurate solution while subsequent steps compensate higher-order errors as identified from a modified equation analysis. One important consequence of this approach is that MPDATA is fully multidimensional—i.e., has no spatial splitting errors—which implies significantly reduced mesh dependence.

MPDATA is a full fluid solver. In analyzing the truncation error of approximations to the momentum equation, one finds error terms that depend on the interaction of the advection with the forcing terms, including the pressure gradient. In implementations of NFV algorithms that treat advection separately from the forcings, this error is uncompensated, reducing the order of accuracy of the solution and potentially leading to oscillations and even instability (see [14]). In MPDATA we compensate this error effectively by integrating the forcing terms along a flow trajectory rather than at a point.

MPDATA is implemented in the three-dimensional program EULAG for simulating rotating, stratified flows in complex geometries, [8,9]. The name EULAG alludes to the capability to solve the fluid equations in either an Eulerian (flux form) or a Lagrangian (advective form) framework. The latter uses a semi-Lagrangian algorithm in which an MPDATA-type scheme performs as an interpolation routine. However all the simulations in this paper use the Eulerian framework. EULAG can be run for incompressible or anelastic fluids; in either case, we solve an elliptic equation for pressure using a preconditioned generalized conjugate residual solver, [15]. EULAG is fully parallelized using message-passing and runs efficiently on a variety of platforms, [16].

3 Theory

In this section, we summarize the theoretical results of [10] and describe an extension to support our analysis.

3.1 Background. In [10], the authors describe a rationale for implicit turbulence modeling. Their analysis begins by deriving the modified equation for MPDATA applied to one-dimensional Burgers' equation. Among the third-order truncation terms, there appears a nonlinear dispersive term of the form $\Delta x^2 u_x u_{xx}$. The authors then construct the governing equation for a finite volume of Burgers' fluid. These equations are derived from the point equations, but are different due to the nonlinearity of the latter, a fact that has long been appreciated by theorists and modelers studying turbulence. What is unexpected is that a straightforward and justifiable derivation of the finite volume equations leads directly to nonlinearly dispersive terms similar to those in the MPDATA modified equation. The rationale for implicit turbulence modeling then is the more accurate approximation of the finite-volume governing equations by MDPATA (and more generally, by NFV algorithms).

The finite scale Burgers' equation merits further discussion. In particular, one might be tempted to interpret the nonlinear dispersive terms as a model for the effects of the unresolved scales of motion—i.e., as a subgrid scale stress. However a careful examination of the derivation shows that this is not the case, a point that is emphasized by the authors. In fact, the finite-scale equation governs the evolution of the volume-averaged velocity independent of the details of the subgrid scale velocity field. In other words, the nonlinear dispersive term regularizes the flow in much the same way that artificial viscosity regularizes shocks in high-speed flows (see [17] and [5] for a similar point of view).

There is another, complementary point of view presented in [10]. The finite scale equation can be considered as a model for the measurements (experimental or computational) made by some observer. Experimental devices and simulations both have finite scales of length and time, implying that information about unresolved scales is lost and the measurements do not exactly correspond to "the flow." Since we are in a regime of classical physics, we are not concerned that the measurement process alters the flow, and so we should expect that the measurements accurately reflect the resolved scales. In this sense, the finite-scale equation is a better model of the observations than the point equation. One of our principal results in Section 4 is to verify that the MPDATA simulations do accurately reproduce the large scales of the turbulence.

3.2 Extensions. The generalization of the analysis in [10] to three-dimensional Navier-Stokes is beyond the scope of this paper. Instead, we shall assume that the basic result of the Burgers' equation analysis—that MPDATA accurately estimates the volume-averaged velocity—remains true for more general equations. This simple and reasonable assumption will allow us to predict the relationship of turbulent energy spectra produced at different resolutions. The verification of this relationship then reinforces our understanding of the performance of MPDATA.

Consider a one-dimensional periodic domain of length L. A measurable velocity $u(x)$ can be expanded in a Fourier series:

$$u(x)=\sum_{k=0}^{\infty}\left[a_k\cos\left(\frac{2\pi kx}{L}\right)+b_k\sin\left(\frac{2\pi kx}{L}\right)\right]. \tag{1}$$

Now consider a small segment $[x-\Delta x/2, x+\Delta x/2]$. In a one-dimensional simulation, this would represent a computational cell, and $\Delta x/L\equiv 1/N$ where N is the total number of cells. We now compute the averaged component $\overline{u}$ in this "cell":

$$\overline{u}(x)\equiv\frac{1}{\Delta x}\int_{x-\Delta x/2}^{x+\Delta x/2}u(x')dx'. \tag{2}$$

An elementary calculation leads to the result

$$\overline{u}(x)=\sum_{k=0}^{\infty}\left[a_k\cos\left(\frac{2\pi kx}{L}\right)+b_k\sin\left(\frac{2\pi kx}{L}\right)\right]f\left(\frac{\pi k\Delta x}{L}\right) \tag{3}$$

where the function

$$f(X)\equiv\frac{\sin X}{X} \tag{4}$$

attenuates each of the spectral coefficients of the original velocity in a wave number dependent fashion. The one-dimensional volume-averaged energy associated with $\overline{u}$ can now be written as

$$\overline{E}(k)=(a_k^2+b_k^2)f^2\left(\frac{\pi k\Delta x}{L}\right)=E(k)f^2\left(\frac{\pi k\Delta x}{L}\right). \tag{5}$$

These calculations can be easily extended to three-dimensions; however, using the anticipated isotropy of the velocity field, the above result can be applied directly in our simulations. In fact we have calculated the energy spectra shown later in Figs. 2–4 by averaging the one-dimensional spectra calculated in each of the three coordinate directions.

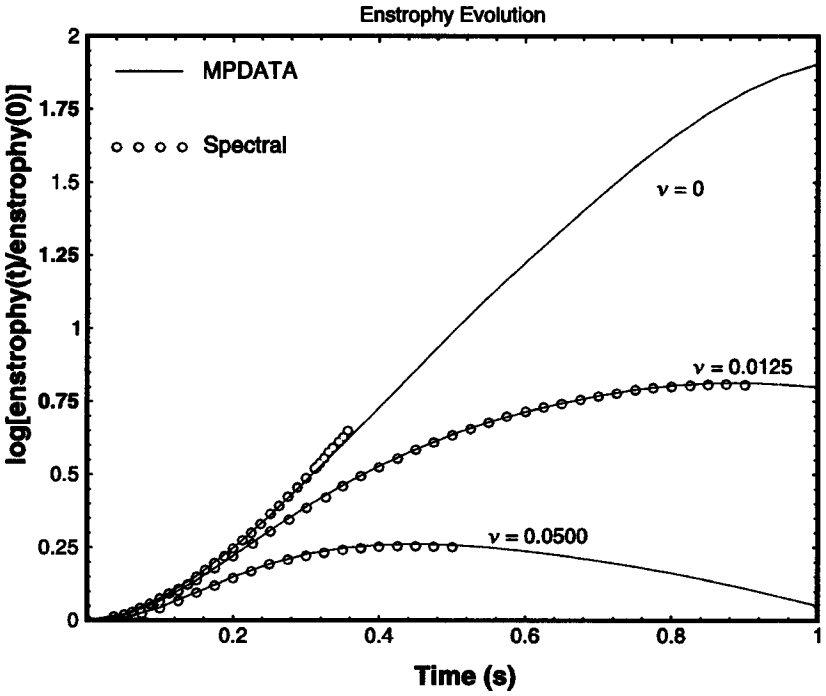

Fig. 1 Enstrophy history in pseudo-spectral and MPDATA simulations of isotropic decaying turbulence. All simulations use the same resolution of 256^3 points.

Let us now identify $\overline{\mathbf{u}}$ as the vector of the three discrete values of the velocity components in an MPDATA simulation. Equation (5) can be used to estimate the underlying energy spectrum *in part*—up to the finite wave number determined by the resolution of the simulation. We term

$$E(k) \equiv \frac{\overline{E}(k)}{f^2(\pi k/N)} \tag{6}$$

the asymptotic spectrum. Furthermore, since the simulated spectrum at each resolution has the same asymptotic spectrum, we can relate the energy spectral coefficients of two simulations at resolutions N_1 and N_2

$$\frac{\overline{E}_1(k)}{f^2(\pi k/N_1)} = \frac{\overline{E}_2(k)}{f^2(\pi k/N_2)} \tag{7}$$

where this relation holds up to the largest wave number of the more coarsely resolved simulation.

We close this section with these remarks about our result. First, the derivation of Eqs. (6) and (7) does not depend on the form of the governing equations, and are not specific to Navier-Stokes. Second, these equations allow us to estimate an asymptotic spectrum, given a simulated spectrum at finite resolution, but do not predict any universal form for this spectrum. Third, for small values of its argument, Eq. (6) implies convergence of the simulated spectra to the asymptotic spectrum as $1/N^2$. Finally, we note that related ideas of spectral deconvolution have been used for the purpose of constructing explicit subgrid models, cf. [18–20].

4 Analysis and Results

We will analyze the simulations of decaying turbulence of a homogeneous incompressible fluid in a triply periodic cube—a generic problem in turbulence studies. The assumed homogeneity of the thermodynamics and the lack of near-wall effects focus attention on the modeling of the convective derivatives $\mathbf{u}\nabla\mathbf{u}$ in the momentum equation. Our NFV experiments with MPDATA will mirror the 256^3 DNS and inviscid pseudo-spectral simulations of Herring and Kerr [12].

Figure 1 displays the numerical data for the evolution of enstrophy for three values of viscosity, $\nu=0.0500$, $\nu=0.0125$,[3] and $\nu=0$ $m^2\,s^{-1}$ (as indicated). Solid lines are for MPDATA experiments, while the data from [12] are marked as circles. One striking result in Fig. 1 is the remarkable agreement of the NFV and the pseudo-spectral solutions for DNS ($\nu>0$). This agreement is maintained uniformly for all flow characteristics, including spectra (see [12] for other diagnostics). Traditionally, pseudo-spectral methods are valued for their accuracy and have been considered the tool of choice to study turbulent flows. Since all convergent methods become accurate as the flow is fully resolved, one may wonder whether this agreement is due to excess resolution. This is definitely not the case for $\nu=0.0125$ where the Kolmogorov scale is about one grid-interval (Kerr, personal communication) and the energy dissipation is marginally resolved.

The $\nu=0$ results expose the essential difference between the pseudo-spectral and MPDATA approaches. Without viscous dissipation, enstrophy blowup occurred in the pseudo-spectral solution. The rapid growth of enstrophy was accompanied by an energy buildup at the highest wave numbers; the spectral calculations became unstable, and were terminated after $\sim$0.35 s, [12]. Up to this point, the spectral and MPDATA results agree closely. Beyond this point, MPDATA continues to produce a plausible solution. However, it is not clear whether the MPDATA simulation is physically realizable.

Based on the large-eddy simulations (LES) of boundary layers in [7], we interpret the $\nu=0$ MPDATA result as the finite-scale representation of the $\mathrm{Re}\to\infty$ limit of viscous flows. This contrasts with the pseudo-spectral result, which at $\nu=0$ represents the solution of the pointwise Euler equations where finite-scale effects have been already discarded. To substantiate our interpretation, we have compiled two convergence studies of the inviscid solution. The first study shows the convergence of the energy spectra as a function of resolution for zero viscosity. The second study shows the convergence of the energy spectra as a function of viscosity.

[3]The initial Taylor microscale Reynolds number is 250, see Fig. 1(c) in [12].

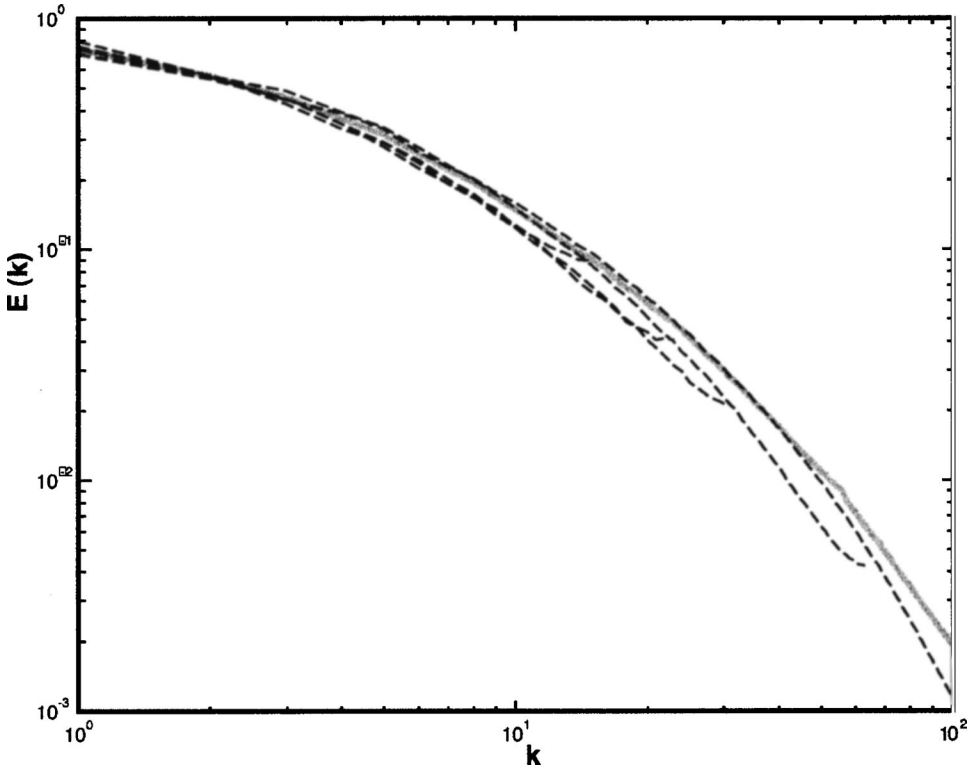

Fig. 2 MPDATA simulated spectra for zero viscosity at 32^3, 48^3, 64^3, 128^3, and 256^3 resolutions

Figure 2 compares the energy spectra from MPDATA simulations at $\nu=0$ for a series of resolutions 32^3, 48^3, 64^3, 128^3, and 256^3, as indicated. The spectra follow each other closely at the large scales of motion, but tend to separate at the smaller scales. This separation is predicted theoretically in Section 3, which also implies the existence of the unique asymptotic spectrum (Eq. 6). Figure 3 displays the asymptotic spectra generated from those shown in Fig. 2. In the absence of truncation errors, all asymptotic spectra should coincide for the resolved scales. Except for the highest wave numbers, the discrepancies of the asymptotic spectra are small compared to the separation of the simulated spectra in Fig. 2. (N.B., The simulated and asymptotic spectra show the well-known bottleneck effect, [21], which only affects the highest resolved wave numbers. These data have been ignored while constructing the average asymptotic spectrum—i.e., the solid line in Fig. 2.) This agreement indicates that the MPDATA results should be interpreted as a finite-resolution projection of the continuum limit. Note that the solid line in Fig. 2, showing the asymptotic spectrum averaged over all five resolutions, estimates the converged limit of the simulated spectra.

As remarked earlier, all physical flows have viscous dissipation. Although the viscous scale lengths may be small compared to finite resolution of a numerical model, they never vanish in the continuum limit. To assess the effects of small but finite viscosity we show in Fig. 4, the convergence of the asymptotic energy spectra as $\nu\rightarrow 0$; these spectra are estimated from MPDATA simulations at 256^3 resolution. The results shown demonstrate that the viscous spectra converge uniformly to the inviscid limit as $\nu\rightarrow 0$. Taken together, our computations substantiate our contention that the inviscid MPDATA runs can be interpreted as the finite-scale representations of the $\mathrm{Re}\rightarrow\infty$ limit of viscous flows.

5 Summary and Conclusions

In this paper, we have continued our study of the use of the nonoscillatory finite volume scheme MPDATA to simulate turbulent flow without need for any explicit subgrid model. We refer to this property as implicit turbulence modeling. We began by comparing simulations of a turbulent flow using MPDATA to a pseudo-spectral simulation. When the physical viscosity is large enough so that all dynamical scales are well resolved, we have shown that MPDATA accurately reproduces the flow predicted by the pseudo-spectral model, thus validating the utility of this NFV scheme for direct numerical simulation.

In the limit of vanishing physical viscosity, the pseudo-spectral model predicts a enstrophy blowup in finite time, and the cessation of meaningful calculation after this point. In contrast, MPDATA does not predict any blowup of enstrophy and continues to produce plausible solutions. Our principal result in this paper has been to analyze these solutions, to demonstrate that they are in fact realizable, and to identify them with a physical problem. Our demonstration relies on mathematical analysis and a computational study of convergence in resolution and viscosity.

Our analytic result is derived in Section 3 and represents a relationship between the energy spectra generated in simulations at different resolutions. The results assume that the numerical algorithm MPDATA accurately estimates the volume-averaged velocity; this result has been demonstrated rigorously for the Burgers' equation in [10]. Our analytic result further implies the existence of an ''asymptotic'' spectrum, representing the continuum limit, and verifies that at fixed wave number the convergence rate goes like the inverse square of the resolution.

Our numerical results in Section 4 validate the analytic relations, and confirm the existence of a unique asymptotic energy spectrum. We further showed a computational study of the convergence of the asymptotic viscous spectra to the inviscid spectrum. This leads to our main conclusion, that the MPDATA simulations with zero-explicit viscosity may correctly model turbulent flow in a high Reynolds number limit.

Throughout this paper, we have emphasized that numerical simulation and physical observation are both carried out at finite

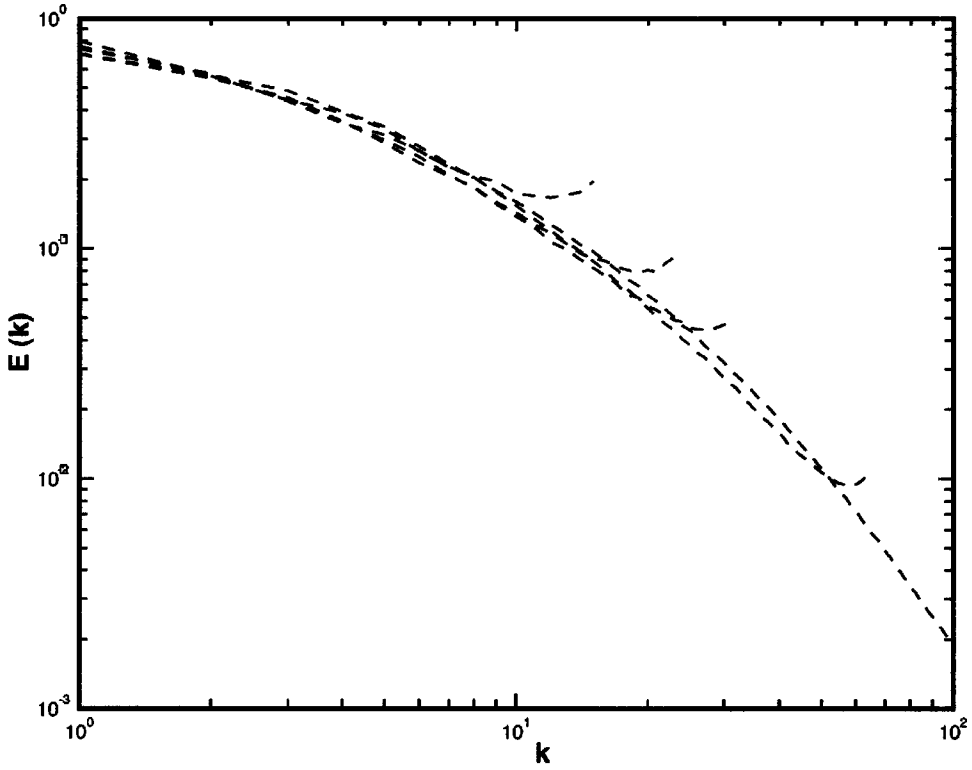

Fig. 3 Asymptotic spectra for zero viscosity estimated from simulated spectra in Fig. 2

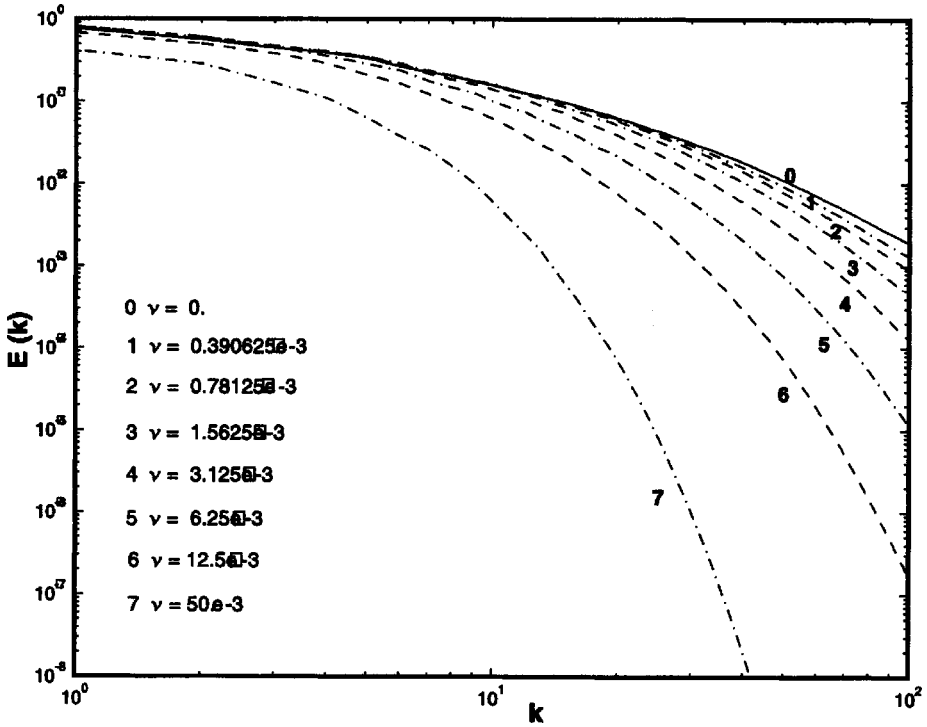

Fig. 4 Asymptotic spectra for finite viscosities

scales. In creating a model for numerical simulation of high Reynolds number flow, one is effectively considering the limit as two different length scales become small. The first is the viscous scale, sometimes termed the Kolmogorov scale. The second is the scale of nonlinear effects (see Section 3) which is the scale of observation or, in the case of simulation, the size of the computational cell. The latter is never negligible in a simulation—so the Euler equations cannot be an adequate model for numerical simulation of high Reynolds number flow—and the finite scale effects must be taken into account. Based on the results presented, we surmise

that MPDATA (and likely other NFV algorithms) accurately models coarse-grained solutions of three-dimensional Navier-Stokes equations, and appears to be a valuable tool for large-eddy simulation free of explicit subgrid-scale parameterization.

Acknowledgments

Helpful discussions with Shiyi Chen and Robert Kerr are gratefully acknowledged. Los Alamos National Laboratory is operated by the University of California for the U.S. Department of Energy. National Center for Atmospheric Research is sponsored by the National Science Foundation. This work has been supported in part by the Department of Energy ''Climate Change Prediction Program'' research initiative.

References

[1] Clarke, A. C., 1973, *Profiles of the Future*, Harper & Row, New York, p. 21.
[2] Oran, E. S., and Boris, J. P., 1993, ''Computing Turbulent Shear Flows—A Convenient Conspiracy,'' Comput. Phys., **7**, pp. 523–533.
[3] Porter, D. H., Pouquet, A., and Woodward, P. R., 1994, ''Kolmogorov-Like Spectra in Decaying Three-Dimensional Supersonic Flows,'' Phys. Fluids, **6**, pp. 2133–2142.
[4] Linden, P. F., Redondo, J. M., and Youngs, D. L., 1994, ''Molecular Mixing in Rayleigh-Taylor Instability,'' J. Fluid Mech., **265**, pp. 97–124.
[5] Fureby, C., and Grinstein, F. F., 1999, ''Monotonically Integrated Large Eddy Simulation of Free Shear Flows,'' AIAA J., **37**, pp. 544–556.
[6] Smolarkiewicz, P. K., and Margolin, L. G., 1998, ''MPDATA: A Finite Difference Solver for Geophysical Flows,'' J. Comput. Phys., **140**, pp. 459–480.
[7] Margolin, L. G., Smolarkiewicz, P. K., and Sorbjan, Z., 1999, ''Large Eddy Simulations of Convective Boundary Layers Using Nonoscillatory Differencing,'' Physica D, **133**, pp. 390–397.
[8] Smolarkiewicz, P. K., and Margolin, L. G., 1997, ''On Forward-in-Time Differencing for Fluids; An Eulerian/Semi-Lagrangian Nonhydrostatic Model for Stratified Flows,'' Atmos.-Ocean., **35**, pp. 127–152.
[9] Smolarkiewicz, P. K., Margolin, L. G., and Wyszogrodzki, A. A., 2001, ''A Class of Nonhydrostatic Global Models,'' J. Atmos. Sci., **58**, pp. 349–364.
[10] Margolin, L. G., and Rider, W. J., 2001, ''A Rationale for Implicit Turbulence Modeling,'' Int. J. Numer. Methods Eng., **39**, pp. 821–841.
[11] Frisch, U., 1995, *Turbulence, The Legacy of A. N. Kolmogorov*, Cambridge University Press, Cambridge, UK.
[12] Herring, J. R., and Kerr, R. M., 1993, ''Development of Enstrophy and Spectra in Numerical Turbulence,'' Phys. Fluids A, **5**, pp. 2792–2798.
[13] Kolmogorov, A. N., 1941, ''The Local Structure of Turbulence in Incompressible Viscous Fluid for Very Large Reynolds Numbers,'' Dokl. Akad. Nauk SSSR, **30**, pp. 301–305.
[14] Smolarkiewicz, P. K., and Margolin, L. G., 1993, ''On Forward-in-Time Differencing for Fluids,'' Mon. Weather Rev., **121**, pp. 1847–1859.
[15] Smolarkiewicz, P. K., and Margolin, L. G., 1994, ''Variational Solver for Elliptic Problems in Atmospheric Flows,'' Appl. Math. Comput., **4**, pp. 527–551.
[16] Prusa, J. M., Smolarkiewicz, P. K., and Wyszogrodzki, A. A., 2001, ''Simulations of Gravity Wave Induced Turbulence Using 512 PE CRAY T3E,'' Int. J. Appl. Math. Comput. Sci., **11**, pp. 101–115.
[17] Smagorinsky, J., 1993, ''Some Historical Remarks on the Use of Nonlinear Viscosities,'' *Large Eddy Simulation of Complex Engineering and Geophysical Flows*, Cambridge University Press, Cambridge, UK, pp. 3–36.
[18] Domaradzki, J. A., and Loh, K-C., 1999, ''The Subgrid-Scale Estimation Model in the Physical Space Representation,'' Phys. Fluids, **11**, pp. 2330–2342.
[19] Geurts, B. J., 1997, ''Inverse Modeling for Large-Eddy Simulation,'' Phys. Fluids, **9**, pp. 3585–3587.
[20] Stolz, S., and Adams, N. A., 1999, ''An Approximate Deconvolution Procedure for Large-Eddy Simulation,'' Phys. Fluids, **11**, pp. 1699–1701.
[21] Lohse, D., and Miller-Groeling, A., 1995, ''Bottleneck Effects in Turbulence: Scaling Phenomena in *r*-Versus *p*-space,'' Phys. Rev. Lett., **74**, pp. 1747–1750.

Large-Eddy Simulation of Supersonic Flat-Plate Boundary Layers Using the Monotonically Integrated Large-Eddy Simulation (MILES) Technique

H. Yan
e-mail: honyan@jove.rutgers.edu

D. Knight
Professor
e-mail:ddknight@rci.rutgers.edu

Department of Mechanical and
Aerospace Engineering,
Rutgers—The State University of New Jersey,
Piscataway, NJ 08854-8058

A. A. Zheltovodov
Senior Scientist,
Institute of Theoretical and Applied Mechanics,
Russian Academy of Sciences,
Siberian Branch,
Novosibirsk 630090, Russia
e-mail: zhelt@itam.nsc.ru

A supersonic flat-plate boundary layer at a Reynolds number of 2×10^4 based on the inflow boundary layer thickness is investigated at different Mach numbers ($M=2.88$ and 4) using the monotonically integrated large-eddy simulation (MILES) technique. The inherent numerical dissipation is taken as an implicit subgrid scales (SGS) model to close the Favre-filtered compressible Navier-Stokes (NS) equations. A finite volume method with second-order accuracy in time and space is implemented for the solution of the Navier-Stokes equations on an unstructured grid of tetrahedra. The heat transfer coefficient is predicted by simulating both adiabatic and isothermal cases. The mean flowfield and turbulent stresses are in good agreement with experiment. The relationship between the predicted skin friction coefficient and heat transfer coefficient is in close agreement with the Reynolds analogy factor. The variation of turbulent Prandtl number cross the boundary layer falls within the experimental envelope. These are the first LES predictions of adiabatic and isothermal supersonic flat plate boundary layers using the MILES technique. [DOI: 10.1115/1.1516578]

Introduction

Important developments in the study of supersonic turbulent boundary layer have been studied by theoretical [1–3], experimental [4–9], and numerical works [10–24]. A significant number of experimental investigations on supersonic turbulent boundary layers have been performed that have greatly improved our knowledge of the effects of compressibility on turbulence. Measurement of turbulence quantities in this flow configuration is difficult and is restricted away from the near-wall region [4–6]. In addition, the data collected in most experiments are limited to basic turbulence quantities. Numerical methods include Reynolds-averaged Navier-Stokes equations (RANS), Large-eddy simulation (LES), and direct numerical simulation (DNS). RANS methods successfully predict the mean flowfield but do not resolve the time-dependent large-scale motions of turbulence. For high Reynolds number flow, DNS is very expensive to perform due to its significant computational effort in resolving all scales of motion. LES is a more practical approach for simulating the flows of engineering importance, in which eddy scales smaller than the grid spacing (subgrid scales (SGS)) are removed by low-pass filtering, while their effects on the resolved flow are incorporated by an SGS model.

Most work using LES has focused on incompressible flows [25,26]. In 1986, Yoshizawa [27] first proposed an SGS model suitable for slightly compressible turbulent flows. Additional studies of compressible LES have been made by other researchers [10,28,29]. In general, compressible LES models can be divided into two categories. The first is the traditional LES approach, in which SGS models are explicitly introduced in the filtered Navier-Stokes (NS) equations. The second is based on monotonically integrated large-eddy simulation (MILES) [30], where the effects of the SGS flow on the resolved flow are implicitly incorporated into the functional reconstruction of the convective fluxes. From a physical standpoint, strong inhomogeneous effects are present in high Reynolds number supersonic shear flows, thus limiting the usefulness of Smagorinsky-type isotropic eddy-viscosity models. From a numerical point of view, the numerical discretization errors have the possibility of masking the SGS stress and flux terms by the leading-order truncation error. Researchers [31], have argued that the effect of discretization errors on LES needs to be studied further before proceeding with application to flows of engineering interest. This became a main motivation of constructing the MILES model. The MILES technique has been successfully applied to free jets [32–34], supersonic confined mixing layers [35], decaying supersonic homogeneous turbulent flow [36], free shear flow [37], axisymmetric supersonic base flow [38], free and wall-bounded flows [39], supersonic flat-plate boundary layer [24], supersonic expansion-compression corner [40], and compression corner [20,41,42]. This paper presents the simulation of supersonic flat plate boundary at different Mach numbers and $Re_\delta=2.0\times10^4$ using the MILES method. Both adiabatic and isothermal boundary conditions are implemented to compute the heat transfer coefficient for each case with different Mach numbers. The objective of this paper is to access the capability of LES to accurately predict the flowfield and heat transfer process in this supersonic flow. The paper introduces the governing equations followed by the description of the numerical methodology and grid configuration, then the results are shown in comparison with experiment and conclusions are drawn.

Governing Equations

The governing equations are the spatially filtered compressible Navier-Stokes equations. The spatial filtering removes the small-scale (high-frequency) components of the fluid motion, while the behavior of the three-dimensional time-dependent details of the large-scale energy containing eddies is accurately simulated. The

Contributed by the Fluids Engineering Division for publication in the JOURNAL OF FLUIDS ENGINEERING. Manuscript received by the Fluids Engineering Division Mar. 25, 2002; revised manuscript received May 29, 2002. Associate Editor: F. F. Grinstein.

filtering operation introduces the subgrid scale (SGS) stresses and heat transfer analogous to the Reynolds stress and turbulent heat flux in RANS.

For an arbitrary function $\mathcal{F}(x_i,t)$, the filtered variable $\overline{\mathcal{F}}(x_i,t)$ is defined as

$$\overline{\mathcal{F}}(x_i,t)=\int_D G(x_i-\xi_i,\Delta)\mathcal{F}(\xi_i,t)d\xi_i \tag{1}$$

where G is the filter function, and Δ is a measure of the filter width and is related to the computational mesh size [43].

For our system of equations we use Favre-filtering with filtered variable $\tilde{\mathcal{F}}(x_i,t)$ defined as

$$\tilde{\mathcal{F}}(x_i,t)=\frac{\overline{\rho\mathcal{F}}}{\overline{\rho}}. \tag{2}$$

The filtered governing equations for the resolved scales in Cartesian tensor notation (using the Einstein notation) are

$$\frac{\partial\overline{\rho}}{\partial t}+\frac{\partial\overline{\rho}\tilde{u}_i}{\partial x_i}=0 \tag{3}$$

$$\frac{\partial\overline{\rho}\tilde{u}_i}{\partial t}+\frac{\partial\overline{\rho}\tilde{u}_i\tilde{u}_j}{\partial x_j}=-\frac{\partial\overline{p}}{\partial x_i}+\frac{\partial\mathcal{T}_{ij}}{\partial x_j} \tag{4}$$

$$\frac{\partial\overline{\rho}\tilde{e}}{\partial t}+\frac{\partial}{\partial x_j}(\overline{\rho}\tilde{e}+\overline{p})\tilde{u}_j=\frac{\partial\mathcal{H}_j}{\partial x_j} \tag{5}$$

$$\overline{p}=\overline{\rho}R\tilde{T} \tag{6}$$

where x_i represents the Cartesian coordinates ($i=1,2,3$), $\overline{\rho}$ is the mean density, $\tilde{u}_i$ are the Cartesian components of the filtered velocity, $\overline{p}$ is the mean pressure,

$$\mathcal{T}_{ij}=\tau_{ij}+\overline{\sigma}_{ij} \tag{7}$$

and

$$\mathcal{H}_j=Q_j+\overline{q}_j+\mathcal{T}_{ij}\tilde{u}_i \tag{8}$$

are the total stress and the energy flux, respectively, and $\tilde{e}$ is the filtered total energy per unit mass

$$\overline{\rho}\tilde{e}=\overline{\rho}c_v\tilde{T}+\frac{1}{2}\overline{\rho}\widetilde{u_iu_i}+\overline{\rho}k \tag{9}$$

where $\overline{\rho}k$ is the subgrid scale turbulence kinetic energy per unit volume

$$\overline{\rho}k=\frac{1}{2}\overline{\rho}(\widetilde{u_iu_i}-\tilde{u}_i\tilde{u}_i) \tag{10}$$

and $\overline{q}_j$ is the molecular heat flux

$$\overline{q}_j=\lambda(\tilde{T})\frac{\partial\tilde{T}}{\partial x_j}, \tag{11}$$

where $\lambda(\tilde{T})$ is the molecular thermal conductivity, and the molecular viscous stress tensor $\overline{\sigma}_{ij}$ is approximated [44], by

$$\overline{\sigma}_{ij}=\mu(\tilde{T})\left(-\frac{2}{3}\frac{\partial\tilde{u}_k}{\partial x_k}\delta_{ij}+\frac{\partial\tilde{u}_i}{\partial x_j}+\frac{\partial\tilde{u}_j}{\partial x_i}\right) \tag{12}$$

where $\mu(\tilde{T})$ is the molecular viscosity based on the Favre-filtered static temperature $\tilde{T}$.

The closure of the system of Eqs. (3) to (6) requires specification of appropriate initial and boundary conditions for the flow variables and a model for the subgrid scale stress

$$\tau_{ij}=-\overline{\rho}(\widetilde{u_iu_j}-\tilde{u}_i\tilde{u}_j) \tag{13}$$

and heat flux

$$Q_j=-c_p\overline{\rho}(\widetilde{u_jT}-\tilde{u}_j\tilde{T}). \tag{14}$$

The monotonically integrated large-eddy simulation technique [30], is used, wherein no explicit subgrid scale (SGS) model is utilized to close the above equation system (i.e., $\tau_{ij}=0$ and $Q_j=0$). The inherent numerical dissipation is taken as the implicit SGS model.

Numerical Methodology

A finite volume method with second-order spatial and temporal accuracy is implemented to solve the Favre-filtered compressible Navier-Stokes equations on an unstructured grid of tetrahedra. We simplify the notation by dropping the tilde ~ and overbar ¯.

The governing equations may be written in finite volume form for a control volume V with surface ∂V as

$$\frac{d}{dt}\int_V QdV+\int_{\partial V}E\mathbf{n}dA=0 \tag{15}$$

where Q is the vector of dependent variables

$$Q=\begin{Bmatrix}\rho\\ \rho u\\ \rho v\\ \rho w\\ \rho e\end{Bmatrix} \tag{16}$$

where $\mathbf{n}$ is the outward unit normal on the surface. The flux tensor E is

$$E=F\mathbf{i}+G\mathbf{j}+H\mathbf{k} \tag{17}$$

where $\mathbf{i}$, $\mathbf{j}$, $\mathbf{k}$ are unit vectors in the x, y, and z directions, respectively, and

$$F=\begin{Bmatrix}\rho u\\ \rho uu+p-\mathcal{T}_{xx}\\ \rho vu-\mathcal{T}_{xy}\\ \rho wu-\mathcal{T}_{xx}\\ \rho eu+pu-\mathcal{Q}_x-\beta_x\end{Bmatrix} \tag{18}$$

$$G=\begin{Bmatrix}\rho v\\ \rho uv-\mathcal{T}_{xy}\\ \rho vv+p-\mathcal{T}_{yy}\\ \rho wv-\mathcal{T}_{xx}\\ \rho ev+pv-\mathcal{Q}_y-\beta_y\end{Bmatrix} \tag{19}$$

$$H=\begin{Bmatrix}\rho w\\ \rho uw-\mathcal{T}_{xz}\\ \rho vw-\mathcal{T}_{yz}\\ \rho ww+p-\mathcal{T}_{zz}\\ \rho ew+pw-\mathcal{Q}_z-\beta_z\end{Bmatrix} \tag{20}$$

where

$$\beta_x=\mathcal{T}_{xx}u+\mathcal{T}_{xy}v+\mathcal{T}_{xz}w \tag{21}$$

$$\beta_y=\mathcal{T}_{xy}u+\mathcal{T}_{yy}v+\mathcal{T}_{yz}w \tag{22}$$

$$\beta_z=\mathcal{T}_{xz}u+\mathcal{T}_{yz}v+\mathcal{T}_{zz}w \tag{23}$$

and

$$\mathcal{Q}_x=Q_x+\overline{q}_x \tag{24}$$

$$\mathcal{Q}_y=Q_y+\overline{q}_y \tag{25}$$

$$\mathcal{Q}_z=Q_z+\overline{q}_z, \tag{26}$$

assuming that control volume is fixed.

The contribution of inviscid fluxes to Eq. (15) is

$$\int_{dV} E_{inv}\mathbf{n}dA=\sum_{k=1}^{4} T^{-1}MdA \tag{27}$$

where k is the index of faces forming the tetrahedra. The flux vector and rotation matrix are

$$M=\begin{Bmatrix} \rho\hat{u} \\ \rho\hat{u}^2+p \\ \rho\hat{u}\hat{v} \\ \rho\hat{u}\hat{w} \\ \rho e\hat{u}+p\hat{u} \end{Bmatrix} \tag{28}$$

$$T^{-1}=\begin{bmatrix} 1 & 0 & 0 & 0 & 0 \\ 0 & n_x & s_x & t_x & 0 \\ 0 & n_y & s_y & t_y & 0 \\ 0 & n_z & s_z & t_z & 0 \\ 0 & 0 & 0 & 0 & 1 \end{bmatrix} \tag{29}$$

where

$$\begin{aligned} \hat{u}&=un_x+vn_y+wn_z \\ \hat{v}&=us_x+vs_y+ws_z \\ \hat{w}&=ut_x+vt_y+wt_z \end{aligned} \tag{30}$$

where (n_x,n_y,n_z) is the outwards unit normal on ∂V, (s_x,s_y,s_z) is an arbitrary unit normal on the surface of ∂V and $(t_x,t_y,t_z)=\mathbf{n}\times\mathbf{s}$ is the second unit normal on the surface ∂V.

The inviscid fluxes are computed using an exact one-dimensional Riemann solver (the second-order Godunov's method [45]) applied normal to each face. The least-squares method [46], is used to reconstruct the values of each variable on each side of the cell faces. The viscous fluxes and heat transfer flux at each cell face are computed by the application of Gauss' Theorem to the control volume. The second-order accurate scheme is developed by Knight [47]. The more details are given in Okong'o and Knight [48]. The temporal integration is performed by using a second-order accurate Runge-Kutta method [49]. Our LES code is parallelized in spanwise direction using domain decomposition with portable message passing interface model implementation (Mpich). One layer of the halo cells is attached to each side of subdomain in spanwise direction, thus these two layers of the halo cells are used for the data exchange with the adjacent subdomains [42]. Since the computational domain is rectangular parallelepiped, a simple one-dimensional decomposition is sufficient.

A compressible extension [24], of the method of Lund et al. [50] is used to generate the time-dependent inflow boundary condition. The flowfield at a downstream station is rescaled and reintroduced at the inflow boundary at every time-step. The distance between the inflow boundary and downstream station is larger than the streamwise correlation length [9], in order to avoid unphysical perturbations to the flow.

Grid Configuration. The computational domain is $L_x=14.8\delta$, $L_y=3.4\delta$, and $L_z=1.925\delta$ in streamwise, transverse, and spanwise directions, respectively. The reference quantities for nondimensionalization are the incoming boundary layer thickness δ, velocity U_∞, density ρ_∞, static temperature T_∞, and molecular viscosity μ_∞ (where the subscript ∞ denotes the freestream condition). The unstructured grid is utilized to access its adaptation ability of concentrating cells in the viscous sublayer to handle complex geometries. The grid resolution near the wall is evaluated in terms of Δx^+, Δy^+, and Δz^+, where $\Delta x^+=\Delta x/\eta$, $\Delta y^+=\Delta y/\eta$, and $\Delta z^+=\Delta z/\eta$. The inner length scale is $\eta=\nu_w/u_\tau$, where ν_w is the kinematic viscosity at the wall, $u_\tau=\sqrt{\tau_w/\rho_w}$ is the friction velocity, τ_w is the wall shear stress, and ρ_w is the density at the wall. Before we proceed with the discussion about the grid resolution, we first describe how to obtain η in our cases.

Table 1 Details of grid

	A2.88	I2.88	A4	I4
Δx^+	20	18	12	11
Δy^+	1.8	1.6	1.8	1.6
Δz^+	7	6.4	4	3.4
$\Delta x/\delta$	0.1	0.1	0.1	0.1
$\Delta y/\delta$	0.18	0.18	0.18	0.18
$\Delta z/\delta$	0.034	0.034	0.034	0.034

The theoretical value of the friction velocity u_τ for a supersonic flat plate boundary is obtained from the combined Law of the Wall and Wake evaluated at $y=\delta$

$$\frac{U_{VD}}{u_\tau}=\frac{1}{\kappa}\ln\left(y\frac{u_\tau}{\nu_w}\right)+C+\frac{2\Pi}{\kappa}\sin^2\left(\frac{\pi}{2}\frac{y}{\delta}\right) \tag{31}$$

where

$$U_{VD}=\frac{U_\infty}{A}\left\{\sin^{-1}\left[\frac{2A^2\left(\frac{U}{U_\infty}\right)-B}{\sqrt{B^2+4A^2}}\right)+\sin^{-1}\left[\frac{B}{\sqrt{B^2+4A^2}}\right]\right\} \tag{32}$$

$$\nu_w=\nu_\infty\left(\frac{T_w}{T_\infty}\right)^{1+\omega} \tag{33}$$

$$A=\left(\frac{\gamma-1}{2}\mathrm{Pr}_{tm}M_\infty^2\frac{T_\infty}{T_w}\right)^{1/2} \tag{34}$$

$$B=\frac{T_{aw}}{T_w}-1 \tag{35}$$

$$T_{aw}=T_\infty\left[1+\frac{(\gamma-1)}{2}\mathrm{Pr}_{tm}M_\infty^2\right] \tag{36}$$

where $\kappa=0.4$ is von Karman's constant, $C=5.1$, the wake parameter Π is 0.12 at $\mathrm{Re}_\delta=2\times10^4$, the exponent ω is 0.76, the mean turbulent Prandtl number Pr_{tm} is 0.89 and the ratio of specific heats γ is 1.4. The wall temperature T_w is fixed at 10% above the theoretical adiabatic temperature T_{aw} for the isothermal boundary. In the computation, u_τ and ν_w are obtained from $u_\tau=\sqrt{\tau_w/\rho_w}$ and $\nu_w=\nu_\infty(T_w/T_\infty)^{1+\omega}$, respectively.

The grid refinement study for the supersonic flat-plate boundary layer performed by Urbin [24] indicates that $\Delta x^+=18$, $\Delta y^+=1.5$, and $\Delta z^+=6.5$ at the wall is adequate for LES. The variation of Mach number and the different temperature boundary condition have an effect on η, and therefore on Δx^+, Δy^+, and Δz^+. At the same Mach number, the wall temperature for the isothermal case is 10% higher than that for the adiabatic case, leading to a larger η and the smaller Δx^+ if keeping the same Δx. However, this effect is very small in our case, therefore we keep the same Δx, Δy, and Δz for the different temperature condition at the same Mach number. The grid details are shown in Table 1, where A and I stand for the adiabatic and isothermal cases, respectively and the number followed indicates the Mach number. The Δx^+, Δy^+, and Δz^+ are measured at the wall and the Δx, Δy, and Δz are measured at $y/\delta=1.0$. The grid is uniform in the x and z directions and stretched in the y direction with about 23 layers of tetrahedra in the boundary layer for each case. The total number of the cells is about 1.4 million compared to about 2.3 million of the cells for a structured grid.

Results

The LES of flat-plate boundary layer at different Mach numbers with adiabatic and isothermal boundary conditions is performed.

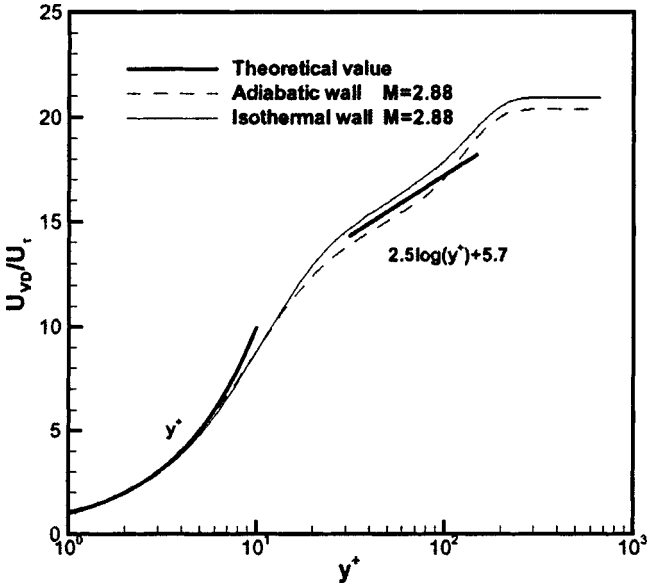

Fig. 1 Van Driest velocity at $M=2.88$

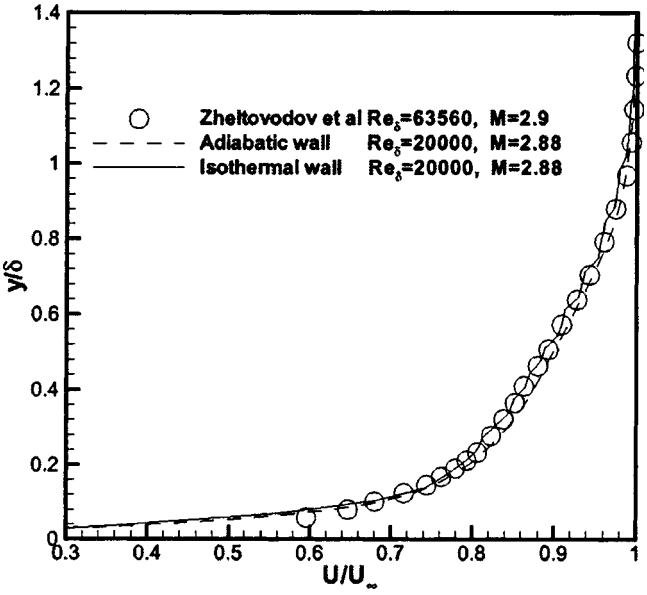

Fig. 3 Mean streamwise velocity at $M=2.88$

First, the mean quantities and turbulence stresses are presented in comparison with the available experiment [51–55], and DNS [56]. Second, the heat transfer character is presented in comparison with the experiment in [57] and the Reynolds analogy.

Mean Flowfield and Turbulence Feature. The mean quantities are averaged in time and in the spanwise direction and are denoted as $\langle f \rangle$. The time-averaging period is set to three times the flow-through time, where one flow-through time is defined as the time for the freestream flow to traverse the computational domain. The averaging is performed once the initial transient has decayed (i.e., after four flow-through times). The results are all shown at the recycle position ($x=11.88\delta$). The initial condition for Mach 4 cases is extracted from the Mach 2.88 flowfield, therefore seven flow-through times is performed before starting the time-averaging.

The mean streamwise velocity profiles using the Van Driest transformation are plotted in Fig. 1 and Fig. 2 (where u_τ is obtained from the simulation). Good agreement is shown with the viscous sublayer linear approximation $U_{VD}/u_\tau = y^+$ and Law of the Wall formulated in (31).

The mean velocity profiles shown in Fig. 3 and Fig. 4 exhibit virtually identical distributions for adiabatic and isothermal cases and show good agreement with the experiment [53,58]. The mean temperature profile in Fig. 5 and Fig. 6 display a higher temperature distribution for the isothermal case with the wall temperature higher than the adiabatic and experiment data [58], which are also obtained at the adiabatic boundary condition. The difference is expected since the wall temperature for the isothermal case is fixed at 10% higher than the adiabatic case.

The discrepancies between Mach 4 cases and experiments in Fig. 4 and Fig. 6 are due to the effects of Mach number and Reynolds number. The Reynolds number in the simulation is one magnitude lower than experiments due to the significant computation cost in LES. The outer portion of the velocity profiles in

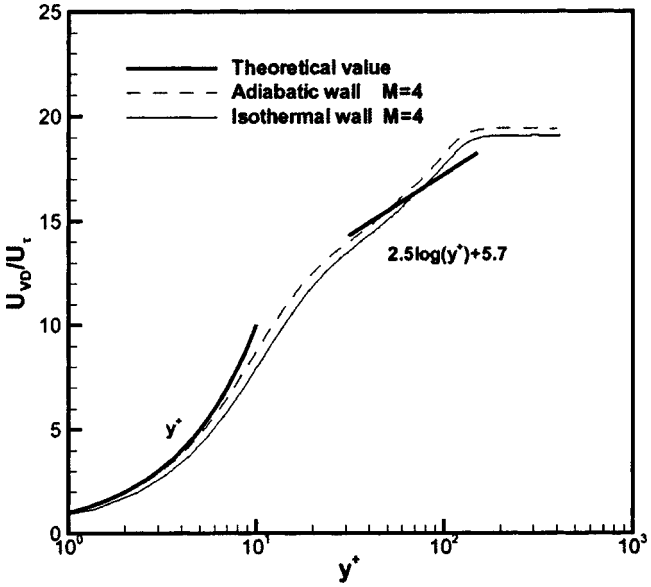

Fig. 2 Van Driest velocity at $M=4$

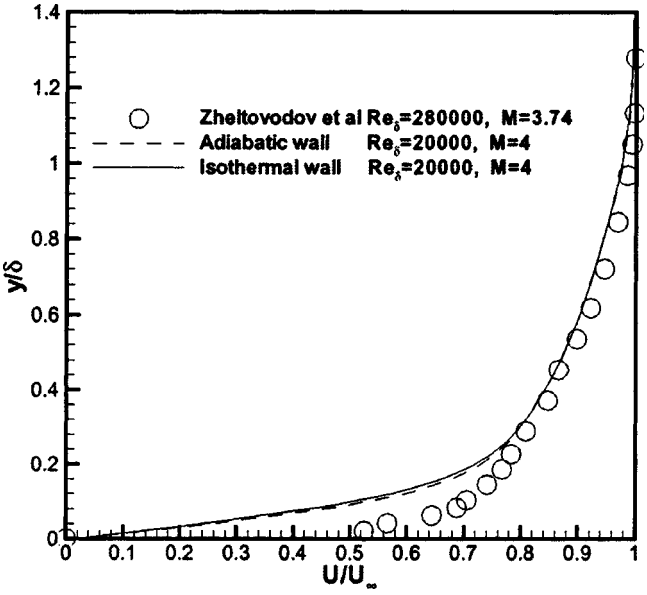

Fig. 4 Mean streamwise velocity at $M=4$

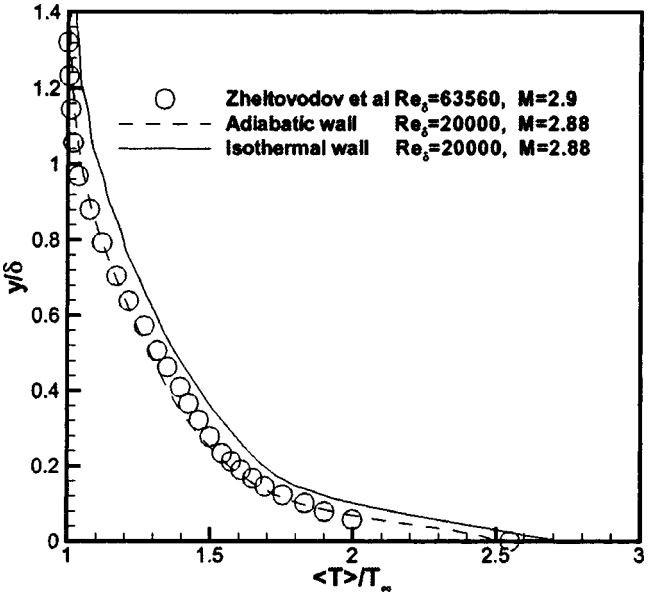

Fig. 5 Mean temperature at $M=2.88$

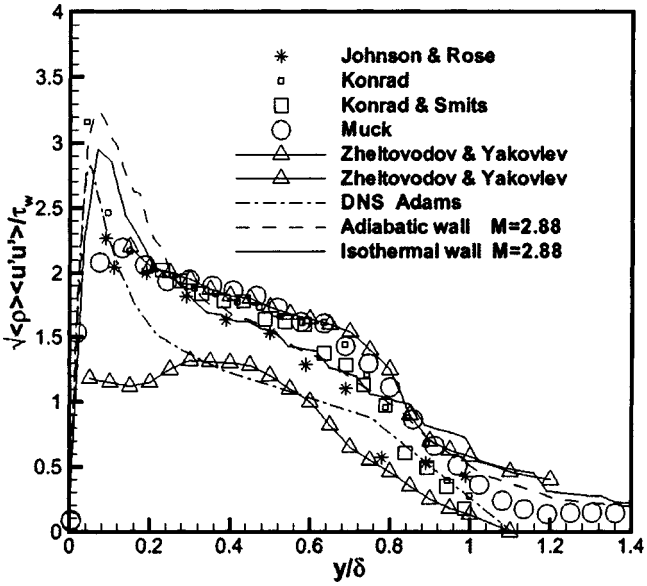

Fig. 7 Streamwise Reynolds stress at $M=2.88$

Fig. 4 is in good agreement with experiment since this portion is not sensitive to the Reynolds number. The discrepancy in the inner portion is due to the effect of the Reynolds number. The effect of the Mach number is observed in Fig. 6, which can be explained using Crocco's relationship between the mean temperature and mean velocity profiles

$$\frac{T}{T_\infty}=\frac{T_w}{T_\infty}+\frac{T_{aw}-T_w}{T_\infty}\frac{U}{U_\infty}-r\frac{\gamma-1}{2}M_\infty^2\left(\frac{U}{U_\infty}\right)^2 \tag{37}$$

where r is the recovery factor defined as

$$r=\frac{T_r-T_\infty}{T_0-T_\infty} \tag{38}$$

where T_r is the adiabatic or recovery temperature and T_0 is the freestream stagnation temperature. For the adiabatic case, Eq. (37) becomes

$$\frac{T}{T_\infty}=\frac{T_w}{T_\infty}-r\frac{\gamma-1}{2}M_\infty^2\left(\frac{U}{U_\infty}\right)^2. \tag{39}$$

Equations (37) and (39) show the trend that under the same mean velocity distribution, the mean temperature decreases with increasing Mach number, leading to the discrepancy between the calculation and experiment in the outer portion of the mean temperature profiles in Fig. 6. The discrepancy in the inner portion is mainly due to the effect of the Reynolds number.

The streamwise Reynolds stresses shown in Fig. 7 and Fig. 8 are compared with the experiments [51–55], and DNS [56]. The experimental range provided by Zheltovodov and Yakovlev [53] was obtained for Mach number range of 1.74–9.4. The distributions for the adiabatic and isothermal cases are very similar except

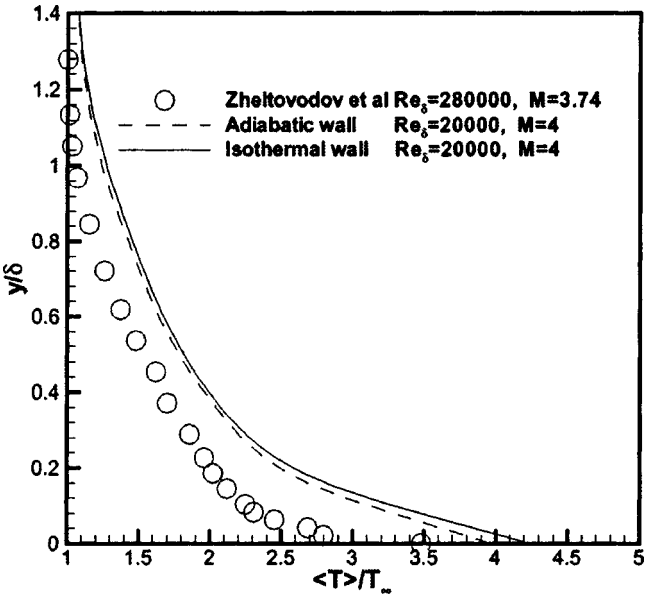

Fig. 6 Mean temperature at $M=4$

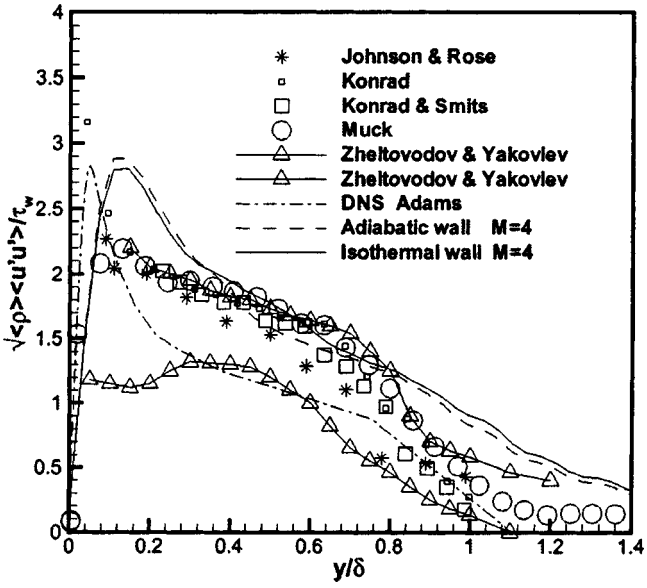

Fig. 8 Streamwise Reynolds stress at $M=4$

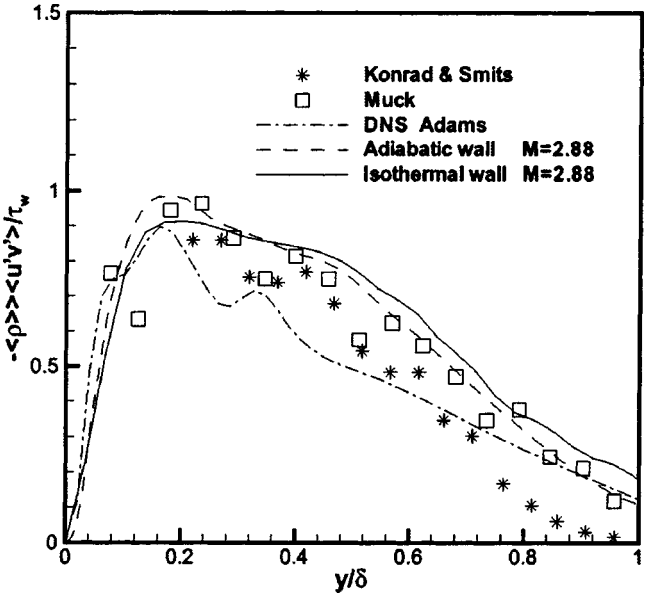

Fig. 9 Reynolds shear stress at $M=2.88$

close to the wall. The good agreement is shown in the outer portion of the boundary layer ($y/\delta>0.2$). The peak in the near-wall region ($y/\delta<0.2$) is supported by experimental data by Konrad [54] and the DNS result [56]. The Reynolds shear stresses displayed in Fig. 9 and Fig. 10 also show the good agreement. The Reynolds stresses as normalized are insensitive to the Reynolds number [9].

Heat Transfer. The capability of our LES method to accurately predict the heat transfer in the flat-plate boundary layer is evaluated. The Reynolds analogy relates the skin friction coefficient C_f and heat transfer coefficient C_h by the Prandtl number as follows:

$$\frac{2C_h}{C_f}=\frac{1}{\mathrm{Pr}_{tm}} \tag{40}$$

where C_h and C_f are written as

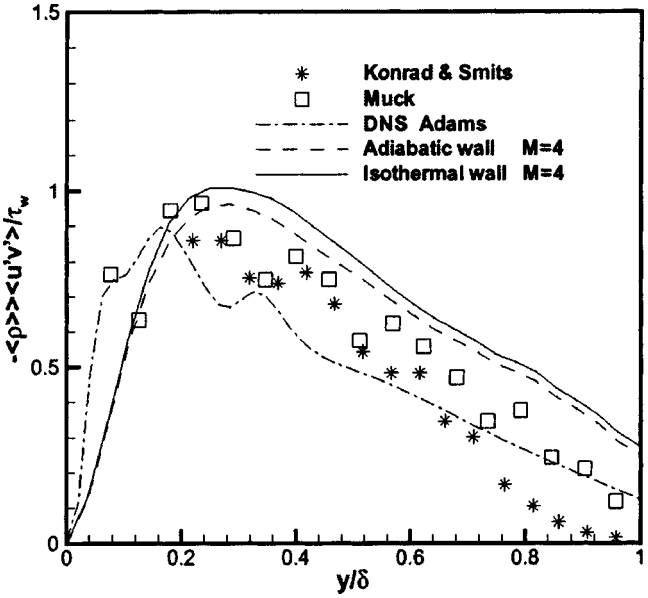

Fig. 10 Reynolds shear stress at $M=4$

Table 2 LES predictions

Name	T_w/T_∞	C_f	C_h
A2.88	2.51	2.44×10^{-3}	0
I2.88	2.72	2.32×10^{-3}	1.27×10^{-3}
A4	3.95	1.97×10^{-3}	0
I4	4.23	2.00×10^{-3}	1.24×10^{-3}

$$C_h=\frac{q_w}{\rho_\infty U_\infty c_p(T_w-T_{aw})} \tag{41}$$

$$C_f=\frac{\tau_w}{\frac{1}{2}\rho_\infty U_\infty^2} \tag{42}$$

where c_p is the specific heat at constant pressure. The wall heat flux (q_w) and skin friction (τ_w) are obtained from the isothermal case and the adiabatic wall temperature (T_{aw}) is calculated from the adiabatic case. The wall heat flux is

$$q_w=-\lambda\left.\frac{\partial T}{\partial y}\right|_w \tag{43}$$

and the wall shear stress is

$$\tau_w=\mu_w\left.\frac{\partial u}{\partial y}\right|_w. \tag{44}$$

The wall temperature T_w is fixed at $T_w=1.1T_{aw}$, where the empirical adiabatic wall temperature $T_{aw}=[1+(\gamma-1)/2\mathrm{Pr}_{tm}M_\infty^2]T_\infty$. All the predicted results are listed in Table 2, where the wall temperature for the isothermal case is fixed. The comparison with experiment is shown in Table 3. The experimental adiabatic wall temperature is computed from $T_{aw}=[1+(\gamma-1)/2\mathrm{Pr}_{tm}M_\infty^2]T_\infty$. The computed mean turbulent Prandtl number from (40) shows good agreement with experiment value of 0.89, indicating the consistency of LES results with the Reynolds analogy.

The turbulent Prandtl number changes across the boundary layer. Simpson et al. [57] have established the uncertainty envelope of the turbulent Prandtl number for incompressible zero-pressure-gradient turbulent boundaries. The experimental predictions by Meier and Rotta [59] at Mach number up to 4.5 at the wall and Horstman and Owen [60] at $M=7.2$ and cooled wall conditions fall into this uncertainty envelope. According to the eddy viscosity hypothesis, the turbulent stress and heat flux can be expressed as

Table 3 Comparison of LES and experiment

Cases	Name	LES	Experiment	Error
Mach=2.88	T_{aw}/T_∞	2.51	2.549	1.5%
	C_f	2.32×10^{-3}	2.56×10^{-3}	9.4%
	C_h	1.27×10^{-3}	1.44×10^{-3}	11.8%
	$2C_h/C_f$	1/0.91	1/0.89	2.2%
	Pr_{tm}	0.91	0.89	2.2%
Mach=4.0	T_{aw}/T_∞	3.95	3.848	2.6%
	C_f	2.0×10^{-3}	1.22×10^{-3}	7.8%
	C_h	1.24×10^{-3}	1.22×10^{-3}	1.6%
	$2C_h/C_f$	1/0.81	1/0.89	9.9%
	Pr_{tm}	0.81	0.89	9.0%

Note:
Experimental T_{aw} from Eq. (36)
Experimental C_f from Eqs. (31), (32), and (42)
Experimental C_h from Eq. (40)

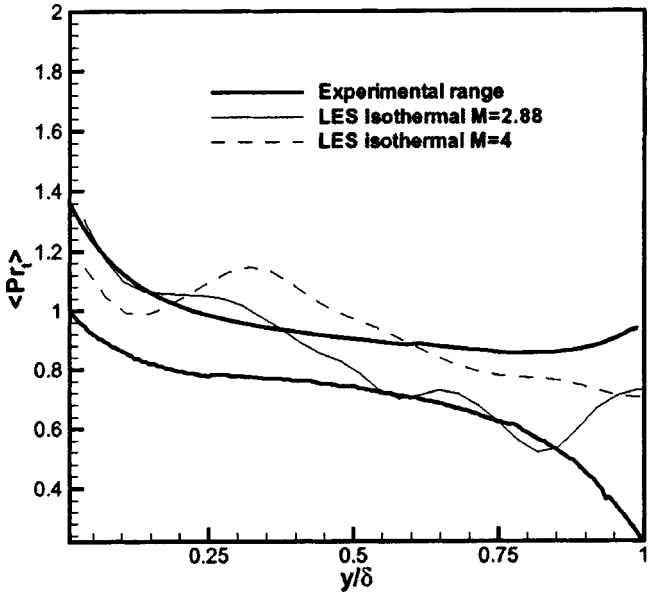

Fig. 11 Turbulent Prandtl number

$$\tau_{ik} = -\overline{\rho u_i' u_k'} = \mu_t \left(\frac{\partial \tilde{u}_i}{\partial x_k} + \frac{\partial \tilde{u}_k}{\partial x_i} - \frac{2}{3} \frac{\partial \tilde{u}_j}{\partial x_j} \delta_{ik} \right) - \frac{2}{3} \overline{\rho} \tilde{k} \delta_{ik} \quad (45)$$

$$Q_k = -c_p \overline{\rho T' u_k'} = \lambda \frac{\partial \tilde{T}}{\partial x_k} \quad (46)$$

where the bar $\bar{}$ denotes the filtered flow variables and the tilde $\tilde{}$ denotes the Favre-averaged filter flow variables. The local turbulent Prandtl number (Pr_t) for a two-dimensional boundary layer can be derived from the above two equations as

$$\mathrm{Pr}_t = \frac{\dfrac{\partial \tilde{T}}{\partial y} \overline{\rho u' v'}}{\dfrac{\partial \tilde{u}}{\partial y} \overline{\rho T' v'}}. \quad (47)$$

The calculated turbulent Prandtl number profile is shown compared with the experimental range in Fig. 11. The Prandtl number reaches the maximum at the wall and starts to decrease away from the wall. In the outer portion of boundary layer, the fluctuation of Prandtl number is relatively greater than the inner portion, which is consistent with the experimental trend.

Conclusions

The first LES predictions of adiabatic and isothermal supersonic flat-plate boundary layer using MILES are presented. An LES of an adiabatic and an isothermal supersonic flat-plate boundary layer at $\mathrm{Re}_\delta = 2 \times 10^4$ and Mach 2.88 and 4 has been performed. The computed flowfield is in good agreement with experiment. The relationship between the computed heat transfer coefficient and skin friction coefficient obeys the Reynolds analogy. The variation of turbulent Prandtl number cross the boundary layer is consistent with the experimental trend.

Acknowledgments

The research is supported by AFOSR under grant No. F49620-99-1-0008 monitored by Drs. R. Herklotz, L. Sakell, J. Schmisseur, and S. Walker and by SCOPES 2000-2003 program under project No. 7SUPJ062351. All computations were performed at Rutgers University.

References

[1] Masad, J. A., and Abid, R., 1995, "On Transition in Supersonic and Hypersonic Boundary Layers," Int. J. Eng. Sci., **33**, pp. 1893–1919.
[2] Dussauge, Jean-Paul, and Smits, A. J., 1997, "Characteristic Scales for Energetic Eddies in Turbulent Supersonic Boundary Layers," Exp. Therm. Fluid Sci., **14**, pp. 85–91.
[3] Debiève, J., Dupont, P., Laurent, H., Menaa, M., and Dussauge, Jean-Paul, 2000, "Compressibility and Structure of Turbulence in Supersonic Shear Flows," Eur. J. Mech. B—Fluids, **19**, pp. 597–614.
[4] Kistler, A. L., 1959, "Fluctuation Measurements in a Supersonic Turbulent Boundary Layer Flow," Phys. Fluids A, **2**, pp. 290–296.
[5] Bradshaw, P., 1977, "Compressible Turbulent Shear Layers," Annu. Rev. Fluid Mech., **9**, pp. 33–54.
[6] Spina, E. F., Donovan, J. F., and Smits, A. J., 1991, "On the Structure of High-Reynolds-Number Supersonic Turbulent Boundary Layers," J. Fluid Mech., **222**, pp. 293–327.
[7] Spina, E. F., Smits, A. J., and Robinson, S. K., 1994, "The Physics of Supersonic Turbulent Boundary Layers," Annu. Rev. Fluid Mech., **26**, pp. 287–319.
[8] Lele, S. K., 1994, "Compressibility Effects on Turbulence," Annu. Rev. Fluid Mech., **26**, pp. 211–254.
[9] Smits, A. J., and Dussauge, Jean-Paul, 1996, *Turbulent Shear Layers in Supersonic Flow*, American Institute of Physics, Woodbury, NY.
[10] Erlebacher, G., Hussaini, M. Y., Speziale, C., and Zang, T. A., 1992, "Toward the Large-Eddy Simulation of Compressible Turbulent Flows," J. Fluid Mech., **238**, pp. 155–185.
[11] Sommer, T. P., So, R. M. C., and Zhang, H. S., "Supersonic Flow Calculations Using a Reynolds-Stress and a Thermal Eddy Diffusivity Turbulence Model," ASME J. Fluids Eng., **116**, pp. 469–476.
[12] Childs, R. E., and Reisenthel, P. H., 1995, "Simulation Study of Compressible Turbulent Boundary Layer," AIAA Paper No. 95-0582.
[13] Hatay, F. F., and Biringen, S., 1995, "Direct Numerical Simulation of Low-Reynolds Number Supersonic Turbulent Boundary Layers," AIAA Paper No. 95-0581.
[14] Rai, M. M., Gatski, T. B., and Erlebacher, G., 1995, "Direct Simulation of Spatially Evolving Compressible Turbulent Boundary Layers," AIAA Paper No. 95-0583.
[15] Ducros, F., Comte, P., and Lesieur, M., 1996, "Large Eddy Simulation of Transition to Turbulence in a Boundary Layer Developing Spatially over a Flat Plate," J. Fluid Mech., **326**, pp. 1–36.
[16] Haworth, D., and Jansen, K. E., 1996, "LES on Unstructured Deforming Meshes: Towards Reciprocating IC Engines," *Proceedings of the 1996 Summer Program, Center for Turbulence Research*, Stanford University/NASA Ames Research Center, Stanford University, Stanford, CA, pp. 329–346.
[17] Spyropoulos, E., and Blaisdell, G., 1996, "Evaluation of the Dynamic Model for Simulations of Compressible Decaying Isotropic Turbulence," AIAA J., **34**, pp. 990–998.
[18] Jansen, K. E., 1997, "Large-Eddy Simulation Using Unstructured Grids," *Advances in DNS/LES*, Greyden Press, pp. 117–128.
[19] Knight, D., 1997, "Numerical Simulation of Compressible Turbulent Flows Using the Reynolds-Averaged Navier-Stokes Equations," AGARD FDP/VKI Special Course on Turbulence in Compressible Flows, AGARD Report R-819.
[20] Urbin, G., Knight, D., and Zheltovodov, A. A., 1990, "Compressible Large Eddy Simulation Using Unstructured Grid: Supersonic Turbulent Boundary Layer and Compression Corner," AIAA Paper No. 99-0427.
[21] Guarini, S. E., Moser, R. D., Shariff, K., and Wray, A., 2000, "Direct Numerical Simulation of a Supersonic Turbulent Boundary Layer at Mach 2.5," J. Fluid Mech., **414**, pp. 1–33.
[22] Guezangar, D., Francescatto, J., Guillard, H., and Dussauge, J.-P., 2000, "Variations on a $k-\epsilon$ Turbulence Model for Supersonic Boundary Layer Computation," Eur. J. Mech. B/Fluids, **18**, pp. 713–738.
[23] Adams, N. A., Maeder, T., Guo, Y., and Kleiser, L., 2001, "Direct Simulation of Turbulent Supersonic Boundary Layers by Extended Temporal Approach," J. Fluid Mech., **429**, pp. 187–216.
[24] Urbin, G., and Knight, D., 2001, "Large Eddy Simulation of Supersonic Turbulent Boundary Layer Using an Unstructured Grid," AIAA J., **39**, pp. 1288–1295.
[25] Piomelli, U., Zang, T. A., Speziale, C. G., and Hussaini, M. Y., 1990, "On the Large-Eddy Simulation of Transitional Wall-Bounded Flows," Phys. Fluids A, **A2**, pp. 257–265.
[26] Lesieur, M., and Metais, O., 1996, "New Trends in Large-Eddy Simulations of Turbulence," Annu. Rev. Fluid Mech., **28**, pp. 45–82.
[27] Yoshizawa, A., 1986, "Statistical Theory for Compressible Turbulent Shear Flows, With the Application to Subgrid Modeling," Phys. Fluids, **29**, pp. 127–140.
[28] Speziale, C. G., Erlebacher, G., Zang, T. A., and Hussaini, M. Y., 1988, "The Subgrid-Scale Modeling of Compressible Turbulence," Phys. Fluids, **31**, pp. 940–942.
[29] Zang, T. A., Dahlburg, R. B., and Dahlburg, J. P., 1992, "Direct and Large Eddy Simulations of Compressible Navier-Stokes Turbulence," Phys. Fluids A, **A1**, pp. 127–140.
[30] Boris, J., Grinstein, F., Oran, E., and Kolbe, R., 1992, "New Insights into Large Eddy Simulation," Fluid Dyn. Res., **10**, pp. 199–228.
[31] Spyropoulos, E., and Blaisdell, G., 1998, "Large Eddy Simulation of a Spatially Evolving Supersonic Turbulent Boundary Layer Flow," AIAA J., **36**, pp. 1983–1990.

[32] Grinstein, F. F., 1995, ''Self-Induced Vortex Ring Dynamics in Subsonic Rectangular Jets,'' Phys. Fluids, **7**, pp. 2519–2521.
[33] Grinstein, F. F., Gutmark, E. J., Parr, T., Hanson-Parr, D., and Obeysekare, U., 1996, ''Streamwise and Spanwise Vortex Interaction in an Axisymmetric Jet, A Computational and Experimental Study,'' Phys. Fluids, **8**, pp. 1515–1524.
[34] Grinstein, F. F., and DeVore, C. R., 1996, ''Dynamics of Coherent Structures and Transition to Turbulence in Free Square Jets,'' Phys. Fluids, **8**, pp. 1237–1251.
[35] Gathmann, R. J., Si-Ameur, M., and Mathey, F., 1993, ''Numerical Simulations of Three-Dimensional Natural Transition in the Compressible Confined Shear Layer,'' Phys. Fluids, **5**, pp. 2946–2968.
[36] Porter, D. H., Pouquet, A., and Woodward, P. R., 1994, ''Kolmogorov-Like Spectra in Decaying Three Dimensional Supersonic Flows,'' Phys. Fluids, **6**, pp. 2133–2142.
[37] Fureby, C., and Grinstein, F. F., 1999, ''Monotonically Integrated Large Eddy Simulation of Free Shear Flows,'' AIAA J., **37**, pp. 544–556.
[38] Fureby, C., Nilsson, Y., and Andersson, K., 1999, ''Large Eddy Simulation of Supersonic Base Flow,'' AIAA Paper No. 99-0426.
[39] Fureby, C., and Grinstein, F. F., 2000, ''Large Eddy Simulation of High Reynolds-Number Free and Wall Bounded Flows,'' AIAA Paper No. 2000-2307.
[40] Knight, D., Yan, H., and Zheltovodov, A. A., 2001, ''Large Eddy Simulation of Supersonic Turbulent Flow in Expansion-Compression Corner,'' Third AFOSR International Conference on DNS and LES, University of Texas at Arlington, Aug.
[41] Urbin, G., Knight, D., and Zheltovodov, A. A., 2000, ''Large Eddy Simulation of a Supersonic Compression Corner Part I,'' AIAA Paper No. 2000-0398.
[42] Chernyavsky, B., Yan, H., and Knight, D., 2001, ''Analyses of Some Numerical Problem in LES,'' AIAA Paper No. 2001-0436.
[43] Moin, P., and Jimenez, J., 1993, ''Large Eddy Simulation of Complex Turbulent Flows,'' AIAA Paper No. 93-3099.
[44] Moin, P., Squires, K., Cabot, W., and Lee, S., 1991, ''A Dynamic Subgrid-scale Model for Compressible Turbulence and Scalar Transport,'' Phys. Fluids A, **11**, pp. 2746–2757.
[45] Gottlieb, J., and Groth, C., 1988, ''Assessment of Riemann Solvers for Unsteady One-Dimensional Inviscid Flows of Perfect Gases,'' J. Comput. Phys., **78**, pp. 437–458.
[46] Ollivier-Gooch, C., 1997, ''High Order ENO Schemes for Unstructured Meshes Based on Least Squares Reconstruction,'' AIAA Paper No. 97-0540.
[47] Knight, D., 1994, ''A Fully Implicit Navier-Stokes Algorithm Using an Unstructured Grid and Flux Difference Splitting,'' Appl. Numer. Math. **16**, pp. 101–128.
[48] Knight, D., and Okong'o, N., 1998, ''Accurate Three-Dimensional Unsteady Flow Simulation Using Unstructured Grids,'' AIAA Paper No. 98-0787.
[49] Press, W. H., Teukolsky, S. A., Vetterling, W. T., and Flannery, B. P., 1992, *Numerical Recipes in C: The Art of Scientific Computing*, 2nd ed., Cambridge University Press, Cambridge, NY.
[50] Lund, T., Wu, X., and Squires, K., 1998, ''Generation of Turbulent Inflow Data for Spatially Developing Boundary Layer Simulation,'' J. Comput. Phys., **140**, pp. 233–258.
[51] Johnson, D., and Rose, W., 1975, ''Laser Velocimeter and Hot Wire Anemometer Comparison in a Supersonic Boundary Layer,'' AIAA J., **13**, pp. 512–515.
[52] Muck, K., Spina, E., and Smits, A., 1984, ''Compilation of Turbulence Data for an 8 Degree Compression Corner at Mach 2.9,'' Report MAE-1642.
[53] Zheltovodov, A. A., and Yakovlev, V. N., 1986, ''Stages of Development, Gas Dynamic Structure and Turbulence Characteristics of Turbulent Compressible Separated Flows in the Vicinity of 2-D Obstacles,'' Preprint No. 27-86, Inst. of Theoretical and Applied Mechanics, USSR Acad. of Sciences, Novosibirsk (in Russian).
[54] Konrad, W., 1993, ''Three Dimensional Supersonic Turbulent Boundary Layer Generated by an Isentropic Compression,'' Ph.D. thesis, Princeton University, Princeton, NJ.
[55] Konrad, W., and Smits, A., 1998, ''Turbulence Measurements in a Three-Dimensional Boundary Layer in a Supersonic Flow,'' J. Fluid Mech., **372**, pp. 1–23.
[56] Adams, N. A., 1997, ''Direct Numerical Simulation of Turbulent Supersonic Boundary Layer Flow,'' *Advances in DNS/LES*, Greyden Press, pp. 29–40.
[57] Simpson, R. L., Whitten, D. G., and Moffat, R. J., 1970, ''An Experimental Study of the Turbulent Prandtl Number of Air With Injection and Suction,'' Int. J. Heat Mass Transf., **13**, pp. 125–143.
[58] Zheltovodov, A. A., Trofinov, V. M., Schülen, E., and Vakovlev, V., 1990, ''An Experimental Documentation of Supersonic Turbulent Flows in the Vicinity of Forward- and Backward-Facing Ramps,'' Report No. 2030, Institute of Theoretical and Applied Mechanics, USSR Academy of Sciences.
[59] Meier, H. U., and Rotta, J. C., 1971, ''Temperature Distributions in Supersonic Turbulent Boundary Layer,'' AIAA J., **9**, pp. 2149–2150.
[60] Horstman, C. C., and Owen, F. K., 1972, ''Turbulent Properties of a Compressible Boundary Layer,'' AIAA J., **10**, pp. 1418–1424.

Computing Blunt Body Flows on Coarse Grids Using Vorticity Confinement

M. Fan
University of Tennessee Space Institute,
411 BH Goethert Parkway,
Tullahoma, TN 37388

Y. Wenren

W. Dietz

Flow Analysis, Inc.,
256 93rd Street,
Brooklyn, NY 11209

M. Xiao

J. Steinhoff

University of Tennessee Space Institute,
411 BH Goethert Parkway
Tullahoma, TN 37388

Over the last few years, a new flow computational methodology, vorticity confinement, has been shown to be very effective in treating concentrated vortical regions. These include thin vortex filaments which can be numerically convected over arbitrary distances on coarse Eulerian grids, while requiring only ~2 grid cells across their cross section. They also include boundary layers on surfaces "immersed" in nonconforming uniform Cartesian grids, with no requirement for grid refinement or complex logic near the surface. In this paper we use vorticity confinement to treat flow over blunt bodies, including attached and separating boundary layers, and resulting turbulent wakes. In the wake it serves as a new, simple effective large-eddy simulation (LES). The same basic idea is applied to all of these features: At the smallest scales (~2 cells) the vortical structures are captured and treated, effectively, as solitary waves that are solutions of nonlinear discrete equations on the grid. The method does not attempt to accurately discretize the Euler/Navier-Stokes partial differential equations (pde's) for these small scales, but, rather, serves as an implicit, nonlinear model of the structures, directly on the grid. The method also allows the boundary layer to be effectively "captured." In the turbulent wake, where there are many scales, small structures represent an effective small scale energy sink. However, they do not have the unphysical spreading due to numerical diffusion at these scales, which is present in conventional computational methods. The basic modeling idea is similar to that used in shock capturing, where intrinsically discrete equations are satisfied in thin, modeled regions. It is argued that, for realistic high Reynolds number flows, this direct, grid-based modeling approach is much more effective than first formulating model pde's for the small scale, turbulent vortical regions and then discretizing them. Results are presented for three-dimensional flows over round and square cylinders and a realistic helicopter landing ship. Comparisons with experimental data are given. Finally, a new simpler formulation of vorticity confinement is given together with a related formulation for confinement of passive scalar fields. [DOI: 10.1115/1.1517573]

1 Introduction

Many real-world flows are characterized by regions of concentrated vorticity. These are typically turbulent at realistic Reynolds numbers and can convect over long distances, either as thin vortex filaments or blunt body wakes containing small-scale vortical structures. Also, boundary layers are typically thin, turbulent vortical structures near solid surfaces. Even though the Navier-Stokes equations apply to these flows, it is not feasible to solve them on foreseeable computers due to the ever-present small scales. As a result, conventional computational fluid dynamics (CFD) methods involve first formulating the partial differential equations (pde's) that model these turbulent regions. These pde's are then discretized in the turbulent regions and then solved. This typically requires large computer resources and difficult grid generation. The problem is that resolving even the model pde's requires very fine computational grids, which must conform to the surface for the boundary layer. Further, these methods typically dissipate thin filaments and vortical structures in the wake as they convect. This is true even if on the order of ten grid points are devoted to the cross section of each structure and complex, high order discretizations are used. The problem is intrinsic to the discretization of the convective terms and made worse by the use of dissipative terms to model the turbulent effects. Finally, even if the model pde's *are* resolved, the result is, of course, still a model approximation of the turbulent flow.

In this paper, we describe an entirely new CFD methodology where very different numerical models are used for small-scale vortical regions. Instead of first hypothesizing a turbulence model based on pde's and then trying to accurately discretize and resolve them, we model the internal structure of the vortical regions *directly* on the grid using generalized nonlinear *difference* equations, rather than using finite difference discretizations of partial differential equations that attempt to approximately resolve the model equations. This approach allows treatment of small vortical structures as objects spread over only one to two grid cells on coarse, essentially uniform Cartesian computational grids. For the smooth, large-scale components of the flow, the method acts like conventional CFD ones with conventional discretization of the pde's.

These ideas are implemented in the methodology termed *vorticity confinement*. Although new for vortical regions, these ideas are old for the treatment of shocks, starting with Von Neumann and Richtmyer [1], Lax [2], and others. There, as is well known, shocks that are treated as thin regions spread over a few grid cells that obey discrete, grid-based nonlinear model equations that conserve certain quantities. This approach has been shown to be more effective than trying to discretize and solve the applicable Navier-Stokes pde's in those thin regions. One difference, however, is that with shocks, unlike vortical regions, characteristics slope inward toward the shock. As a result, the modeling is simpler than that with vortical structures. One of the first confinement-type schemes for contact discontinuities, where, unlike shocks, physical characteristics do not help, was developed by Harten [3], but was specialized to one-dimensional compressible flow.

Contributed by the Fluids Engineering Division for publication in the JOURNAL OF FLUIDS ENGINEERING. Manuscript received by the Fluids Engineering Division March 21, 2002; revised manuscript received May 3, 2002. Associate Editor: G. E. Karniadakis.

It is interesting to compare the vorticity confinement approach to other schemes.

- The main difference is that there is a stable, overall *negative* diffusion at scales larger than ~2 grid cells. The effect of this is very small at the larger scales but very important at the smaller scales. This is necessary to maintain structures as compact, stable solitary waves.
- Methods that merely cancel any added numerical diffusion in the convection part will not do this, since then these structures will still distort when they convect through regions of nonuniform flow. Distorted vortex cores will then develop large multipole moments in the outer, induced flow and not capture the physical characteristics of rolling up vortices. This feature sets confinement apart from methods that add numerical terms to make the total effective diffusion small (but still positive) for the larger scales and do not effectively capture the small scales of the order of a grid cell.
- It has been explained above how the confinement method is very different from conventional large-eddy simulation (LES) schemes that use pde-based turbulence models that must be resolved.
- The idea of using the difference equations themselves as implicit small-scale models is used in other approaches such as ''MILES'' [4]. However, usually a stabilizing positive diffusion results from these schemes, which, as explained above, is different from our approach.

Many results have been obtained in recent years using vorticity confinement, [5–24]. Lohner has a very good short review of this work, [20]. Initial results were for isolated, convecting vortex filaments, [15–17]. Then, vortices convecting past airfoils and wings (blade—vortex interactions) were treated, [14]. In this early study, unlike in our current studies, near the surface a surface-fitted grid was used for the wing with surface grid refinement to resolve the actual Navier-Stokes equations, since only a low Reynolds number, laminar case was treated. To accommodate this grid refinement with vorticity confinement, the parameter specifying the strength of the vorticity confinement term (ε) was made to be proportional to grid size so that it automatically vanished in the fine-grid boundary layer region, but was able to confine the convecting vortex in the external, coarse-grid region. Our current studies, like those described in this paper, involve surfaces ''immersed'' in uniform, nonconforming grids with no grid refinement and use a constant value for ε.

Recently, vorticity confinement has been used together with unstructured grids, [20,21]. When using these grids, which have rapidly changing cell sizes, care must be taken not only that ε varies properly with cell size, but also that the confinement correction does not extend beyond the vortex core due to numerical artifacts of the implementation. This property is true in the continuum limit, as shown in the description of Section 2, and should be preserved in the discretization. If the correction *does* extend beyond the vortex, then it could erroneously affect surface pressure if a vortex is passing near a surface. This could be important, for example, for delta wings, [20], and similar cases, where vortices convect near surfaces. In fact, for delta wings, it is well known that there is a feeding sheet from the leading edge causing the vortex to grow in strength as it convects and causing the characteristics to point towards it. In such cases, for a reasonable grid, confinement is not really needed (until the vortex convects past the trailing edge). If confinement is used correctly, however, it should not change the nearby pressure on the surface even in these cases for high Reynolds number flow. Finally, in low Reynolds number viscous flow cases where laminar flow occurs, the proper Navier-Stokes equations should, of course, be used, since the vortical scales are then not small and there is no need to discretize model equations for small scales.

An important issue in CFD is always grid dependence—whether the basic pde's are adequately resolved. One of the goals of vorticity confinement is to remove some of this dependence. The basic idea is that the smallest resolved structures can be only one or two grid cells wide, and are defined directly on the grid. Thus there are no unknown unresolved structures with uncontrolled numerical errors. These small structures can be controlled and can also be larger than the minimum size, by varying a simple parameter. The larger scales are resolved, as in conventional CFD.

In this paper, vorticity confinement is applied to a series of blunt bodies, a circular and a square cylinder, and a realistic helicopter landing ship. In the cylinder cases, for which unsteady experimental results are available, comparison is made. The ship case demonstrates the ability of vorticity confinement to preserve thin, concentrated vortical structures over long distances. Also velocity and vortex trajectory computations are shown to agree well with experimental results. All cases were run on grids much coarser than those required by conventional CFD methods and did not require body-conforming grid generation or refinement near the surfaces.

As stated, the cases computed all involve solid surfaces ''immersed'' in uniform Cartesian grids. Vorticity confinement allows us to do this in a very simple way and to use no-slip boundary conditions with a simple, implicit boundary layer model, even though the grid is coarse.

First, the surface is represented implicitly by a smooth ''level set'' function ''F,'' defined at each grid point. This is just the (signed) distance from each grid point to the nearest point on the surface—positive outside, negative inside. Then, each time-step during the solution any velocities added by the solver in the interior are set to zero. This results in a concentrated vortical region along the surface. If we only had a conventional CFD solver this vorticity would quickly convect and diffuse away from the surface regions, destroying the accuracy of the outer solution. However, we use vorticity confinement near $F=0$ to confine vorticity to one to two grid cells along the surface when it is attached. The simple boundary layer can still separate, however, especially at edges and in regions of strong adverse pressure.

2 Vorticity Confinement

Vorticity confinement can be implemented in a pre-existing flow solver, for both incompressible and compressible flow, by adding a pair of terms to the discretized momentum conservation equations, [13].

For general unsteady incompressible flows, the governing equations with the vorticity confinement term are discretizations of the continuity equation and the momentum equations, with added terms:

$$\nabla \cdot \mathbf{q} = 0 \tag{2.0.1}$$

$$\partial_t \mathbf{q} = -(\mathbf{q}\cdot\nabla)\mathbf{q} - \frac{1}{\rho}\nabla p + [\mu\nabla^2\mathbf{q} - \varepsilon\mathbf{s}] \tag{2.0.2}$$

where $\mathbf{q}$ is the velocity vector, p is the pressure, ρ is the density, and μ is a diffusion coefficient that includes numerical effects (we assume physical diffusion is much smaller). For the last term, $\varepsilon\mathbf{s}$, ε is a numerical coefficient that, together with μ, controls the size and time scales of the convecting vortical regions or vortical boundary layers. For this reason, we refer to the two terms in the brackets as ''confinement terms.''

It is important to realize that the *pair* of the terms, positive diffusion and ''contraction,'' together create confined structures. Unless the convection operator has its own diffusion, if there is no positive diffusion term it is difficult to get stable solutions, which occur when the two terms are balanced. This has been shown by extensive numerical experience, by closed-form discrete solutions for passive scalars (without convection) and by exact closed-form solutions of related partial differential equations for the original vorticity confinement formulation, where the confined length scale is μ/ε, [19].

There are many possible forms for the second confinement term. First, the original one used in this and earlier studies will be described. Then, a new more elegant, simpler form will be described, together with a simple demonstration.

2.1 Original Form.

$$\mathbf{s} = \hat{n} \times \boldsymbol{\omega} \tag{2.1.1}$$

where

$$\hat{n} = \nabla \eta / |\nabla \eta| \tag{2.1.2}$$

the vorticity vector is given by

$$\boldsymbol{\omega} = \nabla \times \mathbf{q} \tag{2.1.3}$$

and

$$\eta = |\boldsymbol{\omega}|. \tag{2.1.4}$$

In general, for boundary layers and convecting vortex filaments, computed flow fields *external* to the vortical regions are not sensitive to the parameters ε and μ over a wide range of values. For example, the flow outside an axisymmetric two-dimensional vortex core is independent of the vortical distribution, and hence does not depend on ε and μ as long as the core is thin. Hence, the issues involved in setting them are similar to those involved in setting numerical parameters in other standard computational fluid dynamics schemes, such as artificial dissipation in many conventional compressible solvers. There, the flow outside one-dimensional captured shock regions also does not depend on the exact internal structure, as long as it is thin. For wake flows, ε can be used to approximately simulate finite Reynolds number effects, since it controls the intensity of the small vortical scales.

An important feature of the vorticity confinement method is that the confinement terms are nonzero only in the vortical regions, since both the diffusion term and the anti-diffusion term vanish outside those regions (care has to be taken in the numerical implementation to preserve this feature).

Another important feature concerns the total change induced by the confinement correction in mass, vorticity and momentum, integrated over a cross section of a convecting vortex. It can be shown, [15,17], that mass is conserved because of the pressure projection step in the solver and vorticity is explicitly conserved because of the vanishing of the correction outside the vortical regions. Momentum is almost exactly conserved. An extension of the original method, [10], explicitly conserves the momentum. The new formulation, described below in Section 2.2, also explicitly conserves momentum in a simpler way.

It should be mentioned that the above pde form for the confinement cannot, of course, be said to be resolved since vortices are captured in only a few grid cells. Accordingly, we can only say that the pde form is only used to *motivate* the final discrete form and that a large body of numerical evidence has been given that the terms result in confined vortices. The new formulation described below, on the other hand, allows an intrinsically discrete analysis.

2.2 New Vorticity Confinement Formulation. Because of the above issue concerning the pde form and that additional corrections must be added to make it explicitly conserve momentum, a new, simpler formulation that does not have these problems has been developed. This new, intrinsically discrete formulation is presented in this section.

A more detailed description is presented in [25]. First, a formulation for scalar confinement is given. Then, a velocity-based vorticity confinement correction is given that reduces to the scalar confinement in terms of vorticity when the curl is taken.

The scalar formulation presented here is related to that presented in [13] in one dimension. In this section no convection is used, only the two confinement terms, so that the behavior can be seen more clearly. Excellent results are found with convection in [25].

We start with an iteration for a scalar ϕ. This tests the use of the method for passive scalar convection in the simpler zero velocity limit.

$$\phi^{n+1} = \phi^n + \mu \nabla^2 \phi^n - \varepsilon \nabla^2 \Phi^n \tag{2.2.1}$$

where

$$\Phi^n = \left[\frac{\sum_l C_l (\tilde{\phi}_l^n)^{-1}}{\sum_l C_l} \right]^{-1} \tag{2.2.2}$$

$$\tilde{\phi}_l^n = |\phi_l^n| + \delta \tag{2.2.3}$$

where the sum is over a set of grid nodes near and including the node where Φ is computed, and δ is a small positive constant ($\sim 10^{-8}$) to prevent problems due to finite precision. The coefficients, C_l, can be varied but good results are obtained by simply setting them to 1.

For example, in two dimensions, one possibility is

$$\Phi_{ij}^n = \left[\frac{\sum_{\alpha=-1}^{+1} \sum_{\beta=-1}^{+1} (\tilde{\phi}_{i+\alpha, j+\beta}^n)^{-1}}{N} \right]^{-1} \tag{2.2.4}$$

$$\tilde{\phi}_{ij}^n = |\phi_{ij}^n| + \delta \tag{2.2.5}$$

where N neighboring terms are taken.

Here, we assume $\phi^n \geqslant 0$. Both positive and negative values can also be accommodated with a small extension. Both μ and ε are positive.

An important feature is that all terms are homogeneous of degree 1 in Eq. (2.2.1). This is important because the confinement should not depend on the scale of the quantity being confined. Another important feature is the nonlinearity. It is easy to show that a linear combination of terms of different order in the derivatives cannot lead to a stable confinement for any finite range of coefficients: It will either diverge or diffuse.

For smooth ϕ fields, the last term represents a negative diffusion. If $\mu \leqslant \varepsilon$, where N is the number of terms in Eq. (2.2.2), the *total* diffusion is negative. However, the iteration Eq. (2.2.1) is still stable and converges for values of ε up to about 5 μ, resulting in a (small) effective negative diffusion coefficient in the long wavelength limit. Also, the discrete converged solution can be given exactly in terms of sech functions.

The next step involves letting ϕ be the magnitude of vorticity and deriving an equation for the corresponding velocity correction that leads to Eq. (2.2.1) when the curl is taken (exactly in two dimensions or for a straight vortex in three dimensions). This will result in a new formulation of vorticity confinement.

We simply define

$$\mathbf{q}^{n+1} = \mathbf{q}^n + \mu \nabla^2 \mathbf{q}^n + \varepsilon \boldsymbol{\nabla} \times \mathbf{w}^n \tag{2.2.6}$$

or, for $\boldsymbol{\nabla} \cdot q = 0$,

$$\mathbf{q}^{n+1} = \mathbf{q}^n - \boldsymbol{\nabla} \times (\mu \boldsymbol{\omega}^n - \varepsilon \mathbf{w}^n) \tag{2.2.7}$$

where

$$\boldsymbol{\omega}^n = \boldsymbol{\nabla} \times \mathbf{q}^n \tag{2.2.8}$$

and

$$\mathbf{w}^n = \frac{\boldsymbol{\omega}^n}{\tilde{\omega}^n} \left[\frac{\sum_l (\tilde{\omega}_l^n)^{-1}}{N} \right]^{-1} \tag{2.2.9}$$

$$\tilde{\omega}_l^n = |\boldsymbol{\omega}_l^n| + \delta \tag{2.2.10}$$

where the sum is the same as in Eq. (2.2.2).

Results are presented in Fig. 1 after 0, 8, and 100 iterations, for vorticity and velocity for a vortex in two dimensions. Values used

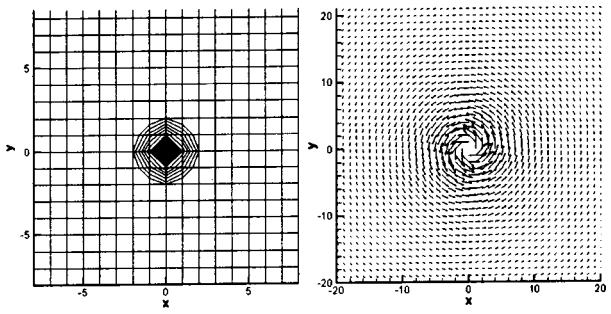

(*a*) the initial condition

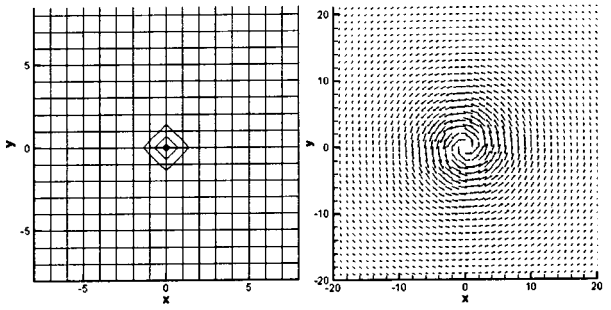

(*b*) time steps = 8, $\varepsilon = 0$

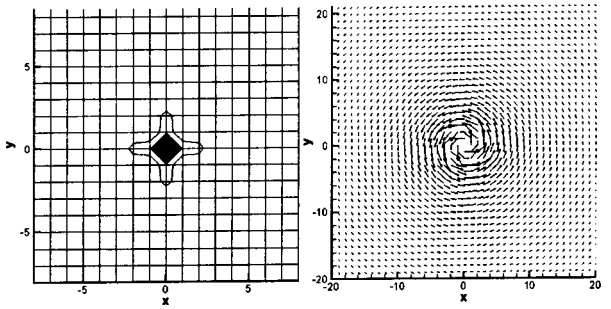

(*c*) time steps = 8, $\varepsilon = 5\mu$

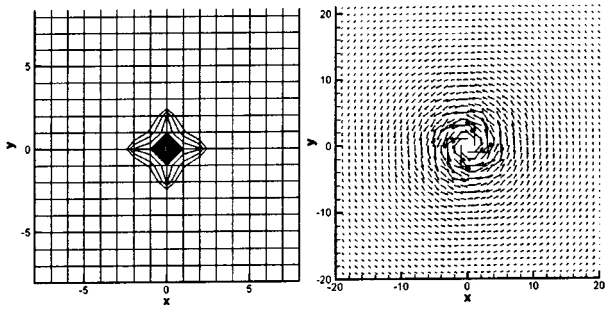

(*d*) time steps = 100, $\varepsilon = 5\mu$

Fig. 1 Vorticity contours and vector fields of velocity

were $\mu = .2$, $\varepsilon = 0$, and $\varepsilon = 5\mu$. In this figure, the vorticity contour levels extend from about 1/4 of the maximum initial value to the maximum so that a measure of the size of the confined region can be determined. We are currently investigating the new method for implementation in our codes. In addition, the use of the ''scalar confinement'' version, Eq. (2.2.1), is being used for flows where thin streams of passive scalars, such as contaminants, must be convected over long distances.

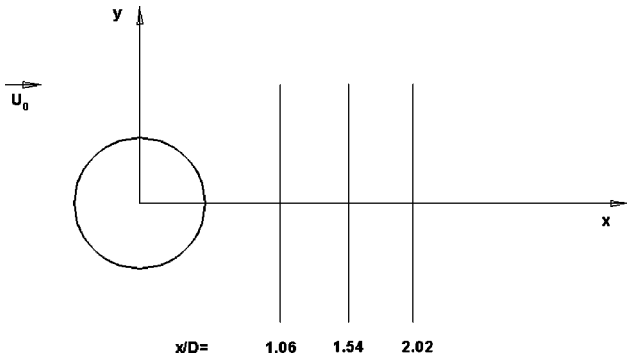

Fig. 2 Measurement positions for circular cylinder

Obviously, any nonlinear equations that result in a stable structure for a feature can be thought of as producing an implicit model of the feature. Further (very interesting) work should be done in developing equations (added terms) that result in structures with specified attributes.

While the vorticity confinement terms are written as positive and negative numerical diffusion terms and act like these in the long wavelength limit, it should be emphasized that they represent an overall *negative* diffusion that creates stable structures of the size of a grid cell. Unlike shock capturing, characteristics do not point inward towards the feature and automatically ''capture'' it.

3 Results

Three test cases are presented in this section. First, the effects of vorticity confinement on the wake structure of a three-dimensional circular and square cylinder are presented. The third example shows the application of vorticity confinement to a realistic flow simulation for a ship configuration. A standard, incompressible pressure-projection solution method was used.

3.1 Three-Dimensional Cylinder

3.1.1 Three-Dimensional Circular Cylinder. Flow over a three-dimensional circular cylinder was calculated to assess the ability of vorticity confinement to accurately model the wake flow behind a blunt body. A long cylinder was ''immersed'' in a uniform $141\times101\times61$ Cartesian grid in the streamwise, normal, and spanwise directions, respectively. Periodic conditions were imposed at the lateral boundaries. The diameter of the cylinder was 15 grid cells. The origin of the coordinate system used is located in the center of the cylinder, and all distances are nondimensionalized by the diameter, shown in Fig. 2. Results of the computations were compared to the experimental results of Lourenco and Shih at a Reynolds number of about 3900, described in Ref. [26]. The computational results were all averaged over the spanwise direction.

The diffusion coefficient μ was held constant for this study. The confinement coefficient, ε, was adjusted to impose different levels of confinement. This resulted in different levels of the intensity of the small vortical scales in the wake, and approximately simulated different Reynolds numbers.

Figure 3 depicts the mean streamwise velocities resulting from three values of the confinement coefficient. Figures 3(*a*) and 3(*b*) depict the result of two levels of confinement, where the flow is measured along lines which are normal to the cylinder axis and the mean stream, at three different locations in the wake of the cylinder shown in Fig. 2. For both values of ε the agreement can be seen to be very good, indicating that the effect of the confinement parameter is small over a range of values. Results from a case without confinement are depicted in Fig. 3(*c*). Without confinement, the flowfield is dominated by diffusive effects that are not counterbalanced by the antidiffusive confinement term and approximates a steady, low Reynolds number flow.

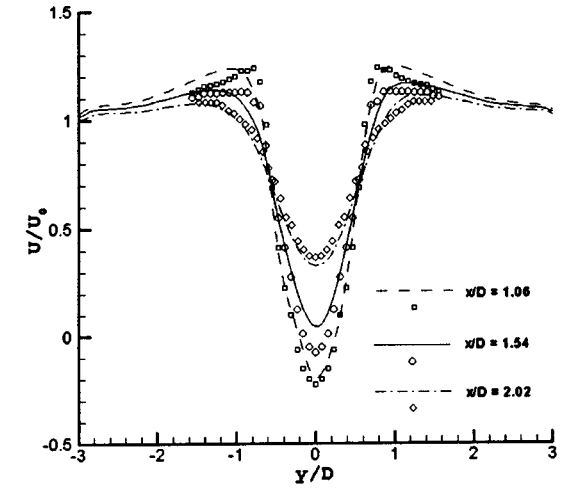

(*a*) $\mu = 0.15,\ \varepsilon = 0.25$

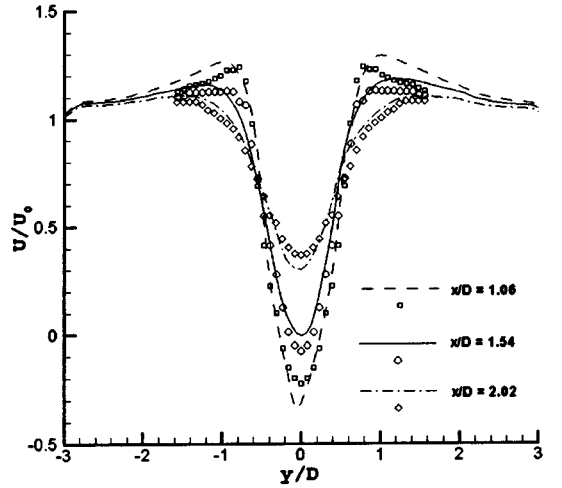

(*b*) $\mu = 0.15,\ \varepsilon = 0.5$

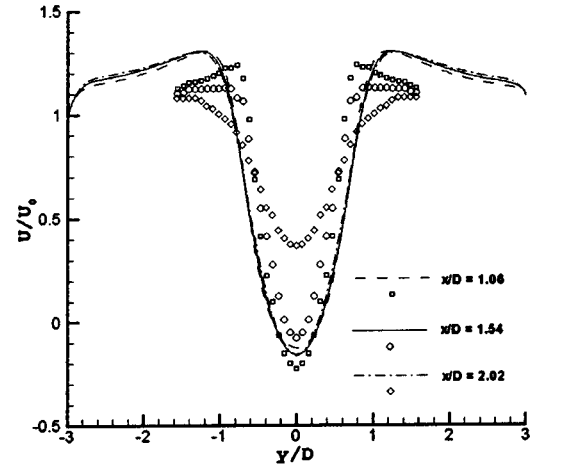

(*c*) $\mu = 0.15,\ \varepsilon = 0.0$ (no confinement)

Fig. 3 Mean streamwise velocity profiles. Symbols are experimental data.

The ability of vorticity confinement to model a turbulent wake was assessed by computing the rms streamwise velocity fluctuations in the wake region. Comparisons of these fluctuations with the experimental data were made along the same lines in the wake as for the mean velocity, for the same three values of ε. Figure 4(*a*) ($\varepsilon = 0.25$) shows very good agreement. The effect of increasing confinement to 0.5 is depicted in Fig. 4(*b*). In general, the effect of increased confinement is to thin the shear layer comprising the wake boundary, and to increase the fluctuation of the time-dependent flow from the mean flow. Figure 4(*c*) depicts results without confinement. Without confinement, the flow can be seen to be steady and exhibits none of the fluctuations that occur when confinement is used.

Figure 5 depicts isosurfaces of vorticity magnitude for the same three levels of confinement. The use of confinement results in chaotic flow patterns, as would be expected in three-dimensional turbulent flows. This does not occur in two-dimensional simulations, indicating that this chaotic behavior is not due to numerical instability created by the confinement. Increasing confinement increases the chaotic nature of the flow in three dimensions and reduces the characteristic size of the vortical structures, analogous to what would be expected with an increase in Reynolds number. Clearly, the use of confinement allows small-scale time-dependent wake structures to be generated on extremely coarse grids with the small-scale structure captured over only 1~2 grid cells. Also, these small-scale structures serve as a viscous sink for turbulent energy, as in physical turbulence.

3.1.2 Three-Dimensional Square Cylinder. Flow over a square cylinder was also calculated. As in the circular case, the cylinder was ''immersed'' in a uniform $141\times101\times61$ Cartesian grid and periodic conditions imposed at the lateral boundaries. The diameter (length of each side) of the cylinder was also 15 grid cells. The same coordinate system was used as for the circular cylinder, as shown in Fig. 6. Results of the computations were compared to the experimental results of Lyn et al. [27] at a Reynolds number of about 21,400. The computational results were all averaged over the spanwise direction.

As in the circular cylinder case, the diffusion coefficient μ was also held constant at 0.15. The confinement coefficient, ε, was adjusted to impose different levels of confinement so as to approximate the effects of different Reynolds numbers.

Figure 7 depicts the comparison with experimental data of the time-averaged streamwise velocity along a streamwise line extending downstream from the middle of the leeward face of the cylinder. Results of two values of the confinement coefficient are plotted. Figure 8 shows the time-averaged velocity along a line normal to the cylinder axis and the mean stream at $x = 1$. Symbols represent the experimental data. Our numerical results agree well with the experimental data.

Comparisons of the computed turbulence level with the experimental results also show reasonably good agreement in Fig. 9(*a*). The effect of decreasing confinement is shown in Fig. 9(*b*). Comparing this case with the previous three-dimensional circular cylinder case, it is easy to see that a higher value of ε is required for better results. This is apparently because the Reynolds number has increased from about 3900 in the three-dimensional circular cylinder case to roughly 21,400 in the present three-dimensional square cylinder case.

3.1.3 Synopsis of Cylinder Study. In subsequent studies, the correlation between ε and Reynolds number will be studied by comparisons between computation and experiment for other cases and a useful calibration of ε determined. Also, it should be emphasized that our agreement with experiment is closer than many much finer, body-fitted grid studies with much more complex LES

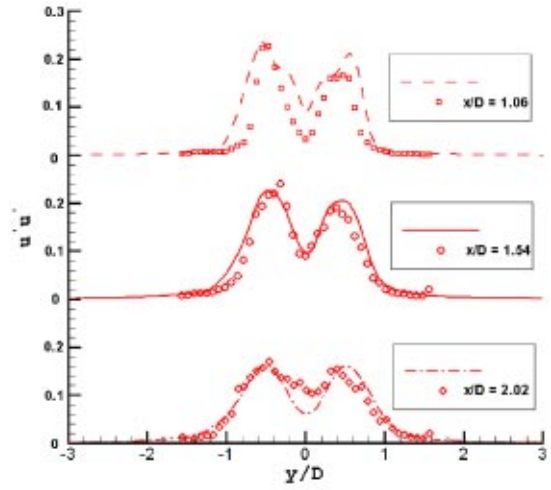

(a) $\mu = 0.15,\ \varepsilon = 0.25$

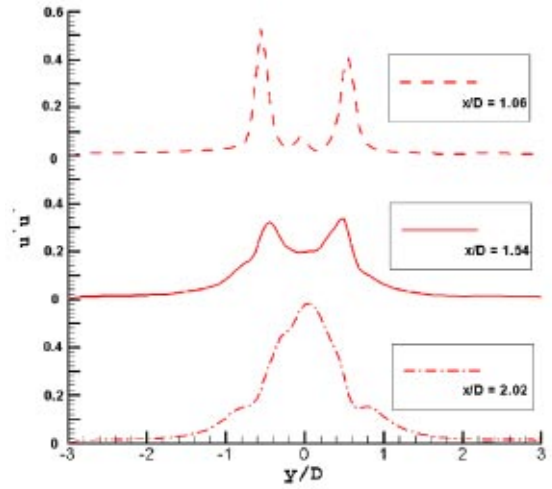

(b) $\mu = 0.15,\ \varepsilon = 0.5$

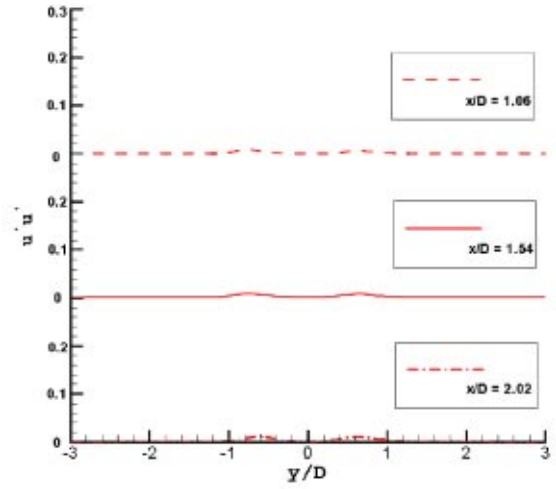

(c) $\mu = 0.15,\ \varepsilon = 0.0$ (no confinement)

Fig. 4 Streamwise Reynolds stresses. Symbols denote experimental data.

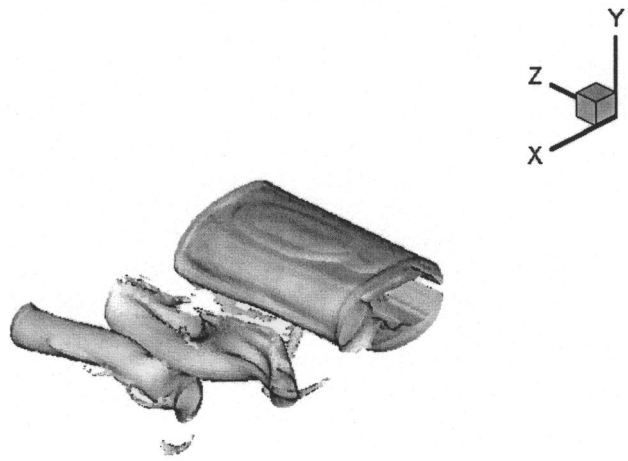

a) $\mu = 0.15,\ \varepsilon = 0.25$, Isosurface Level = ±0.15

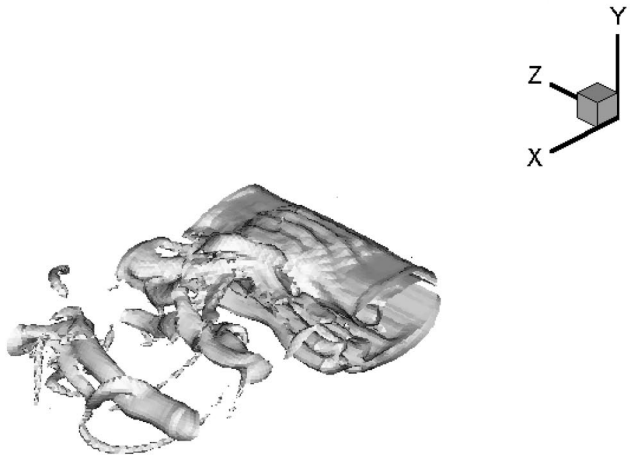

b) $\mu = 0.15,\ \varepsilon = 0.5$, Isosurface Level = ±0.15

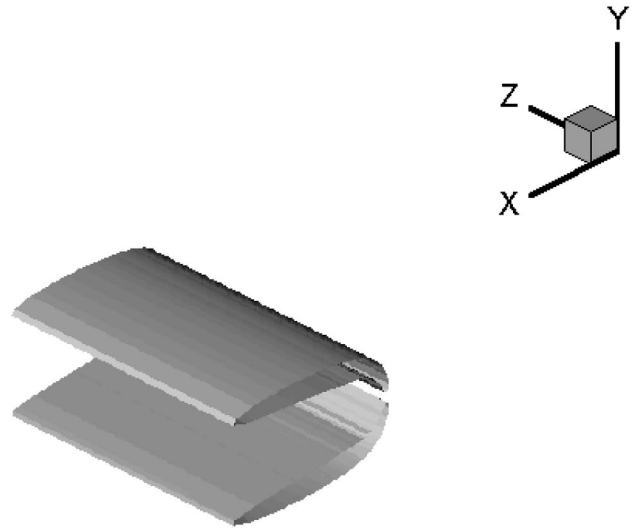

c) $\mu = 0.15,\ \varepsilon = 0.$, Isosurface Level = ±0.15

Fig. 5 Isosurfaces of vorticity magnitude

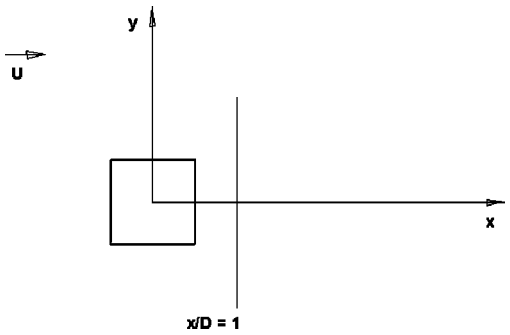

Fig. 6 Measurement positions for square cylinder

pde models, [28], each requiring a number of empirical coefficients. Just one coefficient is adjusted here, on a simple, coarse uniform Cartesian grid.

3.2 Ship Configuration. The present method of developing the operating limits for helicopters landing or taking off from ships is accomplished largely through flight tests, which are time-consuming, costly, and potentially dangerous. The ability to develop the operational limits using computational methods as an adjunct to present methods has the potential of significantly reducing cost, time, and risk. Figure 10 depicts the ship configuration used in this study, which has undergone wind tunnel testing, [29].

The ship configuration is 80 units from bow to stern. The front

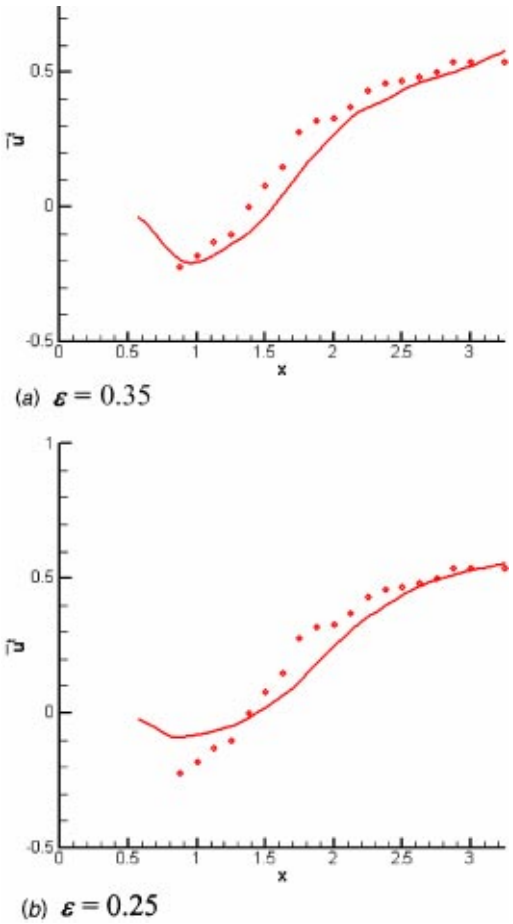

Fig. 7 Comparison of time-averaged streamwise velocity along a streamwise line. Symbols denote experimental data.

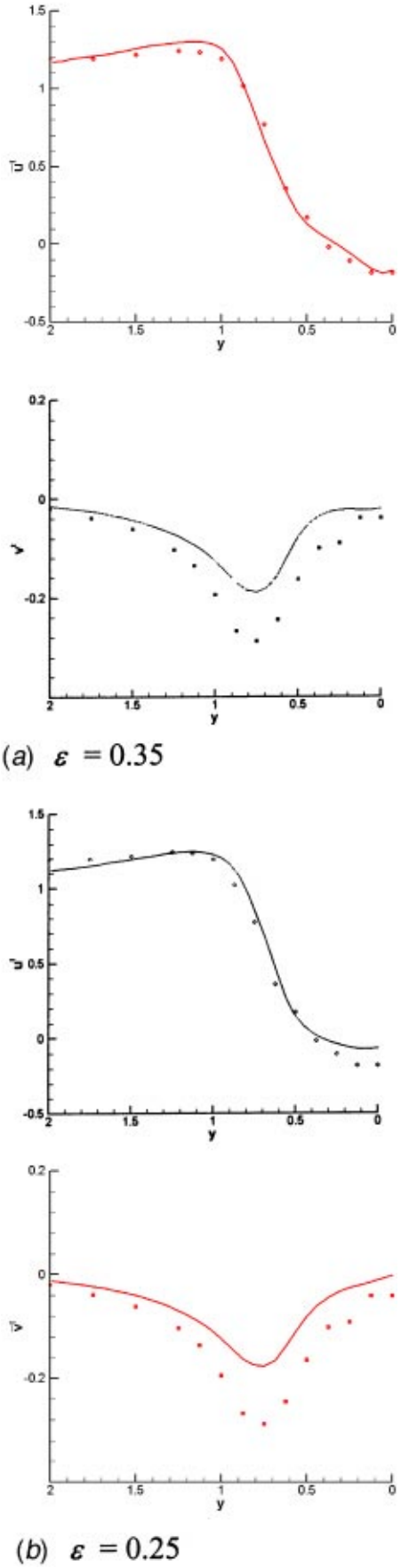

Fig. 8 Comparison of time-averaged velocity profiles at $x=1$. Symbols are experimental data.

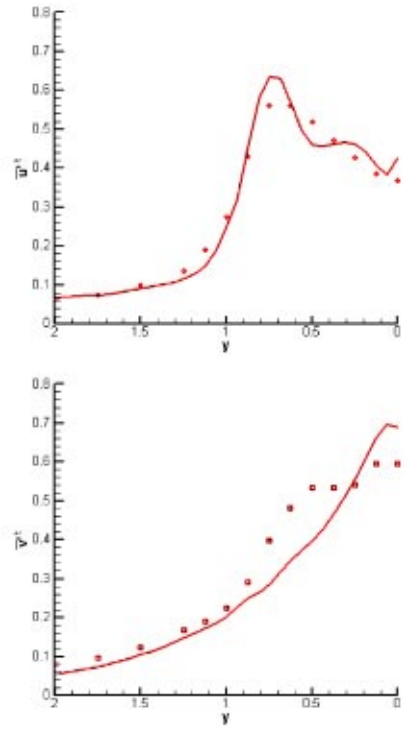

(a) $\varepsilon = 0.35$

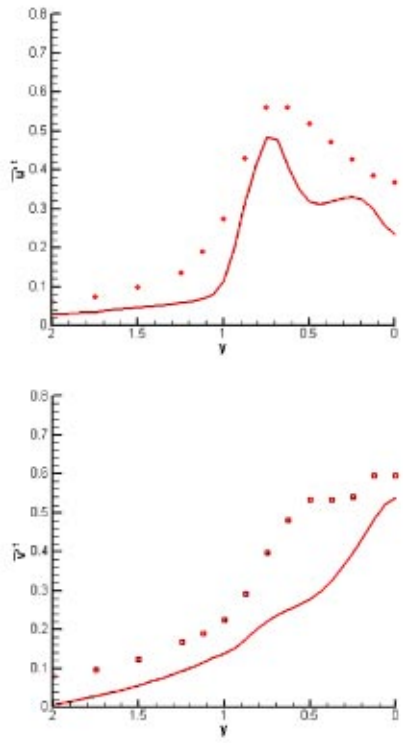

(b) $\varepsilon = 0.25$

Fig. 9 Comparison of root mean square velocity fluctuation profiles at $x=1$. Symbols are experimental data.

of the bow is located at $X=0$; the $Y=0$ plane is perpendicular to the deck and is coincident with the deck midplane. The deck is 13 units wide, extending from $Y=-6.5$ to 6.5. The deck surface is located at $Z=0$, with positive Z upwards. The aerodynamic domain was modeled with two grids: a $401\times121\times74$ grid extended

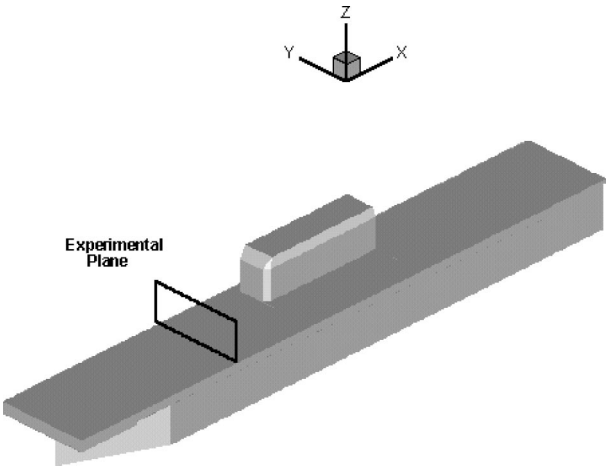

Fig. 10 Helicopter landing ship

from $X=-50$ to 150, $Y=\pm30$, and $Z=-6.5$ to 30. Far-field boundary conditions were imposed on the surfaces of this grid. A second grid was used to more highly resolve the forward deck region. The second grid ($501\times92\times51$) extended from $X=-10$ to 50, $Y=-8$ to 2.92, and $Z=-2.5$ to 3.5. Boundary conditions were imposed on the inner grid via interpolation. In addition, the outer grid obtained flow field information from the inner grid via interpolation at interior boundaries. As a result, two-way flow field communication was effected to obtain a globally consistent flow field. Velocities were measured on a plane ($X=23.63$) for a number of Z locations and were compared with computational results.

Figure 11 depicts vorticity isosurfaces over the ship deck for a wind aspect angle of 20 deg. Ship flowfields are often characterized by the development of a strong vortex at the windward edge of the deck that subsequently convects across the ship deck. The effect of vorticity confinement is illustrated in a comparison between the isosurfaces of Figs. 11(*a*) and 11(*b*). Without confinement (Fig. 11(*a*)), the vortex is greatly dissipated; with confinement (Fig. 11(*b*)), the deck vortex persists indefinitely over the deck surface. The view in Fig. 11 is looking down from above the deck with the bow at the bottom of the figure.

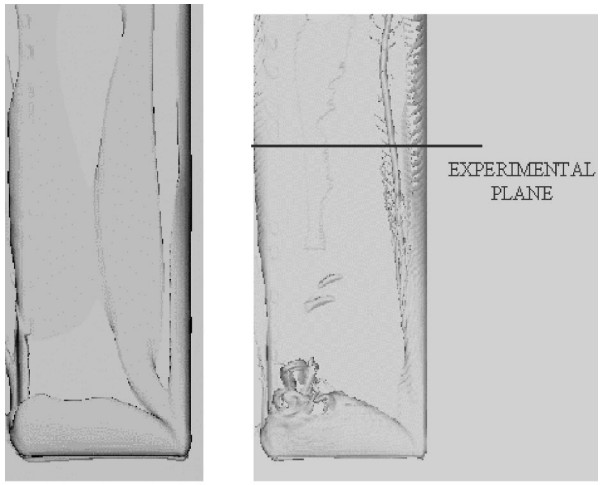

(*a*) **No Confinement** (*b*) **With Confinement**

Fig. 11 Isosurface of vorticity on ship deck

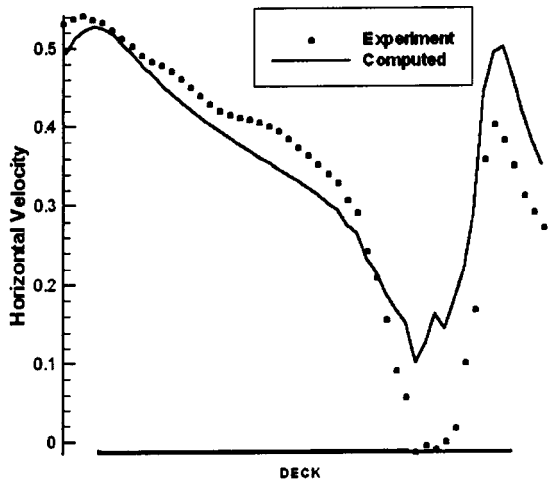

(*a*) Horizontal Velocity

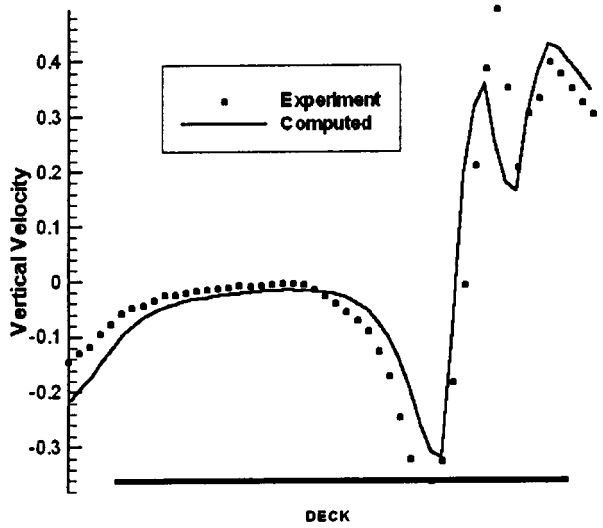

(*b*) Vertical Velocity

Fig. 12 Comparison of experimental and computed velocity over deck, $Z=1.0$

It can be seen that the computed vortex location is very close to the experimental location. These vortical structures are major features of the ship flowfield, and would be difficult to resolve and maintain with conventional CFD methods without a much finer mesh. By contrast, the vortical structures are resolved and persist on a relatively coarse mesh with vorticity confinement. This is in accordance with physical expectations, in that the strength and structure of the vortices are maintained without significant dissipation. Quantitative results are presented in Fig. 12, which depicts velocity one unit above the deck at a constant height horizontal line that goes across the deck through the vortex center. The line is depicted (from above) in Fig. 11(*b*) as the "experimental plane." Additional information on the computation is given in Ref. [5].

4 Conclusions

Vorticity confinement has been shown to provide an efficient, promising means of computing the turbulent wake behind a round and a square cylinder, on a coarse mesh. Results were presented for the mean flow and the rms fluctuations, and the effects of different levels of confinement (and no confinement) were demonstrated. It appears that the ability to resolve scales down to 1 $\sim$2 grid cells and absorb energy there suffices to quantitatively solve for the dynamics of the large scale turbulent eddies in the wake. This makes the method an effective, simple type of LES. Also, the method was shown to allow the embedding of the surface in a uniform, coarse Cartesian grid without body-fitting, refinement, or complex logic near the surface.

It can be seen that the vorticity confinement results for the cylinder wakes, when compared to experiment, are comparable to conventional LES results. The difference is that the confinement solutions employ immersed boundaries with simple, coarse Cartesian grids, with only 15 grid cells across the cylinder diameter, and no complex LES turbulence pde models. As a result, no grid generation was required and the computations were very simple to set up and fast to run. Based on these results, it appears that vorticity confinement should be very useful for rapid engineering solutions for complex flows. Additional validation is being done for surface pressures and forces in these cases (beyond that already done), [6,10]. Further, the functional dependence of our single constant, ε, on the Reynolds number is being calibrated by computing additional cases.

Vorticity confinement was also applied to a helicopter landing ship. In this case, the use of confinement was shown to be necessary, for the grid used, for the development of a deck vortex. This vortex is a major feature of ship flowfields at general wind aspect angles. The ship solution is of particular interest because, unlike the cylinder, the main vortical structures remain close to the configuration for a long distance. Although a very coarse mesh was able to reproduce small-scale turbulent structure quite well with the cylinder, the ship required a more dense mesh in a small region near the corner of the bow to correctly predict the vortex generation. Similar results have been found in other cases. This is due to the interaction of the confinement terms with boundary conditions imposed by solid surfaces. This interaction is a subject of current research, as many structures (e.g., buildings) shed vortices, and the ability to model these structures with coarse grids is of great importance.

Finally, a new, more elegant, fully conservative vorticity confinement formulation was presented with preliminary results with diffusion but without convection. This is currently being implemented in realistic flow simulations.

Acknowledgments

The authors would like to acknowledge the support of the Army Research Office and the Army Aeroflightdynamics Directorate for their support of this effect, and discussions with Dr. Frank Caradonna. The authors would also like to thank the anonymous reviewers for their helpful suggestions.

References

[1] Von Neumann, J., and Richtmyer, R. D., 1950, "A Method for the Numerical Calculation of Hydrodynamic Shocks," J. Appl. Phys., **21**, pp. 232–237.
[2] Lax, P. D., 1957, "Hyperbolic Systems of Conservation Laws II," Commun. Pure Appl. Math., **10**, pp. 537–566.
[3] Harten, A., 1978, "The Artificial Compression Method for Computation of Shocks and Contact Discontinuities III, Self-Adjusting Hybrid Schemes," Math. Comput., **32**, pp. 363–389.
[4] Fureby, C., and Grinstein, F. F., 1999, "Monotonically Integrated Large Eddy Simulation of Free Shear Flows," AIAA J., **37**, pp. 544–556.
[5] Fan, M., Dietz, W., Wenren, Y., and Steinhoff, J., 2002, "Computing Complex Flows on Coarse Grids Using Vorticity Confinement," AIAA Paper No. 02-0135.
[6] Steinhoff, J., Wenren, Y., Braun, C., Wang, L., and Fan, M., 2002, "Application of Vorticity Confinement to the Prediction of the Flow Over Complex Bodies," *Frontiers of Computational Fluid Dynamics 2002*, D. A. Caughey and M. M. Hafez, eds., World Scientific, Singapore, pp. 197–226.
[7] Dietz, W., Fan, M., Steinhoff, J., and Wenren, J., 2001, "Application of Vorticity Confinement to the Prediction of the Flow Over Complex Bodies," AIAA Paper No. 01-2642.

[8] Wenren, Y., Fan, M., Dietz, W., Hu, G., Braun, C., Steinhoff, J., and Grossman, B., 2001, ''Efficient Eulerian Computation of Realistic Rotorcraft Flows Using Vorticity Confinement,'' AIAA Paper No. 01-0996.
[9] Hu, G., Grossman, B., and Steinhoff, J., 2000, ''A Numerical Method for Vortex Confinement in Compressible Flow,'' AIAA Paper No. 00-0281.
[10] Wenren, Y., Steinhoff, J., Wang, L., Fan, M., and Xiao, M., 2000, ''Application of Vorticity Confinement to the Prediction of the Flow Over Complex Bodies,'' AIAA Paper No. 00-2621, Fluids 2000, Denver, CO.
[11] Moulton, M., and Steinhoff, J., 2000, ''A Technique for the Simulation of Stall With Coarse-Grid CFD,'' AIAA Paper No. 00-0277.
[12] Steinhoff, J., Wenren, Y., and Wang, L., 1999, ''Efficient Computation of Separating High Reynolds Number Incompressible Flows Using Vorticity Confinement,'' AIAA Paper No. 99-3316-CP.
[13] Steinhoff, J., Puskas, E., Babu, S., Wenren, Y., and Underhill, D., 1997, ''Computation of Thin Features Over Long Distances Using Solitary Waves,'' *AIAA Proceedings, 13th Computational Fluid Dynamics Conference*, AIAA, Washington, DC, pp. 743–759.
[14] Steinhoff, J., and Raviprakash, G., 1995, ''Navier-Stokes Computation of Blade-Vortex Interaction Using Vorticity Confinement,'' AIAA Paper No. 95-0161.
[15] Steinhoff, J., and Underhill, D., 1994, ''Modification of the Euler Equations for Vorticity Confinement Application to the Computation of Interacting Vortex Rings,'' Phys. Fluids, **6**, pp. 2738–2743.
[16] Steinhoff, J., 1994, ''Vorticity Confinement: A New Technique for Computing Vortex Dominated Flows,'' D. A. Caughey and M. M. Hafez, eds., *Frontiers of Computational Fluid Dynamics*, John Wiley and Sons, New York, pp. 235–264.
[17] Steinhoff, J., Wenren, Y., Mersch, T., and Senge, H., 1992, ''Computational Vorticity Capturing: Application to Helicopter Rotor Flow,'' AIAA Paper No. 92-0056.
[18] Steinhoff, J., Wang, C., Underhill, D., Mersch, T., and Wenren, Y., 1992, ''Computational Vorticity Confinement: A Non-Diffusive Eulerian Method for Vortex-Dominated Flows,'' UTSI preprint.
[19] Steinhoff, J., Mersch, T., and Wenren, Y., 1992, ''Computational Vorticity Confinement: Two Dimensional Incompressible Flow,'' *Proceedings of the Sixteenth Southeastern Conference on Theoretical and Applied Mechanics*, Beaver Press, Manchester, TN, pp. III.II.73–III.II.82.
[20] Lohner, R., and Yang, C., 2002, ''Vorticity Confinement on Unstructured Grids,'' AIAA Paper No. 02-0137.
[21] Murayama, M., Nakahashi, K. and Obayashi, S., 2001, ''Numerical Simulation of Vortical Flows Using Vorticity Confinement Coupled With Unstructured Grid,'' AIAA Paper No. 01-0606.
[22] Grossman, B., and Hu, G., 2002, ''The Computation of Vortex Dominated Flows Using Compressible Vorticity Confinement Methods,'' AIAA Paper No. 02-0136.
[23] Fedkiw, R., Stam, J., and Jensen, H. W., 2001, ''Visual Simulation of Smoke,'' *Proc. SIGGRAPH 2001*, Los Angeles, CA, ACM, Inc., New York, pp. 15–22.
[24] Caradonna, F., 2000, ''Developments and Challenges in Rotorcraft Aerodynamics,'' AIAA Paper No. 00-0109.
[25] Steinhoff, J., Fan, M., and Wang, L., 2002, ''Convection of Concentrated Vortices and Passive Scalars as Solitary Waves,'' UTSI preprint.
[26] Ma, X., Karamanos, G., and Karniadakis, G., 2000, ''Dynamics and Low-Dimensionality of a Turbulent Near Wake,'' J. Fluid Mech., **410**, pp. 29–65.
[27] Lyn, D. A., Einav, S., Rodi, W., and Park, J. H., 1995, ''A Laser-Doppler Velocimetry Study of Ensemble-Averaged Characteristics of the Turbulent Near Wake of a Square Cylinder,'' J. Fluid Mech., **304**, pp. 285–319.
[28] Rodi, W., 1997, ''Large-Eddy Simulation and Statistical Turbulence Models: Complementary Approaches,'' *New Tools In Turbulence Modelling*, O. Metais and J. Ferziger, eds., Springer-Verlag, New York, pp. 49–72.
[29] Caradonna, F., 2001, Wind Tunnel Measurements, Army Aeroflight Dynamics Group, Moffett Field, CA, private communication, Feb.

Robert M. Kirby
e-mail: kirby@cs.utah.edu

George Em Karniadakis
e-mail: gk@cfm.brown.edu

Division of Applied Mathematics,
Brown University,
Providence, RI 02912

Coarse Resolution Turbulence Simulations With Spectral Vanishing Viscosity—Large-Eddy Simulations (SVV-LES)

We present a new implementation of the spectral vanishing viscosity method appropriate for alternative formulations of large-eddy simulations. We first review the method and subsequently present results for turbulent incompressible channel flow.
[DOI: 10.1115/1.1511321]

Introduction

Turbulence simulations using *monotonicity preserving* schemes initially considered homogeneous turbulence, employing both PPM and FCT-type algorithms, [1,2], but more recently emphasis has shifted to wall-bounded flows, [3,4]. Unlike other strictly monotonic discretizations (monotone schemes) of nonlinear conservation laws which are total-variation-diminishing (TVD) and thus at most first-order accurate everywhere (see theorem of LeVeque and Goodman in two dimensions, [5]), the PPM and FCT algorithms employ nonlinear limiters and guarantee monotonicity locally while preserving at least second-order accuracy both in phase and amplitude, [6,7]. These schemes honor the weaker total-variation-bounded (TVB) or other maximum principle conditions, which may allow for small amplitude oscillations. It is worth mentioning that sign-preserving schemes are monotonicity preserving and can be of high order; e.g., see [8]. The intriguing feature of the monotonically integrated LES (or MILES) approach (see [9], also [2], and references therein) is the activation of the limiter on the convective fluxes and its role in generating *implicitly* a tensorial form of eddy viscosity that acts to stabilize the flow and suppress oscillations. It was reported in [2] that if the resolution is fine enough to ensure that the cutoff wave number lies in the inertial range, then the simulation results seem to be independent of the generated viscosity.

In the aforementioned PPM and FCT algorithms for convection, use of nonlinear limiters or reconstruction procedures is in some form equivalent to adding diffusion to the hyperbolic conservation laws so that entropy dissipation is created, and hence a unique solution is obtained (see [10]). If the discretization lacks entropy dissipation, Gibbs oscillations are produced which eventually render the solution unstable. In convection-dominated high Reynolds number flows the situation is analogous. However, this mechanism is implicit and although the induced artificial diffusion may scale with the local resolution as $\propto(\Delta x)^s$, $s>1$, it is an uncontrollable process that may compromise the solution accuracy. This conflict between monotonicity and accuracy, first analyzed by Godunov [11], was revisited by Tadmor [12] who has developed the first *theoretical result* on the convergence and stability of spectral approximations for nonlinear conservation laws. A revised formulation for polynomial spectral methods was presented more recently in [13]. Specifically, Tadmor introduced artificial dissipation via the spectral vanishing viscosity (SVV), which is sufficiently large to suppress oscillations, yet small enough not to affect the solution accuracy. In the context of spectral discretizations, for example, SVV can be viewed as a compromise between the classical TVB viscosity approximation and the exponentially accurate yet unstable spectral approximation.

The spectral vanishing viscosity approach guarantees an essentially nonoscillatory behavior although some small oscillations of *bounded amplitude* may be present in the solution. This theory is based on three key components:

1. a vanishing viscosity amplitude, which decreases with increasing resolution;
2. a viscosity-free spectrum for the lower, most energetic modes; and
3. an appropriate viscosity kernel for the high wave numbers.

If hierarchical discretizations are employed, the combined formulation inherits the scale dependence attempted by other authors, e.g., in the multiscale variational method of Hughes [14] or in the nonlinear Galerkin method of Temam [15]. On the other hand, monotonicity of the TVB kind is preserved, but the high-frequency regularization employed is controlled by parameters whose *range* is given directly by the theory.

In previous work, [16], the SVV approach was used for simulating incompressible turbulent flows using multidomain spectral methods based on the spectral/hp Galerkin approach, see [17]. The *unfiltered* Navier-Stokes equations enhanced on the right-hand side with a spectrally vanishing viscous operator were used. Although reasonably successful, the previous implementation was limited in two ways:

- First, the SVV filtering was accomplished on the C^0 basis, which is hierarchical but only semi-orthogonal.
- Second, the SVV implementation did not discriminate between fully resolved and unresolved regions, thereby possibly applying dissipation in regions where it was not needed.

In the current paper we address these issues by presenting two new enhancements to SVV:

1. First, we present a new SVV filtering for the *continuous* Galerkin method in which filtering is accomplished on a *fully orthogonal* set of modes.
2. Second, we propose a method to compute *adaptively* the viscosity amplitude according to the local strain.

The Spectral Vanishing Viscosity Method

Static Implementation. Tadmor [12] first introduced the concept of spectral vanishing viscosity (SVV) using the inviscid Burgers equation

$$\frac{\partial}{\partial t}u(x,t)+\frac{\partial}{\partial x}\left(\frac{u^2(x,t)}{2}\right)=0, \tag{1}$$

Contributed by the Fluids Engineering Division for publication in the JOURNAL OF FLUIDS ENGINEERING. Manuscript received by the Fluids Engineering Division March 18, 2002; revised manuscript received May 29, 2002. Associate Editor: F. F. Grinstein.

subject to prescribed initial and boundary conditions. The distinct feature of solutions to this problem is that spontaneous jump discontinuities (shock waves) may be developed, and hence *a class* of weak solutions can be admitted. Within this class, there are many possible solutions, and in order to single out the physically relevant one an additional entropy condition is applied, of the form

$$\frac{\partial}{\partial t}\left(\frac{u^2(x,t)}{2}\right)+\frac{\partial}{\partial x}\left(\frac{u^3(x,t)}{3}\right)\leqslant 0. \tag{2}$$

In practical applications, spectral methods are often augmented with smoothing procedures in order to reduce the Gibbs oscillations, [18], associated with discontinuities arising at the domain boundaries or due to underresolution. However, with nonlinear problems, convergence of the Fourier method, for example, may fail despite additional smoothing of the solution. Tadmor [12] introduced the spectral vanishing viscosity method, which adds a small amount of *controlled dissipation* that satisfies the entropy condition, yet retains spectral accuracy. It is based on viscosity solutions of nonlinear Hamilton-Jacobi equations, which have been studied systematically in [19]. Specifically, the viscosity solution for the Burgers equation has the form

$$\frac{\partial}{\partial t}u(x,t)+\frac{\partial}{\partial x}\left(\frac{u^2(x,t)}{2}\right)=\varepsilon\frac{\partial}{\partial x}\left[Q_\varepsilon\frac{\partial u}{\partial x}\right], \tag{3}$$

where $\varepsilon(\rightarrow 0)$ is a viscosity amplitude and Q_ε is a viscosity kernel, which may be nonlinear and, in general, a function of x. Convergence may then be established by compactness estimates combined with entropy dissipation arguments, [12]. To respect spectral accuracy, the SVV method makes use of viscous regularization, and Eq. (3) may be rewritten in discrete form (retaining N modes) as

$$\frac{\partial}{\partial t}u_N(x,t)+\frac{\partial}{\partial x}\left[P_N\left(\frac{u^2(x,t)}{2}\right)\right]=\varepsilon\frac{\partial}{\partial x}\left[Q_N*\frac{\partial u_N}{\partial x}\right], \tag{4}$$

where the star $(*)$ denotes convolution and P_N is a projection operator. Q_N is a (possibly nonlinear) viscosity kernel, which is only activated for high wave numbers. In Fourier space, this kind of spectral viscosity can be efficiently implemented as multiplication of the Fourier coefficients of u_N with the Fourier coefficients of the kernel Q_N, i.e.,

$$\varepsilon\frac{\partial}{\partial x}\left[Q_N*\frac{\partial u_N}{\partial x}\right]=-\varepsilon\sum_{M\leqslant|k|\leqslant N}k^2\hat{Q}_k(t)\hat{u}_k(t)e^{ikx},$$

where k is the wave number, N the number of Fourier modes, and M the wave number above which the spectral vanishing viscosity is activated.

Originally, Tadmor [12] used

$$\hat{Q}_k=\begin{cases}0, & |k|\leqslant M\\ 1, & |k|>M,\end{cases} \tag{5}$$

with $\varepsilon M\sim 0.25$ based on the consideration of minimizing the total variation of the numerical solution. In subsequent work, however, a smooth kernel was used, since it was found that the C^∞ smoothness of $\hat{Q}_k$ improves the resolution of the SVV method. For Legendre pseudo-spectral methods, Maday, Kaber, and Tadmor [20] used $\varepsilon\approx N^{-1}$, activated for modes $k>M\approx 5\sqrt{N}$, with

$$\hat{Q}_k=e^{-(k-N)^2/(k-M)^2},\quad k>M. \tag{6}$$

In order to see the difference between the convolution operator on the right-hand side in Eq. (4) and the usual viscosity regularization, following Tadmor [21] we expand as

$$\varepsilon\frac{\partial}{\partial x}\left[Q_N*\frac{\partial u_N}{\partial x}\right]=\varepsilon\frac{\partial^2 u_N}{\partial x^2}-\varepsilon\frac{\partial}{\partial x}\left[R_N*\frac{\partial u_N}{\partial x}\right]$$

where

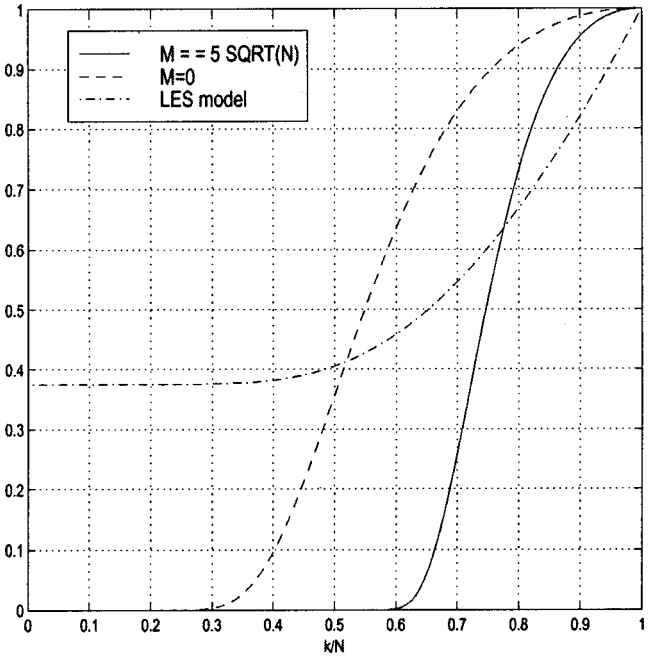

Fig. 1 Normalized viscosity kernels for the spectral vanishing viscosity (dash line $C=0$ and solid line $C=5$) and the Kraichnan/Chollet-Lesieur viscosity (dashed-dot line)

$$R_N(x,t)\equiv\sum_{k=-N}^{N}\hat{R}_k(t)e^{ikx}$$

and

$$\hat{R}_k(t)\equiv\begin{cases}1-\hat{Q}_k(t) & |k|\geqslant M\\ 1 & |k|<M.\end{cases}$$

The extra term appearing in addition to the first standard viscosity term makes this method different. It measures the distance between the spectral (vanishing) viscosity and the standard viscosity. This term is bounded in the L_2 norm similar to the spectral projection error. We refer to the viscosity as vanishing as the theory requires that

$$\varepsilon\approx\frac{1}{N^\theta\log N},\quad \theta\leqslant 1$$

and thus $\varepsilon\rightarrow 0$ for high wave numbers. In more recent work, Tadmor and his collaborators refer to it as simply *spectral viscosity* but this terminology may be confused with the one used by Lesieur and his group, [22].

At this point it is also instructive to compare the spectral vanishing viscosity to the spectral eddy-viscosity introduced by Kraichnan [23] and Chollet-Lesieur [22,24]. The latter has the nondimensional form, [24],

$$\nu(k/N)=K_0^{-3/2}[0.441+15.2\exp(-3.03N/k)],$$

where $K_0=2.1$.

Comparing the Fourier analog of this eddy viscosity employed in LES, [22], to the viscosity kernel $Q_k(k,M,N)$ introduced in the SVV method, Fig. 1 shows both viscosity kernels normalized by their maximum value at $k=N$. For SVV two different values of the cutoff wave number are considered,

$$M=C\sqrt{N}\ \text{ for }\ C=0\ \text{ and }\ C=5. \tag{7}$$

This range has been used in most of the numerical experiments so far (see, for example [16,20]) and is consistent with the theoretical results in [12]. In the plot it is shown that, in general, the two

forms of viscosity have similar distributions but the SVV form does not affect the first one-third or one-half of the spectrum (viscosity-free portion), and it increases faster than the Kraichnan/Chollet-Lesieur eddy viscosity in the higher wave numbers range, e.g., in the second half of the spectrum.

Continuous Galerkin Discretization. In previous work, [16], the SVV concept was implemented in the context of a *modal* spectral/hp discretization in which a C^0 formulation was used for the simulation of incompressible flows, [17]. The SVV filtering was accomplished within the context of the C^0 basis. Although the basis in hierarchical, the C^0 continuity involved in the Galerkin projection destroys partially the orthogonality of the basis. A new modification compared to previous work is now the filtering operation is applied to an orthogonal basis which results from a "rotation" of the semi-orthogonal basis. Equation (8) shows the difference in these two operations. For the SVV as implemented in [16], the Q operator which acts directly on the *semi-orthogonal* basis was used. In the new implementation, the $\tilde{Q}$ operator is used which filters on a *fully orthogonal* set of basis functions. This is accomplished element-by-element by first rotating from the local nonorthogonal basis to a corresponding orthogonal basis spanning the same polynomial space; the filtering is then applied, and the resulting coefficients transformed back to the local basis.

$$
\begin{aligned}
u^N &= \sum_{i=1}^{N} \hat{u}_i \varphi_i \\
Qu^N &= \sum_{i=1}^{N} \hat{q}_i \hat{u}_i \varphi_i \\
\tilde{Q}u^N &= \sum_{i=1}^{N} \sum_{j=1}^{N} a_{ij}^{-1} \hat{q}_j \sum_{k=1}^{N} a_{jk} \hat{u}_k \varphi_i
\end{aligned}
\tag{8}
$$

Technical details are provide in [25], where it is also shown that this new operator remains symmetric and semi-positive definite.

Dynamic Implementation. In the dynamic approach the viscosity amplitude in the SVV kernel varies as a function of space and time. We first apply this idea to the inviscid Burgers equation and subsequently we implement it in the context of Navier-Stokes equations. We thus rewrite the inviscid Burgers equation, and subsequently we implement it in the context of Navier-Stokes equations. A revised formulation of SVV for polynomial spectral methods involving application of the Q kernel at two stages was presented more recently in [13]. We adapt the proposed form and rewrite the inviscid Burgers equation in strong form with a *modified SVV kernel* as follows:

$$
\frac{\partial u}{\partial t} + \frac{1}{2}\frac{\partial u^2}{\partial x} = c(x,t) Q \frac{\partial^2}{\partial x^2} Qu \tag{9}
$$

where

$$
c(x,t) = \varepsilon = \frac{\kappa}{N} \frac{|u_x(x,t)|}{\|u_x(x,t)\|_\infty}. \tag{10}
$$

Here κ is a scalar that can be determined by optimizing the quality of the solution as we shall see below. In other words, we have incorporated the solution into determining the magnitude of the viscosity through the coefficient $c(x,t)$. In this one-dimensional case, we have employed a normalized gradient to accomplish this. This form of $c(x,t)$ is meant to be analogous to the adaptive coefficient for the Navier-Stokes equations $C(\mathbf{x},t) = \nu_e(\mathbf{x};t)/\nu$ (where ν is the physical viscosity and ν_e is the eddy viscosity) proposed in [16]. The use of the rate of strain tensor in the computation of ν_e is mimicked by the use of the magnitude of the first derivative for this one-dimensional example.

For ease of implementation, we have chosen to use the discontinuous Galerkin formulation for this investigation of Burgers equation. We first examine how the dynamic coefficient affects the quality of the solution. First, we evaluate the dynamic coefficient $c(x,t)$ a posteriori from the numerical solution of inviscid Burgers without any viscosity treatment (Fig. 2: case A). We then compute $c(x,t)$ using the global $\|u_x(x,t)\|_\infty$, i.e., max norm obtained *across* all elements, involving the inviscid Burgers equation with dynamic SVV applied to it (Fig. 2: case B). Finally, we compute $c(x,t)$ using local $\|u_x(x,t)\|_\infty$ i.e., max norm obtained in *each* element, involving the inviscid Burgers equation with dynamic SVV applied to it (Fig. 2: case C). We observe in Fig. 2 that if the global $\|u_x(x,t)\|_\infty$ is used in the definition of $c(x,t)$, the form of the $c(x,t)$ when dynamic SVV is acting on the system is the same in shape as when $c(x,t)$ is obtained a posteriori. When a local definition of $\|u_x(x,t)\|_\infty$ is used, however, the form of $c(x,t)$ greatly changes. From this we conclude that

- to effectively utilize dynamic SVV, a global scaling quantity such as $\|u_x(x,t)\|_\infty$ taken over the entire domain must be used.

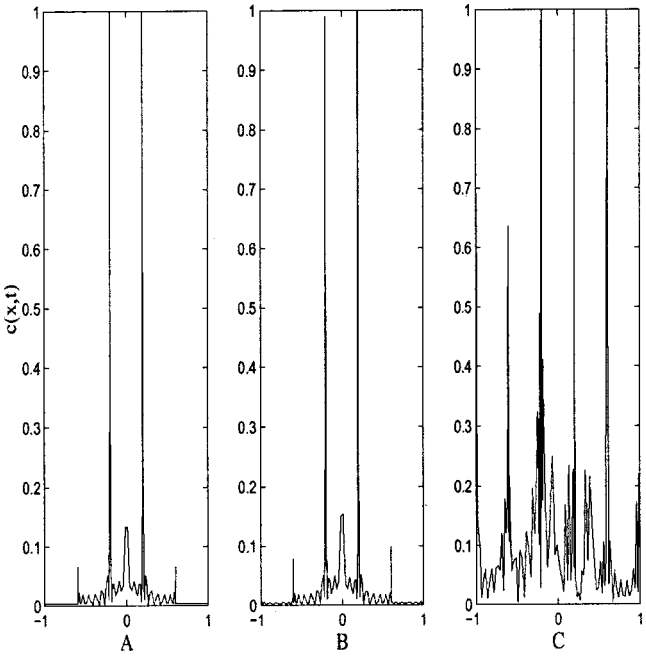

Fig. 2 Plot of the dynamic coefficient $c(x,t)$ at the final time $T=0.5$. The three cases are explained in the text.

To understand the effect of the scaling parameter κ/N (where N is the number of modes on an individual element), we performed a comparison of static SVV ($c(x,t)=\kappa/N$) versus dynamic SVV ($c(x,t)$ as given in Eq. (10)). The inviscid Burgers equation was solved with the added SVV term. Five equally spaced elements spanning the interval $[-1,1]$ were used, each element containing $N=16$ modes. Comparisons of the L_2 error and the L_∞ error for different values of κ are presented in Table 1. Several observations can be made based on our studies:

Table 1 Comparison of L_2 and L_∞ errors for the inviscid Burgers equation using dynamics SVV with $M=8$; $\varepsilon=1/16$

Form	L_2 Error	L_∞ Error
Inviscid	0.133395	0.17006
Static SVV	0.131833	0.44753
Local SVV $\kappa=1$	0.155219	0.699105
Global SVV $\kappa=1$	0.133296	1.15936
Global SVV $\kappa=5$	0.131130	1.04961
Global SVV $\kappa=10$	0.140145	0.775494

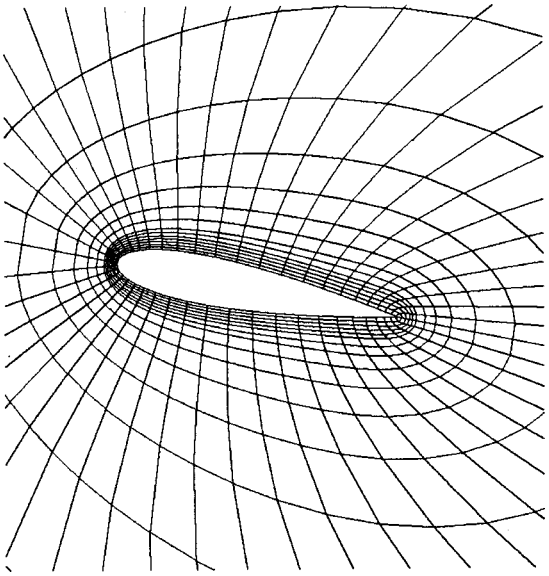

Fig. 3 Segment of the mesh used for simulating the flow past an airfoil at 10 deg angle of attack and Re=10,000

• At the default value of $1/N$, the static SVV does slightly better than the no SVV cases in the L_2 norm. However, the static SVV does noticeably better in the L_∞ than the no SVV case.

• For all values of κ/N less than $1/N$, the static and dynamic SVV perform identically.

• For both static and dynamic SVV, there exists an optimal value of κ/N which is greater than $1/N$. As viscosity in the form of SVV is added to the system, the numerical solution becomes monotonic. However, at some point, too much viscosity is added and degradation in the solution occurs as monotonicity is traded for accuracy.

Alternative LES Implementation. We apply this idea of dynamic SVV to compressible Navier-Stokes equations. Specifically, the SVV kernel is applied to the density, momentum, and energy equations with a variable viscosity amplitude given by

$$c(x,t)=\frac{\rho|S|}{\|\rho|S|\|_\infty}$$

where

$$|S|=\sqrt{Tr(S_{ij}S_{ij})},\quad S_{ij}=\frac{1}{2}\left(\frac{\partial u_i}{\partial x_j}+\frac{\partial u_j}{\partial x_i}\right)$$

and ρ is the local density. As not to affect the flow at the wall we incorporate the Panton function, [26], given by

$$g(y^+)=\frac{2}{\pi}\tan^{-1}\left(\frac{2ky^+}{\pi}\right)\left[1-\exp\left(-\frac{y^+}{C^+}\right)\right]^2$$

where all quantities are expressed in viscous wall units denoted by $+$. This function is multiplied pointwise by the coefficient $c(\mathbf{x},t)$.

In Figs. 3 and 4 we plot, respectively, a segment of the mesh around an airfoil and contours of the SVV amplitude computed using the aforementioned procedure. The spectral/*hp* element simulation is for a two-dimensional flow past an airfoil at 10 deg angle of attack. The mesh involved 912 quadrilateral elements with sixth-order ($N=7$) polynomial interpolation. It is clear that the SVV is nonzero in regions of high vorticity which are the most probable candidates for underresolution.

SVV-LES Coarse Resolution Simulations

The effectiveness of SVV in simulations of turbulent flows using low resolution has been first demonstrated in [16]. Here, we revisit this problem using the aforementioned modification of the continuous Galerkin SVV operator to study the effect of the viscosity amplitude ε and the wave number cutoff M on the solution quality. Specifically, we apply the $\widetilde{Q}$ kernel as in Eq. (8) which filters on an orthogonal trial basis instead of the semi-orthogonal basis employed previously in [16].

Channel flow at $\mathrm{Re}_\tau=180$ is simulated, with periodic boundary conditions in the streamwise and spanwise directions following the benchmark solutions of Kim, Moin, and Moser [27]. The mesh used here is the same as in [16], but the resolution was doubled in the streamwise direction and was substantially reduced in the crossflow plane. Specifically, the size of the computational domain was $L_x=5$, $L_y=2$, and $L_z=2$. In contrast to the previous simulations in [16], we increased the streamwise resolution to 32 Fourier modes (64 points) to test more carefully the effect of SVV acting only the crossflow planes and not in the streamwise direction. In the Fourier direction a 3/2 de-aliasing rule was applied for all simulations. The spectral element mesh has 25 elements (see Fig. 5) in the crossflow plane, with a polynomial order of $N=8$ compared to previous simulations in [16] where $N=21$. We note that the resolution in the wall-normal direction in the current simulations involves only 35 points!

In Fig. 6 we plot the mean-velocity profiles versus the distance from the wall, and in Fig. 7 we plot the turbulence intensities versus the distance from the wall for four different cases. The

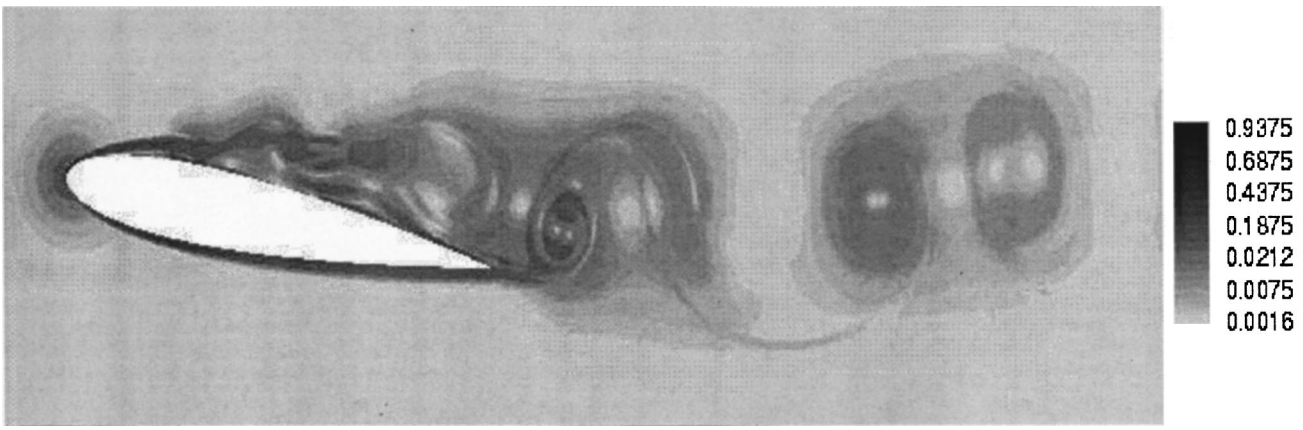

Fig. 4 Amplitude at one time instance of spectral vanishing viscosity in flow past an airfoil at 10 deg angle of attack and Re =10,000

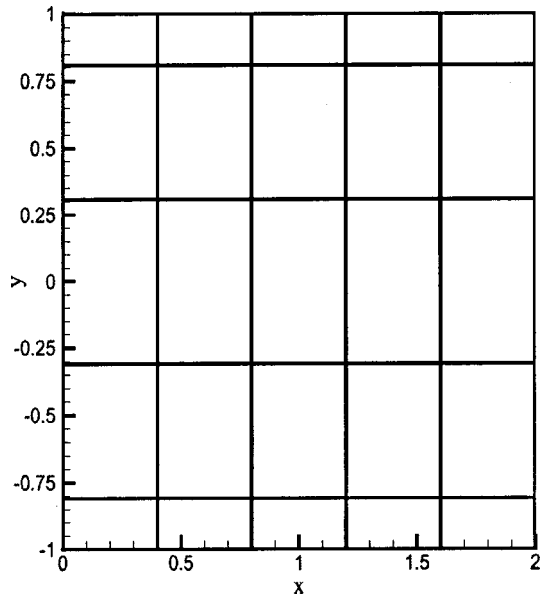

Fig. 5 Mesh in the crossflow plane for turbulent channel flow at $Re_\tau = 180$

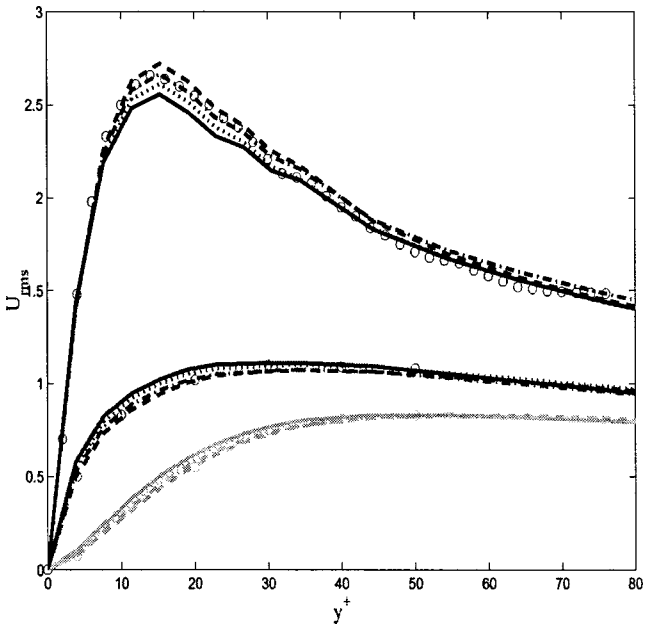

Fig. 7 Turbulence intensities for the turbulent channel flow. The symbols correspond to the benchmark solutions of Kim, Moin, and Moser [27]. The solid line corresponds to the underresolved DNS, the dotted line to ($M=2,\varepsilon=1/8$), the dot-dashed line to ($M=5,\varepsilon=5/8$), and the dashed line to ($M=5,\varepsilon=9/8$).

symbols denote the DNS of Kim, Moin, and Moser [27]. First, we obtained converged (in-time) statistics without SVV using the aforementioned low resolution. The corresponding results underestimate the mean velocity at the centerline ($U_c/u_\tau = 17.67$ versus $U_c/u_\tau = 18.2$ in [27]) as shown in Fig. 6 (solid line). Examining the turbulent intensities, the corresponding results underestimate the streamwise velocity component and overestimate the crossflow, as shown in Fig. 7 (solid line). In our initial runs, we tried two modifications. First, we applied polynomial overintegration which effectively removes any aliasing in the crossflow direction, but the results remained effectively the same. Secondly, we applied the new SVV operator with the default parameters ($M=5,\varepsilon=1/8$), which also gave results similar to the untreated case.

We then experimented with several combinations of the SVV parameters (M, ε). The SVV kernel is scaled with the given physical viscosity, so the actual term included in the Navier-Stokes equation is proportional to $\mathrm{Re}^{-1}\varepsilon$.

The best results for the turbulent intensities are shown in Fig. 7 (dash-dot line) correspond to

$$M=5 \quad \text{and} \quad \varepsilon=5/8.$$

This set of parameters yields a mean velocity at the centerline $U_c/u_\tau = 17.9$ as shown in Fig. 6 (dash-dot line). The other curves in the Figs. 6 and 7 correspond to ($M=2,\varepsilon=1/8$) (dot) and ($M=5,\varepsilon=9/8$) (dashed). The ($M=2,\varepsilon=1/8$) case shows improvement in both the turbulent intensities and mean-velocity profile compared to the untreated case (solid line); however, dissipation is being added over a larger number of modes compared to the ($M=5,\varepsilon=5/8$) case. Observe that for ($M=5,\varepsilon=9/8$) too much dissipation has been added to the system, and hence the solution overestimates the streamwise velocity component as shown in Fig. 7. This case, however, yields the best mean-velocity profile with $U_c/u_\tau = 18.15$ at the centerline. Although case specific, these results confirm the theoretical results that only the upper one-third of the spectrum should be treated with SVV, and that there is an optimum (but unknown) viscosity amplitude level. We propose computing dynamically the viscosity amplitude level using the methodology outlined earlier. Future work will consist of comparisons of static and dynamic SVV for high Reynolds number flow.

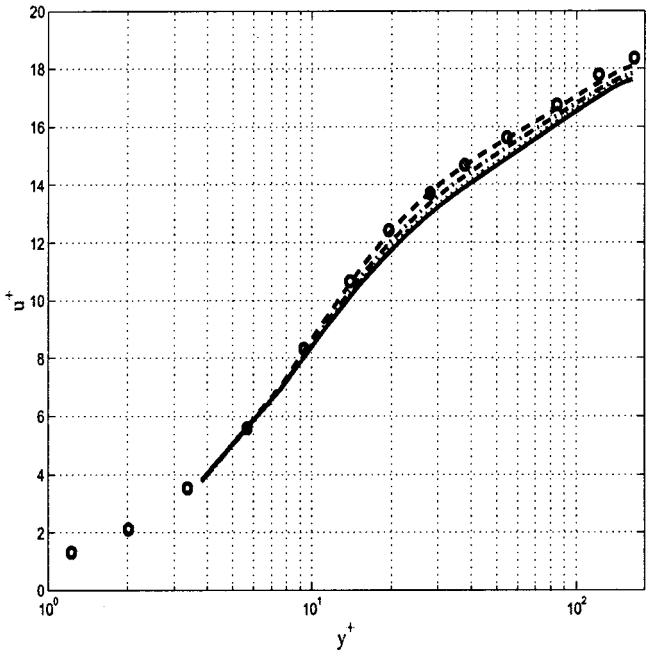

Fig. 6 Mean-velocity profile for the turbulent channel flow. The symbols correspond to the benchmark solutions of Kim, Moin, and Moser [27]. The solid line corresponds to the underresolved DNS, the dotted line to ($M=2,\varepsilon=1/8$), the dot-dashed line to ($M=5,\varepsilon=5/8$), and the dashed line to ($M=5,\varepsilon=9/8$).

Acknowledgments

We acknowledge Mr. Igor Pivkin for his assistance in running the simulations. This work was supported by the Computational Mathematics program of AFOSR. Computations were performed on the IBM SP3 at MHPCC and NPACI.

References

[1] Porter, D. H., Pouquet, A., and Woodward, P. R., 1994, ''Kolmogorov-Like Spectra in Decaying Three-Dimensional Supersonic Flows,'' Phys. Fluids, **6**(6), pp. 2133–2142.

[2] Fureby, C., and Grinstein, F. F., 1999, ''Monotonically Integrated Large Eddy Simulation of Free Shear Flows,'' AIAA J., **37**(5), pp. 544–556.

[3] Urbin, G., and Knight, D., 1999, ''Large Eddy Simulation of the Interaction of a Turbulent Boundary Layer With a Shock Wave Using Unstructured Grids,'' Second AFSOR International Conference on DNS and LES, Rutgers, NJ.

[4] Fureby, C., and Grinstein, F. F., 2000, ''Large Eddy Simulation of High Reynolds Number Free and Wall Bounded Flows,'' AIAA Paper No. 2000-2307.

[5] LeVeque, R. J., 1992, *Numerical Methods for Conservation Laws*, 2nd Ed., Birtkhuser Verlag, Berlin.

[6] Giannakouros, I. G., and Karniadakis, G. E., 1994, ''A Spectral Element-FCT Method for the Compressible Euler Equations,'' J. Comput. Phys., **115**(1), pp. 65–85.

[7] Oran, E. S., and Boris, J. P., 1987, *Numerical Simulation of Reactive Flow*, Elsevier, New York.

[8] Margolin, L. G., Smolarkiewicz, P. K., and Wyszogrodzki, A. A., 2002, ''Implicit Turbulence Modeling for High Reynolds Number Flows,'' AIAA Paper No. 2002-1129, 40th AIAA Aerospace Sciences Meeting, Reno, NV.

[9] Boris, J. P., Grinstein, F. F., Oran, E. S., and Kolbe, R. J., 1992, ''New Insights in Large Eddy Simulations,'' Fluid Dyn. Res., **10**, pp. 199.

[10] Lax, P. D., 1972, ''Hyperbolic Systems of Conservation Laws and the Mathematical Theory of Shock Waves,'' ABMS-NSF Regional Conference Series in Applied Mathematics, Vol. **11**, Society for Industrial and Applied Mathematics, Philadelphia, PA.

[11] Godunov, S. K., 1959, ''A Difference Method for Numerical Calculation of Discontinuous Solutions of the Equations of Hydrodynamics,'' Mat. Sb., **47**, p. 271.

[12] Tadmor, E., 1989, ''Convergence of Spectral Methods for Nonlinear Conservation Laws,'' SIAM (Soc. Ind. Appl. Math.) J. Numer. Anal., **26**(1), pp. 30–44.

[13] Guo, B.-Y., Ma, H.-P., and Tadmor, E., 2001, ''Spectral Vanishing Viscosity Method for Nonlinear Conservation Laws,'' SIAM (Soc. Ind. Appl. Math.) J. Numer. Anal., **39**(4), pp. 1254–1268.

[14] Hughes, T. J. R., Mazzei, L., and Jansen, K. E., 1999, ''Large Eddy Simulation and the Variational Multiscale Methods,'' Comput Visual. Sci., submitted for publication.

[15] Dubois, T., Jauberteau, F., and Temam, R., 1993, ''Solution of the Incompressible Navier-Stokes Equations by the Nonlinear Galerkin Method,'' J. Sci. Comput., **8**, p. 167.

[16] Karamanos, G.-S., and Karniadakis, G. E., 2000, ''A Spectral Vanishing Viscosity Method for Large-Eddy Simulations,'' J. Comput. Phys., **163**(1), pp. 22–50.

[17] Karniadakis, G. E., and Sherwin, S. J., 1999, *Spectral/hp Element Methods for CFD*, Oxford University Press, Oxford, UK.

[18] Don, W. S., 1994, ''Numerical Study of Pseudospectral Methods in Shock Wave Applications,'' J. Comput. Phys., **110**(1), pp. 103–111.

[19] Crandall, M. G., and Lions, P. L., 1983, ''Viscosity Solutions of Hamilton-Jacobi Equations,'' Trans. Am. Math. Soc., **61**, p. 629.

[20] Maday, Y., Ould Kaber, S. M., and Tadmor, E., 1993, ''Legendre Pseudospectral Viscosity Method for Nonlinear Conservation Laws,'' SIAM (Soc. Ind. Appl. Math.) J. Numer. Anal., **30**(2), pp. 321–342.

[21] Tadmor, E., 1993, ''Total Variation and Error Estimates for Spectral Viscosity Approximations,'' Math. Comput., **60**, pp. 245–266.

[22] Lesieur, M., and Metais, O., 1996, ''New Trends in Large-Eddy Simulation,'' Annu. Rev. Fluid Mech., **28**, pp. 45–82.

[23] Kraichnan, R. H., 1976, ''Eddy Viscosity in Two and Three Dimensions,'' J. Atmos. Sci., **33**, p. 1521.

[24] Chollet, J. P., 1984, ''Two-Point Closures as a Subgrid Scale Modeling for Large Eddy Simulations,'' *Turbulent Shear Flows IV* (Lecture Notes in Physics) F. Durst and B. Launder, eds. Springer-Verlag, New York.

[25] Kirby, R. M., 2002, ''Toward Dynamic Spectral/hp Refinement: Algorithms and Applications to Flow-Structure Interactions,'' Ph.D. thesis, Division of Applied Mathematics, Brown University, Providence, RI.

[26] Panton, R. L., 1997, ''A Reynolds Stress Function for Wall Layers,'' ASME J. Fluids Eng., **119**(2), pp. 325–330.

[27] Kim, J., Moin, P., and Moser, R., 1987, ''Turbulence Statistics in Fully Developed Channel Flow at Low Reynolds Number,'' J. Fluid Mech., **117**, p. 133.

On Homogenization-Based Methods for Large-Eddy Simulation

L. Persson
The Swedish Defense Research Agency, FOI,
Department of NBC Defense,
Environment and Protection,
SE-901 82 Umea, Sweden

C. Fureby
The Swedish Defense Research Agency, FOI,
Department of Weapons and Protection
Warheads and Propulsion,
SE-172 Stockholm, Sweden

N. Svanstedt
Chalmers University of Technology,
Department of Mathematics,
SE-412 96 Gothenburg, Sweden

The ability to predict complex engineering flows is limited by the available turbulence models and the present-day computer capacity. In Reynolds averaged numerical simulations (RANS), which is the most prevalent approach today, equations for the mean flow are solved in conjunction with a model for the statistical properties of the turbulence. Considering the limitations of RANS and the desire to study more complex flows, more sophisticated methods are called for. An approach that fulfills these requirements is large-eddy simulation (LES) which attempts to resolve the dynamics of the large-scale flow, while modeling only the effects of the small-scale fluctuations. The limitations of LES are, however, closely tied to the subgrid model, which invariably relies on the use of eddy-viscosity models. Turbulent flows of practical importance involve inherently three-dimensional unsteady features, often subjected to strong inhomogeneous effects and rapid deformation that cannot be captured by isotropic models. As an alternative to the filtering approach fundamental to LES, we here consider the homogenization method, which consists of finding a so-called homogenized problem, i.e. finding a homogeneous "material" whose overall response is close to that of the heterogeneous "material" when the size of the inhomogeneity is small. Here, we develop a homogenization-based LES-model using a multiple-scales expansion technique and taking advantage of the scaling properties of the Navier-Stokes equations. To study the model simulations of forced homogeneous isotropic turbulence and channel flow are carried out, and comparisons are made with LES, direct numerical simulation and experimental data. [DOI: 10.1115/1.1516577]

1 Introduction

For high Reynolds (Re) number complex flows present-day computers are not powerful enough to solve the Navier-Stokes equations (NSE) describing fluid flow, and alternative methods must be formulated. The usual way of doing this is by means of Reynolds averaged numerical simulation (RANS), [1]. In RANS, equations for the statistical average $\langle\cdot\rangle$ of the variables are obtained by averaging the NSE over homogeneous directions, time, or across an ensemble of equivalent flows. The turbulent fluctuations are not represented directly, but are included by way of a turbulence model, which makes it possible to reduce the number of scales or degrees-of-freedom. The statistical character of RANS prevents a detailed description of the physical mechanisms, and is unsuitable for problems where the dynamics is significant. However, RANS is appropriate for analyzing performance characteristics, provided the turbulence models can correctly represent the Reynolds stresses. The most advanced turbulence modeling method at hand is large-eddy simulation (LES), [2–5], which has matured to be a reliable tool for studying flows at parameter ranges infeasible for direct numerical simulation (DNS). In LES, the motion is separated into small and large eddies and equations are solved for the latter. The separation is achieved by means of a low-pass filter, for additional details see [2–6]. Convoluting the NSE with a pre-defined filter kernel $G=G(\mathbf{x},\Delta)$ yields the LES equations,

$$\begin{cases} \nabla\cdot\overline{\mathbf{v}}=m^{\rho}, \\ \partial_t(\overline{\mathbf{v}})+\nabla\cdot(\overline{\mathbf{v}}\otimes\overline{\mathbf{v}})=-\nabla\overline{p}+\nabla\cdot(\overline{\mathbf{S}}-\mathbf{B})+\overline{\mathbf{f}}+\mathbf{m}^{v}, \end{cases} \tag{1}$$

where $\mathbf{v}$ is the velocity, p the pressure, $\mathbf{S}=2\nu\mathbf{D}$ the viscous stress tensor, $\mathbf{D}=1/2(\mathbf{L}+\mathbf{L}^{T})$ the rate-of-strain tensor, ν the viscosity, $\mathbf{L}=\nabla\mathbf{v}$ and $\mathbf{f}$ the specific body force. Specific to LES are the resolved parts, denoted by an overbar, the subgrid scale stress tensor $\mathbf{B}=(\overline{\mathbf{v}\otimes\mathbf{v}}-\overline{\mathbf{v}}\otimes\overline{\mathbf{v}})$ and the commutation errors $m^{\rho}=[G^{*},\nabla]\mathbf{v}$ and $\mathbf{m}^{v}=[G^{*},\nabla](\mathbf{v}\otimes\mathbf{v}+p\mathbf{I}-\mathbf{S})$, where $[G^{*},\nabla]f=\overline{\nabla f}-\nabla\overline{f}$ is the commutation operator. Only the resolved scales are thus retained in LES whereas the subgrid scales are grouped into $\mathbf{B}$, which has to be modeled using an expression of the type $\mathbf{B}(\mathbf{x},t)=\mathbf{B}[\overline{\mathbf{v}}(\mathbf{x}',t');\mathbf{x},t]$. The commutation errors, m^{ρ} and $\mathbf{m}^{v}$, reflect the fact that filtering and differentiation do not generally commute, [7,8], and the effects of these terms on the resolved flow is currently not well known, in particular for complex flows, and must be further investigated. For further details on the filtering and the mathematical and physical properties of $\mathbf{B}$ we refer to [7–10].

Two modeling strategies for $\mathbf{B}$ exists, [3,5]: *Functional modeling* which consists of modeling the action of the subgrid scales on the resolved scales, whereas *structural modeling* consists of modeling $\mathbf{B}$ without incorporating any knowledge about the interactions between the subgrid and the resolved scales. The most frequently used subgrid models belong to the first category—assuming that the energy transfer from the resolved to the subgrid scales is similar to that of a Brownian motion superimposed on the motion of the resolved scales, we have

$$\mathbf{B}=-2\nu_k\overline{\mathbf{D}}, \tag{2}$$

where ν_k is the subgrid (eddy) viscosity. To close (2) we need models for the eddy viscosity ν_k and the specific turbulent kinetic energy k, and for this we assume the existence of characteristic length and velocity scales, and we infer total separation between resolved and subgrid scales. Among the eddy viscosity models we have the Smagorinsky (SMG) model, [11], the one-equation eddy viscosity model (OEEVM), [12], and more recently we have seen the development and use of dynamic eddy-viscosity models, e.g., [13].

Contributed by the Fluids Engineering Division for publication in the JOURNAL OF FLUIDS ENGINEERING. Manuscript received by the Fluids Engineering Division March 12, 2002; revised manuscript received June 24, 2002. Associate Editor: F. F. Grinstein.

When performing LES of simple building block flows the agreement with experimental data is generally good, e.g., [6], and not much can be gained by improving the resolution or the modeling. However, when attempting LES of engineering flows a number of difficulties are present that LES in its current form does not handle very well. (i) As Re increases, the demands on the subgrid model increase, and improved models may be required to handle, e.g., nonequilibrium, transition, and anisotropy effects. (ii) For high Re number wall-bounded flows, the small but dynamically important vortical structures in the near-wall region will become small compared to any grid as Re increases. One alternative is to use local grid refinement to perform wall-resolved LES, however, at some point even this becomes prohibitively expensive. To circumvent the severe near-wall resolution requirement, the subgrid models can either be modified to accommodate integration all the way to the wall, or one may try to introduce explicit wall models, or subgrid simulation models may be developed, which is the topic of this paper. For more complex flows further complications arise due to compressibility effects, shock-waves and their interaction with turbulence and chemical reactions and phase changes. (iii) Another difficulty for LES (and DNS) is how to prescribe inflow boundary conditions. Unlike RANS methods, LES requires large-scale turbulence information at inlet boundaries, an issue that is hard to comply with from a practical point of view.

The present work is concerned with the development of a new class of LES subgrid models that will improve predictions for complex high Re number flows using a relatively coarse grid designed to resolve the outer flow. Since turbulence has a rapidly varying spatio-temporal structure it is necessary to reduce the problem of solving the NSE to solving equations that do not have that rapidly varying structure. In a sense we search for equations that correctly describe the evolution of eddies with a typical size larger than the computational grid. As an alternative to low-pass filtering, we here consider the homogenization method, [14], which consists of finding a so-called homogenized problem, i.e., finding a homogeneous material whose overall response is close to that of the heterogeneous material when the size of the inhomogeneity is small. The homogenization method has been around for about two decades, and has mainly been applied to problems relating to composite materials, e.g., [15], flow in porous media, macroscopic properties of polymer or crystalline structures or optimal design of, e.g., plates consisting of several materials. We here develop a LES methodology based on homogenization using a multiple-scales expansion technique, using the scaling symmetries of the NSE. This computational model, which consists of solving the equations for the supergrid scales separately from those of the subgrid scales, is based on the assumption that the cutoff is located within the inertial subrange at each point.

2 Outline and Main Results of the Paper

The plan of the paper is the following. In Section 2.1, we introduce a two-scale expansion of the Navier-Stokes equations (NSE). The main goal is to obtain a model equation for $(\overline{\mathbf{v}},\overline{p})$, similar to a filtered NSE for conventional large-eddy simulation (LES). Introducing a scaling parameter δ and small-scale variables $\xi=\mathbf{x}/\delta$ and $\tau=t/\delta^2$, the velocity field is decomposed, $\mathbf{v}=\mathbf{v}_\delta+\mathbf{v}'_\delta$, into a stochastic ''subgrid'' part $\mathbf{v}'_\delta=\delta^{-1}\mathbf{w}(\xi,\tau)$ and a remaining ''gridscale'' part $\mathbf{v}_\delta=\overline{\mathbf{v}}(\mathbf{x},t)+\delta\mathbf{v}_1(\mathbf{x},t,\xi,\tau)+\delta^2\mathbf{v}_2(\mathbf{x},t,\xi,\tau)+\ldots$, Eq. (7_1). We assume a similar expansion for the pressure, $p_g=\delta^{-2}p_{-2}(\mathbf{x},t,\xi,\tau)+\delta^{-1}p_{-1}(\mathbf{x},t,\xi,\tau)+\overline{p}(\mathbf{x},t)+\delta p_1(\mathbf{x},t,\xi,\tau)+\ldots$ Eq. (7_2). We suppose that a model for the velocity field $\mathbf{w}$ is given (one possible model is considered in Section 3.3). The higher-order coefficients are determined by a cascade of equations, obtained by identifying coefficients in an expansion of the NSE (13), and the incompressibility condition (14). All fields are assumed to be periodic in $\boldsymbol{\xi}$ and τ. Note that the expansions (7) contain singular terms, so convergence as $\delta\to 0$ should be understood in a weak sense (convergence of distributions), and the singular terms must have mean zero in the fine scale variables, Eq. (9). Using the expansion (14) of the incompressibility condition, we thus rewrite the Navier-Stokes expansion (13) on conservative form (22), and compute averaged expansions (23) and (24). The lowest-order terms in the averaged expansion (24) gives a ''homogenized'' problem for $\overline{\mathbf{v}}$, Eq. (25), which contains a subgrid stress tensor $\overline{\mathbf{w}\otimes\mathbf{v}_1+\mathbf{v}_1\otimes\mathbf{w}}$. Hence, to derive the LES model, we need to compute $\mathbf{v}_1$. To this end, starting with necessary conditions (26) on the modeled $\mathbf{w}$, we conclude that the leading pressure term $p_{-2}(\xi,\tau)$ is independent of $\mathbf{x}$ and t, and that p_{-1} must vanish. Using these facts and identifying coefficients for δ^{-1} in the Navier-Stokes expansion (22) and (23) we get equations for $\mathbf{v}_1$ in (29). A unique solution $\tilde{\mathbf{v}}_1$ is obtained if we impose the additional condition that the average vanishes on the fine scale, Eq. (30).

In Section 2.2, we represent the solution to (30) by a set of cell-problems (31) containing no dependence on the large-scale variables, and obtain the subgrid stress tensor in (32). An important point is that we get the subgrid stress tensor from a fourth-rank eddy-viscosity tensor. Hence, we obtain an anisotropic eddy-viscosity model not by an ad-hoc assumption, but as a direct consequence of the NSE and the assumption of a valid two-scale expansion. We neglect the transport terms in (31) and obtain an approximate cell problem in (33). Assuming a Fourier series representation for $\mathbf{w}$, we solve the approximate problem (33) by considering the corresponding system (34) for the Fourier coefficients, and making some approximations pertaining to high Re number flows, we arrive at a series representation (38) for the eddy-viscosity tensor. In Section 2.3, we consider the modeling of $\mathbf{w}$, assuming a scaling similar to the Kolmogorov energy spectrum. We want to emphasize that this is one of many possible choices. Other choices are certainly appropriate, and in particular near solid walls. The assumption on the energy spectrum and incompressibility gives the eddy-viscosity tensor (48), written on dimensionless form in (49)–(50). It remains to determine the value of the expansion parameter δ and the model constant c_w in (48). Both are determined by the conditions that $\mathbf{v}'_\delta(\mathbf{x},t)=\delta^{-1}\mathbf{w}(\mathbf{x}/\delta,\tau/\delta^2)$ have a Kolmogorov energy spectrum, giving the Eq. (55) for the eddy-viscosity tensor. To close the model, we assume a standard transport model for the turbulent kinetic energy, giving the final result (57).

In Section 4 we introduce the numerical methods to be used for discretization of the resolved continuity (15_1) and momentum Eqs. (25) together with the homogenization-based subgrid model (32), (50), (55), and (56). Since we are aiming at complex engineering-type flows, we use an unstructured, second-order accurate, finite volume scheme. In Section 5 we present results from the homogenization-based LES model applied to forced homogeneous isotropic turbulence and fully developed turbulent channel flows and compare with conventional LES, direct numerical simulation (DNS), and experimental data. These preliminary results indicate that the proposed model performs well and captures the primary features and trends in the experimental and DNS data.

3 Homogenization of the Navier-Stokes Equations (NSE)

The theory of homogenization was developed in structural mechanics in order to study composite materials that are inhomogeneous but have a periodic (micro) structure, [15]. The theory shows that if the structure is very fine, the composite material is then equivalent to a homogeneous material whose characteristics can be computed. The theory is more general, e.g., [16], and applies to problems involving partial differential equations with oscillating coefficients. First, however, we examine the scaling prop-

erties of the NSE. To this end we introduce the scaled variables $\tau = t/\delta^{1-h}$, $\xi = \mathbf{x}/\delta$, $\mathbf{v}_\delta = \mathbf{v}/\delta^h$ and $p_\delta = p/\delta^{2h}$, in which the NSE can be expressed as

$$\begin{cases} \nabla_\xi \cdot \mathbf{v}_\delta = 0, \\ \partial_\tau(\mathbf{v}_\delta) + \nabla_\xi \cdot (\mathbf{v}_\delta \otimes \mathbf{v}_\delta) = -\nabla_\xi p_\delta + \nabla_\xi \cdot (\delta^{-(h+1)} \nu \nabla_\xi \mathbf{v}_\delta) + \mathbf{f} \end{cases}. \quad (3)$$

To obtain scale invariance for finite viscosity, only $h = -1$ is permitted. The corresponding symmetry is then equivalent to the similarity principle of fluid dynamics, because the scaling transformations are then seen to keep the Re number unchanged. If the viscous term is ignored, or allowed to tend to zero, as can be justified at very high Re numbers, then we find that there are infinitely many scaling groups, labeled by their scaling exponent h. In the Kolmogorov theory of turbulence, e.g., [17], the fluctuating part of the flow is considered a random process, and for an energy spectrum of power-law type, i.e., $E(|\mathbf{k}|) \propto |\mathbf{k}|^{-n}$, the second-order structure function is also of power-law type, i.e., $\langle |\delta \mathbf{v}|^2 \rangle \propto |\mathbf{x}' - \mathbf{x}|^{n-1}$, where $\delta \mathbf{v} = \mathbf{v}(\mathbf{x}') - \mathbf{v}(\mathbf{x})$. For $n = 5/3$ the velocity scale is of order $\delta^{1/3}$, and thus $h = 1/3$, which, however, is in contrast to the scaling symmetries.

3.1 Application of the Multiple-Scales Expansion Method to the Navier-Stokes Equations (NSE). For the purpose of developing a LES model based on homogenization by multiple-scales expansion we adopt the decomposition $\mathbf{v} = \mathbf{v}_\delta + \mathbf{v}'_\delta$, where $\mathbf{v}_\delta = \mathbf{v}_\delta(\mathbf{x}, t, \boldsymbol{\xi}, \tau)$ and $\mathbf{v}'_\delta = \mathbf{v}'_\delta(\mathbf{x}, t; \boldsymbol{\xi}, \tau)$ in which $\boldsymbol{\xi}$ denotes the local spatial (subgrid) variable and τ the scaled fast time (subgrid) variable. Furthermore, we let $\overline{\mathbf{v}} = \lim_{\delta \to 0} \mathbf{v}_\delta$. Since we cannot expect to be able to resolve all scales of motion for arbitrary high Re number flows it is appropriate to represent $\mathbf{v}'$ by a stochastic process $\mathbf{v}'_\delta = \mathbf{v}'_\delta(\mathbf{x}, t; \xi, \tau)$ which is to be specified later. Hence, $\mathbf{v}_\delta$ is the solution to the equations,

$$\begin{cases} \nabla \cdot \mathbf{v}_\delta = -\nabla \cdot \mathbf{v}'_\delta, \\ \partial_t(\mathbf{v}_\delta) + (\nabla \mathbf{v}_\delta)\mathbf{v}_\delta - \nabla \cdot (\nu \nabla \mathbf{v}_\delta) + (\nabla \mathbf{v}_\delta)\mathbf{v}'_\delta + (\nabla \mathbf{v}'_\delta)\mathbf{v}_\delta \\ \quad = -\nabla p + \mathbf{f} - (\partial_t(\mathbf{v}'_\delta) + (\nabla \mathbf{v}'_\delta)\mathbf{v}'_\delta - \nabla \cdot (\nu \nabla \mathbf{v}'_\delta)). \end{cases} \quad (4)$$

The choice of the random process $\mathbf{v}'_\delta = \mathbf{v}'_\delta(\mathbf{x}, t; \xi, \tau)$ is not trivial. From the scaling symmetries of the NSE the only obvious choice for the short frequency high wavelength variables τ and $\boldsymbol{\xi}$ is $\tau = t/\delta^2$ and $\xi = \mathbf{a}/\delta$, where $\mathbf{a} = \mathbf{a}(\mathbf{x}, t)$ is the Lagrangian coordinate, i.e., the position at time t of the particle advected by the velocity $\overline{\mathbf{v}}$ from position $\mathbf{x}$ at $t = 0$ given as the solution to the Lagrange invariant,

$$\partial_t(\mathbf{a}) + \nabla \cdot (\mathbf{a} \otimes \overline{\mathbf{v}})\overline{\mathbf{v}} = \partial_t(\mathbf{a}) + (\nabla \mathbf{a})\overline{\mathbf{v}} = \mathbf{0}. \quad (5)$$

This problem fits well into the framework of homogenization, and in order to perform a two-scales expansion of (4) we introduce the expansions

$$\begin{cases} \mathbf{v}_\delta(\mathbf{x}, t) = \overline{\mathbf{v}}(\mathbf{x}, t) + \sum_{k=1}^{\infty} \delta^k \mathbf{v}_k(\mathbf{x}, t; \boldsymbol{\xi}, \tau), \\ p_\delta(\mathbf{x}, t) = \delta^{-2} p_{-2}(\mathbf{x}, t; \boldsymbol{\xi}, \tau) + \delta^{-1} p_{-1}(\mathbf{x}, t; \boldsymbol{\xi}, \tau) \\ \qquad + \overline{p}(\mathbf{x}, t) + \sum_{k=1}^{\infty} \delta^k p_k(\mathbf{x}, t; \boldsymbol{\xi}, \tau), \end{cases} \quad (6)$$

where $\overline{\mathbf{v}} = \lim_{\delta \to 0} \mathbf{v}_\delta$ and $\overline{p} = \lim_{\delta \to 0} p_\delta$ (with limits taken in a weak sense) define the resolved or grid-scale flow. An equivalent two-scale expansion for $\mathbf{v}$ and p is thus

$$\begin{cases} \mathbf{v} = \mathbf{v}_\delta + \mathbf{v}'_\delta = \overline{\mathbf{v}} + \sum_{k=1}^{\infty} \delta^k \mathbf{v}_k + \mathbf{v}'_\delta = \sum_{k=-1}^{\infty} \delta^k \mathbf{v}_k, \\ p = p_\delta = \sum_{k=-2}^{\infty} \delta_k p_k, \end{cases} \quad \forall \mathbf{v}_k, p_k \text{ periodic in } \boldsymbol{\xi}, \tau, \quad (7)$$

from which we identify $\mathbf{v}_0 = \overline{\mathbf{v}}(\mathbf{x}, t)$, $p_0 = \overline{p}(\mathbf{x}, t)$ and $\delta^{-1}\mathbf{v}_{-1} = \mathbf{v}'_\delta = \delta^{-1}\mathbf{w}(\xi, \tau)$. We assume that all dependent variables are periodic in $\boldsymbol{\xi}$ and τ, with period Ξ_j in ξ_j, and period T in τ. Furthermore, we introduce two different averages of functions $f(\mathbf{x}, t, \xi, \tau)$ such that

$$\overline{f}(\mathbf{x}, t) = \frac{1}{\Xi_1 \Xi_2 \Xi_3 T} \int \int \int_{\Xi} \int_0^T f(\mathbf{x}, t, \xi, \tau) d\xi_1 d\xi_2 d\xi_3 d\tau,$$
$$\overline{f}^{\xi}(\mathbf{x}, t, \tau) = \frac{1}{\Xi_1 \Xi_2 \Xi_3} \int \int \int_{\Xi} f(\mathbf{x}, t, \xi, \tau) d\xi_1 d\xi_2 d\xi_3. \quad (8)$$

Note that by construction $\overline{f}(\mathbf{x}, t) = 1/T \int_0^T \overline{f}^{\xi}(\mathbf{x}, t, \tau) d\tau$. A necessary condition for the weak convergence of $(\mathbf{v}_\delta, p_\delta)$ as $\delta \to 0$ is that

$$\overline{\mathbf{v}_{-1}}^{\xi} = \overline{\mathbf{w}}^{\xi} = \mathbf{0}, \quad \overline{\mathbf{p}_{-2}}^{\xi} = 0, \quad \overline{\mathbf{p}_{-1}}^{\xi} = 0, \text{ and, consequently,}$$
$$\overline{\mathbf{w}} = \mathbf{0}, \quad \overline{\mathbf{p}_{-2}} = 0, \quad \overline{\mathbf{p}_{-1}} = 0. \quad (9)$$

The chain rule of differentiation transforms the differential operators ∂_t and ∇ according to

$$\begin{cases} \partial_t = \partial_t + \delta^{-1}\partial_t(\mathbf{a})\nabla_\xi + \delta^{-2}\partial_\tau - \delta^{-1}(\mathbf{G}\overline{\mathbf{v}})\nabla_\xi + \delta^{-2}\partial_\tau, \\ \nabla = \nabla_x + \delta^{-1}(\nabla_x \mathbf{a})\nabla_\xi = \nabla_x + \delta^{-1}\mathbf{G}\nabla_\xi, \end{cases} \quad (10)$$

where $\mathbf{G} = \nabla \mathbf{a}$. For the Laplace operator the successive use of (10_2) yields

$$\begin{aligned} \nabla^2 &= (\nabla_x + \delta^{-1}\mathbf{G}\nabla_\xi)^2 = (\nabla_x + \delta^{-1}\mathbf{G}\nabla_\xi) \cdot (\nabla_x + \delta^{-1}\mathbf{G}\nabla_\xi) \\ &= \nabla_x^2 + \delta^{-1}(\mathbf{G}\nabla_\xi \cdot \nabla_x + \nabla_x \cdot \mathbf{G}\nabla_\xi) + \delta^{-2}\mathbf{G}\nabla_\xi \cdot \mathbf{G}\nabla_\xi \\ &= \nabla_x^2 + \delta^{-1}[2\mathbf{G}\nabla_\xi \cdot \nabla_x + (\nabla_x^T \mathbf{G})\nabla_\xi] + \delta^{-2}(\mathbf{G}\nabla_\xi)^2. \end{aligned} \quad (11)$$

Formal expansion of the NSE using the multiple-scales expansion (7) together with the Lagrange invariant (5) and the chain rule of differentiation (10) and (11) yields

$$
\begin{cases}
(\nabla_x+\delta^{-1}\mathbf{G}\nabla_\xi)\cdot\displaystyle\sum_{k=-1}^{\infty}\delta^k\mathbf{v}_k=0,\\[2ex]
(\partial_t-\delta^{-1}\overline{\mathbf{v}}\cdot\mathbf{G}\nabla_\xi+\delta^{-2}\partial_\tau)\displaystyle\sum_{k=-1}^{\infty}\delta^k\mathbf{v}_k-\nu(\nabla_x^2+\delta^{-1}(2\mathbf{G}\nabla_\xi\cdot\nabla_x+(\nabla_x^T\mathbf{G})\nabla_\xi)+\delta^{-2}(\mathbf{G}\nabla_\xi)^2)\displaystyle\sum_{k=-1}^{\infty}\delta^k\mathbf{v}_k\\[2ex]
\quad+\left(\displaystyle\sum_{k=-1}^{\infty}\delta^k\mathbf{v}_k\right)\cdot(\nabla_x+\delta^{-1}\mathbf{G}\nabla_\xi)\displaystyle\sum_{l=-1}^{\infty}\delta^1\mathbf{v}_1+(\nabla_x+\delta^{-1}\mathbf{G}\nabla_\xi)\left(\displaystyle\sum_{k=-2}^{\infty}\delta^k\mathbf{p}_k\right)=\mathbf{f}.
\end{cases}
\tag{12}
$$

Next we replace $\mathbf{G}$ by the identity matrix $\mathbf{I}$, which means that we are considering the flow on an intermediate timescale between the fine scale and the coarse scale, $\delta^2\ll t\ll 1$, so that $\mathbf{a}(\mathbf{x},t)=\mathbf{x}+\overline{\mathbf{v}}(\mathbf{x},0)t+\mathcal{O}(t^2)$ and hence $\mathbf{G}=\mathbf{I}+\mathcal{O}(t)$. Then (12) may be expanded and rearranged, using the definitions $\mathbf{v}_{-1}=\delta\mathbf{v}'_\delta=\mathbf{w}(\xi,\tau)$, $\mathbf{v}_0=\overline{\mathbf{v}}$ and $p_0=\overline{p}$, to give the expansion

$$
\begin{cases}
\delta^{-2}[\nabla_\xi\cdot\mathbf{w}]+\delta^{-1}[\nabla_x\cdot\mathbf{w}+\nabla_\xi\cdot\bar{\mathbf{v}}]+[\nabla_x\cdot\bar{\mathbf{v}}+\nabla_\xi\cdot\mathbf{v}_1]+\displaystyle\sum_{k=1}^{\infty}\delta^k[\nabla_x\cdot\mathbf{v}_k+\nabla_\xi\cdot\mathbf{v}_{k+1}]=0,\\
\delta^{-3}[\partial_\tau\mathbf{w}-\nu\nabla_\xi^2\mathbf{w}+(\mathbf{w}\cdot\nabla_\xi)\mathbf{w}+\nabla_\xi p_{-2}]+\delta^{-2}[\nabla_x p_{-2}+\nabla_\xi p_{-1}]\\
\quad+\delta^{-1}[(\mathbf{w}\cdot\nabla_{\mathbf{x}})\bar{\mathbf{v}}+\nabla_x p_{-1}+\partial_\tau\mathbf{v}_1-\nu\nabla_\xi^2\mathbf{v}_1+(\mathbf{w}\cdot\nabla_\xi)\mathbf{v}_1+(\mathbf{v}_1\cdot\nabla_\xi)\mathbf{w}+\nabla_\xi p_0]\\
\quad+[\partial_t\bar{\mathbf{v}}-\nu\nabla_x^2\bar{\mathbf{v}}-2\nu(\nabla_\xi\cdot\nabla_x)\mathbf{v}_1+(\mathbf{w}\cdot\nabla_x)\mathbf{v}_1+(\bar{\mathbf{v}}\cdot\nabla_x)\bar{\mathbf{v}}+\nabla_x p_0+\partial_\tau\mathbf{v}_2-\nu\nabla_\xi^2\mathbf{v}_2+(\mathbf{w}\cdot\nabla_\xi)\mathbf{v}_2+(\mathbf{v}_2\cdot\nabla_\xi)\mathbf{w}+\nabla_\xi p_1]\\
\quad+\delta[\partial_t\mathbf{v}_1-\nu\nabla_x^2\mathbf{v}_1-2\nu(\nabla_\xi\cdot\nabla_x)\mathbf{v}_2+(\mathbf{w}\cdot\nabla_x)\mathbf{v}_2+(\bar{\mathbf{v}}\cdot\nabla_x)\mathbf{v}_1+(\mathbf{v}_1\cdot\nabla_x)\bar{\mathbf{v}}+\nabla_x p_1\\
\quad+\partial_\tau\mathbf{v}_3-\nu\nabla_\xi^2\mathbf{v}_3+(\mathbf{w}\cdot\nabla_\xi)\mathbf{v}_3+(\mathbf{v}_1\cdot\nabla_\xi)\mathbf{v}_1+(\mathbf{v}_3\cdot\nabla_\xi)\mathbf{w}+\nabla_\xi p_2]\\
\quad+\displaystyle\sum_{k=2}^{\infty}\delta^k[\partial_t\mathbf{v}_k-\nu\nabla_x^2\mathbf{v}_k-2\nu(\nabla_\xi\cdot\nabla_x)\mathbf{v}_{k+1}+(\mathbf{w}\cdot\nabla_x)\mathbf{v}_{k+1}+(\bar{\mathbf{v}}\cdot\nabla_x)\mathbf{v}_k\\
\quad+\displaystyle\sum_{j=1}^{k-1}[(\mathbf{v}_j\cdot\nabla_x)\mathbf{v}_{k-j}]+(\mathbf{v}_k\cdot\nabla_x)\bar{\mathbf{v}}+\nabla_x p_k+\partial_\tau\mathbf{v}_{k+2}-\nu\nabla_\xi^2\mathbf{v}_{k+2}+(\mathbf{w}\cdot\nabla_\xi)\mathbf{v}_{k+2}\\
\quad+\displaystyle\sum_{j=1}^{k}[(\mathbf{v}_j\cdot\nabla_\xi)\mathbf{v}_{k+1-j}]+(\mathbf{v}_{k+2}\cdot\nabla_\xi)\mathbf{w}+\nabla_\xi p_{k+1}]=\mathbf{f}.
\end{cases}
\tag{13}
$$

Note that the second term in the continuity Eq. (13_1) is zero by definition. Averaging the continuity Eq. (13_1) over one full period yields

$$
\delta^{-2}[\underbrace{\overline{\nabla_\xi\cdot\mathbf{w}}^{\xi}}_{=0}]+[\underbrace{\overline{\nabla_x\cdot\bar{\mathbf{v}}}^{\xi}}_{=\nabla_x\cdot\bar{\mathbf{v}}}+\underbrace{\overline{\nabla_\xi\cdot\mathbf{v}_1}^{\xi}}_{=0}]+\sum_{k=1}^{\infty}\delta^k[\underbrace{\overline{\nabla_x\cdot\mathbf{v}_k}^{\xi}}_{=\nabla_x\cdot\bar{\mathbf{v}}_k^{\xi}}+\underbrace{\overline{\nabla_\xi\cdot\mathbf{v}_{k+1}}^{\xi}}_{=0}]
$$

$$
=[\nabla_x\cdot\bar{\mathbf{v}}]+\sum_{k=1}^{\infty}\delta^k[\nabla_x\cdot\bar{\mathbf{v}}_k^{\xi}]=0. \tag{14}
$$

Identifying coefficients in (14), with the use of the relation between the two averages, we have

$$
\nabla_x\cdot\overline{\mathbf{v}}=0\quad\text{and}\quad\nabla_x\cdot\overline{\mathbf{v}}_k^{\xi}=0, \tag{15}
$$

for $k=1,2,3,\ldots,$ and hence, identifying coefficients in the continuity Eq. (13_1) yields

$$
\nabla_\xi\cdot\mathbf{w}=0,\quad\nabla_\xi\cdot\mathbf{v}_1=0\quad\text{and}\quad\nabla_x\cdot\mathbf{v}_k+\nabla_\xi\cdot\mathbf{v}_{k+1}=0, \tag{16}
$$

for $k=1,2,3,\ldots.$ With the additional relations (15)–(16) we may write the expansion of the momentum Eq. (13_2) above on conservative form. To this end we use (16) to obtain

$$
(\mathbf{w}\cdot\nabla_x)\mathbf{v}_{k+1}=\nabla_x\cdot(\mathbf{w}\otimes\mathbf{v}_{\mathbf{k}+1}),\quad(\mathbf{w}\cdot\nabla_\xi)\mathbf{v}_{\mathbf{k}+2}=\nabla_\xi\cdot(\mathbf{w}\otimes\mathbf{v}_{k+2}), \tag{17}
$$

for $k=1,2,3,\ldots$ and similarly for $(\overline{\mathbf{v}}\cdot\nabla_x)$, $(\overline{\mathbf{v}}\cdot\nabla_\xi)$, $(\mathbf{v}_1\cdot\nabla_x)$ and $(\mathbf{v}_1\cdot\nabla_\xi)$. Moreover, (16) gives

$$
(\mathbf{v}_{k+2}\cdot\nabla_\xi)\mathbf{w}=\nabla_\xi\cdot(\mathbf{v}_{k+2}\otimes\mathbf{w})+\nabla_x\cdot(\mathbf{v}_{k+1}\otimes\mathbf{w}), \tag{18}
$$

$$
(\mathbf{v}_k\cdot\nabla_{\mathbf{x}})\overline{\mathbf{v}}=\nabla_\xi\cdot(\mathbf{v}_{k+1}\otimes\overline{\mathbf{v}})+\nabla_x\cdot(\mathbf{v}_k\otimes\overline{\mathbf{v}}), \tag{19}
$$

$$
\begin{aligned}
&(\mathbf{v}_j\cdot\nabla_\xi)\mathbf{v}_{k+1-j}+(\mathbf{v}_{j-1}\cdot\nabla_x)\mathbf{v}_{k+1-j}\\
&\quad=\nabla_\xi\cdot(\mathbf{v}_j\otimes\mathbf{v}_{k+1-j})+\nabla_x\cdot(\mathbf{v}_{j-1}\otimes\mathbf{v}_{k+1-j}),
\end{aligned}
\tag{20}
$$

for $k=1,2,3,\ldots$ and $j=1,\ldots,k$. Consequently,

$$
\begin{aligned}
&\sum_{j=1}^{k}(\mathbf{v}_j\cdot\nabla_\xi)\mathbf{v}_{k+1-j}+\sum_{j=1}^{k-1}(\mathbf{v}_j\cdot\nabla_x)\mathbf{v}_{k-j}\\
&\quad=\sum_{j=1}^{k}[\nabla_\xi\cdot(\mathbf{v}_j\otimes\mathbf{v}_{k+1-j})]+\sum_{j=1}^{k-1}[\nabla_x\cdot(\mathbf{v}_j\otimes\mathbf{v}_{k-j})].
\end{aligned}
\tag{21}
$$

By applying these formulas to the momentum Eq. (13_2) we obtain the conservative form

$$\delta^{-3}[\partial_\tau \mathbf{w}-\nu\nabla_\xi^2\mathbf{w}+\nabla_\xi\cdot(\mathbf{w}\otimes\mathbf{w})+\nabla_\xi p_{-2}]+\delta^{-2}[\nabla_x p_{-2}+\nabla_\xi p_{-1}]+\delta^{-1}[\nabla_x\cdot(\mathbf{w}\otimes\overline{\mathbf{v}})+\nabla_x p_{-1}+\partial_\tau\mathbf{v}_1-\nu\nabla_\xi^2\mathbf{v}_1$$
$$+\nabla_\xi\cdot(\mathbf{w}\otimes\mathbf{v}_1+\mathbf{v}_1\otimes\mathbf{w})+\nabla_\xi p_0]+[\partial_t\overline{\mathbf{v}}-\nu\nabla_x^2\overline{\mathbf{v}}-2\nu(\nabla_\xi\cdot\nabla_x)\mathbf{v}_1+\nabla_x\cdot(\mathbf{w}\otimes\mathbf{v}_1+\overline{\mathbf{v}}\otimes\overline{\mathbf{v}}+\mathbf{v}_1\otimes\mathbf{w})+\nabla_x p_0+\partial_\tau\mathbf{v}_2-\nu\nabla_\xi^2\mathbf{v}_2$$
$$+\nabla_\xi\cdot(\mathbf{w}\otimes\mathbf{v}_2+\mathbf{v}_2\otimes\mathbf{w})+\nabla_\xi p_1]+\delta[\partial_t\mathbf{v}_1-\nu\nabla_x^2\mathbf{v}_1-2\nu(\nabla_\xi\cdot\nabla_x)\mathbf{v}_2+\nabla_x\cdot(\mathbf{w}\otimes\mathbf{v}_2+\overline{\mathbf{v}}\otimes\mathbf{v}_1+\mathbf{v}_1\otimes\overline{\mathbf{v}}+\mathbf{v}_2\otimes\mathbf{w})$$
$$+\nabla_x p_1+\partial_\tau\mathbf{v}_3-\nu\nabla_\xi^2\mathbf{v}_3+\nabla_\xi\cdot(\mathbf{w}\otimes\mathbf{v}_3+\mathbf{v}_1\otimes\mathbf{v}_1+\mathbf{v}_2\otimes\overline{\mathbf{v}}+\mathbf{v}_3\otimes\mathbf{w})+\nabla_\xi p_2]$$
$$+\sum_{k=2}^{\infty}\delta^k\Bigg[\partial_t\mathbf{v}_k-\nu\nabla_x^2\mathbf{v}_k-2\nu(\nabla_\xi\cdot\nabla_x)\mathbf{v}_{k+1}+\nabla_x p_k+\partial_\tau\mathbf{v}_{k+2}+\nabla_x\cdot\Bigg(\mathbf{w}\otimes\mathbf{v}_{k+1}+\overline{\mathbf{v}}\otimes\mathbf{v}_k+\sum_{j=1}^{k-1}[\mathbf{v}_j\otimes\mathbf{v}_{k-j}]+\mathbf{v}_k\otimes\overline{\mathbf{v}}+\mathbf{v}_{k+1}\otimes\mathbf{w}\Bigg)$$
$$-\nu\nabla_\xi^2\mathbf{v}_{k+2}+\nabla_\xi\cdot\Bigg(\mathbf{w}\otimes\mathbf{v}_{k+2}+\sum_{j=1}^{k}[\mathbf{v}_j\otimes\mathbf{v}_{k+1-j}]+\mathbf{v}_{k+1}\otimes\overline{\mathbf{v}}+\mathbf{v}_{k+2}\otimes\mathbf{w}\Bigg)+\nabla_\xi p_{k+1}\Bigg]=\mathbf{f}. \tag{22}$$

Averaging the momentum Eq. (22) over Ξ and $\Xi\times T$, respectively, using (9), gives

$$\partial^{-1}[\partial_\tau\overline{\mathbf{v}_1}^\xi]+[\partial_t\overline{\mathbf{v}}-\nu\nabla_x^2\overline{\mathbf{v}}+\nabla_x\cdot(\overline{\mathbf{v}}\otimes\overline{\mathbf{v}})+\nabla_{\mathbf{x}}\cdot(\overline{\mathbf{w}\otimes\mathbf{v}_1}^\xi+\overline{\mathbf{v}_1\otimes\mathbf{w}}^\xi)+\nabla_x\overline{p_0}^\xi+\partial_\tau\overline{\mathbf{v}_2}^\xi]+\delta[\partial_t\overline{\mathbf{v}_1}^\xi-\nu\nabla_x^2\overline{\mathbf{v}_1}^\xi$$
$$+\nabla_{\mathbf{x}}\cdot(\overline{\mathbf{v}}\otimes\overline{\mathbf{v}_1}^\xi+\overline{\mathbf{v}_1}^\xi\otimes\overline{\mathbf{v}})+\nabla_x\cdot(\overline{\mathbf{w}\otimes\mathbf{v}_2}^\xi+\overline{\mathbf{v}_2\otimes\mathbf{w}}^\xi)+\nabla_x\overline{p_1}^\xi+\partial_\tau\overline{\mathbf{v}_3}^\xi]$$
$$+\sum_{k=2}^{\infty}\delta^k\Bigg[\partial_t\overline{\mathbf{v}_k}^\xi-\nu\nabla_x^2\overline{\mathbf{v}_k}^\xi+\nabla_x\cdot(\overline{\mathbf{v}}\otimes\overline{\mathbf{v}_k}^\xi+\overline{\mathbf{v}_k}^\xi\otimes\overline{\mathbf{v}})+\nabla_x\overline{p_k}^\xi+\partial_\tau\overline{\mathbf{v}_{k+2}}^\xi+\nabla_x\cdot\Bigg(\overline{\mathbf{w}\otimes\mathbf{v}_{k+1}}^\xi+\sum_{j=1}^{k-1}\overline{\mathbf{v}_j\otimes\mathbf{v}_{k-j}}^\xi+\overline{\mathbf{v}_{k+1}\otimes\mathbf{w}}^\xi\Bigg)\Bigg]=\mathbf{f}, \tag{23}$$

and

$$[\partial_t\overline{\mathbf{v}}-\nu\nabla_x^2\overline{\mathbf{v}}+\nabla_x\cdot(\overline{\mathbf{v}}\otimes\overline{\mathbf{v}})+\nabla_x\cdot(\overline{\mathbf{w}\otimes\mathbf{v}_1}+\overline{\mathbf{v}_1\otimes\mathbf{w}})+\nabla_x\overline{\mathbf{p}_0}]+\delta[\partial_t\overline{\mathbf{v}_1}$$
$$-\nu\nabla_x^2\overline{\mathbf{v}_1}+\nabla_x\cdot(\overline{\mathbf{w}\otimes\mathbf{v}_2}+\overline{\mathbf{v}}\otimes\overline{\mathbf{v}_1}+\overline{\mathbf{v}_1}\otimes\overline{\mathbf{v}}+\overline{\mathbf{v}_2\otimes\mathbf{w}})+\nabla_x\overline{p_1}]$$
$$+\sum_{k=2}^{\infty}\delta^k\Bigg[\partial_t\overline{\mathbf{v}_k}-\nu\nabla_x^2\overline{\mathbf{v}_k}+\nabla_x\cdot\Bigg(\overline{\mathbf{w}\otimes\mathbf{v}_{k+1}}+\overline{\mathbf{v}}\otimes\overline{\mathbf{v}_k}$$
$$+\sum_{j=1}^{k-1}\overline{\mathbf{v}_j\otimes\mathbf{v}_{k-j}}+\overline{\mathbf{v}_k}\otimes\overline{\mathbf{v}}+\overline{\mathbf{v}_{k+1}\otimes\mathbf{w}}\Bigg)+\nabla_x\overline{p_k}\Bigg]=\mathbf{f}. \tag{24}$$

From (24) we recognize the LES equations by identifying the terms of order zero,

$$\partial_t\overline{\mathbf{v}}-\nu\nabla_x^2\overline{\mathbf{v}}+\nabla_x\cdot(\overline{\mathbf{v}}\otimes\overline{\mathbf{v}})+\nabla_x\cdot(\overline{\mathbf{w}\otimes\mathbf{v}_1}+\overline{\mathbf{v}_1\otimes\mathbf{w}})+\nabla_x\overline{p_0}=\mathbf{f}, \tag{25}$$

which contains the subgrid stress tensor $\mathbf{B}=\overline{\mathbf{w}\otimes\mathbf{v}_1}+\overline{\mathbf{v}_1\otimes\mathbf{w}}$, a function of the stochastic process $\mathbf{w}$, and the first-order perturbation velocities $\mathbf{v}_1$ averaged over $\Xi\times T$. In order to close the LES Eq. (25) we need to specify $\mathbf{w}$ and to determine $\mathbf{v}_1$. Identifying coefficients for δ^{-3} in (22), using (9) and (16) gives

$$\begin{cases}\partial_\tau\mathbf{w}-\nu\nabla_\xi^2\mathbf{w}+\nabla_\xi\cdot(\mathbf{w}\otimes\mathbf{w})+\nabla_\xi p_{-2}=\mathbf{0},\\ \nabla_\xi\cdot\mathbf{w}=0,\\ \overline{\mathbf{w}}^\xi=\mathbf{0}.\end{cases} \tag{26}$$

Assuming these conditions on $\mathbf{w}$ fulfilled, we proceed to find $\mathbf{v}_1$. Assume that $(\mathbf{w},p_{-2})$ is a solution to (26). Using (9) we see that $p_{-2}(\mathbf{x},t,\boldsymbol{\xi},\tau)$ is a solution to the problem

$$\begin{cases}\nabla_\xi^2 p_{-2}=-\nabla_\xi\cdot(\nabla_\xi\cdot(\mathbf{w}\otimes\mathbf{w})),\\ \overline{p_{-2}}^\xi=0,\\ \partial_t p_{-2}=0,\\ \nabla_x p_{-2}=\mathbf{0}.\end{cases} \qquad p_{-2}(\mathbf{x},t,\boldsymbol{\xi},\tau)\ \text{periodic in}\ \boldsymbol{\xi}, \tag{27}$$

Note that the problem (27_1) and (27_2) has no explicit dependence on $\mathbf{x}$, t, so since the solution is unique, we have $p_{-2}=p_{-2}(\xi,\tau)$ and hence $(27_3,\ 27_4)$ is a consequence of (27_1) and (27_2). Identifying coefficients for δ^{-2} in (22) results in $\nabla_\xi p_{-1}=-\nabla_x p_{-2}=\mathbf{0}$, and hence,

$$p_{-1}=\overline{p}^\xi_{-1}=0. \tag{28}$$

Identification of coefficients for δ^{-1} in Eqs. (22) and (23) now results in the problem

$$\begin{cases}\partial_\tau\mathbf{v}_1-\nu\nabla_\xi^2\mathbf{v}_1+\nabla_\xi\cdot(\mathbf{w}\otimes\mathbf{v}_1+\mathbf{v}_1\otimes\mathbf{w})+\nabla_\xi p_0=-\nabla_x\cdot(\mathbf{w}\otimes\overline{\mathbf{v}}),\\ \nabla_\xi\cdot\mathbf{v}_1=0,\\ \partial_\tau\overline{\mathbf{v}_1}^\xi=0\end{cases}. \tag{29}$$

Assume that $(\mathbf{w},\overline{\mathbf{v}})$ are given and that $(\mathbf{v}_1,p_0)$ is a solution to (29), and let $\tilde{\mathbf{v}}_1=\mathbf{v}_1-\overline{\mathbf{v}_1}^\xi$, then

$$\begin{cases}\partial_\tau\tilde{\mathbf{v}}_1-\nu\nabla_\xi^2\tilde{\mathbf{v}}_1+\nabla_\xi\cdot(\mathbf{w}\otimes\tilde{\mathbf{v}}_1+\tilde{\mathbf{v}}_1\otimes\mathbf{w})+\nabla_\xi p_0=-\nabla_x\cdot(\mathbf{w}\otimes\overline{\mathbf{v}}),\\ \nabla_\xi\cdot\tilde{\mathbf{v}}_1=0,\\ \overline{\tilde{\mathbf{v}}_1}^\xi=\mathbf{0},\end{cases} \qquad \tilde{\mathbf{v}}_1,\ \ p_0\ \text{periodic in}\ \xi, \tag{30}$$

and $\tilde{\mathbf{v}}_1$ satisfying (30) is unique. Since $\overline{\mathbf{w}}^\xi=\mathbf{0}$ we can replace $\mathbf{v}_1$ by $\tilde{\mathbf{v}}_1$ in the definition of the subgrid stress tensor $\mathbf{B}=\overline{\mathbf{w}\otimes\mathbf{v}_1}+\overline{\mathbf{v}_1\otimes\mathbf{w}}=\overline{\mathbf{w}\otimes\tilde{\mathbf{v}}_1}+\overline{\tilde{\mathbf{v}}_1\otimes\mathbf{w}}$. In order to determine $\mathbf{B}$ we thus need to solve the cell problem (30) and specify the stochastic process $\mathbf{w}$. Given $\mathbf{w}$, which is to be discussed in a forthcoming section, this amounts to solving the cell problem (30) within each LES cell using a so-called ''grid-within-the-grid'' approach. In this paper we will, however, solve a simplified version of the cell-problem (30) using analytical techniques.

3.2 A Homogenization-Based Subgrid Model. The solution $\mathbf{v}_1$ to (30) depends on the variables $\boldsymbol{\xi}$ and τ, and parametri-

cally on $\nabla_x \overline{\mathbf{v}}$. This allows us to construct solutions by superposition from problems without parameter dependence. To this end, if (χ_{kl}^j, π_{kl}) is the unique solution to the problem

$$\begin{cases} \partial_\tau \chi_{kl}^j - \nu \nabla_\xi^2 \chi_{kl}^j + \partial_{\xi^m}(w^m \chi_{kl}^j + \chi_{kl}^m w^j) + \partial_{\xi^j} \pi_{kl} = -\delta_k^j \mathbf{w}^1, \\ \partial_{\xi^m} \chi_{kl}^m = 0, \\ \overline{\chi_{kl}^i}^\xi = 0, \quad \overline{\pi_{kl}}^\xi = 0, \end{cases} \tag{31}$$

we see that since $-\delta_k^j w^l \partial_{x^l} \overline{v^k} = -w^1 \partial_{x^l} \overline{v^j} = -\partial_{x^l}(w^l \overline{v^j})$, so by linearity, the unique solution $(\tilde{\mathbf{v}}_1, p_0)$ to (30) satisfying the additional condition $\overline{p_0}^\xi = 0$ is given by $\tilde{v}_1^j = \chi_{kl}^j \partial_{x^l} \overline{v^k}$ and $p_0 = \pi_{kl} \partial_{x^l} \overline{v^k}$. Finally, we may compute the subgrid stress tensor $\mathbf{B}$ according to

$$\begin{aligned} B_{ij} &= \overline{w^i \tilde{v}_1^j} + \overline{\tilde{v}_1^i w^j} = \overline{w^i \chi_{kl}^j \partial_{x^1} \overline{v^k}} + \overline{w^j \chi_{kl}^j \partial_{x^1} \overline{v^k}} \\ &= (\overline{w^i \chi_{kl}^j + w^j \chi_{kl}^i}) \partial_{x^1} \overline{v^k} = A_{ijkl} \partial_{x^1} \overline{v^k}, \end{aligned} \tag{32}$$

where $A_{ijkl} = \overline{w^i \chi_{kl}^j + w^j \chi_{kl}^i}$ is an anisotropic (fourth-rank) eddy-viscosity tensor. It would be interesting to solve this system in general, but at the moment we will neglect the subgrid transport terms in (31), and consider instead the following simplified cell problem:

$$\begin{cases} \partial_\tau \chi_{kl}^j - \nu \nabla_\xi^2 \chi_{kl}^j + \partial_{\xi^j} \pi_{kl} = -\delta_k^j w^1, \\ \sum_{j'=1}^{3} \partial_{\xi^{j'}} \chi_{kl}^{j'=0}, \\ \overline{\chi_{kl}^j}^\xi = 0. \end{cases} \tag{33}$$

Consider a grid cell, with side lengths Δ_i, $i=1, 2, 3$, and introduce the nondimensionalized lengths $l_i = \Delta_i / \delta$. Then under natural integrability conditions on $\mathbf{w} = \mathbf{w}(\xi, \tau)$, $\chi_{kl}^j = \chi_{kl}^j(\boldsymbol{\xi}, \tau)$ and $\pi_{kl} = \pi_{kl}(\boldsymbol{\xi}, \tau)$ we have the Fourier series expansions $w^j(\boldsymbol{\xi}, \tau) = \Sigma_{\mathbf{m}} \hat{w}^j(\mathbf{m}, \tau) e^{i\mathbf{m} \cdot D\xi}$, $\chi_{kl}^j(\boldsymbol{\xi}, \tau) = \Sigma_{\mathbf{m}} \hat{\chi}_{kl}^j(\mathbf{m}, \tau) e^{i\mathbf{m} \cdot D\xi}$ and $\pi_{kl}(\boldsymbol{\xi}, \tau) = \Sigma_{\mathbf{m}} \hat{\pi}_{kl}(\mathbf{m}, \tau) e^{i\mathbf{m} \cdot D\xi}$, respectively, where $D\boldsymbol{\xi} = 2\pi[\xi_1/l_1, \xi_2/l_2, \xi_3/l_3]^T$ is the lattice vector and $\mathbf{m} \in \mathbf{Z^3}$. Note that $\hat{w}^j(\mathbf{m}, \tau) = \overline{w^j}^\xi = 0$ and similarly for χ_{kl}^j. Then the cell problem (33) is equivalent to an infinite-dimensional system of ordinary differential equations for the Fourier coefficients,

$$\begin{cases} \partial_\tau \hat{\chi}_{kl}^j(\mathbf{m}, \tau) + \nu \|D\mathbf{m}\|^2 \hat{\chi}_{kl}^j(\mathbf{m}, \tau) + (2\pi i m_j / l_j) \hat{\pi}_{kl}(\mathbf{m}, \tau) \\ \quad = -\delta_k^j \hat{w}^1(\mathbf{m}, \tau), \\ \sum_{j'=1}^{3} (2\pi i m_{j'} / l_{j'}) \hat{\chi}_{kl}^{j'} = 0, \\ \hat{\chi}_{kl}^j(\mathbf{0}, \tau) = 0. \end{cases} \tag{34}$$

Taking the divergence of the (33_1), using (33_2) yields $-\nabla_\xi^2 \pi_{kl} = \partial_{\xi^k} w^l$, and thus π_{kl} has the Fourier coefficients $\hat{\pi}_{kl}(\mathbf{m}, \tau) = (2\pi i m_k \hat{w}^l(\mathbf{m}, \tau)) / (l_k \|D\mathbf{m}\|^2)$, and from (34_1) we obtain the equations for the Fourier coefficients of the simplified cell problem (33), viz.,

$$\partial_\tau \hat{\chi}_{kl}^j(\mathbf{m}, \tau) + \nu \|D\mathbf{m}\|^2 \hat{\chi}_{kl}^j(\mathbf{m}, \tau) = \left(-\delta_k^j + \frac{4\pi^2 m_j m_k}{\|D\mathbf{m}\|^2 l_j l_k} \right) \hat{w}^l(\mathbf{m}, \tau). \tag{35}$$

Since $\mathbf{w}$ is assumed to be periodic in τ, we see that the coefficient $\hat{\chi}_{kl}^j$ is the sum of a periodic part and a transient part of the form $Ce^{-\nu \|D\mathbf{m}\|^2 \tau}$. Since we are only interested in the periodic part we assume that $\hat{\chi}_{kl}^j$ has reached a steady state being periodic in τ, i.e., $\hat{w}^j(\mathbf{m}, \tau) = \Sigma_{m'} \tilde{w}^j(\mathbf{m}, m') e^{2\pi i m' \tau / T}$ and $\hat{\chi}_{kl}^j(\mathbf{m}, \tau) = \Sigma_{m'} \tilde{\chi}_{kl}^j(\mathbf{m}, m') e^{2\pi i m' \tau / T}$ so from (35) we obtain the following algebraic system:

$$\left(\frac{2\pi i m'}{T} + \nu \|D\mathbf{m}\|^2 \right) \tilde{\chi}_{kl}^j(\mathbf{m}, \mathbf{m}') = \left(-\delta_k^j + \frac{4\pi^2 m_j m_k}{\|D\mathbf{m}\|^2 l_j l_k} \right) \tilde{w}^l(\mathbf{m}, \mathbf{m}'), \tag{36}$$

from which $\tilde{\chi}_{kl}^j$ can be determined, and from which we obtain the time averages

$$\begin{aligned} \overline{\hat{w}^h \hat{\chi}_{kl}^j}^\tau(\mathbf{m}) &= \sum_{m', n'} \tilde{w}^h(\mathbf{m}, n') \tilde{\chi}_{kl}^j(\mathbf{m}, \hat{m}') \overline{e^{2\pi i (m' + n') \tau / T}}^\tau \\ &= \sum_{m'} \tilde{w}^h(\mathbf{m}, -m') \tilde{\chi}_{kl}^j(\mathbf{m}, m') \\ &= \sum_{m'} \tilde{w}^h(\mathbf{m}, -m') \\ &\quad \times \frac{-\delta_k^j + 4\pi^2 m_j m_k / (\|D\mathbf{m}\|^2 l_j l_k)}{(2\pi i m'/T) + \nu \|D\mathbf{m}\|^2} \tilde{w}^l(\mathbf{m}, m'), \end{aligned} \tag{37}$$

where we have used the notation $\overline{f}^\tau = 1/t \int_0^T f d\tau$. Next, we obtain the anisotropic eddy-viscosity tensor directly from its definition $A_{ijkl} = \overline{w^i \chi_{kl}^j + w^j \chi_{kl}^i}$, viz.,

$$\begin{aligned} A_{hjkl} = \sum_{\mathbf{m}} \Bigg[& \overline{\hat{w}^h(-\mathbf{m}, \tau)}^\tau \frac{(-\delta_{jk} + 4\pi^2 m_j m_k / \|D\mathbf{m}\|^2 l_j l_k)}{\nu \|D\mathbf{m}\|^2} \\ & \times \overline{\hat{w}^1(\mathbf{m}, \tau)}^\tau + \overline{\hat{w}^j(-\mathbf{m}, \tau)}^\tau \\ & \times \frac{(-\delta_{hk} + 4\pi^2 m_h m_k / \|D\mathbf{m}\|^2 l_h l_k)}{\nu \|D\mathbf{m}\|^2} \overline{\hat{w}^1(\mathbf{m}, \tau)}^\tau \Bigg], \end{aligned} \tag{38}$$

where we have neglected the phase shift between $\hat{w}^j(\mathbf{m}, \tau)$ and $\hat{\chi}_{kl}^j(\mathbf{m}, \tau)$ and used the fact that $\overline{\hat{w}^j(\mathbf{m}, \tau)}^\tau = \tilde{w}^j(\mathbf{m}, 0)$. To neglect the phase shift is reasonable for finite sums and high Re number flows, since T is determined by the time step in numerical scheme, so $(2\pi i m'/T) \gg \nu \|D\mathbf{m}\|^2$ as the Reynolds number increases, so terms with $m' = 0$ will dominate in (37) for large Re numbers.

3.3 Choices of *w*. We are interested in $\mathbf{w}(\xi) = \overline{\mathbf{w}(\xi, \tau)}^\tau$ and the corresponding Fourier coefficients $\hat{\mathbf{w}}(\mathbf{m}) = \overline{\hat{\mathbf{w}}(\mathbf{m}, \tau)}^\tau$. The choice of $\mathbf{w}$ is not obvious, to say the least. Considering the expected features of $\mathbf{w}$ it is natural to impose the constraints $\nabla \cdot \mathbf{w} = 0$, and that the energy spectrum obeys the Kolmogorov inertial subrange scaling law, $E(\mathbf{k}) = c_K \varepsilon^{1/3} \mathbf{k}^{-5/3}$, where c_K is the Kolmogorov constant taking the value $c_K \approx 1.4 \pm 0.2$, cf. [17], which puts further restrictions on the Fourier coefficients. The first requirement is fulfilled by choosing each vector Fourier series coefficients $\hat{\mathbf{w}}(\mathbf{m}) = [\hat{w}^1(\mathbf{m}), \hat{w}^2(\mathbf{m}), \hat{w}^3(\mathbf{m})]^T$ orthogonal to the lattice vector $D\mathbf{m}$. To fulfill the second requirement, we note that the energy spectrum is confined to a lattice $\mathbf{k} = 2\pi[m_1/l_1, m_2/l_2, m_3/l_3]$, thus each point is associated with a reciprocal volume $V = (2\pi)^3 / (l_1 l_2 l_3)$. The one-point correlation tensor $\mathbf{R}$ is defined

$$\begin{aligned} \mathbf{R}(\mathbf{r}) &= \overline{\mathbf{w}(\mathbf{x}) \otimes \mathbf{w}(\mathbf{x} + \mathbf{r})}^\xi \\ &= \sum_{\mathbf{m}, \mathbf{n}} (\hat{\mathbf{w}}(\mathbf{m}) \otimes \hat{\mathbf{w}}(\mathbf{n}) / (l_1 l_2 l_3)) \int e^{i(\mathbf{m} + \mathbf{n}) \cdot D\mathbf{x} + \mathbf{n} \cdot D\mathbf{r}} d\mathbf{x} \\ &= \sum_{\mathbf{n}} e^{i\mathbf{n} \cdot D\mathbf{r}} \hat{\mathbf{w}}(-\mathbf{n}) \otimes \hat{\mathbf{w}}(\mathbf{n}) = \sum_{\mathbf{n}} e^{i\mathbf{n} \cdot D\mathbf{r}} \hat{\mathbf{w}}^*(\mathbf{n}) \otimes \hat{\mathbf{w}}(\mathbf{n}), \end{aligned} \tag{39}$$

so that the spectrum tensor becomes

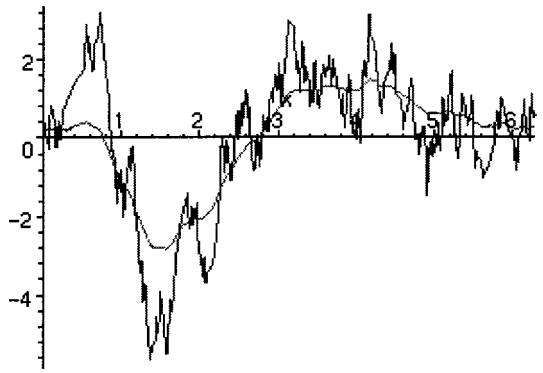

Fig. 1 A typical sample path of w, according to Eq. (40), in green with a sample path of the Brownian motion (in red) in the one-dimensional case

$$\Phi(\mathbf{k}) = \sum_{\mathbf{n}} \hat{\mathbf{w}}^*(\mathbf{n}) \otimes \hat{\mathbf{w}}(\mathbf{n})\, \delta_{D\mathbf{n}}(\mathbf{k}), \tag{40}$$

and hence the full three-dimensional energy spectrum is

$$E(\mathbf{k}) = \frac{1}{2}\mathrm{tr}\boldsymbol{\Phi}(\mathbf{k}) = \frac{1}{2}\sum_{\mathbf{n}} \mathrm{tr}(\hat{\mathbf{w}}^*(\mathbf{n}) \otimes \hat{\mathbf{w}}(\mathbf{n}))\, \delta_{D\mathbf{n}}(\mathbf{k})$$

$$= \frac{1}{2}\sum_{\mathbf{n}} \|\hat{\mathbf{w}}(\mathbf{n})\|^2 \delta_{D\mathbf{n}}(\mathbf{k}), \tag{41}$$

where $\delta_{D\mathbf{n}}$ is the Dirac delta function concentrated at $D\mathbf{n}$. The energy in the shell $k \leqslant \|\mathbf{k}\| \leqslant k+\Delta k$, with the volume $4\pi k^2 \Delta k$, is $\Sigma_{k\leqslant\|D\mathbf{n}\|\leqslant k+\Delta k}\|\hat{\mathbf{w}}(\mathbf{n})\|^2$. Hence, the number of lattice points within this shell is $4\pi k^2 \Delta k/V = l_1 l_2 l_3 k^2 \Delta k/2\pi^2$. In consistency with the energy spectrum we assume that the Fourier components scale like $\|\hat{\mathbf{w}}(\mathbf{n})\| = 2\pi c_w (l_1 l_2 l_3)^{-1/2} \varepsilon^{1/3} \|D\mathbf{n}\|^{\alpha}$, which further implies that the energy in a spherical shell becomes $1/2\Sigma_{k\leqslant\|D\mathbf{n}\|\leqslant k+\Delta k}\|\mathbf{w}(\mathbf{n})\|^2 = c_w^2 \varepsilon^{2/3} k^{2(1+\alpha)} \Delta k$, so that $E(\mathbf{k}) = c_w^2 \varepsilon^{2/3} k^{2(1+\alpha)}$. In order to have the Kolmogorov inertial range scaling we must have that $\alpha = -11/6$. With these properties in mind, and analogous to Wiener's classical Fourier series representation of Brownian motion (cf. [18], p. 21) we propose the following Fourier series representation of $\mathbf{w}$, which is a kind of smoothed three-parameter Brownian motion projected on the subspace of divergence-free vector fields,

$$\mathbf{w}(\boldsymbol{\xi}) = \overline{\mathbf{w}(\boldsymbol{\xi},\tau)}^{\tau}$$

$$= 2\pi c_w (l_1 l_2 l_3)^{-1/2} \varepsilon^{1/3} \sum_{\mathbf{m}} (\mathbf{g}_{\mathbf{m}} \|D\mathbf{m}\|^{-11/6}) e^{i(D\mathbf{m})\cdot\mathbf{x}}, \tag{42}$$

so that $\hat{w}^j(\mathbf{m}) = 2\pi c_w (l_1 l_2 l_3)^{-1/2} \varepsilon^{1/3} g^j_{\mathbf{m}} \|D\mathbf{m}\|^{-11/6}$, where $\mathbf{g}_{\mathbf{m}}$ denotes two-dimensional independent standard Gaussian random variables, with $\mathbf{g}_{\mathbf{m}}$ orthogonal to $D\mathbf{m}$, and c_w is a nondimensional model coefficient to be determined. In order to illustrate the properties of $\mathbf{w}$ Fig. 1 shows a sample path of $\mathbf{w}$ together with a sample path of a Brownian motion the one-dimensional case.

3.4 Computation of the Eddy-Viscosity Tensor. From (38) we get the Fourier series representation for the anisotropic eddy-viscosity tensor,

$$A_{hjkl} = -\frac{4\pi^2 c_w^2 \varepsilon^{2/3}}{\nu l_1 l_2 l_3} \sum_{\mathbf{m}} \frac{1}{\|D\mathbf{m}\|^{17/3}} \left\langle \mathbf{g}^{h*}_{\mathbf{m}} \left(\delta_{jk} - \frac{4\pi^2 m_j m_k}{\|D\mathbf{m}\|^2 l_j l_k} \right) g^l_{\mathbf{m}} + g^{j*}_{\mathbf{m}} \left(\delta_{hk} - \frac{4\pi^2 m_h m_k}{\|D\mathbf{m}\|^2 l_h l_k} \right) g^1_{\mathbf{m}} \right\rangle, \tag{43}$$

where $\langle\cdot\rangle$ denotes the expectation value operator. To compute the expectation values in (43), we need a more explicit representation of $\mathbf{g}_{\mathbf{m}}$. To this end, consider an orthonormal basis generated by $D\mathbf{m}$, e.g.,

$$\mathbf{e}_{1,\mathbf{m}} = \frac{1}{\mathrm{R}} \begin{bmatrix} m_1/l_1 \\ m_2/l_2 \\ m_3/l_3 \end{bmatrix}, \quad \mathbf{e}_{2,\mathbf{m}} = \frac{1}{r} \begin{bmatrix} m_2/l_2 \\ -m_1/l_1 \\ 0 \end{bmatrix},$$

$$\mathbf{e}_{3,\mathbf{m}} = \frac{1}{r\mathrm{R}} \begin{bmatrix} m_1 m_3/(l_1 l_3) \\ m_2 m_3/(l_2 l_3) \\ -r^2 \end{bmatrix}, \tag{44}$$

where $R = \|D\mathbf{m}\|/2\pi = \sqrt{\Sigma_{k=1}^3 (m_k/l_k)^2}$ and $r = \sqrt{(m_1/l_1)^2 + (m_2/l_2)^2}$. Then

$$g^h_{\mathbf{m}} = (a_{2,\mathbf{m}} + i b_{2,\mathbf{m}}) \mathbf{e}^h_{2,\mathbf{m}} + (a_{3,\mathbf{m}} + i b_{3,\mathbf{m}}) \mathbf{e}^h_{3,\mathbf{m}}, \tag{45}$$

where $a_{j,\mathbf{m}}$ and $b_{j,\mathbf{m}}$ are real-valued coefficients. By the assumptions on $\mathbf{g}_{\mathbf{m}}$ we furthermore have that $\langle (a_{j,\mathbf{m}})^2 + (b_{j,\mathbf{m}})^2 \rangle = 1$, and therefore,

$$\langle g^{h*}_{\mathbf{m}} g^l_{\mathbf{m}} \rangle = \sum_{j=2}^{3} \langle (a_{j,\mathbf{m}})^2 + (b_{j,\mathbf{m}})^2 \rangle \mathbf{e}^h_{j,\mathbf{m}} \mathbf{e}^l_{j,\mathbf{m}} = \mathbf{e}^h_{2,\mathbf{m}} \mathbf{e}^l_{2,\mathbf{m}} + \mathbf{e}^h_{3,\mathbf{m}} \mathbf{e}^l_{3,\mathbf{m}}$$

$$= \delta_{hl} - \frac{(m_h/l_h)(m_l/l_l)}{R^2}, \tag{46}$$

where the last equality can be verified by an explicit calculation using (44). Insertion of (46) in (43), using (44), yields

$$A_{hjkl} = -\frac{c_w^2 \varepsilon^{2/3}}{(2\pi)^{11/3} \nu l_1 l_2 l_3} \sum_{\mathbf{m}} R^{-17/3} \left[\left(\delta_{hl} - \frac{(m_h/l_h)(m_l/l_l)}{R^2} \right) \times \left(\delta_{jk} - \frac{(m_j/l_j)(m_k/l_k)}{R^2} \right) + \left(\delta_{jl} - \frac{(m_j/l_j)(m_l/l_l)}{R^2} \right) \times \left(\delta_{hk} - \frac{(m_h/l_h)(m_k/l_k)}{R^2} \right) \right]. \tag{47}$$

Expanding the terms in (47), and taking into account that sums of terms with odd powers of the components of $\mathbf{m}$ vanish by antisymmetry, (47) may be simplified to

$$A_{hjkl} = -\frac{c_w^2 \varepsilon^{2/3}}{(2\pi)^{11/3} \nu l_1 l_2 l_3} \sum_{\mathbf{m}} R^{-17/3} \left[\left(1 - \frac{(m_k/l_k)^2 + (m_l l_l)^2}{R^2} + \frac{(m_k/l_k)^2 (m_l/l_l)^2 (2-\delta_{kl})}{R^4} \right) (\delta_{hl}\delta_{jk} + \delta_{jl}\delta_{hk}) + 2\frac{(m_h/l_h)^2 (m_k/l_k)^2 (1-\delta_{jl})}{R^4} \delta_{hj}\delta_{kl} \right]. \tag{48}$$

To obtain the anisotropic eddy-viscosity tensor A_{hjkl} in dimensionless form, we introduce the isotropic length scale $\Delta = (\Delta_1 \Delta_2 \Delta_3)^{1/3}$, and the nondimensional cell-lengths, $\tilde{\Delta}_j = \Delta_j/\Delta$. Hence, we get the fine scale cell lengths $l_j = \Delta_j/\delta = (\Delta/\delta)\tilde{\Delta}_j$ and $l_1 l_2 l_3 = \Delta_1 \Delta_2 \Delta_3/\delta^3 = (\Delta/\delta)^3$. Furthermore, by introducing $\tilde{R} = \sqrt{(m_1/\tilde{\Delta}_1)^2 + (m_2/\tilde{\Delta}_2)^2 + (m_3/\tilde{\Delta}_3)^2} = (\Delta/\delta)R$, Eq. (48) may be expressed as

$$A_{hjkl} = \frac{c_w^2 \varepsilon^{2/3} (\Delta/\delta)^{8/3}}{(2\pi)^{11/3} \nu} \tilde{A}_{hjkl}, \tag{49}$$

where the dimensionless tensor $\tilde{A}_{hjkl}$ is defined by

$$\tilde{A}_{hjkl}=-\sum_{\mathbf{m}} R^{-17/3}\Bigg[\Bigg(1-\frac{(m_k/\tilde{\Delta}_k)^2+(m_l/\tilde{\Delta}_l)^2}{\tilde{R}^2}+\frac{(m_k/\tilde{\Delta}_k)^2(m_l/\tilde{\Delta}_l)^2(2-\delta_{kl})}{\tilde{R}^4}\Bigg)(\delta_{hl}\delta_{jk}+\delta_{jl}\delta_{hk})+2\frac{(m_h/\tilde{\Delta}_h)^2(m_k/\tilde{\Delta}_k)^2(1-\delta_{jl})}{\tilde{R}^4}\delta_{hj}\delta_{kl}\Bigg]. \quad (50)$$

Finally, we need to determine the model coefficient c_w. The most natural way is by comparison to the properties of the three-dimensional energy spectrum. Hence, we consider, for simplicity, the isotropic three-dimensional spectrum, $E_{\mathbf{w}}(k)=\int\int E_{\mathbf{w}}(k\mathbf{n})k^2 d\sigma(\mathbf{n})$, which scales according to

$$\begin{aligned}E_{\mathbf{w}(\cdot/\delta)}(k)&=\int\int E_{\mathbf{w}(\cdot/\delta)}(k\mathbf{n})k^2 d\sigma(\mathbf{n})\\&=\int\int \delta^3 E_{\mathbf{w}}(\delta k\mathbf{n})k^2 d\sigma(\mathbf{n})\\&=\delta\int\int E_{\mathbf{w}}((\delta k)\mathbf{n})(\delta k)^2 d\sigma(\mathbf{n})=\delta E_{\mathbf{w}}(\delta k),\end{aligned} \quad (51)$$

and thus, by homogeneity, we get

$$E_{\delta^a\mathbf{w}(\cdot/\delta)}(k)=\delta^{1+2a}E_{\mathbf{w}}(\delta k). \quad (52)$$

Note that the isotropic energy spectrum $E_{\mathbf{w}}(k)$ is computed in local coordinates $\mathbf{x}/\delta$. Transformed to physical coordinates $\mathbf{x}$ we obtain

$$E_{(1/\delta)\mathbf{w}(\cdot/\delta)}(k)=\delta^{-1}c_{\mathbf{w}}^2\varepsilon^{2/3}(\delta k)^{2(1+\alpha)}=\delta^{1+2\alpha}c_{\mathbf{w}}\varepsilon^{2/3}k^{2(1+\alpha)}. \quad (53)$$

In order to have the Kolmogorov inertial range scaling we must have that $\alpha=-11/6$, and hence, $E_{\mathbf{w}}(k)=c_{\mathbf{w}}^2\varepsilon^{2/3}k^{-5/3}$ and $E_{(1/\delta)\mathbf{w}(\cdot/\delta)}(k)=\delta^{-8/3}c_{\mathbf{w}}^2\varepsilon^{2/3}k^{-5/3}$ and thus to obtain the Kolmogorov spectrum for the leading term $(1/\delta)\mathbf{w}(\cdot/\delta)$ we should choose $c_{\mathbf{w}}=\sqrt{c_K}\delta^{4/3}$. However, this choice cannot be valid for all values of δ, since $\mathbf{w}$ is not allowed to depend explicitly on δ. Hence it should be viewed as a matching condition applied after the choice of δ in the expansion. Hence, if we choose c_w according to $c_{\mathbf{w}}=\sqrt{c_K}\delta^{4/3}$ the eddy-viscosity tensor A_{hjkl} is independent of δ, namely,

$$A_{hjkl}=\frac{c_k\varepsilon^{2/3}\Delta^{8/3}}{(2\pi)^{11/3}\nu}\tilde{A}_{hjkl}. \quad (54)$$

Hence to compute the eddy-viscosity tensor A_{ijkl} we do not need to assume a particular value of δ, we need only to assume that there exists a value of δ such that the series expansion is a good approximation. To close this expression we need to model the dissipation ε of k. By deriving a transport equation for $k=1/2\mathrm{tr}\mathbf{B}=1/2(\overline{|\mathbf{v}|^2}-|\overline{\mathbf{v}}|^2)$ we find that the dissipation of k is $\varepsilon=\overline{\mathbf{S}\cdot\mathbf{D}}-\overline{\mathbf{S}}\cdot\overline{\mathbf{D}}=2\nu(\overline{\|\mathbf{D}\|^2}-\|\overline{\mathbf{D}}\|^2)$. Within the inertial subrange only inviscid mechanisms are active and energy is transferred from large to small scales. The rate of transfer from the smallest scales may therefore be estimated as $\varepsilon\propto k^{3/2}/\lambda$, where λ is an isotropic length scale, such as $\lambda=\Delta=\sqrt[3]{\Delta_1\Delta_2\Delta_3}$. Following, e.g., [12,19,20], we use the modeled, and modified, transport equation,

$$\begin{aligned}\partial_t(k)+\nabla\cdot(k\overline{\mathbf{v}})&=-\mathbf{B}\cdot\overline{\mathbf{D}}+\nabla\cdot(\nu\nabla k)-\varepsilon\\&=-((A_{ijkl}(\nabla v)_{kl})\overline{D}_{ij})+\nabla\cdot(\nu\nabla k)-\varepsilon,\end{aligned} \quad (55)$$

where $\varepsilon=c_\varepsilon k^{3/2}/\Delta$ in which $c_\varepsilon\approx 1.05$, cf. [19,20]. Substituting this into (54) yields

$$A_{hjkl}=\frac{c_k c_\varepsilon^{2/3}k\Delta^2}{(2\pi)^{11/3}v}\tilde{A}_{hjkl}. \quad (56)$$

For numerical purposes it is convenient to decompose the dimensionless eddy-viscosity tensor $\tilde{A}_{hjkl}$ into a scalar part, $\tilde{A}_{hk}\delta_{jl}$, and the remainder $\tilde{A}_{hjkl}-\tilde{A}_{hk}\delta_{jl}$, where,

$$\tilde{A}_{hk}=\frac{1}{3}\sum_{j=1}^{3}\tilde{A}_{hjkj}=-\sum_{\mathbf{m}} R^{-17/3}\Bigg(1-\frac{(m_k/\tilde{\Delta}_k)^2}{\tilde{R}^2}\Bigg)\delta_{hk}. \quad (57)$$

The scalar part gives a scalar elliptic operator term $\partial_{x^h}(\tilde{A}_{hk}\delta_{jl}\partial_{x^k}\overline{v^l})=\partial_{x^h}(\tilde{A}_{hk}\partial_{x^k}\overline{v^j})$, which may be handled implicitly in the numerical scheme, whereas the remainder may be implemented as an explicit source term—this in order to increase the overall stability.

4 Numerical Methods for Large-Eddy Simulation (LES)

LES requires high-order numerical methods to avoid masking $\nabla\cdot\mathbf{B}$ by the leading-order truncation error. In general, Δ is related to the grid, i.e., $\Delta\propto|\mathbf{d}|$, where $|\mathbf{d}|$ is the grid size, which makes the modeled subgrid stresses $O(|\mathbf{d}|^2)$ terms. In LES, spectral and high-order finite volume, element or difference methods are used for spatial discretization, whilst explicit semi-implicit or predictor-corrector methods are used for time-integration. For complex geometries the finite volume (FV) method is the most convenient technique. Here, the domain $\mathbf{D}$ is partitioned into cells Ω_P so that $\cup_P(\Omega_P)=D\cup\partial D$ and $\cap_P(\Omega_P)=\varnothing$. The cell average of f over the Pth cell is $f_P=1/\delta V\int_\Omega f dV$ so that Gauss theorem may be used to formulate the semi-discretized LES equations. By integrating these over time, using, e.g., a multistep method, [21], the discretized LES equations become

$$\begin{cases}\dfrac{\beta_i\Delta t}{\delta V_P}\displaystyle\sum_f [F_f^{C,\rho}]^{n+i}=0,\\ \displaystyle\sum_{i=0}^{m}\Bigg(\alpha_i(\overline{\mathbf{v}})_P^{n+i}+\frac{\beta_i\Delta t}{\delta v_P}\sum_f[\mathbf{F}_f^{C,v}+\mathbf{F}_f^{D,v}+\mathbf{F}_f^{B,v}]^{n+i}\Bigg)\\ \quad=-\beta_i(\nabla\overline{p})_P^{n+i}\Delta t+\beta_i(\overline{\mathbf{f}})_P^{n+i}\Delta t,\end{cases} \quad (58)$$

where m, α_i and β_i are parameters of the temporal scheme whereas $F_f^{C,\rho}=(\overline{\mathbf{v}}\cdot d\mathbf{A})_f$, $\mathbf{F}_f^{C,v}=(\overline{\mathbf{v}}\cdot d\mathbf{A})_f\overline{\mathbf{v}}_f$, $\mathbf{F}_f^{D,v}=(\nu\nabla\overline{\mathbf{v}})_f d\mathbf{A}$ and $\mathbf{F}_f^{B,v}=(\mathbf{B})_f d\mathbf{A}$ are the convective, viscous and subgrid fluxes. The closure of these requires flux interpolation for the convective fluxes and difference approximations for the inner derivatives of the viscous and subgrid fluxes, respectively. In order to obtain second-order accuracy a cell-centered FV scheme is used, in which linear interpolation is used for the convective fluxes and central difference approximations are used to approximate the inner gradients in the viscous and subgrid fluxes. The time-integration is performed by a three-point scheme defined by $m=2$, $\alpha_0=1/2$, $\alpha_1=-2$, $\alpha_2=3/2$, $\beta_0=\beta_1=0$ and $\beta_2=1$, and hence,

$$\begin{aligned}&a_P(\overline{\mathbf{v}})_P^{n+2}=H(\overline{\mathbf{v}})-(\nabla\overline{p})_P^{n+2}+(\overline{\mathbf{f}})_P^{n+2},\\&\text{where } H(\overline{\mathbf{v}})=\sum_N a_N(\overline{\mathbf{v}})_N^{n+2}+\frac{1}{2\Delta t}(\overline{\mathbf{v}})_P^n-\frac{2}{\Delta t}(\overline{\mathbf{v}})_P^{n+1},\end{aligned} \quad (59)$$

where the coefficients a_P and a_N are complex functions involving, e.g., $F_f^{C,\rho}$, ν and ν_k or A_{hjkl}. By combining (58_1) and (58_2), the continuity equation can be replaced by the Poisson equation,

$$\nabla\cdot(a_P^{-1}(\nabla\overline{p})^{n+2})=\sum_f(a_P^{-1}(H\overline{\mathbf{v}}))_f\cdot d\mathbf{A}+\sum_f(a_P^{-1}(\overline{\mathbf{f}})_P^{n+2}\cdot d\mathbf{A}, \quad (60)$$

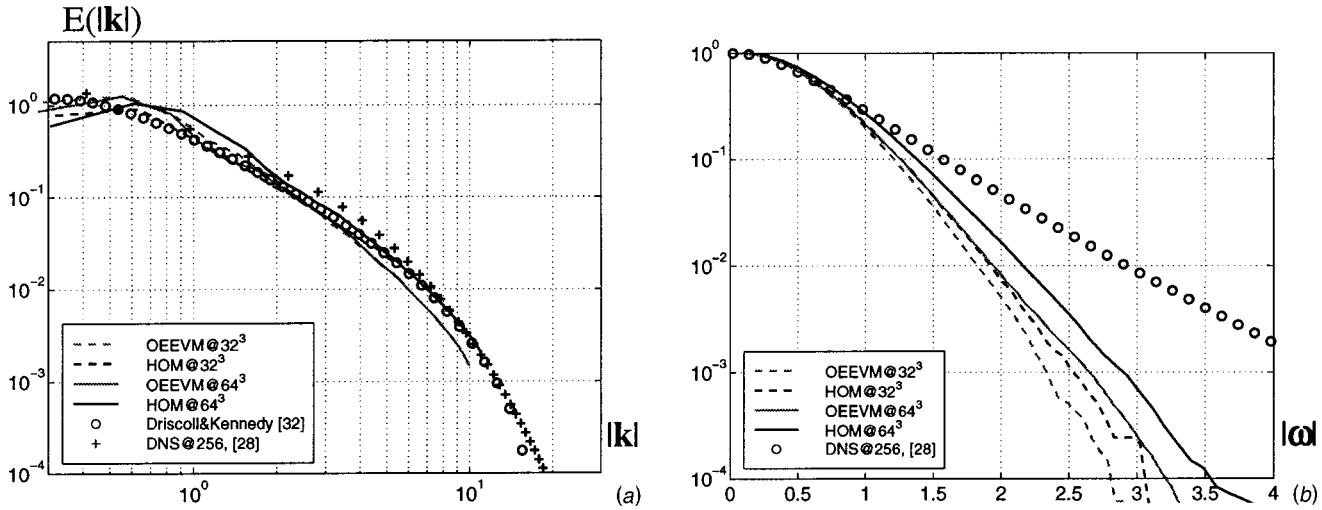

Fig. 2 Comparison of (*a*) the energy spectrum *E* and (*b*) the PDF of the vorticity magnitude $|\overline{\omega}|$ of forced homogeneous isotropic turbulence at $Re_T=96$ at 64^3 resolution for conventional LES, using the OEEVM, and the homogenisation-based LES model

where the Laplace operator is discretized in a standard manner. $F_f^{C,\rho}$ is evaluated from the interpolated velocity field $\overline{\mathbf{v}}_f^{n+2}=(a_P^{-1}H(\overline{\mathbf{v}}))_f-(a_P^{-1}(\nabla\overline{p})_P^{n+2})_f+(a_P^{-1}\overline{\mathbf{f}}_P^{n+2})_f$. The scalar equations are usually solved sequentially, with iteration over the explicit source terms to obtain rapid convergence, with the additional requirement that the Courant number $Co<0.5$.

5 Application of the Proposed Large-Eddy Simulation (LES) Model

In order to test the homogenization-based LES model we have performed simulations of forced homogeneous isotropic turbulence at a target Taylor Re number of $Re_T=96$ and fully developed turbulent channel flow at target friction-velocity based Re number of $Re_\tau=395$, using the scalar part (57) of the eddy viscosity tensor (56). Simulations with the full eddy-viscosity tensor (56) remains to be investigated. The first case is mainly used to examine the dependence of the eddy viscosity on k and Δ, and to verify the scaling properties of the energy spectrum discussed earlier. The aim of the second case is to study the anisotropic properties of the subgrid model, and how well the proposed model can handle wall bounded flows with marginal wall-normal resolution. For both cases we compare predictions from the proposed homogenization-based LES subgrid model with results from conventional LES (typically using the constant coefficient Smagorinsky (SMG) and the one equation eddy-viscosity model (OEEVM) subgrid models), experimental data and DNS state-of-the-art results.

5.1 Homogeneous Isotropic Turbulence. For the purpose of examining the dependence of the eddy viscosity on k and Δ, and to verify the scaling properties of the energy spectrum we first perform LES of forced homogeneous isotropic turbulence for a Taylor Re number of $Re_T=96$ at 32^3 and 64^3 resolution, for which DNS data is available, [22–24]. In these simulations the specific body force, $\mathbf{f}$, is used to create random forcing of the large scales. For this specific purpose we use the forcing scheme of Eswaran and Pope, [25], in which the specific body force is $\mathbf{f}(\mathbf{k},t)=\mathbf{P}(\mathbf{k})\mathbf{w}(\mathbf{k},t)[\Theta(\mathbf{k})-\Theta(\mathbf{k}-\mathbf{k}_F)]$, where Θ is the step-function, $\mathbf{P}(\mathbf{k})=\mathbf{I}-|\mathbf{k}|^{-2}(\mathbf{k}\otimes\mathbf{k})$ and $\mathbf{w}(\mathbf{k},t)$ is a vector valued Uhlenbeck-Ornstein process that is characterized by $\langle\mathbf{w}(\mathbf{k},t)\otimes\mathbf{w}^*(\mathbf{k},t+s)\rangle=2\sigma^2\exp(-s/\tau)\mathbf{I}$ in the equilibrium limit. In this forcing scheme four parameters are introduced: the amplitude σ of the body force, the time scale τ and the wave numbers k_L and k_F. To avoid any influence of the forcing on the smaller scales, only the largest velocity scales are driven. Moreover, the initial velocity field $\overline{\mathbf{v}}=\overline{\mathbf{v}}(\mathbf{x},0)$ is created by superimposing Fourier modes, having a prescribed energy spectrum but random phases.

Figure 2(*a*) presents the time-averaged energy spectra for the $Re_T=96$ case at 32^3 and 64^3 resolution together with a DNS spectrum, [22], and the theoretical model spectrum of Driscoll and Kennedy [26]. The energy spectra are found to depend on the effects of the LES models only towards the high wave number end of the inertial range, and into the viscous subrange. In the 64^3 results a larger fraction of the turbulence is resolved as compared to the 32^3 results, and hence the influence of the subgrid model is comparatively smaller. Concerning the model parameter $c_w=\sqrt{c_K}\delta^{4/3}$, with $c_K=1.4$ being the Kolmogorov constant, these results suggests that this particular choice, eliminating δ from ν_{ijkl}, is appropriate in terms of reproducing the shape of the energy spectra. In general, we find that the spectra from the homogenization-based LES model is in better agreement with DNS data at high wave numbers than the OEEVM model. This is further confirmed by Fig. 2(*b*), which shows comparisons between probability density functions (PDF's) of the resolved vorticity magnitude $|\overline{\boldsymbol{\omega}}|$ and PDF's of the unfiltered vorticity magnitude $|\boldsymbol{\omega}|$ from DNS, where $\overline{\boldsymbol{\omega}}=1/2\nabla\times\overline{\mathbf{v}}$ is the vorticity vector. These plots are presented in semi-logarithmic format in order to highlight the differences occurring at the higher values of the vorticity magnitude due mainly to spatial resolution of the vortical structures of the flow. Plotted in linear format we would hardly see any differences between LES and DNS, or between the different subgrid models. The distributions of $|\overline{\boldsymbol{\omega}}|$ and $|\boldsymbol{\omega}|$ are far from Gaussian, although the LES data are more Gaussian than the DNS data. Hence, most of the resolved values are accommodated in a comparatively weak background that would not affect low-order statistical moments, although it will dominate high-order moments. The homogenization-based model is observed to give slightly better agreement with the unfiltered DNS data than the conventional LES model, using OEEVM. This further suggests that the homogenization-based model is less diffusive than the OEEVM, and that we should expect the vorticity populations and the viscosities from the two LES models to be quite different from each other.

Figures 3(*a*) and 3(*b*) show volumetric visualizations at 64^3 resolution in terms of iso-surfaces of the vorticity magnitude $|\overline{\boldsymbol{\omega}}|$, and contours of the eddy viscosity, ν_k and $|\nu_{ijkl}|$, from conventional LES using the OEEVM, and from the homogenization-based LES model, respectively. The structure of the vorticity field

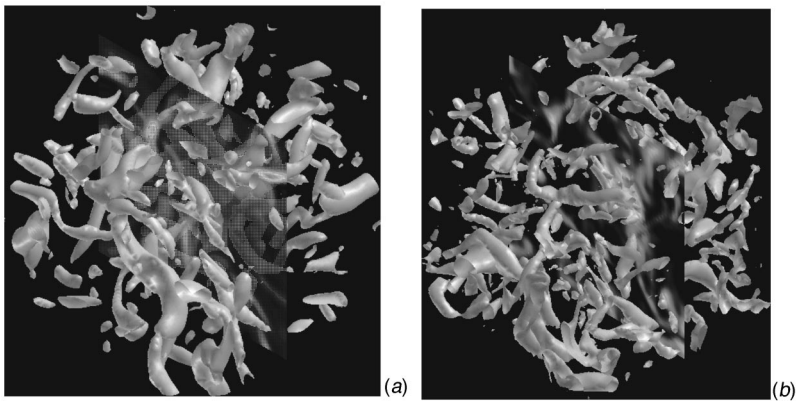

Fig. 3 Volumetric visualization in terms of iso-surfaces of the vorticity magnitude $|\omega|$ and contours of the eddy viscosity ν_k and $|A|$ of forced homogeneous isotropic turbulence at $Re_T=96$ at 64^3 resolution from (*a*) conventional LES using the OEEVM, and from (*b*) the homogenization based LES model

$|\overline{\omega}|$ implies that weak and strong vortices have distinct topology; while there is no evident structure in the lower intensity regions, the higher intensity regions tend to be organized in slender tubes or elongated filaments. This observation is in agreement with the PDF's of Fig. 2(*b*) and volumetric visualizations of DNS results. The thickness of the vortical structures in the LES calculations are considerable larger than in the corresponding DNS calculations, due to lack of spatial resolution. However, filtering the DNS data results in considerably thicker vortical structures—qualitatively similar to those of the LES results. Comparing the volume visualizations in Fig. 3(*a*) and 3(*b*) suggests that the homogenization-based LES model give thinner and more coherent vortical structures as compared to the OEEVM. Comparing the distribution of the eddy viscosity it is clear that the homogenization model produces more localized regions of viscosity than the OEEVM. This is due to the fact that $\nu_k \propto k^{1/2}$, whereas $\nu_{ijkl} \propto k$, which further implies that the homogenization-based LES subgrid model is less diffusive than the ordinary LES OEEVM model. For both models, however, the eddy viscosity tends to peak between vortical structures, in regions of intense strain $\|\overline{\mathbf{D}}\|$ and stretching $\overline{\boldsymbol{\omega}}\cdot\overline{\mathbf{D}}\overline{\boldsymbol{\omega}}$, see also [22].

5.2 Turbulent Channel Flow. The channel is confined between two parallel plates at a distance $2h$ apart, where h is the channel half-width. The flow is driven by a constant mass flow in the streamwise ($\mathbf{e}_1$) direction defining the mean velocity $\langle\overline{\mathbf{v}}\rangle$. No-slip conditions are imposed in the cross-stream ($\mathbf{e}_2$) direction and periodic conditions are used in the spanwise ($\mathbf{e}_3$) direction. As initial conditions we use a parabolic velocity profile with 5% Gaussian white noise. After reaching a statistically steady state the simulations were continued for another $40\cdot h/u_\tau$ time units to obtain statistics. Here, $u_\tau=\tau_w^{1/2}$ denotes the friction velocity, and τ_w is the wall shear stress. The size of the channel is $6h\times 2h\times 3h$ in the streamwise, cross-stream, and spanwise directions, and the friction-velocity based Re number is $Re_\tau=395$ for which DNS data, [27,28], is available. The grid consists of 60^3 cells with uniform spacing in the $\mathbf{e}_1$ and $\mathbf{e}_3$ directions whereas geometrical progression is used in the $\mathbf{e}_2$ direction to concentrate the grid towards the walls. The first grid point is located at $y^+\approx 5$, where the superscript "+" denotes nondimensionalization using u_τ and the viscous length scale ν/u_τ.

In Fig. 4 the flow features in the lower half of the channel are presented in terms of contours of the streamwise vorticity $\overline{\omega}_1$ on side and bottom walls and regions of intense vorticity. The regions of intense vorticity are defined as the regions with positive second invariant Q of the velocity gradient $\nabla\overline{\mathbf{v}}$, with the additional condition that $\overline{p}$ should be lower than its ambient value so that $Q=1/2(\|\overline{\mathbf{W}}\|^2-\|\overline{\mathbf{D}}\|^2)$, where $\overline{\mathbf{W}}=1/2(\nabla\overline{\mathbf{v}}-\nabla\overline{\mathbf{v}}^T)$ and $\overline{\mathbf{D}}=1/2(\nabla\overline{\mathbf{v}}+\nabla\overline{\mathbf{v}}^T)$. In Fig. 4(*a*) we present volume visualizations of Q from $Re_\tau=395$ using OEEVM and in Fig. 4(*b*) show the corresponding results from the homogenization-based model. The flow in the

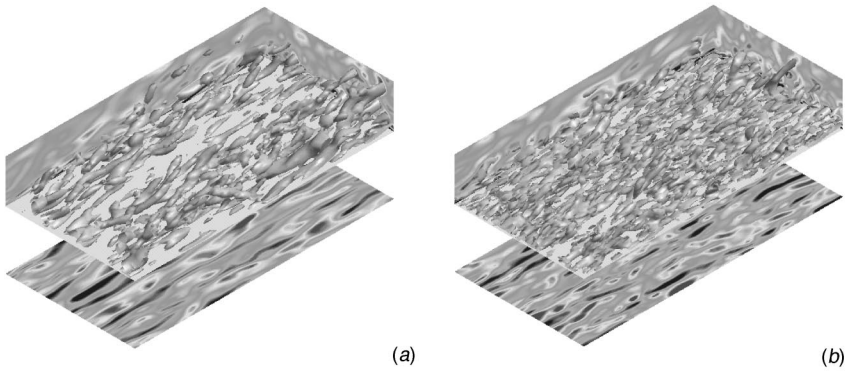

Fig. 4 Contours of streamwise vorticity $\overline{\omega}_1$ projected onto the side and bottom walls together with contours of the streamwise velocity fluctuations $v_1'=\overline{v}_1-\langle\overline{v}_1\rangle$ at $y^+\approx 20$, and iso-surfaces of the second invariant of the velocity gradient tensor Q for (*a*) OEEVM and (*b*) the homogenization-based subgrid model at 60^3 resolution at $Re_\tau=395$

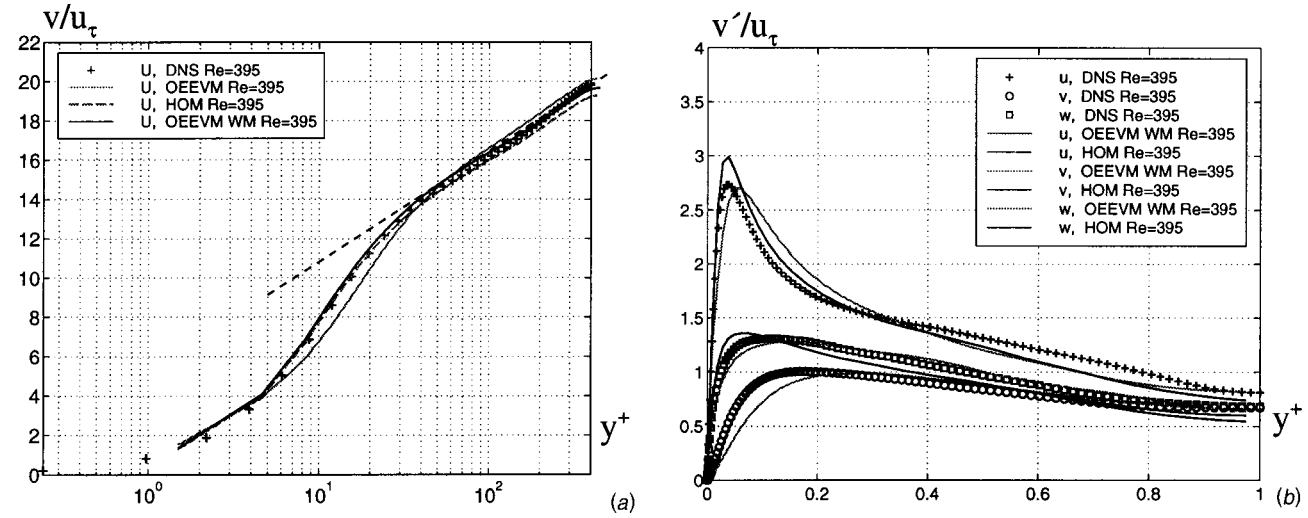

Fig. 5 Time-averaged velocity profiles $\langle \overline{v}_1 \rangle$ (*a*) in outer scaling and the corresponding rms velocity fluctuations $\overline{v}_1^{\text{rms}}$ (*b*) in inner scaling for the fully developed turbulent channel flow case at Re_τ=395

near-wall region consists of recurrent streamwise rolls of high or low-speed fluid, having a length of $\sim 1000\delta_\tau$, where δ_τ is the viscous length scale, a radius of $\sim 15\delta_\tau$, and a mean streak spacing of $\sim 100\delta_\tau$. These structures originate in a layer of vorticity, having a thickness of $\sim 10\delta_\tau$ and situated at a distance $\sim 15\delta_\tau$ from the wall. Ejections of low-speed fluid or inrushes of high-speed fluid at a shallow angle towards the wall are observed, and away from the walls most organized structures disappear. The high-speed fluid elements are inclined with respect to the walls as a consequence of shear acting on a typical fluid element from the outer layer moving towards the lower wall. High-pressure regions occur whenever high-speed fluid impacts on low-speed fluid forming a stagnation point. Most low-pressure regions are elongated and concur with the vortex cores. The near-wall region is densely populated by streamwise or ω_1 vortices having an upward inclination that increase with distance from the wall. In the near-wall region ω_1 vortices occur separately, although sporadic, counterrotating, vortex pairs may occur. Due to the isotropic nature of the viscosity of the OEEVM model processes associated with mainly spanwise topology are overly damped as compared with the results from the homogenization-based model, thus resulting in weaker spanwise and cross-stream rms velocity fluctuations and lower shear stresses, due to a reduced production of turbulent kinetic energy.

In Figs. 5(*a*) and 5(*b*) we present profiles of the time-averaged streamwise velocity $\langle \overline{v}_1 \rangle$ and the corresponding rms-fluctuations $\overline{v}_i^{\text{rms}}$ from conventional LES using OEEVM, homogenization-based LES and DNS data, [27,28]. Concerning the mean flow field, $\langle \overline{v}_1 \rangle$, only minor differences between the LES models can be observed and the von Karman constant can be predicted with essentially no dependence on the SGS model. For $\overline{v}_i^{\text{rms}}$ we directly observe that the homogenization based LES model gives better agreement with DNS data than the ordinary LES model. Not only is the relative distribution of the $\overline{v}_i^{\text{rms}}$ components improved, but also is the location of the peak $\overline{v}_i^{\text{rms}}$ better predicted by the homogenization-based subgrid model. The reason for this improvement lies mainly in the anisotropic nature of the eddy viscosity, taking into account the simultaneous flow and grid anisotropies in the near-wall region. Furthermore, the differences between the DNS and LES in the core of the channel are mainly attributed to the different forcing schemes used in the DNS and LES codes, for further details, we refer to [29,30].

6 Concluding Remarks

In this study we have developed a LES model using a two-scale expansion technique within the framework of the homogenization method. This approach for developing LES models is profoundly different from the conventional filtering approach. The method is tractable since it automatically provides a subgrid closure model, based directly on the underlying NSE. The drawbacks are:

- limitations imposed by assuming two scales, and not a cascade of scales;
- and that the approach is mathematically demanding.

The first, and most serious drawback, can be remedied by using a multiscale expansion, or by using recursive two-scale expansions, but this is beyond the scope of the present paper.

The subgrid model is obtained as the solution to the cell or microstructure problem, describing the small-scale dynamics. In this particular study we have developed a simplified analytical subgrid model, by neglecting the transport of subgrid fluctuations in the cell problem. The subgrid model takes the form of a generalized eddy-viscosity model, with the viscosity being a (nonlinear) fourth-rank tensor. As a direct consequence of this, the homogenization based subgrid model can handle simultaneous grid and flow anisotropies better than most conventional (scalar) eddy-viscosity models. A conceptually similar method was developed more than 20 years ago by Perrier and Pironneau [30], but appears not to have found general application. The model developed here has been applied to forced homogeneous isotropic turbulence in a box and fully developed turbulent channel flows. Comparisons are made with conventional LES (using SMG and OEEVM), experimental data and DNS results. Based on the theoretical work and the associated simulations the main conclusions are:

- the subgrid model is derived directly from the Navier-Stokes dynamics;
- a family of subgrid models is obtained, with the most advanced model being based on solving the partial differential equations for the cell problem along with the LES equations;
- here, we have simplified the cell problem in order to obtain analytical solutions in order to develop a subgrid model of conventional eddy-viscosity type;

- the scaling parameter δ is evaluated as the ratio between the Kolmogorov scale and the isotropic filter width, but other choices may be equally appropriate;
- in the homogenization based subgrid model wall-effects are automatically incorporated, as well as effects from nonuniform grids.

Further modifications to the model may involve investigating multiscale expansions, other types of solutions to the simplified cell problem in order to better account for boundary layer effects, and (iii) the full numerical solution to the cell (or microstructure) problem.

Acknowledgment

These computations were preformed with an earlier research version of the FOAM™ code, for further details see http://www.nabla.com.uk.

References

[1] Speziale, C. G., 1996, ''Modeling of Turbulent Transport Equations,'' *Simulation and Modeling of Turbulent Flows*, Eds., T. B. Gatski, M. Y. Hussaini, and J. L. Lumeley, eds., Oxford University Press, New York.
[2] Lesieur, M., and Metais, O., 1996, ''New Trends in Large Eddy Simulations of Turbulence,'' Annu. Rev. Fluid Mech., **28**, p. 45.
[3] Sagaut, P., 2001, *Large Eddy Simulation for Incompressible Flows*, Springer-Verlag, Heidelberg.
[4] Boris, J. P., 1992, ''On Large Eddy Simulations Using Subgrid Turbulence Models,'' *Wither Turbulence? Turbulence at the Crossroads* (Lecture Notes in Physics), J. L. Lumly, ed., Springer-Verlag, Berlin, **357**, p. 344.
[5] Fureby, C., 2001, ''Towards Large Eddy Simulation of Complex Flows,'' *Direct and Large Eddy Simulation IV*, R. Friedrich and W. Rodi, eds., Kluwer, Dordrecht, The Netherlands.
[6] Ferziger, J. H., and Leslie, D. C., 1979, ''Large Eddy Simulation—A Predictive Approach to Turbulent Flow Computation,'' AIAA Paper No. 79-1441.
[7] Fureby, C., and Tabor, G., 1997, ''Mathematical and Physical Constraints on Large Eddy Simulations,'' J. Theoret Fluid Dyn., **9**, p. 85.
[8] Ghosal, S., and Moin, P., 1995, ''The Basic Equations for the Large Eddy Simulation of Turbulent Flows in Complex Geometry,'' J. Comput. Phys., **118**, p. 24.
[9] Speziale, C. G., 1985, ''Galilean Invariance of Sub Grid Scale Stress Models in Large Eddy Simulations of Turbulence,'' J. Fluid Mech., **156**, p. 55.
[10] Vreman, B., Geurts, B., and Kuerten, H., 1994, ''Realizability Conditions for the Turbulent Stress Tensor in Large Eddy Simulation,'' J. Fluid Mech., **278**, p. 351.
[11] Smagorinsky, J., 1963, ''Numerical Study of Small Scale Intermittency in Three-Dimensional Turbulence,'' Mon. Weather Rev., **91**, p. 99.
[12] Schumann, U., 1975, ''Subgrid Scale Model for Finite Difference Simulation of Turbulent Flows in Plane Channels and Annuli,'' J. Comput. Phys., **18**, p. 376.
[13] Germano, M., Piomelli, U., Moin, P., and Cabot, W. H., 1994, ''A Dynamic Sub Grid Scale Eddy-Viscosity Model,'' Phys. Fluids A, **3**, p. 1760.
[14] Persson, L. E., Persson, L., Svanstedt, N., and Wyller, J., 1993, *The Homogenization Method—An Introduction*, Studentlitteratur, Lund.
[15] Avellaneda, M., 1987, ''Optimal Bounds and Microgeometrics for Elastic Two-Phase Composites,'' SIAM (Soc. Ind. Appl. Math.) J. Appl. Math., **47**, p. 1216.
[16] Bensoussan, A., Lions, J. L., and Papanicolaou, G., 1978, *Asymptotic Analysis for Periodic Structures*, North-Holland, Amsterdam.
[17] Frisch, U., 1995, *Turbulence*, Cambridge University Press, Cambridge, UK.
[18] Itô, K., and McKean, Jr., H. P., 1974, *Diffusion Processes and Their Sample Paths*, Springer-Verlag, New York.
[19] Kim, W.-W., and Menon, S., 1994, ''A New Dynamic One Equation Sub Grid Scale Model for Large Eddy Simulations,'' AIAA Paper No. 95-0356.
[20] Yoshizawa, A., 1993, ''Bridging Between Eddy-Viscosity-Type and Second-Order Models Using a Two-Scale DIA,'' *Ninth Symp. on Turbulent Shear Flows*, Kyoto, Japan, Aug.
[21] Hirsch C., 1999, *Numerical Computation of Internal and External Flows*, John Wiley and Sons, New York.
[22] Jimenez, J., Wray, A., Saffman, P., and Rogallo, R., 1993, ''The Structure of Intense Vorticity in Isotropic Turbulence,'' J. Fluid Mech., **255**, p. 65.
[23] Kerr, R. M., 1985, ''Higher Order Derivative Correlation and the Alignment of Small Scale Structures in Numerical Turbulence,'' J. Fluid Mech., **153**, p. 31.
[24] Fureby, C., Tabor, G., Weller, H., and Gosman, D., 1997, ''A Comparative Study of Sub Grid Scale Models in Homogeneous Isotropic Turbulence,'' Phys. Fluids, **9**, p. 1416.
[25] Eswaran, V., and Pope, S. B., 1988, ''An Examination of Forcing in Direct Numerical Simulation of Turbulence,'' Comput. Fluids, **16**, p. 257.
[26] Driscoll, R. J., and Kennedy, L. A., 1983, ''A Model for the Turbulent Energy Spectrum,'' Phys. Fluids, **26**, p. 1228.
[27] Sandham, N. D., and Howard, R. J. A., 1995, ''Statistics Databases From Direct Numerical Simulation of Fully-Developed Turbulent Channel Flow,'' QMW-EP-1106, Queen Mary & Westfield College, Department of Engineering, London.
[28] Antonia, R. A., Teitel, M., Kim, J., and Browne, L. W. B., 1992, ''Low-Reynolds-Number Effects in a Fully Developed Turbulent Channel Flow,'' J. Fluid Mech., **236**, p. 579.
[29] Fureby, C., Gosman, A. D., Sandham, N., Tabor, G., Weller, H. G., and Wolfstein, M., 1997, ''Large Eddy Simulation of Turbulent Channel Flows,'' *Turbulent Shear Flows 11*, Grenoble.
[30] Perrier, P., and Pironneau, O., 1981, ''Subgrid Turbulence Modelling by Homogenization,'' Math. Model., **2**, p. 295.

George S. Constantinescu
Center for Integrated Turbulence Simulations,
Stanford University,
Stanford, CA 94305

Hugo Pasinato

You-Qin Wang

Mechanical and Aerospace Engineering
Department,
Arizona State University,
Tempe, AZ 85287-6106

James R. Forsythe
United States Air Force Academy,
2354 Fairchild Hall,
Colorado Springs, CO 80840

Kyle D. Squires
Mechanical and Aerospace Engineering
Department,
Arizona State University,
Tempe, AZ 85287-6106

Numerical Investigation of Flow Past a Prolate Spheroid

The flowfield around a 6:1 prolate spheroid at angle of attack is predicted using solutions of the Reynolds-averaged Navier-Stokes (RANS) equations and detached-eddy simulation (DES). The calculations were performed at a Reynolds number of 4.2×10^6, the flow is tripped at $x/L=0.2$, and the angle of attack α is varied from 10 to 20 deg. RANS calculations are performed using the Spalart-Allmaras one-equation model. The influence of corrections to the Spalart-Allmaras model accounting for streamline curvature and a nonlinear constitutive relation are also considered. DES predictions are evaluated against experimental measurements, RANS results, as well as calculations performed without an explicit turbulence model. In general, flowfield predictions of the mean properties from the RANS and DES are similar. Predictions of the axial pressure distribution along the symmetry plane agree well with measured values for 10 deg angle of attack. Changes in the separation characteristics in the aft region alter the axial pressure gradient as the angle of attack increases to 20 deg. With downstream evolution, the wall-flow turning angle becomes more positive, an effect also predicted by the models though the peak-to-peak variation is less than that measured. Azimuthal skin friction variations show the same general trend as the measurements, with a weak minima identifying separation. Corrections for streamline curvature improve prediction of the pressure coefficient in the separated region on the leeward side of the spheroid. While initiated further along the spheroid compared to experimental measurements, predictions of primary and secondary separation agree reasonably well with measured values. Calculations without an explicit turbulence model predict pressure and skin-friction distributions in substantial disagreement with measurements. [DOI: 10.1115/1.1517571]

1 Introduction

Flow separation in three-dimensional configurations constitutes one of the more interesting topics of fluid dynamics research. Boundary layer detachment is almost always accompanied by undesirable effects such as loss of lift, increases in drag, amplification of unsteady effects including fluctuations in the pressure field. Prediction of three-dimensional separation and the features with which it is associated is difficult, forming one of the main obstacles to more widespread use of computational fluid dynamics (CFD) in analysis and design. It is predicting the three-dimensional separated flows over maneuvering bodies that forms the over-arching interest of the present investigations. The particular focus of this contribution is on the flow field that develops around a prolate spheroid at a fixed angle of attack.

Three-dimensional separations strongly challenges analysis and models. Work on two-dimensional separations, by comparison, is more developed and has provided detailed descriptions of the conditions influencing many separated flows, e.g., the effects of adverse pressure gradient and flow reversal. In three-dimensional flows, separation characteristics can be sensitive to the body geometry and angle of attack and Reynolds number, among other factors. Flow reversal and vanishing of the shear stress are two well-known effects that may not accompany three-dimensional separations.

In addition to the complex topology of the flow patterns, three-dimensional separated flows are difficult to predict using numerical simulation and modeling. In this work, computations are used to predict the flow around a 6:1 prolate spheroid at angle of attack. Recent calculations of the flow over a prolate spheroid include the Reynolds-averaged calculations of Tsai and Whitney [1] and Rhee and Hino [2] and large-eddy simulations (LES) of Alin et al. [3] and Hedin et al. [4]. Reynolds-averaged methods (RANS) possess the advantage of being computationally efficient, though application of RANS models to flows with massive separation appears beyond the reach of conventional RANS closures [5]. LES is a powerful approach since it resolves, rather than models, the large energy-containing scales of motion that are responsible for the bulk of momentum transport. Application to high Reynolds number flows requires additional empiricism in treatment of the wall layer, an active and unresolved area of current research.

Detached-eddy simulation (DES) is a hybrid approach which attempts to capitalize on the often adequate performance of RANS models in predicting boundary layer growth and separation, and to use LES away from solid surfaces to model the typically geometry-dependent and unsteady scales of motion in separated regions [5,6]. DES is well suited for prediction of massively separated flows and applications of the technique to a range of configurations have been favorable, [7–10]. In massively separated flows, turbulence structure in the wake develops rapidly through amplification of instabilities that overwhelm whatever structural content (or lack of) is transported from upstream in the boundary layers. The lack of eddy content in the attached boundary layers that are treated using a RANS closure has not resulted in substantial errors in predicting flows experiencing massive separation.

The flow over a prolate spheroid is a difficult test for DES because it is not massively separated, i.e., characterized by a region of chaotic, recirculating fluctuations, etc. The advantage of DES in providing more realistic descriptions of three-dimensional and unsteady motions in the wake of a massively separated flow is less clear cut in the spheroid since the structures in the separated region may not possess any region of reversed flow, for example. In addition, experiments show that an important element of the structure on the lee side of the spheroid are coherent streamwise vortices, structures that are relatively stable compared to the eddies that dominate the wakes of cylinder, spheres, or the region behind an airfoil at high angle of attack.

The main goal of this study is to apply DES to prediction of the

Contributed by the Fluids Engineering Division for publication in the JOURNAL OF FLUIDS ENGINEERING. Manuscript received by the Fluids Engineering Division March 25, 2002; revised manuscript received July 26, 2002. Associate Editor: G. E. Karniadakis.

flow around a prolate spheroid. The computations are assessed not only via comparison to the experimental measurements of Chesnakas and Simpson [11] and Wetzel et al. [12], but also using RANS predictions and solution of the flowfield without any explicit turbulence model. The standard Spalart-Allmaras model [13] (referred to as S-A throughout) forms the backbone for the RANS solutions in this study (as well as comprising the base model in DES). Enhancements to the RANS model are investigated, specifically corrections for streamline curvature [14] and the use of a nonlinear constitutive relation [5]. The interest is to gauge the level of improvement possible in RANS when an existing model for which there is a substantial experience base is augmented in an attempt to account for particular effects. In the longer term, such enhancements could be easily incorporated into a DES formulation.

Presented in the next section is an overview of the numerical approach. The Spalart-Allmaras one-equation model is summarized along with the modification require to obtain the DES formulation. Details of the numerical method, grids, etc., are then summarized. Evaluation of the flowfield predictions is then presented and, following, a summary of the study.

2 Overview and Approach

2.1 Spalart-Allmaras (S-A) Model. In the S-A RANS model, a transport equation is used to compute a working variable used to form the turbulent eddy viscosity,

$$\frac{D\tilde{\nu}}{Dt} = c_{b1}[1-f_{t2}]\tilde{S}\tilde{\nu} - \left[c_{w1}f_w - \frac{c_{b1}}{\kappa^2}f_{t2}\right]\left[\frac{\tilde{\nu}}{d}\right]^2 + \frac{1}{\sigma}[\nabla\cdot((\nu + \tilde{\nu})\nabla\tilde{\nu}) + c_{b2}(\nabla\tilde{\nu})^2] + f_{t1}\Delta U^2, \quad (1)$$

where $\tilde{\nu}$ is the working variable. The eddy viscosity ν_t is obtained from

$$\nu_t = \tilde{\nu}f_{v1}, \quad f_{v1} = \frac{\chi^3}{\chi^3 + c_{v1}^3}, \quad \chi \equiv \frac{\tilde{\nu}}{\nu}, \quad (2)$$

where ν is the molecular viscosity. The production term is expressed as

$$\tilde{S} \equiv S + \frac{\tilde{\nu}}{\kappa^2 d^2}f_{v2}, \quad f_{v2} = 1 - \frac{\chi}{1+\chi f_{v1}}, \quad (3)$$

where S is the magnitude of the vorticity. The function f_w is given by

$$f_w = g\left[\frac{1+c_{w3}^6}{g^6+c_{w3}^6}\right]^{1/6}, \quad g = r + c_{w2}(r^6 - r), \quad r \equiv \frac{\tilde{\nu}}{\tilde{S}\kappa^2 d^2}. \quad (4)$$

The function f_{t2} is defined as

$$f_{t2} = c_{t3}\exp(-c_{t4}\chi^2). \quad (5)$$

The trip function f_{t1} is specified in terms of the distance d_t from the field point to the trip, the wall vorticity ω_t at the trip, and ΔU which is the difference between the velocity at the field point and that at the trip

$$f_{t1} = c_{t1}g_t\exp\left(-c_{t2}\frac{\omega_t^2}{\Delta U^2}[d^2 + g_t^2 d_t^2]\right), \quad (6)$$

where $g_t = \min(0.1, \Delta U/\omega_t\Delta x)$ and Δx is the grid spacing along the wall at the trip. The wall boundary condition is $\tilde{\nu} = 0$ and the constants are $c_{b1} = 0.1355$, $\sigma = 2/3$, $c_{b2} = 0.622$, $\kappa = 0.41$, $c_{w1} = c_{b1}/\kappa^2 + (1+c_{b2})/\sigma$, $c_{w2} = 0.3$, $c_{w3} = 2$, $c_{v1} = 7.1$, $c_{v2} = 5$, $c_{t1} = 1$, $c_{t2} = 2$, $c_{t3} = 1.1$, and $c_{t4} = 2$.

2.2 Detached-Eddy Simulation (DES). The DES formulation is based on a modification to the Spalart-Allmaras RANS model [13] such that the model reduces to its RANS formulation near solid surfaces and to a subgrid model away from the wall [5]. The basis is to attempt to take advantage of the usually adequate performance of RANS models in the thin shear layers where these models are calibrated and the power of LES for resolution of geometry-dependent and three-dimensional eddies. The DES formulation is obtained by replacing in the S-A model the distance to the nearest wall, d, by $\tilde{d}$, where $\tilde{d}$ is defined as

$$\tilde{d} \equiv \min(d, C_{\mathrm{DES}}\Delta), \quad (7)$$

with

$$\Delta \equiv \max(\Delta x, \Delta y, \Delta z) \quad (8)$$

where Δx, Δy, and Δz are the grid spacings. In ''natural'' applications of DES, the wall-parallel grid spacings (e.g., streamwise and spanwise) are at least on the order of the boundary layer thickness and the S-A RANS model is retained throughout the boundary layer, i.e., $\tilde{d} = d$. Consequently, prediction of boundary layer separation is determined in the ''RANS mode'' of DES. Away from solid boundaries, the closure is a one-equation model for the SGS eddy viscosity. When the production and destruction terms of the model are balanced, the length scale $\tilde{d} = C_{\mathrm{DES}}\Delta$ in the LES region yields a Smagorinsky-like eddy viscosity $\tilde{\nu} \propto S\Delta^2$. Analogous to classical LES, the role of Δ is to allow the energy cascade down to the grid size; roughly, it makes the pseudo-Kolmogorov length scale, based on the eddy viscosity, proportional to the grid spacing. The additional model constant $C_{\mathrm{DES}} = 0.65$ was set in homogeneous turbulence [7] and used without modification in this work.

2.3 Numerical Approach. Turbulent flow around the spheroid has been calculated using numerical solution of both the incompressible and compressible Navier-Stokes equations. The incompressible flow is computed using a fractional step method in which the governing equations are transformed to generalized curvilinear coordinates with the primitive velocities and pressure retained as the dependent variables. The method has previously been applied to computation of unsteady turbulent flow using DES by Constantinescu et al. [9] and is briefly summarized. Within a physical time-step, the momentum and turbulence model equations are integrated in pseudo-time using a fully implicit algorithm. In the first step of the fractional step method, an intermediate velocity field is obtained by advancing the convection and diffusion terms using an alternate direction implicit (ADI) approximate factorization scheme. The intermediate field is obtained using the current pressure field and does not satisfy the continuity constraint. A Poisson equation is then solved for the pressure and the resulting solution is used to update the intermediate velocities so that continuity is satisfied. Advancement in pseudo-time is continued until a converged solution of the equations is obtained. The convergence criterion at each physical time-step was that the maximum value of the dimensionless velocity and pressure residuals be smaller than 10^{-4}. Local time-stepping techniques are used to accelerate the convergence of the resulting system of equations. Source terms in the turbulence-model equations are also treated implicitly. The extension of the method to time-accurate calculations using double-time-stepping is reasonably straightforward, as modifications are required only in the right-hand side of the momentum and turbulence model transport equations that now contain a physical time derivative. The time derivative is discretized using a second-order accurate backward difference approximation. As shown by Arnone et al. [15], the pseudo-time-step should be smaller than the physical time-step to maintain numerical stability. A more detailed discussion of the implementation is presented in Johnson and Patel [16]. The numerical method is fully implicit with the momentum and turbulence transport equations discretized using fifth-order accurate upwind differences for the convective terms. All other operators are calculated using second-order central differences. The overall discretization scheme is second-order accurate in space, including at the boundaries.

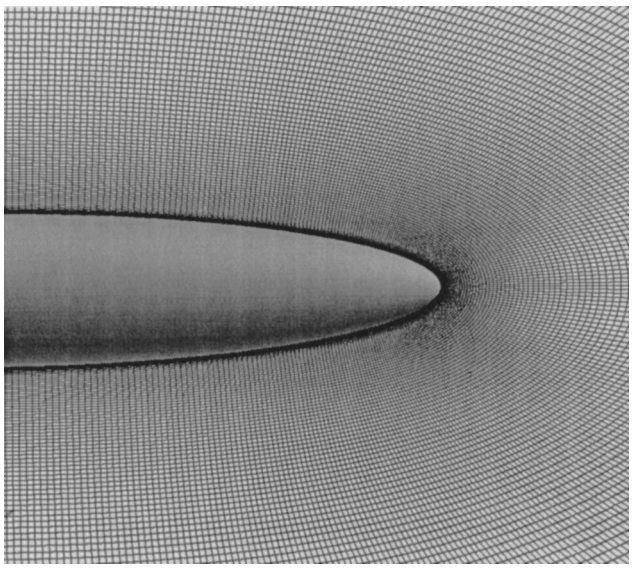

Fig. 1 Side view of the computational domain, showing increase in mesh density towards aft region. Flow is from left to right at angle of attack. Grids are uniformly spaced in the azimuthal direction (out of the plane of the figure).

One of the overall goals of the present research effort is development of accurate predictive methods for three-dimensional separated flows over maneuvering geometries. To this end, a compressible Navier-Stokes solver—Cobalt—capable of computing the flow around geometries undergoing rigid-body motion has been used to predict the static-geometry flow over the spheroid. The numerical method is a cell-centered finite volume approach applicable to arbitrary cell topologies (e.g, hexahedrals, prisms, tetrahdrons). The spatial operator uses the exact Reimann solver of Gottlieb and Groth [17], least-squares gradient calculations using QR factorization to provide second-order accuracy in space, and TVD flux limiters to limit extremes at cell faces. A point implicit method using analytic first-order inviscid and viscous Jacobians is used for advancement of the discretized system. For time-accurate computations, a Newton subiteration scheme is employed, the method is second order accurate in time. The domain decomposition library ParMETIS [18] is used for parallel implementation and provides optimal load balancing with a minimal surface interface between zones. Communication between processors is achieved using message passing interface (MPI), with parallel efficiencies above 95% on as many as 1024 processors [19]. Calculations to date show that averaged quantities (e.g., azimuthal pressure distributions) obtained around the spheroid using the compressible flow solver Cobalt and those obtained with the incompressible flow code used by Constantinescu et al. [9] are similar. In the results that follow in Section 3, the computations performed without an explicit turbulence model were performed using Cobalt. Other predictions shown in Section 3 were obtained using the incompressible flow solver employed by Constantinescu et al. [9].

Structured grids for the spheroid were generated using the control technique of Hsu and Lee [20]. Using this approach it is possible to control grid density and enable a reasonably efficient distribution of points in the leeward region. The grids are single block, calculations were carried out on a series of meshes ranging in grid sizes from 100 to 125 points along the body, 75 to 150 points in the azimuth, and 125 to 140 points normal to the spheroid. A view of the mesh illustrating the density of points in the aft region of the spheroid is shown in Fig. 1. The computations are of the complete geometry, i.e., no symmetry conditions are imposed. For time-dependent solution via DES, it is essential to consider the entire geometry, without resorting to imposition of symmetry conditions. Steady-state RANS could be applied to a half-geometry configuration, though for the time-accurate RANS performed in the present calculations, the simulations also considered the flow over the entire geometry.

The outer boundary shape of the computational domain was elliptic, extending 12 minor axes in front of the spheroid and 15 minor axes in the downstream direction. The first wall-normal grid point was within one viscous unit of the surface. In the cross-stream direction the outer boundary of the domain was eight minor axes from the spheroid surface. The grid distribution in the azimuthal direction was uniform, which is a drawback of the present approach in that it is not optimal for the flow structures that develop in the leeward region. An effect not considered in the present simulations is the confining influence of the wind-tunnel walls. In the experimental facility used to acquire the measurements [11,12] the ratio of the minor axis dimension of the spheroid to the hydraulic radius of the tunnel is about 1/5. At the outer boundaries of the computational domain in the present contribution the conditions are freestream, i.e., either inflow or outflow. Any influence of the tunnel, e.g., on the pressure distribution experienced by the spheroid and its separation pattern would obviously not be accounted for in the simulations. The reader is referred to the work Hedin [4] as an example in which the flow about the spheroid was computed in a domain with the same hydraulic radius as the facility used for the experiments. As described in greater detail below, the present investigations enable comparison of predictions obtained using various turbulence models, an assessment against the experimental measurements is also useful, though a degree of ambiguity is introduced into the comparisons by not including the tunnel walls. Finally, the range of mesh resolutions used in the current work are comparable to or larger than those applied by previous investigators in computing the spheroid. Over the range of resolutions considered the quantities presented in Section 3 did not exhibit strong sensitivity to the grid.

The inflow eddy viscosity was set to zero, with the trip terms active on the surface of the spheroid at $x/L=0.2$. It should be noted that, while the results presented in this manuscript used the trip term to cause laminar-to-turbulent transition, preliminary calculations of the fully turbulent flow, i.e., with turbulent boundary layers initiated from the nose of the spheroid did not yield appreciable changes in azimuthal distributions of the skin friction or pressure coefficient at the downstream stations for which most of the measurements are available, $x/L=0.6$ and $x/L=0.77$. For the incompressible flow, the velocity components and turbulent viscosity at the downstream boundary are obtained using second-order extrapolation from the interior of the domain. Far-field boundary values for solution of the compressible equation are obtained from the Riemann invariants. No-slip conditions on the spheroid surface are imposed. The pressure boundary condition on the spheroid and at the upstream and downstream boundaries in the incompressible solution are obtained from the surface-normal momentum equation. On the polar axes, ($\theta=0,\pi$), the dependent variables are obtained by averaging over the azimuth a second-order accurate extrapolation of these variables in the incompressible flow. Periodic boundary conditions are imposed on all variables in the azimuthal direction. A timestep study showed no significant influence on the computed solutions using a timestep of 0.01 (made dimensionless using the minor axis of the spheroid and freestream velocity).

3 Results

At low incidence angles, viscous effects around a prolate spheroid are confined to thin three-dimensional boundary layers attached to the geometry. As the angle of attack is increased, an attached three-dimensional boundary layer characterizes the state of the flow on the windward side. The adverse pressure gradient along the azimuthal coordinate leads to flow detachment and the rollup of coherent longitudinal vortices that strongly influence the

Fig. 2 Surface flows from DES prediction at 20 deg angle of attack. Flow is tripped at $x/L=0.2$.

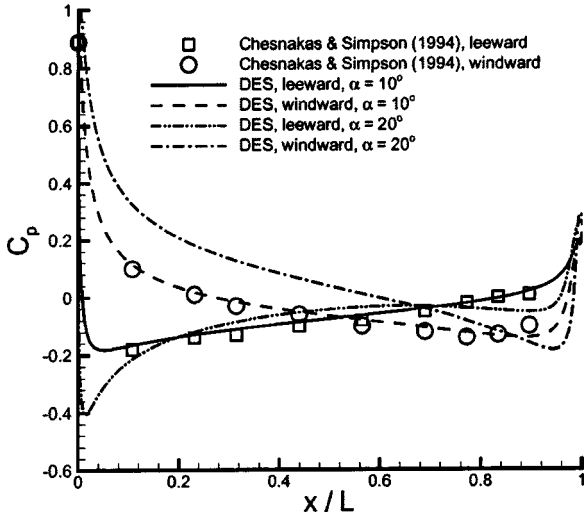

Fig. 3 Axial pressure distribution along windward and leeward surfaces for $\alpha=10$ deg and 20 deg, DES prediction. Profiles taken along the symmetry plane.

character of the flow in the leeward region. For continuing increases in the angle of attack, secondary separations are noted (e.g., see Fu et al. [21] and references therein). Some of these features can be deduced from the surface flow visualization shown in Fig. 2. The surface flows shown in the figure are of the averaged flowfield predicted using DES. At $x/L=0.2$, the surface flows are turned, corresponding to the position at which the turbulence model is activated using the trip terms in (1), also corresponding to the position in which trip posts are used in the experiments [11,12] to cause laminar-to-turbulent transition. Though not shown here, the effectiveness of the trip terms is very apparent in the skin friction distribution over the spheroid. On the windward side an attached three-dimensional boundary layer is formed over the spheroid. As the flow evolves downstream, boundary layer separation occurs on the lee side, corresponding to the convergence of the surface flows in Fig. 2. Wetzel et al. [12] observed that separation from the spheroid was well correlated to local minima in the skin friction, a similar feature found in the present investigations. Further downstream, the surface flow pattern in Fig. 2 diverges, corresponding to a reattaching region. The shed vorticity that rolls up into a pair of longitudinal structures induces a secondary separation that is predicted in the aft region shown in Fig. 2.

The pressure coefficient in the symmetry plane from DES predictions of the flow at 10 deg and 20 deg angle of attack are shown in Fig. 3. Measurements of the distribution at 10 deg angle of attack are available from Chesnakas and Simpson [11]. As can be observed in the figure, the agreement between simulation and experiment for $\alpha=10$ deg is mostly good, especially on the leeward side. Along the windward side in the aft region there is some discrepancy, one contributor could be the presence of the support sting used in the experiments and not included in the computations. Compared to the distribution at $\alpha=10$ deg, the profiles from the DES prediction at 20 deg angle of attack exhibit greater streamwise variation near the nose and tail. Along the windward side, the axial pressure gradient is more favorable than that predicted at 10 deg. For much of the axial coordinate in the leeward side, i.e., between about $x/L=0.2$ and $x/L=0.8$ the pressure gradient change with angle of attack is less significant.

Chesnakas and Simpson [11] measured boundary layer profiles along the spheroid at 10 deg angle of attack in a wall-collateral coordinate system with the wall-normal velocity measured along a radial coordinate, the streamwise component perpendicular to the wall-normal value and in the direction of the mean flow at the boundary layer edge, and the remaining coordinate defined to complete definition of a right-handed coordinate system. The mean velocity components from the DES prediction of the flow at 20 deg angle of attack are shown in Fig. 4. The profiles drawn are at an axial position $x/L=0.6$ and azimuthal angle of $\phi=90$ deg. In Fig. 4 and throughout the azimuthal angle ϕ is measured from the symmetry plane on the windward side of the spheroid. The plot has been made dimensionless using the local boundary layer thickness and freestream speed. Overall, the agreement with measurements is adequate. The near-wall flow is resolved, with sufficient resolution of the viscous region closest to the wall and capture of the logarithmic range from around $0.02<r/\delta<0.60$. The figure shows fair agreement in the y and z component velocities is fair.

The wall-flow turning angle, β_w, is shown in Fig. 5. The angle β_w measures the direction of the flow at the wall relative to the streamwise direction. Predictions using the standard S-A model are plotted along with results obtained using a nonlinear constitutive relation. The nonlinear model is that proposed by Spalart [6] in which the Reynolds stress from the linear model (S-A, in this case) is related to the nonlinear stress via

$$\tau_{ij}=\overline{\tau}_{ij}-c_{nl}[O_{ik}\overline{\tau}_{jk}+O_{jk}\overline{\tau}_{ik}], \tag{9}$$

where

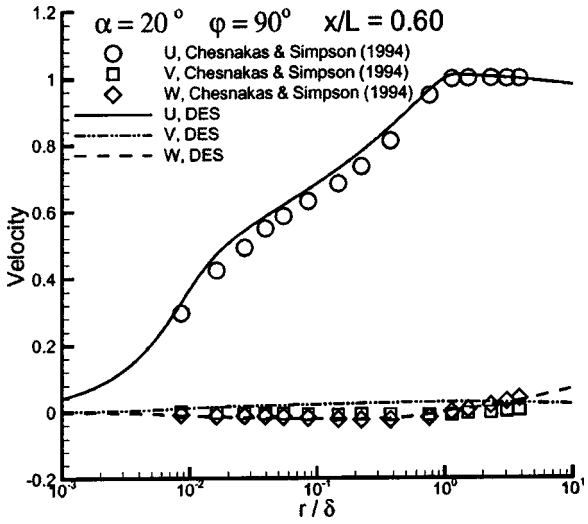

Fig. 4 Mean velocity profile for flow at $\alpha=20$ deg, DES prediction. Profile at $x/L=0.60$ and $\phi=90$ deg.

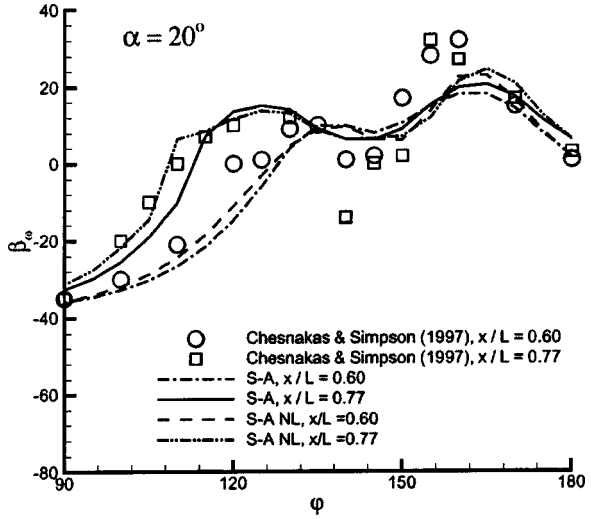

Fig. 5 Azimuthal distribution of wall-flow turning angle, freestream at $\alpha=20$ deg angle of attack, DES prediction

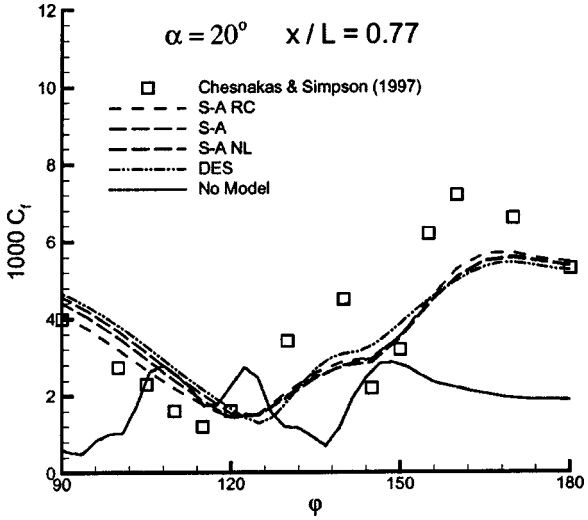

Fig. 6 Azimuthal distribution of skin friction coefficient at $x/L=0.77$, flow at 20 deg angle of attack

$$O_{ik}=\frac{\partial_k U_i-\partial_i U_k}{\sqrt{\partial_n U_m-\partial_m U_n}} \tag{10}$$

is the normalized rotation tensor. An advantage of the nonlinear model (9) is that it provides a better accounting of Reynolds-stress anisotropy, an influence that can create secondary flows of the second kind in a square duct [22]. The second term on the right-hand side of (9) represents one of many possible quadratic combinations of strain and vorticity. As also described in Spalart [5], the constant $c_{nl}=0.3$ was calibrated in the outer region of a simple boundary layer by requiring a fair level of anisotropy. Application of (9) to prediction of the fully developed flow in a square duct was positive, with secondary flows predicted and skin friction estimations closer to measurements [5] than those obtained using the linear model.

The solutions and measurements shown in Fig. 5 are for the flow at 20 deg angle attack and at axial positions $x/L=0.6$ and $x/L=0.77$. The calculations closing the stress using (9) are denoted "S-A NL" in the figure. Note also that the region plotted corresponds to $90\leqslant\phi\leqslant180$ deg. For $x/L=0.6$, there is not a significant difference in predictions of the turning angle for the two models. In general, there is a lag in the predicted turning compared to the measurements for ϕ less than about 135 deg. As the flow evolves downstream the wall-flow angle becomes more positive, together with a reduction in the skin friction coefficient. The strong variation in β_w measured in the vicinity of 150 deg coincides with the positions of the primary and secondary separations. Figure 5 shows the azimuthal variation is not as pronounced in the simulations, using either model. Some differences emerge in predictions obtained using the two models at $x/L=0.77$. The closure using the nonlinear constitutive relation (9) exhibits less lag compared to the experimental measurements as found using the standard S-A model. The shift toward lower ϕ in the minima in β_w at $x/L=0.77$ compared to $x/L=0.6$ seems consistent with the measurements, though Fig. 5 shows greater scatter in β_w measurements at $x/L=0.77$.

Skin friction and pressure coefficients are shown in Fig. 6 and Fig. 7, respectively, for $\alpha=20$ deg and at an axial position $x/L=0.77$. For this angle of attack and streamwise station measurements show the existence of both a primary and secondary separation on the spheroid. In addition to S-A results using the standard (linear) model, the nonlinear relation (9), and DES, RANS predictions obtained using the S-A model with an explicit correction for rotation/curvature effects [14] are included (labeled S-A RC in the figures). The correction outlined by Spalart and Shur [14] respects Galilean invariance, is fully defined in three dimensions, and unifies rotation and curvature effects. The correction reduces the eddy viscosity in regions where streamline curvature is a stabilizing influence, raising ν_t in regions where streamline curvature is destabilizing. In addition to these model predictions, also shown in Fig. 6 and Fig. 7 are results from computations performed without any explicit turbulence model. The concept of "coarse-grid DNS" or LES without an explicit subgrid-scale model has been advocated and employed in previous investigations of various flows (e.g., see Tamura et al. [23] and Boris et al. [24]). The approach is based on use of the dissipation inherent in an upwind flux-limited or flux-corrected transport scheme to act "automatically" as a natural spatial filter for wavelengths in the solutions with scales comparable to the mesh size. These approaches are often denoted MILES (monotone integrated large-eddy simulation), although results obtained in the present work are simply referred to as "no-model" in the following. Detailed investigations have not been undertaken using the current computational approach in evaluating the numerical dissipation and its

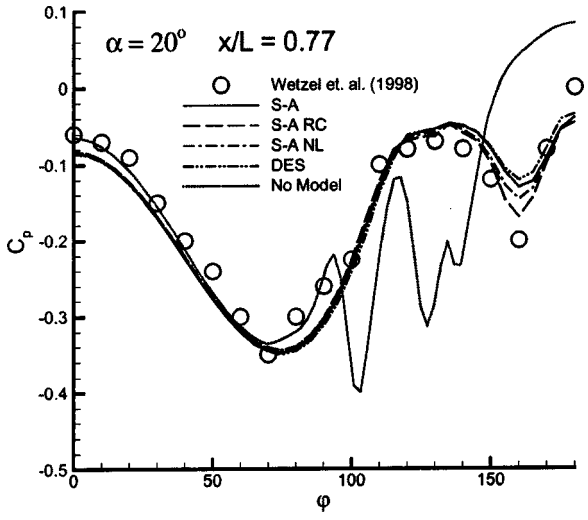

Fig. 7 Azimuthal distribution of the pressure coefficient at $x/L=0.77$, flow at $\alpha=20$ deg angle of attack. Experimental measurements summarized in Wetzel et al. [12].

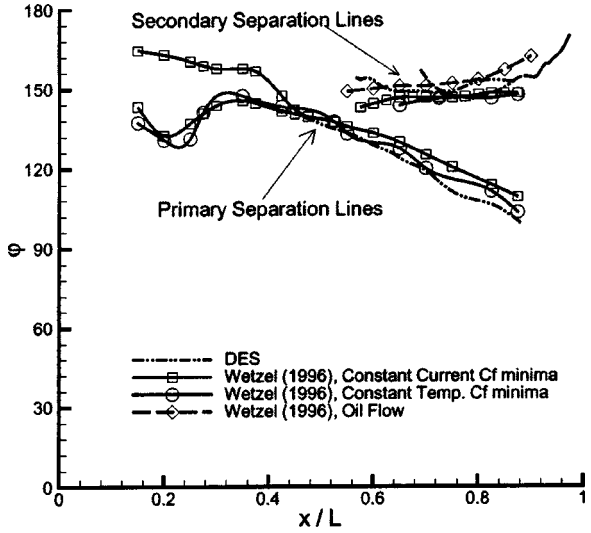

Fig. 8 Primary and secondary separation line predictions from DES compared to various indicators from experiments, $\alpha = 20$ deg

role as a subgrid model. The reader is referred to Fureby and Grinstein [25] for a more detailed discussion of the MILES approach.

With the exception of the no-model result, the general trend of all the skin friction predictions in Fig. 6 is similar, following the data, but less peak-to-peak variation. The minima in C_f near $\phi \approx 150$ deg, for example, is one approach used to identify the separation location. The C_f distributions from all of the simulations show an inflection point in that vicinity, but without a clear secondary minima, indicative of a weaker shed structure in the calculations as compared to the experiments. Based on the skin friction, there is relatively little basis to distinguish the various models in terms of accuracy considerations, though the DES result shows a slightly lower global minimum around $\phi \approx 125$ deg and perhaps greater peak-to-peak variation compared to the RANS model results. The no-model predition of the skin friction agree very poorly with measurements, providing an illustration of the importance of an accurate turbulence treatment in the boundary layer. On the windward side at $\phi = 0$, the skin friction prediction in the no-model result is low, consistent with the fact that for the Reynolds number under consideration, it is not feasible to directly resolve boundary layer turbulence and predictions without an explicit turbulence model yield an effectively laminar boundary layer. Another substantial error source is that the no-model predictions separate substantially earlier than in calculations performed with an explicit turbulence model.

The skin friction and pressure distributions show somewhat analogous features, though skin friction minima more accurately identify flow separation ([13]). In Fig. 6 the pressure coefficient distribution shows that the signature of the shed structures via the second minima in C_p is weaker in the calculations as compared to the experiments. The S-A calculation including the rotation/curvature correction is closest to the experimental measurement of the second minima, slightly superior to the DES result. Analogous to the skin friction, the no-model result for the pressure distribution differs substantially from both the experimental measurements and calculations performed using an explicit turbulence model.

The DES prediction of the primary and secondary separation lines is compared to measured values for $\alpha = 20$ deg in Fig. 8. Various experimental techniques have been employed to deduce separation locations. The figure shows some discrepancy in the position of the separation line prior to $x/L \approx 0.3$, but with generally good agreement among the different techniques in determination of the separation line further along the body. In general, the DES predictions of the onset of both the primary and secondary separations is delayed relative to that from the experiments, e.g., the primary separation is initiated slightly downstream of $x/L \approx = 0.4$. Considering the difficulty in unambiguously identifying the onset of separation in three-dimensional flows, the agreement in the separation lines from DES and experiments seems mostly adequate.

4 Summary

The three-dimensional separated flow over a prolate spheroid has been predicted using RANS and DES. Simulation results were compared both to experimental measurements as well as to calculations in which an explicit turbulence model was not included. Variations of the Spalart-Allmaras one-equation model were employed in the RANS. A nonlinear constitutive relation was applied and shows some differences in prediction of quantities such as the wall flow turning angle. Prediction of the azimuthal variations of the skin friction and pressure coefficient using the nonlinear model showed relatively small differences compared to the standard S-A model. A slightly stronger effect on the pressure variation was observed in calculations that incorporated the rotation/curvature correction to S-A [14]. While improving prediction of the signature of the longitudinal vortex on the mean pressure on the surface, it is noteworthy that in other regions the effect of the rotation/curvature correction did not interfere with already adequate predictions. In general, for the angles of attack considered, grid resolutions, and across two Navier-Stokes solvers, there are not significant differences in predictions of the mean quantities obtained using RANS and DES.

In interpreting DES predictions it should be noted that three-dimensional separated flows over the spheroid at low angles of attack are not characterized by overwhelming new instabilities as the boundary layer detaches from the surface. These and similar flows (or regions of a flow) comprise ''gray area'' applications for hybrid methods such as DES in which turbulent eddies may not rapidly develop following boundary layer detachment. The Reynolds-averaged treatment suppresses substantial eddy content near solid surfaces and the lack of structural features in the detaching boundary layers may contribute to more substantial errors in spheroid predictions as compared to other separated flows, especially those experiencing massive separation. Noteworthy is that the most significant unsteadiness occurred in the simulations performed without an explicit turbulence model, with variations on the order of 15% in the lift. As shown, however, boundary layer treatment without an explicit model can yield very poor predictions of skin friction, inaccurate separation prediction, and consequently poor predictions of forces and moments. The degree to which DES predictions can be altered by incorporating effects such as corrections for streamline curvature, for example, as well substantial refinement of the mesh in the LES region constitute important areas of future work.

Acknowledgments

The authors gratefully acknowledge the support of the Office of Naval Research (Grant Numbers N00014-96-1-1251, N00014-97-1-0238, and N00014-99-1-0922, Program Officers: Dr. L. P. Purtell and Dr. C. Wark). The authors are also grateful for the insight and many useful comments from Dr. P. R. Spalart.

References

[1] Tsai, C.-Y., and Whitney, A. K., 1999, ''Numerical Study of Three-Dimensional Flow Separation for a 6:1 Ellipsoid,'' AIAA Paper No. 99-0172.
[2] Rhee, S. H., and Hino, T., 2000, ''Computational Investigation of 3D Turbulent Flow Separation Around a Spheroid Using an Unstructured Grid Method,'' J. Soc. Nav. Arch. Jpn., **188**, pp. 1–9.
[3] Alin, N., Berglund, M., and Fureby, C., 2000, ''A VLES Approach Applied to Flows Around Underwater Vehicle Hulls,'' AIAA Paper No. 00-0543.
[4] Hedin, P.-O., Berglund, M., Alin, N., and Fureby, C., 2001, ''Large Eddy

Simulation of the Flow Around an Inclined Prolate Spheroid,'' AIAA Paper No. 2001-1035.
[5] Spalart, P. R., 2000, ''Strategies for Turbulence Modeling and Simulations,'' International Journal of Heat and Fluid Flow, **21**, pp. 252–263.
[6] Spalart, P. R., Jou, W. H., Strelets, M., and Allmaras, S. R., 1997, ''Comments on the Feasibility of LES for Wings, and on a Hybrid RANS/LES Approach,'' First AFOSR International Conference on DNS/LES, Ruston, LA.
[7] Shur, M., Spalart, P. R., Strelets, M., and Travin, A., 1999, ''Detached-Eddy Simulation of an Airfoil at High Angle of Attack,'' 4th Int. Symp. Eng. Turb. Modelling and Measurements, Corsica, May 24–26.
[8] Travin, A., Shur, M., Strelets, M., and Spalart, P. R., 2000, ''Detached-Eddy Simulations Past a Circular Cylinder,'' Flow, Turbul. Combust., **63**, pp. 293–313.
[9] Constantinescu, G. S., and Squires, K. D., 2000, ''LES and DES Investigations of Turbulent Flow Over a Sphere,'' AIAA Paper No. 2000–0540.
[10] Strelets, M., 2001, ''Detached Eddy Simulation of Massively Separated Flows,'' AIAA Paper No. 01-0879.
[11] Chesnakas, C. J., and Simpson, R. L., 1997, ''Detailed Investigation of the Three-Dimensional Separation About a 6:1 Prolate Spheroid,'' AIAA J., **35**(6), pp. 990–999.
[12] Wetzel, T. G., Simpson, R. L., and Chesnakas, C. J., 1998, ''Measurement of Three-Dimensional Crossflow Separation,'' AIAA J., **36**(4), pp. 557–564.
[13] Spalart, P. R., and Allmaras, S. R., 1994, ''A One-Equation Turbulence Model for Aerodynamic Flows,'' Rech. Aerosp., **1**, pp. 5–21.
[14] Spalart, P. R., and Shur, M., 1997, ''On the Sensitization of Simple Turbulence Models to Rotation and Curvature,'' Aerosp. Sci. Technol., **1**(5), pp. 297–302.
[15] Arnone, A., Liou, M. S., and Povinelli, L. A., 1995, ''Integration of the Navier-Stokes Equations Using Dual Time Stepping and a Multigrid Method,'' AIAA J., **33**(6), pp. 985–990.
[16] Johnson, T. A., and Patel, V. C., 1999, ''Flow Past a Sphere up to a Reynolds Number of 300,'' J. Fluid Mech., **378**(1), pp. 19–70.
[17] Gottlieb, J. J., and Groth, C. P. T., 1988, ''Assessment of Riemann Solvers for Unsteady One-Dimensional Inviscid Flows of Perfect Gases,'' J. Comput. Phys., **78**, pp. 437–458.
[18] Karypis, G., Schloegel, K., and Kumar, V., 1997, ''ParMETIS: Parallel Graph Partitioning and Sparse Matrix Ordering Library Version 1.0,'' Department of Computer Science, University of Minnesota, Minneapolis, MN.
[19] Grismer, M. J., Strang, W. Z., Tomaro, R. F., and Witzemman, F. C., 1998, ''Cobalt: A Parallel, Implicit, Unstructured Euler/Navier-Stokes Solver,'' Adv. Eng. Software, **29**, pp. 365–373.
[20] Hsu, K., and Lee, S. L., 1991, ''A Numerical Technique for Two-Dimensional Grid Generation With Grid Control at all of the Boundaries,'' J. Comput. Phys., **11**, pp. 451–469.
[21] Fu, T. C., Shekarriz, A., Katz, J., and Huang, T. T., ''The Flow Structure in the Lee of an Inclined 6: Prolate Spheroid,'' J. Fluid Mech., **269**, pp. 79–106.
[22] Speziale, C. G., 1987, ''On the Non-linear K-l and K-ε Models of Turbulence,'' J. Fluid Mech., **178**, p. 459.
[23] Tamura, T., and Kuwahara, K., 1990, ''On the Reliability of Two-Dimensional Simulation for Unsteady Flows Around Cylinder-Type Structure,'' J. Wind. Eng. Ind. Aerodyn., **35**, pp. 275–298.
[24] Boris, J. P., Grinstein, F. F., Oran, E. S., and Kolbe, R. L., 1992, ''New Insights into Large Eddy Simulation,'' Fluid Dyn. Res., **10**, pp. 199–228.
[25] Fureby, C., and Grinstein, F. F., 1999, ''Monotonically Integrated Large Eddy Simulation of Free Shear Flows,'' AIAA J., **37**, pp. 544–556.

Detached-Eddy Simulation With Compressibility Corrections Applied to a Supersonic Axisymmetric Base Flow

James R. Forsythe
Associate Professor,
Department of Aeronautics,
United States Air Force Academy,
USAF Academy, CO 80840

Klaus A. Hoffmann
Professor
Department of Aerospace Engineering,
Wichita State University,
Wichita, KS 67260

Russell M. Cummings
Professor,
Department of Aerospace Engineering,
California Polytechnic State University,
San Luis Obispo, CA 93407

Kyle D. Squires
Professor,
Department of Mechanical Engineering,
Arizona State University,
Tempe, AZ 85287

Detached-eddy simulation is applied to an axisymmetric base flow at supersonic conditions. Detached-eddy simulation is a hybrid approach to modeling turbulence that combines the best features of the Reynolds-averaged Navier-Stokes and large-eddy simulation approaches. In the Reynolds-averaged mode, the model is currently based on either the Spalart-Allmaras turbulence model or Menter's shear stress transport model; in the large-eddy simulation mode, it is based on the Smagorinski subgrid scale model. The intended application of detached-eddy simulation is the treatment of massively separated, high-Reynolds number flows over complex configurations (entire aircraft, automobiles, etc.). Because of the intented future application of the methods to complex configurations, Cobalt, an unstructured grid Navier-Stokes solver, is used. The current work incorporates compressible shear layer corrections in both the Spalart-Allmaras and shear stress transport-based detached-eddy simulation models. The effect of these corrections on both detached-eddy simulation and Reynolds-averaged Navier-Stokes models is examined, and comparisons are made to the experiments of Herrin and Dutton. Solutions are obtained on several grids—both structured and unstructured—to test the sensitivity of the models and code to grid refinement and grid type. The results show that predictions of base flows using detached-eddy simulation compare very well with available experimental data, including turbulence quantities in the wake of the axisymmetric body.
[DOI: 10.1115/1.1517572]

1 Introduction

As airplanes, missiles, and launch vehicles require greater performance in ever-expanding flight regimes, the methods and procedures used for their design must be re-evaluated. The theories and capabilities that were state of the art only a handful of years ago may not adequately address the design requirements of current and future flight vehicles. All aerodynamic predictive methods have as their primary goal the prediction of lift and drag. Specifically, a major constraint on the performance of flight vehicles is the total configuration drag. A supersonic body experiences major drag contributions from skin friction drag, wave drag, and pressure drag (especially in the form of base drag). Obtaining valid predictions for these drag components, and thus having valid tools for design purposes, is difficult at best. Specifically, the prediction of base drag in an accurate manner has long eluded the practicing engineer. Depending on the vehicle's base geometry and flight conditions, the prediction of base drag can range from mildly irritating to incredibly difficult, yet the importance of base drag mandates that the engineer be able to make a credible prediction. Experimental and semi-empirical approaches to predicting base flow have been attempted for the past 50 years, with varying degrees of success. In the past 20 years, various numerical approaches have been used to solve the base flow problem, but the necessity for predicting turbulence in the base region has limited the quality of the predictions, [1,2].

There are various techniques for the numerical prediction of turbulent flows. These range from Reynolds-averaged Navier-Stokes (RANS), to large-eddy simulation (LES), to direct numerical simulation (DNS). DNS attempts to resolve all scales of turbulence, from the largest to the smallest. Because of this, the grid resolution requirements are very high, and increase drastically with Reynolds number. LES attempts to model the smaller, more homogeneous scales, while resolving the larger, energy containing scales, which makes the grid requirements for LES significantly less than for DNS. To accurately resolve the boundary layer, however, LES must accurately resolve the energy-containing eddies in the boundary layer, which requires very small streamwise and spanwise grid spacing. Finally, the RANS approach attempts to solve the time-averaged flow, which means that all scales of turbulence must be modeled. RANS models often fail to provide accurate results for these flows since the large turbulence scales for separated flows are very dependent on the geometry. RANS models, however, can provide accurate results for attached boundary layer flows and thin shear layers. Spalart [3] provides a discussion and comparison of these various techniques.

These various techniques have very different computational requirements. Spalart et al. [4] estimated that the LES computation over an entire aircraft would not be possible for over 45 years. Their estimate led to the formulation of detached-eddy simulation (DES), which combines the advantages of LES and RANS into one model. RANS is used in the boundary layer, where it performs well (and with much lower grid requirements than LES), and LES is then used in the separated regions where its ability to predict turbulence length scales is important. Shur et al. [5] calibrated the model for isotropic turbulence, and applied it to a NACA 0012 airfoil section; the model agreed well with lift and drag predictions to 90 deg angle of attack. Consantinescu and Squires [6] applied detached-eddy simulation to the turbulent flow over a sphere at several Reynolds numbers. Issues of grid resolution, numerical accuracy, and values of the model constant were examined, and the model was compared to predictions using LES and RANS models. Travin et al. [7] applied DES to a circular cylinder at sub and supercritical Reynolds numbers, and obtained

Contributed by the Fluids Engineering Division for publication in the JOURNAL OF FLUIDS ENGINEERING. Manuscript received by the Fluids Engineering Division, March 20, 2002; revised manuscript received July 2, 2002. Associate Editor: F. F. Grinstein.

a grid-converged solution that agreed well with experiments. Strelets [8] presented numerous cases using DES: a cylinder, airfoil, backstep, triangle in a channel, raised runway section, and a landing gear. Although some cases showed very little improvement over RANS, none performed worse than RANS, and many performed far better. Forsythe et al. [1] performed DES on the supersonic axisymmetric base flow of Herrin and Dutton [9] using an unstructured solver; good solutions were obtained only by reducing the DES constant. This article is an attempt to improve upon these preliminary results by using a larger selection of grids to further examine the sensitivity of the model to grid refinement. Menter's shear stress transport-based DES is used for the first time on this flow, and both RANS and DES models are run with and without compressibility corrections.

2 Base Flow Description

Base flows are an important form of separation found in supersonic flowfields. This kind of flow is commonly found behind such objects as missiles, rockets, and projectiles. The low pressure found behind the base causes base drag which can be a sizable portion of the total drag. To make computational fluid dynamics useful as a design tool, it is important to be able to predict the base pressure accurately.

An axisymmetric base flow depicted with pressure contours and streamlines is shown in Fig. 1. The large turning angle behind the base causes separation and the formation of a region of reverse flow (known as the recirculation region or the separation bubble). The size of the recirculation region determines the turning angle of the flow coming off the back of the base, and therefore the strength of the expansion waves. A smaller recirculation region causes the flow to turn sharply, leading to a stronger expansion wave, and lower pressures behind the base. Therefore, small separated regions cause larger base drag than large regions.

Directly behind the base, in the recirculation region, the reverse flow can be seen. The point along the axis of symmetry where the streamwise velocity is zero is considered to be the shear layer reattachment point. As the shear layer reattaches, the flow is forced to turn along the axis of symmetry, causing the formation of a reattachment shock. Figure 1 shows the time average of the flowfield; for high Reynolds numbers, the incoming boundary layer and the flow behind the base will be turbulent, leading to highly unsteady flow behind the base. Bourdon et al. [10] present planar visualizations of the large-scale turbulent structures in axisymmetric supersonic base flows, which provides evidence for the unsteadiness and complexity of the flowfield.

Murthy and Osborn [11] provide an excellent overview of the base flow problem, including a collection of semi-empirical approaches to model base pressure and base drag, while Dutton et al. [12] provide a good overview on the progress in computing

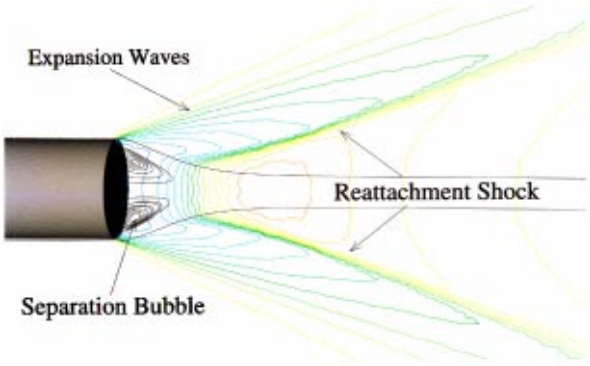

Fig. 1 Axisymmetric base flow—expansion and shock waves. SST RANS simulation, contours of pressure and streamlines.

high-speed separated base flows. Some of the difficulties and complicating factors in modeling the base flow problem are

1. the upstream effects of the presence of a corner in various Mach number flows at different Reynolds numbers;
2. the effects of separation, compression, expansion, and/or shock formation in the vicinity of the corner;
3. the influence of the expansion wave at the base corner on the initial turbulence structure of the shear layer, and the impact of that shear layer on the formation of the recirculating flow region;
4. the shear layer exists under highly compressible conditions (i.e., at high convective Mach numbers), which alters the turbulence structure, [13–16];
5. the shear layer encounters a strong adverse pressure gradient at reattachment;
6. the strong streamline curvature at the reattachment point;
7. the enclosed recirculating region imposes a highly energetic and nonuniform upstream velocity at the inner edge of the shear layer;
8. the structure and shape of the recirculating zone; and
9. and the effects of the configuration (e.g., diameter, boattail, fins, etc.).

Taken in total, these flow features yield a complex flowfield that is considerably difficult to model analytically or numerically.

3 A Brief Overview Of Experimental and Computational Studies

The complexities of the flow in the base region, and the difficulties associated with accurately predicting the flow processes, led researchers to utilize various semi-empirical prediction methods which were valuable but limited in their application. Early attempts to predict base flows are summarized by Murthy and Osborn [11], as well as Delery and Lacau [17]. These methods include data correlations (such as those performed by von Karman and Moore, Hoerner, and Kurzweg) as well as theortically based models (such as the Chapman-Korst component model, and the viscid-inviscid integral interaction technique of Crocco and Lees). These models were limited in applicability by the lack of experimental results for flowfield quantities in supersonic flow. This is partially due to the difficulty in measuring turbulence quantities in compressible flow, as well as the difficulty in interpreting the meaning of what is being measured. According to Murthy and Osborn [11], future experiments, ''will have to be carried out both to assess the gross effects of various parameters as well as to obtain detailed velocity, pressure, enthalpy, and concentration profiles in the base region.'' This recommendation was originally made in 1974, and has only been marginally fulfilled in the ensuing quarter century.

In spite of the importance of the semi-empirical methods, ''solution of the full, Reynolds-averaged Navier-Stokes equations using currently available numerical methods offers the ability to more realistically predict the details of the base flow structure, i.e., to remove many of the assumptions inherent in the component and integral techniques.'' [12] Over the past 30 years, advances in computational capabilities (namely increased computer memory size and processing speed), as well as improved numerical methods, have enabled attempts at solving various levels of the Navier-Stokes equations for the flow around a base. Early predictions were limited in size and scope by the solution algorithm method and by capabilities of the computer, but eventually practical solutions were obtained.

Eventually, computations were made using RANS-based solutions and algebraic turbulence models, but inadequate results quickly showed that higher-level models for turbulence would be required for base flows [18]. Putnam and Bissinger [19] summarize these early attempts and concluded that the current (mid 1984) methods were unable to accurately predict the pressures after separation. They also recommended that, ''the assessment

criteria of numerical predictions should be based on the surface pressure distributions and flowfield characteristics and not simply on the overall afterbody drag.'' Petrie and Walker [20] tested the predictive capabilities of RANS calculations by soliciting solutions from a number of groups for a power-on base flow configuration, for which they had experimental data (the experimental data was not released to the groups performing the calculations). Many fundamental parameters such as the base pressure magnitude and radial variation, as well as the recirculation region size, were not accurately predicted, with large variations among the different groups.

More recently, several groups have obtained results with much better agreement, including Benay et al. [21], Caruso and Childes [22], Childs and Caruso [23,24], Peace [25], Tucker and Shyy [26], Suzen et al. [27], Sahu [28], Chuang and Chieng [29], and Forsythe et al. [30]. Factors that affected the accuracy of the RANS simulation of these flows included the solution-adapted grid alignment in the high gradient shear layer regions and improved turbulence modeling (especially modeling the effects of compressibility and streamline curvature). Childs and Caruso [23] suggested that, ''comparison of simply the base pressure between computation and experiment, without any complementary flowfield data, can lead to false conclusions regarding the accuracy of the numerical solutions, due to cancellation of errors caused by inaccurate turbulence modeling and insufficient grid resolution.'' Dutton et al. [12] also state that, ''the difficult problem of turbulence modeling is the most critical outstanding issue in the accurate RANS predictions of these complex flows.''

Since Herrin and Dutton [9] published their detailed experimental results on a $M_\infty = 2.46$ axisymmetric supersonic base flow, several researchers have performed RANS computations on this flow, attempting to find an accurate RANS turbulence model. Sahu [28] used two algebraic turbulence models (Baldwin-Lomax and Chow) and Chien's low Reynolds number $k-\epsilon$ model. Chuang and Chieng [29] published results for three higher-order models: a two-layer algebraic stress model, Chien's two-equation $k-\epsilon$ model, and Shima's Reynolds stress model. Tucker and Shyy [26] used several variations of two-equation $k-\epsilon$ models, including the original Jones-Launder formulation, and extensions to allow improved response to the mean strain rate and compressibility effects. Both Sahu's $k-\epsilon$ computation and Chuang and Chieng's Reynolds stress prediction of the base pressure were in reasonable agreement with the experimental results. However, all of the models poorly predicted the mean velocity and turbulence fields. Also, even though all three studies employed a ''standard'' $k-\epsilon$ model, they obtained substantially different predictions of the base pressure distribution. This points to possible dependence on numerical implementation, grid resolution, turbulence model implementation, and/or boundary conditions. Suzen et al. [27] tested several popular RANS models on a two-dimensional base, and obtained good agreement for base pressure by adding compressibility corrections to Menter's model. Forsythe et al. [30] applied several RANS models to the two-dimensional and axisymmetric base. Although the two-dimensional base pressure was well predicted by two-equation models with compressibility corrections, no model predicted the constant pressure profile for the axisymmetric base.

Based on the unsatisfactory results of RANS calculations to date, other approaches such as large-eddy simulation or direct numerical simulation should be considered. Dutton et al. [12] state that, ''In order to avoid the difficulties inherent in turbulence modeling for the Reynolds-averaged Navier-Stokes (RANS) approach, the large-eddy simulation (LES) or direct numerical simulations (DNS) techniques will eventually be applied to high-speed flows.'' Harris and Fasel [31] performed DNS on a $M_\infty = 2.46$ two-dimensional base flow with the goal of addressing, ''the nature of the instabilities in such wake flows and to examine the structures that arise from these instabilities.'' Fureby et al. [32] performed large-eddy simulation on the axisymmetric $M_\infty = 2.46$ base flow of Mathur and Dutton [33] and Herrin and Dutton [9], including the effects of base bleed. Subgrid scale models used were the Monotone Integrated LES (MILES) model, the one-equation eddy-viscosity model, and the Smagorinski model. In general, agreement with the experimental data were quite good, however, the size of the recirculation region was slightly underpredicted. A potential source of error cited was that the approaching boundary layer thickness in the computations was smaller than reported in the experimental data. This is presumably because the grid resolution in the boundary layer was inadequate for an LES computation, although the grid was not shown.

Forsythe et al. [1] applied detached-eddy simulation on the supersonic axisymmetric base flow using an unstructured solver. The boundary layer was treated entirely by RANS, which was able to adequately predict the boundary layer thickness prior to separation. Two grids were used, with the coarse grid being clearly inadequate. The fine grid gave a DES solution that agreed quite well with experiments if the DES model constant was reduced enough. Although the good agreement with the experiments was encouraging, the lack of a grid-refined solution, and the need to adjust the DES constant kept the results from being conclusive. Additionally, the poor performance of the Spalart-Allmaras RANS model on this flow created skepticism on the part of the authors that the Spalart-Allmaras model was a good base for a hybrid model for this flow. Menter's model and Wilcox's $k-\omega$ model performed far better than the Spalart-Allmaras model, especially when compressibility corrections were included.

Baurle et al. [34] later explored hybrid RANS/LES for the supersonic axisymmetric base flow. A separate RANS simulation was run upstream of the base to obtain a fully turbulent velocity profile of the correct thickness just prior to the base, then a monotone integrated LES (MILES) was performed in the base region. This approach allowed the authors to examine numerical issues (apart from modeling issues) since a pure LES approach was used behind the base. The agreement with experiments was quite good.

4 Governing Equations And Flow Solver

The unstructured flow solver Cobalt was chosen because of its speed and accuracy (Cobalt is a commercial version of Cobalt_{60}). The relevant improvements in the commercial version for this study were the inclusion of SST-based DES, faster per-iteration times, the ability to calculate time-averages and turbulent statistics, an improved spatial operator, and improved temporal integration. Strang et al. [35] validated the code on a number of problems, including the Spalart-Allmaras model (which forms the core of the DES model). Tomaro et al. [36] converted Cobalt_{60} from explicit to implicit, enabling CFL numbers as high as one million. Grismer et al. [37] then parallelized the code, yielding a linear speedup on as many as 1024 processors. Forsythe et al. [30] provided a comprehensive testing and validation of the RANS models: Spalart-Allmaras, Wilcox's $k-\omega$, and Menter's models. The Parallel METIS (ParMetis) domain decomposition library of Karypis and Kumar [38] and Karypis et al. [39] is also incorporated into Cobalt. ParMetis divides the grid into nearly equally sized zones that are then distributed among the processors.

The numerical method is a cell-centered finite volume approach applicable to arbitrary cell topologies (e.g, hexahedrals, prisms, tetrahdra). The spatial operator uses the exact Riemann solver of Gottlieb and Groth [40], least squares gradient calculations using QR factorization to provide second-order accuracy in space, and TVD flux limiters to limit extremes at cell faces. A point implicit method using analytic first-order inviscid and viscous Jacobians is used for advancement of the discretized system. For time-accurate computations, a Newton subiteration scheme is employed, and the method is second-order accurate in time.

The compressible Navier-Stokes equations were solved in an inertial reference frame. To model the effects of turbulence, a turbulent viscosity (μ_t) is provided by the turbulence model. To obtain k_t (the turbulent thermal conductivity), a turbulent Prandtl

number is assumed with the following relation: $\mathrm{Pr}_t = c_p \mu_t / k_t = 0.9$. In the governing equations, μ is replaced by $(\mu + \mu_t)$ and k (the thermal conductivity) is replaced by $(k + k_t)$. The laminar viscosity, μ, is defined using Sutherland's law.

5 Spalart-Allmaras (S-A) Model

The Spalart-Allmaras (SA) one-equation model, [41] solves a single partial differential equation for a variable $\tilde{\nu}$ which is related to the turbulent viscosity. The differential equation is derived by, "using empiricism and arguments of dimensional analysis, Galilean invariance and selected dependence on the molecular viscosity." The model includes a wall destruction term that reduces the turbulent viscosity in the log layer and laminar sublayer, and trip terms that provide a smooth transition from laminar to turbulent. For the current research, the trip term was turned off. Spalart [42] suggested the use of the compressibility correction of Secundov [43]. In order to effect the correction, the following destruction term is added to right-hand side of the Spalart-Allmaras model equation:

$$-C_5 \tilde{\nu}^2 U_{i,j} U_{i,j} / a^2 \tag{1}$$

where a is the speed of sound and $C_5 = 3.5$, which is empirically determined. The term accounts for the reduced spreading rates in a compressible shear layer by reducing the turbulent eddy viscosity. Cases run with the compressibility correction active are denoted by "CC."

6 Menter's Shear Stress Transport Model

Wilcox's $k-\omega$ model is well behaved in the near-wall region, where low Reynolds number corrections are not required. However, the model is generally sensitive to the freestream values of ω. This sensitivity seems to be a factor mainly for free shear flows, and does not seem to adversely affect boundary layer flows. On the other hand, the $k-\epsilon$ equations are relatively insensitive to freestream values, but behave poorly in the near wall region, [44]. Menter [45,46] proposed a combined $k-\epsilon/k-\omega$ model (known as Menter's SST model) which uses the best features of each model. The model uses a parameter F_1 to switch from $k-\omega$ to $k-\epsilon$ in the wake region to prevent the model from being sensitive to freestream conditions.

Menter did not include compressibility corrections in his model. Suzen and Hoffmann [47], however, added compressible dissipation and pressure dilatation terms to the $k-\epsilon$ portion of Menter's model. When Menter's blending process is applied, the following equations result:

$$\frac{D}{Dt}(\rho k) = \tau_{ij}\frac{\partial u_i}{\partial x_j} + (1-F_1)\overline{p''d''} - \beta^* \rho \omega k (1 + \alpha_1 M_t^2 (1-F_1)) + \frac{\partial}{\partial x_j}\left[(\mu + \sigma_k \mu_t)\frac{\partial k}{\partial x_j}\right] \tag{2}$$

$$\frac{D}{Dt}(\rho \omega) = \frac{\gamma \rho}{\mu_t}\tau_{ij}\frac{\partial u_i}{\partial x_j} + (1-F_1)\beta^* \alpha_1 M_t^2 \rho \omega^2 + \frac{\partial}{\partial x_j}\left[(\mu + \sigma_\omega \mu_t)\frac{\partial \omega}{\partial x_j}\right] - \beta \rho \omega^2 + 2\rho(1-F_1)\sigma_{\omega 2} \times \frac{1}{\omega}\frac{\partial k}{\partial x_j}\frac{\partial \omega}{\partial x_j} - (1-F_1)\frac{\overline{p''d''}}{\nu_t} \tag{3}$$

where the pressure dilatation term is

$$\overline{p''d''} = -\alpha_2 \tau_{ij}\frac{\partial u_i}{\partial x_j} M_t^2 + \alpha_3 \rho \epsilon M_t^2 \tag{4}$$

and the closure coefficients for the compressible corrections are: $\alpha_1 = 1.0$, $\alpha_2 = 0.4$, and $\alpha_3 = 0.2$. By adding these corrections only to the $k-\epsilon$ portion of the model, the near wall solution ($k-\omega$ portion) is unaffected, as observed by Forsythe et al. [48]. Cases run with the compressibility correction active are denoted by "CC."

7 Detached-Eddy Simulation (DES)

Detached-eddy simulation (DES) was proposed by Spalart et al. [4] as a method to combine the best features of large-eddy simulation with the best features of the Reynolds-averaged Navier-Stokes approach. RANS tends to be able to predict attached flows very well with a low computation cost. Traditional LES (i.e., LES without using a wall model), on the other hand, has a high computation cost, but can predict separated flows more accurately. The model was originally based on the Spalart-Allmaras one-equation RANS turbulence model discussed above and in [41]. The wall destruction term is proportional to $(\tilde{\nu}/d)^2$, where d is the distance to the closest wall. When this term is balanced with the production term, the eddy viscosity becomes $\tilde{\nu} \propto S d^2$, where S is the local strain rate. The Smagorinski LES model varies its subgrid-scale (SGS) turbulent viscosity with the local strain rate and the grid spacing, Δ (i.e., $\nu_{\mathrm{SGS}} \propto S\Delta^2$). If, therefore, d is replaced by Δ in the wall destruction term, the S-A model will act as a Smagorinski LES model.

To exhibit both RANS and LES behavior, d in the SA model is replaced by

$$\tilde{d} = \min(d, C_{\mathrm{DES}}\Delta) \tag{5}$$

where C_{DES} is the DES model constant. When $d \ll \Delta$, the model acts as a RANS model. When $d \gg \Delta$, the model acts as a Smagorinski LES model. Therefore, the model can be "switched" to LES mode by locally refining the grid. In an attached boundary layer, a RANS simulation will have highly stretched grids in the streamwise direction. To retain RANS behavior in this case, Δ is taken as the largest spacing in any direction ($\Delta = \max(\Delta x, \Delta y, \Delta z)$). The model was calibrated by Shur et al. [5] using isotropic turbulence to give C_{DES} of 0.65. Although C_{DES} was reduced previously, [1], the current study uses 0.65 for all cases.

Strelets [8] introduced a DES model based on Menter's SST model. In the SST model, the turbulent length scale is given by $l_{k-\omega} = k^{1/2}/(\beta^* \omega)$. The DES modification replaces the length scale by $\tilde{l} = \min(l_{k-\omega}, C_{\mathrm{DES}}\Delta)$ in the dissipative term of the k-transport equation (i.e., the dissipation term is $D^k_{\mathrm{DES}} = \rho k^{3/2}/\tilde{l}$). Since the compressibility corrections outlined above are designed to decrease the turbulence length scale, it was decided to include them in the equation for $\tilde{l}$ (i.e., $l_{k-\omega} = k^{1/2}/(\beta^*(1 + \alpha_1 M_t^2 (1 - F_1))\omega)$). Since Menter's SST model is based on a blending of $k-\epsilon$ and $k-\omega$, Strelets [8] calibrated the model by running both the $k-\epsilon$ and $k-\omega$ DES models on isotropic turbulence. This lead to $C^{k-\epsilon}_{\mathrm{DES}} = 0.61$ and $C^{k-\omega}_{\mathrm{DES}} = 0.78$. The traditional blending function was used to blend between the two constants (i.e., $C_{\mathrm{DES}} = (1 - F_1)C^{k-\epsilon}_{\mathrm{DES}} + F_1 C^{k-\omega}_{\mathrm{DES}}$). The recommended constants were used in the current study.

Since Cobalt accepts arbitrary cell types, a combination of tetrahedra and prisms were used in the current study. This is in contrast to structured grids which use hexahedral cells. Prisms were used in the boundary layer to reduce the number of cells needed and to increase the accuracy of the boundary layer computation by increasing the orthogonality of the cells. Previously, Forsythe et al. [1] used the longest edge in each cell as Δ. However it was pointed out that a tetrahedron with an edge length equal to a hexahedron will have roughly 1/6th the volume (imagine a cube cut into 6 tetrahedra). A more consistent method of defining the length scale is used in the current study—the largest distance between the cell center and all the neighboring cell centers. Since Cobalt is cell-centered, this definition provides a length scale based on the distance between neighboring degrees-of-freedom. In the current study, the streamwise and spanwise grid spacing was slightly larger than the boundary layer thickness, en-

suring that the model was operating in a RANS mode in the boundary layer (since $d<\Delta$ in the boundary layer).

8 Results

The current article is an attempt to resolve many of the issues revealed in the previous study, [1], in order to build confidence in DES for compressible flows. Four grids (both structured and unstructured) are used to examine the sensitivity of the DES model to grid refinement and grid type. DES based on Menter's shear stress transport model is applied to determine the sensitivity of DES on the RANS model for this flow. Compressibility corrections are applied to both Spalart-Allmaras and shear stress transport-based DES. Comparisons are made to RANS solutions and experiments.

8.1 Test Conditions. The experimental conditions for the axisymmetric base of Herrin and Dutton [9] were matched in the current computations. Freestream conditions of $M_\infty=2.46$ and a unit Reynolds number of $\mathrm{Re}=45\times10^6$ per meter were imposed at the inflow boundary. With a base radius of 31.75 mm, the resulting Reynolds number based on the diameter was $\mathrm{Re}=2.858\times10^6$. The test conditions are summarized in Table 1.

8.2 Grids and Boundary Conditions. Two unstructured grids and two structured grids were used in the current study to examine the effects of grid resolution and grid type. All grids used a cylinder of length $8R$, where R is the base radius. This length was determined by running Wilcox's boundary layer code, EDDYBL, [49], with the Spalart-Allmaras model to see what length was needed to match the experimental momentum thickness.

The two structured grids were provided by Baurle et al. [34], with the fine grid shown in Fig. 2(*a*). The grids contained only a short portion upstream of the base, so an additional set of points was added to extend the cylinder upstream to $8R$. Two grids were used, with the fine grid having twice as many points in each coordinate direction. The grid densities of the coarse and fine grids were 330,000 and 2.60×10^6, respectively. The average first y^+ for the coarse grid on a Spalart-Allmaras calculation was 14, while the fine grid was half that value. This is well above the recommended value of $y^+=1$ [42]. Since Baurle et al. [34] were using wall functions, this spacing was adequate. In the current study, however, the boundary layer was treated without the use of wall functions, so the resolution was inadequate. The outflow was placed $10R$ downstream, while the farfield boundary was at $4.15R$ from the axis of symmetry. The structured coarse and fine grids are denoted by SGC and SGF, respectively.

The two unstructured grids had the same basic dimensions as each other. The outflow boundary was placed $12R$ downstream, and the experimental wind tunnel walls were modeled as a slip boundary at $10R$ from the axis of symmetry. The first unstructured grid, pictured in Fig. 2(*b*) was created using VGRIDns [50], and was used for previous computations, [1]. Although VGRIDns is a pure tetrahedral grid generator, a Cobalt utility *blacksmith* was used to recombine the tetrahedra in the boundary layer into

Table 1 Test conditions for the axisymmetric base flow, [9]

M_∞	2.46
ρ_∞	$0.7549\ \frac{\mathrm{kg}}{\mathrm{m}^3}$
p_∞	$3.1415\times10^4\ \frac{\mathrm{N}}{\mathrm{m}^2}$
T_∞	145 K
Re	$\frac{45\times10^6}{\mathrm{m}}$
R	31.75 mm
$U_\infty=U_0$	$593.8\ \frac{\mathrm{m}}{\mathrm{sec}}$

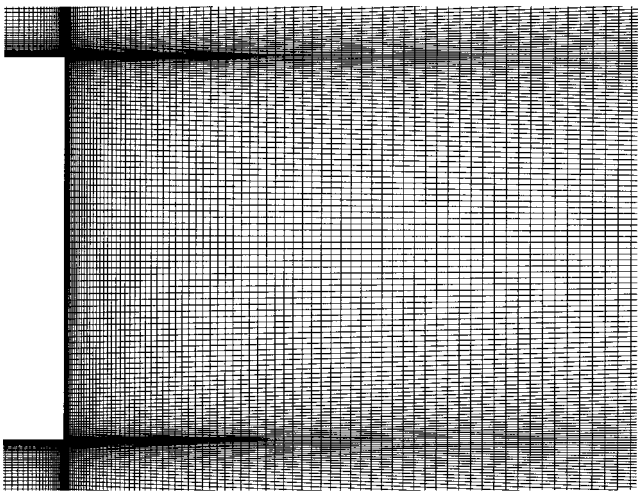

(*a*)

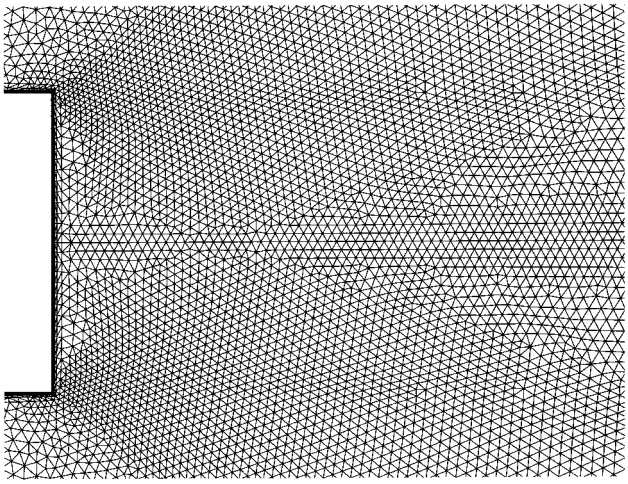

(*b*)

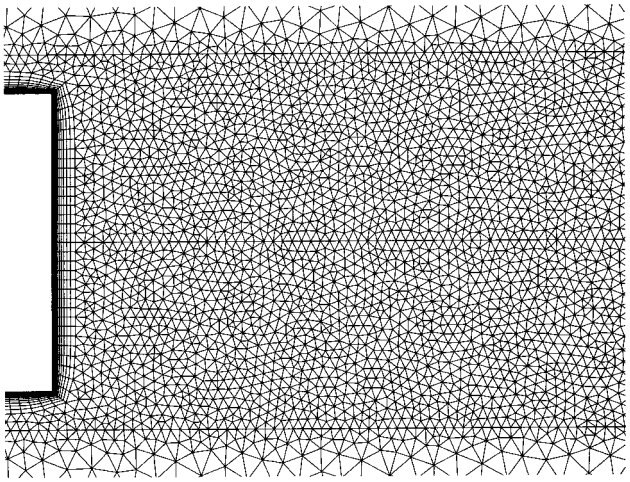

(*c*)

Fig. 2 Closeup views of grids used. (*a*) Fine structural grid (SGF)—2.60×10^6 cells; (*b*) VGRIDns grid (VG)—2.86×10^6 cells; (*c*) Gridgen grid (GG)—2.75×10^6 cells.

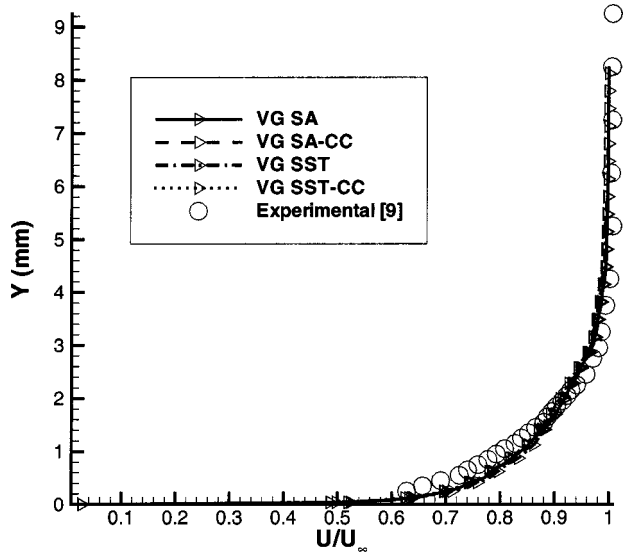

Fig. 3 Boundary layer profile 1 mm prior to the base—RANS models

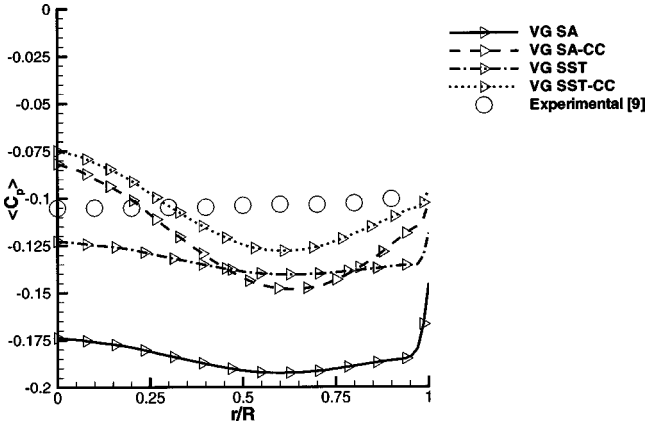

Fig. 4 Pressure along the base—RANS models

prisms. The average first y^+ spacing was 0.7 for the Spalart-Allmaras model, with cells concentrated in the shear layer and in the separated region. The grid consisted of 2.86×10^6 cells, and is denoted by "VG." (See Fig. 3.)

The second unstructured grid was created with Gridgen [51], and is shown in Fig. 2(*c*). This grid was created using the concepts in the "Young-Person's Guide to Detached-Eddy Simulation Grids," [52]. Gridgen's multiblock unstructured gridding capability was used to pack points in the separated region (or focus region [52]) to give better LES resolution. Approximately half of the 2.75×10^6 cells were in a region that extended $4R$ downstream, and $1.3R$ from the axis of symmetry. The boundary layer consisted of prisms, with an average first y^+ spacing of less than 0.2 for the Spalart-Allmaras model. This grid is denoted by "GG."

All farfield, inflow, and outflow boundaries used the modified Reimmann invarient boundary condition in Cobalt. It should be noted that no synthetic turbulence was added to the farfield boundaries. This was considered appropriate even for DES since the boundary layer was treated in RANS mode. It was expected that the instabilities at the separation point would then provide the unsteady content for the simulation. Solid walls on the cylinder were set to be adiabatic no slip, while the outer wind tunnel walls were set to a slip boundary condition. For the no-slip boundary conditions, the normal gradient of pressure was assumed to be zero. No wall functions were used for the turbulence models either for DES or RANS.

8.3 Calculation Details. A timestep study was performed previously and reported in [1]. Pressure was monitored at ten locations along the axis of symmetry, and the timestep was varied. Also, two full DES calculations were done with a timestep that varied by a factor of two, with little effect on the mean flow. The current calculations reduced the timestep from the previous study value of 5.0×10^{-6} to 3.2×10^{-6}. This gives a nondimensional timestep (by base diameter and freestream velocity) of 0.025. In the base region, the velocities are far lower than the freestream velocity, leading to local CFL numbers that are less than one outside the boundary layer. The other parameters used for the temporal integration were two Newton subiterations, 32 matrix sweeps, and a temporal damping of 0.025 (inviscid) and 0.01 (viscous). The calculations were run for 4000 iterations prior to beginning to take time averages, and statistics were calculated internally by Cobalt for a minimum of 10,000 iterations. The code was run second-order accurate in both time and space, and RANS calculation were done with a CFL of 1×10^6 to rapidly obtain a steady-state solution. Previous runs suggested that the RANS calculations would not give an unsteady solution.

As in the previous study, asymmetries were observed in the mean flow. In the previous study, only 4000 total iterations were used to calculate time averages. The current study showed that these asymmetries were greatly reduced, but not eliminated, by running as many as 40,000 iterations. This many iterations was considered impracticable, so averages were taken both in time and in the azimuthal direction.

Calculations were performed on an IBM SP3 and a Linux cluster, with between 32 and 256 processors being used. With 256 processors, the most expensive calculations (14,000 iterations, 2.85×10^6 cells, DES-SST model) took around 30 wall-clock hours. The steady-state calculations took about a tenth that time, since less than 2000 iterations were necessary with less subitera-

Table 2 Test matrix showing range of time averaged pressure coefficient across the base—take from Figs. 4 and 9. Turbulence models: SA=Spalart-Allmaras, SST=Menter's shear stress transport, DES=detached-eddy simulation, CC=compressibility correction; Grids: SGC=structured grid coarse, SGF=structured grid fine, VG=VGRIDns grid, GG=Gridgen grid.

	SGC	SGF	VG	GG
SA			−0.174/−0.192	
SA-CC			−0.082/−0.148	
SST			−0.123/−0.141	
SST-CC			−0.075/−0.128	
DES-SA	−0.117/−0.172	−0.107/−0.118	−0.097/−0.102	−0.098/−0.101
DES-SA-CC	−0.122/−0.165		−0.097/−0.102	−0.099/−0.102
DES-SST			−0.088/−0.094	−0.088/−0.090
DES-SST-CC			−0.093/−0.100	−0.094/−0.097
Experimental [9]		−0.100/−0.105		

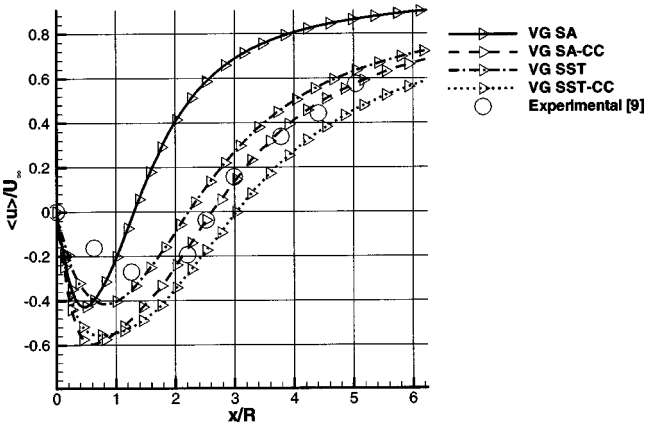

Fig. 5 Centerline velocity—RANS models

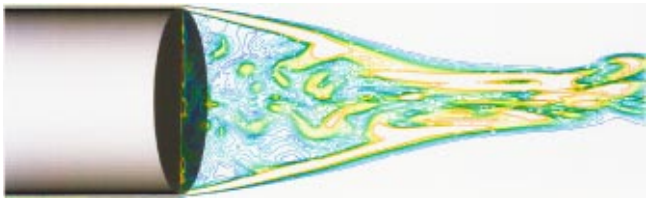

Fig. 7 Vorticity contours—DES Spalart-Allmaras model on the fine structured grid

tions. The test matrix for the turbulence models and the different grids is shown in Table 2. The matrix contains the range of time averaged pressure coefficients on the base for each calculation as well as the experimental values. These values were obtained by finding the maximum and minimum pressure coefficients from Figs. 4 and 9 in the range measured experimentally. All of the RANS runs were performed on the VGRIDns grid, since RANS calculations on that grid were shown previously to match well with a more fine two dimensional structured grid (see [1] and Forsythe et al. [30]).

8.4 RANS Results. Figures 3 through 6 show results for the Spalart-Allmaras and Menter's shear stress transport/RANS models on the VGRIDns grid. As seen in Fig. 3, both models (with and without the compressibility corrections) match the boundary layer thickness prior to the base quite well, although the shape of the velocity profile is slightly different than the experimental profile. This discrepancy was previously seen by Forsythe et al. [1] and later by Baurle et al. [34], who performed a calculation of the actual converging/diverging nozzle section to try to remove this discrepancy, but it made little difference.

The base pressure is next examined in Fig. 4. The Spalart-Allmaras model predicts far too low of a base pressure, with a

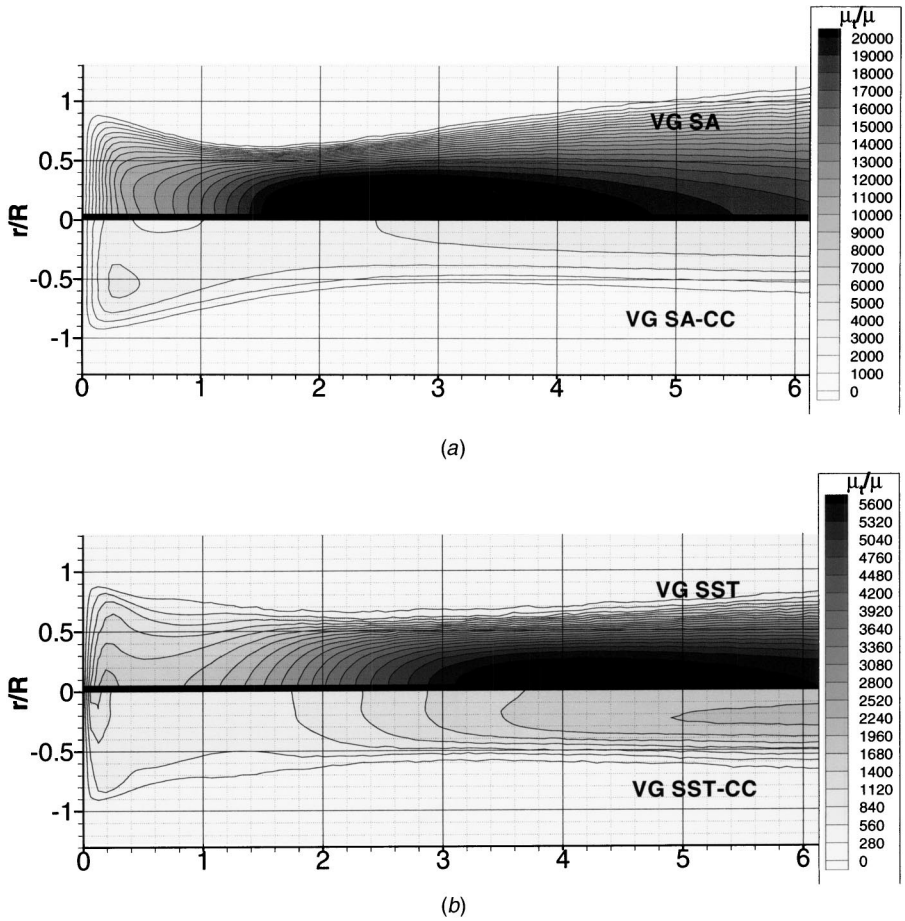

Fig. 6 Nondimensional turbulent eddy viscosity behind the base; (*a*) Spalart-Allmaras model with and without compressibility corrections on VGRIDns grid; (*b*) shear stress transport model with and without compressibility corrections on VGRIDns grid

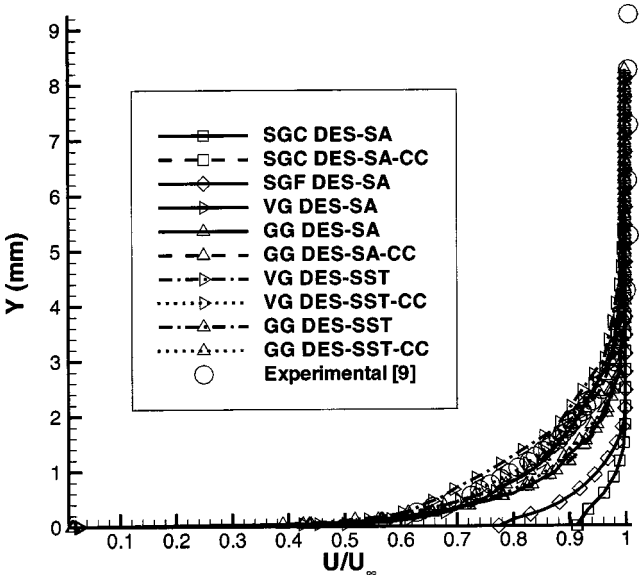

Fig. 8 Boundary layer profile 1 mm prior to the base—DES model

slight radial variation. The compressibility correction has a strong effect, putting the results much closer to the experiments, but introducing a larger radial variation. The SST model without the compressibility corrections does about as well as SA with the correction, and with a flatter radial profile. The compressibility correction then further improves the pressure level; however, it again introduces more radial variation.

The centerline velocity behind the base is next plotted in Fig. 5. The SA model greatly underpredicts the shear layer reattachment location. The peak reverse velocity is overpredicted by the models with compressibility corrections, which helps explain the increased variation in pressure along the base. Streamlines flowing along the centerline towards the base stagnate on the center of the base, leading to the high pressure seen there. The large reduction in turbulent eddy viscosity seen in Fig. 6(*a*) has the effect of increasing the recirculation region size, which makes the turning angle at the base more realistic, but allows a larger reverse velocity, which leads to a larger variation in pressure. The SST model starts with much lower turbulent viscosity than SA, as seen in Fig. 6(*b*), which allows for the larger recirculation region as seen in Fig. 5. The compressibility correction further reduces the levels of eddy viscosity, increasing the size of the recirculation region further, and increasing the peak reverse velocity.

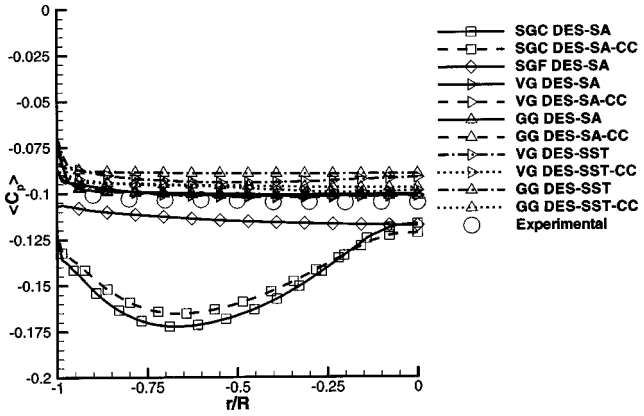

Fig. 9 Pressure along the base—DES model

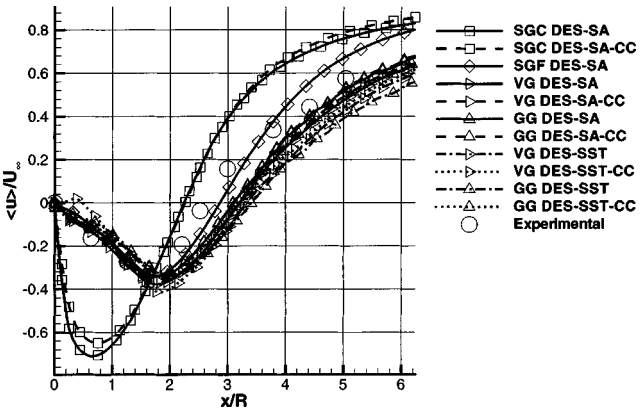

Fig. 10 Centerline velocity—DES model

8.5 DES Results. Figure 7 shows an instantaneous plot of vorticity contours in a cross-plane behind the base for DES based on Spalart-Allmaras on the fine structured grid. Although the shear layer roll up was not captured, the turbulent structures seem otherwise well resolved. This figure as well as subsequent plots of resolved turbulent kinetic energy provide evidence that DES is operating in LES mode behind the base. Three-dimensional volumetric rendering of isosurfaces of vorticity showed numerous small scale structures behind the base.

Boundary layer profiles for all DES runs are plotted in Fig. 8. The coarse and fine structured grids fail to predict the proper boundary layer thickness due their large average first y^+ values of 14 and 7, respectively; coarse streamwise grid spacing also may have contributed to this underprediction. All other profiles match reasonably well.

The base pressure is plotted in Fig. 9. The coarse structured grid is clearly underresolved. The compressibility correction aids the result somewhat, but not significantly. The fine structured grid underpredicts the base pressure by about 10% but has the flat pressure profile observed experimentally. (Note that the base pressure for this grid was plotted incorrectly in Forsythe et al. [53].) The poor boundary layer prediction on this grid is a possible source of error. Both unstructred grid DES-SA results are in good agreement with the experiments, and are insensitive to the presence of the compressibility corrections. The SST results overpredict the base pressure by 5%–10%, depending on the grid. The compressibility correction moves the pressure towards the experimental values.

The centerline velocity plotted in Fig. 10 exhibits a similar behavior as the grid is varied. The coarse structured grid is again underresolved, giving a high peak reverse velocity too close to the base. The fact that LES without an explicit subgrid scale model (predicted by Forsythe et al. [1]) gives a much better result for base pressure and centerline velocity on the coarse grid compared with DES shows that there is a significant effect of the model on this grid, in addition to the numerical errors. The nature of DES is that the coarse grid limit yields a RANS model. As the grid is refined, the eddy viscosity will drop lower than a RANS prediction, yet may still be too high to allow an LES prediction.

Mach contours are compared to the experiments for various models and grids in Figs. 11. Besides the coarse grid, the results all look quite similar, even when comparing SA-based DES to SST-based DES, and the fine structured vs. an unstructured grid. Figure 11 shows that DES is able to predict a realistic shear layer growth on the various grids. Plots of resolved turbulent kinetic energy (Fig. 12), however, suggest that the shear-layer rollup is not being resolved. The shear-layer growth is aided, however, by the presence of turbulent eddy viscosity as seen in Fig. 13. The turbulent kinetic energy is underpredicted on all grids (Fig. 12), especially in the shear layer. Grid refinement should enhance the

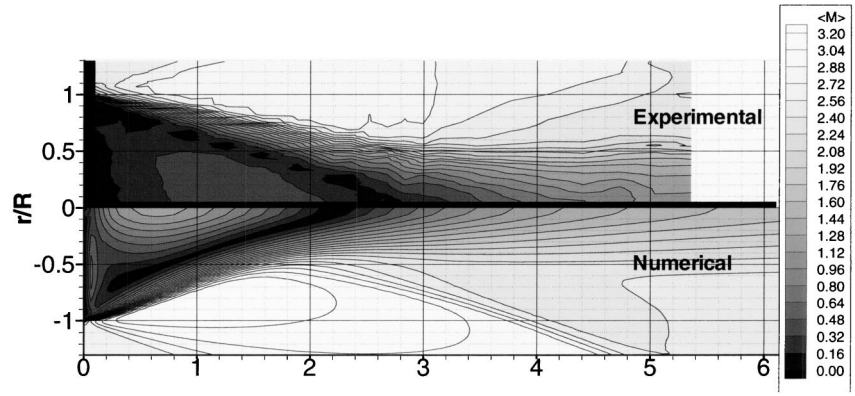

(*a*)

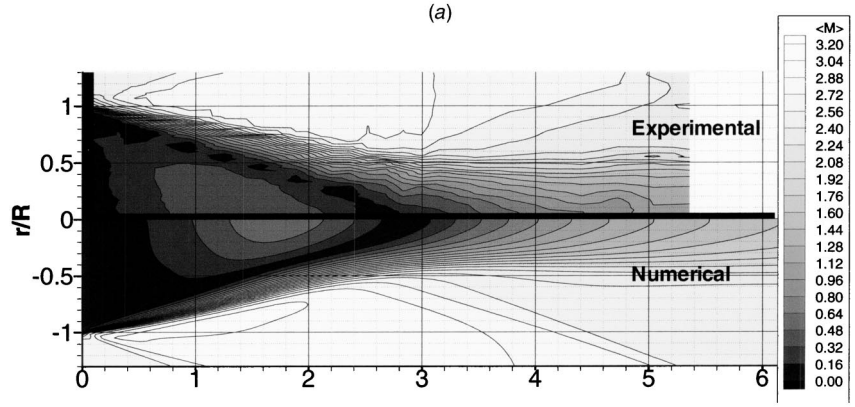

(*b*)

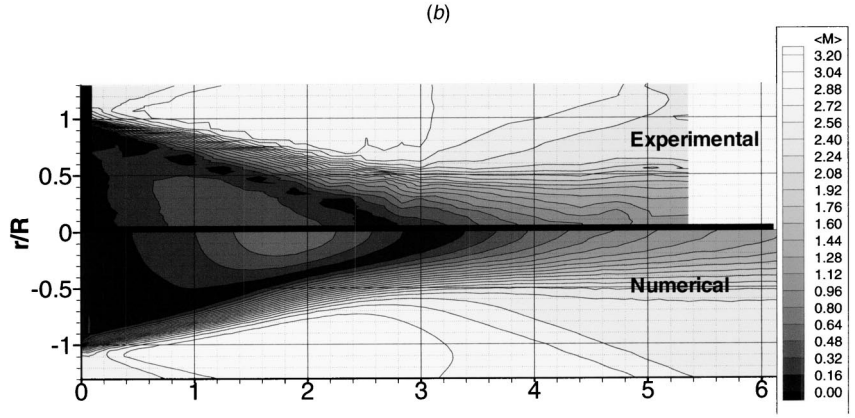

(*c*)

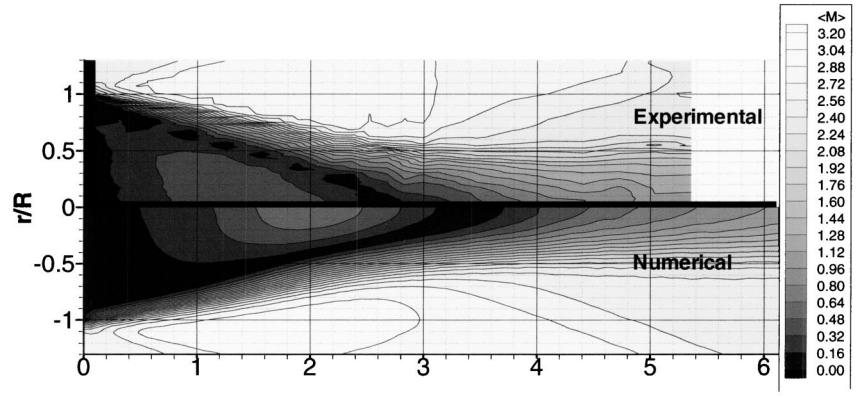

(*d*)

Fig. 11 Mach contours behind the base; (*a*) DES Spalart-Allmaras on the coarse structured grid versus Experiment [9]; (*b*) DES Spalart-Allmaras on the fine structured grid versus Experiment [9]; (*c*) DES Spalart-Allmaras on the Gridgen grid versus Experiment [9]; (*d*) DES shear stress transport model on Gridgen grid versus Experiment [9]

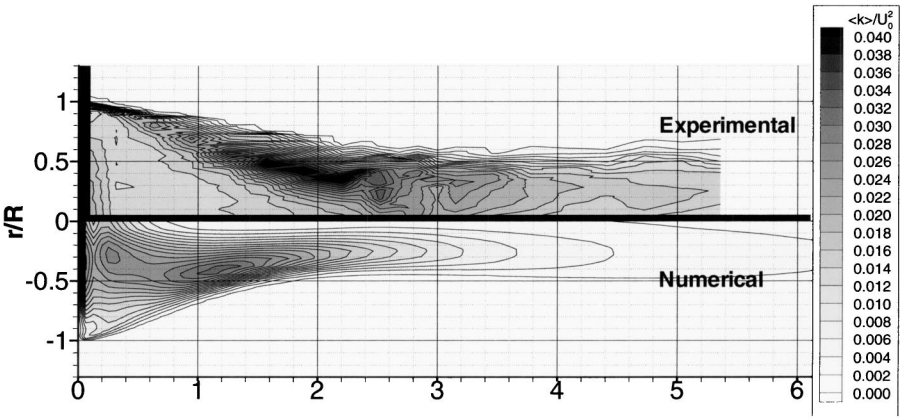

(*a*)

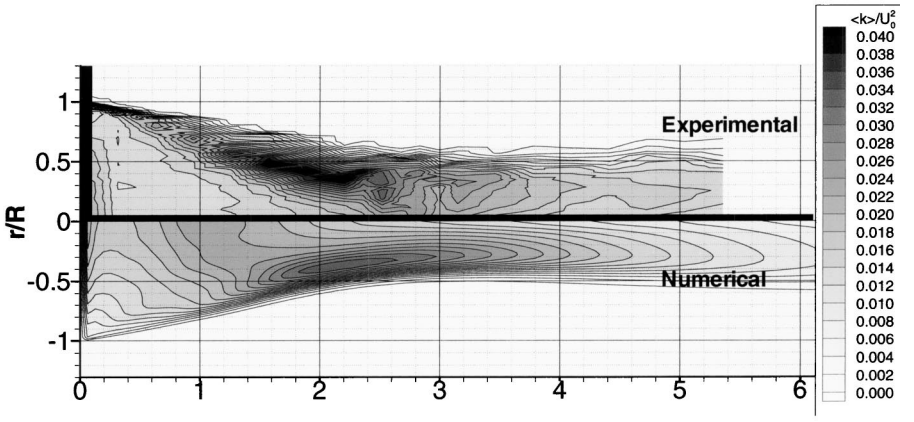

(*b*)

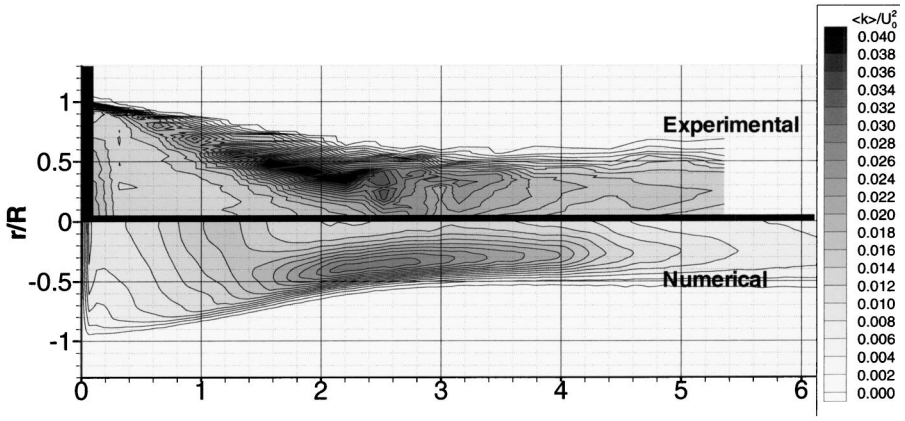

(*c*)

Fig. 12 Resolved turbulent kinetic energy behind the base; (*a*) DES Spalart-Allmaras model on the coarse structured grid versus Experiment [9]; (*b*) DES Spalart-Allmaras model on the fine structured grid versus Experiment [9]; (*c*) DES Spalart-Allmaras model on the Gridgen grid versus Experiment [9]

agreement with the experiments, but since some turbulence is still being modeled (especially in the shear layer), the mean flow properties are reasonable. The fine structured grid underpredicts the shear layer growth rate, which is likely to be the cause for the underprediction of the base pressure. This could be because the structured grid has finer grid resolution in the shear layer, lowering the eddy viscosity below RANS levels. However, as previously mentioned, the shear layer rollup is not being resolved, so the model is not acting in LES mode.

It should be noted that the VGRIDns grid was previously used by Forsythe et al. [1], yet the current results are much improved with the standard model constant, $C_{\mathrm{des}}=0.65$. This is partially attributed to the redefinition of the length scale on tetrahedral cells as discussed previously. Part of the improvement also comes from improvements in the time-accuracy of Cobalt over Cobalt_{60}. This evaluation is based on the fact that a calculation was performed using Cobalt_{60} after the redefinition of the length scale, with base

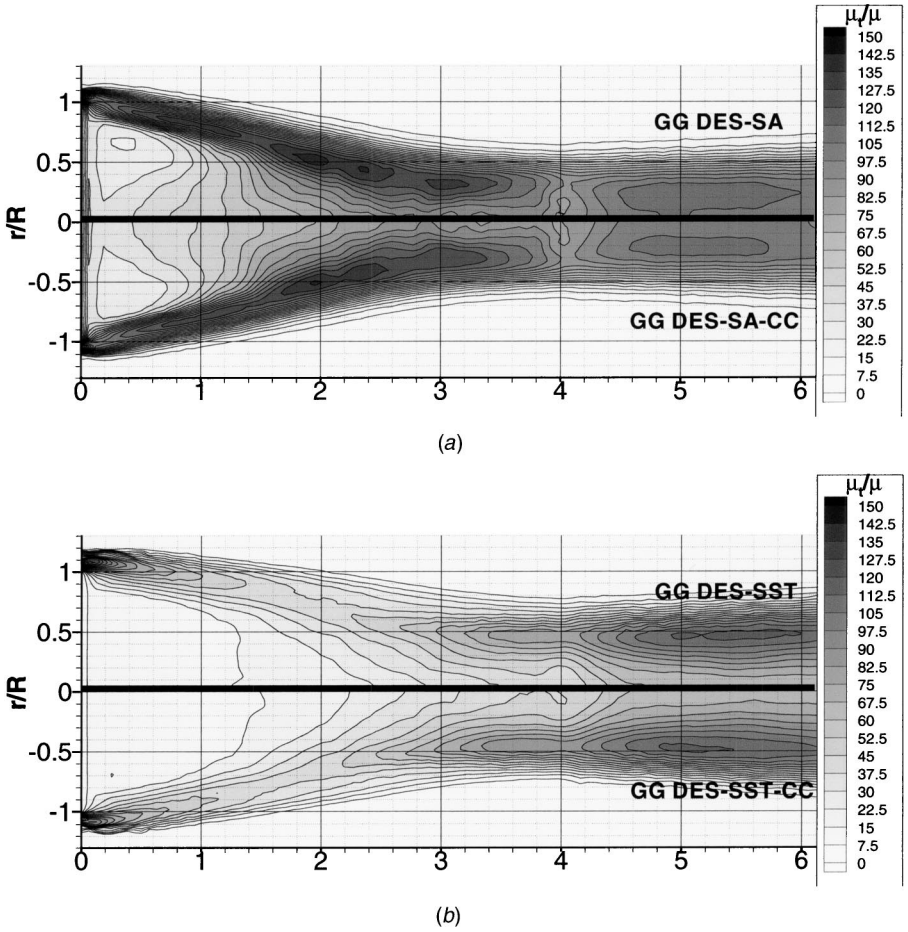

Fig. 13 Nondimensional turbulent eddy-viscosity behind the base; (*a*) DES Spalart-Allmaras model with and without compressibility corrections on Gridgen grid, (*b*) DES shear stress transport model with and without compressibility corrections on Gridgen grid

pressures and levels of resolved turbulent kinetic energy somewhere between that seen in Forsythe et al. [1] and the current study.

Figure 14 shows turbulent statistics for DES-SA on the Gridgen grid. Although underpredicting the statistics in general, the agreement is fair. The resolved radial turbulence intensity is furthest from the experiments.

9 Conclusions

A detailed testing of DES based on both the Spalart-Allmaras and the shear stress transport model was conducted on the supersonic axisymmetric base of Herrin and Dutton [9]. The grids were constructed so that the boundary layer would be treated fully in RANS mode. Comparisons were made to the Spalart-Allmaras and shear stress transport RANS models and experiments. Compressibility corrections were examined for the RANS and DES models.

Both the SA and the SST RANS models seem unable to realistically model this flowfield, with Mach contours for both models being in significant disagreement with the experimental data. Compressibility corrections aid the models in predicting a more realistic level of pressure on the base, but increase the radial variation of the pressure due to the increased centerline velocity. DES, in contrast, predicts a flat pressure profile due to its ability to model the unsteady flow that helps equalize the base pressure. DES successfully predicted the boundary layer thickness prior to the base by operating in RANS mode in the boundary layer, while retaining LES's ability to predict the flat base pressure profile.

Calculations were performed on two structured and two unstructured grids to examine the effect of grid resolution and topology. Good agreement with experimental base pressure was obtained on all but the coarse structured grid. The coarse grid DES results were actually quite similar to the Spalart-Allmaras RANS results with the compressibility correction active on a fine grid. This highlights the need for assessing the resolution of the grid—a fact that is true for RANS, and crucial for DES. The use of the DES modification drew down the eddy viscosity low enough to improve the poor Spalart-Allmaras RANS results, mimicking a compressibility correction, yet not low enough to allow for good LES content. The fine structured grid DES underpredicted the boundary layer thickness prior to the base due to coarse wall normal spacing. This grid also underpredicted the base pressure by about 10%, although this is not necessarily due to the underprediction of the boundary layer thickness. thickness is quite small compared to the base diameter. Unstructured grids gave solutions that agreed well with the experimental data.

The sensitivity of DES on the underlying RANS model was examined by running both Spalart-Allmaras and SST-based DES with and without compressibility corrections. Spalart-Allmaras-based DES predicted the base pressure to within a few percent on the unstructured grids. SST-based DES predicted higher pressures than the experiments (the worst disagreement was 10%). Compressibility corrections helped improve the agreement with base

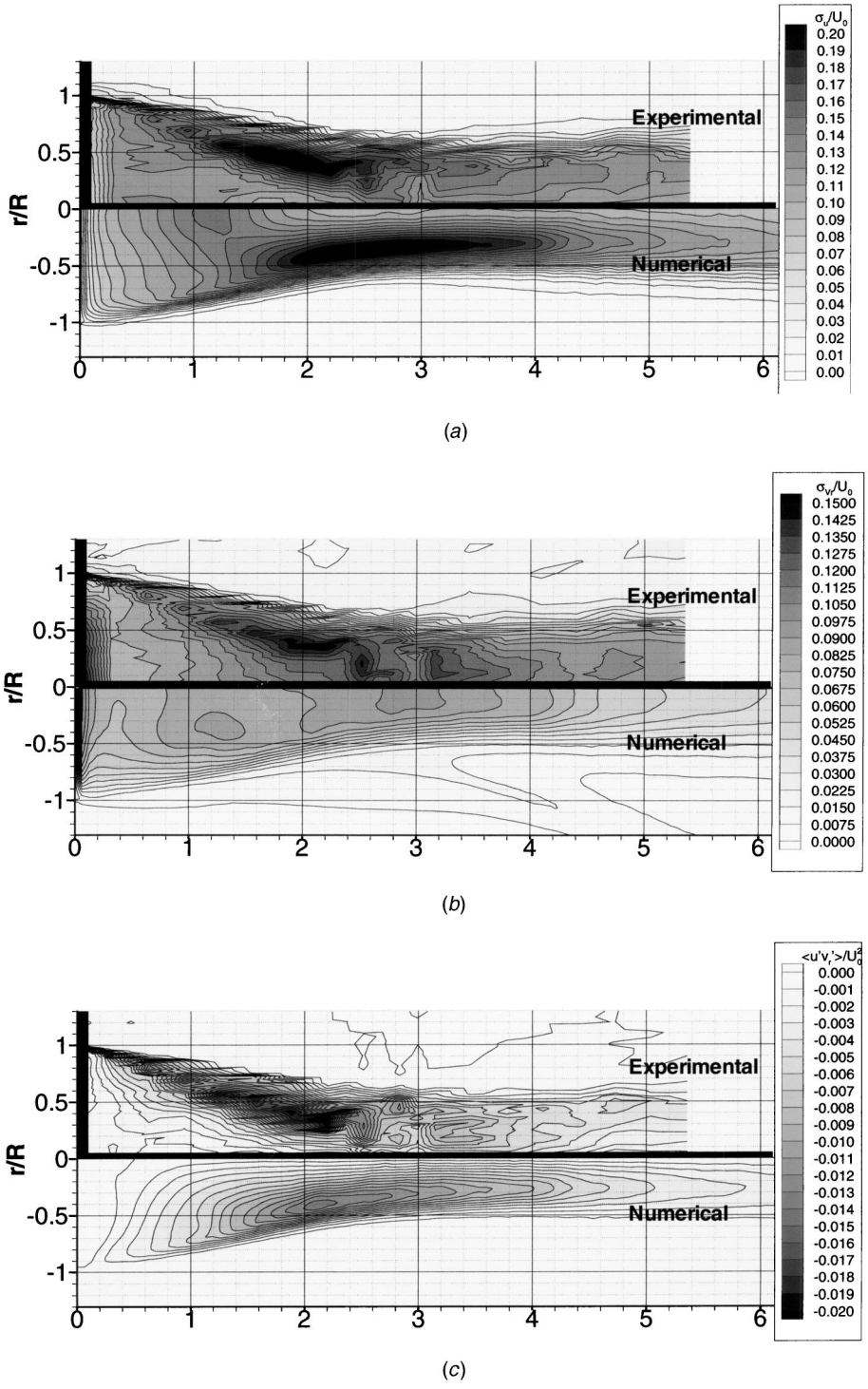

Fig. 14 Resolved turbulent statistics on the Gridgen grid; (*a*) resolved streamwise turbulent intensity versus Experiment [9], (*b*) resolved radial turbulence intensity versus Experiment [9], (*c*) resolved Reynolds stress versus Experiment [9]

pressure for the SST-based DES, however, the turbulent eddy-viscosity contours were so similar it is difficult to understand the reason for the improvement. Compressibility corrections had a negligible impact on Spalart-Allmaras-based DES. The lack of sensitivity of DES to the underlying RANS model is likely due to the fact that the role of the RANS model within DES is confined mainly to the boundary layer and the thin shear layers.

The results of this study show that it is now possible to accurately model axisymmetric base flowfields using appropriate numerical techniques, turbulence models, and grids. While RANS turbulence models give relatively poor results for these flowfields, and pure LES models are excessively expensive to use if the boundary layer is to be resolved, the hybrid DES models were able to give good comparisons with available experimental data. The DES results also show, however, that careful attention must be paid to grid size and density, and boundary conditions (especially the inflow boundary layer profile). While this study was able to sufficiently match the detailed flowfield data of Herrin and

Dutton, including turbulence quantities in the baseflow region, there is still a lack of experimental data for CFD validation—similar data should be taken at a variety of Mach numbers, Reynolds numbers, and for geometries with and without boattails. In spite of this, however, it is apparent that the accurate computation of turbulent base flow at supersonic speeds is now possible.

Acknowledgments

Computer time was provided by the Maui High Performance Computing Center and the NAVO Major Shared Resource Center. Dr. Spalart provided some very helpful discussions and originally motivated this work. Dr. Strelets provided results from other runs to ensure that the Spalart-Allmaras compressibility correction was coded correctly. Bill Strang of Cobalt Solutions coded the compressibility corrections to Spalart-Allmaras model as well as many other features that made this study possible. Dr. Dutton provided the experimental data.

References

[1] Forsythe, J. R., Hoffmann, K. A., and Dieteker, F.-F., 2000, ''Detached-Eddy Simulation of a Supersonic Axisymmetric Base Flow With an Unstructured Solver,'' AIAA Paper No. 2000-2410.

[2] Cummings, R. M., Yang, H. T., and Oh, Y. H., 1995, ''Supersonic, Turbulent Flow Computation and Drag Optimization for Axisymmetric Afterbodies,'' Comput. Fluids, **24**(4), pp. 487–507.

[3] Spalart, P. R., 1999, ''Strategies for Turbulence Modeling and Simulations,'' *4th International Symposium on Engineering Turbulence Modelling and Measurements*, Elsevier Science, Oxford, UK, pp. 3–17.

[4] Spalart, P. R., Jou, W-H., Strelets, M., and Allmaras, S. R., 1997, ''Comments on the Feasibility of LES for Wings, and on a Hybrid RANS/LES Approach,'' *Advances in DNS/LES, 1st AFOSR International Conference on DNS/LES*, Greyden Press, Columbus, OH.

[5] Shur, M., Spalart, P. R., Strelets, M., and Travin, A., 1999, ''Detached-Eddy Simulation of an Airfoil at High Angle of Attack,'' *4th International Symposium on Engineering Turbulence Modelling and Measurements*, Elsevier Science, Oxford, UK, pp. 669–678.

[6] Constantinescu, G. S., and Squires, K. D., 2000, ''LES and DES Investigations of Turbulent Flow Over a Sphere,'' AIAA Paper No. 2000-0540.

[7] Travin, A., Shur, M., Strelets, M., and Spalart, P. R., 2000, ''Detached-Eddy Simulation Past a Circular Cylinder,'' Int. J. Flow, Turb. Combust., **63**(1–4), pp. 293–313.

[8] Strelets, M., 2001, ''Detached Eddy Simulation of Massively Separated Flows,'' AIAA Paper No. 2001-0879.

[9] Herrin, J. L., and Dutton, J. C., 1994, ''Supersonic Base Flow Experiments in the Near Wake of a Cylindrical Afterbody,'' AIAA J., **32**(1), pp. 77–83.

[10] Bourdon, C. J., Smith, K. M., Dutton, M., and Mathur, T., 1998, ''Planar Visualizations of Large-Scale Turbulent Structures in Axisymmetric Supersonic Base Flows,'' AIAA Paper No. 98-0624.

[11] Murthy, S. N. B., and Osborn, J. R., 1976, ''Base Flow Phenomena With and Without Injection: Experimental Results, Theories, and Bibliography,'' *Aerodynamics of Base Combustion*, S. N. B. Murthy et al., eds. (Vol. 40 of Progress in Astronautics and Aeronautics), AIAA, Melville, NY, pp. 7–210.

[12] Dutton, J. C., Herrin, J. L., Molezzi, M. J., Mathur, T., and Smith, K. M., 1995, ''Recent Progress on High-Speed Separated Base Flows,'' AIAA Paper No. 95-0472.

[13] Morkovin, M. V., 1964, ''Effects of Compressibility on Turbulent Flows,'' *The Mechanics of Turbulence*, A. Favre, ed., Gordon and Breach, New York, pp. 367–380.

[14] Rubesin, M. W., ''Compressibility Effects in Turbulence Modeling,'' 1980-81 AFOSR-HTTM-Stanford Conference On Complex Turbulent Flows, Stanford University, Department of Mechanical Engineering, pp. 713–723.

[15] Goebel, S. G., and Dutton, J. C., 1991, ''Experimental Study of Compressible Turbulent Mixing Layers,'' AIAA J., **29**(4), pp. 538–546.

[16] Clemens, N. T., and Mungal, M. G., 1992, ''Two- and Three-Dimensional Effects in the Supersonic Mixing Layer,'' AIAA J., **30**(4), pp. 973–981.

[17] Delery, J., and Lacau, R. G., 1987, ''Prediction of Base Flows,'' AGARD Report 654.

[18] Pope, S. B., and Whitelaw, J. H., 1976, ''The Calculation of Near-Wake Flows,'' J. Fluid Mech., **73**(1), pp. 9–32.

[19] Putnam, L. E., and Bissinger, N. C., 1985, ''Results of AGARD Assessment of Prediction Capabilities for Nozzle Afterbody Flows,'' AIAA Paper No. 85-1464.

[20] Petrie, H. L., and Walker, B. J., 1985, ''Comparison of Experiment and Computation for a Missile Base Region Flowfield With a Centered Propulsive Jet,'' AIAA Paper No. 85-1618.

[21] Benay, R., Coet, M. C., and Delery, J., 1987, ''Validation of Turbulence Models Applied to Transonic Shock-Wave/Boundary-Layer Interaction,'' Rech. Aerosp., **3**, pp. 1–16.

[22] Caruso, S. C., and Childs, R. E., 1988, ''Aspects of Grid Topology for Reynolds-Averaged Navier-Stokes Base Flow Computations,'' AIAA Paper No. 88-0523.

[23] Childs, R. E., and Caruso, S. C., 1987, ''On the Accuracy of Turbulent Base Flow Predictions,'' AIAA Paper No. 87-1439.

[24] Childs, R. E., and Caruso, S. C., 1989, ''Assessment of Modeling and Discretization Accuracy for High Speed Afterbody Flows,'' AIAA Paper No. 89-0531.

[25] Peace, A. J., 1991, ''Turbulent Flow Predictions for Afterbody/Nozzle Geometries Including Base Effects,'' J. Propul. Power, **24**(3), pp. 396–403.

[26] Tucker, P. K., and Shyy, W., 1993, ''A Numerical Analysis of Supersonic Flow Over an Axisymmetric Afterbody,'' AIAA Paper No. 93-2347.

[27] Suzen, Y. B., Hoffmann, K. A., and Forsythe, J. R., 1999, ''Application of Several Turbulence Models for High Speed Shear Layer Flows,'' AIAA Paper No. 99-0933.

[28] Sahu, J., 1994, ''Numerical Computations of Supersonic Base Flow with Special Emphasis on Turbulence Modeling,'' AIAA J., **32**(7), pp. 1547–1549.

[29] Chuang, C. C., and Chieng, C. C., 1996, ''Supersonic Base Flow Computations Using Higher Order Turbulence Models,'' J. Spacecr. Rockets, **33**(3), pp. 374–380.

[30] Forsythe, J. R., Strang, W., and Hoffmann, K. A., 2000, ''Validation of Several Reynolds-Averaged Turbulence Models in a 3D Unstructured Grid Code,'' AIAA Paper No. 2000-2552.

[31] Harris, P. J., and Fasel, H. F., 1998, ''Numerical Investigation of the Unsteady Behavior of Supersonic Plane Wakes,'' AIAA Paper No. 98-2947.

[32] Fureby, C., Nilsson, Y., and Andersson, K., 1999, ''Large Eddy Simulation of Supersonic Base Flow,'' AIAA Paper No. 99-0426.

[33] Mathur, T., and Dutton, J. C., 1996, ''Base Bleed Experiments With a Cylindrical Afterbody in Supersonic Flow,'' J. Spacecr. Rockets, **33**(1), pp. 30–37.

[34] Baurle, R. A., Tam, C.-J., Edwards, J. R., and Hassan, H. A., 2001, ''An Assessment of Boundary Treatment and Algorithm Issues on Hybrid RANS/LES Solution Strategies,'' AIAA Paper No. 2001-2562.

[35] Strang, W. Z., Tomaro, R. F., and Grismer, M. J., 1999, ''The Defining Methods of Cobalt_{60}: A Parallel, Implicit, Unstructured Euler/Navier-Stokes Flow Solver,'' AIAA Paper No. 99-0786.

[36] Tomaro, R. F., Strang, W. Z., and Sankar, L. N., 1997, ''An Implicit Algorithm for Solving Time Dependent Flows on Unstructured Grids,'' AIAA Paper No. 97-0333.

[37] Grismer, M. J., Strang, W. Z., Tomaro, R. F., and Witzemman, F. C., 1998, ''Cobalt: A Parallel, Implicit, Unstructured Euler/Navier-Stokes Solver,'' Adv. Eng. Software, **29**(3–6), pp. 365–373.

[38] Karypis, G., and Kumar, V., 1997, ''METIS: Unstructured Graph Partitioning and Sparse Matrix Ordering System Version 2.0,'' Department of Computer Science, University of Minnesota, Minneapolis, MN.

[39] Karypis, G., Schloegel, K., and Kumar, V., 1997, ''ParMETIS: Parallel Graph Partitioning and Sparse Matrix Ordering Library Version 1.0,'' Department of Computer Science, University of Minnesota, Minneapolis, MN.

[40] Gottlieb, J. J., and Groth, C. P. T., 1988, ''Assessment of Reimann Solvers for Unsteady One-Dimensional Inviscid Flows of Perfect Gases,'' J. Comput. Phys., **78**, pp. 437–458.

[41] Spalart, P. R., and Allmaras, S. R., 1992, ''A One-Equation Turbulence Model for Aerodynamic Flows,'' AIAA Paper No. 92-0439.

[42] Spalart, P. R., 2000, ''Trends in Turbulence Treatments,'' AIAA Paper No. 2000-2306.

[43] Shur, M., Strelets, M., Zaikov, L., Gulyaev, A., Kozlov, V., and Secundov, A., ''Comparative Numerical Testing of One- and Two-Equation Turbulence Models for Flows with Separation and Reattachment,'' AIAA Paper No. 95-0863.

[44] Menter, F. R., 1991, ''Influence of Freestream Values on $k-\omega$ Turbulence Model Predictions,'' AIAA J., **30**(6), pp. 1657–1659.

[45] Menter, F. R., 1992, ''Improved Two-Equation $k-\omega$ Turbulence Models for Aerodynamic Flows,'' NASA-TM-103975.

[46] Menter, F. R., 1994, ''Two-Equation Eddy-Viscosity Turbulence Models for Engineering Applications,'' AIAA J., **32**(8), pp. 1598–1605.

[47] Suzen, Y. B., and Hoffmann, K. A., 1998, ''Investigation of Supersonic Jet Exhaust Flow by One- and Two-Equation Turbulence Models,'' AIAA Paper No. 98-0322.

[48] Forsythe, J. R., Hoffmann, K. A., and Suzen, Y. B., 1999, ''Investigation of Modified Menter's Two-Equation Turbulence Models for Supersonic Applications,'' AIAA Paper No. 99-0873.

[49] Wilcox, D. C., 1998, *Turbulence Modeling for CFD*, 2nd Ed., DCW Industries, La Cañada, CA.

[50] Pirzadeh, S., 1996, ''Three-Dimensional Unstructured Viscous Grids by the Advancing Layers Method,'' AIAA J., **34**(1), pp. 43–49.

[51] Steinbrenner, J., Weyman, N., and Chawner, J., 2000, ''Development and Implementation of Gridgen's Hyperbolic PDE and Extrusion Methods,'' AIAA Paper No. 2000-0679.

[52] Spalart, P., 2001, ''Young-Person's Guide to Detached-Eddy Simulation Grids,'' NASA CR 2001-211032.

[53] Forsythe, J. R., Hoffmann, K. A., and Squires, K. D., 2002, ''Detached-Eddy Simulation With Compressibility Corrections Applied to a Supersonic Axisymmetric Base Flow,'' AIAA Paper No. 2002-0586.

Detached-Eddy Simulations and Reynolds-Averaged Navier-Stokes Simulations of Delta Wing Vortical Flowfields

Scott Morton
Associate Professor

James Forsythe
Associate Professor

Anthony Mitchell
Assistant Professor

David Hajek

Department of Aeronautics,
United States Air Force Academy
USAF Academy, CO 80840-6400

An understanding of vortical structures and vortex breakdown is essential for the development of highly maneuverable vehicles and high angle of attack flight. This is primarily due to the physical limits these phenomena impose on aircraft and missiles at extreme flight conditions. Demands for more maneuverable air vehicles have pushed the limits of current CFD methods in the high Reynolds number regime. Simulation methods must be able to accurately describe the unsteady, vortical flowfields associated with fighter aircraft at Reynolds numbers more representative of full-scale vehicles. It is the goal of this paper to demonstrate the ability of detached-eddy Simulation (DES), a hybrid Reynolds-averaged Navier-Stokes (RANS)/large-eddy Simulation (LES) method, to accurately predict vortex breakdown at Reynolds numbers above 1×10^6. *Detailed experiments performed at Onera are used to compare simulations utilizing both RANS and DES turbulence models.* [DOI: 10.1115/1.1517570]

Introduction

The delta wing flowfield is dominated by vortical structures, the most prominent of which are the leading-edge vortices. As the angle of attack increases, these leading-edge vortices experience a sudden disorganization, known as vortex breakdown, which can be described by a rapid deceleration of both the axial and swirl components of the mean velocity and, at the same time, a dramatic expansion of the vortex core. Henri Werlé first photographed the vortex breakdown phenomenon in 1954, during water tunnel tests of a slender delta wing model at Onera [1]. This work was quickly confirmed by Peckham and Atkinson [2], Elle [3], and Lambourne and Bryer [4] and spawned a large number of experimental, computational, and theoretical studies which continue today. These investigations led to the development of several theories governing vortex breakdown, although none have been universally accepted [5–9]. Despite this lack of a unified theoretical interpretation, several forms of vortex breakdown have been identified, [7,10] (i.e. bubble, helical, etc.), and the global characteristics of the phenomena are understood. During the breakdown process, the mean axial velocity component rapidly decreases until it reaches a stagnation point and/or becomes negative on the vortex axis. This stagnation point, called the breakdown location, is unsteady and typically oscillates about some mean position along the axis of the vortex core [11,12]. As the angle of attack is increased, the mean vortex breakdown location moves upstream over the delta wing (from the trailing edge toward the apex).

The leading-edge vortex over a slender delta wing at angle of attack is principally inviscid. Unfortunately, the location of the vortex is strongly affected by a secondary vortex formed by the inter-relationship between the surface boundary layer and the leading-edge vortex. In addition, the vortex breakdown phenomenon creates turbulent kinetic energy that must be either modeled properly or resolved. Several researchers [13–15], have demonstrated that typical turbulence models create excessive turbulent eddy viscosity in the leading-edge vortex core, which significantly alters the flowfield, and in some cases eliminates breakdown, which is observed experimentally at high Reynolds numbers. For these reasons, an accurate prediction of the flowfield over a slender delta wing at high angles of attack and high Reynolds numbers must correctly capture the boundary layer, leading-edge and secondary vortices, and turbulent kinetic energy.

Gordnier [13] demonstrated the inability of a typical Reynolds averaged Navier-Stokes (RANS) methods ($k-\varepsilon$) to accurately predict high Reynolds number vortical flowfields, by computing solutions of a 65 deg delta wing at 15 deg and 30 deg angle of attack at a root-chord-based Reynolds number of 3.67 million. He applied a correction to the $k-\varepsilon$ turbulence model proposed by Menter [16] to limit the production of eddy viscosity in regions where the vorticity overwhelms the strain rate. For the 15 deg angle of attack case he found a significant improvement in comparison with experiment when applying the correction. Unfortunately, he also found that at the 30 deg angle of attack case that exhibits vortex breakdown, the model produced a mean flow solution with a bubble-type breakdown when the experiments showed a helical-type breakdown. He postulated that the RANS formulation would only predict the mean flow characteristics even when an unsteady RANS simulation was being performed. Dacles-Mariani [17] proposed a similar correction to the Spalart-Allmaras turbulence model but was shown by Murman and Chaderjian [14] to have a limited improvement when applied to the same 65 deg delta wing case if the model was based on production limiting when the vorticity magnitude was in direct proportion to the strain rate. He also found the computed solution's comparison with experiment degraded with improved grid resolution on the delta wing studied. Murman [15] developed a Galilean invariant and computationally efficient correction to the Spalart-Allmaras turbulence model called "vortex filtering." His vortex filtering method utilized the velocity gradient tensor to determine whether the vorticity is generated inside or outside of the boundary layer and limit the production of eddy viscosity outside of the boundary layer in a free vortex. Murman [15] applied the method to a tangent-ogive cylinder and demonstrated successful comparison with experiments for steady-state pressures on the delta-wing surface. Spalart and Shur [18] proposed corrections to the baseline Spalart-Allmaras model to account for streamline curvature and system rotation and applied it successfully to wing tip vortices. Unfortunately, the formulation has not been adopted by many re-

Contributed by the Fluids Engineering Division for publication in the JOURNAL OF FLUIDS ENGINEERING. Manuscript received by the Fluids Engineering Division March 20, 2002; revised manuscript received June 13, 2002. Associate Editor: F. F. Grinstein.

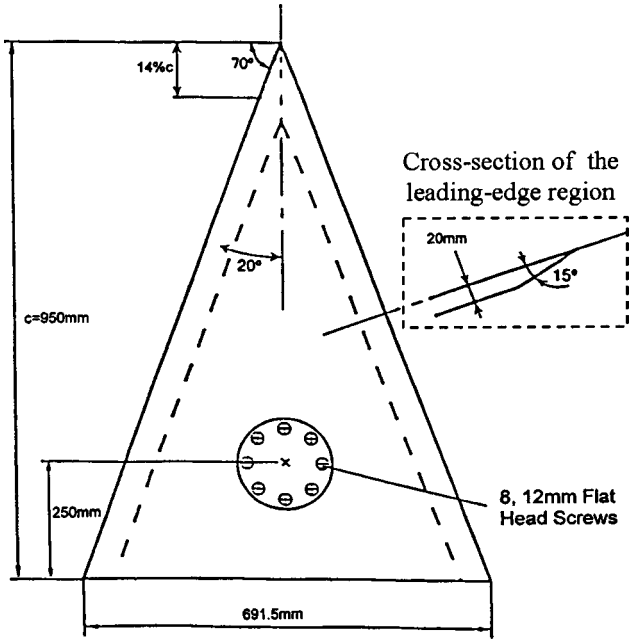

Fig. 1 Sketch of the experimental delta wing model of Onera

searchers due to its complicated formulation and large computational requirements. The advantage of Spalart and Shur's [18] correction to the Spalart-Allmaras turbulence model is its applicability to a very general set of problems. None of these corrections were shown to accurately reproduce the experimentally observed unsteady vortex breakdown phenomenon.

Even with the corrections described above, the turbulence models employed in RANS methods are designed to model, rather than resolve, the entire spectrum of turbulent motions and have been shown to be inadequate in capturing the flows characterized by massive separation and inherent unsteadiness. Unsteady massively separated flows are characterized by geometry-dependent and three-dimensional turbulent eddies; it is probable that these eddies are what make RANS turbulence models inadequate for these flowfields. There are many instances where the time-accurate description of these three-dimensional turbulent structures must be accurately determined (i.e., aeroelasticity, aeroacoustics, engine inlet design). If the primary goal is to simulate the unsteady loads on surfaces, a new approach must be developed.

To overcome the deficiencies of RANS models for predicting massively separated flows, Spalart et al. [19] proposed detached-eddy simulation (DES) with the objective of developing a numerically feasible and accurate approach combining the most favorable elements of RANS models and LES. The primary advantage of DES is that it can be applied at high Reynolds numbers (as can RANS techniques), but also resolve geometry-dependent, unsteady three-dimensional turbulent motions as in LES. DES predictions to date have demonstrated favorable results, [20–22], forming one of the motivations for this research. The specific aim of this work is to apply and assess RANS and DES methods for the problem of vortex breakdown over slender delta wings at high Reynolds number.

Numerical Method

In this section a brief description of the numerical method is provided with full details of the computational scheme and the solution method presented in Ref. [23]. The delta wing surface description is based on Onera's experimental sharp-edged, 70 deg sweep angle (Λ) delta wing with a root chord (c) of 950 mm (Fig. 1). The model has a wingspan of 691.5 mm at its trailing edge, is 20 mm thick, and is beveled on the windward side at an angle of 15 deg to form a sharp leading edge. Solutions were obtained for a freestream velocity of 24 m/s, an angle of attack of 27 deg, and a freestream pressure and temperature resulting in a Reynolds number of 1.56×10^6. The numerical simulation matched the angle of attack, Reynolds number, and Mach number of the wind tunnel experiments, [12,24].

Solutions are computed using the commercially available solver Cobalt. Cobalt is an unstructured finite volume method developed for solution of the compressible Navier-Stokes equations with details of the approach described in Ref. [23]. The method is a cell-centered finite volume approach applicable to arbitrary cell topologies including hexahedrals, prisms, and tetrahedra. The spatial operator uses an exact Riemann solver, least-squares gradient calculations using QR factorization to provide second-order accuracy in space, and TVD flux limiters to limit extremes at cell faces. A point implicit method using analytic first-order inviscid and viscous Jacobians is used for advancement of the discretized system. A Newton subiteration scheme is employed to improve time accuracy. All solutions were computed with at least two Newton subiterations, allowing second-order accuracy in both time and space.

The computational mesh used in all simulations, unless otherwise noted, is a 2.45×10^6 cell, unstructured mesh, generated with the software packages GridTool, [25], and VGRIDns, [26]. It consists of an inner region of 13 layers of prisms for the boundary layer, with a wall normal spacing in viscous wall units less than 1, and an outer region of tetrahedra. The prism dimensions on the surface were a factor of approximately 200 times larger than the wall normal dimension. Figure 2 depicts one of the delta wing grids used for this study. Additional grids were used to perform a grid sensitivity study and are described in detail in a later section. As is evident in the figure, cells are clustered in the boundary layer and in the region of the vortex core. Also, the grid represents only the half-span of the delta wing and does not include the sting or wind tunnel walls of the experiment. All simulations of the current work are for the half-span geometry.

Turbulence Models. Cobalt has several choices of turbulence models including Spalart Allmaras (SA), [27], and shear stress transport (SST), [28], RANS, as well as DES based on either SA or SST models, [20]. In addition, an SA turbulence model with approximate rotation corrections (ASARC), [17,29], was implemented for the current study. The following subsections describe the turbulence models used for comparison in the current work, and provides references for more detailed descriptions.

Spalart-Allmaras (SA) Turbulence Model. The Spalart-Allmaras [27], one-equation turbulence model solves a single partial differential equation for a working variable related to the turbulent viscosity. The differential equation is derived by using empiricism arguments of dimensional analysis, Galilean invariance, and selected dependence on the molecular viscosity [27]. The model includes a wall destruction term that reduces the turbulent viscosity in the laminar sublayer and the log layer. Details of the model implementation and all coefficients are given in Ref. [29]. Solutions presented in the current work using the Spalart-Allmaras model are referred to as SA.

Approximate SA-Rotation Correction Model. The Dacles-Mariani [17], correction to the Spalart-Allmaras (SA) turbulence model was implemented to provide a comparison case for the DES method. The modification to SA includes a destruction term in the modified vorticity based on the magnitude of vorticity and the strain rate. The modified vorticity is expressed as

$$\tilde{S}\equiv S+\frac{\tilde{\nu}}{\kappa^2 d^2}f_{v2}+C_{\mathrm{vor}}\min(0,\hat{S}-S)$$

where S is the magnitude of the vorticity, $\hat{S}$ is the strain rate, $\tilde{\nu}$ is the modified turbulent viscosity, κ is the turbulent kinetic energy, d is the distance to the nearest wall, f_{v2} is defined in Ref. [17],

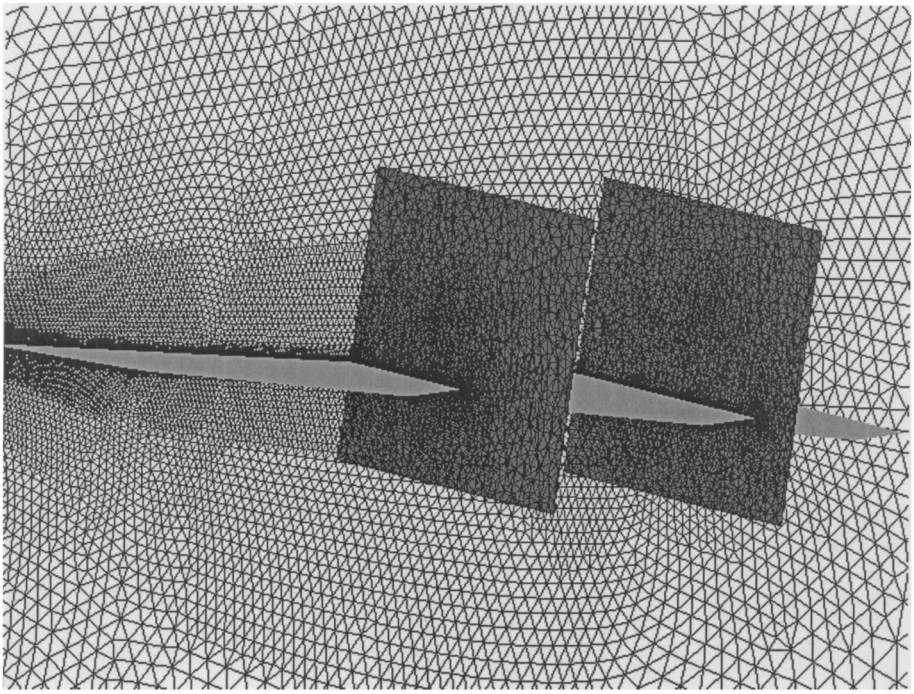

Fig. 2 Unstructured prism/tetrahedra grid with vortex core refinement, 2.45×10^6 cells

and C_{vor} is a constant taken to be 4 for all runs. It should be noted that this value of C_{vor} provides a very strong correction—when the strain rate magnitude is 3/4 of the vorticity magnitude, the production term will be essentially zero. This allows vortical, turbulent flows to be calculated with a RANS turbulence model without too much dissipation being added to the vortex core, which typically eliminates the vortex breakdown phenomenon seen in experiments. The SA model with the approximate rotation corrections will be referred to as ASARC in the results section.

Menter's Shear Stress Transport Model. Menter's shear stress transport model [28], is a hybrid of the $k-\varepsilon$ and $k-\omega$ turbulence models. Typical $k-\omega$ models are well behaved in the near wall region where low Reynolds number corrections are not required. However, they are generally sensitive to the freestream values of ω. On the other hand, $k-\varepsilon$ models are relatively insensitive to freestream values, but behave poorly in the near-wall region. Menter proposed a hybrid model. The SST model uses a parameter F_1 to switch from $k-\omega$ to $k-\varepsilon$ in the wake region to prevent the model from being sensitive to freestream conditions. The governing differential equations, including a compressibility correction, along with the complete set of constants, are detailed in Ref. [29].

Detached-Eddy Simulation. The DES model was originally based on the Spalart-Allmaras one-equation RANS turbulence model (detailed above, with a more detailed presentation in Ref. [19]). The wall destruction term presented above is proportional to $(\tilde{\nu}/d)^2$. When this term is balanced with the production term, the eddy viscosity becomes proportional to $\hat{S}d^2$. The Smagorinski LES model varies its subgrid-scale (SGS) turbulent viscosity with the local strain rate, and the grid spacing described by $\nu_{\text{SGS}} \propto \hat{S}\Delta^2$, where $\Delta=\max(\Delta x,\Delta y,\Delta z)$. If d is replaced with Δ in the wall destruction term, the SA model will act as a Smagorinski LES model. To exhibit both RANS and LES behavior, d in the SA model is replaced by

$$\tilde{d}=\min(d,C_{\text{DES}}\Delta), \quad C_{\text{DES}}=0.65$$

When $d\ll\Delta$, the model acts in a RANS mode and when $d\gg\Delta$ the model acts in a Smagorinski LES mode. Therefore, the model switches into LES mode when the grid is locally refined. DES was implemented in an unstructured grid method by Forsythe et al. [21]. They determined the C_{DES} constant could be 0.65, consistent with the structured grid implementation of Shur et al. [30], when the grid spacing Δ was taken to be the longest distance between the cell center and all of the neighboring cell centers. The DES turbulence model based on the SA RANS model is referred to as SADES in all following sections.

Strelets [20] introduced a DES model based on Menter's shear stress transport (SST) model (called SSTDES in all following sections). The DES modification to the SST model replaces the length scale, $l_{k-\omega}$, by

$$\tilde{l}=\min(l_{k-\omega},C_{\text{DES}}\Delta)$$

where

$$l_{k-\omega}=\frac{k^{1/2}}{\beta^*\omega}, \quad \beta^*=0.09, \quad C^{k-\varepsilon}{}_{\text{DES}}=0.61, \quad C^{k-\omega}{}_{\text{DES}}=0.78,$$

in the dissipation term of the k-transport equation.

Experimental Method and Facilities

The experimental data used for comparison were obtained by Mitchel et al. [12] from ONERA's F2 wind tunnel. ONERA's F2 wind tunnel has a rectangular test section with a width of 1.4 m, a height of 1.8 m, and a length of 5 m. It is powered by a 680 kW DC motor that drives a fan with blades spanning 3.15 m and provides a maximum freestream velocity in the test section of 105 m/s. A cooling system in the closed-return portion of the wind tunnel facility maintains a constant freestream temperature in the test section. The relative freestream velocity, $\Delta U_0/U_0$, is estimated to have an accuracy of 1%, while the mean intensity of turbulence has an accuracy of 0.1%, [12].

In the wind tunnel, the delta wing model depicted in Fig. 1 was mounted on a sting with a horizontal support and flexible joint for adjusting the angle of attack, with an accuracy of ±0.05 deg. The horizontal support was manipulated in height along a vertical column so as to maintain the model close to the center axis of the test

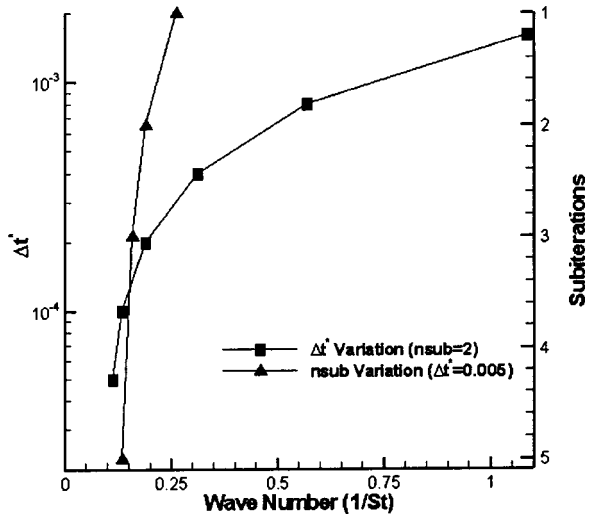

Fig. 3 Wave number convergence for a variation in time-step and subiteration using the SADES turbulence model and the baseline grid

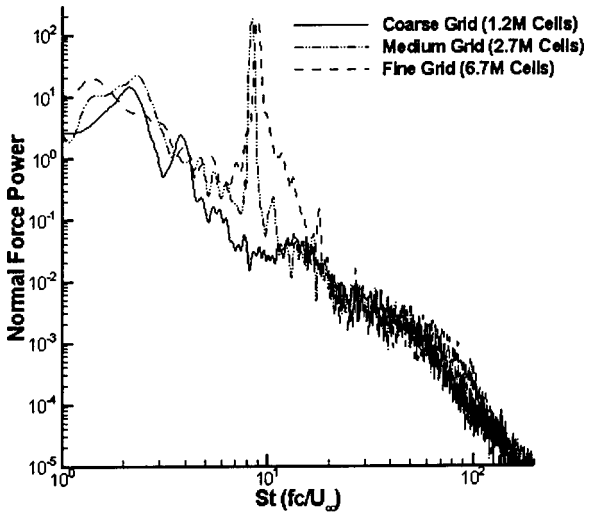

Fig. 4 MATLAB power spectral density analysis of normal force for three grids

section. The model was mounted in the test section with no yaw angle with respect to the freestream flow (estimated accuracy of ± 0.1 deg). The experimental dataset consists of steady surface pressure data on the leeward surface of the delta wing and laser Doppler velocimeter data in planes parallel to the top surface, perpendicular to the top surface spanwise, and perpendicular to the top surface along the vortex core [12].

Results

This section presents results of the numerical simulations, as well as comparison of these simulations to the Onera experimental data. All cases were run at a freestream velocity of 24 m/s, a Mach number of 0.069, an angle of attack of 27 deg, and other freestream conditions consistent with a Reynolds number of 1.56×10^6. No attempt was made to model transition from laminar to turbulent flow on the delta wing. In all cases the spatial and temporal operators were second-order accurate. Typical unsteady simulations were run for 9000 time-steps, with an iteration plus two subiterations per time-step. The baseline time-step, nondimensionalized by the root chord and freestream velocity, was 0.005.

Time Accuracy Study. When computing solutions for unsteady flowfields such as vortex breakdown, it is important to determine the degree to which the solution is time accurate. Since a major goal is to reproduce unsteady surface loads, the unsteady normal force was used to determine the time accuracy of the simulations. The delta wing normal force was analyzed with MATLAB's power spectral density (PSD) function. The PSD power was scaled by the number of iterations analyzed and the output frequency was nondimensionalized by the root chord and freestream velocity, giving the Strouhal number, $\mathrm{St}=fc/U_\infty$. To show a convergence of frequency with time-step, the data from SADES simulations was plotted versus the inverse of the Strouhal number (or the wave number) and the wave number with the highest power was tracked to determine if there was any change with respect to time step. After analyzing the time-accurate data and correlating the dominant frequency with structures in the flowfield, it was determined that the wave number chosen is created by the formation of alternating vortical structures shed from the blunt trailing edge. If this dominant frequency is scaled by the trailing edge base height instead of the root chord, the resulting St number is approximately 0.21, a typical shedding frequency. As can be seen in Fig. 3, as the nondimensional time step is halved, the wave number decreases. For the three largest time-steps, a change in the wave number is approximately equivalent to the decrease in time-step; the three most refined time steps rapidly approach an asymptotic value of wave number.

Cobalt also utilizes Newton subiteration to improve time accuracy. In the previous cases, an initial iteration plus two Newton subiterations were performed. To determine the effect of varying the number of subiterations, four different subiteration values were used with a nondimensional time step of 0.005 and the results are presented in Fig. 3, demonstrating that the wave number is reduced as the number of subiterations is increased. Figure 3 displays the primary wave number versus the time-step and number of subiterations. One can see from the figure that the asymptotic value of the wave number is approximately 0.1 ($\mathrm{St}=10$). The baseline nondimensional time step of 0.005 and two subiterations results in a wave number of 0.188, and were used for the majority of the simulations hereafter. Although the choices of time step and number of Newton subiterations result in a simulation with a dominant wave number different than the asymptotic value, the simulation is qualitatively correct and can be used to analyze the effect of changing the turbulence model if the choices are used consistently.

Grid Resolution Study. A detailed grid resolution study was performed and documented in Ref. [31]. The baseline grid of 2.45×10^6 cells discussed above is approximately equivalent to the medium grid of Ref. [31]. Figure 4 depicts a normal force PSD plot comparison between course, medium, and fine grids of 1.2×10^6, 2.7×10^6, and 6.7×10^6 cells, respectively. The grid refinement study was accomplished by first developing a consistent set of three grids. The medium grid, similar to the baseline grid discussed above, was produced first. The coarse and fine grids were developed by modifying the growth rates by either a factor of a square root of two or the inverse of a square root of two. This produces a set of grids with cell sizes in the vortex breakdown region varying by a square root of two in each coordinate direction. The viscous region is approximately the same in the wall normal direction for each grid but the surface distribution was modified by the same scaling factor. A nondimensional time-step of 0.0025 was used for the medium grid and the coarse and fine grid time-steps were a factor of square-root-two larger and smaller, respectively. Figure 4 demonstrates the ability of the medium grid to capture the dominant frequency of 10 within 6%. Although higher frequency content is improved on the fine grid (Fig. 4), the medium grid seems sufficient to explore the effects of the various turbulence models.

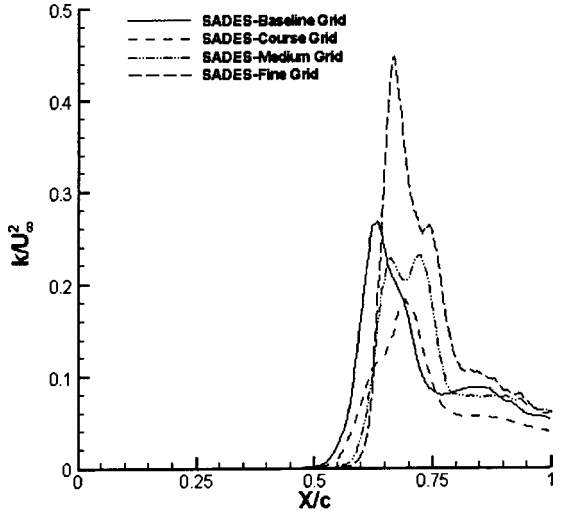

Fig. 5 Resolved turbulent kinetic energy along the vortex core scaled by the freestream velocity squared for four different grids

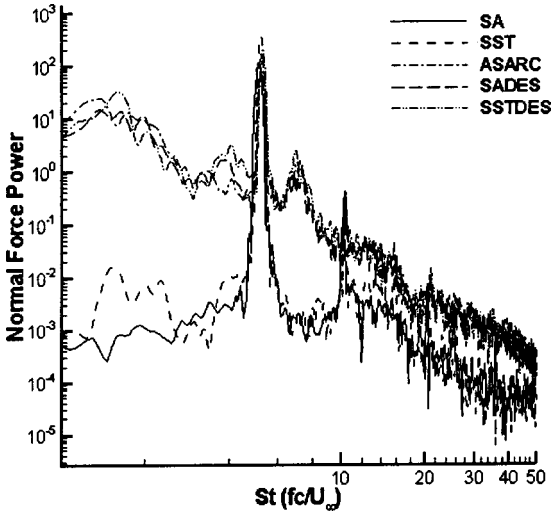

Fig. 6 MATLAB power spectral density analysis of the unsteady normal force for various turbulence models

Figure 5 depicts the resolved turbulent kinetic energy along the core, nondimensionalized by the freestream velocity squared, for the four grids used in the current work. The medium and fine grids capture the vortex breakdown position, as measured by a sharp rise in resolved turbulent kinetic energy, but are a factor of two different in peak resolved turbulent kinetic energy. The experiments documented in Ref. [12] show a peak value of nondimensional turbulent kinetic energy of 0.5, which is within 10% of the fine-grid peak. The baseline grid core resolved turbulent kinetic energy peak is within 10% of the medium grid peak but the vortex breakdown position is upstream of the medium grid breakdown position. This difference can be attributed to the larger time-step and smaller number of subiterations, which produces larger temporal error. Nevertheless, the comparison is in close enough agreement to use the baseline grid, time-step, and number of subiterations to perform a valid comparison between the various turbulence models.

Turbulence Model Study. After determining that the relevant vortical flow features were being captured by the grid, and that a reasonable level of time accuracy was obtained, a study of various RANS and DES turbulence models was accomplished. Figure 6 depicts the normal force PSD power versus Strouhal frequency for the SA, SST, ASARC, SADES, and SSTDES turbulence models. All cases were run for at least 9000 iterations. Transients from the initiation of the run were eliminated from the datasets analyzed by eliminating the first 1000 iterations in the frequency analysis.

Several conclusions can be made from Fig. 6. First, the SA and SST RANS models used widely in industry are not able to capture the majority of the frequencies in the spectrum. In the case of both RANS models, all frequencies, except the dominant frequency previously discussed, have a power which could be reasonably associated with random noise. On the other hand, the ASARC model compares surprisingly well with the DES methods. This is most likely due to the fact that the rotation correction is very effective in eliminating the affects of turbulence dissipation in the core of the vortex. The only range of frequencies the ASARC model is not able to capture as well as the DES methods is $3 < St < 5$, where the power is not as high as the DES methods. Finally, both DES methods are able to capture the full range of frequencies resident in the simulation of delta wings at high angles of attack. This additional frequency content not captured by the ASARC, SA, or SST turbulence models is most likely coming from the post-breakdown LES resolved eddies. One further note concerning the ASARC model is the fact that although it is able to capture the high Reynolds number vortex breakdown phenomena fairly well, the simulation has little hope of improving with a refinement in grid, as is the case with the DES methods, since RANS models have no grid dependence. Also, ASARC is only an improvement in typical RANS models for vortical flows, while simulations with either DES method can also simulate massive separation not associated with strong vortices [22].

Figures 7–10 depict the flowfields for all of the turbulence models except the SST RANS model (the SST RANS model results are not visibly different than the SA RANS model). The left side of the figure depicts an iso-surface of vorticity magnitude and the right side depicts an iso-surface of total pressure. All of the figures use consistent iso-surface values. Notice the SA model's inability to predict the vortex breakdown core enlargement commonly seen in experiments, [12]. Also, note the similarity between the ASARC and DES solutions. It is a matter of further research whether the ASARC method is over correcting for the streamline curvature effects due to the simplified formulation. It is apparent that the two DES methods are consistent in their ability to capture vortex breakdown, the post-breakdown helical structures, and the tertiary vortices observed in experiments, [12].

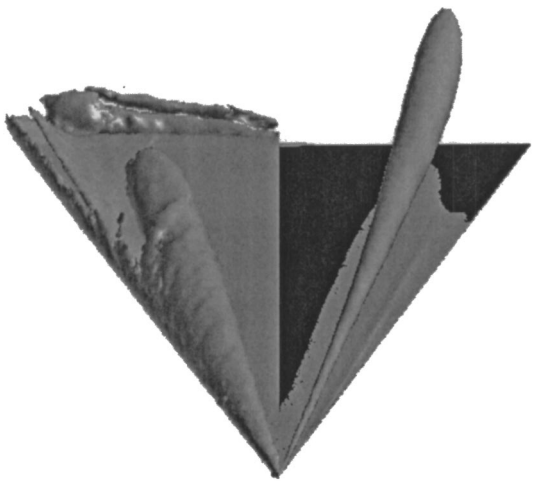

Fig. 7 Instantaneous iso-surfaces of vorticity magnitude (left side) and total pressure (right side) for the Spalart-Allmaras turbulence model

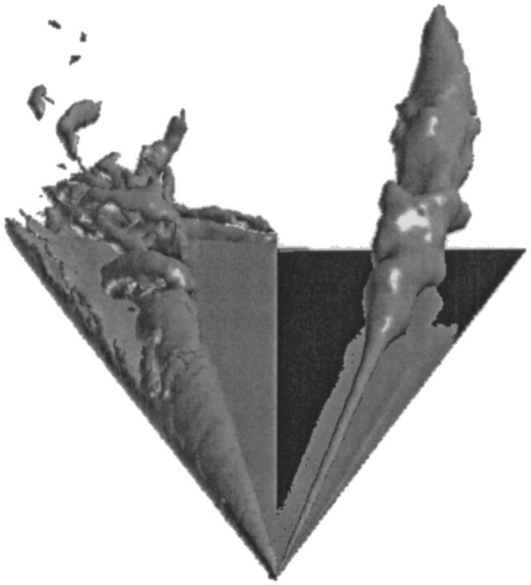

Fig. 8 Instantaneous iso-surfaces of vorticity magnitude (left side) and total pressure (right side) for the Spalart-Allmaras turbulence model with approximate rotation corrections

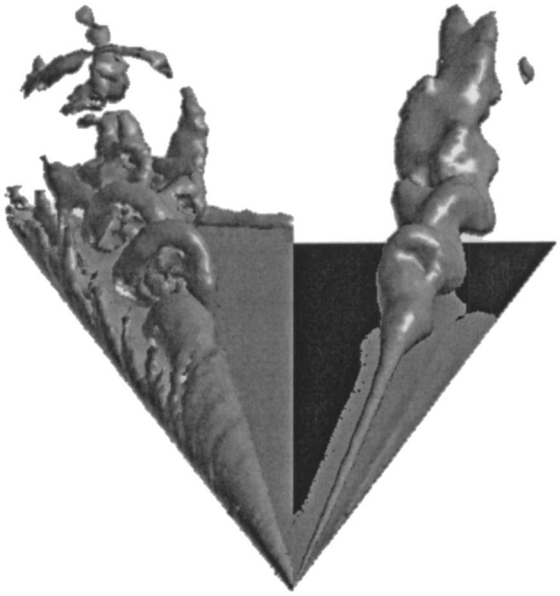

Fig. 10 Instantaneous iso-surfaces of vorticity magnitude (left side) and total pressure (right side) for the shear stress transport detached eddy simulation turbulence model

One of the most difficult quantities to capture accurately in a numerical simulation is the turbulent kinetic energy. Figure 11 demonstrates the ability of the simulations with various turbulence models to produce the resolved turbulent kinetic energy in the core of the vortex aft of the vortex breakdown location. Figure 9 is a plot of resolved turbulent kinetic energy, nondimensionalized by the freestream velocity squared, versus the location along the chord. All of the turbulence models have a value of resolved turbulent kinetic energy of zero prior to the vortex breakdown position. Aft of the breakdown position, the two RANS methods still have essentially zero-resolved turbulent kinetic energy along the core. The ASARC, SADES, and SSTDES turbulence models all predict very similar resolved turbulent kinetic energy profiles.

The probable cause of typical turbulence models inability to accurately capture vortex breakdown is the excessive amount of eddy viscosity they generate in the core of strong vortices. Figure 12 depicts the eddy-viscosity ratio along the vortex core as a function of chordwise position. The SA RANS method produces extremely large values of eddy viscosity all along the vortex core. The SST model is much more limited in its production of eddy viscosity prior to vortex breakdown but then produces similarly large values of eddy viscosity post-breakdown. The ASARC model virtually eliminates the eddy viscosity produced pre-breakdown but then produces significantly larger values post-breakdown. The SADES model produces fairly large values of eddy viscosity pre-breakdown but not post-breakdown due to the grid refinement in the post-breakdown region. The SSTDES

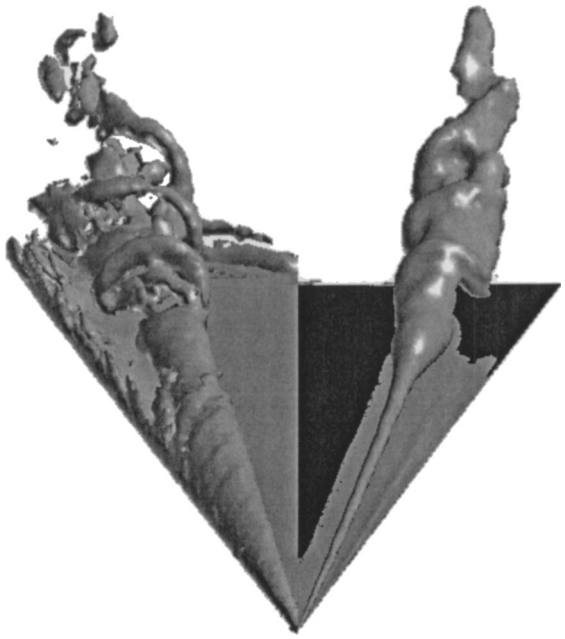

Fig. 9 Instantaneous iso-surfaces of vorticity magnitude (left side) and total pressure (right side) for the Spalart-Allmaras detached eddy simulation turbulence model

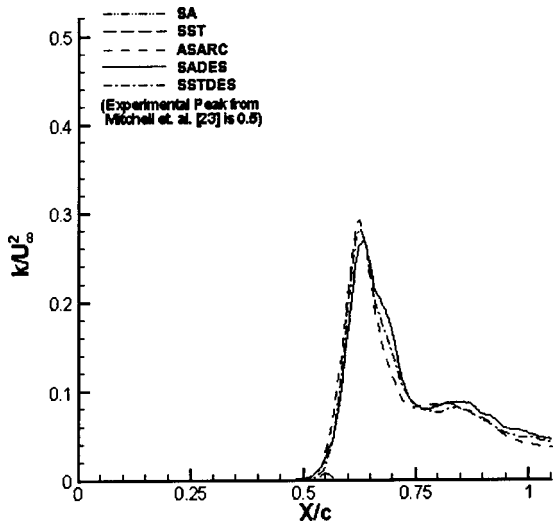

Fig. 11 Resolved turbulent kinetic energy along the vortex core scaled by the freestream velocity squared for five different turbulence models

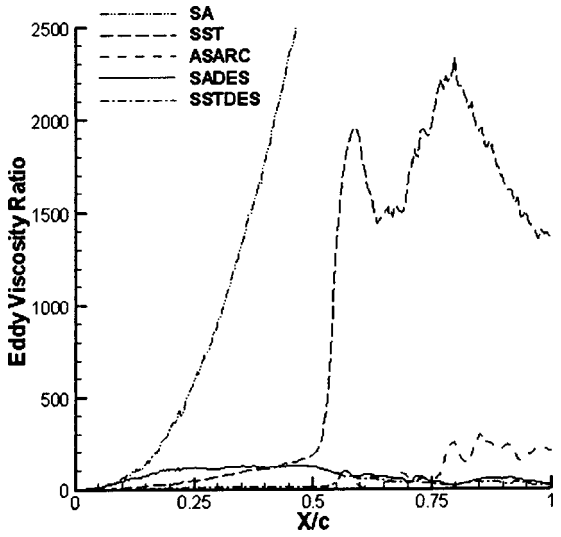

Fig. 12 Eddy-viscosity ratio along the vortex core for five different turbulence models

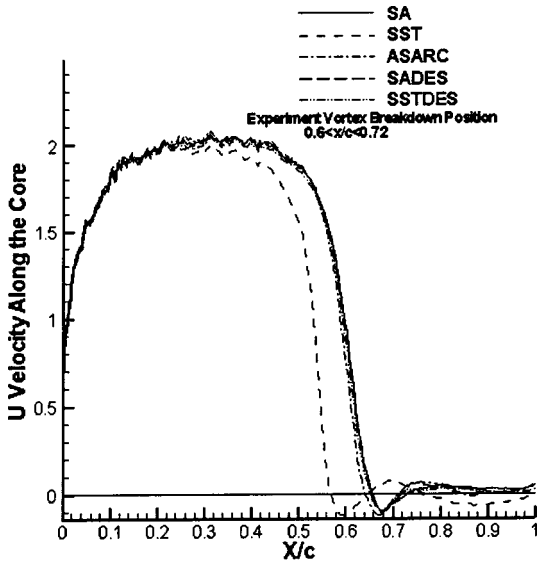

Fig. 14 Streamwise velocity along the vortex core as a function of chord location

method produces limited values pre and post-breakdown. Figure 12 demonstrates the need for a DES method with rotation corrections in the RANS part of the hybrid method even though post-breakdown is in LES mode because of the grid resolution.

Comparison With Experiment. The experimental data of Mitchel et al. [12] was next used to determine if there is qualitative agreement between the experiments and the simulations. It should be noted that the grids used in the numerical simulations did not model either the sting or the wind tunnel walls. Since the Onera model created a blockage of approximately 14% at a 24 deg angle of attack, it is expected that there will be some disagreement between the experiments and the simulations since tunnel blockage typically manifests itself as a change in the effective angle of attack. Figure 13 depicts the vortex breakdown position as a function of angle of attack for the experiments. The variation in vortex breakdown position ranged from 60% to 72% in the experiments. Figure 14 depicts the streamwise velocity along the core of the vortex as a function of chord location. A very common method of defining vortex breakdown position is when the streamwise component of velocity is equal to zero. All of the turbulence models except for the SST RANS model produced vortex breakdown positions within the range of the experiments, with the SST RANS method upstream by approximately 10%. This is surprising when considering the vorticity iso-surface differences between the models presented in Figs. 7–10. Although the actual vortex breakdown position seems to be predicted well by the RANS methods, the overall characteristics of the breakdown structure are not consistent with the experiments.

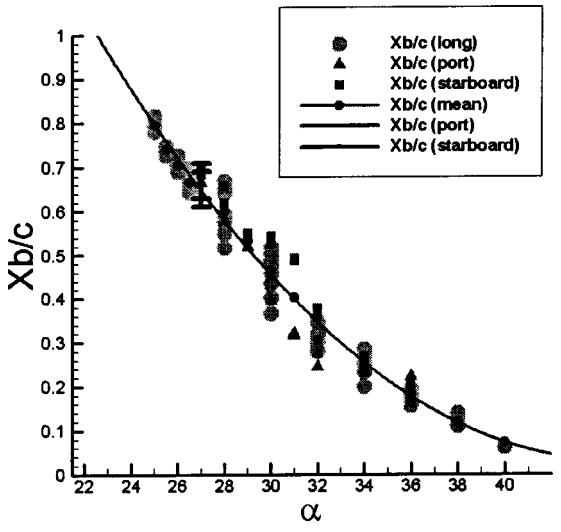

Fig. 13 Chord location of vortex breakdown as a function of angle of attack from the experiments of Mitchell et al. [24]

Figure 15 depicts the resolved turbulent kinetic energy contours of ASARC, SSTDES, and SADES (including a time-step and grid variation) as well as the experimentally determined turbulent kinetic energy contours in a plane essentially parallel to the surface but inclined through the vortex core. The ASARC simulation achieved a peak value similar to the experiments but the region of high intensity extends further aft than the experiment. The SSTDES method shows general agreement in the shape of the contours but does not achieve the peak value of turbulent kinetic energy. The SADES method shows an ability to match the experiment in shape and improve the peak comparison with grid refinement.

Figure 16 depicts cross-plane contours of vorticity at two longitudinal stations for the LDV experiments, and instantaneous contours for the SADES method on the medium and fine grids. The overall shape of the vorticity contours is captured very well by the SADES method at both stations, and the core vorticity magnitude approaches the experiment as the grid is refined at the 500 mm station. At the 600 mm station, the experiment does not show vortex breakdown for the case presented, whereas post-breakdown is observed for the particular instant of time chosen for the simulation. An increase in vorticity level is observed with grid resolution at the 600 mm station as well.

Conclusions and Recommendations

DES simulations of a delta wing experiencing vortex breakdown were successfully computed and compared to RANS simulations and an experiment. These solutions were shown to be sensitive to time accuracy in the frequency domain, but achieved an asymptotic solution as time step was reduced. The SA and SST typical RANS turbulence models were shown to be inadequate in capturing the physics of vortex breakdown at high Reynolds number, whereas, both DES turbulence models and the ASARC turbulence model captured the spectrum of frequencies and compared well with the experimental data.

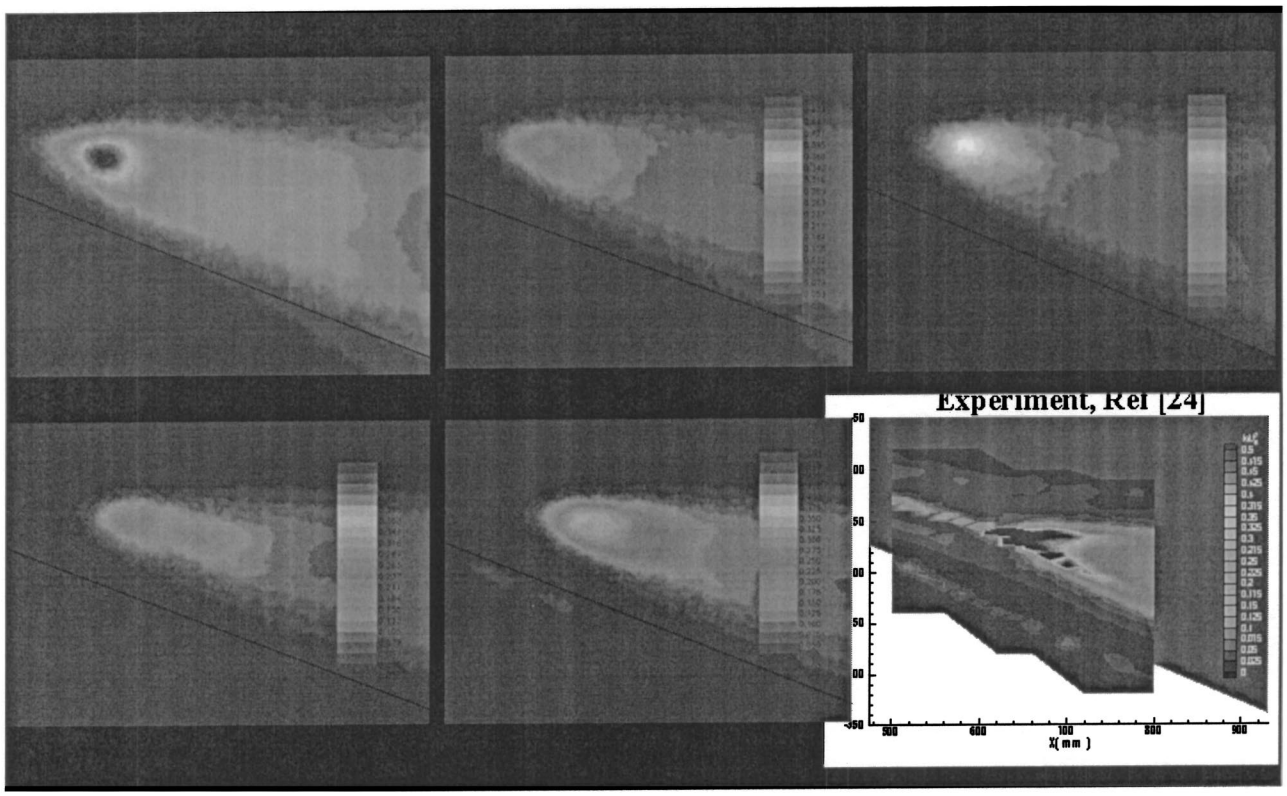

Fig. 15 Longitudinal plane of turbulent kinetic energy nondimensionalized by the freestream velocity squared through the core of the vortex for various turbulence models and from the experiments of Mitchell et al. [24] (* denotes baseline grid and nondimensional time-step of 0.005)

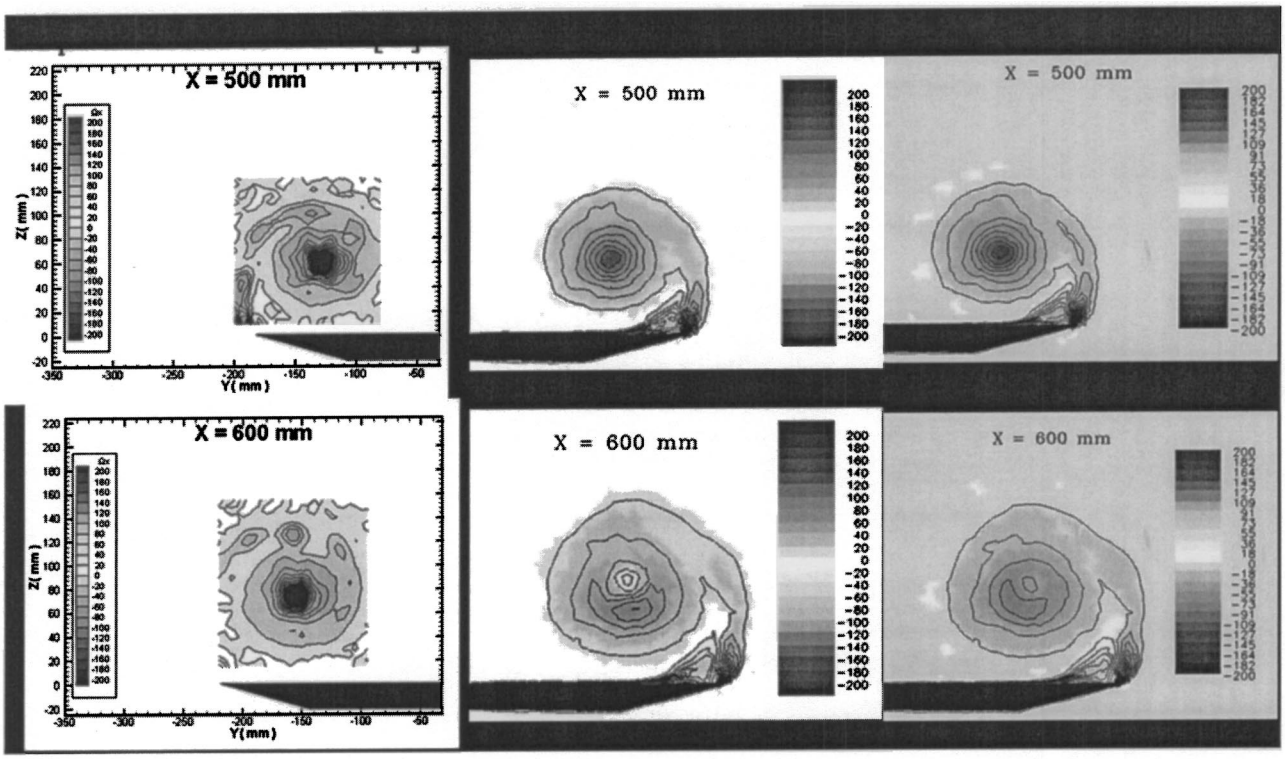

Fig. 16 Cross-planes of vorticity contours at two longitudinal stations from the experiments of Mitchell et al. [24] and SADES for two grids

The success of an approximate rotation correction in predicting the vortex breakdown motivates the inclusion of Spalart's more general rotation correction within the DES method. The rotation correction drives the eddy viscosity down in the vortex core, accounting for the stabilizing effect of strong streamline curvature. The DES method also drives the eddy viscosity down, but for a different reason. As the grid spacing is reduced, DES (or LES in general) reduces the eddy viscosity as more turbulence is resolved on the grid, eventually approaching a direct numerical simulation (DNS). Inclusion of the rotation correction in a DES model may allow the reduction of eddy viscosity in strong vortical flows on more modest grids. The success of DES in capturing the post-breakdown helical structures would be maintained. In summary, the overall success of DES methods in capturing vortical flows, combined with the previous success in capturing massively separated flows, make them extremely useful for full aircraft solutions at high angles of attack and flight Reynolds numbers.

Acknowledgments

The authors would like to express their thanks to Dr. Phillipe Spalart, Dr. Russ Cummings, and Dr. Doug Blake for their enlightening conversation and editorial comments on this work. The authors would also like to express their gratitude for the computational support provided by the DoD HPCMO in general, and the Maui High Performance Computing Center in particular. Finally, the authors would like to express thanks to the Air Force Office of Scientific Research for their funding sponsorship through Dr. John Schmisseur.

References

[1] Werlé, H., 1954, ''Quelques résultats expérimentaux sur les ailes en flèche, aux faibles vitesses, obtenus en tunnel hydrodynamique'' La Rech. Aéronaut., No. 41, Sep.-Oct. pp. 15–21.
[2] Peckham, D. H., and Atkinson, S. A., 1957, ''Preliminary Results of Low Speed Wind Tunnel Tests on a Gothic Wing of Aspect Ration 1.0,'' Aeronautical Research Council Technical Report, C.P. No 508, T. N. Aero 2504, Apr.
[3] Elle, B. J., 1961, ''An Investigation at Low Speed of the Flow near the Apex of Thin Delta Wings With Sharp Leading Edges,'' Aeronautical Research Council R&M, No. 3176.
[4] Lambourne, N. C., and Bryer, D. W., 1962, ''The Bursting of Leading-Edge Vortices-Some Observations and Discussion of the Phenomenon,'' Aeronautical Research Council R&M No. 3282.
[5] Hall, M. G., 1972, ''Vortex Breakdown,'' Annu. Rev. Fluid Mech., **4**, pp. 195–218.
[6] Leibovich, S., 1978, ''The Structure of Vortex Breakdown,'' Annu. Rev. Fluid Mech., **10**, pp. 221–246.
[7] Sarpkaya, T., 1971, ''On Stationary and Traveling Vortex Breakdowns,'' J. Fluid Mech., **45**, Part 3, pp. 545–559.
[8] Nelson, R. C., ''Unsteady Aerodynamics of Slender Wings,'' Aircraft Dynamics at High Angles of Attack: Experiments and Modeling, AGARD-R-776, pp. 1-1–1-26.
[9] Délery, J., 1994, ''Aspects of Vortex Breakdown,'' Prog. Aerosp. Sci., **30**, pp. 1–59.
[10] Faller, J. H., and Leibovich, S., 1977, ''Disrupted States of Vortex Flow and Vortex Breakdown,'' Phys. Fluids, **20**(9), pp. 1385–1400.
[11] Menke, M., Yang, H., and Gursul, I., 1996, ''Further Experiments on Fluctuations of Vortex Breakdown Location,'' Paper No. AIAA-96-0205, 34th AIAA Aerospace Sciences Meeting and Exhibit, Jan. 1996, Reno, NV.
[12] Mitchell, A. M., Molton, P., Barberis, D., and Délery, J., 2000, ''Oscillation of Vortex Breakdown Location and Control of the Time-Averaged Location by Blowing,'' AIAA J., **38**(**5**), pp. 793–803.
[13] Gordnier, R. E., 1996, ''Computational Study of a Turbulent Delta-Wing Flowfield Using Two-Equation Turbulence Models,'' Paper No. AIAA-96-2076, 27th AIAA Fluid Dynamics Conference, June, New Orleans, LA.
[14] Murman, S. M., and Chaderjian, N. M., 1998, ''Application of Turbulence Models to Separated High-Angle-of-Attack Flows,'' Paper No. AIAA-98-4519.
[15] Murman, S. M., 2001, ''Vortex Filtering for Turbulence Models Applied to Crossflow Separation,'' Paper No. AIAA-2001-0114, 39th Aerospace Sciences Meeting & Exhibit, Jan. Reno, NV.
[16] Menter, F. R., 1993, ''Zonal Two Equation $k-\omega$ Turbulence Models for Aerodynamic Flows,'' Paper No. AIAA-93-2906.
[17] Dacles-Mariani, J., Zilliac, G. G., Chow, J. S., and Bradshaw, P., 1995, ''Numerical/Experimental Study of a Wingtip Vortex in the Near Field,'' AIAA J., **33**(9), pp. 1561–1568.
[18] Spalart, P. R., and Shur, M. L., 1997, ''On the Sensitization of Turbulence Models to Rotation and Curvature,'' J. Fluid Mech., **358**, pp. 223.
[19] Spalart, P. R., Jou W-H., Strelets M., and Allmaras, S. R., 1997, ''Comments on the Feasibility of LES for Wings, and on a Hybrid RANS/LES Approach,'' *Advances in DNS/LES, 1st AFOSR Int. Conf. on DNS/LES*, Aug. 4–8, Greyden Press, Columbus OH.
[20] Strelets, M., 2001, ''Detached Eddy Simulation of Massively Separated Flows,'' Paper No. AIAA 01-0879.
[21] Forsythe, J. R., Hoffmann, K. A., Dieteker, F. F., 2000, ''Detached-Eddy Simulation of a Supersonic Axisymmetric Base Flow with an Unstructured Flow Solver,'' Paper No. AIAA 00-2410.
[22] Squires, K. D., Forsythe, J. R., Morton, S. A., Strang, W. Z., Wurtzler, K. E., Tomaro, R. F., Grismer, M. J., and Spalart, P. R., ''Progress on Detached-Eddy Simulation of Massively Separated Flows,'' Paper No. AIAA 2002-1021.
[23] Strang, W. Z., Tomaro, R. F., Grismer, M. J., 1999, ''The Defining Methods of Cobalt: A Parallel, Implicit, Unstructured Euler/Navier-Stokes Flow Solver,'' Paper No. AIAA 99-0786.
[24] Mitchell, A., Molton, P., Barberis, D., and Delery, J., 2000, ''Characterization of Vortex Breakdown by Flow Field and Surface Measurements,'' Paper No. AIAA 2000-0788.
[25] Samareh, J., 1995, ''Gridtool: A Surface Modeling and Grid Generation Tool,'' *Proceedings of the Workshop on Surface Modeling, Grid Generation, and Related Issues in CFD Solution*, NASA CP-3291, May 9–11.
[26] Pirzadeh, S., 1996, ''Progress Toward A User-Oriented Unstructured Viscous Grid Generator,'' AIAA Paper No. 96-0031.
[27] Spalart, P. R., and Allmaras, S. R., 1994, ''A One Equation Turbulence Model for Aerodynamic Flows,'' Rech. Aerosp., **1**, p. 5.
[28] Menter, F. R., and Rumsey, C. L., 1994, ''Assessment of Two-Equation Turbulence Models for Transonic Flows,'' Paper No. AIAA 94-2343.
[29] Morton, S. A., Forsythe, J. R., Mitchell, A. M., and Hajek, D., 2002, ''DES and RANS Simulations of Delta Wing Vortical Flows,'' Paper No. AIAA 2002-0587.
[30] Shur, M., Spalart, P. R., Strelets, M., and Travin, A., 1999, ''Detached Eddy Simulation of an Airfoil at High Angle of Attack,'' 4th International Symposium of Engineering Turbulence Modeling and Measurements, Corsica, May 24–26.
[31] Morton, S. A., Forsythe, J. R., Squires, K. D., and Wurtzler, K. E., 2002, ''Assessment of Unstructured Grids for Detached-Eddy Simulation of High Reynolds Number Separated Flows,'' 8th International Conference on Numerical Grid Generation in Computational Field Simulations, June.

A Methodology for Simulations of Complex Turbulent Flows

H. F. Fasel

J. Seidel

S. Wernz

Department of Aerospace and Mechanical Engineering,
The University of Arizona,
1130 N. Mountain,
Tucson, AZ 85721-0119

A new flow simulation methodology (FSM) for computing turbulent shear flows is presented. The development of FSM was initiated in close collaboration with C. Speziale (then at Boston University). The centerpiece of FSM is a strategy to provide the proper amount of modeling of the subgrid scales. The strategy is implemented by use of a "contribution function" which is dependent on the local and instantaneous "physical" resolution in the computation. This physical resolution is obtained during the actual simulation by comparing the size of the smallest relevant scales to the local grid size used in the computation. The contribution function is designed such that it provides no modeling if the computation is locally well resolved so that the computation approaches a direct numerical simulation in the fine grid limit, or provides modeling of all scales in the coarse grid limit and thus approaches an unsteady RANS calculation. In between these resolution limits, the contribution function adjusts the necessary modeling for the unresolved scales while the larger (resolved) scales are computed as in traditional large-eddy simulations (LES). However, a LES that is based on the present strategy is distinctly different from traditional LES in that the required amount of modeling is determined by physical considerations, and that state-of-the-art turbulence models (as developed for Reynolds-averaged Navier-Stokes) can be employed for modeling of the unresolved scales. Thus, in contrast to traditional LES based on the Smagorinsky model, with FSM a consistent approach (in the local sense) to the coarse grid and fine grid limits is possible. As a consequence of this, FSM should require much fewer grid points for a given calculation than traditional LES or, for a given grid size, should allow computations for larger Reynolds numbers. In the present paper, the fundamental aspects of FSM are presented and discussed. Several examples are provided. The examples were chosen such that they expose, on the one hand, the inherent difficulties of simulating complex wall bounded flows, and on the other hand demonstrate the potential of the FSM approach.
[DOI: 10.1115/1.1517569]

Introduction

In spite of considerable progress in computer technology, numerical methods, and turbulence modeling during the last several decades, reliable prediction of complex turbulent flows at high Reynolds numbers remains an elusive target. Turbulent flows and, in particular, wall-bounded flows exhibit wide ranges of spatial and temporal scales that increase with Reynolds number. Therefore, direct numerical simulations (DNS) are limited to relatively low Reynolds numbers, as the number of grid points required for DNS increases proportionally to Re^3 (Piomelli [1]). Thus today, DNS is used mainly as a research tool. For practical and industrial applications, Reynolds-averaged Navier-Stokes (RANS) calculations continue to be the main tool in spite of the obvious limitations of RANS, which have become clearer after their extensive use for a wide range of applications over several decades. Clearly, RANS calculations are not applicable where the time-dependent behavior of the flow is of interest or when the time-dependent behavior (either natural or imposed) has an impact on the mean flow behavior. Thus, flows where naturally occurring, large, highly energetic coherent structures play an important role, or when such structures are excited by forcing, as in active flow control (AFC), steady RANS calculations are not suitable. Therefore, in recent years, so-called unsteady RANS (URANS) calculations are being employed for applications where capturing the effect of unsteadiness or of the most energetic coherent structures in the flow are believed to be relevant for predicting the mean flow quantities correctly. URANS has also been proposed for AFC applications, although it is obvious that for such calculations the quality of the turbulence model and the numerical method is of crucial importance.

Due to the limitations of DNS on the one hand, and RANS on the other, great expectations have been placed on large-eddy simulation (LES). Although initial progress in developing LES had been relatively rapid, the extensive use of LES in recent years for a wide range of flows has brought the limitations of LES clearly to light. To date the promise of LES remains largely unfulfilled, in particular for wall-bounded flows, which are of great relevance for practical and scientific applications. Although LES does not require as much resolution as DNS, the savings are not significant enough to make LES a useful tool for practical computations of relevant flows. Even worse, in certain situations the turbulence model employed in LES can actually do more harm than good, as the physics of the relevant flow under investigation can be negatively affected by the unphysical diffusion provided by the turbulence model and/or the interaction of the diffusion introduced by the turbulence model and the numerical diffusion caused by the discretization error of the numerical method that is employed for computing the resolved scales. When scrutinizing applications of LES published in the literature, simple estimates often indicate that the dissipation provided by the discretization error far exceeded that provided by the turbulence model, or, in other instances, the grid resolution was so fine that the contribution of the modeled subgrid scales was negligible (''quasi''-DNS, [2]). Thus, not surprisingly, it was proposed in the literature to give up the subgrid-scale model altogether and let the discretization error [3] or filtering [4] provide for the subgrid-scale modeling. Although, and again not surprisingly, results with such ''LES'' (which are actually just coarse ''DNS'') yielded results similar to LES, this approach will hardly help in overcoming the limitations of LES, namely the relatively high-resolution requirements and the limita-

Contributed by the Fluids Engineering Division for publication in the JOURNAL OF FLUIDS ENGINEERING. Manuscript received by the Fluids Engineering Division March 29, 2002; revised manuscript received August 12, 2002. Associate Editor: G. E. Karniadakis.

tion to relatively low Reynolds numbers. As the idea of giving up the subgrid-scale model was motivated by the disappointment with conventional LES, this is a clear signal that LES has not yet lived up to its original promise.

This was essentially the ''state of the art'' of simulating turbulent flows in 1993 when C. Speziale and the first author of this paper joined efforts to develop a new approach for the simulation of turbulent flows. This team effort was proposed for the ONR Accelerated Research Initiative (ARI) for complex turbulent flows in 1993. Both of us were convinced at that time that the drawbacks of traditional LES had to be overcome in order to make LES useful for practical applications. Based on our diverse past research focus (Speziale, development of turbulence models for RANS calculations of complex flows, and Fasel, investigation of transition using high-order accurate methods for DNS) we strongly felt that LES would benefit from (i) the use of high-order accurate codes (higher than first or second order) for computing the resolved scales, (ii) state-of-the-art RANS-type turbulence models for the modeling of the subgrid scales instead of simple eddy-viscosity models (e.g., the Smagorinsky model) that are typically used in traditional LES, and (iii) eliminating explicit filtering.

The focus on the use of high order accurate numerical methods (higher than second order) originated from our experience with DNS of laminar-turbulent transition calculations. For a given resolution, high-order methods exhibit significantly reduced amplitude and phase errors allowing the dynamical behavior of the resolved scale structures to be more accurately captured. In addition, the role of the subgrid scale model can be much better evaluated by use of higher-order methods because this allows for a much better separation of the effects of the truncation error from the contribution of the subgrid-scale model.

To make the proposed new type of LES truly applicable for complex flows and/or for high Reynolds numbers, we also believed that in the new approach the ''transition'' from DNS to RANS had to be time and space-dependent and should be based on the instantaneous and local ''physical'' resolution of the actual computation. This idea was implemented by the use of a contribution function (see below) which determines the necessary modeling of the subgrid scales based on the local, physical resolution during the actual computations.

As our approach represents a new strategy or methodology for simulations of turbulent flows, rather than just the implementation of another turbulence model, we called it ''flow simulation methodology'' (FSM). As mentioned above, initial development was in close collaboration with C. Speziale [5,6]. Unfortunately, due to Charles' severe illness in 1997 and his subsequent tragic death in 1999, we had to continue the development of the FSM without the great inspiration and motivation that Charles had provided to the joint effort in the past. Without the tragic loss, the development of the FSM would have proceeded at a much faster pace and we would be able to report significantly more progress in the development of FSM. Presently the development of the FSM is still not complete. However, all major elements of FSM have been implemented and tested extensively. What is required are many more applications to gain the necessary experience. In the present paper, the fundamental aspects of the FSM as we see them today will be presented. The examples of FSM applications discussed in this paper were chosen to expose, on the one hand, the difficulties encountered in simulations of complex turbulent flows, and, on the other hand, demonstrate the potential of the FSM for complex turbulent flows.

FSM was originally proposed and subsequently developed for incompressible flows only. However, it should be noted that later on, and initially also in collaboration with C. Speziale, we have initiated development of the FSM for compressible flows (v. Terzi and Fasel, [7]). For these computations, we use the compressible Navier-Stokes equations in primitive variables in a conservative formulation. Initial test data indicate that FSM is equally promising for compressible flows. For space considerations, the discussion in the present paper will be limited to the incompressible case.

The Flow Simulation Methodology (FSM)

Applying averaging to the Navier-Stokes equations in incompressible form results in a system of partial differential equations for the resolved scales that contains the turbulent stress tensor $\boldsymbol{\tau} = [\tau_{ij}]$ that has to be modeled to close the equations. The centerpiece of the flow simulation methodology (FSM) is a contribution function, $f(\Delta,L)$, that is employed for the modeling of $[\tau_{ij}]$, $\tau_{ij} = f(\Delta,L)R_{ij}$ where Δ is representative of the local spatial stepsize of the computational grid and L is representative for the smallest relevant spatial scale of the turbulent motion. Thus, Δ/L is a measure of the local ''physical'' resolution, which is obtained by comparing the local grid size to the locally smallest relevant scale. R_{ij} is the Reynolds stress tensor. With the use of the contribution function $f(\Delta,L)$, the required degree of modeling of the un- (or under-) resolved subgrid scales can be determined in a local and time-dependent manner, because even if a time-independent, fixed computational grid is employed (which is usually the case), the relevant smallest scales vary in space and time as the computation progresses in time. Constraints on the design of the contribution function are such that for a coarse local grid (Δ/L large), $f(\Delta,L)\rightarrow 1$, all scales are modeled and, locally, a RANS-type calculation is performed. In the other limit, i.e., for a very fine grid (Δ/L small), $f(\Delta,L)\rightarrow 0$, when all scales can be resolved, a DNS should be recovered. In between, depending on the magnitude of Δ/L, LES-type calculations are being performed as then only the unresolved scales are being modeled, where the degree of (local) modeling is determined directly by $f(\Delta,L)$. For modeling R_{ij}, in principle, any turbulence model may be employed. However, in order to enable a consistent approach to the RANS limit ($f(\Delta,L)\rightarrow 1$), it is obvious that state-of-the-art RANS turbulence models should be used. For our FSM development so far, we have mainly used the explicit algebraic stress model (ASM) by Gatski and Speziale [8].

For our initial development of the FSM we have mainly employed $f(\Delta,L)$ in the form

$$f(\Delta,L) = [1 - \exp(\beta\Delta/L)]^n \tag{1.1}$$

where β and n are calibration constants (so far $n=1$ was used) [5,6]. Thus, this contribution function allows for a consistent local approach to RANS when Δ/L is large, and to DNS when Δ/L becomes small. In between, depending on Δ/L, a more or less resolved ''untraditional'' LES is performed. ''Untraditional,'' because a state-of-the-art turbulence model is used for modeling unresolved scales and because the required model contribution is based on a physical local (and time instantaneous) resolution which is determined during the actual computation and does not require a test filter as in conventional dynamic subgrid scale (DSGS) models.

For L, in principle any relevant length scale can be used as long as it represents the smallest relevant scales and can be used to determine the local ''physical'' resolution (local grid size divided by smallest relevant scale). As the form of $f(\Delta,L)$ was obtained from empirical considerations, it is obvious that other forms may be found that are better suited for given applications, or may be more universally applicable. In other words, it would be desirable to find a contribution function that would allow meaningful simulations with an even coarser resolution than is possible with the form given in Eq. (1.1). Thus, in summary, it is important to emphasize that, for FSM, a particular form of the contribution function, a specific turbulence model, or a specific length scale used for determining the physical resolution, are not the fundamental aspects. Rather, it is the strategy, the approach, by which instantaneous, local, relevant length scales in the flow are used to determine the ''physical resolution'' (by comparing the relevant length scale to the local grid size) and using the local resolution

for determining the degree of modeling required to properly represent the unresolved subgrid scales. Application of the FSM approach to a variety of flow problems will invariably lead to improved, more versatile forms of the contribution function than that of Eq. (1.1). Towards this end, we have experimented with other forms of $f(\Delta,L)$ which, for example, use other length scales, such as an integral length scale [9]. A strategy similar to our FSM has also been tested by Batten et al. [10].

As FSM, the hybrid approach by Cabot [11,12] and the detached eddy simulation (DES) approach by Spalart [13] were also motivated by the realization that traditional LES was computationally too expensive for practical applications. To overcome the high-resolution requirement of the traditional LES, in these hybrid approaches, a two-layer model is used, where in the wall region, RANS-type calculations are performed and then at a specified distance from the wall, the computation switches to LES. Thus, in contrast to FSM, where the ''transition'' from RANS to LES (and DNS) is smooth, in these approaches, the transition is abrupt. As demonstrated by Squires et al. [14], DES can work quite effectively for so-called ''natural'' applications where the flow field is dominated by large, energetic (''detached'') structures. It does not and cannot work as well for wall bounded flows, because the arbitrary and sharp transition between the near wall RANS type model to LES will cause unphysical effects.

Numerical Method

Governing Equations. The governing equations considered in this paper are the incompressible, unsteady Navier-Stokes equations in vorticity-velocity formulation. However, it should be noted that the FSM approach is not limited to any particular formulation. After averaging the Navier-Stokes equations and subsequently applying the curl operator, three transport equations for the averaged vorticity components are obtained,

$$\frac{\partial\overline{\boldsymbol{\omega}}}{\partial t}+\nabla\times(\overline{\boldsymbol{\omega}}\times\overline{\mathbf{u}}-\nabla\cdot\boldsymbol{\tau})=\frac{1}{\mathrm{Re}}\nabla^2\overline{\boldsymbol{\omega}}. \tag{1.2}$$

The velocity vector $\overline{\mathbf{u}}$ is computed from a set of Poisson equations, which are obtained form the definition of vorticity and the continuity equation (see Meitz and Fasel [15] for details). However, it should be pointed out that FSM is not at all tied to a particular form of the Navier-Stokes equations. Using FSM, the turbulent stress tensor, $\boldsymbol{\tau}$, is modeled by the product of a contribution function such as given in Eq. (1.1) and the Reynolds stress

$$\boldsymbol{\tau}=f(\Delta,L)\mathbf{R}. \tag{1.3}$$

Turbulence Models. For modeling the Reynolds stresses in Eq. (1.3), in principle, any state-of-the-art turbulence model can be employed. So far, in our development of FSM, we have mainly used the explicit algebraic stress model (ASM) developed by Gatski and Speziale [8]. In this model, the Reynolds stress tensor is modeled as

$$R_{ij}=\frac{2}{3}k\delta_{ij}-f(\eta,\xi)\left[\alpha_1\frac{k^2}{\varepsilon}S_{ij}+\alpha_2\frac{k^3}{\varepsilon^2}(S_{ik}W_{kj}+S_{jk}W_{ki})-\alpha_3\frac{k^3}{\varepsilon^2}\left(S_{ik}S_{kj}-\frac{1}{3}\delta_{ij}S_{kl}S_{kl}\right)\right] \tag{1.4}$$

where the strain rate tensor and the vorticity tensor are given by

$$S_{ij}=\frac{1}{2}\left(\frac{\partial u_i}{\partial x_j}+\frac{\partial u_j}{\partial x_i}\right),\quad W_{ij}=\frac{1}{2}\left(\frac{\partial u_i}{\partial x_j}-\frac{\partial u_j}{\partial x_i}\right) \tag{1.5}$$

and

$$f(\eta,\xi)=\frac{3(1+\eta^2)}{3+\eta^2+6\xi^2\eta^2+6\xi^2}$$

with the invariants for the strain rate tensor and the vorticity tensor

$$\eta=\frac{1}{2}\frac{\alpha_3}{\alpha_1}\frac{k}{\varepsilon}(S_{ij}S_{ij})^{1/2},\quad \xi=\frac{\alpha_2}{\alpha_1}\frac{k}{\varepsilon}(W_{ij}W_{ij})^{1/2}.$$

The quantities $k=(1/2)\overline{u_i'u_i'}$ and $\varepsilon=1/\mathrm{Re}\overline{(\partial u_i'/\partial x_j)^2}$ are the turbulent kinetic energy and dissipation rate, respectively, which are governed by the following transport equations:

$$\frac{\partial k}{\partial t}+u_j\frac{\partial k}{\partial x_j}=-R_{ij}\frac{\partial u_i}{\partial x_j}-\varepsilon+\frac{\partial}{\partial x_j}\left(\left(\frac{\nu_t}{\sigma_k}+\frac{1}{\mathrm{Re}}\right)\frac{\partial k}{\partial x_j}\right)$$
$$\frac{\partial\varepsilon}{\partial t}+u_j\frac{\partial\varepsilon}{\partial x_j}=-C_{\varepsilon_1}\frac{\varepsilon}{k}R_{ij}\frac{\partial u_i}{\partial x_j}-C_{\varepsilon_2}f_{\varepsilon_2}\frac{\varepsilon^2}{k}+\frac{\partial}{\partial x_j}\left(\left(\frac{\nu_t}{\sigma_k}+\frac{1}{\mathrm{Re}}\right)\frac{\partial\varepsilon}{\partial x_j}\right) \tag{1.6}$$

where $\nu_t=C_\mu k^2/\varepsilon$ is the eddy viscosity and the constants are given by Speziale [6] as $C_{\varepsilon_1}=1.44$, $C_{\varepsilon_2}=1.83$, $\sigma_k=1.0$, $C_\varepsilon=1.3$, $C_\mu=0.09$, and $\alpha_1=0.227$, $\alpha_2=0.0423$, $\alpha_3=0.0396$. The near-wall damping function in the ε transport equation is $f_{\varepsilon_2}=1-\exp(-0.1\,\mathrm{Re}\,yk^{1/2})$.

Numerical Scheme. A detailed description of the numerical scheme used in this study for solving the governing equations is given by Meitz and Fasel [15]. Some key points of the numerical method can be summarized as follows: (i) The streamwise and wall-normal derivatives are approximated by compact differences of fourth-order accuracy; (ii) variable grid, allowing for clustering of grid points near the wall; (iii) for three-dimensional simulations, the flow is assumed to be periodic in the spanwise direction, therefore, this direction is treated pseudo-spectrally; (iv) a fourth-order Runge-Kutta scheme is used for the time integration; (v) a fast Poisson solver is implemented for solving the velocity equations; and (vi) at the outflow boundary a buffer domain technique is implemented to avoid reflections of disturbance waves and vortical structures.

Equations (1.6) are solved using a second-order accurate difference scheme in both the x- and y-directions and an ADI method is utilized to advance in time. It should be noted that the lower formal accuracy of the scheme is used on purpose for the solution of Eqs. (1.6). This does not reduce the overall order of the numerical scheme of the Navier-Stokes equations, because only the subgrid scale stresses are integrated to a lower order which stabilizes the computation of Eq. (1.6).

Boundary Conditions. For the examples discussed below, the boundary conditions are given as follows: At the inflow, Dirichlet conditions are imposed for the vorticity, the velocity components, the turbulent kinetic energy, and the turbulent dissipation rate (if the inflow is turbulent). At the wall ($y=0$), no-slip, no-penetration conditions are imposed on the velocity components. For the turbulent quantities, a Dirichlet condition is used for the turbulent kinetic energy $k=0$, while a Neumann condition is used for ε.

At the freestream boundary ($y=y_{\max}$), the flow is assumed to be irrotational and laminar. At the outflow ($x=x_{\max}$) the second derivatives with respect to x of all variables are set to zero.

Disturbances are introduced into the flow in two ways: (i) a blowing and suction slot near the inflow boundary; (ii) a volume forcing technique, also applied near the inflow. Both disturbance generation techniques are designed to introduce predominantly vortical disturbances into the flow.

Examples

Flat-Plate Boundary Layer. As a first example for an FSM application, results for a flat-plate boundary layer without pressure gradient are presented (see Bachman [16]). This case has been chosen for testing FSM because of the abundance of available data for comparison, both experimental measurements and computations. The inflow of the computational domain is located at $x=0.3$ m from the plate leading edge and the freestream boundary is at $y=0.0627$ m. The number of grid points and Fourier modes

Table 1 Computational parameters

Case	B1	B2	B3	B4
N_x	1281	751	481	301
N_y	80	80	80	80
K_z	25	15	9	5

used for the four different cases presented here are summarized in Table 1. For case B1, the resulting dimensional step-size in the x-direction is $dx=5.83\times10^{-4}$ m and in the z-direction $dz=2.92\times10^{-4}$ m, which yields $dx^+=26$ and $dz^+=13$ at $\mathrm{Re}_\theta\approx1400$. The contribution function employed for these calculations is $f(\Delta,L)=1-\exp(-0.004\Delta/L)$ where $\Delta=(dxdydz)^{1/3}$ is the mean local step-size and $L=L_k=\mathrm{Re}^{-3/4}\varepsilon^{-1/4}$.

Figure 1 shows the mean streamwise velocity profile in wall coordinates at a location $\mathrm{Re}_\theta\approx1400$. The data of cases B1–B3 are virtually identical and also match both the theoretical curves for the viscous sublayer and the logarithmic layer as well as data by Murlis [17] and Spalart [18]. Case B4, however, shows a significant deviation from these data, indicating that for this very coarse resolution, the contribution of the turbulence model is too small. In fact, the resolution in this case is far too coarse (only five modes in the spanwise direction) to allow for a meaningful unsteady simulation. However, we are investigating more general forms of the contribution function that would allow simulations with such an extremely coarse resolution. The spanwise average of the contribution function $f(\Delta,L)$ as a function of wall normal distance is plotted in Fig. 2. As designed, the model contribution increases for reduced streamwise and spanwise resolution. More importantly, the increase in step-size has a more pronounced effect in the inner region of the boundary layer ($y^+<80$), consistent with the reduction in size of the turbulent structures near the wall.

In Fig. 3, instantaneous contours of spanwise vorticity for cases B1 (top) through B4 (bottom) are shown in an x-y plane. The

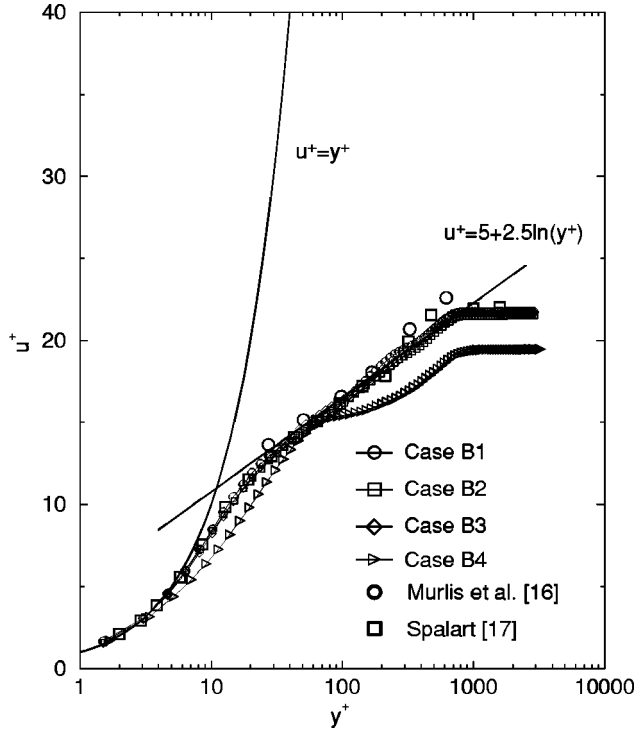

Fig. 1 Streamwise velocity profiles in near-wall scaling—flat-plate boundary layer

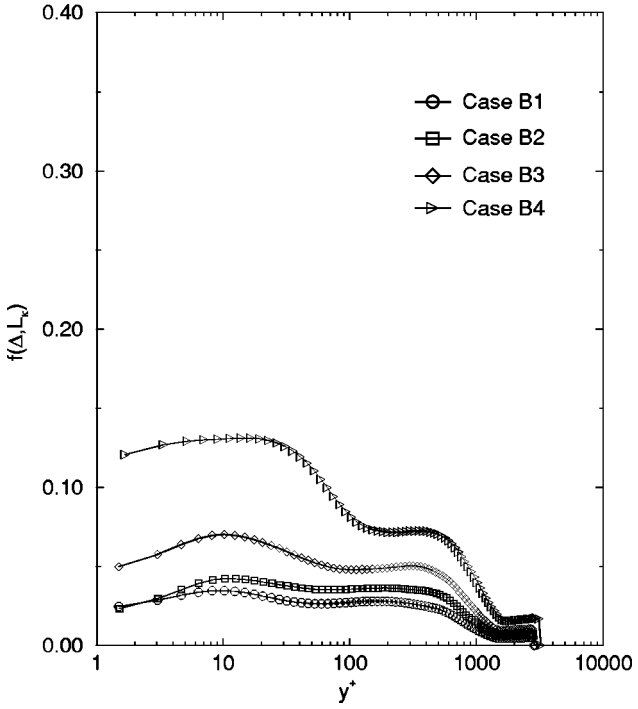

Fig. 2 Time-averaged contribution function profiles—flat-plate boundary layer

figure clearly demonstrates how the decrease in resolution and the concomitant increase in the contribution of the model remove the smallest structures while the large, coherent motion remains largely unchanged. For case B4, this figure again shows that the resolution is too coarse, resulting in spurious oscillations and unphysical structures in the flow. Spanwise vorticity is plotted again in Fig. 4 in an x-z plane at $y=0$. Note how the near wall structures are well resolved in both case B1 and case B2. In contrast, the scale of the structures increases significantly for case B3, but the simulation still yields surprisingly accurate results for the mean velocity profile (see Fig. 1).

Wall Jet. The wall jet is an ideal test case for turbulence models because it combines elements of two important prototypical flows: a turbulent wall boundary layer and a free shear layer. However, as was recognized early on (see Launder [19]), capturing the interaction between these two regions in the turbulent wall jet is crucial in order to obtain numerical results that match experimental measurements.

Numerous experimental investigations of the mean flow have been reported in the literature (see Launder [19]). Although the measurements agree well for the bulk of the wall jet, the data vary considerably in the near wall region, especially for the skin friction. In part, this is due to the large discrepancy in length scales of the inner boundary layer region and the outer shear layer region. The velocity maximum is reached at a wall normal distance of only 15% of the wall jet half-width, while the velocity decays to zero at the outer edge of the shear layer region at a wall normal distance of about three times the half-width. While most experimental investigations of the turbulent wall jet focused on the mean flow quantities, the work by Katz et al. [20] is a notable exception. They showed that large vortical structures with a strong spanwise coherence exist in the turbulent wall jet and play an important role. Although these structures are observed mainly in the shear layer region, they profoundly change the entire velocity profile, as indicated by the significant change in the mean skin friction. This could be observed clearly in the experiments where these structures were deliberately enhanced by periodically forcing the flow.

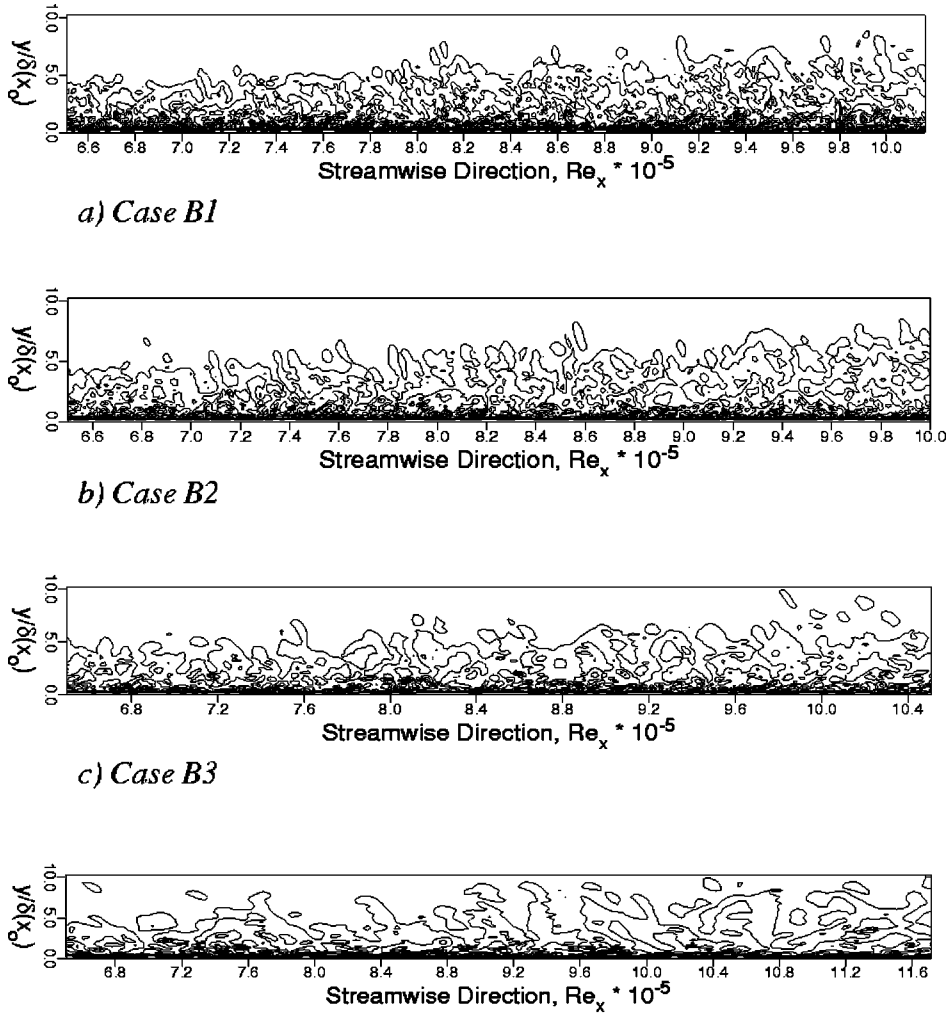

Fig. 3 Instantaneous contours of spanwise vorticity in the *x-y* plane—flat-plate boundary layer

The objective of the present numerical investigations was to determine how well the FSM captures the dynamics of the large coherent structures in the wall jet and their effect on the turbulent mean flow.

Flow Simulation Methodology (FSM) in the Unsteady Reynolds-Averaged Navier-Stokes (URANS) Limit. To assess the quality of the algebraic stress model, FSM was used in the URANS limit. In these calculations (c.f. Seidel and Fasel [21]), agreement similar to other RANS calculations was achieved between experimental mean flow data and the computational results. However, due to the equilibrium turbulence models used in typical RANS simulations, the nonequilibrium character of the turbulent wall jet cannot be captured. This is most clearly seen in the fact that the Reynolds shear stress is zero at the velocity maximum, whereas in the experiments this wall normal distance is reduced by about 30%.

Using FSM in the unsteady RANS limit, the effect of large coherent motion on the mean flow profiles was studied. Although FSM was developed to allow LES type calculations, it is particularly important to evaluate the performance of the model in the URANS limit to establish how well the underlying subgrid scale model is able to predict the flow in the large Reynolds number/coarse resolution limit. Within the FSM framework, this can be accomplished by setting $f(\Delta,L)=1$.

To investigate the effect of the large, coherent motion, disturbances were introduced into the flow using the volume forcing method described above. Forcing was introduced with a frequency of $F=17$ Hz. The amplitudes for the cases presented here are shown in Table 2.

Figure 5 compares the mean flow profiles of case U1 and case U2 with the profile of the unforced base flow at three streamwise locations, $x/b=100$, 150, 200 (b is the nozzle height). The large-amplitude forcing applied in case U2 leads to a significant mean flow distortion. Note that this distortion increases in the streamwise direction, indicating a continuous momentum transfer from the mean flow to the large, coherent structures. Also, the maximum velocity decreases and its location is shifted towards the wall, whereas the wall jet half-width is largely unaffected.

The effect of the large, coherent motion on the Reynolds shear stress distribution is shown in Fig. 6, where R_{12} is plotted as a function of wall normal distance. The large structures increase the shear stress maximum and shift the location of zero shear stress significantly towards the wall, which qualitatively agrees with experimental measurements. Figure 7 shows the computed Reynolds shear stress (case U2) and experimental measurements by Eriksson et al. [22] in wall coordinates. When large coherent structures are present in the calculations, the agreement between the experimental and computational results is significantly improved. This

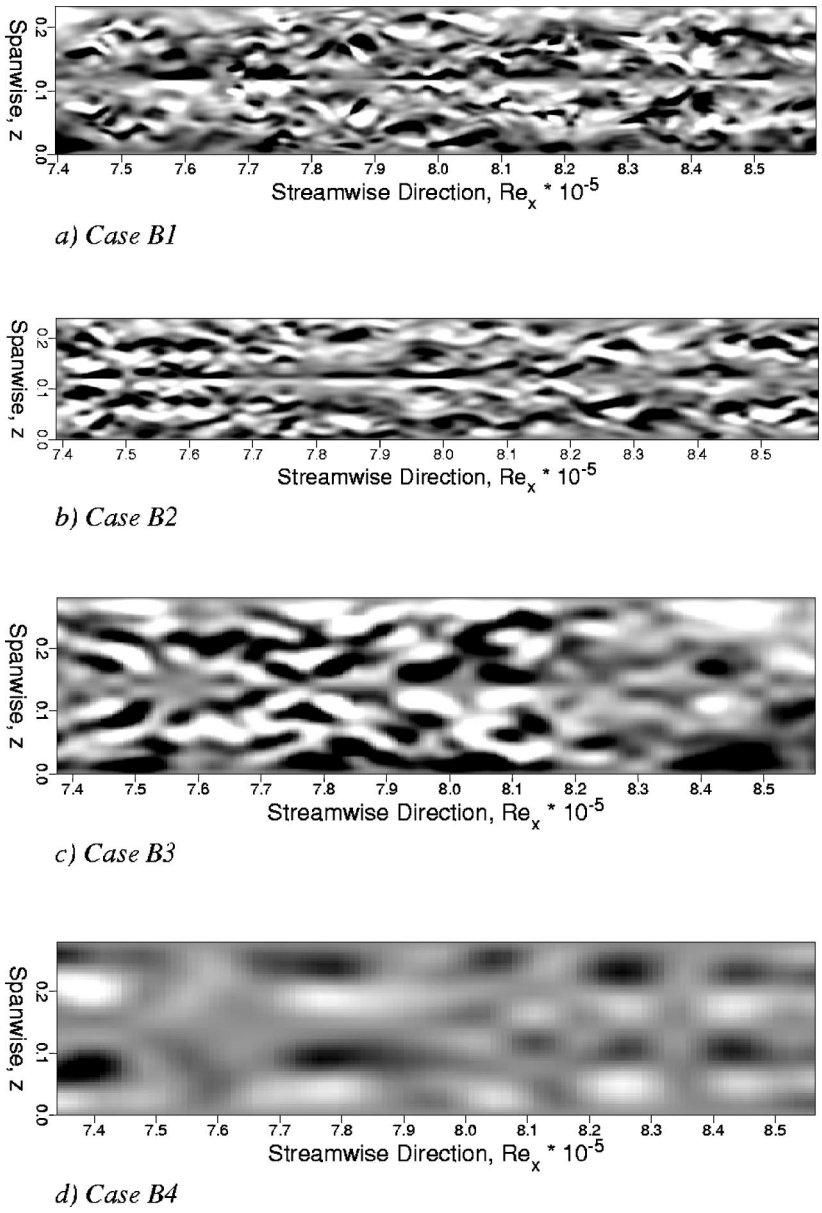

Fig. 4 Instantaneous contours of streamwise vorticity in the *x-z* plane at the wall—flat-plate boundary layer

result is very surprising in light of the fact that for these calculations only a single-frequency disturbance was introduced.

Despite this simplification, URANS evidently captures this important characteristic of the turbulent wall jet, which could not be captured by a steady RANS calculation (''base flow'' in Figure 5). The large coherent structures apparently impact the turbulent mean flow in a fundamentally different way (adding nonequilibrium effects) than the small scale turbulence. Hence, computing the structures in the URANS provides a significant improvement over combining their effect on the mean flow with that of the small scale turbulence in the Reynolds stress, as done in the steady RANS.

Table 2 Disturbance amplitude (normalized by the jet exit velocity)

Case	U1	U2
$\hat{f}/U_j$	1×10^{-2}	2×10^{-2}

Flow Simulation Methodology. A case study is presented to demonstrate the performance of FSM in its entire range of applicability, from DNS with $f(\Delta,L)=0$ in the whole domain (case F1), to URANS with $f(\Delta,L)=1$ (case F5). Cases F2 through F5 use the DNS data as initial condition. The computational parameters for the five cases are summarized in Table 3 (I is the number of points in the streamwise direction, K is the number of Fourier modes in the spanwise direction).

For the simulations presented here, a modified form of the contribution function suggested by Zhang et al. [23] was used $f(\Delta,L)=1-\exp(-\max(0,5\Delta-10L_k)/NL_k)$ with $\Delta=1/3(\Delta x^2+\Delta y^2+\Delta z^2)^{1/2}$. The form of this contribution function is a slight variation from the one proposed originally. It allows for setting the physical resolution in the DNS limit (here five step-sizes

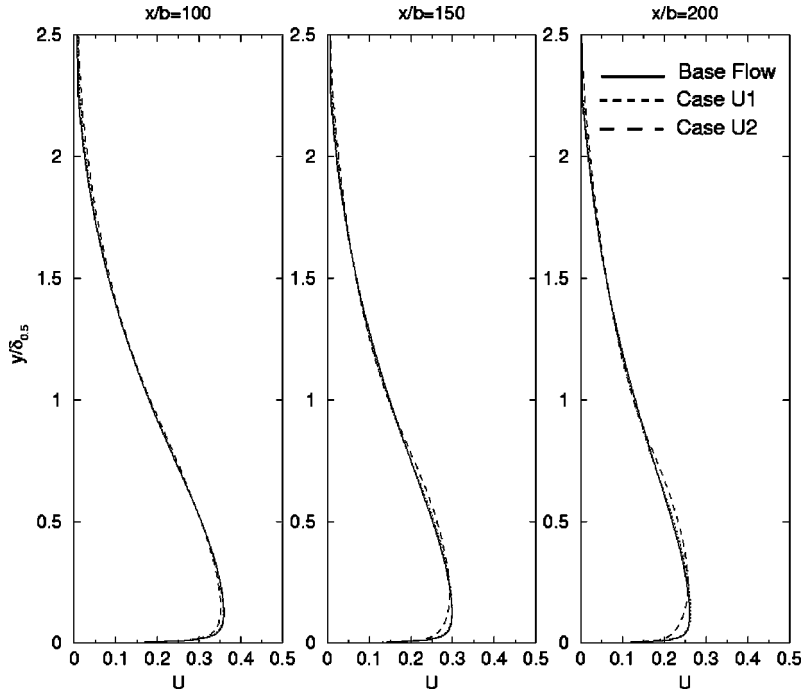

Fig. 5 Effect of large-scale structures on the mean *u*-velocity profile—URANS of turbulent wall jet

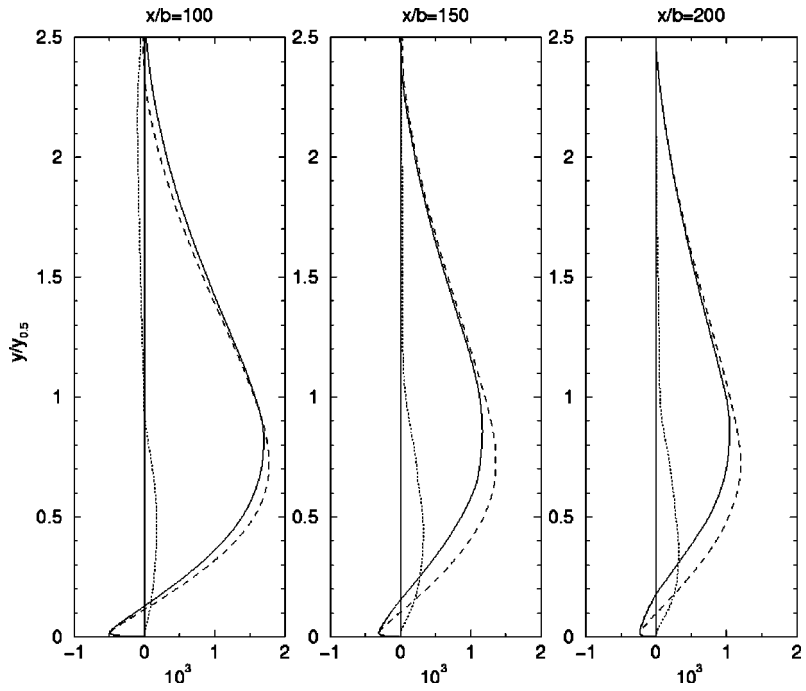

Fig. 6 Reynolds stress R_{12} from URANS of turbulent wall jet; ----- random part (modeled), · · · · coherent part, — — —sum of coherent and random parts

within $10L_k$) and independently choosing a calibration parameter N that determines how rapidly $f(\Delta,L)$ approaches the URANS limit as the physical resolution decreases. N is given in Table 3 for the FSM computations presented.

In the DNS (case F1), a high momentum self-similar Glauert wall jet (Re=16,500 based on the jet half-width at the inflow) is perturbed by volume forcing near the inflow. Only three-dimensional perturbations are introduced close to the inflow. Fig-

Table 3 Simulation-type, model parameters, and resolution

Case	F1	F2	F3	F4	F5
Type	DNS ($f=0$)	LES	LES	LES	URANS ($f=1$)
N	-	2500	1000	1500	-
Δx [mm]	.5	.5	1	1	1
Δz [mm]	.25	.25	.5	.125	.5
I	801	801	401	401	401
K	21	21	11	5	11

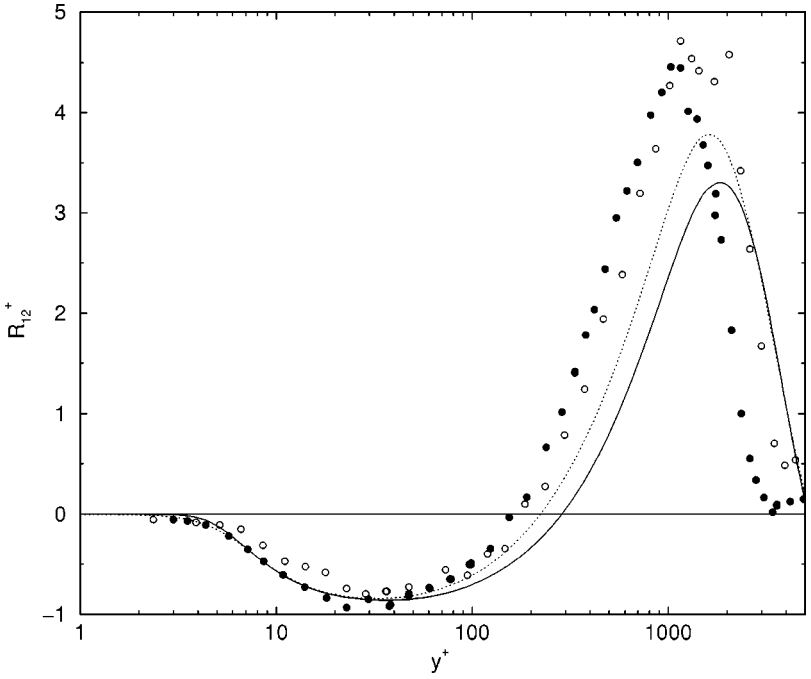

Fig. 7 Reynolds stress R_{12} from URANS of turbulent wall jet in wall coordinates; ----- flow without structures, · · · · mean flow with structures, ○● experimental data from Eriksson [22]

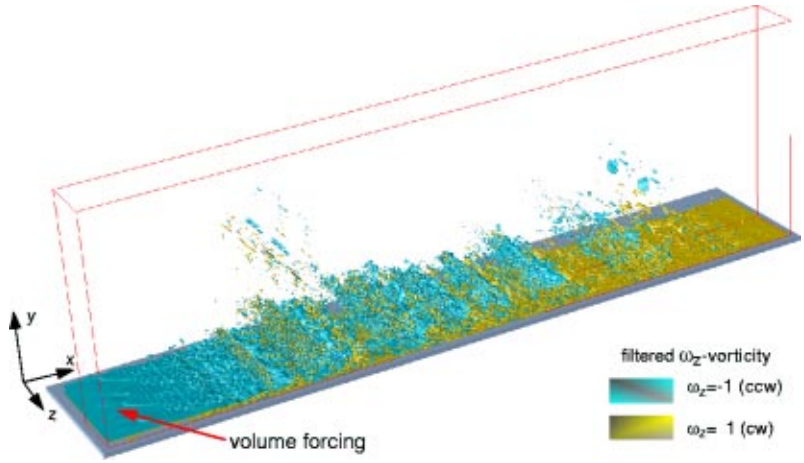

Fig. 8 Direct numerical simulation of wall jet transition. Isolevels of spanwise vorticity.

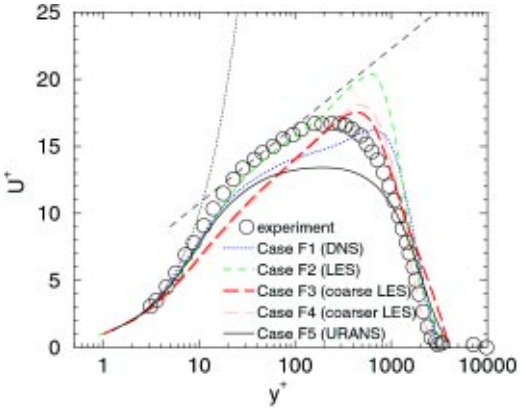

Fig. 9 Mean velocity profiles in wall coordinates

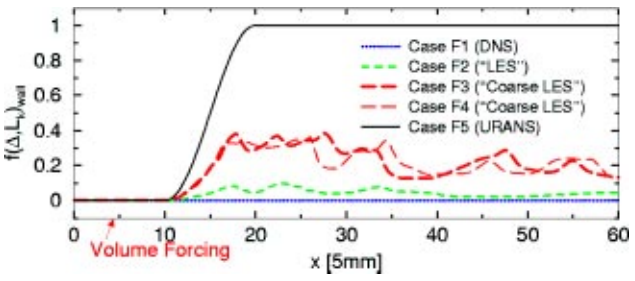

Fig. 10 Wall values of the contribution functions for Cases F1–F5—turbulent wall jet

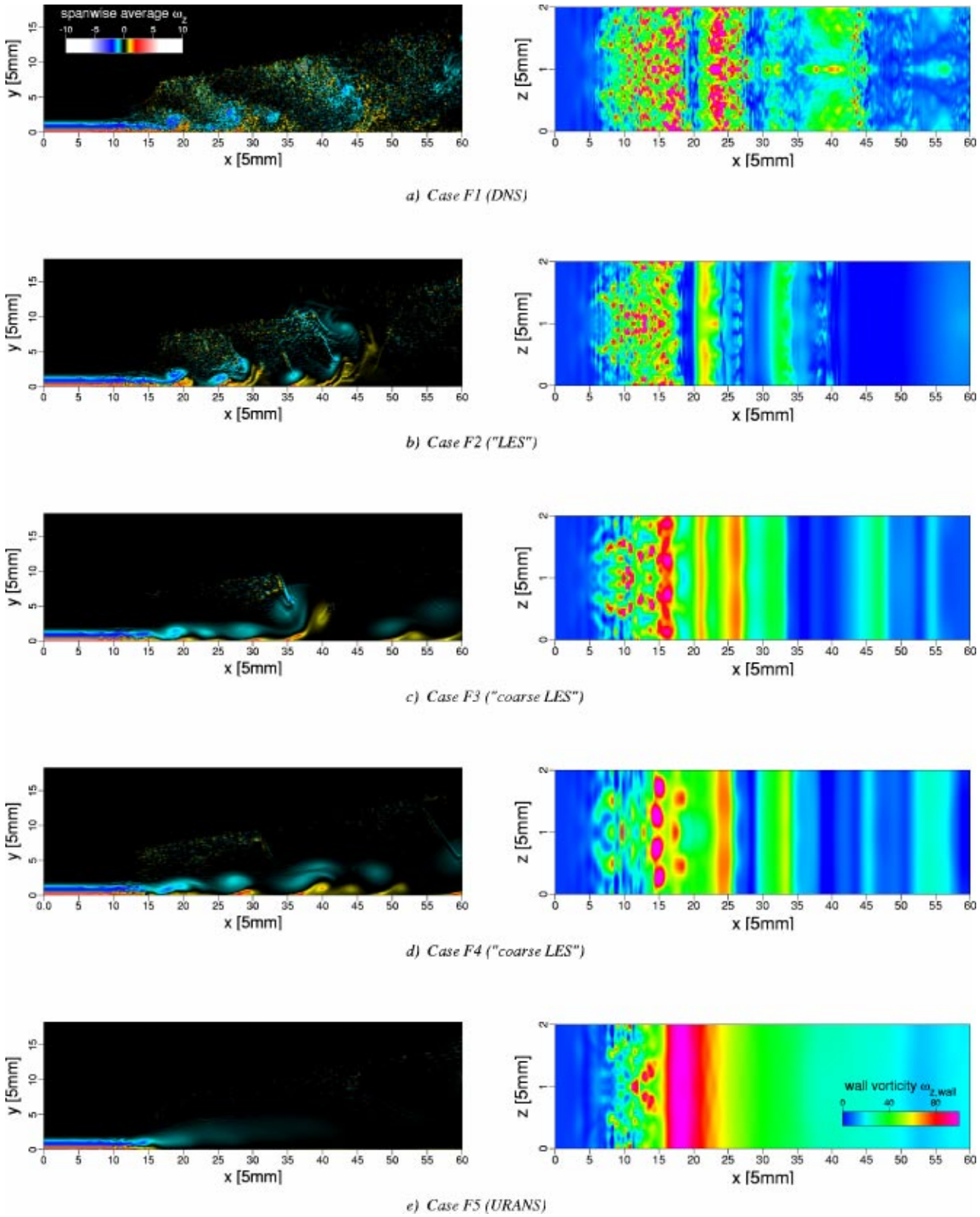

Fig. 11 Isolevels of instantaneous spanwise vorticity in an *x-y* plane (left) and on the wall (right)—turbulent wall jet

ure 8 shows isolevels of instantaneous spanwise vorticity in perspective view. Remarkably, the spanwise coherent structures emerge naturally some distance downstream of the forcing location, despite the lack of a two-dimensional forcing component.

The grid resolution used for case F1 is far too low to constitute a well-resolved DNS calculation (which would be extremely expensive due to the discrepancy in scales between inner and outer flow regions and due to the large spreading of the wall jet in downstream direction). Consequently, gridmesh oscillations are present in case F1.

Despite the coarse resolution, the turbulent wall jet computed with the DNS is remarkably close to experimental measurements. For example, in Fig. 9 streamwise mean velocity profiles from the simulations (cases F1–F5) are compared with profiles from the experiments by Eriksson et al. [22]. The profile from case F1 is quite close to the experimental measurements, in particular it exhibits a similar log-like behavior from $y^+=10$ to $y^+=100$.

Cases F2–F4 are FSM calculations and therefore the modeling contribution adjusts in a time and space-dependent manner. Figure 10 shows the streamwise development of the contribution function at the wall for one time instant. Note that upstream of $x=20$ the contribution function obtained by FSM is multiplied by a ramping function to shut off the model during flow transition.

Case F2 has the same resolution as the DNS, and consequently, the model contribution is very small, comparable to the subgrid scale contribution in an LES (see Fig. 10). The turbulence model mainly acts to reduce gridmesh oscillations that are present in the DNS (case F1). As a result, the mean flow profile for case F2 in Fig. 9 matches the experimental data even better than for case F1. The grid resolution for cases F3 and F4 is such that the small scales have to be modeled, resulting in significant values for $f(\Delta,L)$ (Fig. 10). Nevertheless, the velocity profiles computed from these cases are still remarkably close to the experiments.

An impression of the resolved flow fields for all five cases is provided with the contour plots of instantaneous spanwise vorticity in Fig. 11. The plots in the left column show the spanwise average of the spanwise vorticity versus x and y, the plots in the right column display the spanwise vorticity in the x-z plane at $y=0$. For case F1 (DNS), the flow exhibits small-scale structures embedded in the large scales in the entire computational domain. The large coherent structures consist of a pair of counter rotating vortices, one in the near wall boundary layer region, the other in the shear layer region of the wall jet.

In case F2, the small scale fluctuations are reduced in strength due to the effect of the subgrid model, yet the large-scale structures still correlate very well with the DNS data. Interestingly, the structure at $x=45$ is somewhat stronger than in the DNS computation and in the process of lifting off. This change in behavior can be contributed to the effect of the turbulence model on the very delicate balance of vortex pairs as they are generated and convected downstream. The spatially varying model contribution (especially the wall normal distribution) changes this balance slightly by modeling to a larger degree near the wall. It turns out that these large coherent vortices are an extremely sensitive indicator of the balance between modeled subgrid scale stresses and the resolved scale motion. As cases F2 and F3 indicate, the contribution function is not optimal, but also not very far from optimal, since the results obtained with a quarter of the resolution in an x-z plane essentially match the results of the DNS (case F1).

Case F5, using FSM in the limit of unsteady RANS, significantly attenuates the evolving structures close to the disturbance slot and eventually results in a steady flowfield in the turbulent flow region downstream. It has to be stressed, however, that this steady flowfield is still the result of a RANS computation with a state-of-the-art algebraic stress model and therefore yields very good mean flow results.

Conclusion

In this paper the fundamental aspects of the flow simulation methodology (FSM) have been presented and discussed. The examples of applications of FSM for the present paper have been chosen so that the basic features of the FSM approach could be demonstrated. In particular, the wall jet was chosen because it represents a ''tough'' application, as the turbulent flow physics depend on the interaction between outer (large) coherent structures developing in the free shear layer and the near-wall boundary layer. The results of the FSM calculations demonstrate that the core module of FSM, the contribution function, is doing the job it was designed to do, namely providing the proper amount of subgrid scale modeling based on the local, ''physical'' grid resolution. Development of FSM is far from complete, although all essential modules of FSM have been implemented and tested. Much more experience has to be gathered by applying FSM to other flows. However, the results presented here are very encouraging and demonstrate the potential of FSM for calculating complex turbulent flows.

Dedication/Acknowledgment

This paper is dedicated to the memory of Charles Speziale who passed away in April, 1999. Without Charles' ideas, support, and stimulating discussions, the development of FSM would not have come about.

We also acknowledge the many contributions by several members of the CFD group of the AME department at the University of Arizona: C. Bachman, R. Sandberg, D. von Terzi, P. Valsecchi, and H. L. Zhang.

Funding for the development of FSM was provided by ONR under grants N00014-94-1-0095 and N00014-99-1-885. Funding for the wall jet research was provided by AFOSR under grant F49620-00-1-0069.

References

[1] Piomelli, U., 1994, ''Large-Eddy Simulation of Turbulent Flows,'' University of Illinois at Urbana-Champaign, TAM Report No. 767.
[2] Spalart, P. R., 2000, ''Strategies for Turbulence Modelling and Simulations,'' Int. J. Heat Fluid Flow, **21**, pp. 252–263.
[3] Boris, J., Grinstein, F., Oran, E., and Kolbe, R., 1992, ''New Insights Into Large Eddy Simulation,'' Fluid Dyn. Res., **10**(4–6), pp. 199–228.
[4] Fureby, C., and Grinstein, F., 1999, ''Monotonically Integrated Large Eddy Simulation of Free Shear Flows,'' AIAA J., **37**(5), pp. 544–556.
[5] Speziale, C. G., 1996, ''Computing Non-equilibrium Turbulent Flows With Time-Dependent RANS and VLES,'' 15th International Conference on Numerical Methods in Fluid Dynamics, Monterrey, CA.
[6] Speziale, C. G., 1998, ''Turbulence Modeling for Time-Dependent RANS and VLES: A review,'' AIAA J., **36**(2), pp. 173–184.
[7] v. Terzi, D., and Fasel, H., 2002, ''A New Flow Simulation Methodology Applied to the Turbulent Backward-Facing Step,'' AIAA Paper No. 2002-0429 (invited paper).
[8] Gatski, T. B., and Speziale, C. G., 1993, ''On Explicit Algebraic Stress Models for Complex Turbulent Flows,'' J. Fluid Mech., **254**, pp. 59–78.
[9] Israel, D., and Fasel, H., 2002, ''Numerical Investigation of Turbulent Separation Control Using Periodic Disturbances,'' AIAA Paper No. 2002-0409.
[10] Batten, P., Goldberg, U., and Chakravarthy, S., 2000, ''Sub-grid Turbulence Modeling for Unsteady Flow With Acoustic Resonance,'' AIAA Paper No. 2000-0473.
[11] Cabot, W., 1996, ''Near-Wall Models in Large Eddy Simulations of Flow Behind a Backward-Facing Step,'' Center for Turbulence Research, annual research briefs.
[12] Cabot, W., and Moin, P., 1999, ''Approximate Wall boundary Conditions in the Large-Eddy Simulation of High Reynolds Number Flow,'' Flow, Turbul. Combust., **63**, pp. 269–291.
[13] Spalart, P. R., Jou, W-H., Strelets, M., and Allmaras, S. R., 1997, ''Comments on the Feasibility of LES for Wings, and on a Hybrid RANS/LES Approach,'' Advances in DNS/LES, 1st AFOSR Int. Conf. on DNS/LES.
[14] Squires, K., Forsythe, J., Morton, S. A., Strang, W. Z., Wurtzler, K. E., Tomaro, R. F., Grismer, M. J., and Spalart, P., 2002, ''Progress on Detached-Eddy Simulation of Massively Separated Flows,'' AIAA Paper No. 2002-1021.
[15] Meitz, H., and Fasel, H., 2000, ''A Compact-Difference Scheme for the Navier-Stokes Equations in Vorticity-Velocity Formulation,'' J. Comput. Phys., **157**, pp. 371–403.
[16] Bachman, C., 2001, ''A New Methodology for the Numerical Simulation of Wall Bounded Turbulent Flows,'' Ph.D. dissertation, University of Arizona.
[17] Murlis, J., Tsai, H. M., and Bradshaw, P., 1982, ''The Structure of Turbulent Boundary Layers at Low Reynolds numbers,'' J. Fluid Mech., **122**, pp. 13–56.
[18] Spalart, P. R., 1988, ''Direct Simulation of a Turbulent Boundary Layer Up to Re_θ=1410,'' J. Fluid Mech., **187**, pp. 61–98.
[19] Launder, B. E., and Rodi, W., 1983, ''The Turbulent Wall Jet—Measurements and Modeling,'' Annu. Rev. Fluid Mech., **15**, pp. 429–459.
[20] Katz, Y., Horev, E., and Wygnanski, I., 1992, ''The Forced Turbulent Wall Jet,'' J. Fluid Mech., **242**, pp. 577–609.
[21] Seidel, J., and Fasel, H., 2000, ''Numerical Investigations of Forced Turbulent Wall Jets,'' AIAA Paper No. 2000-2317.
[22] Eriksson, J. G., Karlsson, R. I., and Persson, J., 1998, ''An Experimental Study of a Two-Dimensional Lane Turbulent Wall Jet,'' Exp. Fluids, **25**, pp. 50–60.
[23] Zhang, H. L., Bachman, C., and Fasel, H., 2000, ''Application of a New Methodology for Simulations of Turbulent Flows,'' AIAA Paper No. 2000-2535.

Multidimensional Diagnostics of Turbine Cavitation[1]

Branko Bajic
Managing Director,
Korto Cavitation Services–Korto GmbH,
12, rue Ste Zithe
L-2763 Luxembourg, Luxembourg
e-mail: korto@cavitation.de

A novel technique for vibro-acoustical diagnostics of turbine cavitation is introduced and its use demonstrated on a Francis turbine. The technique enables identification of different cavitation mechanisms functioning in a turbine and delivers detailed turbine cavitation characteristics, for each of the mechanisms or for the total cavitation. The characteristics specify the contribution of every critical turbine part to the cavitation intensity. Typical diagnostic results: (1) enable optimization of turbine operation with respect to cavitation erosion; (2) show how a turbine's cavitation behavior can be improved; and (3) form the basis for setting up a high-sensitivity, reliable cavitation monitoring system.
[DOI: 10.1115/1.1511162]

Introduction

In a long list of recent publications on the methods of vibro-acoustical diagnostics of hydro turbine cavitation ([1–20]), little can be found regarding the problem of identifying turbine parts that cause cavitation. This seems to be the consequence of the fact that most measurements have been performed with *one sensor* using *mean values* of vibro-acoustical signatures. While such measurements can possibly yield an overall description of cavitation performance of a turbine, they can hardly furnish any details as to the cause of cavitation. In order to distinguish between different cavitating elements of a turbine, spatial resolution is needed. Because the space-time configuration of the acoustical field in a turbine is unsuitable for coherent acoustical measurements that might result in directivity or focusing on a source, one has to try incoherent processing based on parametric differences produced by the inhomogeneity of a transfer function or source structure. In one such approach, introduced in Bajic [9] and elaborated in Bajic [16], one analyzes the dependence of cavitation noise power on the instantaneous angular position of a turbine runner. In case of weak or moderate cavitation this yields data that enable estimation of contributions of various pairs of stator/runner blades to the total cavitation intensity. Fundamentally, this method is based on using an *additional dimension* of data which usually has been ignored and omitted by circumferential averaging. Another case in which one distinguishes between spatially separated segments of a cavitating flow and identifies contributions arising from different runner blades has been reported in Hermann et al. [18]. However, the method is not described by the reference.

In this paper an approach to vibro-acoustical diagnostics of turbine cavitation is presented that systematically uses the *multidimensionality* of vibro-acoustical signatures of cavitation in order to infer details of cavitation in a turbine. A number of spatially separated sensors are utilized to pick up differences in the dependence of cavitation on the runner's angular position, and these data are studied as a function of noise frequency and turbine power. By using the resolution in a combination of dimensions—sensors' location, noise frequency, runner's instantaneous angular position, turbine power—it is possible to distinguish between different cavitation mechanisms and their causes (i.e., different turbine parts that cause cavitation), and to quantify their respective contributions to cavitation intensity. As concluded in a critique of the present practice of the vibro-acoustical cavitation diagnostics (Bajic [20]) such an approach has to be truly multidimensional and not a simple series of analyses in which only one independent element is varied in each step.

Experiment

The multidimensional measurement and analysis procedure was verified by means of the data collected on a 17 MW, double-runner, horizontal-axis Francis turbine in which 19 runner blades are rotating behind 20 guide vanes. On the shaft of each guide vane a high-frequency vibro-acoustical sensor was fixed (Fig. 1). The instantaneous angular position of the runner, described by the angle θ (increasing in the direction of rotation and being zero when the reference blade is in the reference position), was controlled. 100 signal samples, each covering one revolution period, were recorded at each sensor and in every operating condition of the turbine. The signal recording was synchronized with runner rotation, and the 100 samples were used to produce deterministic descriptors of random cavitation noise signals by averaging over 100 revolutions. The frequency range from the revolution frequency up to 1 MHz was covered. More than 40 gigabytes of vibro-acoustical data were collected and analyzed. The steps of the analysis are presented in what follows.

Experimental Data

The power density spectra of noise recorded by means of the sensor at the guide vane $v = 1$ are illustrated in Fig. 2. The spectra measured at the other guide vanes were similar. In a broad frequency range between 0.2 kHz and 1 MHz there is a noticeable

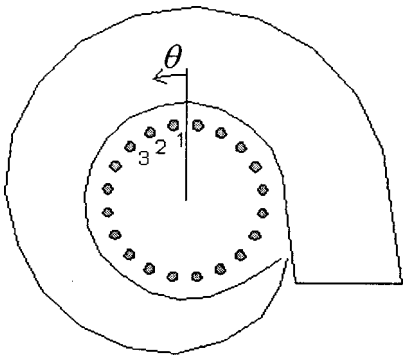

Fig. 1 The sensors placed on the 20 guide vanes react to cavitation in various locations around the spiral

[1]Presented at the Hydraulic Machinery and Systems—20th IAHR Symposium, Aug. 6–9, 2000, Charlotte, NC.

Contributed by the Fluids Engineering Division for publication in the JOURNAL OF FLUIDS ENGINEERING. Manuscript received by the Fluids Engineering Division December 1, 2000; revised manuscript received May 6, 2002. Associate Editor: Y. Tsujimoto.

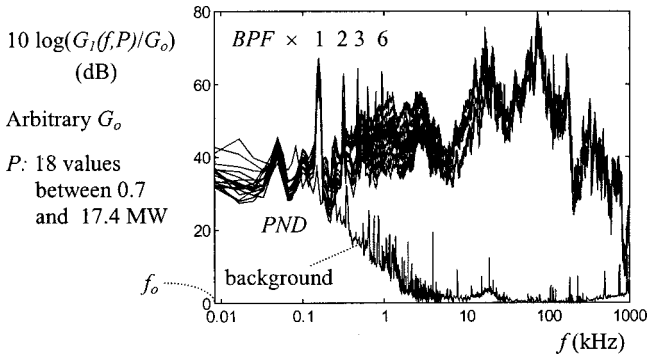

Fig. 2 Typical power density spectra of noise picked up at different power values. There is no noticeable line at the revolution frequency, but the blade-passage frequency (BPF) lines are rather strong. The background noise, recorded in the turbine at rest while the other machinery in the plant was operating, is low enough to enable reliable estimation of the continuous spectrum component between 0.3 and 800 kHz.

dependence on turbine power. Narrow peaks at frequencies above 10 kHz are due to sensor resonances and vibro-acoustic resonances of the turbine.

In another format, as normalized spectra (Bajic and Keller [6]) the data from Fig. 2 are shown in Fig. 3. Most resonance peaks, other traces of transfer functions, and the BPF-harmonics disappear. Free from these cavitation-irrelevant issues, such spectra illuminate the influence of turbine load on cavitation in a more objective way. They also may reveal cavitation details hardly visible in nonnormalized spectra.

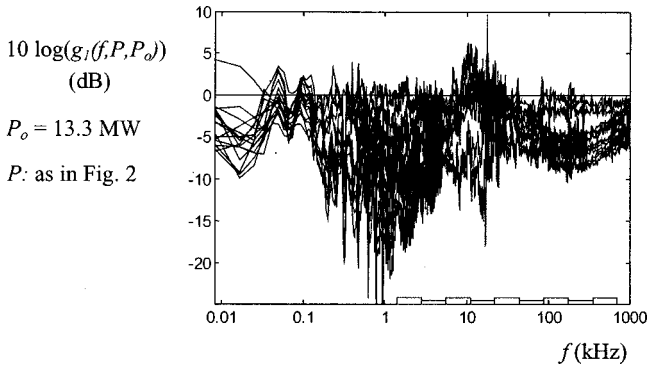

Fig. 3 Overview of the normalized power spectra. The $v=1$ power density spectra recorded at different turbine power values are compared to the one recorded at 13.3 MW. The spectrum related to this reference value is thus represented by the zero-dB line.

The dependence of noise intensity on the angular position of the runner found in the measurements is illustrated by the polar diagrams in Fig. 4. These were obtained by means of the sensor at $v=1$. Similar, but not identical, patterns were recorded at the other guide vanes.

Identification of Cavitation Mechanisms

A two-dimensional representation of the $v=1$ normalized spectra presented in Fig. 5 yields both detailed and overall insight into the structure of data in the (f, P)-domain. Although the information content of the data in Fig. 3 and Fig. 5 is identical, much more can be inferred from Fig. 5. First of all, two dominant patterns can be recognized in the body presented by the two views in Fig. 5. These are drawn in Figs. 6(*a*) and 6(*b*) and are interpreted as the vibro-acoustical signatures of two segments of cavitating flow, i.e., *cavitation mechanisms*. With reference to strongly differing spectra, these mechanisms may be assumed hydraulically independent and thus their respective noise power components additive. After subtracting the two components from the total spectrum of Fig. 5, the third mechanism, presented in Fig. 6(*c*), is identified. In this way a useful decomposition of the total spectrum follows:

$$g_v(f,P,P_o)=\sum_{m=0}^{M} {}^{(m)}g_v(g,P,P_o),$$

$M=3$, $v=1$. Here a possibly existing background component, ${}^{(0)}g_v(f,P,P_o)$, is included to enable the most general description. In the present $v=1$ case such a component was not necessary.

Estimates of cavitation intensity based on noise power measured within a limited frequency band are highly biased due to strong differences in the forms of the spectra of the three mechanisms. In order to suppress this error, the total noise power, $I_v(P)$, should be used as an estimate of cavitation intensity and not an arbitrary part of it (Bajic [16]). This also holds true for the estimates of the cavitation intensity of cavitation mechanisms, ${}^{(m)}I_v(P)$. These follow from the normalized spectra, ${}^{(m)}g_v(f,P,P_o)$, identified by the empirical procedure illustrated above:

$${}^{(m)}G_v(f,P)={}^{(m)}g_v(f,P,P_o)\times G_v(f,P_o),$$

$${}^{(m)}I_v(P)=\int_0^{\infty} {}^{(m)}G_v(f,P)df,$$

and thus

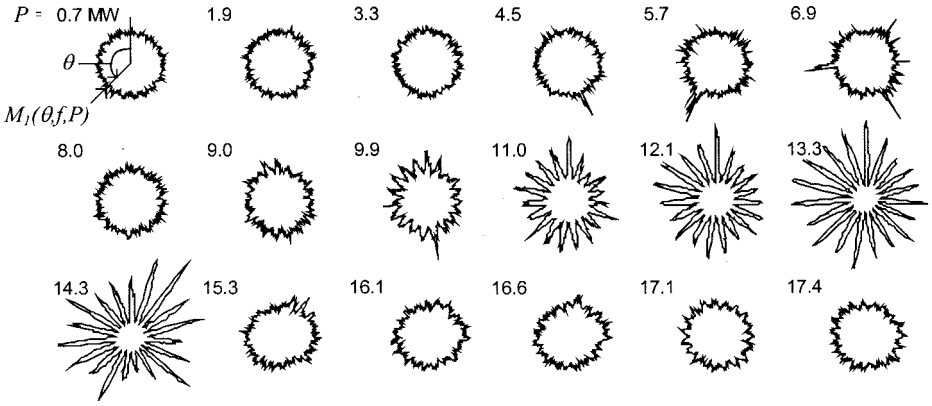

Fig. 4 An example of modulation curves: $M_1(\theta,f,P)$ in an octave band centered at $f=125$ kHz measured at different turbine power values

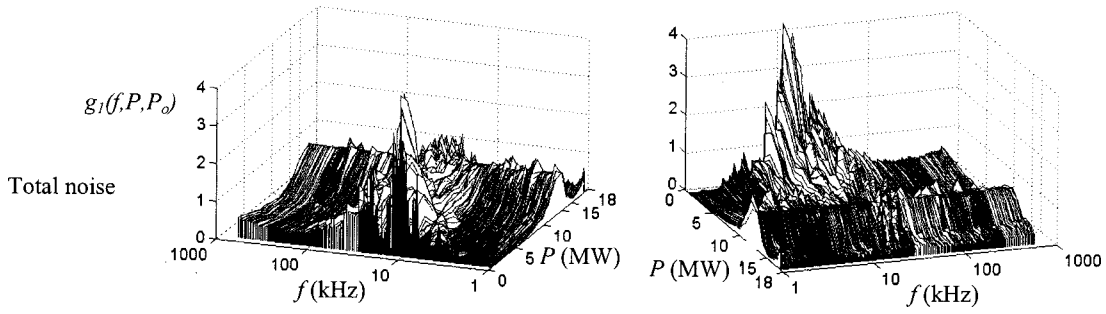

Fig. 5 Normalized spectra of Fig. 3 (P_o=13.3 MW) presented two dimensionally, seen from two perspectives

$$I_v(P)=\sum_{m=0}^{M} {}^{(m)}I_v(P).$$

This last form of the cavitation description, in which there is no longer frequency dependence, will be used as a final cavitation intensity estimate. As to the turbine-power dependence of the relative intensities of the mechanisms, it will be assumed that its form stays the same for all the frequency components contributing to a particular mechanism. Consequently, the dependence found within a narrow frequency range that is typical for the mechanism (Fig. 7) will be used:

$m=1$: octave band centered at $f=31.5$ kHz, $0<P$ (MW)<7;
$m=2$: octave band centered at $f=125$ kHz, $7<P$ (MW)<14;
$m=3$: octave band centered at $f=125$ kHz, $14<P$ (MW).

Cavitation Intensity Estimates

A weak point in the previous discussion derives from the fact that everything in it is based on the results obtained on only one guide vane, $v=1$. While such results may rather safely be used to identify the $(f,P)_m$ ranges and to optimize the analysis, no quantitative estimates of cavitation intensity may be derived from them. Indeed, as stated in Bajic [20], spatial averaging is neces-

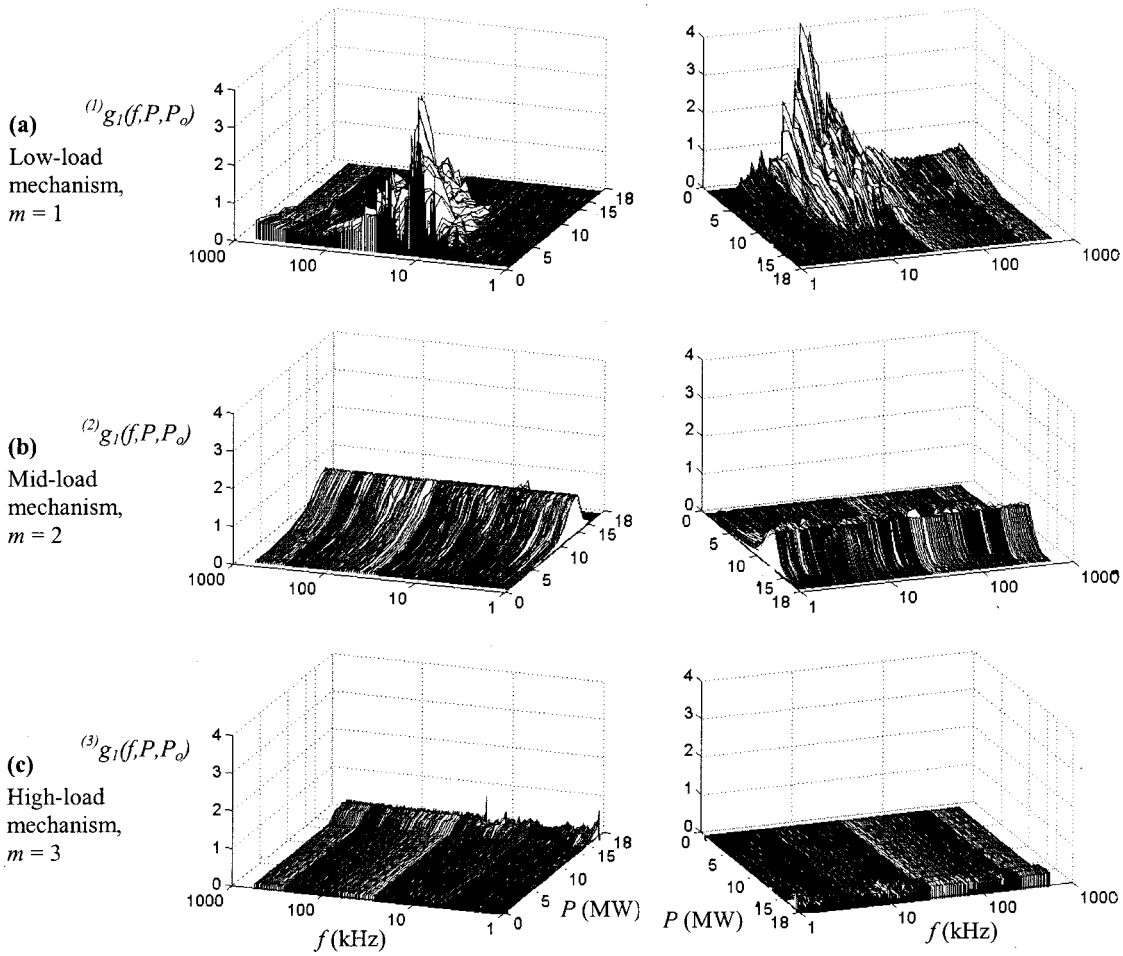

Fig. 6 Noise decomposition: contribution of the three cavitation mechanisms to the total noise

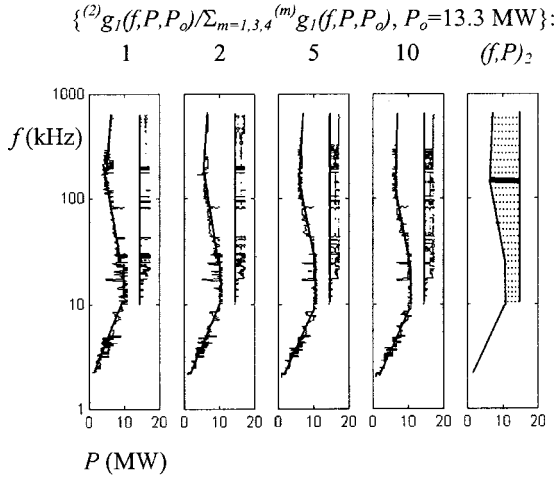

Fig. 7 The way used to determine the range of prevalence of a mechanism m, $(f,P)_m$, in the total noise is illustrated here by the $m=2$ case. At the P-values between the pairs of curves the $m=2$ intensity is equal resp. 2, 5, or 10 times stronger than the rest of the intensity. There from the $(f,P)_2$ denoted; the ratio 5 is assumed sufficiently high.

sary to derive stable estimates of cavitation intensity which would be representative of all the segments of a cavitating flow. Thus, instead of $I_v(P)$ and ${}^{(m)}I_v(P)$, the estimates

$$I(P)=\langle I_v(P)\rangle_v \quad \text{and} \quad {}^{(m)}I(P)=\langle {}^{(m)}I_v(P)\rangle_v$$

should be used. One more calibration step is needed in order to produce a stable and representative estimate of the total cavitation intensity, $C(P)$. The data related to the chosen frequency bands that are found suitable for the estimation of the mechanisms should be combined into the estimates of the mechanisms' intensities. This can be done by making the contribution to the cavitation intensity of the mechanism m, ${}^{(m)}C(P)$, stemming from the vane v, proportional to the quantity

$$\frac{G_v(f,P)}{G_1(f,P)}\times {}^{(m)}I_1(P), \quad (f,P)\in(f,P)m,$$

where stable-in-f low-resolution spectra should be used. Such data, which are based on the total noise power but incorporate the dependence on turbine power as it is described by the spectra determined within the (f, P) ranges specific for the mechanism considered, are then averaged over all the v's to yield the final estimates of the mechanisms' intensity. Considered within their respective (f, P) ranges and summed, these estimates then yield the final estimate of the total cavitation intensity. Additionally, this final estimate—which is not more than a relative estimate of cavitation intensity—is normalized relative to its maximum.

Role of Guide Vanes and Runner Blades

The 19 equidistant peaks in the modulation curves of Fig. 4, noticeable at most power values but strongest between 9.9 and 14.3 MW, are due to interaction of one guide vane (in this case $v=1$) and the 19 runner blades. Such modulation curves obtained at all the guide vanes, in the same frequency band as in Fig. 4 at a power value lying within $(f,P)_2$, are presented in Fig. 8(b). This strong BPF-modulation is found to be characteristic of mechanism 2. As to mechanism 1, the modulation in its (f, P) range, illustrated by the 1.9 MW curve in Fig. 8(a), is undetectable. The small fluctuations observable there are due to random errors. The situations like these in Figs. 8(a) and 8(b) were found within the whole $(f,P)_1$ and $(f,P)_2$ ranges. Therefore, as to the mechanisms 1 and 2, the noise produced by mechanism 1 does not

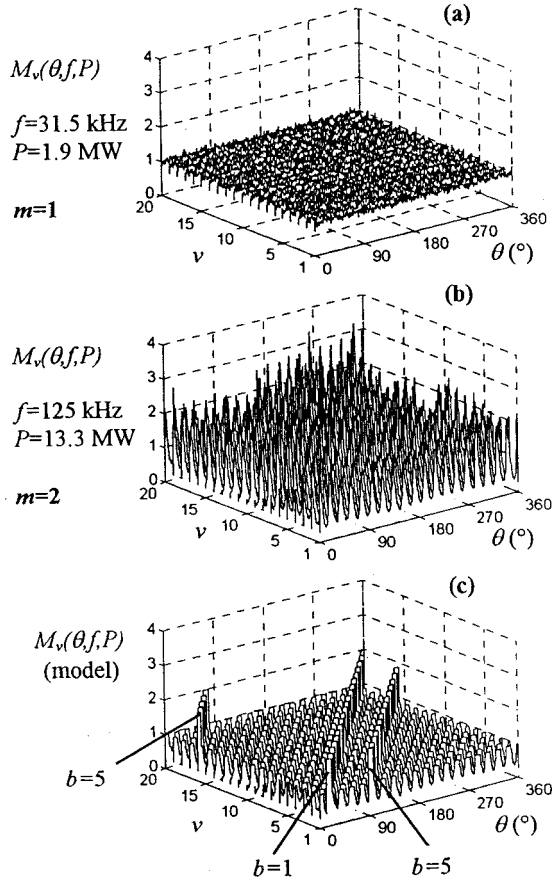

Fig. 8 Typical cases of noise modulation

depend on the angular position of the runner, and there is a series of 19 peaks for every guide vane in the modulation curves of noise produced by mechanism 2.

An interesting regularity can be noted in the set of 19×20 peaks related to mechanism 2. There is a systematic shift of the peaks related to the same runner blade as detected by the subsequent guide vanes. This is illustrated in Fig. 8(c) by the model which was derived by manipulating the amplitudes of the peaks of Fig. 8(b) while leaving their positions unchanged. As an example, two series of peaks are denoted here, the ones due to the interaction of runner blades 1 and 5 with the 20 guide vanes. Obviously, the regularity found in the modulation waveforms can be used to identify the contribution of each runner blade to the noise measured at every guide vane. Here the assumption has to be introduced that a distinct maximum related to a particular b/v-pair stems from cavitation in the vicinity of the guide vane v and thus can be used as a measure of its cavitation activity. Such a heuristic assumption is supported by the form of the peaks and the fact that they do not overlap (cf. Figs. 4 and 8(b)).

A filtering procedure based on the regularity of the described $M_v(\theta,f,P)$ structure has been devised and applied to the modulation data. Allowing for a small random spread of angular positions of the peaks, the peaks' maxima were estimated. These were attributed to the related v's and b's and denoted by $M_v^b(f,P)$. Such data were then classified with respect to the f and P values, so that the estimates, ${}^{(m)}M_v^b(P)$, of the component generated by the mechanisms were derived. These were defined by

$${}^{(m)}M_v^b(P)=M_v^b(f,P)\big|_{(f,P)\in(f,P)_m}$$

because there were no significant variations of $M_v^b(f,P)$ within $(f,P)_m$. An alternative for the opposite case reads

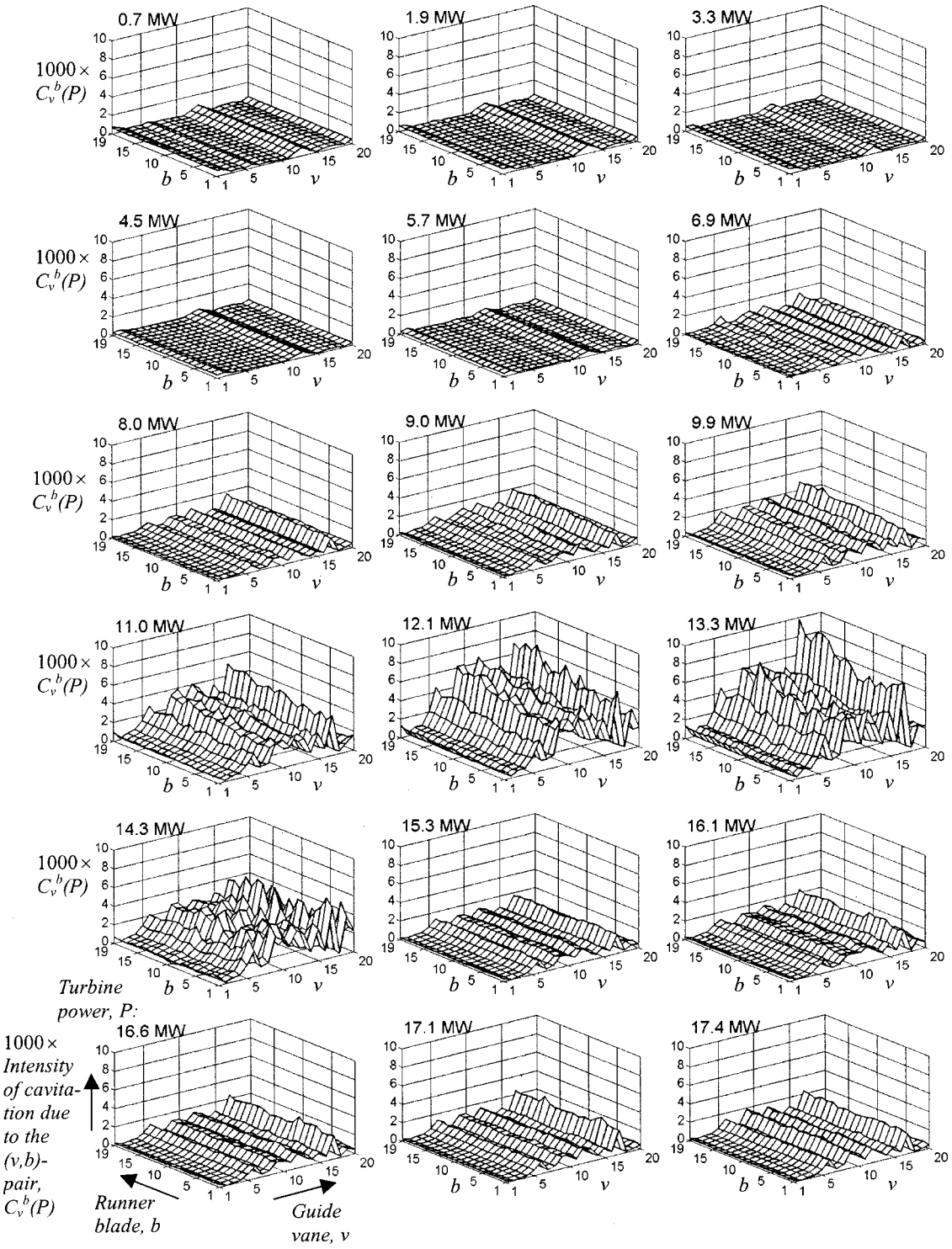

Fig. 9 The fine-structure cavitation characteristics of the turbine: the most detailed description of cavitation that can be obtained by the multidimensional method. For each tested turbine-power value, *P*, there are 380 (number-of-runner-blades×number-of-guide-vanes) dimensionless values, C_v^b, that stand for the intensity of cavitation caused by the interaction of a pair consisting of the runner blade *b*, and the guide vane *v*. The C_v^b-values specify the relative intensity of cavitation. Their use in cavitation erosion estimation is discussed elsewhere (Bajic [14,17]). The data presented in the figure describe total cavitation. The method also enables identification of different segments of a cavitating flow—cavitation mechanisms—and yields data like this for each of them.

$$^{(m)}M_v^b(P)=\langle M_v^b(f,P)|_{(f,P)\in(f,P)_m}\rangle_f .$$

Note that there are only four variables in these estimates: m, v, b, and P; noise frequency has disappeared.

In order to transform these results of modulation analysis into the estimates of true intensities like those presented in Fig. 9, the quantities

$$^{(m)}I_v^b(P)=^{(m)}I_v(P)\left[^{(m)}M_v^b(P)\Big/\sum_{b'=1}^{B}{}^{(m)}M_v^{b'}(P)\right]$$

were computed and used in the following formulas:

$$^{(m)}C_v^b(P)=k\,^{(m)}I_v^b(P),\quad C_v^b(P)=\sum_{m=1}^{M}{}^{(m)}C_v^b(P),$$

$$^{(m)}C^b(P)=\sum_{v=1}^{V}{}^{(m)}C_v^b(P),\quad C^b(P)=\sum_{v=1}^{V}C_v^b(P),$$

$$^{(m)}C_v(P)=\sum_{b=1}^{B}{}^{(m)}C_v^b(P),\quad C_v(P)=\sum_{b=1}^{B}C_v^b(P),$$

$$^{(m)}C(P)=\sum_{b=1}^{B}\sum_{v=1}^{V}{}^{(m)}C_v^b(P),\quad C(P)=\sum_{b=1}^{B}\sum_{v=1}^{V}C_v^b(P);$$

by means of the calibration constant

$$k=\left[\max_P\sum_{m=1}^{M}\sum_{b=1}^{B}\sum_{v=1}^{V}{}^{(m)}I_v^b(P)\right]^{-1}.$$

$C(P)$ was scaled to a maximum value of 1.

Turbine Cavitation Characteristics

The C-functions of turbine power, P, introduced above, are turbine cavitation characteristics. Four of them deal with all the cavitation mechanisms at once and differ only in the degree and type of resolution with respect to turbine parts—guide vanes, v, and runner blades, b:

$C_v^b(P)$ *fine-structure characteristic*,
$C^b(P)$ *runner characteristic*,
$C_v(P)$ *wicket gate characteristic*, and
$C(P)$ *global turbine characteristic*.

The other four (sets of) characteristics, $^{(m)}C_v^b(P)$, $^{(m)}C^b(P)$, $^{(m)}C_v(P)$, and $^{(m)}C(P)$, yield the same description of cavitation as above but separately for every one of M mechanisms, $m=1,\ldots M$. Some of the characteristics derived for the turbine considered are illustrated in Figs. 9–12.

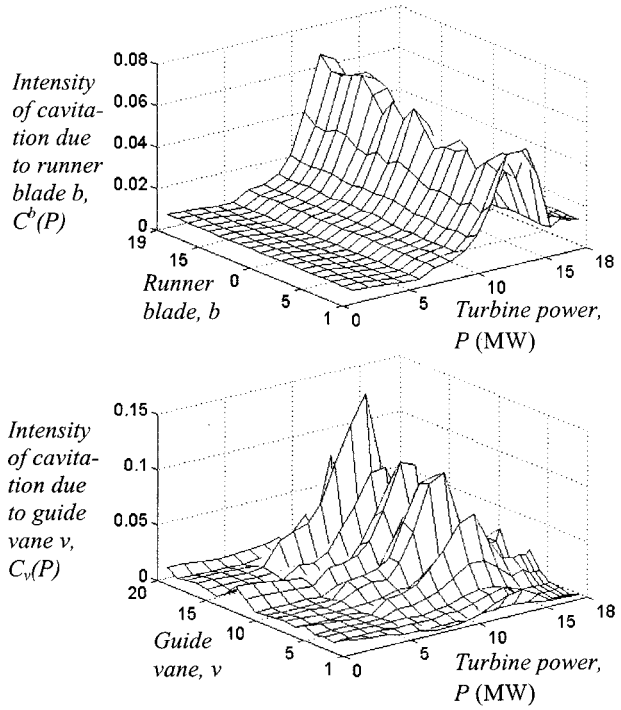

Fig. 10 Runner and wicket gate cavitation characteristics

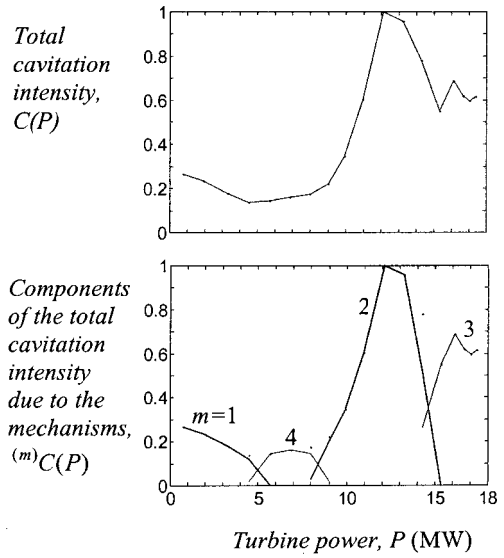

Fig. 11 Global turbine characteristics without and with resolution with respect to cavitation mechanisms

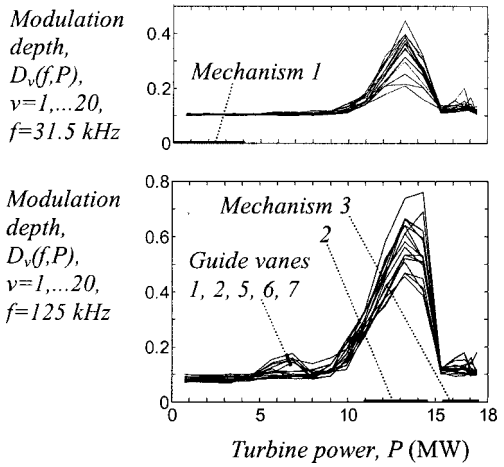

Fig. 12 Check of (in)stationarity: variation of cavitation intensity at the (f,P)-values characteristic of the mechanisms

Conclusion

Vibro-acoustical diagnostics of turbine cavitation based on a number of suitably located sensors and multidimensional data processing, proposed and verified here, utilizes an exhaustive set of measurement data to reconstruct a virtual vibro-acoustic picture of cavitation, which enables iterative adaptive analyses and thus reveals details that otherwise may remain undetected. Such multidi-

mensional diagnostics enables identification of different cavitation mechanisms functioning in a turbine, proves to be a highly sensitive tool for reliable estimation of turbine cavitation characteristics, and yields detailed quantitative descriptions of the role critical turbine parts play in the cavitation process. It removes several disadvantages encountered in practice with simpler approaches.

Typical diagnostic results enable optimizing a turbine's operation with respect to cavitation erosion and improving a turbine's cavitation behavior if necessary. The results may also be used to set up a high-sensitivity, reliable, application-specific cavitation monitoring system.

Acknowledgment

The experimental data used in this paper were collected on a turbine of the Walchensee Hydro Powerplant owned by the Bayernwerk Wasserkraft AG, Bavaria, Germany. The author is grateful to Dr. Andreas-Peter Keller of Hydraulic Research Laboratory of the Munich University of Technology in Obernach and Dipl.-Ing. Hans-Peter Schanderl of the Walchensee Hydro Powerplant for initiating and enabling these measurements.

Nomenclature

b = runner blade
B = number of runner blades, $B=19$
BPF = blade-passage frequency, Bf_o
$C(P)$ = total cavitation intensity
$C_v(P)$ = intensity of the cavitation component due to action of guide vane v
$C^b(P)$ = intensity of the cavitation component due to action of runner blade b
$C_v^b(P)$ = intensity of the cavitation component due to action of the (v,b)-pair
${}^{(m)}C(P)$ = intensity of cavitation mechanism m
${}^{(m)}C_v(P)$ = intensity of the component of cavitation mechanism m due to action of guide vane v
${}^{(m)}C^b(P)$ = intensity of the component of cavitation mechanism m due to action of runner blade b
${}^{(m)}C_v^b(P)$ = intensity of the component of cavitation mechanism m due to action of the (v,b)-pair
$D_v(f,P)$ = $\langle [M_v(\theta,f,P)-1]^2\rangle \theta^{1/2}$
= modulation depth
f = noise frequency
f_o = revolution frequency, $f_o=500\ \mathrm{min}^{-1}$
$(f,P)_m$ = part of the (f, P)-domain within which mechanism m is domineering
G_o = reference power-spectrum value
$g_v(f,P,P_o)$ = $G_v(f,P)/G_v(f,P_o)$
= normalized power spectrum
$G_v(f,P)$ = power spectrum density of noise sensed at guide vane v (various resolutions)
${}^{(m)}g_v(f,P,P_o)$ = component of $g_v(f,P,P_o)$ generated by mechanism m
${}^{(m)}G_v(f,P)$ = component of $G_v(f,P)$ generated by mechanism m
I_o = reference noise-power value
$I(P)$ = total noise power
$I_v(P)$ = total noise power as sensed on v
${}^{(m)}I(P)$ = power of noise component generated by mechanism m
${}^{(m)}I_v(P)$ = power of noise component generated by mechanism m as sensed on v
${}^{(m)}I_v^b(P)$ = power of noise component generated by mechanism m due to action of the (v,b)-pair
k = calibration constant
m = cavitation mechanism $(1,2,\ldots M)$; $m=0$ background
M = number of cavitation mechanisms detected in the turbine
$M_v(\theta,f,P)$ = amplitude modulation of noise power sensed at v at power P within a chosen frequency band centered at f, expressed as a function of θ; $\langle M_v(\theta,f,P)\rangle_0=1$
$M_v^b(f,P)$ = peak value (in θ) of the component of $M_v(\theta,f,P)$ related to the (v,b)-pair
${}^{(m)}M_v^b(P)$ = component of $M_v^b(f,P)$ related to mechanism m
P = turbine power
P_o = reference turbine-power value
PND = power net disturbance
v = guide vane (1, 2, 3, ... in Fig. 1)
V = number of guide vanes, $V\approx 20$
θ = instantaneous angular position of the runner
$\langle\rangle_f$ = averaging over f within a denoted band
$\langle\rangle_v$ = averaging over $v=1,2,\ldots V$
$\langle\rangle_\theta$ = averaging over $\theta\in[0,2\pi]$

References

[1] Abbot, P. A., 1989, "Cavitation Detection Measurements on Francis and Kaplan Hydroturbines," *Proceedings of the International Symposium on Cavitation Noise and Erosion in Fluid Systems*, ASME, New York, FED-Vol. 88, pp. 55–61.

[2] Abbott, P. A., and Morton, D. W., 1991, "Hydroturbine Cavitation Detection Using Advanced Acoustic Emissions Techniques," *Hydroacoustics Facilities, Instrumentation and Experimental Techniques*, ASME, New York, NCA-Vol. 10, pp. 75–84.

[3] Gulich, J.-F., 1992, "Kavitationsdiagnose an Kreiselpumpen," *Technische Rundschau Sulzer*, (1), pp. 30–35.

[4] Knapp, W., Schneider, Ch., and Schilling, R., 1992, "Experience With an Acoustic Cavitation Monitor for Water Turbines," *Cavitation, Proceedings of the ImechE International Conference*, C453/048, ImechE, London, pp. 271–275.

[5] Bourdon, P., Simoneau, R., and Avellan, F., 1993, "Erosion Vibratory Fingerprint of Leading Edge Cavitation of a NACA Profile and of a Francis Model and Prototype Hydroturbine," *Bubble Noise and Cavitation Erosion in Fluid Systems*, ASME, New York, FED-Vol. 176, pp. 51–67.

[6] Bajic, B., and Keller, A., 1996, "Spectrum Normalization Method in Vibro-acoustical Diagnostic Measurements of Hydroturbine Cavitation," ASME J. Fluids Eng., **118**, pp. 756–761.

[7] Farhat, M., Bourdon, P., and Lavigne, P., 1996, "Some Hydro Quebec Experiences on the Vibratory Approach for Cavitation Monitoring," Int. J. on Hydropower Dams, **3**, pp. 151–160.

[8] Vizmanos, C., Egusquiza, E., and Jou, E., 1996, "Cavitation Detection in a Francis Turbine," Int. J. Hydropower Dams, **3**, pp. 161–168.

[9] Bajic, B., 1996, "Vibro-acoustical Diagnosis of Hydroturbine Cavitation: Some Measurement and Analysis Methods," Int. J. on Hydropower Dams, **3,** pp. 169–178.

[10] Kaye, M., Holenstein, A., Dupont, Ph., and Rettich, J., 1996, "Acoustic Methods for Monitoring Mechanical Seal Condition and Cavitation Erosion in Hydro Machinery," Int. J. on Hydropower Dams, **3**, pp. 179–188.

[11] Bourdon, P., Farahat, M., Simoneau, R., Pereira, F., Dupont, Ph., Avellan, F., and Dorey, J.-M., 1996, "Cavitation Erosion Prediction on Francis Turbines—Part I: Measurements on the Prototype," *Proceedings of the XVIII IAHR Symposium on Hydraulic Machinery Cavitation*, Valencia, Spain, **1**, pp. 534–543.

[12] Dorey, J. M., Laperrousaz, E., Avellan, F., Dupont, Ph., Simoneau, R., and Bourdon, P., 1996, "Cavitation Erosion Reduction on Francis Turbines—Part III: Methodologies of Prediction," *Hydraulic Machinery and Cavitation: Proceedings of the XVIII IAHR Symposium on Hydraulic Machinery and Cavitation*, Valencia, Spain, **1**, pp. 564–573.

[13] Dupont, Ph., Caron, J.-F., Avellan, F., Bourdon, P., Lavigne, P., Farhat, M., Simoneau, R., Dorey, J.-M., Archer, A., Laperrousas, E., and Couston, M., 1996, "Cavitation Erosion Prediction on Francis Turbines—Part II: Model Tests and Flow Analysis," *Hydraulic Machinery and Cavitation: Proceedings of the XVIII IAHR Symposium on Hydraulic Machinery and Cavitation*, Valencia, Spain, **1**, pp. 574–583.

[14] Bajic, B., 1996, "A Practical Approach to Vibroacoustical Assessment of Turbine Cavitation," Int. J. Hydropower Dams, **3**, pp. 45–50.

[15] Farhat, M., Bourdon, P., Lavigne, P., and Simoneau, R., 1997, "The Hydrodynamic Aggressive of Cavitating Flows in Hydro Turbines," *Proceedings of the ASME Fluids Engineering Division*, Vancouver, ASME, New York, Vol. FEDS-97, Paper No. 3250.

[16] Bajic, B., 1997, ''Inflow Decomposition: A Vibroacoustical Technique to Reveal Details of Hydroturbine Cavitation,'' Int. J. Hydropower Dams, **4**, pp. 185–196.
[17] Bajic, B., 1999, ''Would Turbine Uprating be Allowable With Respect to Cavitation?—An Example of Vibroacoustic Diagnosis,'' *Proceedings of the Third International Symposium on Cavitation*, Grenoble, **1**, pp. 359–362.
[18] Hermann, O., Holenstein, A., Keck, H., and Rettich, J., 1998, ''Kavitationsmonitoring an Francisturbinen, 4,'' *Symposium Methoden, Nutzen und Trends der Diagnostichen Überwachung von Maschinenschwingungen und weiteren Zustandsgrössen in Wasserkraftanlagen*, Innsbruck, Austria, TIWAG–Schneck, Tagunsband, pp. 207–223.
[19] Bajic, B., 1998, ''Spectrum Tracing: A Vibroacoustic Technique to Identify Mechanisms of Turbine Cavitation,'' Int. J. Hydropower Dams, **5**, pp. 641–652.
[20] Bajic, B., 1998, ''Neue Methoden der Vibroakustischen Diagnostik der Turbinekavitation,'' *10 Internationales Seminar Wasserkraftanlagen*, Vienna, Vienna University of Technology, Tagunsband, pp. 447–458.

J. Chahed
Ecole Nationale d'Ingénieurs de Tunis,
BP No. 37,
1002 Le Belvédère,
Tunis, Tunisia

C. Colin

L. Masbernat

Institut de Mécanique des Fluides de Toulouse,
Avenue Camille Soula,
31400 Toulouse, France

Turbulence and Phase Distribution in Bubbly Pipe Flow Under Microgravity Condition

The role of the turbulence in the void fraction distribution in bubbly pipe flow under microgravity condition is evaluated on the basis of numerical simulations using a Eulerian-Eulerian two-fluid model. In microgravity, the average relative velocity is weak and the void fraction distribution is mainly governed by the turbulence. The simulations show that the turbulent contributions of the added mass force play an important role in the phase distribution phenomenon. It is clearly proved that the turbulence acts on the bubbles distribution not only by the pressure term but also by the turbulent correlations obtained by averaging the added mass force. [DOI: 10.1115/1.1514212]

1 Introduction

In spite of the progress achieved in the bubbly flow modeling, [1–3], some important difficulties subsist; in particular the ability to predict the phase distribution remains limited by the inadequate modeling of the turbulence and of the interfacial forces. Lance and Lopez de Bertodano [4] pointed out, in a remarkable review on the phase distribution phenomena in bubbly two-phase flows, a number of points that are not well considered in the interfacial momentum transfer modeling. Among other effects they have evoked those of the bubble size and of the turbulence.

In bubbly pipe flow, the radial bubble distribution is classically attributed to two main effects. The first one is the lift force due to the slip velocity of the bubble and the vorticity of the liquid flow, [5]. The second one, pointed out by Drew and Lahey [6], is the transversal pressure effect due to the gradient of the turbulence in the radial direction. Since this last work, the development of accurate multidimensional turbulence models has been presented as a requirement for suitable predetermination of two-phase bubbly flows and many experiments have been carried out during the last decades in order to study the turbulence structure in two-phase bubbly flows, [7–11].

In a previous study, Chahed et al. [12] have pointed out the important effect of the turbulent contributions in the modeling of the interfacial momentum transfer: particularly the turbulent correlations generated by the added mass force play an important role in the prediction of the void fraction in a bubbly wake behind a splitter plate. These results were carried out using an Eulerian-Eulerian two-fluid model developed for bubbly flows, [13,14].

In the present paper, the two-fluid model is used to simulate a bubbly pipe flow under microgravity condition. The numerical results are compared to the experimental data of Kamp et al. [15] and the prediction of the void fraction distribution is interpreted according to the role played by the turbulence in the interfacial momentum transfer. Indeed, the experiments of bubbly flows under microgravity condition provide remarkable data that allow to evaluate the specific role of the turbulence in the momentum interfacial exchange: in microgravity, the buoyancy and the interfacial forces associated with the mean relative velocity (drag and lift forces) are close to zero and the interfacial momentum transfer is quite exclusively determined by the turbulence effects.

Contributed by the Fluids Engineering Division for publication in the JOURNAL OF FLUIDS ENGINEERING. Manuscript received by the Fluids Engineering Division November 29, 2000, revised manuscript received May 16, 2002. Associate Editor: L. A. Mondy.

2 Eulerian-Eulerian Two-Fluid Modeling

Eulerian two-fluid models are based on a classical averaging of the balance equations that express in each phase the mass and the momentum conservation. For each variable $\psi_k(\mathbf{x},t)$ defined in the phase k, the mean and fluctuating fields of $\psi_k(\mathbf{x},t)$ are defined, respectively, by $\alpha_k\overline{\overline{\psi_k}}=\langle\chi_k\psi_k(\mathbf{x},t)\rangle$ and $\psi_k'(\mathbf{x},t)=\psi_k(\mathbf{x},t)-\overline{\overline{\psi_k}}$ where χ_k is the characteristic function of the phase k ($\chi_k=1$ in the phase k and 0 everywhere else), α_k is the presence rate of the phase k ($\alpha_k=\langle\chi_k\rangle$) and $\langle\ \rangle$ is an averaging operator that satisfies the Reynolds rules. For steady incompressible bubbly flows ($\rho_k=$const), without mass transfer, the averaged balance equations of mass and momentum for the liquid phase (subscript L) and for the gas phase (subscript G) are, [13],

$$\nabla\cdot(1-\alpha)\overline{\overline{\mathbf{u}_L}}=0 \quad \text{and} \quad \nabla\cdot\alpha\overline{\overline{\mathbf{u}_G}}=0 \tag{1}$$

$$(1-\alpha)\rho_L\frac{D}{Dt}\overline{\overline{\mathbf{u}}}_L=-\nabla\overline{\overline{p_L}}-\nabla\cdot((1-\alpha)\rho_L\overline{\overline{\mathbf{u}_L'\mathbf{u}_L'}})+(1-\alpha)\rho_L\mathbf{g} \quad \text{with} \quad \frac{D}{Dt}=\frac{\partial}{\partial t}+(\overline{\overline{\mathbf{u}}}_L\cdot\nabla) \tag{2}$$

$$0=-\alpha\nabla\overline{\overline{p_L}}+\mathbf{M}_G \tag{3}$$

where $\overline{\overline{\mathbf{u}}}_L$ and $\overline{\overline{\mathbf{u}_G}}$ are the average velocities, respectively, in the liquid and in the gas phases, $\overline{\overline{p}}_L$ is the average pressure in the liquid, $\alpha=\langle\chi_G\rangle$ is the void fraction, and $\mathbf{g}$ is the gravity acceleration.

In Eq. (2), the interfacial momentum transfer M_G has been expressed versus the pressure gradient using Eq. (3). The acceleration and the weight of the gas are neglected in comparison with the force exerted by the liquid on the bubbles; so, Eq. (3) indicates that the total force exerted on the bubbles is zero. This force contains the nonperturbed flow action (pressure term or Tchen force) and the interfacial term $\mathbf{M}_G=\langle\chi_G\mathbf{f}_p^{(1)}\rangle$ where $\mathbf{f}_p^{(1)}$ is the density of the force due to the perturbed flow action. The expression of this force density is

$$\mathbf{f}_p^{(1)}=\frac{1}{\vartheta_B}\int\int_{\partial\vartheta_B}\sigma_L^{(1)}\cdot\mathbf{n}dS=\overline{\nabla\cdot\sigma_L^{(1)}}^{(\vartheta_B)} \tag{4}$$

where $\sigma_L^{(1)}$ designates the stress tensor due to the perturbed flow, ϑ_B and $\partial\vartheta_B$ are the volume and the boundary of the bubble and $^{-(\vartheta_B)}$ is a volume-averaging operator applied on the volume of the bubble. A classical formulation for $\mathbf{f}_p^{(1)}$ is adopted in function of the drag, lift and added mass forces:

$$f_{Pi}^{(1)} = -\frac{3}{4}\rho\frac{C_D}{d}|\mathbf{u}_G - \mathbf{u}_L^{(0)}|(\mathbf{u}_G - \mathbf{u}_L^{(0)}) - C_A\rho\left(\frac{\tilde{d}}{\tilde{d}t}\mathbf{u}_G - \frac{\tilde{D}}{\tilde{D}t}\mathbf{u}_L^{(0)}\right)$$
$$-2\rho C_L\omega^{(0)}\times(\mathbf{u}_G - \mathbf{u}_L^{(0)}) \quad (5)$$

with the material derivatives $\tilde{D}/Dt = \partial/\partial t + \mathbf{u}_L\cdot\nabla$ and $\tilde{d}/dt = \partial/\partial t + u_G\cdot\nabla$. In this expression the velocity $\mathbf{u}_L^{(0)}$ and the vorticity $\omega_L^{(0)}$ are those of the nonperturbed flow, d is the bubble diameter, and (C_D, C_L, C_A), are, respectively, the drag, lift, and added mass coefficients. The formulation of the momentum interfacial exchange set many questions especially concerning the averaging of the fluctuating terms issued from the drag, added mass, and lift forces. The common method consists of only keeping the mean contributions of the interfacial momentum transfer while the turbulent contributions are ignored, [2], or eventually expressed via a supplementary dispersion term proportional to the void fraction gradient, [3,4]. In consideration of the insufficiency of these formulations, Chahed et al. [12] proposed to include the turbulent correlations issued from the added mass force. We consider that the correlation between the fluctuation of velocity and that of the vorticity is relatively weak and we admit that it is possible to adopt a suitable formulation of the drag coefficient that takes into account the effect of the turbulence. Under these conditions, the turbulent contributions of the lift and the drag forces that remain in the average momentum transfer expression are related to the correlation between the velocity fluctuation of the nonperturbed flow and the instantaneous phase distribution. Thus the average interfacial momentum transfer taken in this model is written

$$\mathbf{M}_G = -\frac{3}{4}\alpha\rho_L\frac{C_D}{d}|\overline{\overline{\mathbf{u}}}_R|\overline{\overline{\mathbf{u}}}_R - 2\alpha\rho_L C_L\overline{\overline{\omega}}_L\times\overline{\overline{\mathbf{u}}}_R$$
$$-\alpha\rho_L C_A\left(\frac{d}{dt}\overline{\overline{\mathbf{u}}}_G - \frac{D}{Dt}\overline{\overline{\mathbf{u}}}_L\right) - \rho_L C_A\nabla\cdot\alpha(\overline{\overline{\mathbf{u}'_G\mathbf{u}'_G}} - \overline{\overline{\mathbf{u}'_L\mathbf{u}'_L}}) \quad (6)$$

where $d/dt = \partial/\partial t + (\overline{\overline{\mathbf{u}}}_G\cdot\nabla)$ and $\overline{\overline{\mathbf{u}}}_R$ is the relative velocity given by

$$\alpha\overline{\overline{\mathbf{u}}}_R = \langle\chi_G(\mathbf{u}_G - \mathbf{u}_L)\rangle = \alpha(\overline{\overline{\mathbf{u}}}_G - \overline{\overline{\mathbf{u}}}_L) - \langle\chi_G\mathbf{u}'_L\rangle. \quad (7)$$

It should be observed that in the formulation of the average interfacial momentum transfer, the nonperturbed flow is identified to the continuous phase flow. The average interfacial momentum transfer (Eq. (6)) includes the contribution of the mean flow in the drag, lift and added mass forces as well as the contribution of the turbulence generated by the added mass force. The last term in Eq. (7) represents a correlation between the continuous phase velocity fluctuation and the instantaneous phase distribution. It can be interpreted as a drift velocity associated with a dispersion effect due to bubbles transport by the turbulent fluid motion, [1].

According to the formulation of the interfacial term, the two-fluid model we propose is basically adapted to dilute dispersed gas-liquid flows with small spherical bubbles. In fact this formulation supposes that the bubble diameter is relatively small in comparison with the turbulent scales in the liquid. Besides, the expression of the instantaneous force exerted by the continuous phase on the bubble is only valid for bubbles with low deformation and weak hydrodynamic interactions (low void fraction).

3 Closure of the Turbulence

The two-fluid model presented above requires closure of the turbulent stress tensors in the liquid and in the gas ($\overline{\overline{\mathbf{u}'_L\mathbf{u}'_L}}$, $\overline{\overline{\mathbf{u}'_G\mathbf{u}'_G}}$) and of the dispersion term $\langle\chi_G\mathbf{u}'_L\rangle$. The turbulent stress tensor of the gas $\overline{\overline{\mathbf{u}'_G\mathbf{u}'_G}}$ is related to that of the liquid through a turbulent dispersion model and the turbulent stress tensor of the liquid $\overline{\overline{\mathbf{u}'_L\mathbf{u}'_L}}$ is computed using a second-order closure of the turbulence developed for bubbly flows, [13]. In this model, the Reynolds stress tensor in the liquid is split into two parts: a pseudo-turbulent non-dissipative part $\overline{\overline{\mathbf{u}'_L,\mathbf{u}'_L}}^{(S)}$ induced by the bubbles displacements and controlled by the added mass force and a turbulent dissipative part $\overline{\overline{\mathbf{u}'_L\mathbf{u}'_L}}^{(T)}$ produced by the gradient of the mean velocity which also contains the turbulence generated in the bubble wakes. After modeling, the transport equation for each part writes as follows:

$$\frac{D}{Dt}\overline{\overline{\mathbf{u}'_L\mathbf{u}'_L}}^{(S)} = \mathrm{Diff}(\overline{\overline{\mathbf{u}'_L\mathbf{u}'_L}}^{(S)}) + \frac{3}{20}\frac{D}{Dt}\alpha\|\overline{\overline{\mathbf{u}}}_R\|^2\delta + \frac{1}{20}\frac{D}{Dt}\alpha\overline{\overline{\mathbf{u}}}_R\overline{\overline{\mathbf{u}}}_R \quad (8)$$

$$\frac{D}{Dt}\overline{\overline{\mathbf{u}'_L\mathbf{u}'_L}}^{(T)} = \mathrm{Diff}(\overline{\overline{\mathbf{u}'_L\mathbf{u}'_L}}^{(T)}) - 2\,\mathrm{sym}[\overline{\overline{\mathbf{u}'_L\mathbf{u}'_L}}^{(T)}\cdot\nabla\overline{\overline{\mathbf{u}}}_L] + \Phi - \frac{2}{3}\varepsilon\delta. \quad (9)$$

The transport equation of the pseudo-turbulent part, (Eq. (8)), expresses a diffusive transport (first term of the rhs) and a production-redistribution mechanism related to the added mass force (second and third terms of the rhs). The experimental results in homogenous bubbly flow show that the eddies produced in the wakes of the bubbles are dissipated by viscosity before the spectral transfer takes place, [9]. If we assume that this hypothesis is valid in a wide range of bubbly flows, we can consider that the interfacial production of the turbulent energy and its dissipation rate are balanced in the bubbles wakes. The dissipation rate in the transport equation of the turbulent part (Eq. (9)) is thus identified to the isotropic dissipation at the small scales ε resulting from the energy cascade and the transport equation of the turbulent part has the same form as in single-phase flow.

The diffusion and redistribution terms in Eq. (9) (first and third terms of the rhs) are modified in order to take into account the interfacial effects. In the model of the diffusion term, an additional turbulent transport by the bubbles is introduced with the characteristic time scale τ_b; the single-phase flow model of Launder et al. [16] is thus ''generalized'' in two-phase bubbly flows in the form

$$\mathrm{Diff}(\Psi) = \frac{C_{S\Psi}}{1-\alpha}\nabla[(1-\alpha)(\tau_t\overline{\overline{\mathbf{u}'_L\mathbf{u}'_L}}^{(T)} + \tau_b\overline{\overline{\mathbf{u}'_L\mathbf{u}'_L}}^{(S)})\nabla\Psi] \quad (10)$$

with $\tau_t = \mathrm{trace}(\overline{\overline{\mathbf{u}'_L\mathbf{u}'_L}}^{(T)})/2\varepsilon$ and $\tau_b = C_R\,d/|\overline{\overline{\mathbf{u}}}_R|$.

The redistribution term Φ is, in the same manner as in single-phase flow, split into two parts, a linear part $\Phi^{(L)}$ and a nonlinear part $\Phi^{(\mathrm{NL})}$, so that $\Phi = \Phi^{(L)} + \Phi^{(\mathrm{NL})}$.

The modeling of the nonlinear part $\Phi^{(\mathrm{NL})}$, is based on Lance et al. [17] experimental results in pure shear bubbly flow where they observed a more pronounced tendency to isotropy in two-phase flow in comparison with the equivalent single-phase flow. In order to take into account this effect, they modified the nonlinear part of the single-phase redistribution model by modifying the time scale of turbulent stretching. We adopt their proposition and rewrite the nonlinear term in a different form

$$\Phi^{(\mathrm{NL})} = -C_1(\tau_t^{-1} + \alpha\tau_b^{-1})\left[\overline{\overline{\mathbf{u}'_L\mathbf{u}'_L}}^{(T)} - \frac{1}{3}\mathrm{trace}(\overline{\overline{\mathbf{u}'_L\mathbf{u}'_L}}^{(T)})\right] \quad (11)$$

where we only consider the turbulent part of the Reynolds stress tensor; we thus avoid inappropriate redistribution rates when the pseudo-turbulence is important.

The linear part $\Phi^{(L)}$ is modeled as in single-phase and the Launder et al. [16] model is adopted. We also take into account the wall effect on the redistribution mechanism using a similar single-phase phase model. The transport equation of the dissipation rate ε is also the same as in single-phase flow where the diffusion term is modeled according to Eq. (10).

The dispersion term $\langle\chi_G\mathbf{u}'_L\rangle$ is modeled as a drift velocity that leads to a turbulent diffusion of the void fraction proportional to the void fraction gradient and modeled according to Eq. (10).

4 Simulation of the Bubbly Pipe Flow Under Microgravity Condition

The two-fluid model is used to simulate bubbly pipe flow experiments under microgravity conditions. These experiments described in Kamp et al. [15], were carried out in a transparent Plexiglas tube of 0.04-m inner diameter (D) and 3.17-m length. The water was axially injected in the tube and the air bubbles of 1.2-mm diameter were injected through 24 hypodermic needles of 0.34-mm diameter, uniformly located in the pipe section. At a distance of 70 D from the injection, the tube was equipped with local probes which can be moved in the radial direction: (1) a single hot-film probe for the measurement of the mean and RMS axial velocities of the liquid and (2) a double optical fiber probe for the measurement of the local void fraction and the bubble velocities and diameters. Microgravity conditions were obtained during parabolic flights aboard the Caravelle ''ZERO-G'' aircraft of the ''Center National d'Etudes Spatiales.'' One flight campaign was composed of three flights with thirty parabolas each. During each parabola a microgravity period of 20 seconds was obtained, with a residual level of gravity smaller than 2% of the earth gravity level. In order to obtain convergence of both turbulence intensity and void fraction measurements, five parabolas were used for each probe location, corresponding after subtraction of the 0 g establishment periods to averaging over about 75 seconds. Different flow conditions were investigated, [18]. In the present paper the run corresponding to a superficial velocity of the liquid equal to 1 m/s ($R_{eD}=4.10^4$) and a superficial velocity of gas of 0.023 m/s is simulated. The uncertainty on the measurements is estimated to 2% for the mean velocities of the liquid and to 10% for the RMS velocities. The relative uncertainty is about equal to 5% on the local void fraction, 5% on the mean gas velocity and 15% on the mean bubble diameter, [18]. The shape of the void fraction profile in bubbly flow is similar to the radial distributions of neutrally buoyant particles in a water pipe flow measured by Lahey and Bonneto [19].

The conservation equations are written for quasi-parallel bubbly flows in axisymmetrical cylindrical geometry. The liquid velocity components are noted u, v, w (with the subscript G these velocities are related to the gas), respectively, in the axial x, the radial y and the azimuthal θ coordinates. In absence of gravity, the mass and momentum balances for the liquid are

$$\frac{\partial}{\partial x}(1-\alpha)\bar{\bar{u}}+\frac{1}{y}\frac{\partial}{\partial y}y(1-\alpha)\bar{\bar{v}}=0 \tag{12}$$

$$(1-\alpha)\frac{D\bar{\bar{u}}}{Dt}=-\frac{1}{\rho}\frac{\partial\bar{\bar{p}}}{\partial x}-\frac{1}{y}\frac{\partial}{\partial y}(y(1-\alpha)\overline{\overline{u'v'}}) \tag{13}$$

$$0=-\frac{1}{\rho}\frac{\partial\bar{\bar{p}}}{\partial y}-\frac{1}{y}\frac{\partial}{\partial y}(y(1-\alpha)\overline{\overline{v'^2}})+\frac{1}{y}(1-\alpha)\overline{\overline{w'^2}}. \tag{14}$$

Assuming the isotropy of the turbulence in the plan ($\overline{\overline{v'^2}}=\overline{\overline{w'^2}}$), Eq. (14) reduces to

$$P_e(x)=\bar{\bar{p}}+\rho(1-\alpha)\overline{\overline{v'^2}}. \tag{15}$$

According to the modeling of the interfacial momentum transfer (Eq. (6)) and with the boundary layer approximation, the mass and momentum balance equations of the gas can be written as

$$\frac{\partial}{\partial x}\alpha\overline{\overline{u_G}}+\frac{1}{y}\frac{\partial}{\partial y}(y\alpha\overline{\overline{v_G}})=0 \tag{16}$$

$$0=-\frac{1}{\rho}\frac{\partial\bar{\bar{p}}}{\partial x}-\frac{3}{4}\frac{C_D}{d}|\overline{\overline{\mathbf{u}_R}}|\overline{\overline{u_R}}-C_A\left(\frac{d}{dt}\overline{\overline{u_G}}-\frac{D}{Dt}\bar{\bar{u}}\right)+\frac{C_A}{\alpha y}\frac{\partial}{\partial y}y(\alpha\overline{\overline{u'_Gv'_G}}-\alpha\overline{\overline{u'v'}}) \tag{17}$$

$$0=\frac{\partial}{\partial y}((1-\alpha)\overline{\overline{v'^2}})+(1-\alpha)\frac{\overline{\overline{v'^2}}-\overline{\overline{w'^2}}}{y}-\frac{3}{4}\frac{C_D}{d}|\overline{\overline{\mathbf{u}_R}}|\overline{\overline{v_R}}-\frac{C_A}{y\alpha}\frac{\partial}{\partial y}y(\alpha\overline{\overline{v'^2_G}}-\alpha\overline{\overline{v'^2}})-C_L\overline{\overline{u_R}}\frac{\partial\bar{\bar{u}}}{\partial y}. \tag{18}$$

Equations (17) and (18) show that the turbulence acts on the momentum balance by the pressure term and by the turbulent correlations of the liquid and of the gas generated by the the added mass force. Under microgravity condition, the average contributions of the added mass and lift forces are negligible and the drag adjusts itself to the turbulent terms in the interfacial momentum transfer. As a result, the void fraction distribution is, in this case, principally controlled by the turbulent terms and by the dispersion effect due to the drift velocity.

The Reynolds stress tensor of the gas is related to that of the liquid through a turbulent dispersion model. The components of the Reynolds stress tensor in the gas are expressed versus the corresponding components in the liquid in the form

$$\overline{\overline{u'_Gu'_G}}=C_{11}\overline{\overline{u'u'}}\quad\overline{\overline{v'_Gv'_G}}=C_{22}\overline{\overline{v'v'}}\quad\overline{\overline{u'_Gv'_G}}=C_{12}\overline{\overline{u'v'}}. \tag{19}$$

The coefficients of the normal components are formulated on the basis of the Tchen-Hinze theory developed for homogenous turbulence, [20]:

$$C_{11}=C_{22}=C_T\frac{b^2+\tau_r}{1+\tau_r}\quad\text{with}\quad b=\frac{1+C_A}{\frac{\rho_G}{\rho}+C_A}\approx\frac{1+C_A}{C_A}$$

$$\text{and}\quad\tau_r=\frac{\tau_t}{\tau_p} \tag{20}$$

where $\tau_p=(\rho_G/\rho+C_A)/(\frac{3}{4}C_D/d\,|\mathbf{u}_R|)$ is the bubble relaxation time and τ_t is the time scale of the liquid turbulence. The coefficient C_T is introduced in order to take into account the loss of correlation that might occur because of the bubbles deformation, of the flow inhomogeneity and generally speaking, of the deviation from the Tchen theory hypothesis.

The formulation of the nondiagonal component of the Reynolds stress tensor of the gas is based on the turbulent viscosity concept. The velocity gradients in both phases are assumed to be equal (the relative velocity is small as compared to the liquid velocity), thus the nondiagonal components of the Reynolds stress in the gas can be expressed as a function of that of the liquid in the form

$$\frac{\overline{\overline{u'_Gv'_G}}}{\overline{\overline{u'v'}}}=\frac{\nu_{tG}}{\nu_t}=C_{12} \tag{21}$$

where ν_t is the liquid turbulent viscosity and ν_{tG} is the gas one.

Csanady [21] has proposed to link the turbulent diffusivity of the dispersed phase to the continuous one through an expression that takes into account the crossing trajectory effect. In the absence of mean relative velocity between phases, this effect is negligible and C_{12} is a constant of order unity.

Finally, the drift velocity is modeled as a dispersion effect proportional to the void fraction gradient. With the quasi-parallel approximation, the relative velocity components are written as

$$\overline{\overline{u_R}}=\overline{\overline{u_G}}-\bar{\bar{u}}\ \text{ and }\ \overline{\overline{v_R}}=\overline{\overline{v_G}}-\bar{\bar{v}}-\frac{C_{DT}}{\alpha}D_{yy}\frac{\partial\alpha}{\partial y}$$

$$\text{with}\ \ D_{yy}=C_{sk}(\tau_t\overline{\overline{v'^{2(T)}}}+\tau_b\overline{\overline{v'^{2(S)}}}). \tag{22}$$

A two-dimensional numerical code has been developed for parabolic flow resolution. The numerical method is based on finite difference scheme and the equations are solved with an explicit method. At each iteration, the mass flow rate for the liquid is

calculated with the updated velocity fields and the pressure drop is adjusted considering the actual and computed mass flow rates. The computation is repeated until convergence concerning the liquid velocity is obtained within specified tolerance.

5 Results and Discussion

Velocity Profiles of the Liquid. Figures 1 and 2 present the results of the numerical simulations of the mean velocity profiles of the liquid in single-phase flow (for a superficial velocity of the liquid $j_L=1$ m/s) and in bubbly flow under microgravity condition (for $j_L=1$ m/s and a superficial velocity of the gas $j_G=0.023$ m/s). These results are compared to the experimental data of Kamp et al. [15] obtained for the same flow conditions and we observe a good concordance between the numerical results and the experimental data. In Fig. 2, the liquid velocity is scaled by the friction velocity u^* and plotted versus the wall coordinate $y^+=yu^*/\nu$. Figures 1 and 2 show that the bubble flow structure in microgravity is quite the same as in single-phase flow. Particularly, Fig. 2 indicates that the single-phase logarithmic profile in the wall vicinity is maintained in bubbly flow under microgravity with the same characteristics. This outcome indicates that under microgravity (without relative velocity between phases), the turbulent shear stress is not altered with respect to the single-phase flow. Indeed, in microgravity, the momentum balance of the liquid (Eq. (2)) is, for low void fraction, quite the same as in single-phase flow.

On the other hand, under microgravity condition the relative velocity is very small and the pseudo-turbulence is consequently negligible. In the absence of pseudo-turbulence, the turbulence model reduces to the classical single-phase second-order closure of the turbulence proposed by Launder et al. [16]. Consequently, the numerical results of the turbulent intensity are roughly the same in single-phase in normal gravity and in bubbly flow under microgravity condition, (Fig. 3).

Void Fraction Profiles. In the following, the effect of the interfacial momentum transfer modeling on the phase distribution phenomena is discussed and the analysis is focused on the role played by the turbulent contributions (the only terms that are for importance under microgravity condition). For this purpose, different numerical simulations are performed with various interfacial momentum transfer models and the void fraction distribution is analyzed with respect to the effect of the turbulent terms in the interfacial momentum transfer.

The first test concerns the interfacial models that only consider the turbulent contribution of the interfacial momentum transfer through a diffusion term proportional to the gradient of the void fraction. In the first set of simulations, the lift force is omitted and the dispersion effect is introduced as a drift velocity (Eq. (22)) with four values of the coefficient C_{DT} ($C_{DT}=0.05$, $C_{DT}=0.5$, $C_{DT}=1$ and $C_{DT}=2$). In this case, only the three first terms of the rhs of Eq. (18) remain. The two first terms represent the pressure gradient effect that was pointed out to be responsible for the bubbles migration toward the wall in the vertical bubbly pipe flow in normal gravity, [6,7]. This migration leads to the apparition of the near wall void fraction peaking. An important result of the bubbly flow in microgravity experiments is to show that, even though the gradient of the liquid turbulence is not significantly modified in microgravity, the radial gradient of the void fraction is inverted depending on whether the gravity is active or not (depending on whether the interfacial momentum transfer associated with the average relative velocity is important or not). Since the gradient of the turbulent components of the Reynolds stress tensor is not inverted in microgravity condition, the numerical results of the first set of simulations exhibit a near wall void fraction peaking that is not observed in the experiment (Fig. 4). The dispersion term yields a simple diffusion effect that leads to an attenuation of the near wall void fraction peaking but can't obviously invert the void fraction gradient to produce the void fraction maximum in the centerline of the pipe as observed in the experiment. This result clearly shows that the formulation of the forces exerted by the liquid on the bubbles is incomplete and set the problem of the specific role played by the turbulent contributions in the interfacial transfer.

In the second set of simulations, the small effect of the lift force is highlighted. The dispersion effect is maintained with the coefficient $C_{DT}=1$ and the lift force is introduced with the coefficient C_L that takes values between 0 and 0.2. The numerical results of the second set of simulations presented in Fig. 5 show that the effect of the mean lift force on the phase distribution phenomena

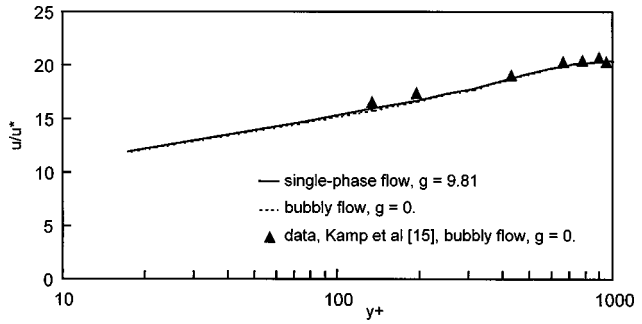

Fig. 2 Logarithmic near wall profiles of the mean velocity simulated in single-phase pipe flow in normal gravity (——) and in bubbly pipe flow (- - -) under microgravity condition. Comparison with the experimental data (▲ bubbly flow in microgravity) of Kamp et al. [15].

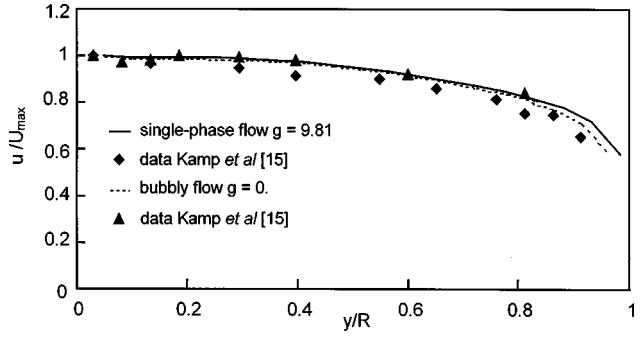

Fig. 1 Mean velocity profiles in single-phase pipe flow in normal gravity and in bubbly pipe flow under microgravity condition. Comparison of the numerical results: (—— single-phase flow, - - - bubbly flow) with the experimental data (♦ single phase flow, ▲ bubbly flow in microgravity) of Kamp et al. [15].

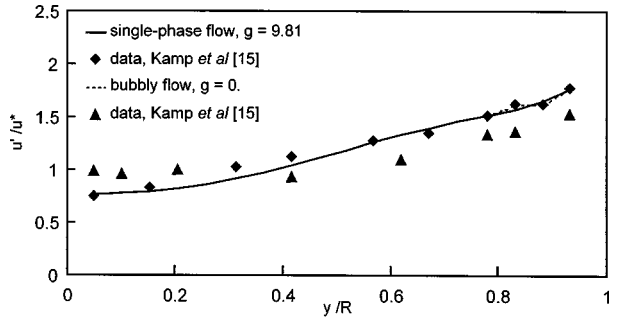

Fig. 3 Longitudinal turbulent intensity profiles in single-phase pipe flow in normal gravity (——) and in bubbly pipe flow under microgravity condition (- - -). Experimental data (♦ single phase flow, ▲ bubbly flow in microgravity) of Kamp et al. [15].

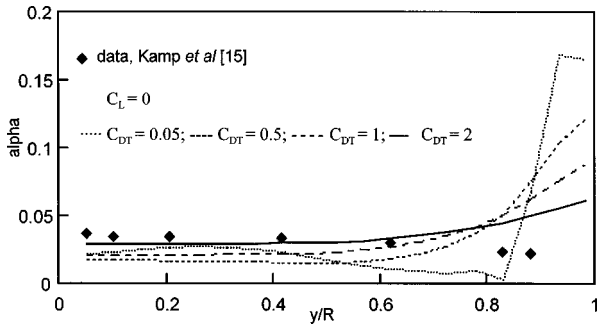

Fig. 4 Effect of the drift on the void fraction profiles in bubbly pipe flow under microgravity condition; simulations without the turbulent contribution of the added mass force (lift force coefficient $C_L=0$): simulations with $\cdots\cdots C_{DT}=0.05$; $---C_{DT}=0.5$; $-\cdot-\cdot-C_{DT}=1$; $——C_{DT}=2$, ♦ experimental data of Kamp et al. [15]

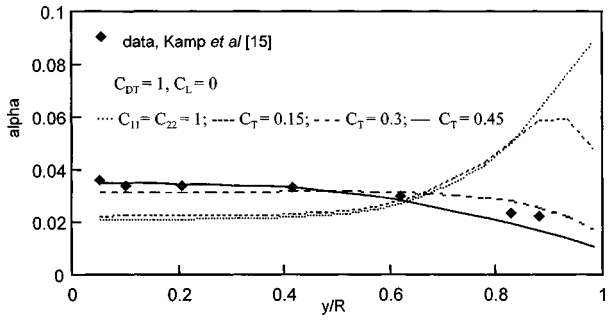

Fig. 6 Effect of the added mass turbulent term in the transversal momentum balance on the void fraction profiles in bubbly pipe flow under microgravity condition (drift coefficient $C_{DT}=1$, lift coefficient $C_L=0$): simulations with $\cdots\cdots C_{11}=C_{22}=1$; $---C_T=0.15$; $-\cdot-\cdot-C_T=0.3$; $——C_T=0.45$, ♦ experimental data of Kamp et al. [15]

is insignificant: As expected in microgravity, the mean relative velocity is very small, then the lift force vanishes.

In the third set of simulations, the sensibility of the void fraction distribution to the turbulent correlations issued from the added mass force is analyzed. For this purpose the turbulent correlations generated by the added mass force are introduced in the expression of the interfacial force (last term of Eq. (17) and fourth term of the rhs of Eq. (18)). In these simulations, the coefficient C_{12} of Eq. (21) is taken equal to 1, and the coefficient C_T takes values between 0.15 and 0.45. Considering the previous numerical results, the mean lift force is neglected, $(C_L=0)$ and the drift effect is maintained with the coefficient $C_{DT}=1$. In Fig. 6, the numerical results are compared to those obtained without the turbulent contribution of the added mass term $(C_{11}=C_{22}=1)$ and to the experimental data of Kamp et al. [15].

Figure 6 shows that the turbulent correlations in the added mass force provoke an inversion of the action of the fluctuating flow field (the only effects considered in these simulations) and allow, after suitable adjustment of the coefficient C_T, to obtain a maximum of the void fraction in the centerline of the pipe as observed in the microgravity experiment. The interpretation of the transversal momentum balance of the gas phase provides an explanation to the effect of the turbulent correlations issued from the added mass force on the interfacial momentum transfer and thus on the phase distribution phenomena. Assuming the turbulence isotropy in the transversal plan, the transversal momentum balance equation of the gas is written as

$$0=\frac{\partial}{\partial y}(1-\alpha)\overline{\overline{v'^2}}-\frac{3}{4}\frac{C_D}{d}|\overline{\overline{\mathbf{u}}_R}|\overline{\overline{v}_R}-C_A\frac{\partial}{\partial y}((C_{22}-1)\overline{\overline{v'^2}})$$
$$-\frac{C_A}{y\alpha}(C_{22}-1)\overline{\overline{v'^2}}\frac{\partial}{\partial y}y\alpha. \tag{23}$$

In Eq. (23), the turbulent contribution of the added mass force is split into two terms (the two last terms). The last one is a turbulent dispersion proportional to the gradient of void fraction; this term is similar to the drift velocity and leads, in a same manner, to a diffusion of the void fraction. The second term due to the turbulent contribution of the added mass force (second to last term in Eq. (23)) is, for low void fraction, opposed to the pressure term (first term) provided that the coefficient C_{22} exceeds the unity. In Fig. 7, we present, for the different simulations, the numerical profiles of the coefficient C_{22}. This figure shows that when the coefficient C_T is greater than 0.3, the turbulent correlations of the gas exceed three times the turbulent correlations of the liquid in the near wall region. Similar turbulent levels of the gas were observed in bubbly mixing layer, [11]. With such a level of fluctuating gas velocity, the action of the turbulent correlations obtained by averaging the added mass force prevails over the pressure term. The action of the turbulent flow field on the bubbles is thus inverted and the model allows to reproduce the maximum of the void fraction in the centerline of the pipe as observed in the experiment.

The coefficient C_T was adjusted from these numerical simulations and the value $C_T=0.35$ yields the better void fraction pre-

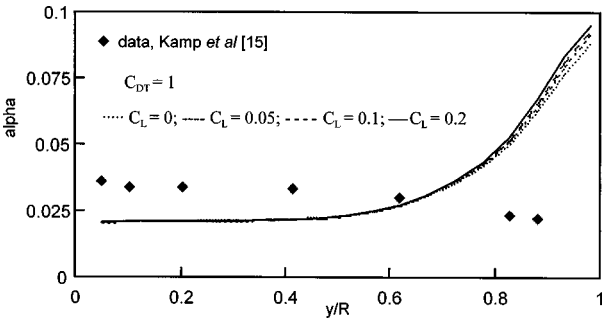

Fig. 5 Effect of the lift force on the void fraction profiles in bubbly pipe flow under microgravity condition; simulations without the turbulent contribution of the added mass force (drift coefficient $C_{DT}=1$): simulations with $\cdots\cdots C_L=0$; $---C_L=0.05$; $-\cdot-\cdot-C_L=0.1$; $——C_L=0.2$, ♦ experimental data of Kamp et al. [15]

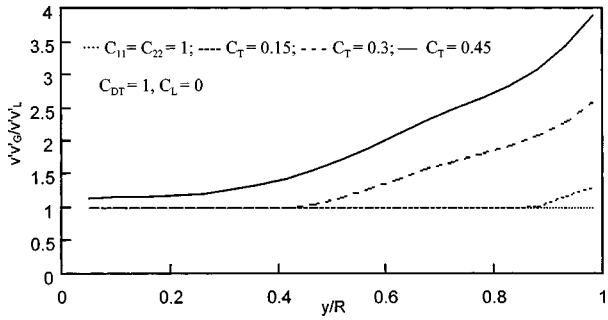

Fig. 7 Ratio between the normal components of the Reynolds stress tensor in the gas and in the liquid phases in bubbly pipe flow under microgravity condition (drift coefficient $C_{DT}=1$, lift coefficient $C_L=0$): simulations with $\cdots\cdots C_{11}=C_{22}=1$; $---C_T=0.15$; $-\cdot-\cdot-C_T=0.3$; $——C_T=0.45$

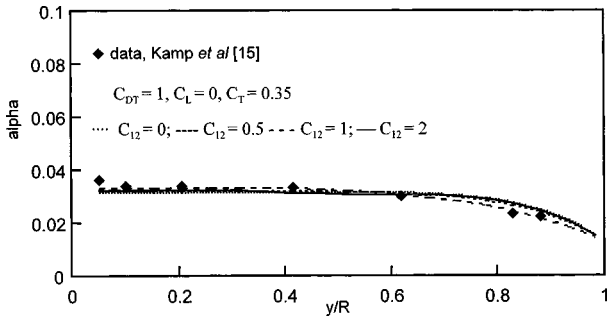

Fig. 8 Effect of the added mass turbulent term in the longitudinal momentum balance on the void fraction profiles in bubbly pipe flow under microgravity condition (drift coefficient $C_{DT}=1$, lift coefficient $C_L=0$, $C_T=0.35$): simulations with $C_{12}=0$; $C_{12}=0.5$ $C_{12}=1$; $C_{12}=2$, ◆ experimental data of Kamp et al. [15]

diction. This value allows also to obtain good prediction of the void fraction distribution in wall bounded bubbly flows in normal gravity, [22].

The previous numerical results are obtained with the coefficient $C_{12}=1$ in Eq. (19): The nondiagonal component of the Reynolds stress tensor of the gas $\overline{\overline{u'_G v'_G}}$ is assumed to be equal to that in the liquid $\overline{\overline{u'v'}}$. In this case the turbulent correlations of the gas and of the liquid in the longitudinal momentum balance equation of the gas (Eq. 17) are in equilibrium and have no effect on the force exerted by the liquid on the bubbles. In the last set of simulations, the effect of these turbulent correlations on the interfacial momentum transfer and thus on the phase distribution phenomena is examined. For this purpose, the same conditions as before are considered ($C_L=0$, $C_{DT}=1$), and the coefficient C_T is taken constant equal to $C_T=0.35$ (this value yields the better void fraction prediction). The numerical results are presented for values of C_{12} varying from 0.5 to 2 and compared to the experimental data of Kamp et al. [15] in Fig. 8. It should be observed that with the value of the coefficient $C_T=0.35$, the dispersion effect due to the drift velocity has low effect in comparison with the dispersion effect due to the last tem of Eq. (23). Figure 8 shows that, in parallel bubbly flow, the turbulent contribution of the added mass force in the longitudinal momentum balance of the gas has a small effect on the transversal void fraction distribution.

Conclusion

The bubbly pipe flow in micro-gravity is an interesting test case for two-fluid models. Indeed, in the absence of a mean velocity between the gas and liquid phases, the lift force vanishes and the radial distribution of the bubbles is mainly controlled by the turbulent effects. This situation allows one to analyze the role played by the turbulence in the interfacial momentum transfer. In fact, the comparison of the numerical simulations with experimental data highlights the shortcomings of the existing models and allows the modeling of the interfacial momentum transfer to be improved. The numerical simulations provide evidence that the turbulence plays a part on the bubbles distribution not only by the pressure term, but also by the turbulent correlations obtained by averaging the interfacial force, particularly in the added mass term.

Despite the relatively simple and perhaps incomplete formulation of the turbulent terms in the interfacial momentum transfer adopted in this two-fluid model, the simulations clearly show some aspects of the role of the turbulent contributions in the interfacial momentum transfer. Of course we are still far from a general modeling of the interfacial transfer in bubbly flows. We have to examine more precisely the role of the other turbulent contributions in the interfacial momentum balance and to improve the representation of the dispersed phase turbulence. We can expect some realistic progress in this direction from direct numerical simulation applied to dispersed two-phase flows.

References

[1] Simonen, O., 1991, "Eulerian Formulation for Particle Dispersion in Turbulent Two-Phase Flows," *Proceedings of the 5th Workshop on Two-Phase Flow Prediction*, M. Sommerfeld and D. Wennerberg, Erlangen, FRG.

[2] Lee, S. J., Lahey, Jr., R. T., and Jones, Jr., O. C., 1989, "The Prediction of Two Phase Turbulence and Phase Distribution Phenomena Using k-ε model," Jpn. J. Multiphase Flow, **3**, pp. 335–368.

[3] Lopez de Bertodano, M., Lee, S. J., Lahey, R. T., and Jones, O. C., 1994, "Development of a k-ε Model for Bubbly Two-Phase Flow," ASME J. Fluids Eng., **116**, pp. 128–134.

[4] Lance, M., and Lopez de Bertodano, M., 1992, "Phase Distribution Phenomena and Wall Effects in Bubbly Two-Phase Flows," Third Int. Workshop on Two-Phase Flow Fundamentals, Imperial College, London, June 15–19.

[5] Auton, T. R., 1987, "The Lift Force on a Spherical Body in a Rotational Flow," J. Fluid Mech., **138**, pp. 199–218.

[6] Drew, D. A., and Lahey, R. T., 1982, "Phase Distribution Mechanisms in Turbulent Low-Quality Two-Phase Flow in Circular Pipe," J. Fluid Mech., **117**, pp. 91–106.

[7] Wang, S. K., Lahey, Jr., R. T., and Jones, Jr., O. C., 1987, "Three Dimensional Turbulence Structure and Phase Distribution Measurements in Bubbly Two Phase Flows," Int. J. Multiphase Flow, **13**, pp. 327–343.

[8] Liu, T. J., and Bankoff, S. G., 1990, "Structure of Air-Water Bubbly Flow in a Vertical Pipe: I—Liquid Mean Velocity and Turbulence Measurements," Int. J. Heat Mass Transf., **36**, pp. 1049–1060.

[9] Lance, M., and Bataille, J., 1991, "Turbulence in the Liquid Phase of an Uniform Bubbly Air Water Flow," J. Fluid Mech., **222**, pp. 95–118.

[10] Serizawa, A., Kataoka, I., and Michiyoshi, I., 1992, "Phase Distribution in Bubbly Flow," *Multiphase Science and Technology*, **6**, G. F. Hewitt, J. M. Delhaye, and N. Zuber, eds., Hemisphere, Washington, DC, pp. 257–301.

[11] Roig, V., Suzanne, C., and Masbernat, L., 1998, "Experimental Investigation of a Turbulent Bubbly Mixing Layer," Int. J. Multiphase Flow, **24(1)**, pp. 35–54.

[12] Chahed, J., Masbernat, L., and Roig, V., 1998, "Turbulence and Void Fraction Prediction in a Bubbly Wake," Third Int. Conf. On Multiphase Flow, Lyon, June 8–12.

[13] Chahed, J., and Masbernat, L., 1998, "Forces interfaciales et turbulence dans les écoulements à bulles," C. R. Acad. Sci. Paris, **326**, pp. 635–642.

[14] Chahed, J., and Masbernat, L., 1998, "Effets de parois sur la distribution de taux de vide dans les écoulements à bulles," C. R. Acad. Sci. Paris, **326**, pp. 719–726.

[15] Kamp, A., Colin, C., and Fabre, J., 1995, "The Local Structure of a Turbulent Bubbly Pipe Flow Under Different Gravity Conditions," *Proceedings of the Second International Conference on Multiphase Flow*, Kyoto, A. Serizawa, T. Fukano, J. Bataille, eds.

[16] Launder, B. E., Reece, G. J., and Rodi, W., 1975, "Progress in the Development of a Reynolds Stress Turbulence Closure," J. Fluid Mech., **68**, Part 3, pp. 537–566.

[17] Lance, M., Marié, J. L., and Bataille, J., 1991, "Homogeneous Turbulence in Bubbly Flows," ASME J. Fluids Eng., **113**, pp. 295–300.

[18] Kamp, A., 1996, "Ecoulements turbulents à bulles dans une conduite en micropesanteur," Ph.D. thesis, Institut National Polytechnique de Toulouse, France.

[19] Lahey, J. R., and Bonetto, F., 1994, "Analysis of Phase Distribution in Microgravity Environments," *Proceedings of the 2nd Microgravity Fluid Physics Conference*, Cleveland, NASA Conference Publication, pp. 193–201.

[20] Hinze, J. O., 1975, *Turbulence*, 2nd Ed., McGraw-Hill, New York.

[21] Csanady, G. T., 1963, "Turbulent Diffusion of Heavy Particles in the Atmosphere," J. Atmos. Sci., **20**, pp. 201–208.

[22] Chahed, J., and Masbernat, L., 2001, "Numerical Simulations of Vertical and Horizontal Wall Bounded Turbulent Bubbly Flows," Fourth Int. Conf. on Multiphase Flow, New Orleans, LA, May 27–June 1.

Modeling and Direct Simulation of Velocity Fluctuations and Particle-Velocity Correlations in Sedimentation

F. R. Cunha
G. C. Abade
A. J. Sousa

Department of Mechanical Engineering,
University of Brasília,
Campus Universitário,
70910-900 Brasília-DF, Brazil

E. J. Hinch
Department of Applied Mathematics
and Theoretical Physics,
University of Cambridge,
Silver Street,
Cambridge CB3 9EW, UK

In this paper we present direct numerical simulations of monodisperse and polydisperse suspensions of non-Brownian particles sedimenting at low Reynolds number. We describe a scheme to generate ergodic ensembles of random particulate systems and a numerical procedure for computing interactions among spherical particles based on Ewald summation technique for hydrodynamic mobility tensors. From the generation process truly random both monodisperse and multimodal size distributions of particles were obtained for dilute and moderate densities based on a minimum energy criterion. Concerned with computations of the Ewald sums our numerical procedure drastically reduces the CPU simulation time providing results of the hindered settling function in good agreement with available experimental data and asymptotic results for ordered and random periodic arrays of particles. We show new computer simulations with no flux boundary perpendicular to gravity and periodic boundary conditions in horizontal direction. The simulations reproduce the experimental correlation-time and anisotropy of the velocity fluctuations, but have the magnitude of these fluctuations increasing proportional to the size of the system. [DOI: 10.1115/1.1502665]

1 Introduction

The sedimentation of solid particles in a viscous fluid is a common industrial process in civil, chemical, and oil engineering. Much theoretical and experimental research has been directed at determining the sedimentation velocity for monodisperse suspensions, [1]. The most popular result is the simple formula of Richardson and Zaki [2]: $\langle U\rangle = U_0(1-\phi)^n$, where $U_0 = 2\Delta\rho a^2 g/9\mu$ is the Stokes velocity for an isolated particle, a is the particle radius, $\Delta\rho$ denotes the difference between the density of the solid particles and fluid, μ is the fluid viscosity, g is the acceleration due to gravity, and $n = 5.1$ for spherical particles with low Reynolds numbers. On the theoretical side, the origin, significance, and interpretation of the convergence difficulties in calculating the sedimentation velocity are well understood after the rigorous theories of Batchelor [3,4] for predicting sedimentation velocities in monodisperse and polydisperse dilute suspensions of spheres at low Reynolds number. On the other hand the problem of velocity fluctuations in sedimentation is still unresolved theoretically, [5,6]. Theories, [7–13], and numerical computations, [14–17], with randomly positioned monodisperse particles find that fluctuations diverge with increasing system size. Most experiments find differently, [18,19].

The first theoretical work to investigate the convergence problem of the rms fluctuations in sedimentation was developed by Caflisch and Luke [7], who pointed out that Batchelor's renormalization does not resolve the divergence associated with calculating the variance of the sedimentation velocity. A physical scaling argument based on buoyancy-driven convection in sedimentation was given by Hinch [8]. The scalings confirmed the predictions of Caflisch and Luke. Koch [10] has adapted Hinch's scalings to gas-solid suspensions and studied the behavior of fluctuations in a range of moderate particle Stokes numbers, $1 \ll \mathrm{St} \ll \phi^{-3/4}$. Several theoretical approaches have attempted to explain the fluctuation screening in sedimentation. Koch and Shaqfeh [9] argued that screening of the velocity fluctuations results from correlations in the particle distribution. The distribution is characterized by a net deficit of exactly one particle surrounding any test particle. This theory predicts that the velocity fluctuations scale like U_0, independent of the solid volume fraction ϕ, and that the correlation length scales as $a\phi^{-1}$, in contrast to the experiments carried out by Segré, Herbolzheimer, and Chaikin [19] and Guazzelli [6] who found velocity fluctuations of order $U_0\phi^{1/3}$ and correlation length of order $10a\phi^{-1/3}$. Recently, Brenner [13] has examined through scaling and numerical simulations the effect of side walls on arguments leading to the prediction of diverging velocity fluctuations with container size. The analysis has not definitively explained the dependence of the velocity fluctuations on the size of the settling box, although it seems to predict a divergence weaker than Caflisch-Luke theory. Dynamical simulations of sedimenting particles with point particles approximation or full hydrodynamic interaction in periodic systems, and large-scale lattice-Boltzmann numerical simulations support the conclusion, finding an increase in the magnitude of the velocity fluctuations and hydrodynamic diffusivity with the size of the numerical box, [14–17,20].

Several experiments have also been carried out to investigate fluctuations in sedimentation. Davis and Hassen [21] examined the spreading of the interface at the top of a sedimenting, slightly polydisperse suspension of non-Brownian particles. An investigation of the simultaneous effects of self-sharpening and velocity fluctuations in a sedimenting suspension of noncolloidal particles has been made by Lee et al. [22]. Ham and Homsy [23] carried out experiments to investigate the nature of the motion of a test particle sedimenting in the midst of a suspension of like particles. Their experiments found that fluctuations in the sedimentation velocity over relatively short settling distances are large (ranging from 25% to 46% of the mean) with dimensionless self-dispersion coefficients parallel to gravity increasing from approximately $2aU_0$ at $\phi = 25\%$ to $6aU_0$ at $\phi = 5\%$, which is about a factor of 5 smaller than the gradient diffusivity reported by Lee et al. [22]. Using a multiple light scattering technique, Xue et al. [24] measured the effects of hydrodynamic interactions on the average

Contributed by the Fluids Engineering Division for publication in the JOURNAL OF FLUIDS ENGINEERING. Manuscript received by the Fluids Engineering Division April 21, 2000; revised manuscript received April 30, 2002. Associate Editor: L. A. Mondy.

sedimentation velocity, its variance and the short-time self-diffusion coefficient in a concentrated hard-sphere colloidal suspension. Important experiments in sedimentation were carried out by Nicolai et al. [25], who have also investigated velocity fluctuations in a monodisperse sedimenting suspension of spheres under conditions of low Reynolds number. These experiments estimated velocity fluctuations between 75% and 170% of the mean, larger than those of Ham and Homsy [23]. In addition they observed a strong anisotropy in the velocity fluctuations and self-diffusivities, $D_{\parallel}/D_{\perp} \approx 5$ at 5%, although substantially smaller than that found by the theory of Koch [14] and numerical simulations of Ladd [15,16]. The indices $\perp$ and $\parallel$ denote quantities parallel and perpendicular to gravity. At moderate concentration, Nicolai and Guazzelli [18] found differently from the theories and computations that particle velocity fluctuations and hydrodynamic self-dispersion coefficients did not depend on the container dimension as the inner width of the vessel varied by a factor of four. The experiments, [18], unfortunately disagree with the theoretical predictions. This contrary result may be an indication that a well mixed particle distribution cannot, in principle, remain unchanged during sedimentation, and that information about the evolution of the microstructure in time is required to understand the behavior of the velocity fluctuations. We argue that after the suspension evolves the strong convection current observed in the initial stages of sedimentation will remove horizontal fluctuations in the number density leading to a saturation of velocity fluctuations. We should also mention here the related phenomenon of shear-induced hydrodynamic diffusion in sheared suspensions, [26,27].

The objective of this paper is to investigate by computer simulation the average sedimentation velocity, the particle velocity fluctuations, and particle-velocity correlations during sedimentation. We examine monodisperse and bidisperse suspensions with randomly positioned particles for different volume fractions and size of the container. In Section 2 we will present scaling arguments for velocity fluctuations and dispersion in sedimentation. The basic method is presented in Section 3 where we describe in detail both the calculation of the far-field interactions and short-range interactions for closing particles. In Section 4 the numerical scheme for polydisperse suspensions will be explained. This computational scheme will then be tested in Section 5 by comparing results of sedimentation velocity for ordered and random suspensions with analytical predictions and Richardson-Zaki empirical correlation. Simulation results for monodisperse and bidisperse sedimentation are presented. Conclusions will be stated in Section 6.

2 Scalings

One can begin to understand the scaling of the velocity fluctuations by considering a box of size l containing N particles distributed uniformly, with the number of particles related to the size of the box and the volume fraction ϕ by $N = l^3\phi/\frac{4}{3}\pi a^3$. If the box is divided into two equal parts by a vertical plane, due to statistical fluctuations one half of the box will typically contain $N/2+\sqrt{N}$ particles, whereas the other half will contain $N/2-\sqrt{N}$. This imbalance drives convection currents during the sedimentation process. The extra weight on the heavy side is $mg\sqrt{N}$, with $m = \frac{4}{3}\pi a^3 \Delta\rho$. Balancing this fluctuation in weight with a Stokes drag $6\pi\mu U' l$ on the velocity fluctuation, and using $U_0 = 2\Delta\rho a^2 g/9\mu$, we find the fluctuation in the velocities.

$$U'^2 \sim U_0^2 \phi \frac{l}{a} \tag{1}$$

With this velocity fluctuation we can estimate the hydrodynamic self-diffusivity as $D \sim U' l$, corresponding to the particle velocity remaining correlated for a time $\tau_c = O(l/U')$. Thus

$$D \sim a U_0 \phi^{1/2} \left(\frac{l}{a}\right)^{3/2}. \tag{2}$$

This scaling argument helps to explain how velocity fluctuations and hydrodynamic self-diffusivity in a random dilute sedimenting suspension depend on the size of the system.

In the simulations we shall be monitoring the horizontal variation of density which is responsible for the convection currents in sedimentation. This is the important origin of the large velocity fluctuations which has not been made clear by previous works who have worried about Koch and Shaqfeh's mass deficit theory, [9].

3 Statement of the Problem

Consider a suspension of N rigid and spherical particles interacting hydrodynamically. The spheres differ in radius and density. The particulate dispersion is subject to a sedimentation process through a Newtonian fluid of viscosity μ and density ρ_f with low-Reynolds-number flow about each particle. The system occupies a three-dimensional unit cell represented by a prismatic container with dimensions $d \times l \times h$. In order to simulate an infinite suspension, the unit cells comprise a periodic spatial structure like a Bravais lattice (see Fig. 1).

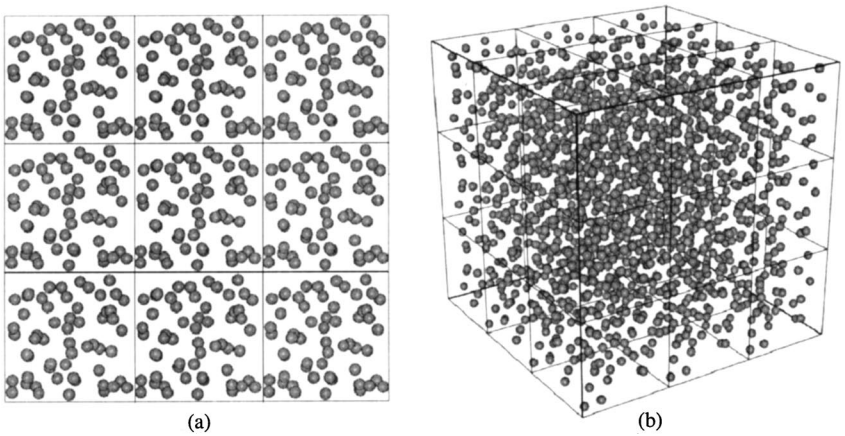

Fig. 1 Representation of a typical lattice used in the simulations. The particles are randomly distributed in a periodic cell with $\phi = 0.03$. (*a*) Side view; (*b*) three-dimensional perspective view.

In the case in which the particulate phase consists of m species of particles, one follows an usual notation and denotes, respectively, the radius, density, number density, and volume fraction of each particle of species s by a_s, ρ_s, n_s, and ϕ_s. The dimensionless polydispersity parameters concerned with species s will be denoted by aspect ratios λ_s and reduced density ratios η_s as follows:

$$\lambda_s=\frac{a_s}{a},\quad \eta_s=\frac{\rho_s-\rho_f}{\rho-\rho_f},\quad (s=1,2,\ldots,m), \tag{3}$$

where a and ρ correspond, respectively, to the characteristic radius and density of the species adopted as the reference for nondimensionalization purposes. The other species are expressed in terms of the parameters λ and η. Thus, the terminal settling velocity of an isolated particle, the Stokes-Einstein diffusivity and the Péclet number of species s are, respectively,

$$\mathbf{U}_0^{(s)}=\eta_s\lambda_s^2\mathbf{U}_0,\quad D_0^{(s)}=\lambda_s^{-1}D_0,\quad \mathrm{Pe}^{(s)}=\eta_s\lambda_s^2\mathrm{Pe}_0,\quad (s=1,\ldots,m) \tag{4}$$

where

$$\mathbf{U}_0=\frac{2}{9\mu}a^2(\rho-\rho_f)\mathbf{g},\quad D_0=\frac{\kappa T}{6\pi\mu a},\quad \mathrm{Pe}_0=\frac{aU_0}{D_0}, \tag{5}$$

$\mathbf{g}$ is the gravitational force per unit mass, κ is the Boltzmann constant and T is the absolute temperature. The length quantities are made nondimensional using a as the characteristic length scale. The Stokes hydrodynamic drag $6\pi\mu a U_0$ is taken as the characteristic reference scale for force.

3.1 Lattice Sums. In view of the well-known convergence problem inherent in the long-range nature of the hydrodynamic interaction, one adopts a formulation based on the Beenakker's Ewald-summed Rotne-Prager tensor, [28–30], under the assumption that pairwise additivity of the hydrodynamic interaction is plausible at dilute conditions. An extension of the formulation proposed by Beenakker for hydrodynamic interactions in a heterogeneous suspension and some basic background information about the periodic array in space are presented next.

Let the center positions of the N spheres within a unit cell be denoted by the set of vectors $\mathcal{C}_N=(\mathbf{x}_1,\ldots,\mathbf{x}_N)$. Consider a periodic lattice in which the set $\mathcal{C}_N$ assumes the general form $\mathcal{C}_N=(\mathbf{x}_{\gamma 1},\ldots,\mathbf{x}_{\gamma N})=(\mathbf{x}_1+\mathbf{x}_\gamma,\ldots,\mathbf{x}_N+\mathbf{x}_\gamma)$ where

$$\mathbf{x}_\gamma=(\gamma_1 d,\gamma_2 l,\gamma_3 h),\quad (\gamma_1,\gamma_2,\gamma_3=0,\pm1,\pm2,\ldots) \tag{6}$$

defines the lattice points, obtained by a linear combination of the basic orthogonal vectors $d\mathbf{e}_1, l\mathbf{e}_2, h\mathbf{e}_3$, $\gamma=\{\gamma_1,\gamma_2,\gamma_3\}$ being the set of integer coefficients, named the cell indices, and the set of vectors $\{\mathbf{e}_1,\mathbf{e}_2,\mathbf{e}_3\}$ being the canonical base of the Euclidian space.

The reciprocal lattice vectors $\mathbf{k}_\zeta$ specifies lattice waves satisfying the periodic boundary condition. Thus the function $e^{i\mathbf{k}_\zeta\cdot\mathbf{x}_\gamma}$ is periodic with respect to the basic vectors and assumes a unit value for all $\gamma\in\mathbb{Z}$. The vectors $\mathbf{k}_\zeta$ have the dimension of the inverse of length and are written as

$$\mathbf{k}_\zeta=2\pi\left(\frac{\zeta_1}{d},\frac{\zeta_2}{l},\frac{\zeta_3}{h}\right),\quad (\zeta_1,\zeta_2,\zeta_3=0,\pm1,\pm2,\ldots) \tag{7}$$

where $\zeta=\{\zeta_1,\zeta_2,\zeta_3\}$ is the cell index of the reciprocal lattice.

The evaluation of the sedimentation velocity $\mathbf{U}^\alpha$ of a test particle (numbered by the index α) considering the flow disturbances induced by the neighboring ones involves the computation of two mobility matrices. The first matrix is relative to an isolated particle being represented by an isotropic tensor. The second one consists of a two-sphere mobility which considers the particle images periodically replicated. The last mobility includes terms with respect to the lattice sums in real and reciprocal space, being the sums convergence rate controlled by a positive parameter ξ. One attributes to the convergence parameter a value $\xi=\pi^{1/2}V^{-1/3}$ suggested by Beenakker [28] as a good choice in the case of a simple cubic lattice, where V denotes the volume of the unit cell.

Now, consider an arbitrary pair of particles numbered by the indices α and β, pertaining to species s and p, respectively. The velocity of a particle α is given by

$$\mathbf{U}^\alpha=\mathbf{M}^\alpha\cdot\mathbf{F}^\alpha+\sum_{\substack{\gamma\\ \mathbf{x}_{\gamma\beta}\neq\mathbf{x}_\alpha}}\sum_{\beta=1}^{N}\mathbf{M}^{(ps)}(\mathbf{x}_{\gamma\beta}-\mathbf{x}_\alpha)\cdot\mathbf{F}^\beta+\frac{1}{V}\sum_{\substack{\zeta\\ \mathbf{k}_\zeta\neq0}}\sum_{\beta=1}^{N}\mathbf{M}^{(rs)}(\mathbf{k}_\zeta)\cdot\mathbf{F}^\beta\cos[\mathbf{k}_\zeta\cdot(\mathbf{x}_\beta-\mathbf{x}_\alpha)], \tag{8}$$

where

$$\mathbf{M}^\alpha=\left(1-6\xi\pi^{-1/2}-\frac{40}{3}\pi^{-1/2}\xi^3\right)\mathbf{I}. \tag{9}$$

$\mathbf{M}^\alpha$ defines the αth isolated particle mobility and $\mathbf{I}$ denotes the unit second rank tensor. The periodic two-sphere mobilities are defined by the following expressions:

$$\mathbf{M}^{(ps)}(\mathbf{r})=\left\{\left[3\xi^3r^2-\frac{9}{2}\xi+(4\xi^7r^4-20\xi^5r^2+14\xi^3+\xi r^{-2})\lambda\right]\pi^{-1/2}\exp(-\xi^2r^2)+\left(\frac{3}{4}r^{-1}+\frac{1}{2}r^{-3}\lambda\right)\times\mathrm{erfc}(\xi r)\right\}\mathbf{I}+\left\{\left[-3\xi^3r^2+\frac{3}{2}\xi+(-4\xi^7r^4+16\xi^5r^2-2\xi^3-3\xi r^{-2})\lambda\right]\pi^{-1/2}\exp(-\xi^2r^2)+\left(\frac{3}{4}r^{-1}-\frac{3}{2}r^{-3}\lambda\right)\mathrm{erfc}(\xi r)\right\}\mathbf{e}_r\mathbf{e}_r \tag{10}$$

$$\mathbf{M}^{(rs)}(\mathbf{k})=\left(1-\frac{1}{3}k^2\lambda\right)\left(1+\frac{1}{4}\xi^{-2}k^2+\frac{1}{8}\xi^{-4}k^4\right)6\pi k^{-2}\times\exp\left(-\frac{1}{4}\xi^{-2}k^2\right)(\mathbf{I}-\mathbf{e}_k\mathbf{e}_k). \tag{11}$$

$\mathbf{M}^{(ps)}$ is the mobility associated to lattice sum in real space, $\mathbf{M}^{(rs)}$ concerns with the sum in reciprocal space, $r=|\mathbf{x}_{\gamma\beta}-\mathbf{x}_\alpha|$, $\mathbf{e}_r=\mathbf{r}/r$, $\mathbf{e}_k=\mathbf{k}/k$, $\lambda=\frac{1}{2}(1+a_p/a_s)$ and erfc is the complementary error function. The mobilities presented from the Eq. (9) to (11) provide two different levels of hydrodynamic interaction approximation. The terms which include λ^2 provide a leading order correction due to the finite size of the particles.

Considering the system under the action of gravity and that the particles are torque-free, the force $\mathbf{F}^\alpha$ acting on a particle α of species s is given by

$$\mathbf{F}^\alpha=-\eta_s\lambda_s^3\mathbf{e}_3+\mathbf{f}_l^\alpha+\mathbf{f}_c^\alpha. \tag{12}$$

The term $-\eta_s\lambda_s^3\mathbf{e}_3$ is the net weight of the particle α and $\mathbf{f}_l^\alpha$ is an artificial short-range repulsive force acting among pairs of particles when they are close together and $\mathbf{f}_c^\alpha$ is a restoring force to prevent eventual overlaps. One discusses short-range interaction next.

For a mobility problem the particle trajectories are obtained simply by integration of the kinematic equation

$$\frac{D\mathbf{x}^\alpha}{Dt}=\mathbf{U}^\alpha,\quad \mathbf{x}^\alpha(0)=\mathbf{x}_o^\alpha. \tag{13}$$

3.2 Short-Range Repulsive Forces. As mentioned above, the mobility tensors include only the far-field interactions which cannot capture the lubrication forces arising from the squeezing

flow within the gap between two approaching spheres. As a consequence, in a time evolution of disordered suspensions it is common the occurrence of numerical errors owing to occasional overlaps between the spheres, even in dilute systems. Such a problem is critical in regions of large solid volume fractions especially when particles have settled at the bottom of the container.

In view of this a lubrication short-range force is modeled here by employing an artificial repulsive force acting among pairs of particles when they are close together, [11]. Introduction of this extra repulsive force to prevent particles clusters is not unrealistic because forces acting between particles in nature and in laboratory practice are often repulsive. Furthermore, the pairwise addition of near-field lubrication forces in Stokesian dynamics simulations of Brady and Bossis [31] requires time steps prohibitively small to prevent overlaps.

The expression for this repulsive force is given by

$$\mathbf{f}_l^\alpha = C_1 \eta_p \lambda_p^3 \exp\left[-\frac{(-\varepsilon_{\alpha\beta})}{\lambda_p C_2} \right] \hat{\mathbf{r}}, \quad \text{for } 0 < (-\varepsilon_{\alpha\beta}) < \varepsilon_0 \tag{14}$$

where C_1 and C_2 are arbitrary numerical parameters which represent, respectively, the intensity and the range of the repulsive force, $\varepsilon_{\alpha\beta} = (\lambda_s + \lambda_p) - |\mathbf{x}_\beta - \mathbf{x}_\alpha|$ is the virtual overlap, and ε_0 is the interparticle gap for which the force $\mathbf{f}_l^\alpha$ is cut off. The parameters C_1, C_2, and ε_0 were determined by means of numerical experiments with two unequal sedimenting spheres with an upstream impact parameter of $a_l = \lambda_p a$. Figure 2 presents the time evolution of the gap between two closing unequal spherical particles. The accuracy of the numerical simulation was tested by performing calculations for two interacting particles that have been studied extensively in the past and for which analytical and simulation results are available for comparison, [32]. For a time step (1/100) Stokes time it is found a minimum gap around 1/10 of the particle radius, when imposing the above short-range repulsive force with the appropriate constants C_1, C_2, and ε_0. Typical values for these constants are: $C_1 = 10$, $C_2 = 0.1$, and $\varepsilon_0 = 0.1$.

Although the lubrication forces have a divergent character when the particles come close at the creeping flow regime, it is considered in addition the restoring force $\mathbf{f}_c^\alpha$ due to eventual elastic collisions. For simplicity it was employed a linear force-displacement relation for interparticle contact in such a way that the normal elastic force is proportional to the virtual overlap of the particles, so that

$$\mathbf{f}_c^\alpha = -K_e \varepsilon_{\alpha\beta} \hat{\mathbf{r}}, \qquad \text{for} \quad \varepsilon_{\alpha\beta} > 0 \tag{15}$$

where K_e denotes the contact stiffness, assumed to be constant, whose value depends upon material and geometric properties of the colliding spheres. After several tests we found a typical value for this constant equal to 100. Here, the repulsive forces may be also employed to model particle-wall interactions in a system with no flux boundaries parallel to gravity.

3.3 Impenetrable Boundaries. The image system is constructed by considering a unit cell with dimensions $d \times l \times 2h$, being the real and reciprocal lattice vectors defined now as $\mathbf{x}_\gamma = (\gamma_1 d, \gamma_2 l, \gamma_3 2h)$ and $\mathbf{k}_\zeta = 2\pi(\zeta_1/d, \zeta_2/l, \zeta_3/2h)$, respectively, where $\{\gamma_1, \gamma_2, \gamma_3\}$ and $\{\zeta_1, \zeta_2, \zeta_3\}$ are sets of integer coefficients. The procedure to obtain the flow solution within a no flux boundary is essentially to consider a linear combination $\mathbf{u}(\mathbf{x}) = \mathbf{u}(\mathbf{x};\mathbf{x}_\alpha^s) + \mathbf{u}(\mathbf{x};\mathbf{x}_\alpha^i)$ satisfying the following boundary conditions:

$$\begin{cases} u(\mathbf{x}), v(\mathbf{x}), w(\mathbf{x}) & \text{periodic in } x \text{ and } y \text{ directions} \\ & \text{with period } d \text{ and } l, \text{ respectively} \\ u(\mathbf{x}), v(\mathbf{x}) & \text{periodic in } z \text{ with period } h \\ w(\mathbf{x}) = 0 & \text{on } z = 0 \text{ and } z = h, \end{cases} \tag{16}$$

where u, v and w denote the components of the fluid velocity. The term $\mathbf{u}(\mathbf{x};\mathbf{x}_\alpha^s)$ corresponds to the periodic flow solution due to a stokeslet located at $\mathbf{x}_\alpha^s = (x,y,z)$. The complementary term $\mathbf{u}(\mathbf{x};\mathbf{x}_\alpha^i)$ corresponds to the image system which consists of a stokeslet equal in magnitude but opposite in sign located at the image point $\mathbf{x}_\alpha^i = (x,y,-z)$, [33].

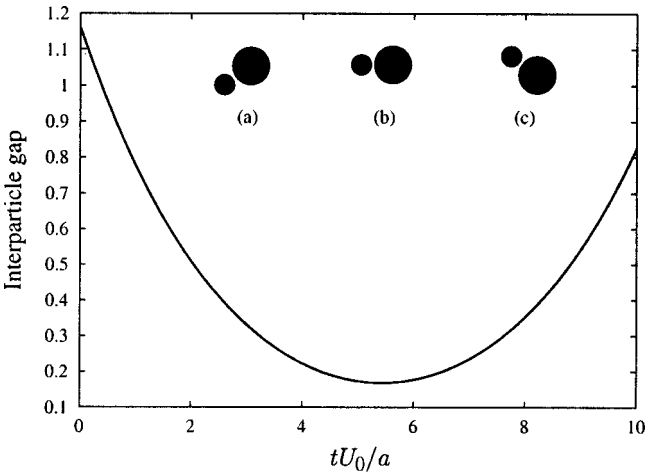

Fig. 2 Time evolution of the dimensionless gap between two unequal sedimenting spheres. The figure is for an aspect ratio of $\lambda_l/\lambda_s = 1.75$ with upstream impact parameter λ_l. In the inset are represented three steps of the time evolution, being (*b*) the step of minimum interparticle gap.

Using such an image system with Ewald's summation technique in the version of Beenakker [28] we arrive at the fundamental solution for the Stokes flow induced by a lattice of stokeslets with side periodicity and impenetrable top and bottom. The general form for the velocity of a particle α is given by

$$\mathbf{U}^\alpha = \mathbf{M}^\alpha(\xi) \cdot \mathbf{F}^\alpha + \sum_{\beta=1}^{N} \mathbf{G}(\mathbf{x}_\beta - \mathbf{x}_\alpha, \xi) \cdot \mathbf{F}^\beta, \tag{17}$$

where $\mathbf{G}(\mathbf{x}_\beta - \mathbf{x}_\alpha, \xi)$ is the Ewald summed mobility tensor, given by

$$\mathbf{G}(\mathbf{x}_\beta - \mathbf{x}_\alpha) = \sum_{\substack{\gamma \\ \mathbf{x}_{\gamma\beta} \neq \mathbf{x}_\alpha}} \mathbf{J}^{(ps)}(\mathbf{x}_{\gamma\beta} - \mathbf{x}_\alpha) + \frac{1}{V} \sum_{\substack{\zeta \\ \mathbf{k}_\zeta \neq \mathbf{0}}} \mathbf{M}^{(rs)}(\mathbf{k}_\zeta) \Theta \tag{18}$$

being the kernel tensor $\mathbf{J}^{(ps)}$ and the function Θ defined as

$$\mathbf{J}^{(ps)} = \mathbf{M}^{(ps)}(\mathbf{x}_{\gamma\beta}^s - \mathbf{x}_\alpha, \xi) - \mathbf{M}^{(ps)}(\mathbf{x}_{\gamma\beta}^i - \mathbf{x}_\alpha, \xi), \tag{19}$$

$$\Theta = \cos[\mathbf{k}_\zeta \cdot (\mathbf{x}_\beta^s - \mathbf{x}_\alpha)] - \cos[\mathbf{k}_\zeta \cdot (\mathbf{x}_\beta^i - \mathbf{x}_\alpha)]. \tag{20}$$

The term $\mathbf{M}^{(ps)}$ is the periodic Green's function in the physical space presented in Section 3.1 and the vectors $\mathbf{x}_{\gamma\beta}^s = (x,y,z) + \mathbf{x}_\gamma$ and $\mathbf{x}_{\gamma\beta}^i = (x,y,-z) + \mathbf{x}_\gamma$ locate the source point and the image point, respectively.

4 Numerical Method

Equations (13) and (17) will be applied to examine the dynamics of N particles sedimenting and interacting hydrodynamically within a container with a no flux boundary perpendicular to gravity direction and periodic boundary conditions in the horizontal direction. This type of formulation represents a mobility problem with hydrodynamic interactions, calculated by using pairwise additivity (i.e., superposition of velocity in the mobility matrix). It should be important to note that the moderate number of particles used in the present simulations makes the effect of periodicity dominate the sedimentation velocity at small particle volume frac-

tion, and the relatively low number of multipoles included (i.e., degenerate quadrupole only) reduces the accuracy at high ϕ. Improvements could be made on both fronts by including more multipole on the one hand and more particles on the other. Either of these approaches, however, increases dramatically the number of degrees-of-freedom and results in prohibitive computation times, even avoiding the costly (N^3) inversion from hydrodynamic lubrication. The simulations here requires for the calculation of the mobility interactions $O(N^2)$ operations, which is still excessive at moderate ϕ.

4.1 Sampling Techniques. In this section, we describe a procedure based on the method proposed by Metropolis et al. [34] to simulate the initial condition for either monodisperse and multimodal size distributions of many interacting spherical particles. The main aim of this method is to generate ergodic ensembles in which each member consists of N mutually impenetrable spheres whose centers are randomly distributed in a prismatic unit cell of volume V.

Consider the rigid sphere system defined in Section 3. The mutual impenetrability of the spheres imposes that the center of a test sphere of radius a_s cannot be located within an excluded volume shell $a_p < |\mathbf{r}| < a_p + a_s$ of any other one of radius a_p. In other words, these systems are characterized by a pair potential which is zero when the interparticle distance is greater than $a_p + a_s$ and infinite when $|\mathbf{r}| \leqslant a_p + a_s$.

In order to simulate a narrow fluid gap separating the spheres when they are in close proximity, a geometric parameter ϵ is incorporated into the excluded volume. The amount of this gap is arbitrary but it is determined by considering the physical phenomenon to be simulated, such as sedimentation or shear flow. This parameter is also considered in order to calibrate numerically the minimum distance between spheres during the generation process. The value of ϵ must be chosen with some care, since it magnifies the exclusion-volume effects, and consequently exerts an important influence upon the randomness degree of the distributions. In terms of the aspect ratios and the mentioned geometric parameter, the numerical excluded volume is written as

$$\lambda_p + \frac{1}{2}\epsilon < |\mathbf{r}| < \lambda_p + \lambda_s + \frac{1}{2}\epsilon \quad (p,s = 1, \ldots, m). \tag{21}$$

The generation procedure for a given volume fraction $\phi = (4/3)\pi \Sigma_{i=1}^{m} n_i \lambda_i^3$ begins by placing sequentially the required number N of particles within the periodic domain under the nonoverlap condition. Increasing ϵ, the impenetrability condition imposes more severe restrictions on available particle arrangements and decreases the physically accessible space.

From the set $\mathcal{C}_N = (\mathbf{x}_1, \ldots, \mathbf{x}_N)$, which characterizes the static initial configuration of the particles, one attributes to the system a potential energy, defined by

$$E(\mathcal{C}_N) = \sum_{\alpha=1}^{N} \sum_{\beta=\alpha+1}^{N} \mathcal{V}(r_{\alpha\beta}), \tag{22}$$

where $\mathcal{V}(r_{\alpha\beta})$ is an arbitrary pair potential which falls off rapidly with distance $r_{\alpha\beta} = |\mathbf{x}_\beta - \mathbf{x}_\alpha|$, and gives a weight $P(\mathcal{C}_N) = \exp(-E)$, which defines an ergodicity criterion.

The system is subject to a temporal evolution simulated numerically as a random diffusive walk governed by the following Brownian-diffusion equation

$$\mathbf{x}_{n+1} = \mathbf{x}_n + \mathrm{Pe}^{(s)}\ \delta t + \sqrt{6\lambda_s^{-1}\delta t}\,\varepsilon_n \tag{23}$$

where ε_n is a random vector with each component having zero mean and unit variance and being generated independently of the other components and independently of previous time steps. Numerically, this random vector is obtained by means of a standard random number generator with enough independence between adjacent numbers, [35]. During the diffusion simulations the deterministic displacement $\mathrm{Pe}^{(s)}\delta t$ was neglected by the imposition of $\mathrm{Pe}^{(s)} \ll 1$, which leads to isotropic particle motion. While the system evolves, the impenetrability condition was employed based upon the excluded volume criterion given by Eq. (21), in which ϵ is set to a value representative of the lubrication gap.

The evolution of the system from the initial distribution to subsequent nonoverlapping configurational states, in particular the motion of each particle, is subject to an energy criterion which prescribes: If the movement of a particle α implies in a reduction of the system energy, the new position vector $\mathbf{x}_\alpha^{n+1}$ will integrate into the set $\mathcal{C}_N$ by substituting the element $\mathbf{x}_\alpha$. Otherwise, one considers the energy increment ΔE due to movement and takes a random number ε between 0 and 1. The position $\mathbf{x}_\alpha^{n+1}$ will be allowed only if $\varepsilon < \exp(-\Delta E)$. In the case in which $\varepsilon > \exp(-\Delta E)$, the new position is forbidden and the prescriptions outlined above are similarly followed for the next particle.

4.2 Computation of Hydrodynamic Interactions. To compute hydrodynamic interactions among spherical multisized particles in a semi-dilute ($\phi \leqslant 0.15$) suspension, one presents a numerical procedure based upon the Ewald summation technique for the Rotne-Prager mobility tensor, [28]. Although the Ewald sum technique overcomes the convergence problems intrinsic to the long-range nature of interparticle interactions, it demands great computational effort which decreases the suitability of the method for large systems. It is the purpose of the method presented below to reduce the computational effort in order to permit a study of some aspects of microstructural dynamics and an evaluation of transport properties based on meaningful statistics. Our computational resource permits the simulation of monodisperse and polydisperse suspensions characterized by N of $O(10^3)$, N being the number of particles in a periodic cell.

The lattice sum computation, in each time step of the temporal evolution, demands $O(n_{pc}N^2)$ computations, n_{pc} being the number of periodic cells in the lattice. A significant computational saving is achieved by tabulating *a priori* the periodic Green's functions (10) and (11) in order to avoid the computation of the mobility tensor during the simulation. This scheme takes advantage of an important feature of the two-sphere mobility, which is a function of the relative separation only. Although the computational effort still scales with N^2, the avoidance of lattice sum computations reduces drastically (about 98%) the CPU time. However, the computational effort growing with N^2 imposes severe constraints on system size and consequently a number of particles greater than few thousands is prohibitively large for dynamic simulations. A typical number of particles we simulated in a unit cell is 300 for dynamic simulations with 10 realizations, and 1000 for static simulations averaging over a hundred particle configurations. Typically it takes 5–10 s CPU time for the simulation of one time step ($\Delta t = 0.01a/U_0$) on a 933 MHz Dell work station. The maximum memory required for the largest problem and the tabulation process is around 25–100 MB. Recently, Sireou and Brady [36] have described a method for calculating the hydrodynamic interactions among particles in suspension at small Reynolds number based on a Stokesian dynamics method with a reduced computational cost of $O(N \ln N)$. However, the work was limited to evaluation of macroscopic properties of static suspensions (not evolving in time). We should also mention here the existence of $O(N)$ algorithms developed by Ladd [37] and by Mo and Sangani [38]. Ladd's method is based on the lattice-Boltzmann technique for finite Reynolds number of $O(N)$, although he recognizes that there are several possible sources of error in his simulations. Sangani and Mo's algorithm follows a well-known approach by calculating the full resistance matrix through a fast multipole summation technique and inverting the resulting matrix iteratively. This method is in principle $O(N)$, although the iterative solution employed for these authors appears to perform poorly.

5 Numerical Results

We first test the accuracy of the method by comparing sedimentation velocities given by the present simulation with some analytical and experimental results available.

5.1 Hindered Settling Function for Ordered Suspensions. The first case we consider is a periodic arrangement of spheres sedimenting in a simple cubic lattice. For this case the theoretical hindered settling function scales as $O(\phi^{1/3})$ for point particle force (i.e., dilute limit), [39]. We verify our numerical scheme by comparing calculated sedimentation rates with the asymptotic, low-volume fraction solutions of Sangani and Acrivos [40], given by

$$f(\phi)=1-1.7601\phi^{1/3}+\phi-1.5593\phi^{2}+3.9799\phi^{8/3}-3.0734\phi^{10/3}+O(\phi^{11/3}). \quad (24)$$

Figure 3 shows the settling velocity for a simple cubic array of spherical particles as a function of $\phi^{1/3}$. It can be seen that the numerical results, obtained by considering the finite size of the particles, yield close agreement with the theoretical predictions given by Eq. (24) in the semi-dilute particle volume fraction range $\phi \leqslant 0.20$. It is also displayed the point-particle numerical results in order to illustrate the effect of the level of the hydrodynamic approximation on the sedimentation velocity.

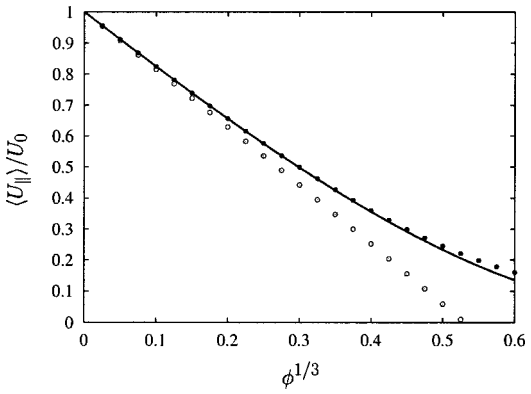

Fig. 3 Dimensionless settling velocity as a function of $\phi^{1/3}$ for a simple cubic arrangement of particles. The numerical results for point-particle approximation (○) and including the finite size of the particle (●) are shown in comparison with the low ϕ asymptotic solution of and Sangani-Acrivos [40] (solid curve).

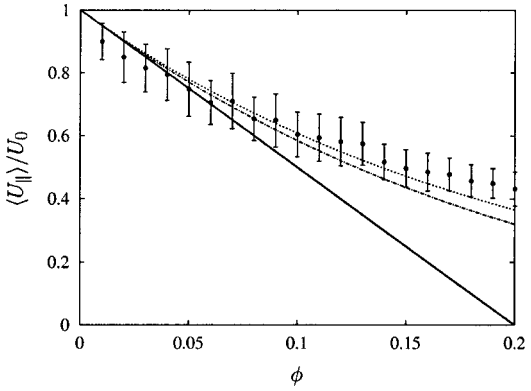

Fig. 4 Dimensionless settling velocity as a function of the solid volume fraction. Simulations results (●) are shown in comparison with the low ϕ asymptotic result of Batchelor [3] (solid curve), the Brady-Durlofsky [41] result (dashed curve) and the Richardson-Zaki correlation [2] (dashed-dotted curve).

5.2 Hindered Settling Function for Disordered Suspensions. The calculation of the settling velocity averaged over several instantaneous random configurations of particles constitutes a more realistic test than the above. In this section we validate the hindered settling function by means of comparisons with Richardson-Zaki [2] correlation,

$$f(\phi)=(1-\phi)^{n}, \quad (25)$$

for which we assumed an exponent $n=5.1$, and with the low ϕ asymptotic result of Batchelor [4] for random and statistically homogeneous suspensions, given by

$$\langle U_\parallel \rangle / U_0 = f(\phi) \sim 1-5\phi+O(\phi^{2}). \quad (26)$$

It is also made a comparison with the analytical expression of Brady and Durlofsky [41]

$$f(\phi)=\frac{\langle U_\parallel \rangle}{U_0}=1+\phi-\frac{1}{5}\phi^{2}-\frac{6}{5}\phi\left(\frac{5-\phi+1/2\phi^{2}}{1+2\phi}\right), \quad (27)$$

derived by considering the Rotne-Prager approximation for the Percus-Yevick hard-sphere radial distribution function, [41].

The instantaneous mean of the velocities of the sedimenting particles is

$$\overline{\mathbf{U}}(t)=\frac{1}{N}\sum_{i=1}^{N}\mathbf{U}_i(t). \quad (28)$$

Figure 4 shows the results for the dimensionless average sedimentation rate as a function of the particle volume fraction for a random monodisperse suspension together with Eqs. (25) to (27). Each point corresponds to the mean velocity over 100 independent particle configurations at a given concentration. Good accuracy for the sedimentation velocity is obtained for the wide range of particle volume fraction simulated ($0<\phi<0.20$). At low volume fraction ($\phi \leqslant 0.03$), however, the numerical results underpredict Batchelor's theory being the agreement within statistical uncertainty. The small degree of scatter suggests that some of the initial random configurations accessible through our simulations were not perfectly statistically homogeneous as assumed by Batchelor's analysis. Actually, the dilute limit is difficult to study through simulation, as very small effects must be compared and issues of system size, the effect of periodic boundary conditions must be considered. In this limit the motion is in essence a superposition of the sedimentation velocity of the dilute periodic array of images which scales like $(\phi/N)^{1/3}$, with that for the random suspension which is $O(\phi)$ for a low-volume fraction. Mo and Sangani [38] have calculated this difference in the velocity induced at the center of a test particle in a periodic suspension and a random suspension. Experimental results do not seem also to give Batchelor's coefficient, generally giving a value less than 6.55. The hindering of the settling observed is due to a back flow outside the particle, which occurs since we imposed the condition of no mean flow, $\langle \mathbf{u} \rangle = 0$. Our method can predict accurate velocity only for low to moderate volume fractions; for higher volume fractions more moments are required to represent the particles correctly. (See Figs. 5 and 6.)

5.3 Hindered Settling Function for Bidisperse Suspensions We now present the calculated hindered settling velocities for a bimodal size suspension of equidensity particles. At dilute conditions the comparisons are made with the theoretical result of Batchelor [4] which states that the mean velocity of a particle of species s in a suspension of m distinct species is given by

$$f_s(\phi)=\frac{\langle U_\parallel^{(s)} \rangle}{U_0^{(s)}} \sim 1+\sum_{p=1}^{m} S_{sp}(\lambda,\eta)\phi_p+O(\phi^{2}) \quad (s=1,2,\ldots,m) \quad (29)$$

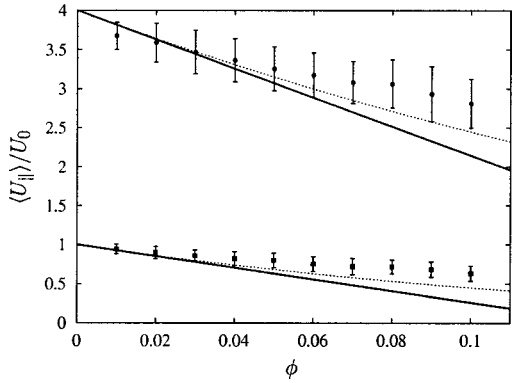

Fig. 5 The settling velocity, nondimensionalized by U_0, as a function of the total solid volume fraction for a bimodal size suspension. Simulation results for small (□) and large (●) species are shown in comparison with the low ϕ asymptotic result of Batchelor-Wen [43] (solid curve) and the Davis-Gecol correlation [42] (dashed curve). The simulations were performed over 100 random and equally probable configurations. The system is comprised of 1000 particles in a cubic periodic cell. The results are for $\phi_s = \phi_l = \phi/2$ and $\lambda_l/\lambda_s = 2$.

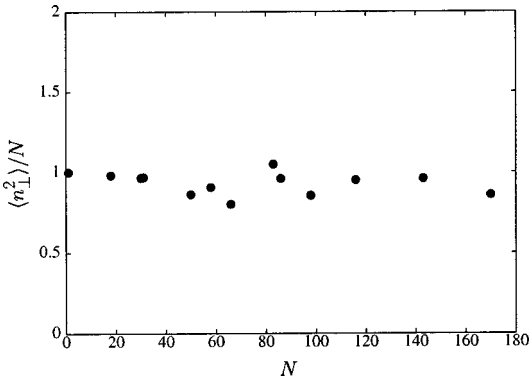

Fig. 6 Dimensionless horizontal density fluctuation obtained over 100 random and independent configurations as a function of the number of particles.

where S_{sp} values are sedimentation coefficients which depend upon the aspect ratio $\lambda = a_p / a_s$ and the reduced density ratio $\eta = (\rho_p - \rho_f)/(\rho_s - \rho_f)$.

As another basis for comparison one adopts the correlation proposed by Davis and Gecol [42], valid for a wider range of total particle volume fraction, given by the following expression:

$$f_s = \frac{\langle U_\parallel^{(s)} \rangle}{U_0} = \lambda_s^2 (1-\phi)^{-S_{ss}} \left(1 + \sum_{p \neq s} (S_{sp} - S_{ss}) \phi_s \right) \quad (30)$$

where the sedimentation coefficients S_{sp} assume the appropriate values calculated by Batchelor and Wen [43].

In Figure 7 it is shown the numerical results for the mean settling velocity as a function of the total particle volume fraction in comparison with those predicted by the Eqs. (29) and (30). For the sedimentation coefficients it was assumed the numerical values $S_{11} = S_{22} = -5$, $S_{12} = -9.81$, $S_{21} = -4.29$ provided by Batchelor and Wen [43]. The simulations were performed under the imposition of equal volume fractions for both particle species. The numerical results were obtained by averaging over 100 random and independent instantaneous configurations. We see that they are in good general agreement with the correlation, [43], thus validating the calculations of the average sedimentation by the present numerical procedure.

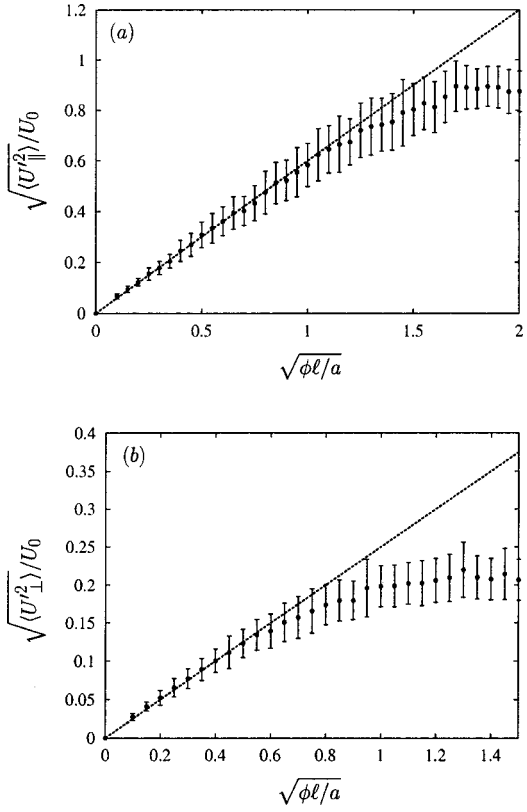

Fig. 7 Dimensionless velocity fluctuation for a monodisperse suspension as a function of the system parameter $\sqrt{\phi l/a}$. The simulations were performed over 100 random and equally probable configurations. The system is comprised of 300 particles in the unit cell with periodic sides and impenetrable boundaries perpendicular to gravity. The dashed lines are the linear fit: (*a*) $\sqrt{\langle U'^2_\parallel \rangle}/U_0 = 0.79\sqrt{\phi l/a}$; (*b*) $\sqrt{\langle U'^2_\perp \rangle}/U_0 = 0.20\sqrt{\phi l/a}$.

5.4 Fluctuations in Sedimentation. Several cases were studied. The particle concentration was varied through the range $0 < \phi < 0.10$. Various different box sizes were studied, with l/a ranging from around 25 to 350. The aspect ratio of the box was kept constant at $h/l = 3$.

The horizontal fluctuations in the density of the suspension are the origin of the large convection currents during the sedimentation. We investigate the magnitude of these fluctuations by constructing the Fourier amplitude for the lowest mode in the x-direction of the number density $\langle n_\perp^2 \rangle$

$$\langle n_\perp^2 \rangle = \sum_{j,k} e^{2\pi i (x_j - x_k)/l}, \quad (31)$$

summing over the differences in the x-coordinates of the positions of the particles.

We collect together in Fig. 6 the average of the horizontal density fluctuations, normalized by N, over the 100 realizations in each of the 12 different cases studied. Although the results are plotted as a function of the number of particles used in the different cases, we see that the horizontal density fluctuations are essentially constant, equal to the standard $\pm\sqrt{N}$ statistical fluctuation. The small degree of scatter around the unit we attribute to the effect of the finite size of the box.

We measure the fluctuations in the velocities with the instantaneous variance

$$\langle U'^2(t) \rangle = \frac{1}{N-1} \sum_{i=1}^{N} (U_i(t) - \overline{U}(t)), \quad (32)$$

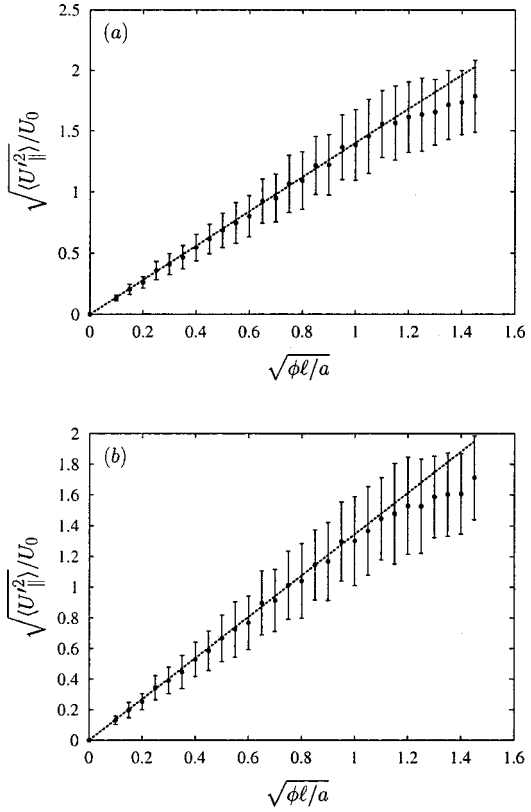

Fig. 8 Dimensionless vertical velocity fluctuation for a bidisperse suspension as a function of the system parameter $\sqrt{\phi l/a}$. The simulations were performed over 100 random configurations. The system is comprised of 300 particles in the unit cell with periodic sides and impenetrable box. The results are for $\phi_s=\phi_l=\phi/2$ and $\lambda_l/\lambda_s=2$. The dashed lines are the linear fit: (*a*) $\sqrt{\langle U_\parallel'^2\rangle}/U_0=1.400\sqrt{\phi l/a}$; (*b*) $\sqrt{\langle U_\perp'^2\rangle}/U_0=1.345\sqrt{\phi l/a}$.

constructed for the vertical and two horizontal components of velocity, the variances of the horizontal components then being averaged to give $\langle U_\parallel'^2\rangle$ and $\langle U_\perp'^2\rangle$.

In Figures 7(a) and 7(b) we examine the variation of the fluctuations in the vertical and horizontal velocities. The system was comprised of 300 particles in a unit cell with no flux boundary perpendicular to gravity, but with side periodicity. The results for the cases with different particle concentrations ϕ and box sizes a/l are plotted against the expected scaling parameter $(\phi l/a)^{1/2}$. We see that for low-volume fractions and small boxes both velocity fluctuations increase linearly with the square root of the box size, with linear fits $\sqrt{\langle U_\parallel'^2\rangle}=0.79U_0(\phi l/a)^{1/2}$ and $\sqrt{\langle U_\perp'^2\rangle}=0.20U_0(\phi l/a)^{1/2}$. Thus in agreement with Caflisch and Luke [7] and with the scaling argument presented here, we conclude that when the particles are positioned randomly in a monodisperse dilute suspension there are initially variances proportional to the size of the box.

The saturation of the velocity fluctuations in Figs. 7(a) and 7(b) are obtained for a volume fraction around 0.19 and l/a 18.7. It is seen that velocity fluctuations parallel to gravity reach the constant value of $0.85U_0$ for $(\phi l/a)^{1/2}$ around 1.5, whereas the velocity fluctuations perpendicular to gravity reach the value $0.20U_0$ for $(\phi l/a)^{1/2}$ around 0.8. The velocity fluctuation of the vertical velocity is comparable to the mean sedimentation velocity. This is in good general agreement with the experiments [23] where the fluctuations ranged between 25% and 50% of the mean in the dilute suspensions. Our results are also in good general agreement with the experiments of Nicolai et al. [25] and Guazzelli [6] who found a relative fluctuation around 80% at $\phi=5\%$. The theoretical value of Koch and Shaqfeh [9] gives a slightly higher value of $\sqrt{\langle U_\parallel'^2\rangle}=2.2U_0$. The ratio in Fig. 7 of the vertical to horizontal velocity fluctuations was found to be 4, indicating a strong anisotropy. This is near to the experiment value of 2.5 found by Nicolai et al. [25] and Guazzelli [6], and near to the ratio of 3.5 found by theory and numerical simulations, [14–16].

We next present simulations results for a bidisperse suspension. These simulations were performed for equal concentration of the large and the small species ($\phi_s=\phi_l=\phi/2$) and for a diameter ratio 2. Figures 8(a) and 8(b) display the results for vertical velocity fluctuations for two species as a function of the system parameter $(\phi l/a)^{1/2}$. It is seen that the hydrodynamic interactions of small particles with larger ones produces an increasing in their velocity fluctuations of about 30% compared to the results shown in Fig. 7(a). It is apparent from these results that random bidisperse suspensions present a system size dependence at low-volume fraction, just as shown above for the monodisperse case. This leaves open the possibility that a dilute homogeneous polydisperse suspension could exhibit hydrodynamic screening.

5.5 Suspension Evolution. Microstructural change, that is the variations in the relative arrangements of the particles, is an important feature of a sedimentation process. The time evolution of the system was analyzed over 10–20 realizations. The main problem that we examine was to know how the initial configurations of the particles evolve in time.

Typical evolutions for the cases of monodisperse and bimodal suspensions simulated are displayed in Fig. 9. Figure 9(a) shows one realization of the monodisperse case for a particle concentration $\phi=5\%$, a box size of $l/a=20$ and an aspect ratio of the box $h/l=3$; a simulation requiring 286 particles. The realization of the bimodal suspension is shown in Fig. 9(b) for $l/a=20$, a total concentration $\phi=0.05$ ($N=185$), $\phi_s=\phi_l=0.025$, and aspect ratio $\lambda_l/\lambda_s=1.5$ and $h/l=3$. We show at five different times (from 0 to 60 a/U_0) the positions of the particles projected onto the vertical xz-plane. The first time in both cases is the initial configuration with the particle distributed randomly inside the box. As time progresses, a sediment accumulates on the lower impen-

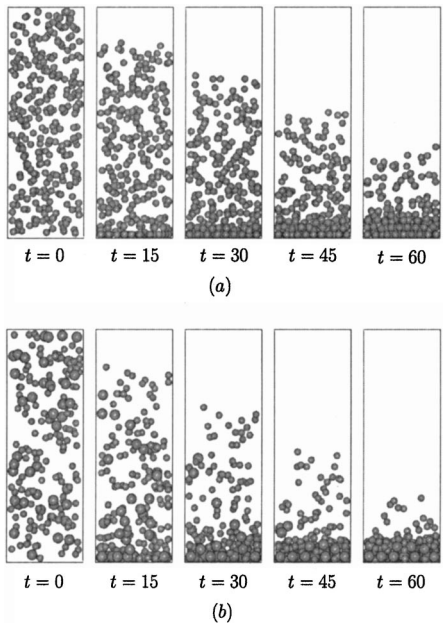

Fig. 9 Typical dynamic simulation of particle configuration at different times during sedimentation: (*a*) monodisperse sedimentation for $a/l=0.05$, $h/l=3$, $N=286$; $\phi=0.05$; (*b*) bimodal sedimentation for $\phi=0.05$ ($N=185$), $\phi_s=\phi_l=0.025$ and aspect ratio $\lambda_l/\lambda_s=1.5$; $h/l=3$.

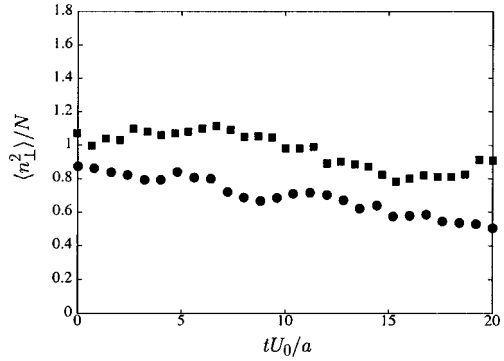

Fig. 10 Time evolution of the dimensionless horizontal density number fluctuations at different conditions of the simulated system with the aspect ratio $h/l=3$. (□): $a/l=0.05$; $\phi=0.03$ ($N=172$), (●): $a/l=0.06$; $\phi=0.02$ ($N=66$).

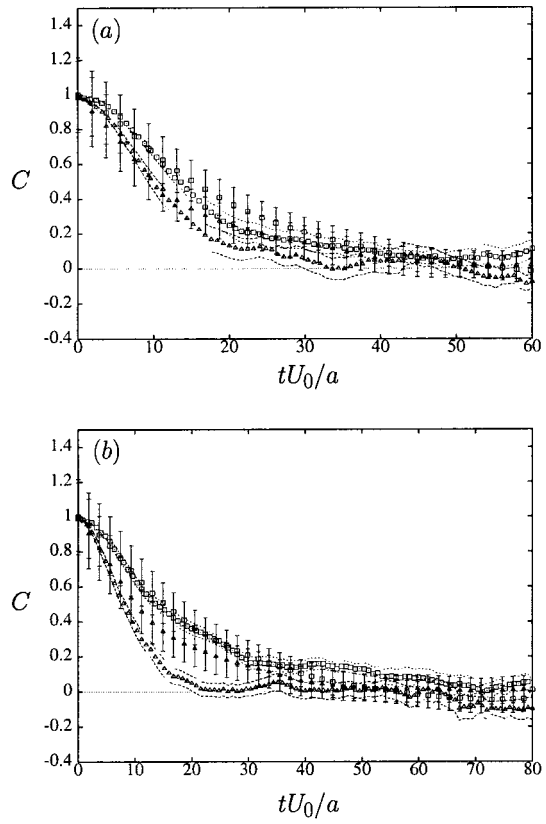

Fig. 11 Normalized velocity fluctuation auto-correlation functions parallel, $C_\parallel$ (□) and perpendicular, $C_\perp$ (△) to the gravity direction. (*a*) Computer simulations for $h/l=3$, $a/l=0.05$, $N=114 \Rightarrow \phi=0.02$; (*b*) Computer simulations for $h/l=3$, $a/l=0.05$, $N=172 \Rightarrow \phi=0.03$. The error bars represent experimental data [25] with $\phi=0.05$, $h/l=4$, $h/d=10$ and $d/a \approx 100$. The dashed lines indicate the uncertainly range of the present computer simulations.

etrable boundary. Note that the impenetrable boundary is slippery and not a no-slip rigid boundary, so that particles can be seen moving along it. The descending upper interface between the suspension and clear fluid above is diffuse and spreads slowly, so that the nearby concentration of particles decreases in time.

For each case studied, dynamic simulations were made for 10 to 20 realizations with different initial configurations. Below we give only averages over these realizations. Moreover in calculating the averages, we select the middle part of the suspension, away from the sediment and the diffuse upper front.

Variations in number density can result from different boundary conditions, such as when a finite height of suspension settles toward an impenetrable plane boundary as considered in our simulations. Figure 10 shows the time evolution of the horizontal density fluctuations, normalized by N, for two different combinations of particle concentrations and box size. In each of the two different cases studied, the horizontal density fluctuations are seen to remain essentially constant up to $t=20a/U_0$, approximately the time to fall through the width of the box l or one third the time to fall the height of the box h. We had expected that during such a time the density fluctuations would drive a convection which would turn the horizontal variations in density into vertical variations, and so the large velocity fluctuations would decay. Our dynamic simulations show, however, that the convection does not lead to a systematic decrease in the horizontal density fluctuations. Further simulations, [11], with a taller box, $h/l=4$ and $h/l=5$ found the same behavior. This result indicates that, even in the case of considering no flux slip boundaries one would not expect the probability density in the bulk of the suspension to be influenced. Thus, the fluctuations seem to be always limited by the box size in the dilute limit of a sedimenting suspension.

Corresponding to the lack of evolution of the density fluctuations, vertical velocity fluctuations therefore remain proportional to the size of the box, as in the parameter $\phi l/a$, and do not evolve to some value which is independent of the size of the box. The computer simulations therefore remain at variance with experimental observations of fluctuations independent of the size of the box. A possible explanation to the discrepancy between experiment and theory is that side walls in the experiments may induce large inhomogeneities as the suspension evolves in time. Furthermore, the experiments are always affected by polydispersity at low-volume fraction. Polydispersity could decrease the correlation time for a particle allowing it to fall through the interaction volume faster than it can sample the same volume by hydrodynamic dispersion. This effect would be important to decrease diffusivity as observed in the experiments.

The velocities of the particles fluctuate randomly in time, apparently with a magnitude which does not evolve during the sedimentation. The persistence in time of the velocity fluctuations is investigated using the auto-correlation function of the velocity fluctuations, which correlates the velocity at time t with itself at various time delays τ. This is constructed for the vertical and two horizontal components. We shall report these auto-correlation functions normalized by the variances, i.e.,

$$C_\parallel(t)=\frac{\langle U'(t)U'(t+\tau)\rangle}{\langle U'(t)U'(t)\rangle} \tag{33}$$

and similarly for $C_\perp(t)$. Here the angle brackets denote a sum over all particles, and an average over all configurations or realizations (i.e., an average over time in dynamic simulation).

Figure 11 gives the auto-correlation function, nondimensionalized by the variance (correlation with zero time delay), for the horizontal and vertical velocity, both for our computer simulations in the case $\phi=3\%$, $a/l=0.05$ and $h/l=3$ and for the experiments of Nicolai et al. [25] in the case $\phi=5\%$, $a/l=0.01$, $h/l=10$, and $l/d=2.5$. There is good general agreement in which the velocities lose correlation over a time of $O(10a/U_0)$ and the horizontal velocity de-correlates slightly faster.

The random motion of the sedimenting particles can be characterized by a diffusion process with diffusivity calculated as the integral over time of the velocity auto-correlation function

$$D=\int_0^\infty \langle U'(t)U'(t+\tau)\rangle dt, \tag{34}$$

constructed for the vertical $D_\parallel$ and averaged over the two horizontal directions for $D_\perp$.

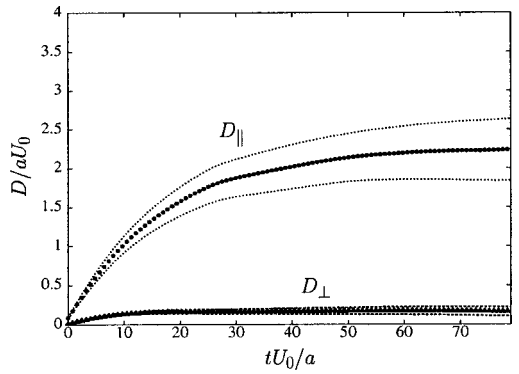

Fig. 12 Dimensionless hydrodynamic self-diffusivities for $h/l=3$, $a/l=0.05$, and $\phi=3\%$. The dashed lines are the error bars.

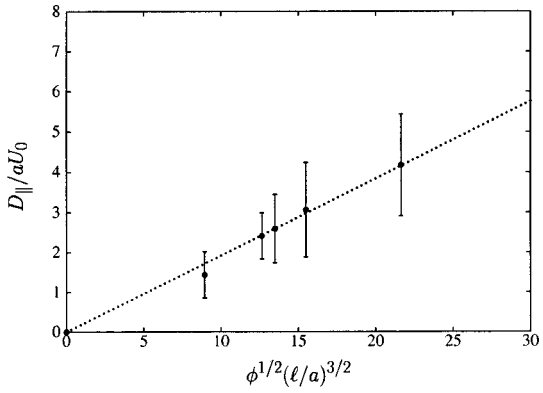

Fig. 13 Vertical dimensionless hydrodynamic self-diffusivity as a function of the scaling $\phi^{1/2}(l/a)^{3/2}$. The dot line is the linear fit $D_\parallel=0.19aU_0\phi^{1/2}(l/a)^{3/2}$.

$$\mathbf{D}=\mathbf{e}_z\mathbf{e}_z D_\parallel+(\mathbf{I}-\mathbf{e}_z\mathbf{e}_z)D_\perp \tag{35}$$

An important question is to examine whether this integral converges at long times: if it does not, the diffusion process is anomalous. The ratio of the diffusivities to the velocity variance gives the integral time-correlation $D/\langle U'^2\rangle$.

Figure 12 shows the time integral increasing to its asymptotic value on the correlation time of $O(10a/U_0)$. For the case $\phi=3\%$, $a/l=0.05$ and $h/l=3$ we find a diffusivity in the direction of gravity $D_\parallel=2aU_0$. This value should be compared with the experimental values of Ham and Homsy [23] increasing from $2aU_0$ at $\phi=2.5\%$ to $6aU_0$ at $\phi=6\%$, and the experimental value of Nicolai et al. [25] around $5aU_s$. Hydrodynamic screening theory gives $D_\parallel=0.52aU_0/\phi$, i.e., the larger value $17aU_s$ at $\phi=3\%$, [9].

Figure 13 shows our results for the self-diffusivity parallel to gravity as a function of the scaling parameter $\phi^{1/2}(l/a)^{3/2}$. The results for various particle concentrations ϕ and box sizes a/l can be approximated by the linear fit $D_\parallel=0.19aU_0\phi^{1/2}(l/a)^{3/2}$. While the values of the diffusivity are comparable with those in laboratory experiments, a direct comparison is not possible because our simulations depend on the size of the box and the laboratory experiments do not.

The random fluctuations during sedimentation exhibit considerable anisotropy. We find that $D_\parallel/D_\perp\approx 10$ in all our simulations. This value should be compared with a value around 5 in the experiments of Nicolai et al. [25], and a value around 25 in the theory of Koch [14]. In fact, Koch's theory shows that it is possible to reduce a degree of anisotropy from 100 to around 25 by increasing the aspect ratio of the box from $h/l=1$ to $h/l=3$. We speculate, however, that this still high value results from the use of a full periodic boundary condition in the vertical rather than our no flux boundary perpendicular to gravity. Ladd [16] reported numerical results of fluctuations and hydrodynamic dispersion in sedimentation for a large homogeneous suspension using 32768 particles ($\phi=10\%$) at finite Reynolds number (Re=0.45), based on the width of the periodic cell. His results show an anisotropy in velocity fluctuations about 3 that agree well with our numerical results and experiments. However, the ratio of diffusivities equal to 24 for $h/l=4$ are larger than the result here and about five times the experimental measurements.

Finally, we consider the results for velocity fluctuation fields across the whole box at $\phi=0.03$. The simulations show how the random initial structure develops in time. Figure 14 displays typical velocity fluctuation fields taken during the dynamical simulation at time t from 0 to $75a/U_0$. The starting time ($t=0$) corresponds to a random suspension generated as described in Section 4.1. It is apparent that coherent large-scale structure that are order of the size of the box forms (convective currents of particles) and persists at later times. This larger scale vortex structure indicates that the velocity fluctuations depend on the system size.

From the above discussion it seems as though that simulations with a finite height of suspension approaching a no-flux boundary with periodic boundary conditions in the horizontal direction is the key to better capture the anisotropic nature of the particle interactions and also to understand the difference between theory and experiments on dilute sedimenting suspensions. This problem can be better explored through simulations considering a box with no-slip boundaries in order to investigate the effect of the container walls on the dynamic of fluctuations as particles sediment.

6 Conclusions

In this paper we report direct numerical simulations of monodisperse and polydisperse suspensions of spherical particles sedimenting at low Reynolds number in a rectangular container with side periodicity and impenetrable slip boundaries perpendicular to gravity. Our method is applicable for static (not developing in time) and dynamic simulations of suspensions at moderately volume fractions. The method of images was peculiarly adapted to the solution of the problem of many interacting particles. The results show the importance of including the effect of a no-flux lower boundary for reducing the vertical-horizontal anisotropy of particle diffusivities to realistic proportions.

We have compared our results of sedimentation velocity for ordered and random (monodisperse and polydisperse) suspensions with theory and experimental correlations and have generally found good agreement for particle volume fraction ranging from 0 to 0.20. It is seen that the sedimentation velocities do not agree particularly well in the very dilute limit due to the effect of periodicity of our numerical system. For higher volume fractions a good agreement of our sedimentation with experiments would require higher-order many-body multipole moments.

The results also show the evolution of the positions of the particles in a finite box. Our numerical computations have found velocity fluctuations of monodisperse and polydisperse dilute suspensions increasing in a predictable way with the system size. It is seen that a saturation of fluctuations occurs only at volume fractions larger than 10%. This result agrees with the scaling arguments presented here, with theory and with large-scale lattice-Boltzmann simulations of dilute suspensions. We conclude that the sedimentation process observed in our simulations has been dominated by convection currents (large structure motion) of the size of the settling box, which is preserved in time. In contrast, the experiments have found that large vortex structures diminishes in size at larger times.

The degree of anisotropy in velocity fluctuations and hydrodynamic self-diffusivities, both experimentally and in the present simulations are independent of the system size. Our simulation results for normalized autocorrelation functions are also in good agreement with experiments at dilute limit.

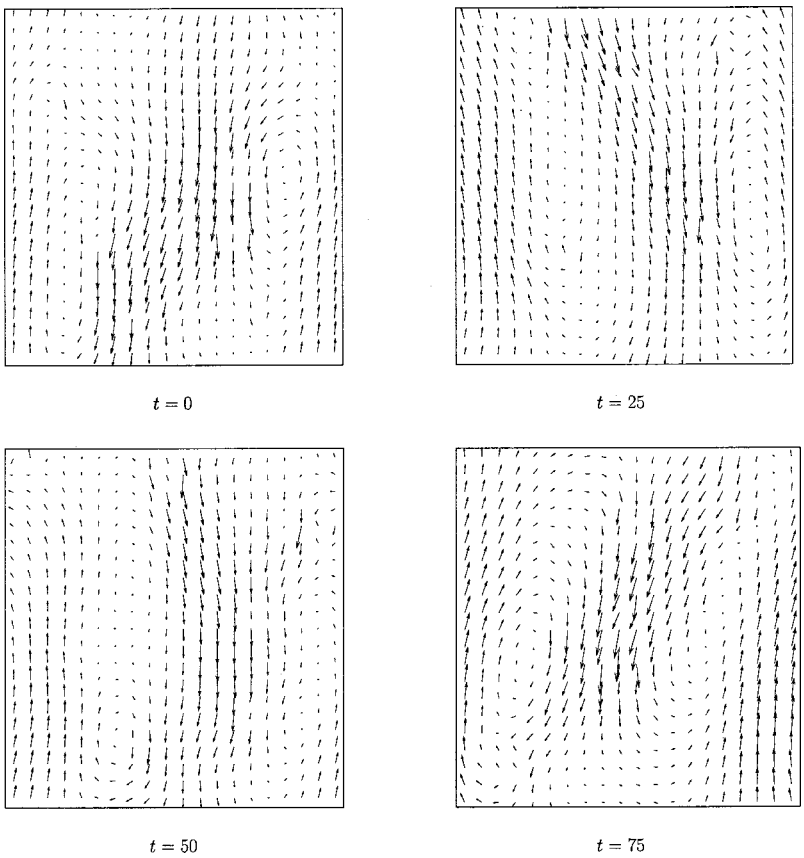

Fig. 14 Time developing of three-dimensional velocity-fluctuation fields across the numerical box (20×20×60) during the sedimentation process of monodisperse particles at $\phi=0.05$. The dimensionless time corresponds to multiples of Stokes time a/U_o. Large-scale motions (i.e., convective currents) dominate the sedimentation process with large swirl depending on the numerical box.

Since the experimental systems are never perfectly homogeneous and the actual particle distribution is unknown, the experimental observations have not a definite answer for the physical mechanism that renormalizes the rms fluctuations in a dilute sedimenting suspension. Certainly new numerical simulations including the effects of the container walls would be important and challenging to explain the experimental observations.

We hope that our simulations have given some new insights into the study of fluctuations and dispersion in sedimentation and may help to stimulate new developments in the future.

Acknowledgments

We acknowledge the support from CNPq-Brasil and Finep-CTPETRO. We wish to thank Elizabeth Guazzelli (LPMH/ESPCI, Paris) for kindly providing the experimental data plotted in Fig. 11.

Nomenclature

a = particle radius
C = velocity autocorrelation function
C_1, C_2 = numerical parameters (see Eq. (14))
D = hydrodynamic self-diffusivity
D_0 = Stokes-Einstein diffusivity
d = box width
$\mathbf{F}$ = force acting on the particles
$\mathbf{f}_l^\alpha$ = artificial lubrication force acting on a particle α
$\mathbf{f}_c^\alpha$ = artificial contact force acting on a particle α
$f(\phi)$ = hindered settling function
$\mathbf{G}$ = Ewald summed mobility tensor
$\mathbf{g}$ = gravitational force per unit mass
h = box height
$\mathbf{I}$ = unit second-rank tensor
$\mathbf{J}$ = kernel tensor
K_e = contact stiffness
$\mathbf{k}_\xi$ = reciprocal lattice vector
l = box length
$\mathbf{M}$ = mobility tensor
m = number of species
N = number of particles within the unit cell
n = number density of particles
Pe = Péclet number
$\mathbf{r}$ = relative distance vector
Re = Reynolds number
$S(\lambda,\eta)$ = sedimentation coefficients
St = Stokes number
U_0 = Stokes velocity
U' = particle velocity fluctuation
u,v,w = fluid velocity components
V = cell volume
$\mathbf{x}$ = position vector
$\mathbf{x}_\gamma$ = physical lattice vector
x,y,z = space coordinates

Greek Symbols

γ = cell index of the physical lattice
ΔE = energy variation
$\Delta\rho$ = particle-fluid density difference

δt = time step
ϵ = geometric parameter (see Eq. (21))
ε_n = random vector
ε_0 = interparticle gap for which the force $\mathbf{f}_l^\alpha$ is cut off
$\varepsilon_{\alpha\beta}$ = virtual overlap between particles α and β
ζ = cell index of the reciprocal lattice
η = reduced density ratio
κ = Boltzmann constant
λ = aspect ratio
μ = fluid viscosity
ξ = convergence parameter
ρ = particle density
ρ_f = fluid density
τ_c = correlation time
ϕ = solid volume fraction

Superscripts

α, β = particle index
(ps) = physical space
(rs) = reciprocal space
$(s), (p)$ = given species

Subscripts

$\parallel$ = parallel to gravity
$\perp$ = perpendicular to gravity
s = small species
s, p = given species
l = large species

References

[1] Davis, R. H., and Acrivos, A., 1985, "Sedimentation of Noncolloidal Particles at Low Reynolds Number," Annu. Rev. Fluid Mech., **17**(91), pp. 91–118.
[2] Richardson, J. F., and Zaki, W. N., 1954, "Sedimentation and Fluidization: I," Trans. Inst. Chem. Eng., **32**(35), pp. 35–52.
[3] Batchelor, G. K., 1972, "Sedimentation in a Dilute Dispersion of Spheres," J. Fluid Mech., **52**, pp. 245–268.
[4] Batchelor, G. K., 1982, "Sedimentation in a Dilute Polydisperse System of Interacting Spheres. Part 1. General Theory," J. Fluid Mech., **119**, pp. 379–408.
[5] Davis, R. H., 1996, "Hydrodynamic Diffusion of Suspended Particles: A Symposium," J. Fluid Mech., **310**, pp. 325–335.
[6] Guazzelli, E., 2001, "Evolution of Particle-Velocity Correlations in Sedimentation," Phys. Fluids, **13**(6), pp. 1537–1540.
[7] Caflisch, R. E., and Luke, J. H. C., 1985, "Variance in the Sedimentation Speed of a Suspension," Phys. Fluids, **28**(3), pp. 759–760.
[8] Hinch, E. J., 1988, *Disorder and Mixing*, Kluwer Academic, Dordrecht, pp. 153–161, Chap. 9.
[9] Koch, D. L., and Shaqfeh, E. S. G., 1991, "Screening in Sedimenting Suspensions," J. Fluid Mech., **224**, pp. 275–303.
[10] Koch, D. L., 1992, "Anomalous Diffusion of Momentum in a Dilute Gas-Solid Suspension," Phys. Fluids, **4**(7), pp. 1337–1346.
[11] Cunha, F. R., 1995, "Hydrodynamic Dispersion in Suspensions," Ph.D. Thesis, Department of Applied Mathematics and Theoretical Physics, Cambridge University, Cambridge, UK.
[12] Cunha, F. R., 1997, "On the Fluctuations in a Random Suspension of Sedimenting Particles," J. Braz. Soc. Mech. Sci., **19**(4), pp. 474–495.
[13] Brenner, M. P., 1999, "Screening Mechanisms in Sedimentation," Phys. Fluids, **11**(4), pp. 754–772.
[14] Koch, D. L., 1994, "Hydrodynamic Diffusion in a Suspension of Sedimenting Point Particles With Periodic Boundary Conditions," Phys. Fluids, **6**(9), pp. 2894–2900.
[15] Ladd, A. J. C., 1993, "Dynamical Simulation of Sedimenting Spheres," Phys. Fluids, **5**(2), pp. 299–310.
[16] Ladd, A. J. C., 1997, "Sedimentation of Homogeneous Suspensions of Non-Brownian Spheres," Phys. Fluids, **9**(3), pp. 491–499.
[17] Cunha, F. R., Rosa, O. S., and Sousa, A. J., 2001, "Do We Understand Hydrodynamic Dispersion in Sedimenting Suspensions?" J. Braz. Soc. Mech. Sci., **23**(4), pp. 379–399.
[18] Nicolai, H., and Guazzelli, E., 1995, "Effect of the Vessel Size on the Hydrodynamic Diffusion of Sedimenting Spheres," Phys. Fluids, **7**(1), pp. 3–5.
[19] Ségre, P. N., Herbolzeimer, E., and Chaikin, P. M., 1997, "Long-Range Correlations in Sedimentation," Phys. Rev. Lett., **79**(13), pp. 2574–2577.
[20] Kalthoff, W., Schwarzer, S., Ristow, G. et al., 1996, "On the Application of a Novel Algorithm to Hydrodynamic Diffusion and Velocity Fluctuations in Sedimenting Systems," Int. J. Mod. Phys. C, **7**(4), pp. 543–561.
[21] Davis, R. H., and Hassen, M. A., 1988, "Spreading of the Interface at the Top of a Slightly Polydisperse Sedimenting Suspension," J. Fluid Mech., **196**, pp. 107–134.
[22] Lee, S., Jang, J., Choi, C., and Lee, T., 1992, "Combined Effect of Sedimentation Velocity Fluctuation and Self-Sharpening on Interface Broadening," Phys. Fluids, **4**(12), p. 2601–2606.
[23] Ham, J. M., and Homsy, G. M., 1988, "Hindered Settling and Hydrodynamic Dispersion in Quiescent Sedimenting Suspensions," Int. J. Multiphase Flow, **14**(5), pp. 533–546.
[24] Xue, J.-Z., Herboltzheimer, E., Rutgers, M. A., Russel, W. B., and Chaikin, P. M., 1992, "Diffusion, Dispersion, and Settling of Hard Spheres," Phys. Rev. Lett., **69**(11), pp. 1715–1718.
[25] Nicolai, H., Herzhaft, B., Hinch, E. J., Oger, L., and Guazzelli, E., 1995, "Particle Velocity Fluctuations and Hydrodynamic Self-Diffusion of Sedimenting Non-Brownian Spheres," Phys. Fluids, **7**(1), pp. 12–23.
[26] Cunha, F. R., and Hinch, E. J., 1996, "Shear-Induced Dispersion in a Dilute Suspension of Rough Spheres," J. Fluid Mech., **309**, pp. 211–223.
[27] Leighton, D. T., and Acrivos, A., 1987, "The Shear-Induced Migration of Particles in Concentrated Suspensions," J. Fluid Mech., **181**, pp. 415–439.
[28] Beenakker, C. W. J., 1986, "Ewald Sum of the Rotne-Prager Tensor," J. Chem. Phys., **85**(3), pp. 1581–1582.
[29] Nijboer, B. R. A., and De Wette, F. W., 1957, "On the Calculation of Lattice Sums," Physica, **23**, pp. 309–321.
[30] Rotne, J., and Prager, S., 1969, "Variational Treatment of Hydrodynamic Interaction in Polymers," J. Chem. Phys., **50**(11), pp. 4831–4837.
[31] Brady, J. F., and Bossis, G., 1988, "Stokesian Dynamics," Annu. Rev. Fluid Mech., **20**, pp. 111–157.
[32] Kim, S., and Karrila, S. J., 1991, *Microhydrodynamics: Principles and Selected Applications*, Butterworth-Heinemann.
[33] Blake, J. R., 1971, "A Note on the Image System for a Stokeslet in a No-Slip Boundary," Proc. Cambridge Philos. Soc., **70**, pp. 303–310.
[34] Metropolis, N., Rosenbluth, A. W., Rosenbluth, M. N., Teller, A. H., and Teller, E., 1953, "Equation of State Calculations by Fast Computing Machines," J. Chem. Phys., **21**(6), pp. 1087–1092.
[35] Press, W. H., Teukolsky, S. A., Vetterling, W. T., and Flannery, B. P., 1992, *Numerical Recipes in Fortran 77*, **1**, Cambridge University Press, Cambridge, UK.
[36] Sierou, A., and Brady, J. F., 2001, "Accelerated Stokesian Dynamics Simulations" J. Fluid Mech., **448**, pp. 115–146.
[37] Ladd, A. J. C., 1994, "Numerical Simulations of Particulate Suspensions via a Discretized Boltzmann Equation. Part 2. Numerical Results," J. Fluid Mech., **271**, pp. 311–339.
[38] Mo, G., and Sangani, A. S., 1994, "A Method for Computing Stokes Flow Interactions Among Spherical Objects and Its Application to Suspensions of Drops and Porous Particles," Phys. Fluids, **6**(5), pp. 1637–1652.
[39] Saffman, P. G., 1973, "On the Settling Speed of Free and Fixed Suspensions," Stud. Appl. Math., **52**(2), pp. 115–127.
[40] Sangani, A. S., and Acrivos, A., 1982, "Slow Flow Through a Periodic Array of Spheres," Int. J. Multiphase Flow, **8**(4), pp. 343–360.
[41] Brady, J. F., and Durlofsky, L. J., 1988, "The Sedimentation Rate of Disordered Suspensions," Phys. Fluids, **31**(4), pp. 717–727.
[42] Davis, R. H., and Gecol, H., 1994, "Hindered Settling Function with No Empirical Parameters for Polydisperse Suspensions," AIChE J., **40**(3), pp. 570–575.
[43] Batchelor, G. K., and Wen, C. S., 1982, "Sedimentation in a Dilute Polydisperse System of Interacting Spheres. Part 2. Numerical Results," J. Fluid Mech., **124**, pp. 495–528.

Thermal Damping in Cavitating Nozzle Flows

Can F. Delale
Department of Aeronautics and Astronautics,
Istanbul Technical University,
80626 Maslak, Istanbul
and
Tübítak Feza Gürsey Institute,
P.O. Box 6,
81220 Cengelköy,
Istanbul, Turkey
e-mail: delale@gursey.gov.tr

Recent investigations of bubbly cavitating nozzle flows using the polytropic law for the partial gas pressure have shown flow instabilities that lead to flashing flow solutions. Here, we investigate the stabilizing effect of thermal damping on these instabilities. For this reason we consider the energy equation within the bubble, assumed to be composed of vapor and gas, in the uniform pressure approximation with low vapor concentration. The partial vapor pressure is fixed by the vapor saturation pressure corresponding to the interface temperature, which is evaluated by assuming the thin boundary layer approximation within the liquid. Consequently, the partial gas pressure is evaluated by its relation to the heat flux through the interface in the uniform pressure approximation. The model is then coupled to the steady-state cavitating nozzle flow equations replacing the polytropic law for the partial gas pressure. The instabilities found in steady cavitating nozzle flows are seen to be stabilized by thermal damping with or without the occurrence of bubbly shock waves. [DOI: 10.1115/1.1511163]

1 Introduction

It is well known that the pressure within the bubble affects bubble dynamics significantly. Thermal effects arising mainly from thermal conduction through the bubble and the surrounding liquid produce temperature changes that can have significant effects on the total pressure p_b', written as the sum of the partial gas pressure p_g' and partial vapor pressure p_v', as has been demonstrated in various studies (e.g., see Chapman and Plesset [1], Nigmatulin et al. [2], Miksis and Ting [3], Prosperetti et al. [4], Prosperetti [5], Brennen [6], Hao and Prosperetti [7], and references therein). Matsumoto and Takemura [8] and Takemura and Matsumoto [9] have also numerically simulated single bubble motion subjected to a stepwise pressure signal by integrating directly the full conservation equations for mass, momentum, and energy inside and outside the bubble. Their results showed that heat conductivity and diffusion affect the bubble motion significantly. For a spherical vapor-gas bubble of radius R' whose partial gas pressure is p_{g0}' at some reference size R_0' and temperature T_0' (usually taken as those values at the mechanical and thermal equilibrium of the bubble with the surrounding liquid), the total bubble pressure at the bubble wall, can be written as

$$p_b' = p_v'(T_R') + p_{g0}' \left(\frac{T_R'}{T_0'}\right)\left(\frac{R_0'}{R'}\right)^3 \tag{1}$$

where T_R' is the bubble wall temperature provided that there is no appreciable mass transfer of the gas to or from the liquid (e.g., see Brennen [6]). It is now clear that the bubble wall pressure p_b' and consequently, bubble dynamics can be strongly influenced by the variation of the bubble wall temperature T_R'. The determination of the bubble wall temperature T_R' requires solving heat diffusion equations within the bubble and in the surrounding liquid. This problem is usually bypassed by assuming a polytropic law for the gas so that Eq. (1) becomes

$$p_b' = p_v'(T_R') + p_{g0}' \left(\frac{R_0'}{R'}\right)^{3k} \tag{2}$$

where $k=1$ for isothermal and $k=\gamma_g$ for isentropic expansion (compression) of the gas. Recent investigations (e.g., see Nigmatulin et al. [2], Prosperetti [5]) have shown that the use of the polytropic law (2) for the gas leads to considerable disagreement between theory and experiment in nonlinear oscillations of bubbles (for an extension to vapor bubbles, see Hao and Prosperetti [7]). It has also been recently demonstrated by Wang and Brennen [10] and by Delale et al. [11] that the use of Eq. (2) in steady-state cavitating nozzle flows can result in instabilities in the flow. Here we abandon Eq. (2) and, instead, concentrate on Eq. (1) to see the effect of thermal damping on bubble dynamics, especially on the instabilities mentioned.

For most cavitating flows, the bubble wall temperature deviates from the cold liquid temperature T_0' only slightly so that we can write

$$T_R' = T_0'(1+\vartheta) \tag{3}$$

where the function $\|\vartheta\| \ll 1$. Substitution of Eq. (3) into Eq. (1) then yields

$$p_b' = p_v'(T_0') + p_{g0}' \left(\frac{R_0'}{R'}\right)^3 + \vartheta\left[\rho_v' L'(T_0') + p_{g0}'\left(\frac{R_0'}{R'}\right)^3\right] + \ldots \tag{4}$$

where ρ_v' is the saturated vapor density at T_0' and $L'(T_0')$ is the latent heat of vaporization at T_0'. Equation (4) shows that, when the normalized radius R'/R_0' is of $O(1)$ during the growth period, the isothermal approximation holds. However, when the radius grows to appreciable size, as observed in the flashing flow instabilities of Wang and Brennen [10] and of Delale et al. [11], the contribution from the $O(\vartheta)$ term can become comparable to the first term so that deviations from isothermal behavior can be substantial. In such a case the effect of thermal damping on bubble dynamics cannot be neglected and the function ϑ has to be determined from the solution of the thermal diffusion equations within the bubble as well as in the surrounding liquid.

In this investigation we consider the heat diffusion equation for a spherical vapor-gas bubble in the uniform pressure approximation and in the limit of low vapor concentration and near-isothermal flow, following the work of Prosperetti [5] for a gas bubble. The bubble wall temperature is evaluated by the Plesset-Zwick [12] solution of the heat equation in the surrounding liquid in the thin boundary layer approximation. Consequently, a general expression for the variation of the bubble pressure, that depends on the variation of the bubble wall temperature and its coupling to bubble dynamics, is obtained. The resulting equation is then coupled to the quasi-one-dimensional nozzle flow equations to

Contributed by the Fluids Engineering Division for publication in the JOURNAL OF FLUIDS ENGINEERING. Manuscript received by the Fluids Engineering Division July 27, 2001; revised manuscript received May 29, 2002. Associate Editor: Y. Matsumoto.

determine the effect of thermal damping. Results obtained for quasi-one-dimensional steady-state cavitating nozzle flows show that the flashing flow instabilities discussed by Wang and Brennen [10] and by Delale et al. [11] can be stabilized with or without the occurrence of bubbly shock waves by thermal damping.

2 The Energy Balance for a Spherical Vapor-Gas Bubble

In this section we discuss the energy balance between a spherical vapor-gas bubble and its surrounding liquid. For this reason it is essential to discuss the processes of energy transfer between the spherical bubble and the surrounding liquid.

2.1 Thermal Conduction Through a Spherical Vapor-Gas Bubble. We consider a spherical bubble with radius R' with content taken as a homogeneous mixture of a gas and a vapor at the same temperature T'. We neglect the inter-diffusion between the gas and vapor. The energy equation can then be written as (see Prosperetti [5])

$$\frac{\gamma_b p_b'}{(\gamma_b-1)T'}\frac{dT'}{dt'}-\frac{dp_b'}{dt'}=\frac{1}{r'^2}\frac{\partial}{\partial r'}\left(r'^2\lambda_b'\frac{\partial T'}{\partial r'}\right) \tag{5}$$

where the isentropic exponent γ_b of the gas-vapor mixture is defined by

$$\gamma_b=\frac{(1-c_g)[\gamma_v\Re_v'/(\gamma_v-1)]+c_g[\gamma_g\Re_g'/(\gamma_g-1)]}{(1-c_g)[\Re_v'/(\gamma_v-1)]+c_g[\Re_g'/(\gamma_g-1)]} \tag{6}$$

with γ_v, $\Re_v'$ and γ_g, $\Re_g'$ denoting, respectively, the isentropic exponents and the gas constants of the vapor and of the gas and with $c_g=\rho_g'/\rho_b'$ denoting the ratio of the gas density to the bubble density. In Eq. (5), p_b' is the total pressure of the bubble (assumed to be uniform throughout the bubble), λ_b' is the thermal conductivity of the bubble, t' denotes the time, r' is the radial coordinate and the operator $d/dt'=\partial/\partial t'+w'\partial/\partial r'$ (where w' is the magnitude of the radial velocity) is the total derivative. Utilizing the thermal equation of state of the bubble for ideal gas mixture with gas constant $\Re_b'=(1-c_g)\Re_v'+c_g\Re_g'$ together with the continuity equation, we can write Eq. (5) in the form

$$\frac{dp_b'}{dt'}+\gamma_b p_b'\frac{1}{r'^2}\frac{\partial}{\partial r'}(r'^2w')=\frac{(\gamma_b-1)}{r'^2}\frac{\partial}{\partial r'}\left[r'^2\lambda_b'(T')\frac{\partial T'}{\partial r'}\right]. \tag{7}$$

Equation (7), in the uniform pressure approximation, can be integrated once with respect to r' to yield

$$w'=\frac{1}{\gamma_b p_b'}\left[(\gamma_b-1)\lambda_b'(T')\frac{\partial T'}{\partial r'}-\frac{1}{3}r'\frac{dp_b'}{dt'}\right]. \tag{8}$$

Assuming that the gas content of the gas-vapor mixture is constant, we have

$$w'|_{r'=R'}=\frac{dR'}{dt'}-\frac{m_v''}{\rho_b'} \tag{9}$$

where m_v'' is the interfacial mass flux of the vapor, determined, in principle, from kinetic theory (e.g., see Nigmatulin et al. [2]). However, for this case, the value of the accommodation coefficient to be used presents a serious difficulty in determining the value of m_v''. Here we determine m_v'' using an approximate overall energy balance. We consider the interfacial condition

$$m_v''L'=\lambda_{lR}'\left(\frac{\partial T_l'}{\partial r'}\right)_{r'=R'}-\lambda_{bR}'\left(\frac{\partial T'}{\partial r'}\right)_{r'=R'} \tag{10}$$

where L' is the latent heat of vaporization, λ_{lR}' and λ_{bR}' are, respectively, the thermal conductivity of the liquid and that of the gas-vapor mixture at the bubble wall, and T_l' denotes the temperature field within the liquid. Assuming that the thermal conductivity of the liquid is much greater than that of the gas-vapor mixture, the phase change at the bubble wall can be thought to be dominated by the liquid side. If, in addition, the vapor density distribution within the bubble is approximated by some average value, e.g., by its saturated value at the bubble wall temperature, the interfacial condition (10) can be approximated as (e.g., see Brennen [6] and Hao and Prosperetti [7])

$$\frac{dR'}{dt'}=\frac{\lambda_{lR}'}{\rho_v'L'}\left(\frac{\partial T_l'}{\partial r'}\right)_{r'=R'} \tag{11}$$

so that we have $m_v''\approx\rho_v'(dR'/dt')$. Using this result, we evaluate Eq. (8) at $r'=R'$ and utilize Eq. (9) to arrive at

$$\frac{dp_b'}{dt'}=\frac{3}{R'}\left[(\gamma_b-1)\lambda_{bR}'\frac{\partial T'}{\partial r'}\bigg|_{r'=R'}-\gamma_b c_g p_b'\frac{dR'}{dt'}\right] \tag{12}$$

where $\lambda_{bR}'=\lambda_b'(T_R')$ with T_R' denoting the temperature of the bubble wall. For a gas bubble ($c_g=1$), Eq. (12) reduces precisely to that derived by Prosperetti [5]. Following Nigmatulin et al. [2] and Prosperetti [5], we introduce the scaled variable y:

$$y=\frac{r'}{R'(t')}. \tag{13}$$

Equations (5), (8), and (12), then, reduce to

$$\begin{aligned}\frac{\gamma_b p_b'}{(\gamma_b-1)T'}&\left\{\frac{\partial T'}{\partial t'}+\frac{(\gamma_b-1)}{\gamma_b p_b' R'^2}\left[\lambda_b'(T')\frac{\partial T'}{\partial y}-\lambda_{bR}'y\frac{\partial T'}{\partial y}\bigg|_{y=1}\right.\right.\\&\left.\left.-\frac{\gamma_b(1-c_g)}{(\gamma_b-1)}yp_b'R'\frac{dR'}{dt'}\right]\frac{\partial T'}{\partial y}\right\}\\&=\frac{dp_b'}{dt'}+\frac{1}{R'^2y^2}\frac{\partial}{\partial y}\left[y^2\lambda_b'(T')\frac{\partial T'}{\partial y}\right]\end{aligned} \tag{14}$$

and

$$\frac{dp_b'}{dt'}=\frac{3}{R'}\left[(\gamma_b-1)\frac{\lambda_{bR}'}{R'}\frac{\partial T'}{\partial y}\bigg|_{y=1}-\gamma_b c_g p_b'\frac{dR'}{dt'}\right] \tag{15}$$

for $0<y<1$. These equations that couple the microscopic energy equation for the bubble temperature T' to the total bubble pressure p_b' and to the bubble radius R' were first derived by Prosperetti [5] for a gas bubble ($c_g=1$). Here, it is shown that they can also be utilized for cavitating flows, except for the very last stages of bubble collapse where the uniform pressure approximation breaks down. This result also assumes that γ_b and $\Re_b'$ can be treated as constants (although the composition of the vapor and of the gas can vary significantly during growth and collapse, γ_b and $\Re_b'$ vary at a much slower rate so that they can be approximated by some average values).

2.2 The Energy Equation in the Surrounding Liquid. The bubble wall temperature T_R' may, in some cases, be significantly different from the ambient liquid temperature T_0' far away from the bubble. In such a case the consideration of the energy equation in the surrounding liquid is essential. If $T_l'(r',t')$ is the temperature in the liquid phase at a distance r' ($R'\leqslant r'<\infty$) from the bubble center at time t', the energy equation in the liquid can be written as

$$\frac{\partial T_l'}{\partial t'}+\frac{dR'}{dt'}\left(\frac{R'}{r'}\right)^2\frac{\partial T_l'}{\partial r'}=\frac{\alpha_l'}{r'^2}\frac{\partial}{\partial r'}\left(r'^2\frac{\partial T_l'}{\partial r'}\right) \tag{16}$$

where α_l' is the thermal diffusivity of the liquid (e.g., see Brennen [6]). Assuming that the radial motion is sufficiently small so that translational motion can be neglected, the temperature difference

$T_0'-T_R'$ can be obtained by the solution of Eq. (16) given by Plesset and Zwick [12] together with Eq. (11) (for details see Brennen [6])

$$T_0'-T_R'=\frac{L'\rho_v'}{c_{pl}'\rho_l'}\left(\frac{1}{\pi\alpha_l'}\right)^{1/2}\int_0^{t'}\frac{R'^2(\xi')(dR'/d\xi')}{\left[\int_{\xi'}^{t'}R'^4(\tau')d\tau'\right]^{1/2}}d\xi'. \quad (17)$$

Equation (17) relates bubble dynamics to the bubble wall temperature T_R'.

2.3 Normalized Equations for Energy Balance of a Spherical Vapor-Gas Bubble. We now introduce the normalized variables

$$p_b=\frac{p_b'}{p_0'},\quad T=\frac{T'}{T_0'},\quad \lambda_b=\frac{\lambda_b'}{\lambda_{bR}'},\quad R=\frac{R'}{R_0'}\quad\text{and}\quad t=\frac{t'}{\Theta'} \quad (18)$$

where R_0' is a typical equilibrium radius, p_0' is the corresponding mixture pressure, T_0' is the liquid temperature at infinity, $\lambda_{bR}'=\lambda_b'(T_R')$ is the thermal conductivity of the bubble evaluated at T_R' and Θ' is a characteristic time for bubble dynamics. With this normalization Eqs. (14) and (15) assume the form

$$\frac{p_b}{T}\left\{\frac{\partial T}{\partial t}+\frac{D}{p_bR^2}\left[\lambda_b(T)\frac{\partial T}{\partial y}-y\frac{\partial T}{\partial y}\bigg|_{y=1}-\frac{(1-c_g)}{D}yp_bR\frac{dR}{dt}\right]\frac{\partial T}{\partial y}\right\}$$
$$=\frac{(\gamma_b-1)}{\gamma_b}\frac{dp_b}{dt}+\frac{D}{R^2y^2}\frac{\partial}{\partial y}\left[y^2\lambda_b(T)\frac{\partial T}{\partial y}\right] \quad (19)$$

and

$$\frac{d}{dt}[R^{3\gamma_b}p_b]=3\gamma_bR^{(3\gamma_b-2)}\left[D\frac{\partial T}{\partial y}\bigg|_{y=1}+(1-c_g)p_bR\frac{dR}{dt}\right] \quad (20)$$

where D is the square of the ratio of the penetration length l_p' to the equilibrium radius R_0' (e.g., see Prosperetti [5]) and it is defined by

$$D=\left(\frac{l_p'}{R_0'}\right)^2=\frac{(\gamma_b-1)\lambda_{bR}'T_0'\Theta'}{\gamma_bp_0'R_0'^2}. \quad (21)$$

In Eq. (21) l_p' is given by

$$l_p'=\left(\frac{\lambda_{bR}'\Theta'}{\rho_0'c_{pb}'}\right)^{1/2} \quad (22)$$

where $\rho_0'=p_0'/(\Re_b'T_0')$ is the density of the bubble at equilibrium. Equations (19) and (20) provide two equations for the normalized temperature T and the bubble pressure p_b coupled to the equations of nonlinear spherical bubble dynamics.

It is worthwhile mentioning that the neglect of gas diffusion at the bubble wall and the assumption of uniform pressure distribution throughout the bubble impose the restriction

$$\int_0^{R'}\rho_g'r'^2dr'=\frac{1}{3}R_0'^3\rho_{g0}', \quad (23)$$

where ρ_{g0}' is the gas density at equilibrium. Equation (23), in normalized form, becomes

$$p_g\int_0^1\frac{y^2}{T}dy=\frac{p_{g0}}{3R^3} \quad (24)$$

where p_g $(=p_g'/p_0')$ denotes the normalized partial gas pressure inside the bubble and p_{g0} is its equilibrium value.

It is also interesting to note that the term $D\partial T/\partial y|_{y=1}$ in Eq. (20) plays a decisive role in the nature of expansion or compression of the gas during the growth or collapse of the bubble. In particular, two cases frequently employed during collapse and growth periods of the bubble are easily identified as limiting cases:

(i) The adiabatic limit ($D\partial T/\partial y|_{y=1}\to 0$ and $c_g\to 1$).

This limit is frequently assumed at the collapse stages of the bubble where most of the vapor has already condensed. Therefore, in this limit Eq. (20) integrates to the adiabatic compression law

$$p_g=\frac{p_{g0}}{R^{3\gamma_g}}. \quad (25)$$

(ii) The isothermal limit ($T=1$ so that $D\to\infty$, $\partial T/\partial y|_{y=1}\to 0$).

In this limit it follows from the normalized Eq. (24) that

$$p_b=p_v+p_g=p_v+\frac{p_{g0}}{R^3}. \quad (26)$$

3 Model Equations for Thermal Damping in Quasi-One-Dimensional Cavitating Nozzle Flows

In this section we consider the model equations for unsteady quasi-one-dimensional nozzle flow equations together with the classical Rayleigh-Plesset equation for bubble dynamics. These equations in normalized form are

$$\rho=1-\beta, \quad (27)$$

$$A\frac{\partial\rho}{\partial t}+\frac{\partial}{\partial x}(\rho uA)=0, \quad (28)$$

$$\rho\frac{du}{dt}=-\frac{\partial p}{\partial x}, \quad (29)$$

$$R^3\left(\frac{1-\beta}{\beta}\right)=\frac{1-\beta_0}{\beta_0}=k_0^3 \quad (30)$$

and

$$\frac{p_b-p}{L^2}=R\frac{d^2R}{dt^2}+\frac{3}{2}\left(\frac{dR}{dt}\right)^2+\frac{S_0}{L^2R}+\frac{4}{L^2(\mathrm{Re})R}\frac{dR}{dt} \quad (31)$$

with

$$S_0=\frac{2S'}{p_0'R_0'},\quad \mathrm{Re}=\frac{H_0'\sqrt{p_0'/\rho_l'}}{\nu_l'}, \quad (32)$$

where β denotes the void fraction, S' is the surface tension at the liquid temperature T_0', ρ_l' is the liquid density at the liquid temperature T_0', ν_l' is the corresponding liquid kinematic viscosity, H_0' is the nozzle inlet height as shown in Fig. 1 and $L=R_0'/H_0'$ is the ratio of bubble to nozzle size. The normalized mixture pressure p, mixture density ρ, mixture flow speed u and nozzle area A entering the system of Eqs. (27)–(32) are defined by

$$p=\frac{p'}{p_0'},\quad \rho=\frac{\rho'}{\rho_l'}=1-\beta,\quad p_b=\frac{p_b'}{p_0'},\quad u=\frac{u'}{\sqrt{p_0'/\rho_l'}}\quad\text{and}$$
$$A=\frac{A'}{A_0'} \quad (33)$$

with A_0' denoting the inlet nozzle area. The nozzle axial coordinate and the time are normalized as

$$x=\frac{x'}{H_0'}\quad\text{and}\quad t=\frac{t'}{\Theta'}=\frac{t'\sqrt{p_0'/\rho_l'}}{H_0'}. \quad (34)$$

The normalized total derivative is $d/dt=\partial/\partial t+u\partial/\partial x$. The system of Eqs. (27)–(31) can now be supplemented by Eqs. (19) and (20), with the total derivative d/dt replacing the partial derivative $\partial/\partial t$ in Eq. (19), constitute a complete system for p, ρ, β, u, T, p_b, and R for a given normalized area $A(x)$ with appropriate initial and boundary conditions. The solution of such a problem is

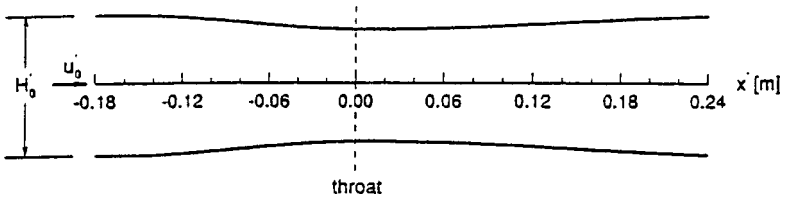

Fig. 1 Investigated nozzle geometry

difficult, even if Eqs. (19) and (20) are replaced by a polytropic law for the gas. Therefore, approximations leading to certain simplifications, especially of Eqs. (19) and (20), are needed. A major difficulty in the coupling of Eqs. (19) (with $\partial T/\partial t$ replaced by dT/dt) and (20) to the rest of the flow equations is the y-dependence of the term $(1/T)(dT/dt)$. However, a close examination shows that the term $(1/T)(dT/dt)$ is a slowly varying function of y for $0<y<1$ (except at violent collapse stages where the model is no longer valid) and can, therefore, be taken to be independent of y, as will be justified below. By applying the operator d/dt to Eq. (24) together with the assumption that $(1/T)(dT/dt)$ is independent of y, it can be shown that

$$p_g=\frac{f(yR)T}{R^3} \tag{35}$$

where $f(yR)$ is some function of the non-dimensional radial coordinate yR, normalized with respect to the equilibrium radius R_0'. This relation, in the uniform pressure approximation, suggests that T is a product of a function of x and t by a function of yR alone ($1/f(yR)$ in this case), showing consistency with the ideal gas law. Equation (35) also shows that the normalized gas density ρ_g is proportional to $f(yR)/R^3$. To proceed further, we need to determine the temperature dependence of the normalized thermal conductivity $\lambda_b(T)$. The thermal conductivity of a gas is proportional to the square root of the temperature according to the kinetic theory of gases (e.g., see Leighton [13]) so that the normalized thermal conductivity of the bubble can be taken as $\lambda_b=\sqrt{T}$. Utilizing this relation together with the assumption that $(1/T)(dT/dt)$ is independent of y, the energy Eq. (19) in cavitating nozzle flows assumes the form

$$\frac{\partial^2 T}{\partial y^2}-\frac{1}{2T}\left(\frac{\partial T}{\partial y}\right)^2+\left[\frac{2}{y}+\frac{y(c+d)}{T^{3/2}}\right]\frac{\partial T}{\partial y}-\frac{1}{T^{1/2}}[3(1+\gamma_b K_g)(c+d)-b]=0 \tag{36}$$

where b, c, and d are defined by

$$b(x,t)=\frac{(1+K_g)}{DR^{(3\gamma_b-2)}}\frac{d}{dt}[p_v R^{3\gamma_b}], \tag{37}$$

$$c(x,t)=\left.\frac{\partial T}{\partial y}\right|_{y=1}, \tag{38}$$

and

$$d(x,t)=\frac{(1-c_g)}{D}p_b R\frac{dR}{dt} \tag{39}$$

with K_g given by

$$K_g=\frac{(1-c_g)}{c_g}\frac{\mathfrak{R}_v'}{\mathfrak{R}_g'}. \tag{40}$$

The partial differential Eq. (36) does not contain the time derivative and depends on the time t and position x implicitly through the functions $b(x,t)$, $c(x,t)$ and $d(x,t)$. It can, therefore, be treated as an ordinary differential equation in y at any fixed x and t. Furthermore, the temperature field at any field point (x,t) should satisfy the boundary conditions

$$\left.\frac{\partial T}{\partial y}\right|_{y=0}=0 \tag{41}$$

and

$$T(y=1,x,t)=T_R(x,t)=1-\mathcal{L}\int_0^t\frac{R^2(x,\xi)(dR/d\xi)d\xi}{\left[\int_\xi^t R^4(x,\tau)d\tau\right]^{1/2}} \tag{42}$$

where we have used the normalized form of the Plesset-Zwick formula [12] for T_R. It is understood that the integration in Eq. (42) is carried out following bubble motion where $\mathcal{L}$ is defined by

$$\mathcal{L}=\left(\frac{L'}{T_0' c_{pl}'}\right)\left(\frac{\rho_v'}{\rho_l'}\right)\frac{R_0'}{(\pi\Theta'\alpha_l')^{1/2}}. \tag{43}$$

All properties entering Eq. (43) can be evaluated at the temperature T_0' since, for most cavitating flows, T_R' and T_0' differ, at most, by a few degrees.

We now introduce the transformation

$$Z=\sqrt{T} \tag{44}$$

so that the boundary value problem to be solved becomes

$$Z^2\frac{\partial^2 Z}{\partial y^2}+\left[\frac{2Z^2}{y}+\frac{y(c+d)}{Z}\right]\frac{\partial Z}{\partial y}-\frac{1}{2}[3(1+\gamma_b K_g)(c+d)-b]=0 \tag{45}$$

subject to

$$\left.\frac{\partial Z}{\partial y}\right|_{y=0}=0 \tag{46}$$

and

$$Z(y=1,x,t)=Z_0(x,t)=\left[1-\mathcal{L}\int_0^t\frac{R^2(x,\xi)(dR/d\xi)}{\left[\int_\xi^t R^4(x,\tau)d\tau\right]^{1/2}}d\xi\right]^{1/2} \tag{47}$$

where $b(x,t)$ and $d(x,t)$ are, respectively, given by Eqs. (37) and (39) and where $c(x,t)$ is now given by

$$c(x,t)=2\left[1-\mathcal{L}\int_0^t\frac{R^2(x,\xi)[dR/d\xi]d\xi}{\left[\int_\xi^t R^4(x,\tau)d\tau\right]^{1/2}}\right]^{1/2}\left.\frac{\partial Z}{\partial y}\right|_{y=1}. \tag{48}$$

Note that Eq. (45) contains the boundary value $\partial Z/\partial y|_{y=1}$ through c. We can now seek an analytical solution to Eq. (45) in the form

$$Z(y,x,t)=Z_0(x,t)+\sum_{k=1}^{\infty}a_k(b,c,d,Z_0)(y-1)^k \tag{49}$$

for $0<y<1$ where $Z_0(x,t)$ is given by Eq. (47) and the coefficients a_k are, in general, functions of b, c, d, and Z_0. It follows from Eq. (48) that

$$c=2Z_0a_1(b,c,d,Z_0). \tag{50}$$

Also the boundary condition (46) yields

$$\sum_{k=1}^{\infty}(-1)^k k a_k(b,c,d,Z_0)=0, \tag{51}$$

from which it follows that the relation to be solved for c is

$$c=2Z_0\sum_{k=2}^{\infty}(-1)^k k a_k(b,c,d,Z_0). \tag{52}$$

The solution of Eq. (52) for c requires, in principle, determining all of the coefficients a_k. Given these coefficients, Eq. (52) could be solved for c as a function of b, d, and Z_0 to yield

$$c(x,t)=\mathcal{F}[b(x,t),d(x,t),Z_0(x,t)] \tag{53}$$

so that Eq. (20) together with Eq. (53) replaces the previously employed polytropic law for the partial gas pressure (e.g., see Wang and Brennen [10] and Delale et al. [11]). In general, the solution of Eq. (52) for c is a difficult task; however, it is possible to simplify the dependence of Eq. (53) in some limiting cases of practical importance. For most cavitating flows, we have $|Z_0-1|\ll 1$ and D, given by Eq. (21), is much greater than unity ($D\gg 1$), as will be demonstrated in Section 4. In this limit, the dependence of c on both b and d in Eq. (53) can be suppressed ($b\to 0$ and $d\to 0$) since $D\gg 1$. Therefore, Eq. (53) reduces to

$$c=\mathcal{H}(Z_0) \tag{54}$$

with $\mathcal{H}(1)=0$. In such a case, we can approximate Eq. (54) by expanding $\mathcal{H}$ in the vicinity of $Z_0=1$ to linear order and then use the Plesset-Zwick formula, Eq. (47), for (Z_0-1) to arrive at

$$c(x,t)=-\kappa\mathcal{L}\int_0^t\frac{R^2(x,\xi)(dR/d\xi)d\xi}{\left[\int_\xi^t R^4(x,\tau)d\tau\right]^{1/2}} \tag{55}$$

where κ is defined by

$$\kappa=\frac{1}{2}\frac{\partial\mathcal{H}}{\partial Z_0}\bigg|_{Z_0=1}. \tag{56}$$

It can be shown that $\kappa\geqslant 0$ by the second law of thermodynamics. The exact value of κ is difficult to estimate. Here it will be treated as a parameter. The polytropic law employed previously for the partial gas pressure in this limit can now be replaced by the law

$$\frac{dp_b}{dt}+\left(\frac{3\gamma_b c_g}{R}\frac{dR}{dt}\right)p_b=\frac{3\gamma_b}{R^2}Dc \tag{57}$$

for the bubble pressure p_b where c is given by Eq. (55) and c_g is close to unity. It is worthwhile to mention that Eq. (57) reduces to that derived by Watanabe and Prosperetti [14] for a gas bubble ($c_g=1$). In this case c, defined by Eq. (38), cannot be evaluated by Eq. (55) since the boundary conditions (9) and (10) differ for a gas bubble and for a vapor-gas bubble, the difference arising from the presence of phase change in the latter case. For a vapor-gas bubble there is a discontinuity in the heat flux at the liquid/vapor-gas bubble interface, given by Eq. (10), in contrast to the case of a gas bubble where the heat flux at the interface is continuous. By assuming that the interfacial temperature gradients in both the liquid and bubble sides are of the same order of magnitude for a vapor-gas bubble, the heat transfer, in this case, can be thought to be dominated by the liquid side due to much higher thermal conductivity of the liquid. On the contrary, for a gas bubble ($m_v''=0$ and $c_g=1$), the interfacial condition (10) implies the continuity of the heat flux at the liquid-gas bubble interface, which shows that the temperature gradients at the bubble wall in the gas side are much higher than those in the liquid side due to higher thermal conductivity of the liquid. Consequently, the bubble wall temperature can, to a good approximation, be replaced by the cold liquid temperature for a gas bubble, an assumption used by Prosperetti [5] and verified by Prosperetti et al. [4] and by Kamath et al. [15]. It should, therefore, be expected that the near-isothermal solution of this work for a vapor-gas bubble and that of Prosperetti [5] for a gas bubble are also different. It should also be mentioned that Eq. (57) can be used more widely, except for the very last stages of the collapse periods of violent cavitating bubbles where the uniform pressure approximation breaks down (e.g., see Prosperetti et al. [4]). In such a case, one would require the full solutions of the thermal diffusion equation for the evaluation of c, Eq. (53), (in contrast to the limiting near-isothermal solution discussed above where c is approximated by Eq. (55)) together with the mass diffusion equations for the evaluation of the gas concentration c_g (in contrast to the low vapor concentration limit discussed above where c_g is close to unity). If simple models of c and c_g, that can be validated by comparison with the results of full numerical simulations of bubble motion (similar to those of Matsumoto and Takemura [8]) during the growth and collapse periods of vapor-gas bubbles, can be constructed, the application of Eq. (57) can then be largely extended. With these remarks in mind, here we limit the application of Eq. (57) to near-isothermal flow in the limit of low vapor concentration. Equations (55) and (57) together with Eqs. (27)–(31) can now be taken as model equations for quasi-one-dimensional cavitating nozzle flows with thermal damping.

4 Some Applications and Results

In this section we investigate the effects of thermal damping on some cavitating nozzle flow solutions by the model developed above. In particular, we consider the effect of thermal damping on the flashing flow instabilities encountered in the quasi-one-dimensional steady-state nozzle flow solutions obtained numerically by Wang and Brennen [10] (or by solving a third-order dynamical system of scaled variables for the flow speed as demonstrated by Delale et al. [11]); therefore, we restrict the Eqs. (27)–(31) to steady-state. As for the nozzle, we use the slender nozzle given in Fig. 1 (also employed by Delale et al.) with origin ($x=0$) at the throat and the inlet at $x=-l$. For the steady-state situation, Eq. (57), in the limit of low vapor concentration, integrates to

$$p_b(x)=\left[1+S_0+3\gamma_b D\int_{-l}^{x}\frac{[R(\xi)]^{(3\gamma_b-2)}}{u(\xi)}c(\xi)d\xi\right]\Big/\,[R(x)]^{3\gamma_b} \tag{58}$$

where c, given by Eq. (55), takes the form

$$c(x)=-\kappa\mathcal{L}\int_{-l}^{x}\frac{R^2(\xi)(dR/d\xi)d\xi}{\left\{\int_\xi^x[R^4(z)/u(z)]dz\right\}^{1/2}} \tag{59}$$

with $\kappa\geqslant 0$. Equations (58) and (59) can now be implemented into the steady-state solution of Delale et al. [11], replacing the polytropic law for the gas pressure. The resulting system form an integro-differential system for the initial value problem. The solution of this system is carried iteratively starting with initial values obtained from a nearby solution.

We consider a bubbly cavitating flow of water-vapor/air bubbles in water at 20°C, with a constant partial vapor pressure $p_v'=0.0234$ bar, a constant surface tension coefficient $S'=7.1\times 10^{-2}$ N/m and a constant water viscosity $\mu_l'=10^{-3}$ kg/m-s. The flow is through the converging-diverging nozzle shown in Fig. 1. The initial cavitation number σ_0, the initial void fraction β_0 and the initial flow speed u_0' are fixed at the values $\sigma_0=0.5$, $\beta_0=10^{-5}$ and $u_0'=10$ m/s, respectively. The initial radius R_0' is

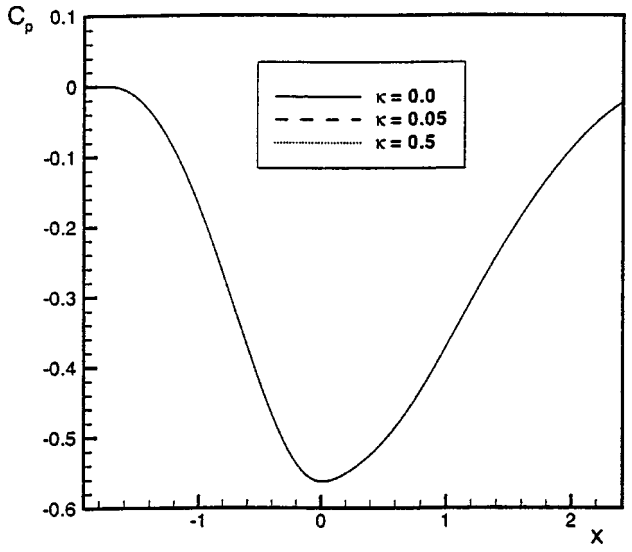

Fig. 2 Distributions of the pressure coefficient C_p without ($\kappa = 0.0$) and with thermal damping ($\kappa = 0.05$ and $\kappa = 0.5$) along the nozzle axis with initial void fraction $\beta_0 = 10^{-5}$, initial cavitation number $\sigma_0 = 0.5$, inlet flow speed $u_0' = 10$ m/s, and initial radius $R_0' = 10$ μm (corresponding to $D = 61{,}841$) for the steady-state solution of water vapor-air bubbles in water at 20°C (note that no difference can be seen between the pressure coefficients in the scale used in the figure)

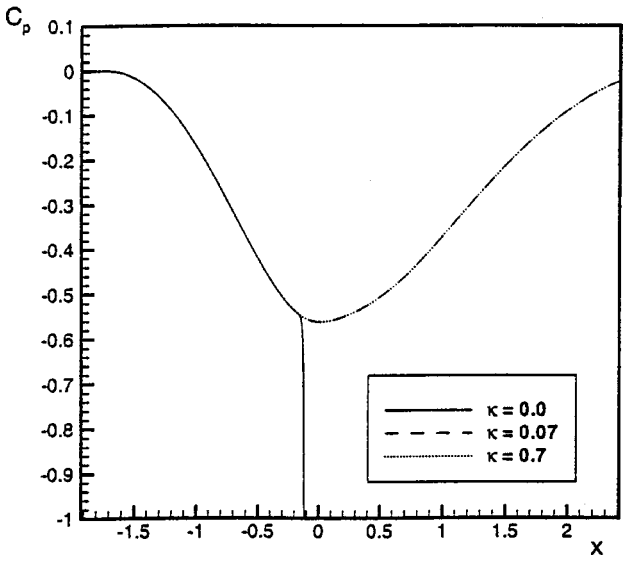

Fig. 4 Distributions of the pressure coefficient C_p without ($\kappa = 0.0$) and with thermal damping ($\kappa = 0.07$ and $\kappa = 0.7$) along the nozzle axis with initial void fraction $\beta_0 = 10^{-5}$, initial cavitation number $\sigma_0 = 0.5$, inlet flow speed $u_0' = 10$ m/s, and initial radius $R_0' = 20$ μm (corresponding to $D = 13{,}289$) for the steady-state solution of water vapor-air bubbles in water at 20°C

varied between 10 μm and 35 μm. When the partial gas pressure is approximated by the polytropic law leaving out the thermal damping effects on the flow field, it has already been demonstrated by Delale et al. [11] that, under the conditions stated above, stable steady-state cavitating nozzle flow solutions in the quasi-one-dimensional approximation are possible if the initial radius R_0' is below some critical value (for the conditions stated above, this critical value is 10.22 μm). When the initial radius exceeds this critical value, flashing flow instabilities, similar to those obtained by Wang and Brennen [10], are observed. Presently, we replace the polytropic law for the gas pressure by Eqs. (58) and (59) to include the damping effect of heat conduction through the bubble, that has already been demonstrated to be quite significant for oscillating gas bubbles (Nigmatulin et al. [2] and Prosperetti [5]).

Figures 2 and 3 show the thermal damping effect on the pressure coefficient C_p and on the normalized radius R for the case with initial radius $R_0' = 10$ μm. In this case a stable configuration is possible even with the polytropic law for the gas pressure. The value of the undetermined parameter κ is varied to quantify the relative effect of thermal damping. The pressure coefficient for this case seems to be unaffected by thermal damping whereas thermal damping seems to reduce the normalized maximum radius, the reduction being greater when the coefficient κ assumes higher values (e.g., for $\kappa = 0.5$). Figures 4 and 5 show how flash-

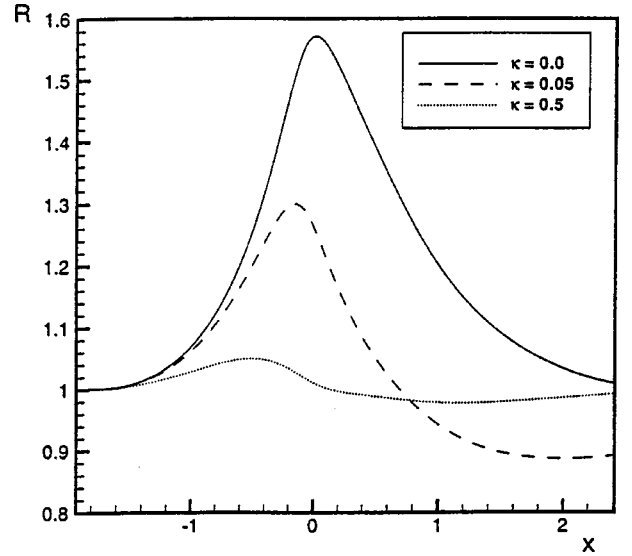

Fig. 3 Distributions of the normalized radius R without ($\kappa = 0.0$) and with thermal damping ($\kappa = 0.05$ and $\kappa = 0.5$) along the nozzle axis under conditions specified in Fig. 2

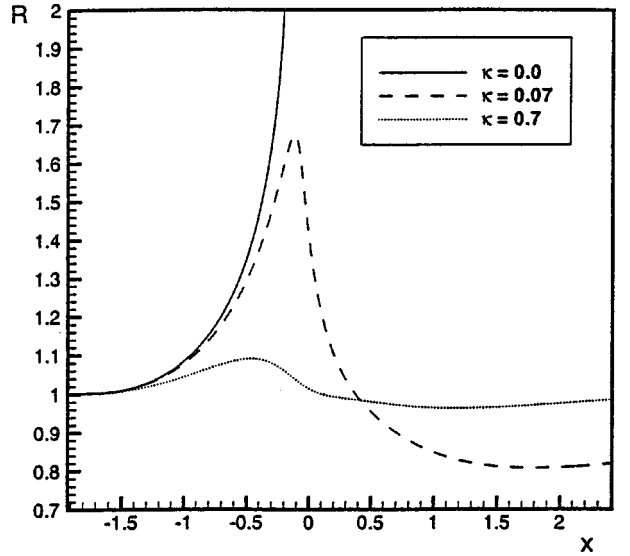

Fig. 5 Distributions of the normalized radius R without ($\kappa = 0.0$) and with thermal damping ($\kappa = 0.07$ and $\kappa = 0.7$) along the nozzle axis under conditions specified in Fig. 4

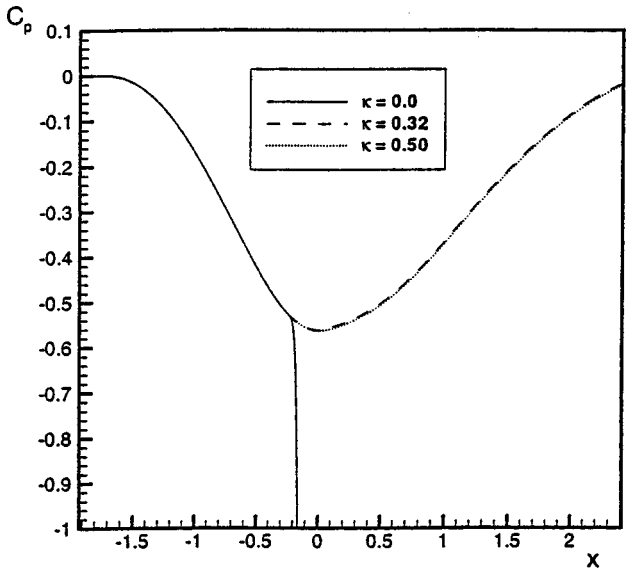

Fig. 6 Distributions of the pressure coefficient C_p without ($\kappa = 0.0$) and with thermal damping ($\kappa = 0.32$ and $\kappa = 0.5$), corresponding to bubbly shock solutions, along the nozzle axis with initial void fraction $\beta_0 = 10^{-5}$, initial cavitation number $\sigma_0 = 0.5$, inlet flow speed $u_0' = 10$ m/s and initial radius $R_0' = 33$ μm (corresponding to $D = 4458$) for the steady-state solution of water vapor-air bubbles in water at 20°C

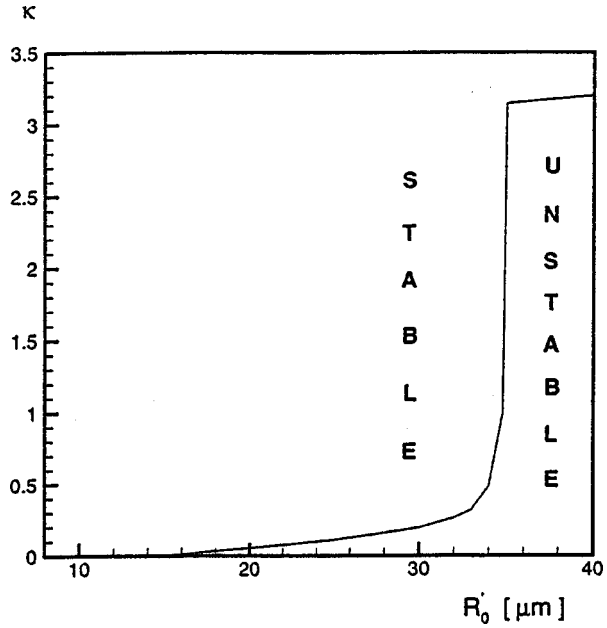

Fig. 8 Stability diagram of the parameter κ versus the initial radius R_0' under nozzle inlet conditions with initial void fraction $\beta_0 = 10^{-5}$, initial cavitation number $\sigma_0 = 0.5$ and inlet flow speed $u_0' = 10$ m/s for the steady-state solution of water vapor-air bubbles in water at 20^{0}C

ing flow instabilities obtained when $R_0' = 20$ μm with other nozzle inlet conditions held fixed, can be stabilized by the present thermal damping model. Figure 4 shows the stabilizing effect on the pressure coefficient C_p as the thermal damping parameter κ is increased from zero (corresponding to a flashing flow instability) to 0.7. Figure 5 demonstrates the effect on the normalized radius distribution along the nozzle axis. When the initial radius R_0' is increased even further (e.g., to a value of $R_0' = 33$ μm) with the same inlet conditions, the flashing flow instabilities become even stronger with much steeper gradients along the nozzle axis. In this case greater values of the thermal damping parameter κ are required to stabilize the flow. Figure 6 demonstrates the thermal damping effect on the pressure coefficient C_p, in a steady-state bubbly shock solution, as the parameter κ is increased from zero to 0.5. The increase in the pressure coefficient can be identified as an increase in the strength of the bubbly shock. The corresponding normalized bubble radius distribution $R(x)$ along the nozzle axis is plotted in Fig. 7. Finally, a stability diagram κ versus R_0', with the same inlet conditions, is shown in Fig. 8. The increase in the thermal damping coefficient towards a bubbly shock solution is observed as the initial radius R_0' is increased, corresponding to an intensified flashing flow instability resulting from the use of the polytropic law for the gas pressure. On the other hand, since κ is independent of the nozzle inlet conditions (see Eq. (56)), the same value of κ should be assumed for all stable steady-state solutions. Therefore, the unique value of κ that would yield stable steady-state solutions is needed. Preston et al. [16], under similar conditions, have recently demonstrated that bubbly shock solutions are unsteady. If this is so, the value of κ that leads to stable steady-state solutions can roughly be taken as that value beyond which flashing flow solutions can only be stabilized by the occurrence of bubbly shock waves (this corresponds to a rough estimate of $\kappa = 0.08 - 0.09$ in the stability diagram of Fig. 8). A better estimate of κ may be obtained from the stability analysis of steady-state solutions of cavitating nozzle flows from the unsteady equations of motion in the quasi-one-dimensional approximation.

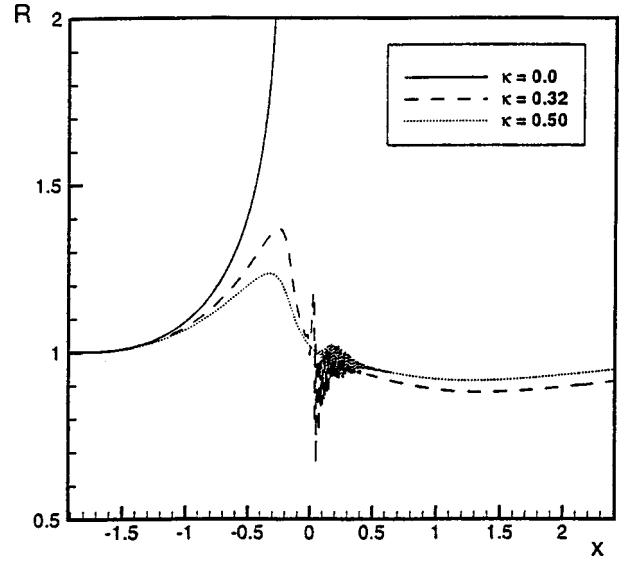

Fig. 7 Distributions of the normalized radius R without ($\kappa = 0.0$) and with thermal damping ($\kappa = 0.32$ and $\kappa = 0.5$), corresponding to bubbly shock solutions, along the nozzle axis under conditions specified in Fig. 6

5 Concluding Remarks

The effect of thermal damping on cavitating flows is investigated by consideration of the heat diffusion equations within the bubble and in the surrounding liquid. In the latter case, the Plesset-Zwick formula [12] in the thin boundary layer approximation is utilized. In particular an approximate expression for the total bubble pressure is derived in the uniform pressure approximation replacing the polytropic law. This expression is coupled to the quasi-one-dimensional steady-state cavitating nozzle flow equations. The effects of thermal damping in such flows are then

demonstrated for both stable and unstable solutions of Wang and Brennen [10] and of Delale et al. [11] using the polytropic gas law. The instabilities observed in quasi-steady nozzle flows are seen to be stabilized by the present thermal damping model with or without the occurrence of bubbly shock waves.

The present thermal damping model utilizes the near-isothermal and uniform bubble pressure approximations in the limit of low vapor concentration for stabilizing the flashing flow instabilities found in the study of steady-state cavitating nozzle flows during bubble growth. The application of the model to other phenomena with bubble dynamics, such as high-temperature boiling flows, requires reconsideration and further improvements on the assumptions made (uniform pressure distribution inside the bubble, the near-isothermal flow approximation, low vapor concentration, neglected inter-diffusion between the vapor and the gas).

Acknowledgments

This work is supported in part by the National Science Foundation under contract number CTS-9979258 at the California Institute of Technology, in part by the Scientific and Technical Research Council of Turkey (TÜBİTAK) and in part by the Turkish Academy of Sciences (TÜBA). The author is indebted to Dr. A. Preston, Prof. T. Colonius, and Prof. C. E. Brennen for numerous valuable comments and suggestions during his visit to Caltech in the summer of 2000. The author would also like to thank Prof. Y. Matsumoto for very valuable comments during the 4th International Cavitation Symposium in June 2001 at Caltech.

Nomenclature

A = cross-sectional area of the nozzle
C_p = pressure coefficient
D = dimensionless parameter defined by Eq. (21) characterizing the square of the penetration length to the equilibrium radius
H_0' = inlet height of nozzle
K_g = weighted ratio of vapor gas constant to noncondensable gas constant
L = ratio of bubble to nozzle size
L' = latent heat of vaporization
R = bubble radius
Re = Reynolds number
$\Re$ = gas constant
S_0 = normalized surface tension
T = temperature
Z = scaled dimensionless temperature
b = dimensionless function defined by Eq. (37)
c = dimensionless temperature gradient of the gas mixture at the bubble wall, defined by Eq. (38)
c_g = mass concentration of the gas in the vapor/gas bubble
c_{pl}' = the specific heat of the liquid
d = dimensionless function defined by Eq. (39)
l_p' = penetration length defined by Eq. (22)
m_v'' = vapor mass flux at the bubble wall
p = pressure
r' = dimensional radial coordinate
t = time
u = flow speed
w' = magnitude of radial velocity due to bubble dynamics
x = nozzle axial coordinate
y = dimensionless radial coordinate

Greek

Θ' = dimensional characteristic time scale
α_l' = thermal diffusivity of the liquid
β = void fraction
γ = isentropic exponent
κ = parameter defined by Eq. (56)
λ = thermal conductivity
ν_l' = kinematic viscosity of the liquid
ρ = density
σ_0 = inlet cavitation number

Subscripts

0 = equilibrium or nozzle inlet value
R = evaluated at the bubble wall
b = bubble
g = gas
l = liquid
v = vapor

Superscripts

$'$ = signifies dimensional quantity (otherwise dimensionless)
k = polytropic index

References

[1] Chapman, R. P., and Plesset, M. S., 1971, ''Thermal Effects in the Free Oscillation of Gas Bubbles,'' ASME J. Basic Eng., **93**, pp. 373–376.
[2] Nigmatulin, R. I., Khabeev, N. S., and Nagiev, F. B., 1981, ''Dynamics, Heat and Mass Transfer of Vapor-Gas Bubbles in a Liquid,'' Int. J. Heat Mass Transf., **24**, pp. 1033–1044.
[3] Miksis, M. J., and Ting, L., 1984, ''Nonlinear Radial Oscillations of a Gas Bubble Including Thermal Effects,'' J. Acoust. Soc. Am., **76**, pp. 897–905.
[4] Prosperetti, A., Crum, L. A., and Commander, K. W., 1988, ''Nonlinear bubble dynamics,'' J. Acoust. Soc. Am., **83**, pp. 502–514.
[5] Prosperetti, A., 1991, ''The Thermal Behavior of Oscillating Gas Bubbles,'' J. Fluid Mech., **222**, pp. 587–616.
[6] Brennen, C. E., 1995, *Cavitation and Bubble Dynamics*, Oxford University Press, Oxford, UK.
[7] Hao, Y., and Prosperetti, A., 1999, ''The Dynamics of Vapor Bubbles in Acoustic Pressure Fields,'' Phys. Fluids, **11**, pp. 2008–2019.
[8] Matsumoto, Y., and Takemura, F., 1994, ''Influence of Internal Phenomena on Gas Bubble Motion (Effects of Thermal Diffusion, Phase Change on the Gas-Liquid Interface and Mass Diffusion Between Vapor and Non-condensable Gas in the Collapsing Phase),'' JSME Int. J. B, **37**(2), pp. 288–296.
[9] Takemura, F., and Matsumoto, Y., 1994, ''Influence of Internal Phenomena on Gas Bubble Motion (Effects of Transport Phenomena and Mist Formation Inside the Bubble in the Expanding Phase),'' JSME Int. J. B, **37**(4), pp. 736–745.
[10] Wang, Y. C., and Brennen, C. E., 1998, ''One-Dimensional Bubbly Cavitating Flows Through a Converging-Diverging Nozzle,'' ASME J. Fluids Eng., **120**, pp. 166–170.
[11] Delale, C. F., Schnerr, G. H., and Sauer, J., 2001, ''Quasi-One-Dimensional Steady-State Cavitating Nozzle Flows,'' J. Fluid Mech., **427**, pp. 167–204.
[12] Plesset, M. S., and Zwick, S. A., 1952, ''A Nonsteady Heat Diffusion Problem With Spherical Symmetry,'' J. Appl. Phys., **23**, pp. 95–98.
[13] Leighton, T. G., 1994, *The Acoustic Bubble*, Academic Press, San Diego, CA.
[14] Watanabe, M., and Prosperetti, A., 1994, ''Shock Waves in Dilute Bubbly Liquids,'' J. Fluid Mech., **274**, pp. 349–381.
[15] Kamath, V., Prosperetti, A., and Egolfopoulos, F. N., 1993, ''A Theoretical Study of Sonoluminescence,'' J. Acoust. Soc. Am., **94**, pp. 248–260.
[16] Preston, A. T., Colonius, T., and Brennen, C. E., 2002, ''A Numerical Investigation of Unsteady Bubbly Cavitating Nozzle Flows,'' Phys. Fluids, **14**, pp. 300–311.

Mach Number Influence on Reduced-Order Models of Inviscid Potential Flows in Turbomachinery

Bogdan I. Epureanu[1]
Department of Mechanical Engineering,
University of Michigan,
Ann Arbor, MI 48109-2125
e-mail: epureanu@umich.edu

Earl H. Dowell
e-mail: dowell@ee.duke.edu

Kenneth C. Hall
e-mail: Kenneth.C.Hall@duke.edu

Department of Mechanical Engineering
and Materials Science,
Center for Nonlinear and Complex Systems,
Duke University,
Durham, NC 27708

An unsteady inviscid flow through a cascade of oscillating airfoils is investigated. An inviscid nonlinear subsonic and transonic model is used to compute the steady flow solution. Then a small amplitude motion of the airfoils about their steady flow configuration is considered. The unsteady flow is linearized about the nonlinear steady response based on the observation that in many practical cases the unsteadiness in the flow has a substantially smaller magnitude than the steady component. Several reduced-order modal models are constructed in the frequency domain using the proper orthogonal decomposition technique. The dependency of the required number of aerodynamic modes in a reduced-order model on the far-field upstream Mach number is investigated. It is shown that the transonic reduced-order models require a larger number of modes than the subsonic models for a similar geometry, range of reduced frequencies and interblade phase angles. The increased number of modes may be due to the increased Mach number per se, or the presence of the strong spatial gradients in the region of the shock. These two possible causes are investigated. Also, the geometry of the cascade is shown to influence strongly the shape of the aerodynamic modes, but only weakly the required dimension of the reduced-order models. [DOI: 10.1115/1.1511165]

1 Introduction

Time histories and frequency domain responses of extremely large dimensional aerodynamic systems, with up to 10^4-10^6 degrees-of-freedom may be computed due to the recent advances in computer technology. However, the computation time required to solve such systems becomes prohibitive especially when numerous parametric analyses are required. Moreover, such computation of fluid dynamics (CFD) codes are practically impossible to use in control applications, because most control schemes are designed for relatively small systems, with less than 100 degrees-of-freedom. Therefore, the direct applicability of the most common control strategies to standard CFD models is significantly limited. Fortunately, many control strategies are robust with respect to model uncertainties and thus may be successful although they are designed and tested using approximate models. These observations lead to the conclusion that reduced-order models, which have a much smaller number of degrees-of-freedom, are desired. Generally a reduced-order model is a simplified model which has a much smaller number of degrees-of-freedom than the original model, but, nevertheless, captures the dynamics of the original model with acceptable accuracy. The tradeoff between accuracy and complexity is determined by each particular application.

Early attempts to construct reduced-order models for fluid dynamic analysis and design used physical insights to reduce the complexity of the model ([1–3]). Although useful, these techniques are usually applicable to a rather limited range of parameter variations, such as small values of the reduced frequency, and small static and dynamic loads. To overcome this limitation, more recent analyses have used more systematically derived reduced-order models. Among these techniques are Padé approximants of the unsteady aerodynamic transfer functions ([4–6]), eigenmode summation techniques in either time or frequency domains ([7,8]), and proper orthogonal decomposition also known as Karhunen-Loève method ([9–13]). Another interesting paper which discusses the proper orthogonal decomposition method and an alternative approach based upon Arnoldi vectors was recently presented also ([14]). Reduced-order models of flows over isolated airfoils have been developed in the time domain. Recently, however, the frequency domain has been more extensively analyzed for both unsteady analyses and reduced-order model construction. The inviscid full potential equation and the eigenmode summation technique in the frequency domain have been used to construct reduced-order models for flows in turbomachinery cascades.

A reduced-order model has by definition a smaller number of degrees-of-freedom than the original CFD model and is typically several orders of magnitude smaller. Ideally, the reduced-order modeling provides accuracy comparable to the original CFD model, but at much less computational cost when used in an aeroelastic analysis. The tradeoff between accuracy and complexity of the model is dependent on the particular application, of course. Nevertheless, using reduced-order modeling in preliminary design and optimization analyses is very promising especially when active control of an aeroelastic system is concerned because most current control strategies require relatively small system models, with 100 degrees-of-freedom or less.

In this paper we apply the proper orthogonal decomposition technique in the frequency domain and construct reduced-order models of unsteady flows in a turbomachinery cascade. The proper orthogonal decomposition is a technique that allows one to obtain good approximations of the spatial modes of vibration and the dynamics of a system using the response of the system to various excitations. The proper orthogonal decomposition technique was first used by experimentalists to analyze test data, and it has recently been applied to a wider variety of problems, such as wind loads calculations and coherent structure identification in turbulent flows. The main assumption made in the proper orthogonal decomposition technique is that the dynamics of large systems

[1]To whom correspondence should be addressed.

Contributed by the Fluids Engineering Division for publication in the JOURNAL OF FLUIDS ENGINEERING. Manuscript received by the Fluids Engineering Division September 20, 2001; revised manuscript received March 12, 2002. Associate Editor: T. B. Gatski.

is in fact low dimensional, i.e., the inertial manifold of the dynamics is low dimensional. For a large category of problems, this assumption holds because in many cases most of the energy of the system being analyzed is contained in the dynamics of a few modes.

In this paper we investigate the problem of a forced excited flow. An inviscid nonlinear model of subsonic and transonic flows in a cascade of turbomachinery airfoils is used to compute the steady flow. Then, a small amplitude motion of the airfoils about their steady flow configuration is considered. The unsteady flow is linearized about the nonlinear steady response based on the observation that in many cases the unsteadiness in the flow has a substantially smaller magnitude than the steady component. Next, a frequency domain model is constructed and validated by showing that it provides similar results when compared to previous computational data presented in the literature. A cascade of airfoils based upon a slightly modified generic compressor cascade geometry established as benchmark test case configuration at the Sixth International Symposium on Unsteady Aerodynamics and Aeroelasticity of Turbomachines is numerically investigated for several cases, i.e., subsonic cases where the upwind far-field Mach number is 0.50, 0.55, and 0.70, and a transonic case where the Mach number is 0.80.

For the subsonic case, three reduced-order models are constructed in the frequency domain using the proper orthogonal decomposition technique. A reduced-order model with only 10 degrees-of-freedom is shown to predict accurately the unsteady response over a wide range of reduced frequencies when compared to a full model with approximately 5000 degrees-of-freedom. Similarly, a second reduced-order model with only 10 degrees-of-freedom is shown to predict accurately the unsteady response over a full spectrum of interblade phase angles and a fixed reduced frequency. Finally, a third-model model with 35 degrees-of-freedom is shown to model accurately the flow dynamics over a full spectrum of interblade phase angles and a wide range of reduced frequencies. These results are obtained for upwind far-field Mach numbers of 0.50, 0.55, 0.70.

For the transonic case, three reduced-order model are constructed in the frequency domain using the proper orthogonal decomposition technique also. A reduced-order model with only 15 degrees-of-freedom is shown to model accurately the unsteady response over a wide range of reduced frequencies when compared to a full model with approximately 17,500 degrees-of-freedom. Similarly, a second reduced-order model with 15 degrees-of-freedom also, is shown to predict accurately the unsteady response over a full spectrum of interblade phase angles and a fixed reduced frequency. Finally, a third-model model with 50 degrees-of-freedom is shown to model accurately the flow dynamics over a full spectrum of interblade phase angles and a wide range of reduced frequencies. These results are obtained for an upwind far-field Mach number of 0.80.

Finally, the dependency of the required number of aerodynamic modes in a reduced-order model on some of the most significant parameters of the system is investigated. Specifically the far-field upstream Mach number and geometrical parameters such as the solidity and airfoil profile are considered. It has been observed that the transonic reduced-order models require a larger number of modes than the subsonic reduced-order models for a similar geometry, range of reduced frequencies and interblade phase angles. The increased number of modes may be due to the increased Mach number per se, or the presence of the strong spatial gradients in the region of the shock. These two possible causes are investigated. Also, the geometry of the cascade is shown to influence strongly the shape of the proper orthogonal decomposition modes, but only weakly the required dimension of the reduced-order model.

2 Unsteady Flow Model

The flow model used is based on a variational formulation of the full potential equation. The nonlinear full potential equations is linearized about the steady nonuniform flow and a small perturbation model is obtained. Distinct from classical linearized potential models, the full potential equation is not linearized about a uniform steady state. Rather, the *nonlinear* steady state is computed first and then the linearization is done around the steady solution. The full potential equation for an isentropic, irrotational flow ([15]) may be expressed as

$$\nabla^2\phi=\frac{1}{c^2}\left[\frac{\partial^2\phi}{\partial t^2}+2\nabla\phi\cdot\nabla\frac{\partial\phi}{\partial t}+\frac{1}{2}\nabla\phi\cdot\nabla(\nabla\phi)^2\right], \tag{1}$$

where c is the local speed of sound given by

$$c^2=c_T^2-(\gamma-1)\left[\frac{\partial\phi}{\partial t}+\frac{1}{2}(\nabla\phi)^2\right], \tag{2}$$

with c_T denoting the stagnation or total speed of sound. Using Bernoulli's equation, one may obtain also the expression of the flow density as a function of the potential and its derivatives. Also, one may compute the expression of the density as a function of stagnation quantities, i.e., the density and pressure at a point in the flow field where $\nabla\phi$ and $\partial\phi/\partial t$ are both zero. From the isentropic relation one may obtain the expression of the local pressure as a function of the potential.

The steady flow is solved first. Then the unsteady flow is computed based on the small disturbance assumption. Making this assumption, one considers the unsteady component of the flow to be much smaller than the steady component. The potential ϕ may, therefore, be decomposed into a large steady component Φ and a much smaller unsteady component $\tilde{\phi}$. The potential may then be expressed as $\phi(t)=\Phi+\tilde{\phi}(t)$, where t is the time, $\tilde{\phi}\ll\Phi$, and all three variables ϕ, Φ, and $\tilde{\phi}$ depend on the spatial location in the flow.

One assumes also that the unsteadiness in the flow is also harmonically varying in time. This analysis is a natural choice generated by the small perturbation assumption. A scale analysis of the differential equations that govern the flow motion quickly shows that the unsteadiness in the flow is governed by a differential equation that is linear in time and has constant coefficients in time. Nevertheless, these coefficients depend on the steady solution and, therefore, on the spatial location. Since the unsteadiness in the flow is, to first order, governed by a linear constant coefficient differential equation in time, the unsteadiness may be decomposed into a Fourier series. The unsteady response is the sum of the responses computed for each excitation frequency separately. In the turbomachinery problem investigated, the unsteadiness in the flow is due to the pitch motion of the airfoils of the cascade. The motion of the airfoils is the excitation.

The unsteady small magnitude potential $\tilde{\phi}$ is, therefore, analyzed in the frequency domain. The potential $\tilde{\phi}$ is assumed to vary periodically in time, i.e.,

$$\tilde{\phi}(t)=\sum_{\omega}\ \varphi(\omega)e^{j\omega t}, \tag{3}$$

where j is the imaginary unit $\sqrt{-1}$, ω are the frequencies of the excitation, and φ is the response of the unsteady flow at frequency ω. The variable φ is a Fourier coefficient and, in general, it is complex. However, from the theory of linear differential equations, one may readily conclude that the real part of φ is the response that is in phase with the corresponding excitation. Similarly, the imaginary part of φ is the out-of-phase component of the response.

The motion of the airfoils is modeled by a moving physical domain, and a fixed computational domain. The physical domain of the flow varies in time. However, the computation domain may be considered constant by using an unsteady coordinate transformation. The coordinate transformation defines the physical domain at each instant in time as a function of the computational domain and the imposed motion of the airfoils. The unsteady co-

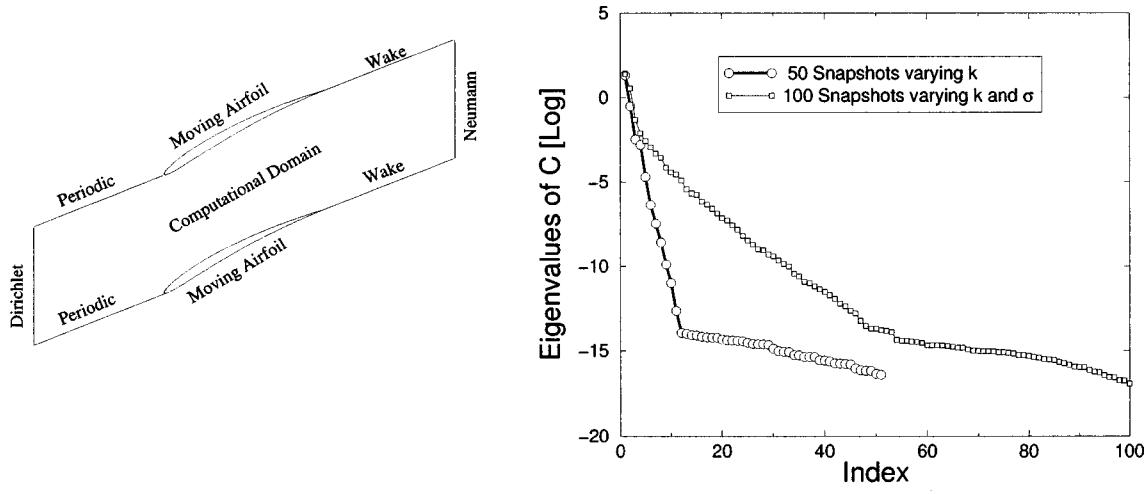

Fig. 1 Left: Cascade geometry and computational domain of the flow. Right: Eigenvalues of the correlation matrix computed using 50 snapshots obtained varying *k* only; and 10×10 snapshots obtained varying both *k* and σ.

ordinate transformation eliminates the need to extrapolate the potential to apply the airfoil boundary conditions or to compute the unsteady pressure.

There are five types of flow boundary conditions that apply to the computational domain ([16]). As shown in Fig. 1, at the inlet, periodic boundary conditions are used in the circumferential direction. The Kutta condition is implemented and the wake is considered an impermeable surface while the continuity of pressure is enforced along this boundary. On the airfoil surfaces, the no-penetration condition is enforced. The far-field boundary conditions are of two types: Dirichlet and Neumann. The Dirichlet boundary condition enforces given values to the potential at the vertical upstream computational boundary. The values of the potential in the upstream far-field are computed so that they correspond to a given vertical flow velocity. The Neumann boundary conditions enforce a certain flux of fluid to exit the computation domain.

There are five types of boundary conditions for the linearized unsteady flow also. They are periodic, wake, upstream far-field, downstream far-field, and airfoil surface boundary conditions. Similar to the steady case, the unsteady wake is also considered an impermeable surface. The continuity of unsteady pressure is enforced along this boundary. On the airfoil surfaces, the unsteady no-penetration condition is enforced. The far-field boundary conditions are exact nonreflecting boundary conditions ([17]) for the linearized unsteady problem. They are based on an eigenanalysis of the wave propagation in the far-field. The eigenanalysis identifies which waves propagate/grow towards the inside of the domain and which propagate/grow towards the outside. The waves that propagate towards the inside of the domain are eliminated to ensure the nonreflectivity of the boundaries. The boundary conditions are, therefore, numerically exactly nonreflective. Their description is dependent on the discretization.

3 Model Reduction Technique

The model reduction technique used is proper orthogonal decomposition. Very well suited for linear systems, the proper orthogonal decomposition is also applicable to nonlinear systems. The applicability of the proper orthogonal decomposition method is limited because the modes (also referred to as coherent structures) strongly exchange energy and therefore the required number of modes that may capture most of the energy of the dynamics increases rapidly. This phenomenon occurs because the dynamics of the system is not low dimensional ([18]). Typical cases of systems where the simple proper orthogonal decomposition technique is not successful are the systems that exhibit spatio-temporal chaos. However, in such situations, the proper orthogonal decomposition may also be used in a local fashion ([19–21]).

In the context of aeroelasticity, the proper orthogonal decomposition method was first introduced in the time domain ([13]), and the frequency domain ([12,22]). In this paper, we used the ''snapshot'' POD method. In this approach the response of the linearized system with L degrees-of-freedom is obtained and stored in a solution vector $\mathbf{\Phi}_i$, for a set of N excitation frequencies ω_i. Please note that $\mathbf{\Phi}_i$, does not refer to the steady potential Φ. Rather, $\mathbf{\Phi}_i$ is a vector containing the unsteady solution φ at all computational nodes. Each solution vector $\mathbf{\Phi}_i$ has L complex entries and, therefore, contains both the phase and the magnitude of the response. A matrix $\mathbf{R}$ of size $L\times N$ is formed such that its ith column is the solution vector $\mathbf{\Phi}_i$ for each $i\leqslant N$. A correlation matrix is then assembled of the form $\mathbf{C}=\mathbf{R}^*\mathbf{R}$, where the superscript $*$ indicate the Hermitian operator.

The eigenvalues of the correlation matrix are then obtained by solving an eigenvalue problem of dimension $N\times N$, i.e., $\mathbf{C}\mathbf{v}_i=\lambda_i\mathbf{v}_i$, where i varies between 1 and N, λ_i is an eigenvalue of the correlation matrix, and $\mathbf{v}_i$ has dimension N. Among the N eigenvalues obtained, the most significant eigenmodes contain most of the energy of the fluid motion and correspond to the largest eigenvalues. One organizes the eigenvectors $\mathbf{v}_i$ and eigenvalues λ_i in descending order, from most important to least important, i.e., largest to smallest eigenvalue.

The most significant n eigenvectors ([22]) are then organized in a matrix $\mathbf{V}$ of size $N\times n$ such that the ith column of $\mathbf{V}$ is the vector $\mathbf{v}_i$, with $i=1,\ldots,n$. The equations of motion and the state space vector are then projected onto the space spanned by these vectors and a reduced-order model is obtained. Formally one may express the equations of motion as

$$\omega^2\mathbf{A}_2\mathbf{\Phi}+\omega\mathbf{A}_1\mathbf{\Phi}+\mathbf{A}_0\mathbf{\Phi}=\mathbf{b}, \tag{4}$$

where $\mathbf{b}$ is the inhomogeneous forcing vector arising from the motion of the airfoil and $\mathbf{\Phi}$ is a vector containing the unsteady solution φ at all computational nodes. The component of the solution $\mathbf{\Phi}$ in the subspace $\mathbf{S}$, is denoted $\mathbf{\Phi}_S$. Then, $\mathbf{\Phi}$ is approximated by $\mathbf{\Phi}_A$ which may be expressed as

$$\mathbf{\Phi}\approx\mathbf{\Phi}_A=\mathbf{P}\mathbf{\Phi}_S. \tag{5}$$

Multiplying Eq. (4) to the left by the Hermitian of the matrix $\mathbf{P}=\mathbf{R}\mathbf{V}$ (which is normalized so that $\Sigma_j P_{ij}^2=1$), and considering

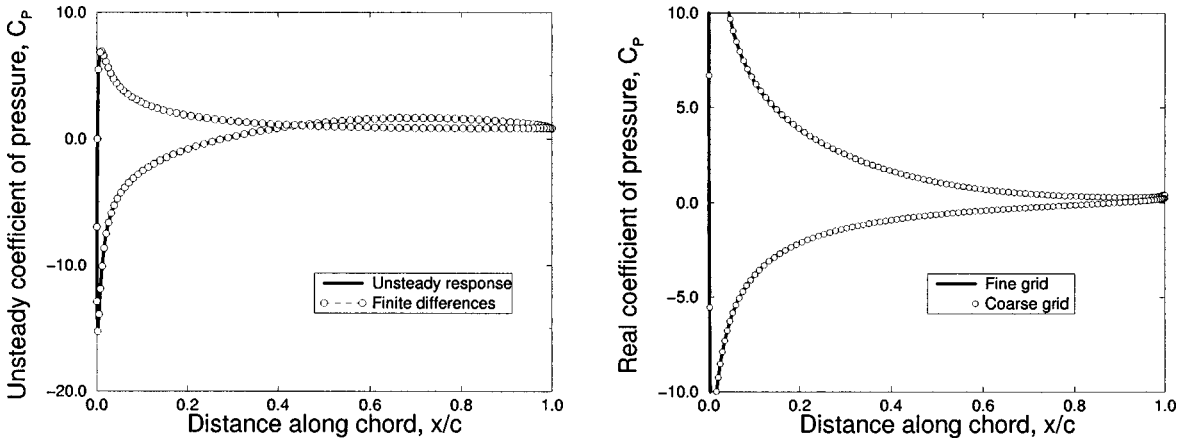

Fig. 2 Unsteady coefficient of pressure C_P for a pitching motion about the mid-chord. Left: zero frequency and zero interblade phase angle. Right: real (in-phase) part of C_P at reduced frequency k of 0.5 and interblade phase angle σ of 90 deg.

only the solutions contained in the subspace **S** spanned by the columns of **P**, one obtains a reduced order system of size n, i.e.,

$$\omega^2 \mathbf{P}^* \mathbf{A}_2 \mathbf{P} \mathbf{\Phi}_S + \omega \mathbf{P}^* \mathbf{A}_1 \mathbf{P} \mathbf{\Phi}_S + \mathbf{P}^* \mathbf{A}_0 \mathbf{P} \mathbf{\Phi}_S = \mathbf{P}^* \mathbf{b}. \tag{6}$$

Equation (6) represents the reduced-order model and it is solved for the n unknowns $\mathbf{\Phi}_S$. The Mach number appears in the matrices $\mathbf{A}_{0,1,2}$ whereas σ appears explicitly in the right-hand side vector **b**. The unknowns $\mathbf{\Phi}_S$ are expanded back into the original physical space using Eq. (5). An important feature of the proper orthogonal decomposition technique is that the eigenvalues of the reduced-order model in Eq. (6) are good approximations to the eigenvalues of the full system. A more detailed mathematical treatment of the proper orthogonal decomposition method in the time and frequency domains may be found in [22–24].

4 Numerical Results

In this section, numerical results are presented. The flow through the Tenth Standard Configuration is investigated. This is a generic compressor cascade geometry established as the benchmark test case configuration at the Sixth International Symposium on Unsteady Aerodynamics and Aeroelasticity of Turbomachines. The airfoil geometry used in the Tenth Standard Configuration is the NACA-5506 configuration ([25]). In addition, the stagger angle is 45 deg, the inflow angle Θ is 55 deg, the solidity is 1, the inflow Mach number is 0.70, and the Reynolds number based on chord and upstream total flow velocity is 10^5. In our investigations we analyze an inviscid flow at various Mach numbers.

4.1 Subsonic Model Validation. The coefficient of lift for an isolated flat plate in inviscid flow may be shown to be 2π. To compare our code with this analytic result, we computed the flow in a two-dimensional cascade of NACA-5506 airfoils, same as the Tenth Standard Configuration, but with a solidity of 5. First, we computed the steady flow for an upstream far-field Mach number of 0.1, and zero inflow and stagger angles. We then calculated the unsteady flow for a pitching motion about the mid-chord point of the airfoils at zero frequency. We obtained a coefficient of lift C_L of $1.003\times 2\pi$. This value of the coefficient of lift obtained with our code is within 0.3% margin of the value 2π. In the following we perform more precise self-consistency tests, and compare our code with other computational data presented in the literature.

First, we investigate the self-consistency of the linearization. Shown in Fig. 2 is the coefficient of pressure obtained for an upstream far-field Mach number of 0.50. A special unsteady solution is compared to a solution obtained by finite differences. To obtain the finite difference solution, we first computed the steady response for two stagger angles of values 44.99 deg and 45.01 deg, while the inflow angle and the solidity were maintained constant. Then, the two steady solutions were subtracted and divided by 0.02 deg. The result is an approximation for the unsteady response of the model in the limit of zero frequency. To obtain the special unsteady solution, we first saved the changes in the grid node location between the two steady solutions computed. These changes were loaded into the unsteady code as prescribed grid motion and unique source of unsteadiness. Finally, the unsteady code was used to obtain the special unsteady solution. A very good agreement between the unsteady solution and the finite difference solution is observed in Fig. 2. The coefficient of pressure C_P plotted in Fig. 2 is defined by $C_P=(p-p_\infty)/(0.5\rho v_\infty^2)$, where v_∞ is the total velocity upstream in the far-field.

Next, we investigate the sensitivity of the solution to grid refinement. First, we investigate the steady calculations. Shown in Fig. 3 is the steady coefficient of pressure when the upstream far-field Mach number is 0.50. A very good agreement between the solutions obtained on the fine and the coarse grid is observed. The coarse grid is composed of 150×30 grid nodes, while the fine grid contains 300×50 grid nodes.

Next, we investigate the grid sensitivity of the unsteady calculations. Shown in Fig. 2 is the real part of the coefficient of pressure computed for a pitching motion of the airfoils about their mid-chord point. The interblade phase angle σ is 90 deg and the reduced frequency $k=\omega b/v_\infty$ is 0.5, where b is the semi-chord and v_∞ is the total velocity upstream in the far-field. Similar to the steady calculations presented above, the coarse grid is composed of 150×30 grid nodes, while the fine grid contains 300×50 grid nodes. A very good agreement between the results obtained with the coarse and the fine grid is observed, indicating the insensitivity of the unsteady results with respect to grid refinement.

Next, we compare our results with the results obtained using a very similar computer code presented by Hall [16]. Shown in Fig. 3 is the steady coefficient of pressure for an upstream far-field Mach number of 0.50. A very good agreement between the results obtained with the two codes is observed. Comparisons with other models and experimental data along with a more detailed discussion of the strengths and weaknesses of the small perturbation potential model are given in [16].

Finally, we compare our unsteady results with the results presented by Hall [16]. Shown in Fig. 3 is the real part of the unsteady coefficient of pressure for a pitching motion of the airfoils about their mid-chord at a reduced frequency k of 0.5 and an interblade phase angle σ of 90 deg. A very good agreement between the results obtained with the two codes is observed. A similar agreement may be observed for the imaginary part of the unsteady coefficient of pressure, which was not shown here.

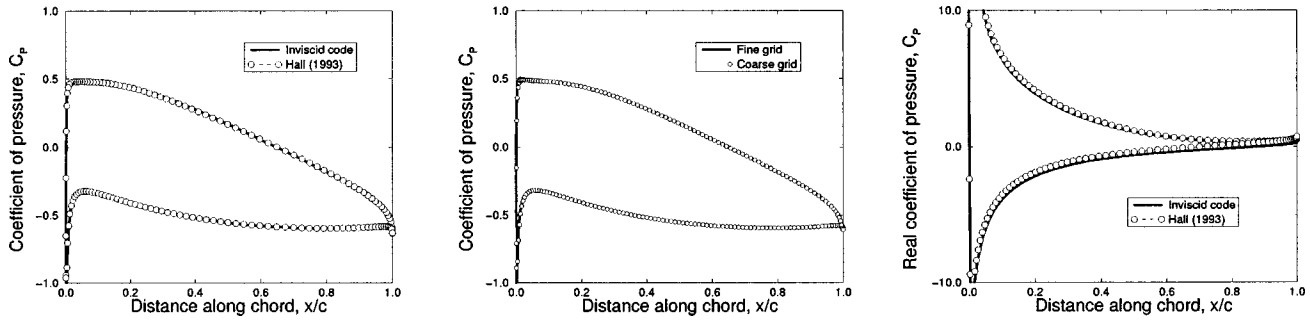

Fig. 3 Coefficient of pressure C_P for an upstream far-field Mach number of 0.50. Left: comparison of steady flows. Center: comparison of steady flows obtained using a fine and a coarse grid. Right: real (in-phase) part of the unsteady flow at reduced frequency k of 0.5.

4.2 Transonic Model Validation. A typical two-dimensional cascade of NACA-5506 airfoils is investigated. The solidity of the cascade is 1, the stagger angle is 45 deg, the upstream far-field Mach number is 0.80, and the inflow angle Θ is 55 deg. For the unsteady calculations, a pitching motion of the airfoils about the mid-chord point is assumed.

First, we perform a self-consistency test of the linearization. Shown in Fig. 4 is the coefficient of pressure obtained for an upstream far-field Mach number of 0.80. A special unsteady solution is compared to a solution obtained by finite differences using a similar technique as done for the subsonic case. To obtain the finite difference solution, we first computed the steady response for two stagger angles of values 44.99 deg and 45.01 deg, while the inflow angle and the solidity were maintained constant. Then, we used the two steady solutions to compute an approximate unsteady response of the model at zero frequency. To obtain the special unsteady solution, we first computed the changes in the grid node location for the two steady solutions. These changes were loaded into the unsteady code as prescribed grid motion and unique source of unsteadiness. Finally, the unsteady code was used to obtain the special unsteady solution. A very good agreement between the unsteady solution and the finite difference solution is observed in Fig. 4.

Next, we investigate the sensitivity of the transonic solution to grid refinement. The steady solution is first considered. Shown in Fig. 4 are the coefficients of pressure obtained using a coarse and a fine grid. The coarse grid has 200×40 nodes, while the fine grid is composed of 300×50 modes. A good agreement between the two solutions is observed, demonstrating the insensitivity of the steady transonic solution to grid refinement.

Next, we investigate the sensitivity of the unsteady transonic solution to grid refinement. Shown in Fig. 4 is the real part of the coefficient of pressure computed for a pitching motion of the airfoils about their mid-chord point. The interblade phase angle σ is 90 deg and the reduced frequency k is 0.5. Similar to the steady calculation presented above, the coarse grid is composed of 200×40 grid nodes, while the fine grid contains 300×50 grid nodes. A good agreement between the results obtained with the coarse and the fine grid is observed.

4.3 Subsonic Reduced-Order Modeling. A typical two-dimensional cascade of NACA-5506 airfoils is investigated. The solidity of the cascade is 1, the stagger angle is 45 deg, the upstream far-field Mach number is 0.50, and the inflow angle Θ is 55 deg. For the unsteady calculations, a pitching motion of the airfoils about the mid-chord point is assumed. The flow is discretized using a grid with 150×30 nodes.

Four reduced-order models have been constructed. The first model was obtained using a proper orthogonal decomposition technique applied to a set of 36 snapshots obtained varying the interblade phase angle σ between -180 deg and 180 deg while the reduced frequency k was maintained constant of value 0.5. This model has 10 degrees-of-freedom. The second model was constructed using a proper orthogonal decomposition technique applied to a set of 51 snapshots obtained varying the reduced frequency k between 0.0 and 2.0 while the interblade phase angle σ was maintained constant of value 90 deg. This model has 10 degrees-of-freedom. The third and the fourth models have 35 and 25 degrees of freedom, respectively. These models were constructed using 11×18 snapshots obtained varying σ between -180 deg and 180 deg and k between 0.0 and 2.0.

First, we investigate the performance of the reduced-order models for various interblade phase angles. Shown in Fig. 5 are the results obtained for a pitching motion of the airfoils with reduced frequency k of 0.5. The reduced-order models with 10 and 35 degrees-of-freedom, are shown to model accurately the response

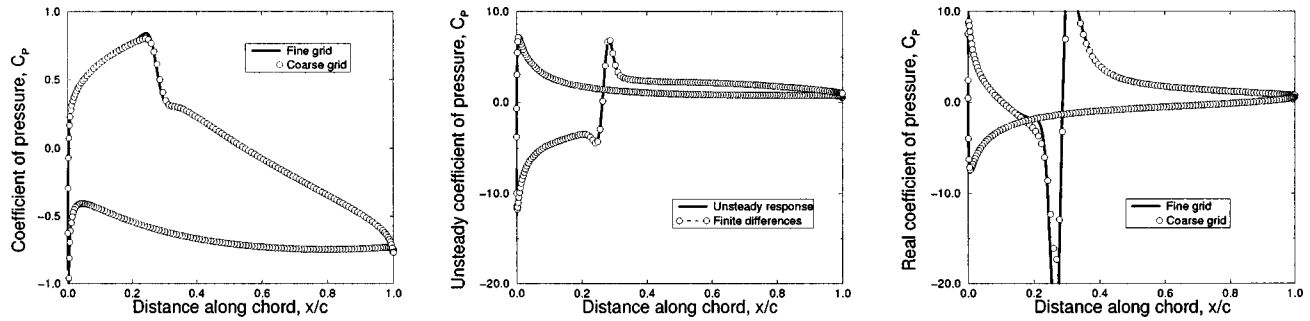

Fig. 4 Coefficient of pressure C_P for an upstream far-field Mach number of 0.80. Left: steady flow computed on a fine and a coarse grid. Center: unsteady flow for a pitching motion about the mid-chord at zero frequency and zero interblade phase angle. Right: real (in-phase) part of the unsteady flow for a pitching motion about the mid-chord at reduced frequency k of 0.5 and interblade phase angle σ of 90 deg.

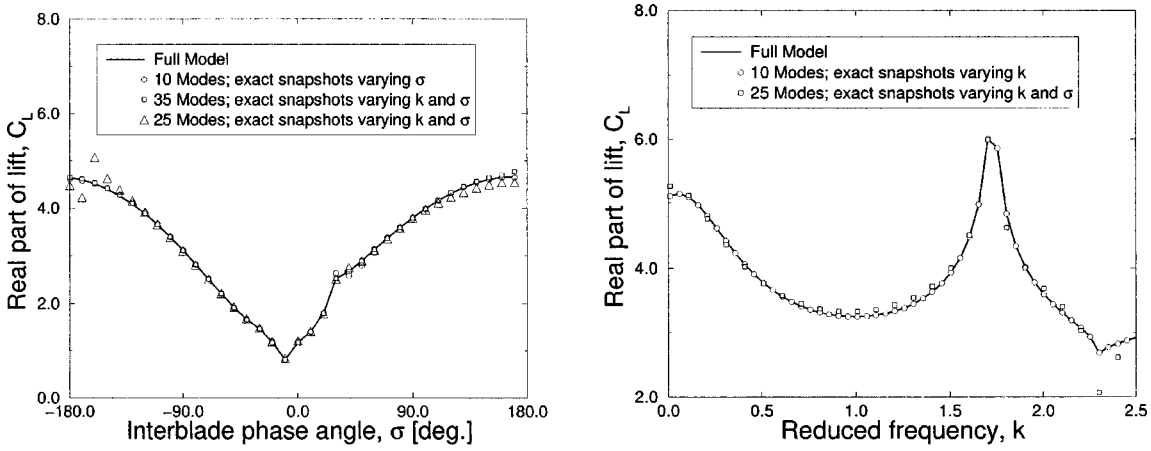

Fig. 5 Real (in-phase) part of the unsteady coefficient of lift C_L for a pitching motion about the mid-chord. Left: reduced frequency k of 0.5. Right: interblade phase angle σ of 90 deg.

computed using the full model. When only 25 modes are used to model the flow using snapshots obtained varying both k and σ, the model is accurate over a limited spectrum of interblade phase angles. When additional number of ten modes are included, the reduced-order model is accurate over the entire spectrum of interblade phase angles. Only the real part of the coefficient of lift is shown. The performance of the reduced-order models in computing the imaginary part of the coefficient of lift is similar and not shown here. The coefficient of lift is defined by $C_L = \int_0^c C_P(\xi) d\xi/(c\alpha)$, where c is the chord and α is the amplitude of the pitch motion. When a plunging motion is investigated, the angle α is replaced by the nondimensional pitch amplitude.

Next, we investigate the performance of the reduced-order models for various reduced frequencies. Shown in Fig. 5 are the responses of the full model and the reduced-order models for an interblade phase angle of 90 deg. The reduced-order models with 10 and 25 degrees-of-freedom are shown to model accurately the dynamics of the full model. The additional ten modes or degrees-of-freedom used for large interblade phase angles, are not required here because the interblade phase angle of 90 deg falls into the region of interblade phase angles where the model with 25 degrees-of-freedom models accurately the full system, as shown in Fig. 5.

The reduced-order model obtained using snapshots computed at an upstream far-field Mach number of 0.50 may be used to construct reduced-order models of flows with other Mach numbers. However, the accuracy of the reduced-order models is dependent on the value of M for which aerodynamic forces are computed. Figure 6 and Fig. 7 show that the 35-mode model referred to in Fig. 5 and computed using snapshots at a Mach number of 0.50 predicts well the trends in the dynamics of the system at a Mach number of 0.35, e.g., increasing or decreasing magnitudes of the coefficient of lift, cuton or cutoff frequencies. Also, this reduced-order model provides reasonable quantitative results at a Mach number of 0.55 although it does not give as accurate results as the same model gives at a Mach number of 0.50. Moreover, the aerodynamic forces computed for values of M closer and closer to 0.50 are more and more accurate when the reduced-order model obtained using snapshots computed for a Mach number of 0.50 is used. Figure 8 and Fig. 9 show that the results predicted at a Mach number of 0.50 by the 35-mode model are very accurate when compared to the results obtained using the full model.

There are two possible factors which determine the number of modes required for constructing a reduced-order model. One factor is the intrinsic dimension of the inertial manifold of the flow dynamics. Another factor is the accuracy of the modal approximations obtained using the proper orthogonal decomposition technique. To separate these two factors, we computed a separate set of 700 snapshots obtained at 35×20 distinct values of the interblade phase angle σ (varying from -180 deg to 180 deg) and

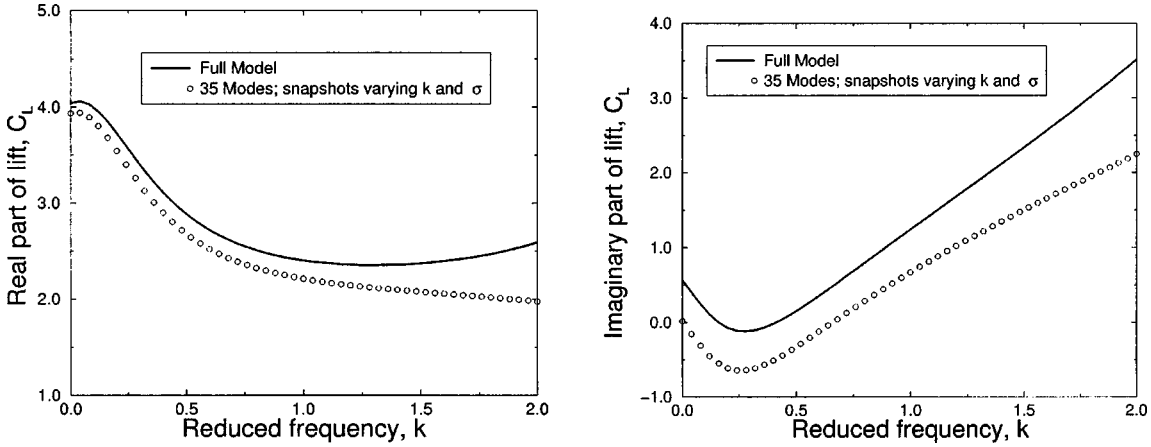

Fig. 6 Unsteady coefficient of lift C_L for a pitching motion about the mid-chord, upstream far-field Mach number of 0.35 and interblade phase angle σ of 90 deg. Snapshots are computed at a Mach number of 0.50. Left: real part. Right: imaginary part.

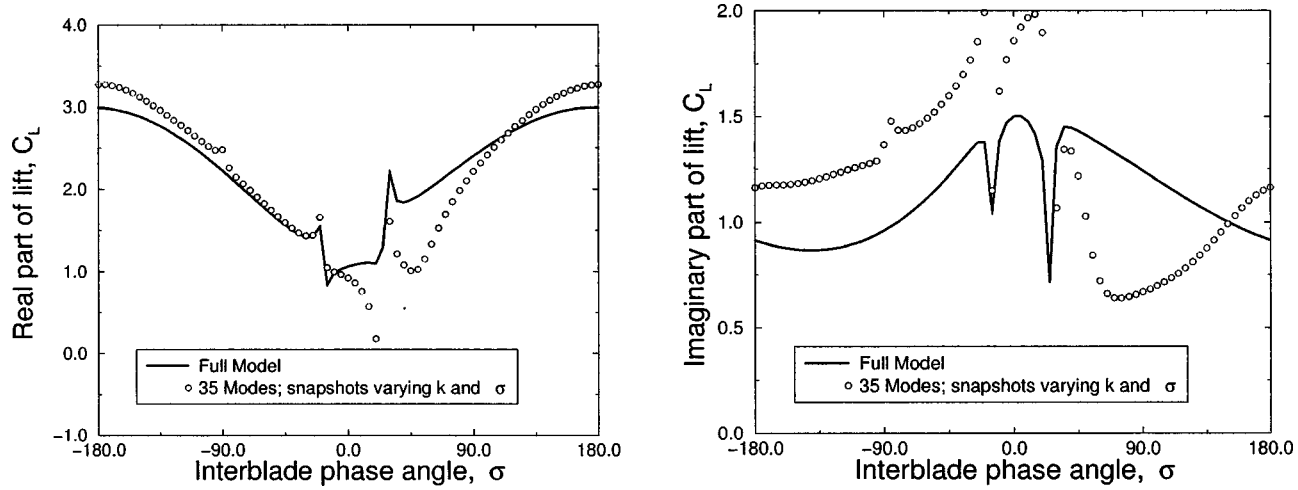

Fig. 7 Unsteady coefficient of lift C_L for a pitching motion about the mid-chord, upstream far-field Mach number of 0.35 and reduced frequency k of 1. Snapshots are computed at a Mach number of 0.50. Left: real part. Right: imaginary part.

reduced frequency k (varying from 0 to 2). The reduced-order models and full model are compared at various Mach numbers. However, the snapshots are computed at one Mach number only. Thus, the reduced-order models obtained using snapshots computed for flows with the same Mach number as the flows computed using the full model are referred to as *exact*. For example, Fig. 8 and Fig. 9 show the coefficient of lift (at a Mach number of 0.55) predicted by the full model, a 35-mode reduced-order model obtained using snapshots computed at a Mach number of 0.50 and two reduced-order models obtained using snapshots referred to as *exact* as they are computed at a Mach number of 0.55.

Figure 8 and Fig. 9 show that the accuracy of the modes obtained using a proper orthogonal decomposition technique is a critical factor. The 25-mode model (based on snapshots computed at a Mach number of 0.55) is shown to predict the flow dynamics as well as the 35-mode model (based on snapshots computes at a Mach number of 0.55) in Fig. 5 although the former uses 10 modes less. The reason for the lower number of modes is the accuracy of the proper orthogonal decomposition modes used for reduction. The 25-mode model was constructed using 700 snapshots whereas the 35-mode model was constructed using only 100 snapshots, obtained for 10×10 parameter values for σ between -180 deg and 180 deg and k between 0.0 and 2.0. Thus, a 25-mode model based on 700 snapshots was shown to be more accurate than a 35-mode model based on 100 snapshots, which in turn is more accurate than a 25-mode model based on 100 snapshots. Also, the 20-mode model shown in Fig. 8 and Fig. 9 predicts accurately the flow response to an oscillation of the airfoils at a reduced frequency k of 1. Nevertheless, this model does not predict accurately the dynamics at other frequencies (as shown in Fig. 8) suggesting that the factor limiting the further decrease below 25 of the required number of modes of the reduced-order models is the dimension of the inertial manifold of the flow dynamics.

The trends in the required number of modes in a reduced-order model are observed at other values of the Mach number as well. Figure 10 and Fig. 11 show that a 25-mode model (based on snapshots computed at a Mach number of 0.70) is accurate for an upstream far-field Mach number of 0.7 while a 20-mode model (based on snapshots computed at a Mach number of 0.70) predicts trends and has limited accuracy as shown in Fig. 10, for example.

4.4 Transonic Reduced-Order Modeling. The upstream far-field Mach number considered is 0.80, and the inflow angle Θ

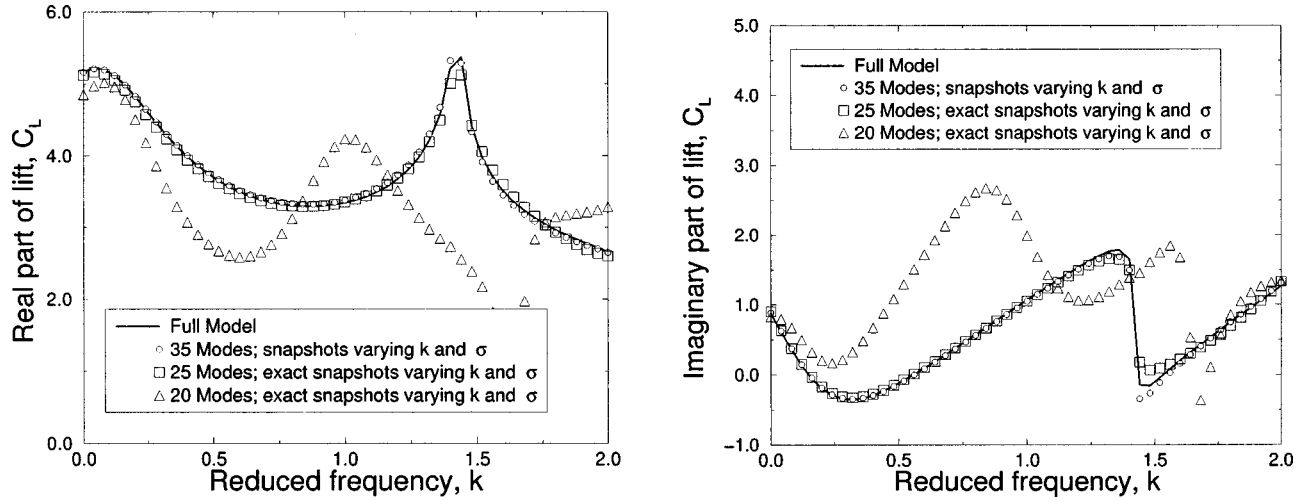

Fig. 8 Unsteady coefficient of lift C_L for a pitching motion about the mid-chord, upstream far-field Mach number of 0.55 and interblade phase angle σ of 90 deg. Snapshots are computed at a Mach number of 0.50 and 0.55. Left: real part. Right: imaginary part.

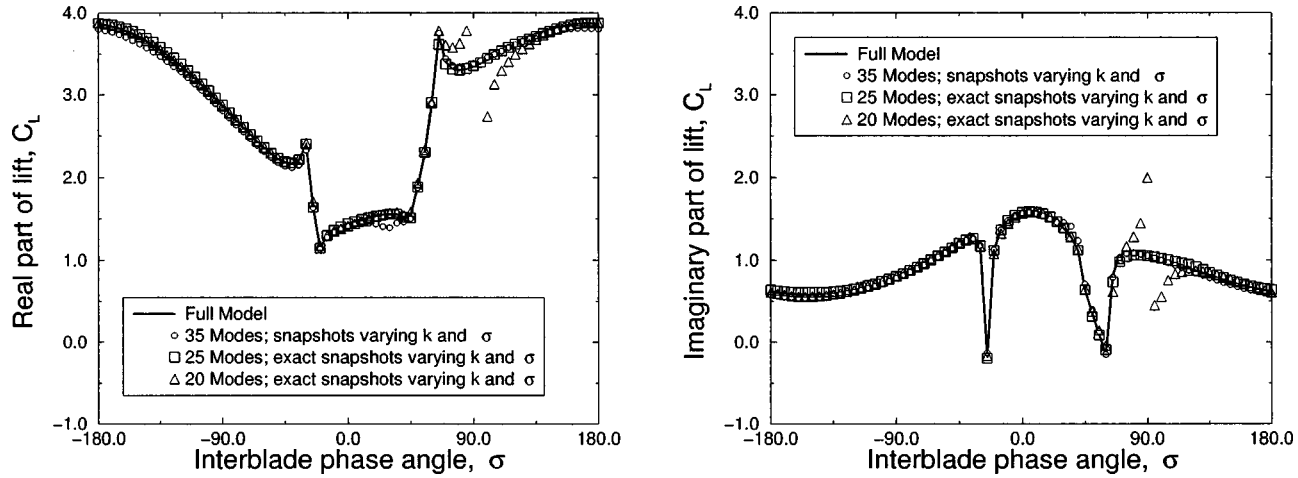

Fig. 9 Unsteady coefficient of lift C_L for a pitching motion about the mid-chord, upstream far-field Mach number of 0.55 and reduced frequency k of 1. Snapshots are computed at a Mach number of 0.50 and 0.55. Left: real part. Right: imaginary part.

is 55 deg. For the unsteady calculations, a pitching motion of the airfoils about the mid-chord point is assumed. The flow is discretized using a grid with 300×40 nodes.

Five reduced-order models have been constructed. First model was constructed using 15 modes obtained using a proper orthogonal decomposition technique applied to a set of 72 snapshots obtained varying the interblade phase angle σ between -180 deg and 180 deg while the reduced frequency k was maintained constant of value 0.5. The second model has 15 modes also. However, it was constructed using a proper orthogonal decomposition technique applied to a set of 51 snapshots obtained varying the reduced frequency k between 0.0 and 2.0 while the interblade phase angle σ was maintained constant of value 90 deg. The third, fourth, and fifth models have 25, 35, and 50 degrees-of-freedom, respectively. These models were constructed using 10×10 snapshots obtained varying σ between -180 deg and 180 deg and k between 0.0 and 2.0.

First, we investigate the performance of the reduced-order models for various interblade phase angles. Shown in Fig. 12 are the results obtained for a pitching motion of the airfoils with reduced frequency k of 0.5. The reduced-order models with 15 and 50 degrees-of-freedom, are shown to capture accurately the response computed using the full model. The model with 25 modes obtained using snapshots for various values of k and σ is accurate over a limited spectrum of interblade phase angles only. However, an additional number of 25 modes are sufficient to construct a reduced-order model which is accurate over the entire spectrum of interblade phase angles. Only the real part of the coefficient of lift is shown. The performance of the reduced-order models in computing the imaginary part of the coefficient of lift is similar and not shown here.

Next, we investigate the performance of the reduced-order models over a range of reduced frequencies. Shown in Fig. 12 are the responses of the full model and the reduced-order models for an interblade phase angle of 90 deg. The reduced-order models with 15 and 25 degrees-of-freedom are shown to model accurately the dynamics of the full model. The additional 25 modes or degrees-of-freedom used for large interblade phase angles, are not required here because the interblade phase angle of 90 deg falls into the region of interblade phase angles where the model with 25 degrees-of-freedom models accurately the full system, as shown in Fig. 12.

Similar to the subsonic calculations, Fig. 13 and Fig. 14 show that the accuracy of the modes obtained using a proper orthogonal decomposition technique is a critical factor. In these two figures, a 25-mode model is shown to predict accurately the flow dynamics.

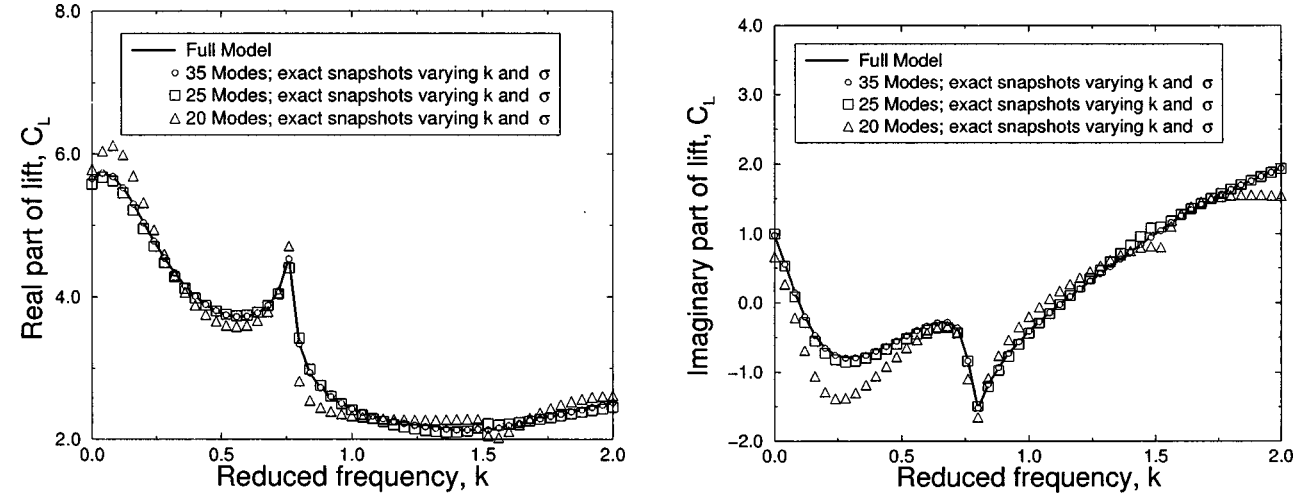

Fig. 10 Unsteady coefficient of lift C_L for a pitching motion about the mid-chord, upstream far-field Mach number of 0.70 and interblade phase angle σ of 90 deg. Left: real part. Right: imaginary part.

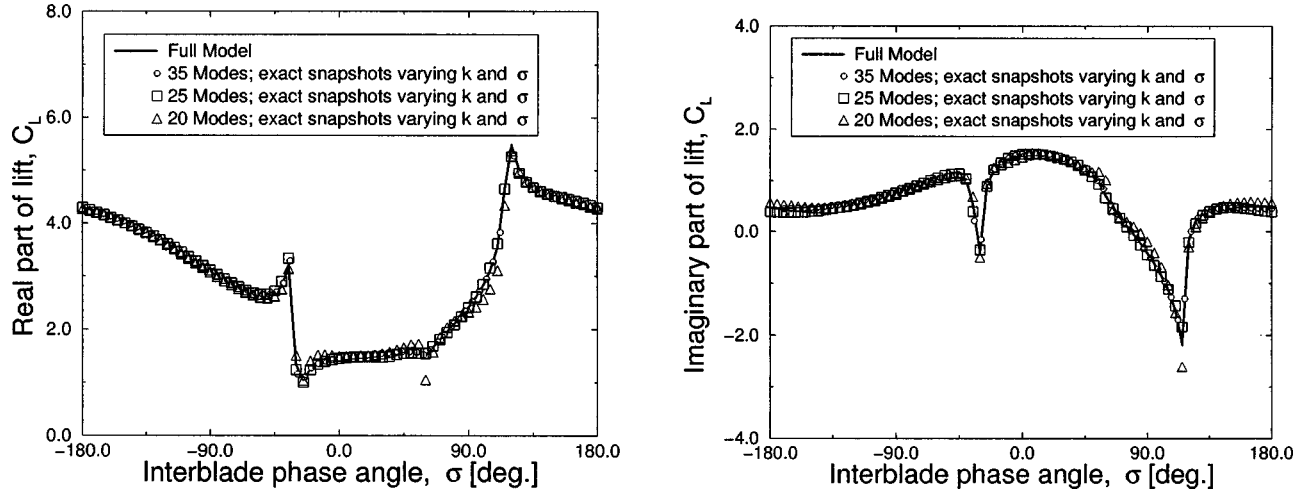

Fig. 11 Unsteady coefficient of lift C_L for a pitching motion about the mid-chord, upstream far-field Mach number of 0.70 and reduced frequency k of 1. Left: real part. Right: imaginary part.

To obtain similar accuracy, a model with 50 modes is required when less accurate proper orthogonal decomposition modes (i.e., modes computed based on a smaller number of snapshots) are available, as shown in Fig. 12. One may note that the 25-mode model used in Fig. 13 and Fig. 14 is distinct from the 25-mode model used in Fig. 12 because the two models were constructed using different snapshots. The reason for the lower number of required modes shown in Fig. 13 and Fig. 14 is the accuracy of the proper orthogonal decomposition modes used for reduction which is very important for the transonic case since large spatial gradients are present in the flow due to shocks. Thus, a larger reduction in the required number of modes is observed for the transonic flows than for subsonic flows, i.e., 25 compared to 10. Similar to the subsonic cases, the 25-mode model was constructed using 700 snapshots whereas the 50-mode model was constructed using 100 snapshots. Also, the 20-mode model shown in Fig. 13 and Fig. 14 predicts well the trends in the flow response although it is not as accurate as the 25-mode model because it has fewer modes. This observation suggests that the factor limiting the further decrease below 25 of the required number of modes of the reduced-order models is the dimension of the inertial manifold of the flow dynamics. It is interesting to note also that for a fixed total frequency of interest, if one continues to increase the number of frequencies within that interval at which snapshots are taken, there is a point beyond which increasing the number of snapshots may not improve the result. This is because if snapshots are taken at adjacent frequencies which are too close, then the information obtained may not be sufficiently linearly independent and this can lead to numerical difficulties.

The subsonic and transonic reduced-order models indicate that the number of modes required to model accurately the flow dynamics is approximately 25 and it is not strongly dependent on the upstream far-field Mach number. The critical factor is the accuracy of the proper orthogonal decomposition modes used for model reduction. Nevertheless, the value of the Mach number has an important influence on the accuracy of the proper orthogonal decomposition modes (for a given number of snapshots) thus indirectly influencing the accuracy of the reduced-order models.

In both the subsonic and transonic cases, the models based on snapshots at one fixed reduced frequency (or interblade phase angle) were observed not to be accurate when used at a different reduced frequency (or interblade phase angle).

5 Conclusions

An inviscid model of a subsonic or low transonic flow in a two-dimensional turbomachinery cascade has been used to com-

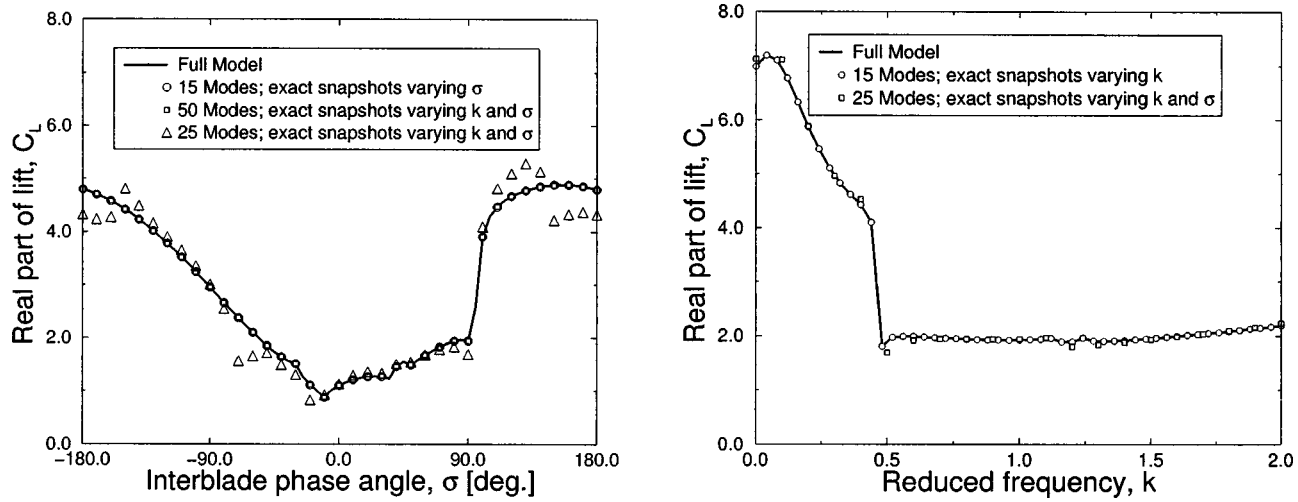

Fig. 12 Real (in-phase) part of the unsteady coefficient of lift C_L for a pitching motion about the mid-chord and upstream far-field Mach number of 0.80. Left: reduced frequency 0.5. Right: interblade phase angle 90 deg.

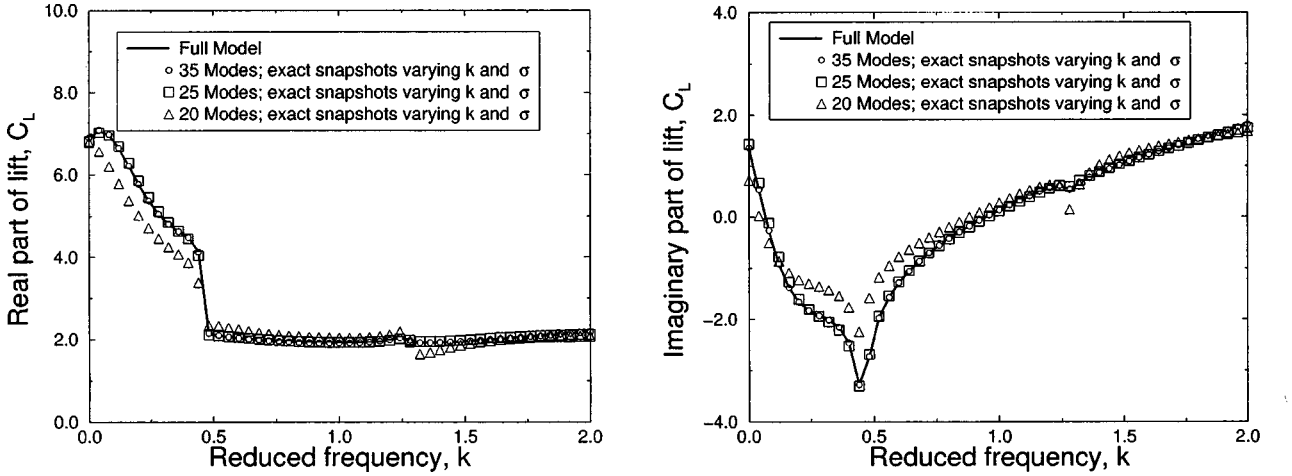

Fig. 13 Unsteady coefficient of lift C_L for a pitching motion about the mid-chord, upstream far-field Mach number of 0.80 and interblade phase angle σ of 90 deg. Left: real part. Right: imaginary part.

pute steady and unsteady flows. The unsteady flow has then been linearized about the nonlinear steady response and a frequency domain model has been constructed. This model has been validated and shown to provide similar results when compared to previous computational data presented in the literature.

Three subsonic and three transonic reduced-order models have been constructed in the frequency domain using proper orthogonal decomposition. A cascade of airfoils forming a slightly modified Tenth Standard Configuration has been investigated. A reduced-order model with only 10 degrees-of-freedom has been shown to predict accurately the unsteady response over a wide range of reduced frequencies when compared to a full model with approximately 5000 degrees-of-freedom. Similarly, a second reduced-order model with only 10 degrees-of-freedom has been shown to predict accurately the unsteady response over a full spectrum of interblade phase angles and a fixed reduced frequency. Finally, a third model model with 35 degrees-of-freedom has been shown to model accurately the flow dynamics over a full spectrum of interblade phase angles and a wide range of reduced frequencies.

Flows with an upwind far-field Mach number of 0.80 have been investigated. A reduced order model with only 15 degrees-of-freedom has been shown to model accurately the unsteady response over a wide range of reduced frequencies when compared to a full model with approximately 17,500 degrees-of-freedom. Similarly, a second reduced-order model, with 15 degrees-of-freedom also, has been shown to predict accurately the unsteady response over a full spectrum of interblade phase angles and a fixed reduced frequency. Finally, a third-model model with 50 degrees-of-freedom has been shown to model accurately the flow dynamics over a full spectrum of interblade phase angles and a wide range of reduced frequencies.

The reduced-order model obtained using snapshots computed at an upstream far-field Mach number of 0.50 were used to construct reduced-order models of flows with other Mach numbers. In such cases, the accuracy of the reduced-order models was found to be dependent on the difference in the Mach number values for the flow and the snapshots. Also, trends in the dynamics of the system were well predicted, e.g., increasing or decreasing magnitudes of the coefficient of lift, cuton or cutoff frequencies. Accurate quantitative results were obtained for a Mach number of 0.55 using snapshots collected at a Mach number of 0.50.

The number of modes required to model accurately the flow dynamics was shown to be approximately 25 for the cascade configuration investigated. The required number of modes in a

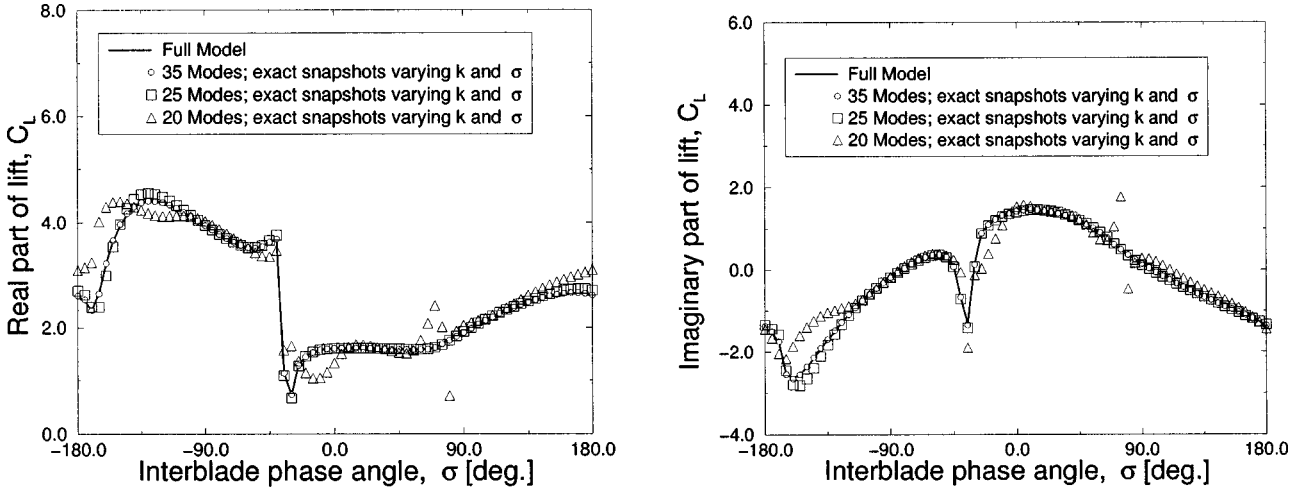

Fig. 14 Unsteady coefficient of lift C_L for a pitching motion about the mid-chord, upstream far-field Mach number of 0.80 and reduced frequency k of 1. Left: real part. Right: imaginary part.

reduced-order model was shown to be only weakly dependent on the upstream far-field Mach number, while the critical factor is the accuracy of the proper orthogonal decomposition modes used for model reduction. As previously observed ([10,11]), the value of the Mach number has an important influence on the accuracy of the proper orthogonal decomposition modes (for a given number of snapshots) thus indirectly influencing the accuracy of the reduced-order models.

The numerical examples provided show that the inertial manifold of the dynamics of subsonic as well as transonic flow has a very small number of degrees-of-freedom for a broad range of Mach numbers. Thus, we have shown numerically that the main assumption made in the proper orthogonal decomposition technique holds as the dynamics the systems is low dimensional. Thus, a proper orthogonal decomposition representation of a more precise full model such as a three-dimensional Navier-Stokes model may not be very large as long as the required proper orthogonal decomposition modes are computed accurately. There are several ways to improve the accuracy of the proper orthogonal decomposition modes used for reduction. One method, used in this paper, is to increase the number of snapshots. However, this method may be computation intensive and not easily available in certain calculations. Thus, alternate techniques are currently under evaluation and are part of the future work. Nevertheless, less accurate proper orthogonal decomposition modes may be used as well. The drawback is an increased number of degrees-of-freedom of the reduced-order models However, this drawback is not major as even the increased the number of degrees-of-freedom constitutes a dramatic model reduction when compared to the full model.

Acknowledgments

The first author would like to acknowledge the financial support of NSERC-Canada and FCAR-Canada.

References

[1] Greitzer, E. M., 1976, ''Surge and Rotating Stall in Axial Flow Compressors. Part I: Theoretical Compression System Model,'' J. Eng. Power, **98**(1), pp. 190–198.
[2] Moore, F. K., and Greitzer, E. M., 1986, ''A Theory of Post-Stall Transients in Axial Compression Systems: Parts I and II,'' ASME J. Eng. Gas Turbines Power, **108**(1), pp. 68–76.
[3] Whitehead, D. S., 1959, ''The Vibration of Cascade Blades Treated by Actuator Disk Methods,'' Proc. Inst. Mech. Eng., **173**(21), pp. 555–563.
[4] Dowell, E. H., 1980, ''A Simple Method for Converting Frequency Domain Aerodynamics to the Time Domain,'' NASA, Lewis Research Center.
[5] Peterson, L. D., and Crawley, E. F., 1988, ''Improved Exponential Time Series Approximation of Unsteady Aerodynamic Operators,'' J. Aircr., **25**(2), pp. 121–127.
[6] Ueda, T., and Dowell, E. H., 1984, ''Flutter Analysis Using Nonlinear Aerodynamic Forces,'' J. Aircr., **21**(2), pp. 101–109.
[7] Dowell, E. H., 1995, ''Eigenmode Analysis in Unsteady Aerodynamics: Reduced Order Models,'' *Proceedings of the 36th AIAA/ASME/ASCE/AHS/ASC Structures, Structural Dynamics, and Materials Conference*, Vol. 1, New Orleans, LA, AIAA, Washington, DC, pp. 1–13.
[8] Hall, K. C., 1994, ''Eigenanalysis of Unsteady Flows About Airfoils, Cascades, and Wings,'' AIAA J., **32**(12), pp. 2426–2432.
[9] Dowell, E. H., Hall, K. C., Thomas, J. P., Florea, R., Epureanu, B. I., and Heeg, J., 1999, ''Reduced Order Models in Unsteady Aerodynamics,'' *Proceedings of the 40th AIAA/ASME/ASCE/AHS/ASC Structures, Structural Dynamics, and Materials Conference and Exhibit*, Vol. 1, AIAA, Waldorf, MD, pp. 622–637.
[10] Epureanu, B. I., Hall, K. C., and Dowell, E. H., 2000, ''Reduced Order Models of Unsteady Transonic Viscous Flows in Turbomachinery,'' J. Fluids Struct., **18**(8), pp. 1215–1235.
[11] Epureanu, B. I., Hall, K. C., and Dowell, E. H., 2001, ''Reduced Order Models of Unsteady Viscous Flows in Turbomachinery Using Viscous-Inviscid Coupling,'' J. Fluids Struct., **15**(2), pp. 255–276.
[12] Hall, K. C., Thomas, J. P., and Dowell, E. H., 1999, ''Reduced-Order Modelling of Unsteady Small-Disturbance Flows Using a Frequency-Domain Proper Orthogonal Decomposition Technique,'' *Proceedings of the 37th Aerospace Sciences Meeting and Exhibit*, Vol. 99-0655, Reno, NV, AIAA, Washington, DC, pp. 1–11.
[13] Romanowski, M. C., 1996, ''Reduced Order Unsteady Aerodynamic and Aeroelastic Models Using Karhunen-Loève Eigenmodes,'' *Proceedings of the 6th AIAA Symposium on Multidis ciplinary Analysis and Optimization*, vol. 1, Bellevue, WA, AIAA, Washington, DC, Paper No. 96-3981, pp. 1–7.
[14] Willcox, K. E., Peraire, J., and White, J., 2000, ''An Arnoldi Approach for Generation of Reduced-Order Models for Turbomachinery,'' presented at the 38th Aerospace Sciences Meeting and Exhibit, Reno, NV, AIAA Paper No. 2000-0884.
[15] Dowell, E. H., and Ilgamov, M., 1988, *Studies in Nonlinear Aeroelasticity*, 1st Ed., Springer-Verlag, New York.
[16] Hall, K. C., 1993, ''Deforming Grid Variational Principle for Unsteady Small Disturbances Flows in Cascades,'' AIAA J., **31**(5), pp. 891–900.
[17] Hall, K. C., Lorence, C. B., and Clark, W. S., 1993, ''Nonreflecting Boundary Conditions for Linearized Unsteady Aerodynamic Calculations,'' *31st Aerospace Sciences Meeting & Exhibit*, Vol. 93-0882, Reno, NV, AIAA, Washington, DC, pp. 1–15.
[18] Strain, M. C., and Greenside, H. S., 1998, ''Size-Dependent Transition to High-Dimensional Chaotic Dynamics in a Two-Dimensional Excitable Medium,'' Phys. Rev. Lett., **80**(11), pp. 2306–2309.
[19] Epureanu, B. I., and Dowell, E. H., 1997, ''System Identification for Ott-Grebogi-Yorke Controller Design,'' Phys. Rev. E, **56**(5), pp. 5327–5331.
[20] Epureanu, B. I., and Dowell, E. H., 1998, ''On the Optimality of the OGY Control Scheme,'' Physica D, **116**(1–2), pp. 1–7.
[21] Epureanu, B. I., Trickey, S. T., and Dowell, E. H., 1998, ''Stabilization of Unstable Limit Cycles in Systems With Limited Controllability: Expanding the Basin of Convergence of OGY-Type Controllers,'' Nonlinear Dyn., **15**(2), pp. 191–205.
[22] Kim, T., 1998, ''Frequency Domain Karhunen—Loéve Method and Its Application to Linear Dynamic Systems,'' AIAA J., **36**(11), pp. 2117–2123.
[23] Sirovich, L., 1987, ''Turbulence and the Dynamics of Coherent Structures, Part I: Coherent Structures,'' Q. Appl. Math., **XLV**(3), pp. 561–571.
[24] Sirovich, L., 1987, ''Turbulence and the Dynamics of Coherent Structures, Part II: Symmetries and Transformations,'' Q. Appl. Math., **XLV**(3), pp. 573–582.
[25] Fransson, T. H., and Verdon, J. M., 1993, ''Panel Discussion on Standard Configurations for Unsteady Flow Through Vibrating Axial-Flow Turbomachine,'' In H. M. Atassi, editor, *Unsteady Aerodynamics, Aeroacoustics and Aeroelasticity of Turbomachines and Propellers*, Vol. 1, H. M. Atassi, ed., Springer-Verlag, New York, pp. 859–889.

Reduced-Order Modeling of Unsteady Flows About Complex Configurations Using the Boundary Element Method

V. Esfahanian
e-mail: evahid@chamran.ut.ac.ir

M. Behbahani-nejad

Department of Mechanical Engineering,
University of Tehran,
North Amin Abad Avenue,
Tehran, Iran

An approach to developing a general technique for constructing reduced-order models of unsteady flows about three-dimensional complex geometries is presented. The boundary element method along with the potential flow is used to analyze unsteady flows over two-dimensional airfoils, three-dimensional wings, and wing-body configurations. Eigenanalysis of unsteady flows over a NACA 0012 airfoil, a three-dimensional wing with the NACA 0012 section and a wing-body configuration is performed in time domain based on the unsteady boundary element formulation. Reduced-order models are constructed with and without the static correction. The numerical results demonstrate the accuracy and efficiency of the present method in reduced-order modeling of unsteady flows over complex configurations. [DOI: 10.1115/1.1511166]

Introduction

Reduced-order modeling is a conceptually novel and computationally efficient technique that is recently used in analysis of unsteady flows. Unsteady flow eigenmodes are used to construct reduced-order unsteady flow models similar to the normal mode analysis in structural dynamics. Although the modal analysis of structures is quite routine, the modal analysis of unsteady flows is still in the developing stage. The advantage to a modal approach is that one may construct a reduced-order model by retaining only a few of the original modes. Eigenanalysis of unsteady potential flows about flat airfoils, cascades, and wings has been applied by Hall [1]. He constructed reduced-order models based on unsteady incompressible vortex lattice method and found that in order to obtain satisfactory results, the static correction technique must be used. Romanowski and Dowell [2] applied reduced-order modeling to the subsonic unsteady flows based on the Euler equations about a NACA 0012 airfoil. Reduced-order modeling of unsteady viscous flow in a compressor cascade based on the coupled potential flow and boundary layer approximation has been applied by Florea et al. [3], and the status of reduced-order modeling of unsteady aerodynamic systems has been reviewed by Dowell et al. [4].

Although less than a decade is spent from application of reduced-order modeling in unsteady aerodynamic systems, almost all of the previous studies have been done for two-dimensional cases. One of the main difficulties with applying reduced-order modeling to the real three-dimensional geometries using field discretization approaches is that the resulting formulation has a very large degree-of-freedom. This makes the computation of eigenvalues and eigenvectors very cumbersome. Therefore, any procedure that reduces the degrees-of-freedom of the problem, makes the eigenanalysis and reduced-order modeling of unsteady flows about real geometries more practical.

The Boundary element method is recently known as a powerful numerical technique in engineering analysis. In CFD analysis and especially heat transfer problems, the boundary element method plays an important and efficient role. At the beginning, this method was used in linear problems but it developed quickly to analyze nonlinear problems too. One of its main advantages is reduction of the problem dimensionality by one, since it will be required to discretize only the boundary of computational domain.

In this context, the boundary element method is used for eigenanalysis and reduced-order modeling of unsteady aerodynamics based on unsteady potential flows in two and three-dimensional cases. Since only the boundary and the wake of the geometry are discretized, the degrees-of-freedom of the problem are reduced considerably. Therefore, one can compute all of the eigenvalues and eigenvectors using the well-known IMSL routines ([5]). Moreover, one can use the Lanczos method to compute only a small subset of the largest eigenvalues and corresponding eigenvectors for complex geometries which require large number of boundary elements ([6]). The present study shows that the number of zero eigenvalues is the same as the number of elements that lie on the body. Therefore, the corresponding eigenmodes behave in quasi-steady fashion. Moreover, the neglected modes which have large natural frequencies compared to the excitation frequency, also respond in an essentially quasistatic fashion. Hence, to include approximately the effects of the neglected eigenmodes, the static correction method is used. In the present work, reduced-order modeling of unsteady flows based on the boundary element method around a NACA 0012 airfoil, a three-dimensional wing with NACA 0012 section and a wing-body configuration are studied. The results show the efficiency of the boundary element method in reduced order modeling of unsteady flows about complex configurations.

Basic Formulation

Consider a body with known boundaries, submerged in a potential flow. The body is modeled as a closed surface which divides the space into two external and internal regions (see Fig. 1). One region contains the flow field of interest and the other contains a fictitious flow. The flow of interest is in the outer region where the governing equation in terms of the total potential, Φ, in the body's frame of reference is

$$\nabla^2\Phi = 0. \tag{1}$$

The first boundary condition is zero normal velocity across the body's solid boundaries, namely,

$$\nabla\Phi \cdot \mathbf{n} = \nabla(\phi + \phi_\infty) \cdot \mathbf{n} = 0 \tag{2}$$

Contributed by the Fluids Engineering Division for publication in the JOURNAL OF FLUIDS ENGINEERING. Manuscript received by the Fluids Engineering Division January 11, 2002; revised manuscript received May 3, 2002. Associate Editor: G. E. Karniadakis.

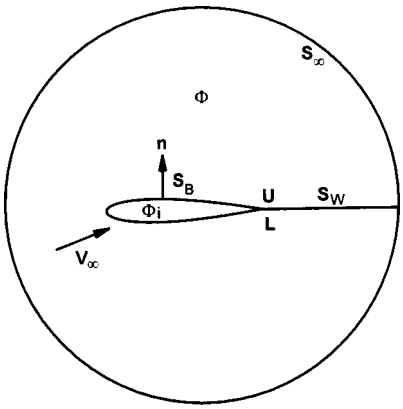

Fig. 1 Potential flow model of a body submerged in fluid

where ϕ_∞ is the freestream potential, ϕ is the perturbation potential and **n** is the outward unit normal on the surface. The second boundary condition requires that the flow disturbance, due to the body's motion through the fluid, should diminish far from the body,

$$\lim_{\rho\to\infty} \nabla\phi = 0, \tag{3}$$

where ρ is the distance from origin of the body's frame of reference. Along the wing's trailing edges, the velocity has to be finite in order to fix the rear stagnation line (Kutta condition). Therefore, at the trailing edge one has

$$\nabla\phi < \infty. \tag{4}$$

Moreover, in the potential flow region the angular momentum can not change, thus the circulation, Γ, is conserved (Kelvin's theorem), i.e.,

$$\frac{d\Gamma}{dt} = 0. \tag{5}$$

Boundary Element Formulation

The potential at any point P in either region may be evaluated by applying Green's theorem to both regions which results in the following boundary integral equation ([7]):

$$\Phi_P = \frac{1}{4\pi}\int_{S_B}\left[(\Phi-\Phi_i)\nabla\frac{1}{r} - \frac{1}{r}\nabla(\Phi-\Phi_i)\right]\cdot\mathbf{n}dS - \frac{1}{4\pi}\int_{S_W+S_\infty}\left(\frac{1}{r}\nabla\Phi - \Phi\nabla\frac{1}{r}\right)\cdot\mathbf{n}dS \tag{6}$$

where r is the distance from the point P to the boundary element dS, Φ_i is the velocity potential of the fictitious flow, **n** is the unit normal vector to the surface pointing into the flow field of interest, and S_B, S_W, and S_∞ are the surface of the body, the surface of the wake and the surface at infinity, respectively, as shown in Fig. 1. It is assumed that the wake is thin and no aerodynamic loads will be supported by the wake which means that the jump in normal velocity across the wake is zero. Therefore, the contribution of the second integral in Eq. (6) can be written as

$$\int_{S_W}\left(\frac{1}{r}\nabla\Phi - \Phi\nabla\frac{1}{r}\right)\cdot\mathbf{n}dS = \int_{S_W^U+S_W^L}\Phi\nabla\left(\frac{1}{r}\right)\cdot\mathbf{n}dS = \int_{S_W^U}\Delta\Phi_W\nabla\left(\frac{1}{r}\right)\cdot\mathbf{n}dS \tag{7}$$

where $\Delta\Phi_W = \Phi_W^U - \Phi_W^L$. At the trailing edge, Kutta condition implies

$$\Delta\Phi_W = \Phi_B^U - \Phi_B^L. \tag{8}$$

For the wake points off the trailing edge, $\Delta\Phi_W$ is determined using Eq. (5). Using Kelvin's theorem, one concludes that the value of $\Delta\Phi_W$ at each time, t, is determined by the corresponding trailing edge value at time $t-t^*$, where t^* is the time at which the fluid particle travels the distance between the trailing edge and the desired point. Using the second boundary condition, Eq. (3), the contribution of the second integral in Eq. (6) is equal to $4\pi\phi_\infty$. Therefore, using Eqs. (3) and (7), Eq. (6) becomes

$$\Phi_P = \frac{1}{4\pi}\int_{S_B}\left[(\Phi-\Phi_i)\nabla\frac{1}{r} - \frac{1}{r}\nabla(\Phi-\Phi_i)\right]\cdot\mathbf{n}dS - \frac{1}{4\pi}\int_{S_W^U}\Delta\Phi_W\nabla\left(\frac{1}{r}\right)\cdot\mathbf{n}dS + \phi_\infty. \tag{9}$$

The first integral in Eq. (9) represents the disturbance potential from a surface distribution of doublets and sources with strength $(\Phi-\Phi_i)$ and $\nabla(\Phi-\Phi_i)\cdot\mathbf{n}$ per unit area, respectively. In addition, the second integral in Eq. (9) represents the surface distribution of doublets with strength $\Delta\Phi_W$ per unit area. To solve Eq. (9), an internal Dirichlet boundary condition ([7]) is used and the potential of the fictitious flow is set equal to the onset potential, ϕ_∞. If the point P lies on the surface, the integrals become singular and it must be excluded from the integration by assuming a hemispherical deformation of the surface centered at P. If the integral is evaluated for this hemispherical deformation and its radius is allowed to go to zero, the contribution at point P is $(\Phi-\Phi_i)/2$. Therefore, using Dirichlet boundary condition and looking at point P inside the surface, Eq. (9) can be written as

$$4\pi c\phi_P = \int_{S_B}\left[\phi\frac{\partial}{\partial\mathbf{n}}\left(\frac{1}{r}\right) - \frac{1}{r}\frac{\partial\phi}{\partial\mathbf{n}}\right]dS + \int_{S_W^U}\Delta\phi_W\frac{\partial}{\partial\mathbf{n}}\left(\frac{1}{r}\right)dS \tag{10}$$

where $c=1/2$ if P is on a smooth part of the inner surface, $c=-1/2$ if P is on a smooth part of the outer surface, and the integrals on S_B are in the sense of Cauchy principal value. In a similar way, one can obtain the following equation for two-dimensional problems ([7]):

$$2\pi c\phi_P = \int_{S_B}\left[\phi\frac{\partial}{\partial\mathbf{n}}(\ln r) - \ln r\frac{\partial\phi}{\partial\mathbf{n}}\right]dS + \int_{S_W^U}\Delta\phi_W\frac{\partial}{\partial\mathbf{n}}(\ln r)dS. \tag{11}$$

In order to obtain an approximate solution for the boundary integral Eq. (10), the surfaces S_B and S_W^U are discretized into small quadrilateral elements. The values of ϕ and $\partial\phi/\partial\mathbf{n}$ are assumed to be constant within each element. Therefore, the collocation method yields the following relation for each collocation point on the body:

$$\phi_{P_h} = \sum_{k=1}^{NB} A_{hk}\phi_{P_k} + \sum_{k=1}^{NB} B_{hk}\left(\frac{\partial\phi}{\partial\mathbf{n}}\right)_{P_k} + \sum_{k=1}^{NW} A_{hk}\Delta\phi_{P_k} \tag{12}$$

where NB and NW are the number of elements on the body and the wake, respectively, and

$$A_{hk} = \frac{1}{2\pi}\int_{S_k}\frac{\partial}{\partial\mathbf{n}}\left(\frac{1}{r}\right)dS_k \tag{13}$$

$$B_{hk} = -\frac{1}{2\pi}\int_{S_k}\left(\frac{1}{r}\right)dS_k \tag{14}$$

where S_k is the surface of element. The coefficients A_{hk} and B_{hk} can be evaluated analytically as ([8])

$$A_{hk} = I_D(1,1) - I_D(1,-1) - I_D(-1,1) + I_D(-1,-1) \tag{15}$$

$$B_{hk} = I_S(1,1) - I_S(1,-1) - I_S(-1,1) + I_S(-1,-1) \tag{16}$$

where

$$I_D(\xi,\eta)=\frac{1}{2\pi}\tan_p^{-1}\left(\frac{\mathbf{r}\times\mathbf{a}_1\cdot\mathbf{r}\times\mathbf{a}_2}{|\mathbf{r}|\mathbf{r}\cdot\mathbf{a}_1\times\mathbf{a}_2}\right) \tag{17}$$

$$I_S(\xi,\eta)=-\frac{1}{2\pi}\left\{-\mathbf{r}\times\mathbf{a}_1\cdot\mathbf{n}\frac{1}{|\mathbf{a}_1|}\sinh^{-1}\left(\frac{\mathbf{r}\cdot\mathbf{a}_1}{|\mathbf{r}\times\mathbf{a}_1|}\right)+\mathbf{r}\times\mathbf{a}_2\times\mathbf{n}\frac{1}{|\mathbf{a}_2|}\sinh^{-1}\left(\frac{\mathbf{r}\cdot\mathbf{a}_2}{|\mathbf{r}\times\mathbf{a}_2|}\right)+\mathbf{r}\cdot\mathbf{n}\tan_p^{-1}\left(\frac{\mathbf{r}\times\mathbf{a}_1\cdot\mathbf{r}\times\mathbf{a}_2}{|\mathbf{r}|\mathbf{r}\cdot\mathbf{a}_1\times\mathbf{a}_2}\right)\right\} \tag{18}$$

and $-\pi/2\leqslant\tan_p^{-1}(\,)\leqslant\pi/2$, ξ and η are local element coordinates, respectively, and $\mathbf{a}_1$ and $\mathbf{a}_2$ are corresponding tangent vectors. For two-dimensional problems A_{hk} and B_{hk} are

$$A_{hk}=\frac{1}{\pi}\int_{S_k}\frac{\partial}{\partial\mathbf{n}}(\ln r)dS_k \tag{19}$$

$$B_{hk}=-\frac{1}{\pi}\int_{S_k}(\ln r)dS_k\,. \tag{20}$$

The relations in Ref. [7] may be used to compute the coefficients A_{hk} and B_{hk} for two-dimensional cases analytically.

The second term in the right-hand side of Eq. (12) is known from the tangency condition, Eq. (2), at each time step. Also, $\Delta\phi$ is determined via the Kutta condition and Kelvin's theorem as explained before. Hence, if Eq. (12) is applied at all of the collocation points over the body and the vector $\boldsymbol{\mu}$ is defined as

$$\boldsymbol{\mu}=\{\phi_1,\phi_2,\ldots,\phi_{NB},\Delta\phi_1,\Delta\phi_2,\ldots,\Delta\phi_{NW}\}^T \tag{21}$$

one can obtain

$$\mathbf{A}\boldsymbol{\mu}^{n+1}+\mathbf{B}\boldsymbol{\mu}^n=\mathbf{w}^{n+1} \tag{22}$$

where $\mathbf{w}$ is a known vector derived using tangency condition.

When the velocity potential is computed, the pressure coefficient may be calculated as ([7])

$$C_p=1-\frac{V^2}{V_\infty^2}-\frac{2}{V_\infty^2}\frac{\partial\Phi}{\partial t} \tag{23}$$

where V is the local fluid velocity on the body's surface.

Reduced-Order Modeling

Consider the homogeneous part of Eq. (22), set $\boldsymbol{\mu}=\mathbf{x}_i e^{\lambda_i t}$ and $z_i=e^{\lambda_i\Delta t}$, therefore, one obtains

$$z_i\mathbf{A}\mathbf{x}_i+\mathbf{B}\mathbf{x}_i=\mathbf{0} \tag{24}$$

that is a generalized eigenvalue problem where z_i is the ith eigenvalue and x_i is the corresponding right eigenvector. More generally, we may write

$$\mathbf{A}\mathbf{X}\mathbf{Z}+\mathbf{B}\mathbf{X}=\mathbf{0} \tag{25}$$

where $\mathbf{Z}$ is a diagonal matrix containing the eigenvalues of the generalized eigenvalue problem, and $\mathbf{X}$ is a matrix whose columns contain the corresponding right eigenvectors. Similarly, the left eigenvector problem is given by

$$\mathbf{A}^T\mathbf{Y}\mathbf{Z}+\mathbf{B}^T\mathbf{Y}=\mathbf{0}. \tag{26}$$

The eigenvectors satisfy the orthogonality conditions

$$\mathbf{Y}^T\mathbf{A}\mathbf{X}=\mathbf{I} \tag{27}$$

$$\mathbf{Y}^T\mathbf{B}\mathbf{X}=-\mathbf{Z}. \tag{28}$$

The eigenvalues and eigenvectors describe the natural modes of fluid motion or, at least, the natural modes of the computational model of fluid motion. In this paper, the boundary element method is used for eigenanalysis and reduced-order modeling of unsteady aerodynamics based on unsteady potential flows. Hence, the resulting eigensystem is usually small, and the eigenvalues and eigenvectors are computed using IMSL routines. However, for more complex configurations which require large number of boundary elements, one can use Lanczos method to compute only a small subset of the largest eigenvalues and corresponding eigenvectors.

Next, as is commonly done in the structural dynamic problems, the dynamic behavior of the fluid is represented as the sum of individual eigenmodes, i.e.,

$$\boldsymbol{\mu}=\mathbf{X}\mathbf{c}, \tag{29}$$

where $\mathbf{c}$ is the vector of normal mode coordinates. Substituting Eq. (29) into Eq. (22), premultiplying by $\mathbf{Y}^T$ and making use of the orthogonality conditions, gives a set of uncoupled equations for the modal coordinates $\mathbf{c}$,

$$\mathbf{c}^{n+1}-\mathbf{Z}\mathbf{c}^n=\mathbf{Y}^T\mathbf{w}^{n+1}. \tag{30}$$

Because the left-hand side of Eq. (30) is now diagonal, each mode can be marched forward in time independently and inexpensively. The advantage to a modal approach is that one may construct a reduced-order model by retaining only a few of the original modes. Hall [1] has shown that reduced order modeling produces satisfactory results whenever the static correction is used. For applying the static correction, one decomposes the unsteady solution into two parts; a part which is equivalent to response of the system if the disturbance were quasi-steady and a dynamic part to be determined, i.e.,

$$\boldsymbol{\mu}^n=\boldsymbol{\mu}_s^n+\tilde{\boldsymbol{\mu}}^n=\boldsymbol{\mu}_s^n+\mathbf{X}\tilde{\mathbf{c}}^n \tag{31}$$

where $\boldsymbol{\mu}_s$ is the quasisteady portion. Therefore, Eq. (30) is replaced by

$$\tilde{\mathbf{c}}^{n+1}-\mathbf{Z}\tilde{\mathbf{c}}^n=\mathbf{Y}^T\mathbf{w}^{n+1}-\mathbf{Y}^T(\mathbf{A}\boldsymbol{\mu}_s^{n+1}+\mathbf{B}\boldsymbol{\mu}_s^n). \tag{32}$$

Results and Discussions

Two-Dimensional Airfoil. The results in this section are presented to show the capability of reduced order modeling with just a few eigenmodes in unsteady flow analysis. A NACA 0012 airfoil is used as a test case. The airfoil is modeled using 72 boundary elements with the cosine distribution. The wake length is taken to be 10 chord length and it is discretized using 100 elements. Figure 2 shows the eigenvalues for the NACA 0012 airfoil in both the z-plane and the λ-plane. The present results are similar with isolated flat airfoil in Ref. [1]. The eigensystem has 172 eigenvalues which are related to the number of elements considered in discretization. The present eigenanalysis reveals that the number of distinct eigenvalues and corresponding eigenvectors that can be used to construct an eigenspace, is equal to the number of the wake elements, i.e., 100 in our case. Moreover, the eigensystem in

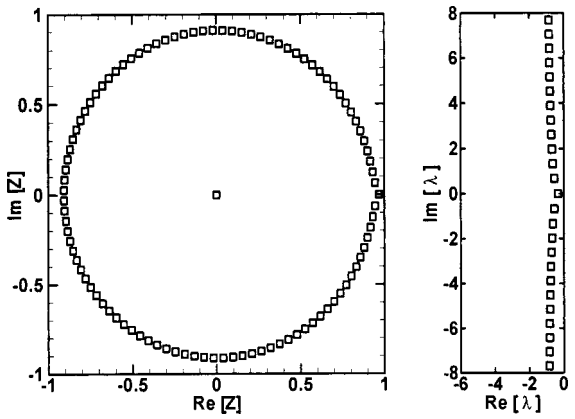

Fig. 2 Eigenvalues of boundary element model of unsteady flow about a NACA 0012 airfoil

the z-plane has 72 zero eigenvalues which correspond to the number of elements used on the body of the airfoil. On the other hand, the eigensystem has 72 eigenmodes which are excited instantly with the motion of the body. In the physical point of view, it means that the behavior of 72 eigenmodes is exactly quasi-steady. Therefore, it will be clear that the reduced order modeling without the static correction can not produce satisfactory results even if a large number of modes is used, since the effects of the eigenmodes corresponding to the zero eigenvalues may be only considered using the static correction.

As reported by Hall [1], the numerical experiments in the present study also reveal that the line of eigenvalues in the λ-plane gets denser as the length of the computational wake is increased with constant the wake element size, Δx_w, and gets longer as Δx_w is reduced with constant wake length. Inspection of the eigenvalue patterns in the z-plane and λ-plane shows that the maximum frequency, λ_I (the imaginary part of λ), that can be resolved, corresponds with the $z=|z|e^{\pm i\pi}$. Therefore, one can conclude that $\max(\lambda_I)=\pi/\Delta t=\pi U_\infty/\Delta x_w$. Hence, changing the wake element size, changes the maximum resolved frequency, and as the size of the wake elements becomes infinitesimal, the eigenvalue arms will cover frequency range ($\pm\infty$). These numerical experiments also reported by Heeg and Dowell [9].

The lift and pitching moment loops for the pitch oscillation of the airfoil are shown in Fig. 3. The pitching axis is at the 1/4 of chord, the angle of attack, $\alpha=3\ \text{deg}+10\ \text{deg}\sin kT$, and the reduced frequency, $k=\omega t/2U_\infty=0.10$. Although the angle of attack varies in a wide range ($-7\ \text{deg}\leqslant\alpha\leqslant+13\ \text{deg}$) and the wake roll-up is not considered, comparison of the present method with Ref. [10] shows satisfactory results. Also the figure shows reduced order modeling results in comparison with the direct method. Although reduced-order modeling with 40 modes without the static correction is not capable to give a suitable result, using the static correction with just one mode, it results in a very good agreement with the direct method.

Figures 4 and 5 present the results of the airfoil, oscillating at $\alpha=\pm1\ \text{deg}$ and Mach 0.50, with the reduced frequencies $k=0.10$ and 0.40, respectively. The Prandtl-Glaurt compressibility correction is used to consider compressibility effects. The present boundary element method and reduced-order modeling results are in excellent agreement with the unsteady Euler solution used in Ref. [11] when the static correction is applied.

Three-Dimensional Wing. The capability of reduced order modeling using the boundary element method in unsteady flow analysis over three-dimensional wings is demonstrated in this section. A three-dimensional wing with the NACA 0012 airfoil section and the aspect ratio 4.0, with heaving oscillation about $\alpha=5$ deg is used as a test case. Figure 6 shows the wing geometry and its wake. The body of the wing is modeled using 20 elements in chordwise and spanwise directions. The wake length is taken to be 10 chord length and discretized using 40 elements in streamwise direction. Eigenvalues of the three-dimensional wing in the z-plane and λ-plane are plotted in Fig. 7. Careful inspection of the results proves that, as the case in Ref. [1], the eigenvalues in λ-plane appear to form 20 branch cuts, the same as the number of elements in the spanwise direction. However, since the distribution of elements in spanwise direction is taken to be denser from the root to the tip, and the wing aspect ratio is smaller than the case in Ref. [1], 15 branch cuts are overlayed with each other. Also as reported by Hall [1], the branch farthest to the right corresponds to the first spanwise mode, that is, the mode in which the doublet elements (vortex ring elements) vary most slowly in the spanwise direction.

Computed results for the lift variation during a heaving oscillation cycle of the wing with an amplitude of $h/c=0.10$ about a

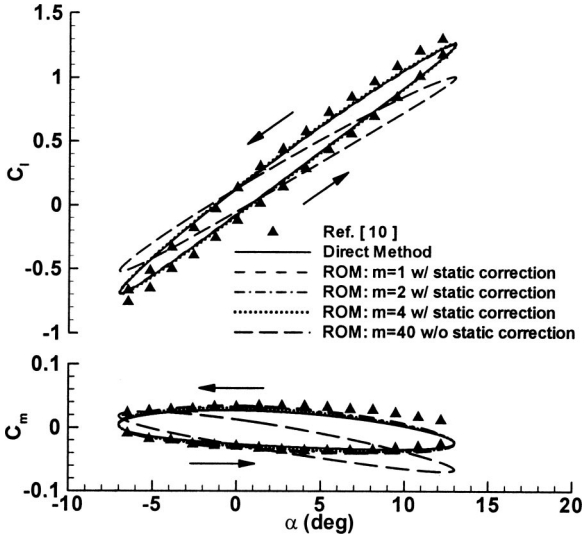

Fig. 3 Lift and pitching moment loops for the pitch oscillation of a NACA 0012 airfoil

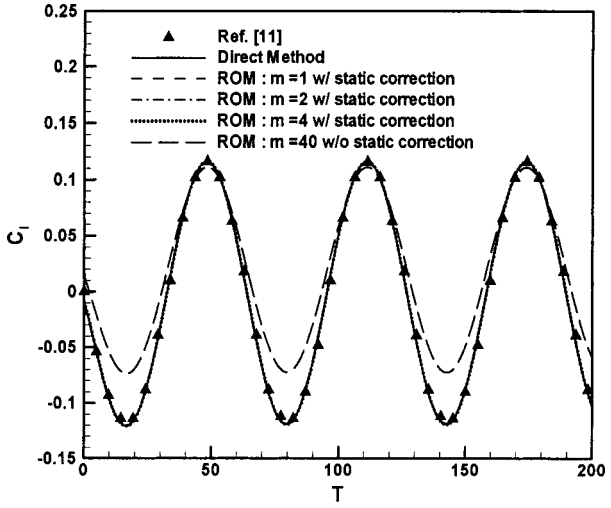

Fig. 4 Lift response versus time for a NACA 0012 airfoil at Mach 0.5 oscillating at ±1 degree about zero angle of attack with $k=0.10$

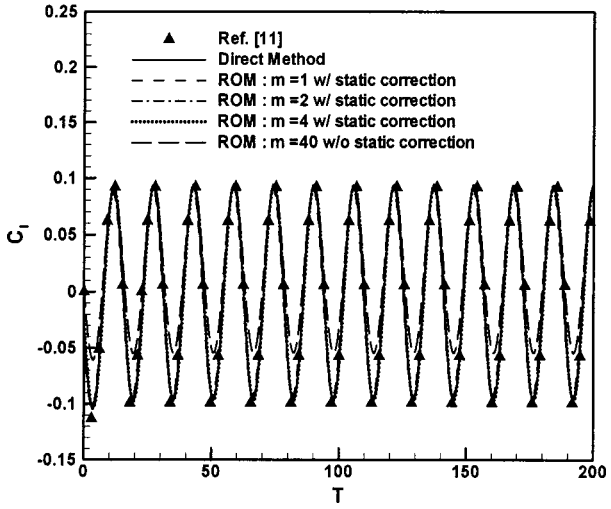

Fig. 5 Lift response vs time for a NACA 0012 airfoil at Mach 0.5 oscillating at ±1 degree about zero angle of attack with $k=0.40$

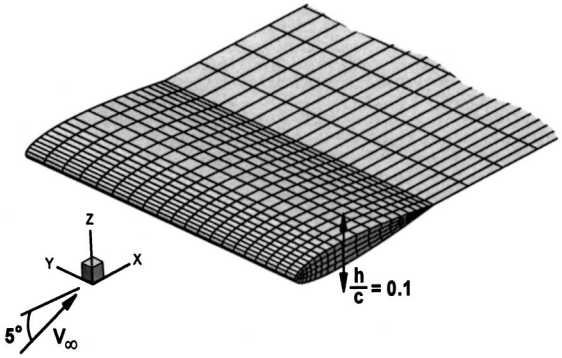

Fig. 6 Geometry of the three-dimensional wing and the wake in heaving oscillation (half of the wing is shown)

5-deg angle of attack with the reduced frequency $k=0.10$ are presented in Fig. 8. The results of the direct method are in excellent agreement with those of presented in Ref. [10]. Also, the figure shows reduced-order modeling results with 1, 2, and 4 eigenmodes with the static correction and reduced-order modeling results with 40 eigenmodes without static correction. As expected,

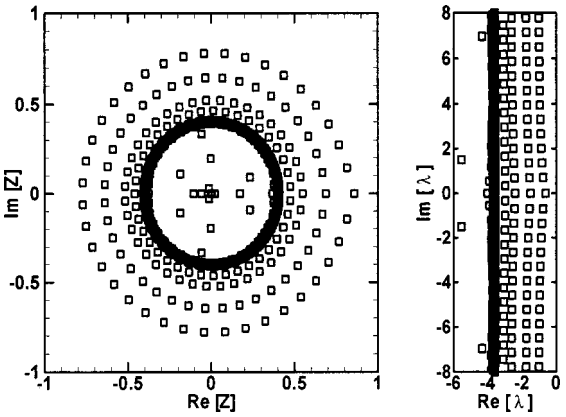

Fig. 7 Eigenvalues of boundary element model of unsteady flow about a rectangular wing with NACA 0012 section

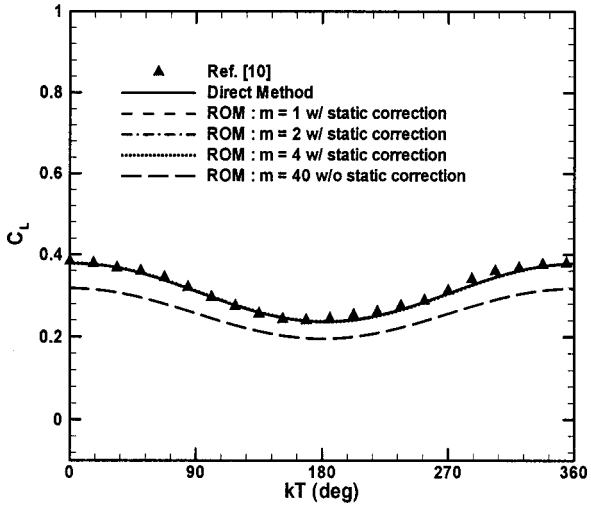

Fig. 8 Periodic lift variation during heaving oscillation with $k=0.10$, of a rectangular wing with NACA 0012 section

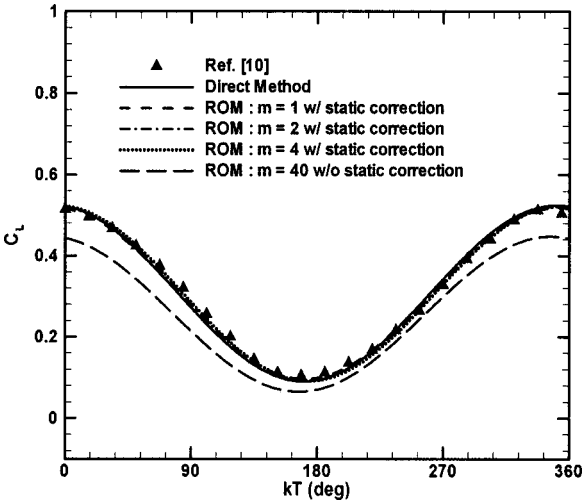

Fig. 9 Periodic lift variation during heaving oscillation with $k=0.30$, of a rectangular wing with NACA 0012 section

reduced-order modeling along with the static correction shows very good agreement with the direct method. The same results for the case with $k=0.30$ are shown in Fig. 9.

Wing-Body Configuration. To show the capability of reduced-order modeling using the boundary element method in unsteady flow analysis over complex configurations, a wing-body combination is considered as shown in Fig. 10. The wing-body combination oscillates in heaving mode with the reduced fre-

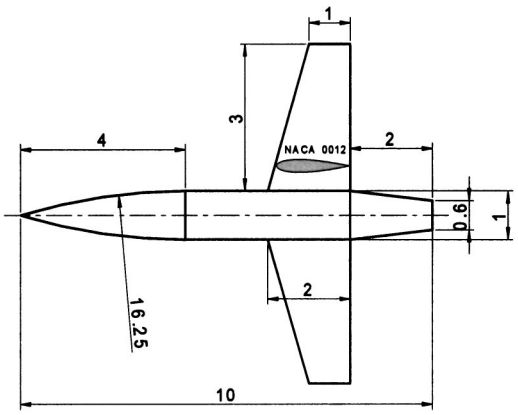

Fig. 10 Dimensions of the wing-body combination

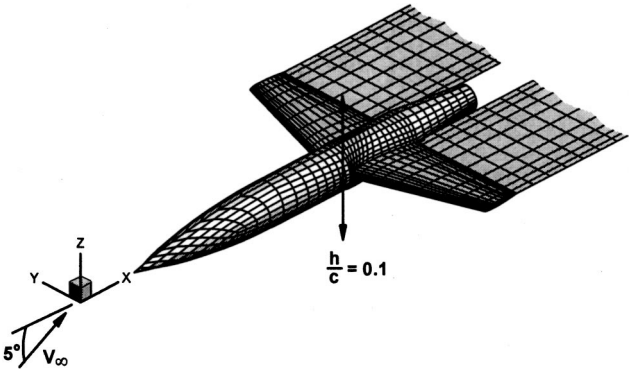

Fig. 11 Geometry of the wing-body combination and its wake in heaving oscillation

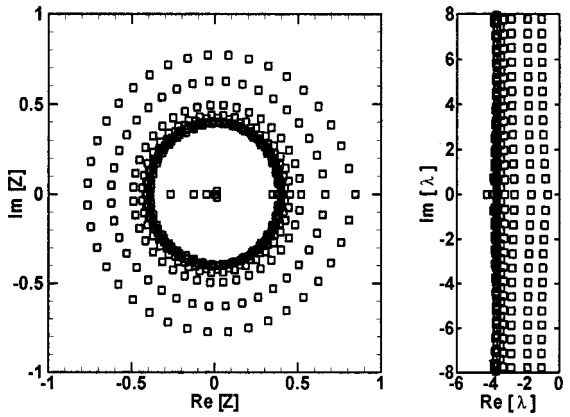

Fig. 12 Eigenvalues of boundary element model of unsteady flow about the wing-body configuration

quency, $k=0.30$, about a 5-deg angle of attack. Figure 11 shows computational mesh over the body and its wake. Because of symmetry, half of the wing-body and its wake is discretized. The surface of the wing-body combination is modeled using 894 elements. The wake length is taken to be ten times of the maximum chord length and is discretized using 10 and 40 elements in spanwise and streamwise directions, respectively.

Eigenvalues of the wing-body combinations in the *z*-plane and λ-plane are plotted in Fig. 12. Since ten elements are used in spanwise direction, ten branch cuts in the λ-plane are expected which are shown in Fig. 12. The eigenvalues spectrum is qualitatively similar to the three-dimensional wing, i.e., the branch farthest to the right corresponds to the first spanwise mode in which the doublet elements vary most slowly in the spanwise direction.

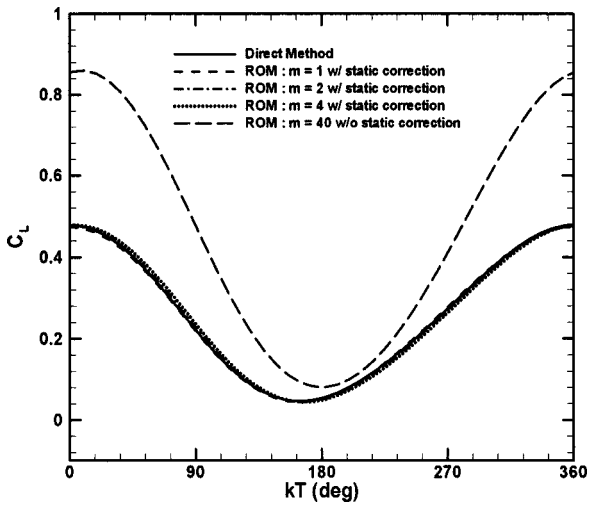

Fig. 13 Periodic lift variation during heaving oscillation with $k=0.30$, of the wing-body configuration

Computed results for the lift variation during a heaving oscillation cycle of the wing-body configuration with an amplitude of $h/c=0.10$ about a 5-deg angle of attack with the reduced frequency $k=0.30$ are presented in Fig. 13. The results of reduced-order modeling with 1, 2, and 4 eigenmodes with the static correction and with 40 eigenmodes without the static correction are compared with those of the direct method. As expected, reduced-order modeling along with the static correction shows very good agreement with the direct method which indicates the efficiency of the boundary element method used for reduced-order modeling of unsteady flows around complex configurations.

Conclusions

This study demonstrates that reduced-order models of unsteady flows in general three-dimensional cases can be constructed efficiently based on the boundary element method. The resulting eigensystem of unsteady flow over a three-dimensional configuration may be solved using well-known IMSL routines. The number of zero eigenvalues of an unsteady flow model based on the boundary element method is equal to the number of elements that lie on the body. Therefore, the maximum number of eigenvectors that may be used, is equal to the number of the wake elements. Hence, some of the eigenmodes which are equal to the body's elements behave exactly in quasi-static fashion and reduced-order modeling without the static correction cannot give satisfactory results even if the large number of eigenmodes is used. However, reduced-order modeling with the static correction based on the boundary element method can accurately predict the unsteady flow characteristics over complex configurations using just a few eigenmodes.

Acknowledgment

The authors would like to thank the University of Tehran for financial support of this research.

References

[1] Hall, K. C., 1994, "Eigenanalysis of Unsteady Flows About Airfoils, Cascades, and Wings," AIAA J., **32**, pp. 2426–2432.
[2] Romanowski, M. C., and Dowell, E. H., 1996, "Reduced Order Euler Equations for Unsteady Aerodynamic Flows: Numerical Techniques," AIAA Paper No. 96-0528.
[3] Florea, R., Hall, K. C., and Cizmas, P. G., 1998, "Reduced-Order Modeling of Unsteady Viscous Flow in a Compressor Cascade," AIAA J., **36**, pp. 1039–1048.
[4] Dowell, E. H., Hall, K. C., and Romanowski, M. C., 1997, "Eigenmode Analysis in Unsteady Aerodynamics: Reduced Order Models," Appl. Mech. Rev., **50**(6), pp. 371–385.
[5] IMSL Library Reference Manual, 1980, IMSL LIB-0008.
[6] Rajakumar, C., and Rogers, C. R., 1991, "The Lanczos Algorithm Applied to Unsymmetric Generalized Eigenvalue Problem," Int. J. Numer. Methods Eng., **32**, pp. 1009–1026.
[7] Katz, J., and Plotkin, A., 1991, *Low-Speed Aerodynamics from Wing Theory to Panel Methods*, McGraw-Hill, New York.
[8] Morino, L., Chen, L. T., and Susiu, E. O., 1975, "Steady and Oscillatory Subsonic and Supersonic Aerodynamics around Complex Configurations," AIAA J., **13**, pp. 368–374.
[9] Heeg, J., and Dowell, E. H., 1999, "Aerodynamic and Aeroelastic Insights Using Eigenanalysis," AIAA Paper No. 99-1473.
[10] Katz, J., and Maskew, B., 1988, "Unsteady Low-Speed Aerodynamic Model for Complete Aircraft Configurations," J. Aircr., **25**(4), pp. 302–310.
[11] Romanowski, M. C., 1995, "Using Fluid Eigenmodes to Develop Euler Based Reduced Order Unsteady Aerodynamic and Aeroelastic Models," PhD. thesis, Duke University, Durham, NC.

Effect of Gap Size on Tip Leakage Cavitation Inception, Associated Noise and Flow Structure

Shridhar Gopalan

Joseph Katz

Han L. Liu[1]

Department of Mechanical Engineering,
The Johns Hopkins University,
3400 N. Charles Street
Baltimore, MD 21218

This paper focuses on the onset of tip-leakage cavitation on a fixed hydrofoil. The objectives are to investigate the effect of gap size on the flow structure, conditions of cavitation inception, the associated bubble dynamics and cavitation noise. The same hydrofoil with three tip gap sizes of 12%, 28%, and 52% of the maximum tip thickness are studied. Controlled cavitation tests are performed after de-aerating the water in the tunnel and using electrolysis to generate cavitation nuclei. The experiments consist of simultaneously detecting cavitation inception using a 2000 fps digital camera (visual) and two accelerometers ("acoustic") mounted on the test section windows. Good agreement between these methods is achieved when the visual observations are performed carefully. To obtain the time-dependent noise spectra, portions of the signal containing cavitation noise are analyzed using Hilbert-Huang transforms. Rates of cavitation events as a function of the cavitation index (σ) for the three gap sizes are also measured. The cavitation inception index decreases with increasing gap sizes. The experiments demonstrate that high-amplitude noise spikes are generated when the bubbles are distorted and "shredded"—broken to several bubbles following their growth in the vortex core. Mere changes to bubble size and shape caused significantly lower noise. High-resolution particle image velocimetry (PIV) with a vector spacing of 180 μm is used to measure the flow, especially to capture the slender tip vortices where cavitation inception is observed. The instantaneous realizations are analyzed to obtain probability density functions of the circulation of the leakage vortex. The circulation decreases with increasing gap sizes and minimum pressure coefficients in the cores of these vortices are estimated using a Rankine model. The diameter of the vortex core varied between 540–720 μm. These coefficients show a very good agreement with the measured cavitation inception indices.
[DOI: 10.1115/1.1514496]

1 Introduction

Cavitation occurs in liquid flows when a nucleus (bubbles, particles, etc.) is captured in a region where the pressure is lower or equal to the vapor pressure (Arndt [1] and Brennen [2]). Such low-pressure regions could be at the cores of vortical structures that frequently occur in shear flows (Arndt [1], Katz and O'Hern [3], O'Hern [4], Ran and Katz [5], Belahadji et al. [6], and Gopalan et al. [7]). Experimental studies on tip vortex formation and resulting cavitation have been addressed, e.g., by Higuchi et al. [8], and Maines and Arndt [9] and a numerical study of steady-state tip vortex aimed at predicting the core pressure has been reported by Hsiao and Pauley [10]. Several papers in recent years have dealt with cavitation in tip leakage or tip clearance flows, i.e., cases where the wing tip is located near a solid boundary leaving only a narrow gap. A tip leakage vortex develops as a result of the clearance between the tip and the wall, which is prone to cavitation (Farrell and Billet [11] and Boulon et al. [12]). Farrell and Billet [11] examine the effect of gap size on tip leakage cavitation in a rotating turbomachine and find that for narrower gaps the cavitation inception indices decrease with increasing gap sizes. They also find a minimum in the cavitation inception index near $\lambda \approx 0.2$; λ being the ratio of tip gap size to the maximum tip thickness. Conversely, experiments performed by Boulon et al. [12] in a setup similar to the present study, i.e., no relative motion between the tip and the end wall, do not show a minimum in the cavitation inception index. This trend is consistent with the present observations and can be explained using a potential flow model, elaborated in Boulon et al. and discussed briefly in Section 4 of this paper. In Boulon et al. the hydrofoil is elliptical and has a NACA 16-020 cross section, a chord length of 0.12 m at root, a span of 0.18 m, and an aspect ratio of 3.8. The noticeable difference is that for gap sizes of 4 mm and smaller, Boulon et al. found attached cavitation on the tip of the hydrofoil along with tip vortex cavitation. For gap sizes higher than 4 mm, tip vortex cavitation is dominant. In our case we do not see attached cavitation at the measured cavitation indices. There is only tip leakage vortex cavitation.

The present paper provides high magnification, high-speed photographs of bubbles during cavitation in the tip leakage vortex along with simultaneous measurements of the resulting noise. The observations demonstrate clearly that high noise spikes occur when the bubbles break up in the vortex core. Mere oscillations in bubble size and shape cause significantly lower amplitude signals. Detailed measurements of the velocity and thus vorticity and circulation of the tip leakage vortex along with vortex core size are used for estimating the minimum pressure coefficients in the core. These coefficients compare well to the cavitation inception indices. The following are addressed: (i) cavitation inception measurements using visual and acoustic techniques, (ii) a comparison between the acoustic signal and the visual occurrence of cavitation, including a detailed spectral analysis of the signal, and (iii) the strength of the tip leakage vortex and the effect of gap size on the leakage flow characteristics. The same hydrofoil with three tip gap sizes of 0.6, 1.4, and 2.6 mm are studied, corresponding to $\lambda = 0.12$, 0.28, and 0.52, respectively.

[1]Formerly at the Naval Surface Warfare Center, West Bethesda, MD.

Contributed by the Fluids Engineering Division for publication in the JOURNAL OF FLUIDS ENGINEERING. Manuscript received by the Fluids Engineering Division March 21, 2002; revised manuscript received May 3, 2002. Associate Editor: G. E. Karniadakis.

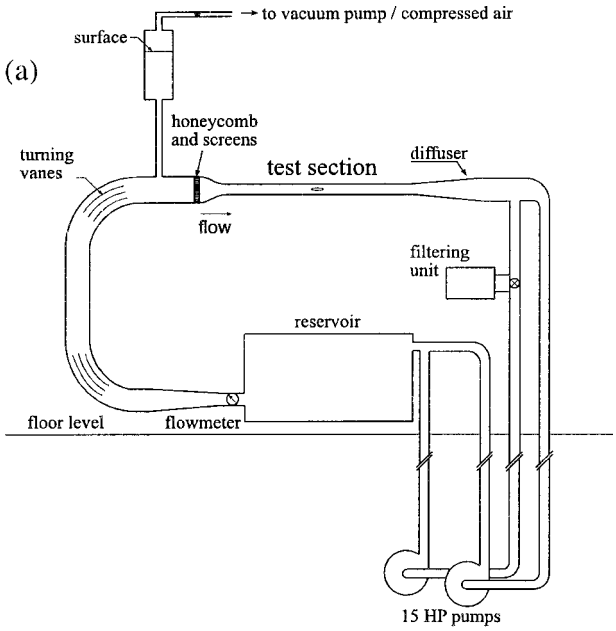

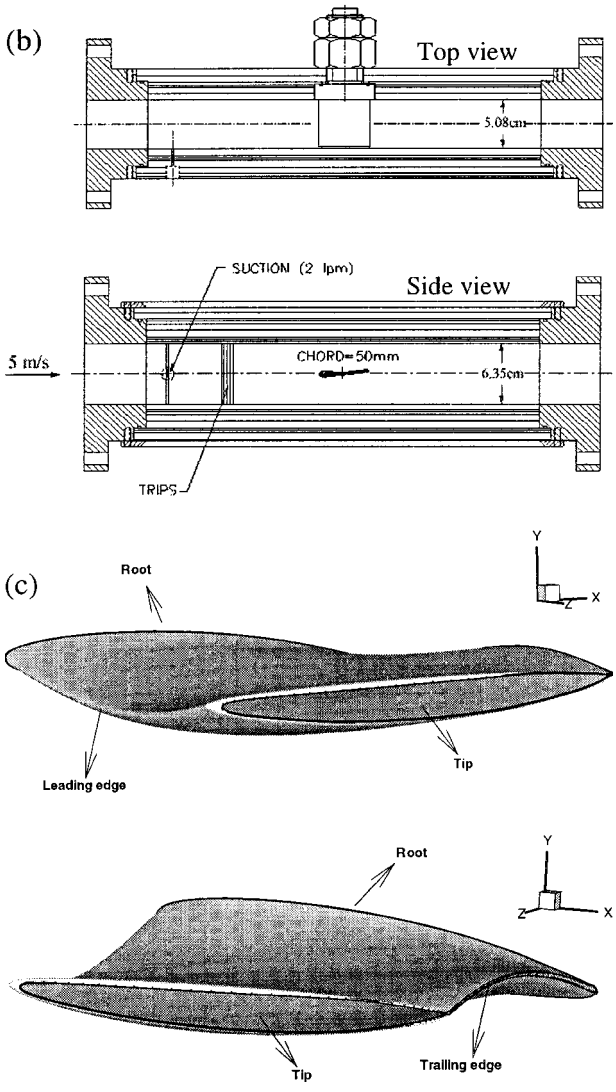

Fig. 1 (*a*) **Experimental facility,** (*b*) **close-up of test section,** (*c*) **two three-dimensional views of the hydrofoil, showing the geometry**

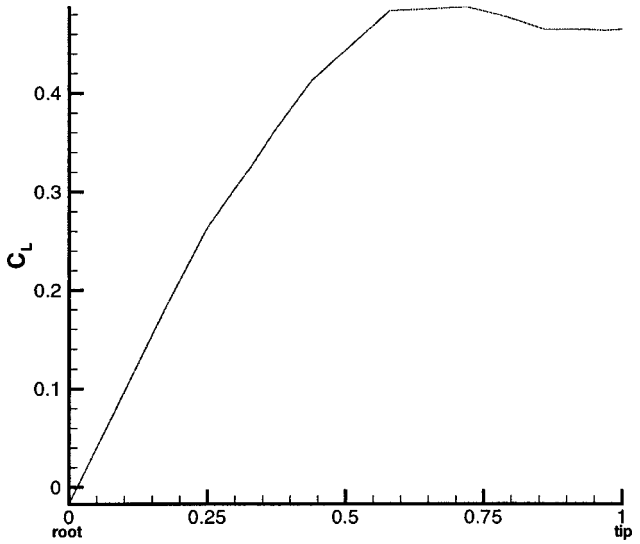

Fig. 2 Estimated spanwise lift distribution on the hydrofoil at 0 deg incidence

2 Experimental Setup and Procedure

The tests are performed in a specially designed water tunnel located at The Johns Hopkins University Fig. 1(*a*). The 6.35 $\times 5.08$ cm^2 test section has a minimum length of 41 cm and maximum entrance velocity of 13 m/s, although the present tests were performed at 5 m/s. The flow is driven by two 11 KW centrifugal pumps located 4 m below the test section to prevent pump cavitation. The facility has windows (made of optical grade lucite) on four sides to enable easy access for PIV measurements. A hydrofoil is attached to the side window and its tip has a small clearance with the opposite side window (Fig. 1(*b*)). The hydrofoil has a thickness to chord ratio of 0.1, constant chord of 50 mm, span of 50 mm, skew and rake is 0 and nonzero pitch and camber. Two three-dimensional views of the hydrofoil are shown in Fig. 1(*c*). The maximum tip thickness is 5 mm (at midchord) and the hydrofoil is loaded towards the tip. The estimated spanwise distribution of the lift coefficient at a 0 deg incidence angle is shown in Fig. 2. Lift coefficient values have been prescribed based on ''real

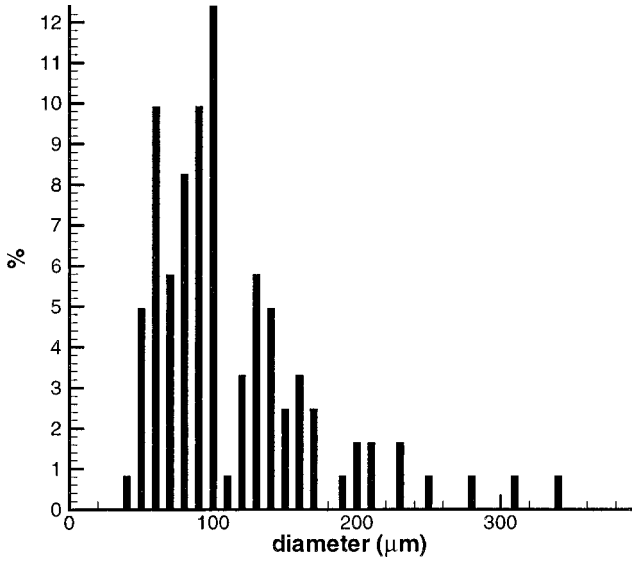

Fig. 3 Size distribution of cavitation nuclei measured upstream of the leading edge of the hydrofoil

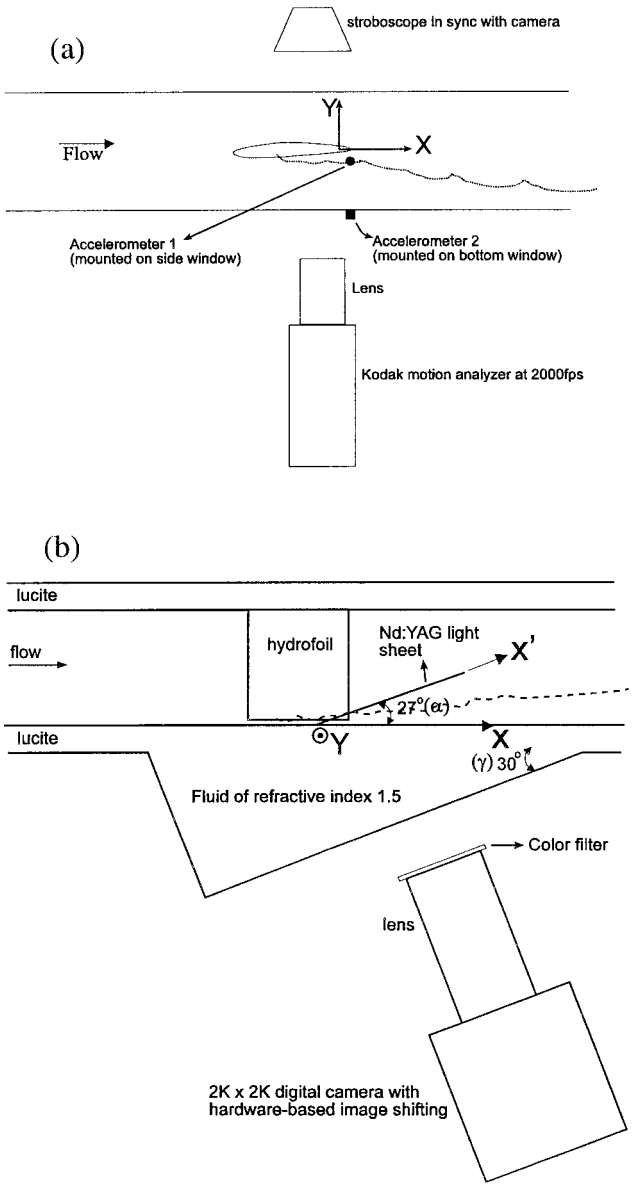

Fig. 4 (*a*) Setup for cavitation inception measurements. (*b*) Setup for PIV measurements in the plane *X′ Y*. Intersection of tip and TE corresponds to *Y*=0.

conditions'' and the hydrofoil has been designed thereafter using a viscous code at NSWC-Carderock (Chen [13], private communication). The tip clearance (or gap) size is varied by varying the thickness of the side window located next to the tip. Boundary layer suction followed by tripping is used on the wall near the tip as shown in Fig. 1(*b*) (side view) to generate a fully developed turbulent boundary layer on the wall. The boundary layer thickness at the hydrofoil location is estimated to be 2.7 mm, based on a flat-plate turbulent boundary layer with a thickness of trip height=0.5 mm at the trip location. Hence the tip gap sizes are 22.2%, 51.8%, and 96.3% of the wall boundary layer thickness.

The freestream velocity in the test-section is fixed at 5 m/s, which corresponds to a Reynolds number Re_c, based on chord, c equal to 2.5×10^5. Plots of cavitation index, σ versus the rate of cavitation events, r_c, where $\sigma=(P_0-P_v)/0.5\rho V^2$, P_0 is the ambient pressure in the test section, P_v is the vapor pressure, and V is the freestream velocity are obtained in nuclei controlled conditions. The cavitation index is regulated by varying the ambient pressure in the test chamber. The air content is reduced to about 3

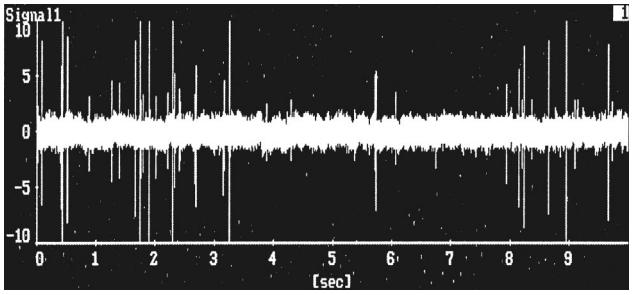

Fig. 5 A sample accelerometer signal showing several spikes caused as a result of cavitation

ppm by keeping the facility under vacuum for extended periods and the dissolved oxygen content measured using an oxygen meter. The cavitation nuclei are supplied by electrolysis using two vertical wires, located in the settling chamber upstream of the test section next to the honeycombs shown in Fig. 1(*a*). The bubble generation rate, approximately 2500/s can be controlled by varying the current through the electrodes. The nuclei size distribution generated by this setup is measured using silhouette photographs at high magnification (following the procedure described in Gopalan et al. [7]). As the distribution shown in Fig. 3 indicates, the bubble diameters vary between 50–250 μm with a median at approximately 100 μm.

Two accelerometers (PCB309A, made by PCB Piezotronics) with a resonant frequency of 120 kHz were used to detect cavitation events. As shown in Fig. 4(*a*), one sensor is attached to the side window and the other to the bottom window, both at the vicinity of the blade trailing edge. A high-speed camera (Kodak Ektapro EM Motion Analyzer, Model 1012) operating at 2000 fps is used to record images of the cavitating bubbles in the tip leakage vortex. The timing of the image acquisition is synchronized with the accelerometer signal. Careful comparisons, examples of which are shown in this paper, result in a good correlation between the physical appearance of the bubbles and the accelerometer signal. A Data Translation, 12 bit, A-D board capable of sampling rates up to 1 MHz is used for acquiring the accelerometer signals and the signal from the stroboscope. The data is acquired at 250 kHz/channel using LabView based software. Using an in-house code, the accelerometer signals are analyzed for counting the rate of cavitation events and for tagging the high-speed frames

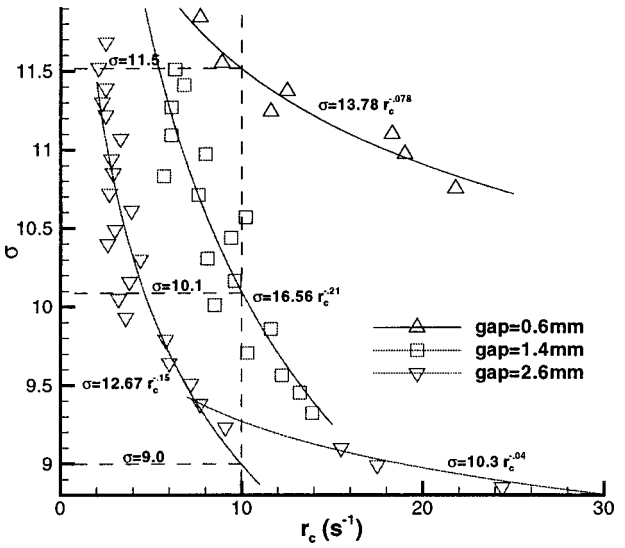

Fig. 6 Cavitation event rates as a function of the cavitation index σ, for three gap sizes

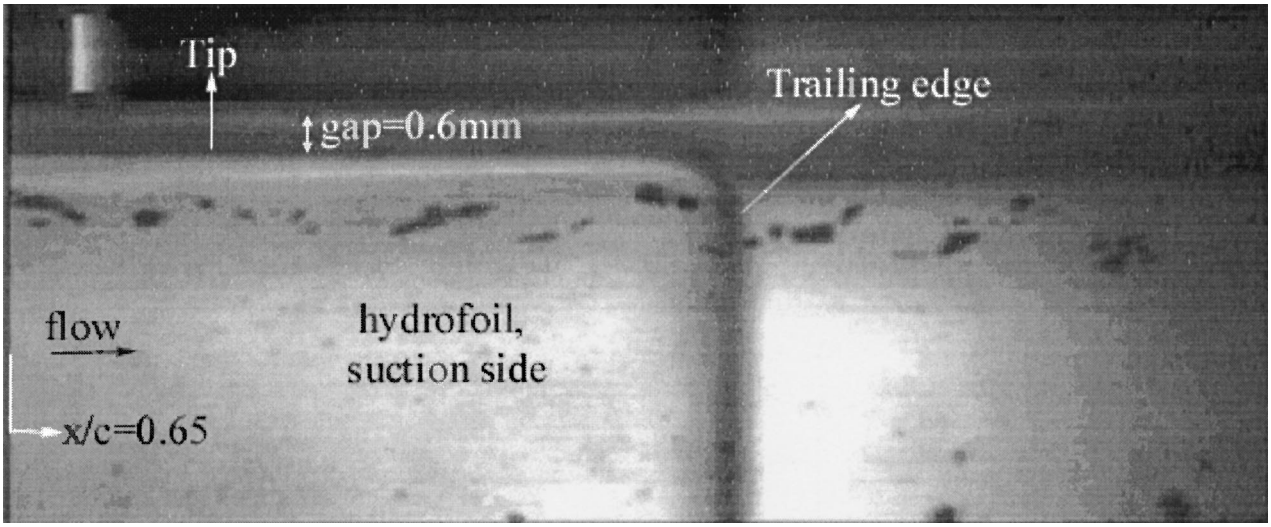

Fig. 7 Six consecutive frames, 1 ms apart, are superimposed to show the trajectory of the bubbly tip leakage vortex. The gap size in this example is 0.6 mm.

(example—Fig. 8(*b*)). Each data point in Fig. 6 is based on a 10 s long signal sampled at 250 kHz. The code used to count the cavitation events, first identifies points in the signal with amplitudes greater than 1.2 V and then searches for amplitudes $\geqslant$3.3 V in a time interval of 0.06 ms from the original point. If it finds such points it is counted as an event. In order to avoid counting the same event more than once, the program jumps 1.4 ms after finding an event and then continues.

PIV experiments are performed using a system described in Roth et al. [14] and Roth and Katz [15]. The light source is Nd:YAG laser and images are recorded using a $2K\times 2K$ pixel^2 digital camera with built in image shifting. Fluorescent particles are used as tracers and a filter in front of the camera lens filters out the incident green light (Sridhar and Katz [16] and Gopalan and Katz [17]). An inclined light sheet (Fig. 4(*b*)) is necessary to measure the circulation of the leakage vortices. When a sheet at an angle α is used in water bounded by material of different refractive index (lucite), a proper interface at an angle, γ, given by $\tan\gamma/\tan\alpha = n(\text{lucite})/n(\text{water})$ (where n is the refractive index) has to be created. As shown in Fig. 4(*b*), we use a triangular lucite canister attached to the side window and filled with Dow Corning 550 fluid, which has a refractive index of 1.5, i.e., the same as lucite. The images are first analyzed initially with a 64×64 pixel^2 interrogation window and a 32 pixel spacing. Then using the output of the first run as a ''guess input,'' the displacements are measured using 32×32 pixel^2 interrogation windows and 16 pixel vector spacing. This approach is feasible only when there is good particle seeding (4–5 per window) in a 32×32 pixel^2 window. Under these conditions, the uncertainty in velocity measurements is about 0.4 pixels as discussed in detail in Roth et al. [14]. This procedure enables to obtain high-resolution velocity fields with vector spacing of 180 μm. Such measurements are imperative since tip vortex core diameters are less than 1 mm. Vorticity is calculated from the velocity using a second order finite difference scheme. The error in the vorticity, based on the characteristic vorticity is approximately 25%.

3 Cavitation Event Rates and Cavitation Noise

A sample accelerometer signal showing noise spikes caused by cavitation is shown in Fig. 5. Without nuclei seeding (i.e. bubble generation) the number of cavitation events for a 10 s period at this cavitation index decreases from 50 to 1. The accelerometer signals are analyzed to obtain plots of cavitation index versus rate of cavitation events, r_c, for the three gap sizes. The results (Fig. 6) show that for all three cases the event rates increase with decreasing σ and with decreasing gap sizes. As an example at 10 events/s, σ for the 0.6 mm gap is 11.5 as compared to 10.1 for the 1.4 mm gap and 9.0 for the 2.6 mm gap. The slope of the 0.6 mm gap is also quite different than those of the 1.4 and 2.6 mm gaps. Since all the experiments are performed with similar nuclei distributions, the substantial differences in event rate indicates that the probability of finding low-pressure regions decreases with increasing gap size. For the 2.6 mm gap at $r_c > 14$, the curve flattens out. This trend occurs due to the increased concentration of nuclei resulting from prior cavitation events, a self-feeding phenomenon. Figure 6 also contains equations of power fit curves for the three gaps.

Farrell and Billet [11], for a rotating turbomachine, have observed a minimum in the cavitation inception index as a function of the gap size (at $\lambda \sim 0.2$), while Boulon et al. (with a fixed wing) do not, similar to our results. Several features of a tip leakage flow in a rotating turbomachine don't occur in this study (and that of Boulon et al.)—the motion of the tip relative to the end wall, effect of centrifugal forces, and unloading of the tip (ours is intentionally loaded). These differences most likely have a significant impact on the flow structure which may explain why some investigators observe a minimum in cavitation index while some do not. Another related issue is the interpretation of the cavitation inception index and the event rates. Bubbles with diameters of 100 μm require little tension to initiate cavitation, thus the bubble size is intentionally not a critical issue in the present study. Also, generation of 2500 bubbles per second makes cavitation inception less sensitive to bubble populations. However, being a very turbulent flow—a vortex embedded in a boundary layer, infrequent cavitation events (e.g., less than 2 per second) are a result of ''extreme'' flow conditions and are not typical of the flow. With increasing events rate a trend can be correctly identified. At least for relatively high σ, the slope of the cavitation event rate curve indicates the distribution of points in the flow with pressure lower than that indicated by the cavitation index. Thus, the slope of the cavitation event rate curve is important in addition to its absolute values.

Figure 7 shows the trajectory of a tip leakage vortex for a gap of 0.6 mm, visualized by cavitating bubbles and superposing six consecutive frames recorded at 1000 fps. The helical shape of the vortex trajectory is clearly evident. Three samples of high-speed image series at time intervals of 0.5 ms and the associated accel-

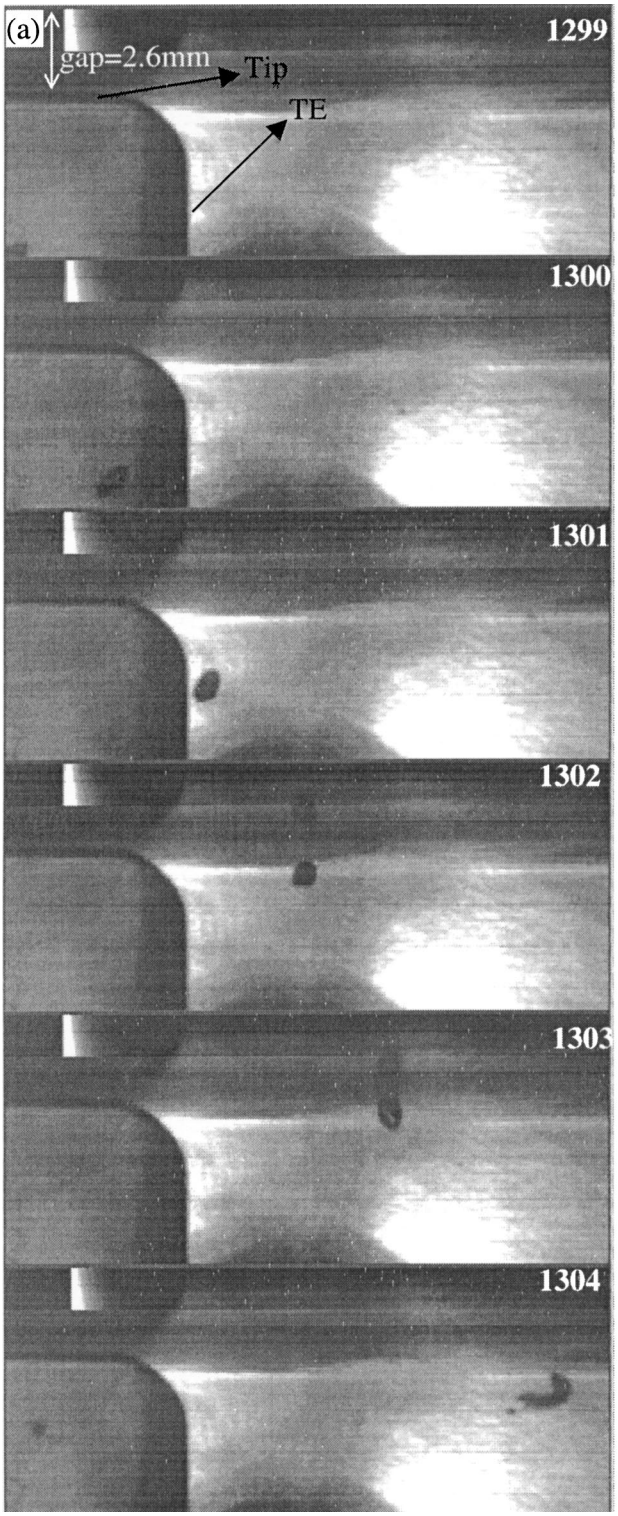

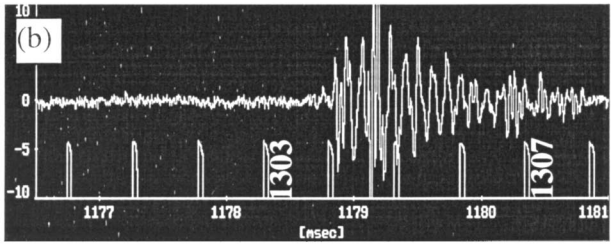

Table 1

Frames	RMS	Frequency peak kHz
1300-1301	0.3	-
1301-1302	0.3	-
1302-1303	0.4	-
1303-1304	4.65	23-28
1304-1305	2.88	5-8
1305-1306	1.54	-
1306-1307	0.94	-
1307-1308	0.38	-

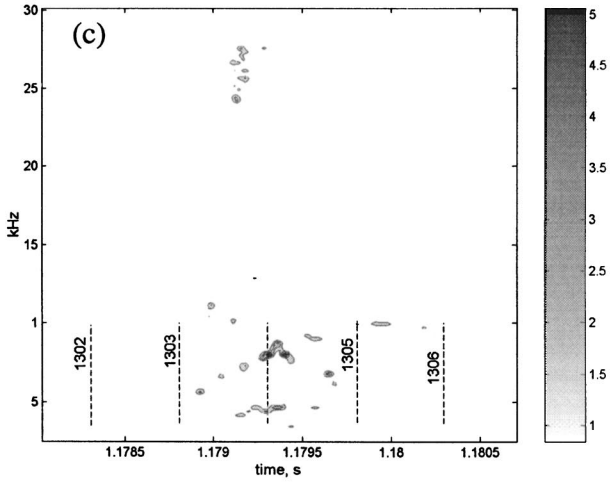

Fig. 8 (*a*) **A high-speed series (frames 1299–1304) at 2000 fps (gap size, 2.6 mm). Flow is from left to right with suction surface, tip and trailing edge (TE) visible ($\sigma=10$). (*b*) Corresponding accelerometer and strobe signals (indicated by vertical bars). (*c*) Hilbert-Huang spectrum of the accelerometer signal. Frame timings are indicated by dashed lines. Table 1 is included in Fig. 8.**

erometer signals are presented in Figs. 8, 9, and 10 (top views). We have carefully examined numerous such matches between ''acoustically'' sensed cavitation and visually observed cavitation. Figure 8 is a high-speed image series for the 2.6 mm gap. Cavitation noise starts at frame 1303 and continues on till frame 1307 (Fig. 8(*b*)). The highest amplitude noise occurs between frame 1303–1304, where the bubble becomes highly distorted and fragmented. Observe that the bubble migrates towards the tip indicating the existence of secondary flows. As will be discussed shortly multiple flow structures exist only in the case of the wider gap. Table 1 shows the RMS values of the signal between consecutive frames. Clearly, the highest RMS values (an order of magnitude

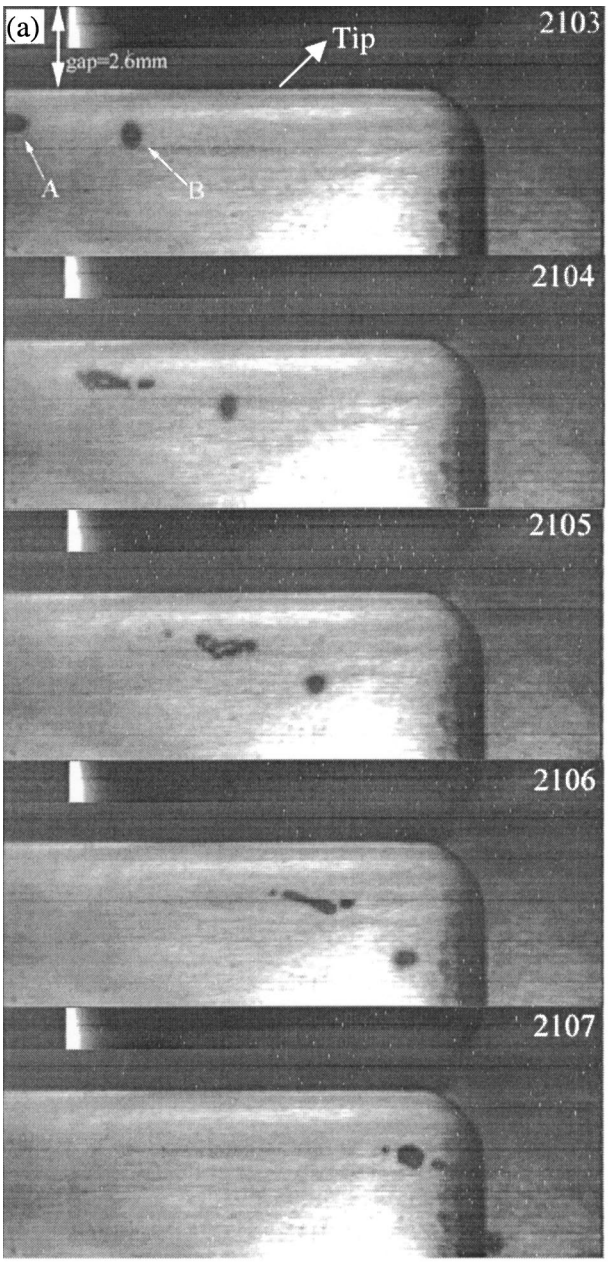

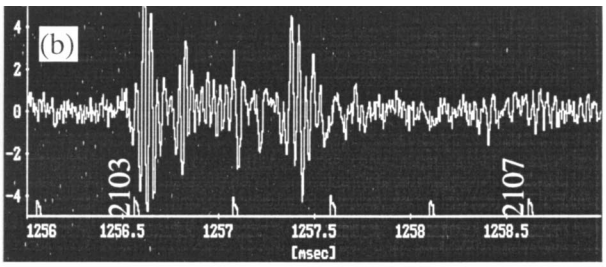

Table 2

Frame numbers	RMS	Frequency peak kHz
2102-2103	0.41	-
2103-2104	1.75	25-28
2104-2105	1.58	23
2105-2106	0.47	-

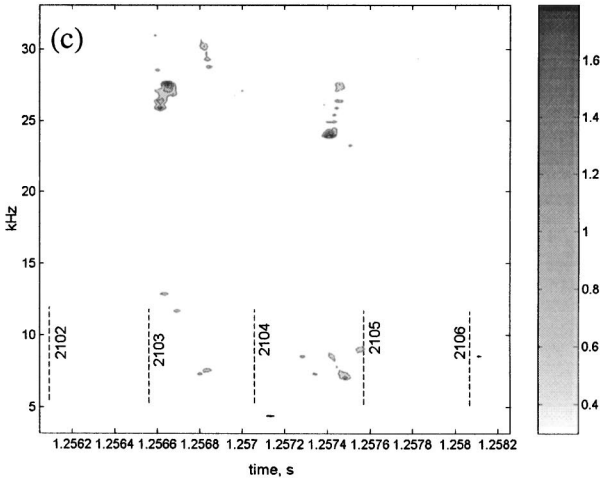

Fig. 9 (*a*) A high-speed series (frames 2103–2107) at 2000 fps (gap size, 2.6 mm). Flow is from left to right with suction surface, tip and trailing edge visible ($\sigma=10$). (*b*) Corresponding accelerometer and strobe signals (indicated by vertical bars at the bottom). (*c*) Hilbert-Huang spectrum of the accelerometer signal. Frame timings are indicated by dashed lines. Table 2 is included in Fig. 9.

higher) are observed between frames 1303–1304 and then they drop to the background levels (0.3) in frames 1307–1308. The Hilbert-Huang ''amplitude'' spectrum for this signal (HHS) (procedures described in Huang et al. [18]) is shown in Fig. 8(*c*) and identifies the spectral peaks associated with cavitation as a function of time. A commercially available software (Princeton Satellite Systems) based on N. E. Huang's code is used for the analysis. The frequencies are included in Table 1.

Figure 9(*a*) shows another high-speed image series with significant noise emission in frames 2103–2105 (Fig. 9(*b*)). Bubble B is out of focus, is not in the plane of the leakage vortex, and simply travels with the freestream, while bubble A cavitates—undergoes considerable growth, distortion, and fragmentation in frames 2103–2105. In frames 2106–2107, the larger part of bubble A begins to shrink and noise is emitted but of considerably lower amplitude. Table 2 summarizes the RMS values and spectral peaks, for this example. High RMS values are observed in frames 2103–2104 and 2104–2105 and the frequencies involved in this cavitation process are extracted from the HHS in Fig. 9(*c*). In Fig. 10(*a*), high-amplitude cavitation noise is emitted between frames 1495–1496. At this time bubble C is fragmented to three elongated bubbles. Bubble D undergoes abrupt elongation in frame 1497, emitting further noise. Bubble E emerges around the tip in frame 1496 and is also seen in 1497. The highest noise spike occurs as bubble C is fragmented and a second spike at a slightly lower amplitude appears as bubble D is elongated and deformed.

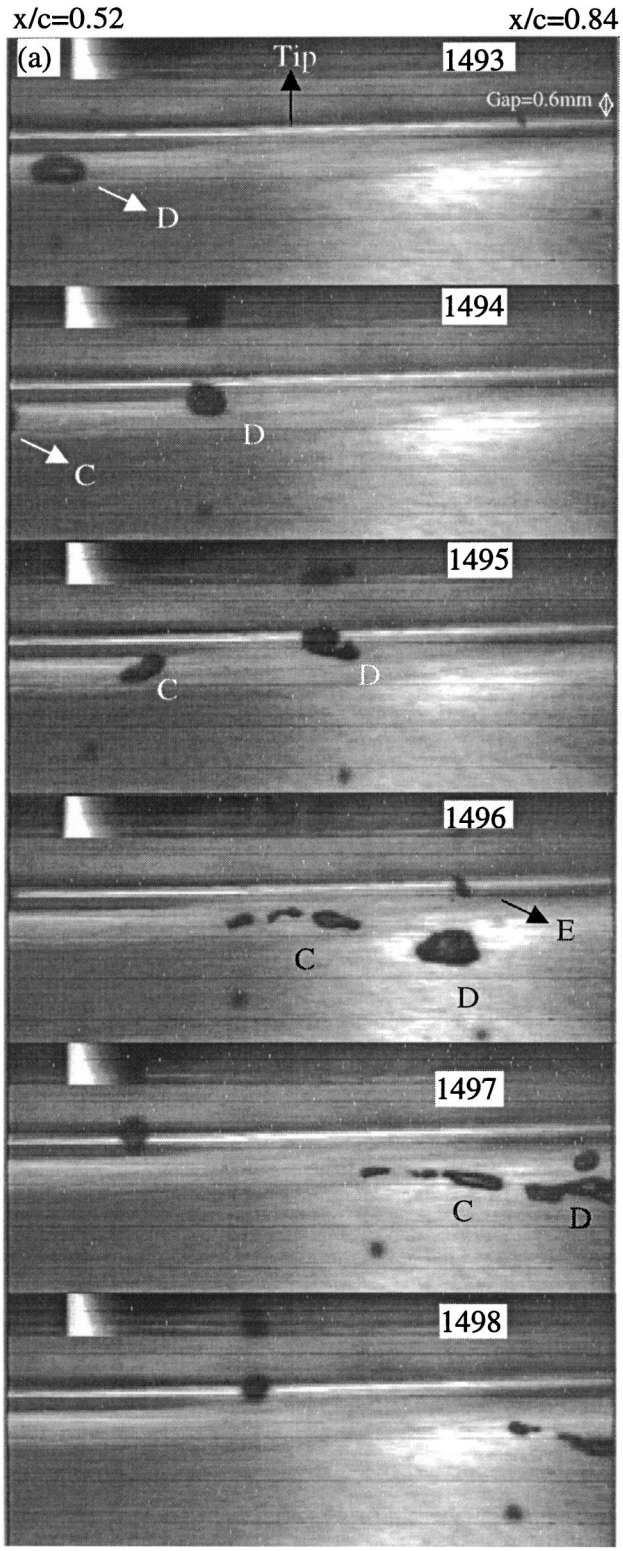

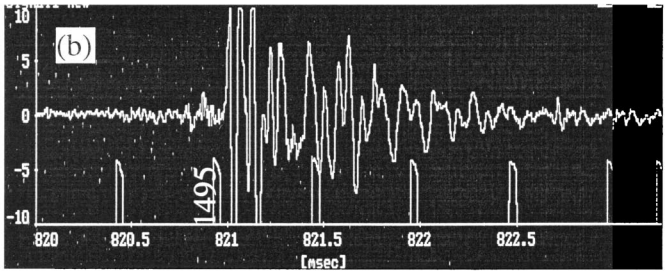

Table 3

Frame numbers	RMS	Frequency peak kHz
1493 -1494	0.21	-
1494 -1495	0.533	-
1495 -1496	5.34	6-8 and 17-20
1496 -1497	3.2	5-6 and 14
1497 -1498	1.25	-
1498 -1499	0.505	-

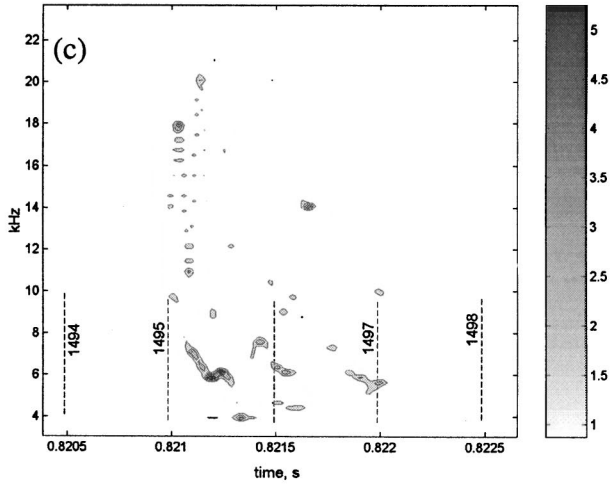

Fig. 10 (*a*) **A high-speed series (frames 1493–1498) at 2000 fps (gap size, 0.6 mm). Flow is from left to right with suction surface and tip visible ($\sigma=10$). (*b*) Corresponding accelerometer and strobe signals (indicated by vertical bars). (*c*) Hilbert-Huang spectrum of the accelerometer signal. Frame timings are indicated by dashed lines. Table 3 is included in Fig. 10.**

Note that mere deformation of bubbles D & C in frames 1493–1495 results in significantly lower noise levels compared to the ones resulting from fragmentation in the later frames. Table 3 summarizes the RMS values and spectral peaks in this example and Fig. 10(*c*) shows the HHS. Very high RMS values (more than 20 times the level with no cavitation event) are observed in frames 1495–1496 where the highest cavitation activity is observed. One can note from the HHS that the characteristic frequencies involved in these cavitation processes are 20–28 kHz and 5–8 kHz. We have examined numerous such data series. They are all con-

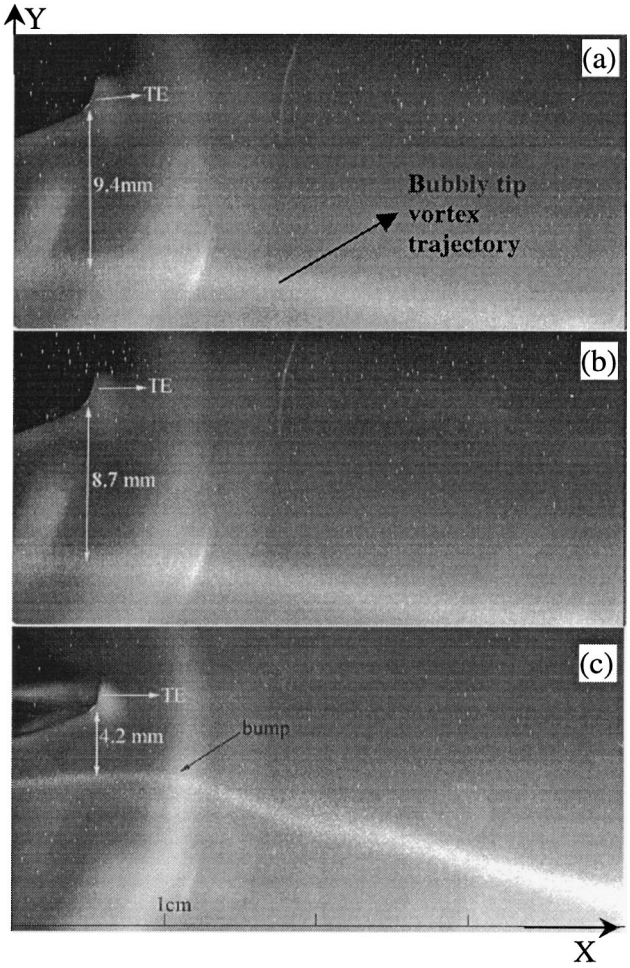

Fig. 11 A 0.25 s long exposure showing the trajectory of the bubbly tip leakage vortex as seen in a side view (Fig. 1(*b*)), for gaps of (*a*) 0.6 mm; (*b*) 1.4 mm; (*c*) 2.6 mm. Flow is from left to right. The hydrofoil with its trailing edge and tip is visible on the left edge of the images.

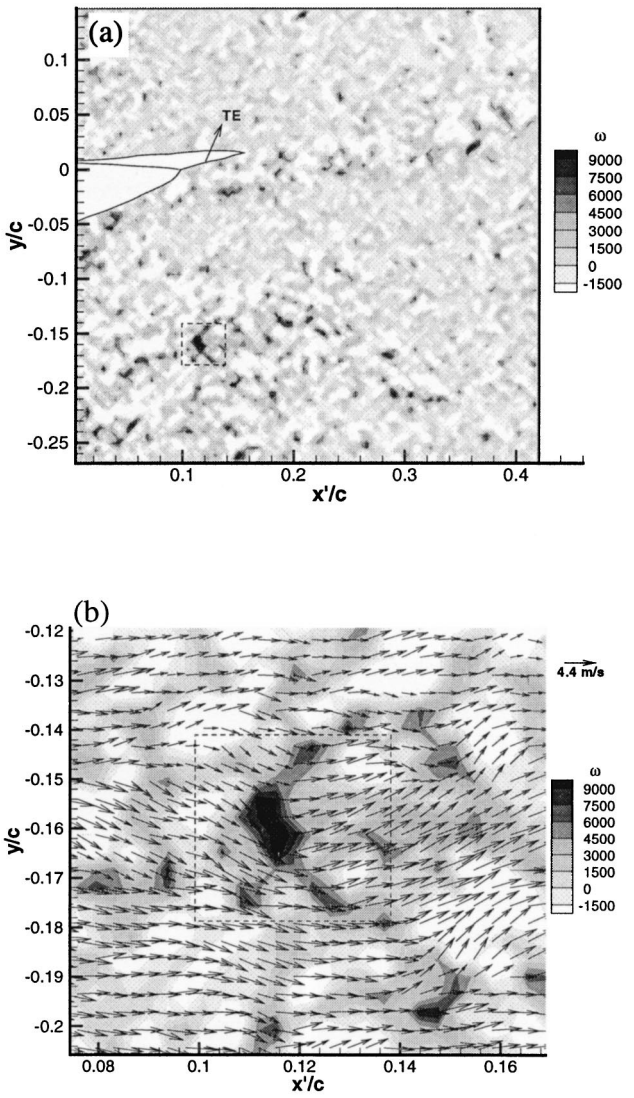

Fig. 12 Sample instantaneous vorticity (*a*, *c*, and *e*) and their "zoomed in" counterparts (*b*, *d*, and *f*) with instantaneous velocity in the plane $x'y$ for gap sizes of 0.6, 1.4, and 2.6 mm, respectively. The dashed boxes in the two views represent the same area.

sistent in showing that high-amplitude noise is associated with substantial distortion and fragmentation of bubbles. Merely changes in shape or volume of the bubble generate substantially weaker noise signals. The differences in bubble size and noise signals (i.e., the frequency content and amplitude) are *not* characteristic to their respective gap sizes, i.e., bubbles of various sizes appeared in all gap sizes.

Figure 11 shows extended exposure images of the trajectory of the *bubbly* tip leakage vortex as seen in a side view for the three gap sizes. The following observations can be made: (a) the vortex trace becomes closer (vertical distance) to the hydrofoil as the gap size is increased; (b) the trajectories in the 0.6 and 1.4 mm gaps are continuous and do not show a *bump*, i.e., a change in slope of the vortex trace that is clearly evident in the case of the 2.6 mm gap (Fig. 11(*c*)); and (c) it is possible that the cause of this bump is the interaction (merging) of multiple vortices. Note also the outward trajectory of the bubbles in Fig. 8, this motion is most likely associated with this complex flow structure.

4 Circulation of the Tip Leakage Vortex

Figures 12(*a*)–(*f*) show sample instantaneous vorticity and velocity, in the inclined plane ($x'y$, Fig. 4(*b*)) with a vector spacing of 180 μm. Figures 12(*b*), (*d*), and (*f*) are the "zoomed in" counterparts of Figs. 12(*a*), (*c*), and (*e*) that correspond to gap sizes of 0.6, 1.4, and 2.6 mm, respectively. A section of the tip leakage vortex can be seen within the dashed boxes for each of the gap size. The object on the left in these maps is the hydrofoil with portions of the trailing edge and tip visible. Since the local flow is generated by an interaction of a wing tip with a turbulent boundary layer, it is not surprising that instantaneous realizations contain multiple vorticity peaks. However, unlike the tip leakage vortex all the others are intermittent and appear in different locations at different images. The tip vortex peak appears consistently although its exact location varies slightly, which is vortex meandering. Furthermore, clearly the tip vortex cores have substantially higher overall circulation. Also, just below the hydrofoil (Fig. 12(*a*) and (*c*) only), we can see a trail of vortical structures that are weaker than the primary leakage vortex. These secondary vortices are similar to those seen by Farrell and Billet [11]. Figure 12(*c*) for the 2.6 mm gap shows a vortex core much closer to the hydrofoil as expected from Fig. 11(*c*).

We have analyzed 70 instantaneous realizations for the 0.6 mm clearance and 65 for the 1.4 mm and 2.6 mm clearances. The regions with peak vorticity where the tip leakage vortices dissect the sheet were selected and regions with vorticity higher than 500 1/s considered to be part of the vortex core. The circulation was

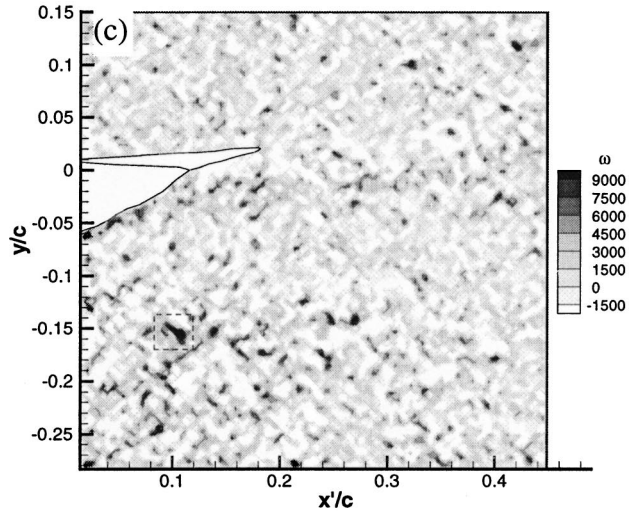

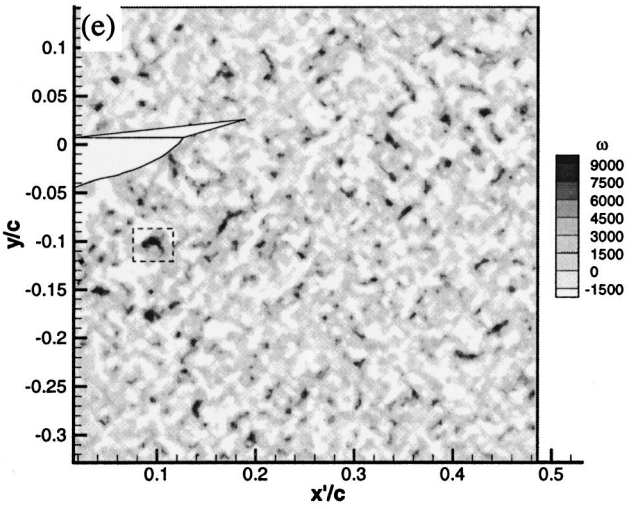

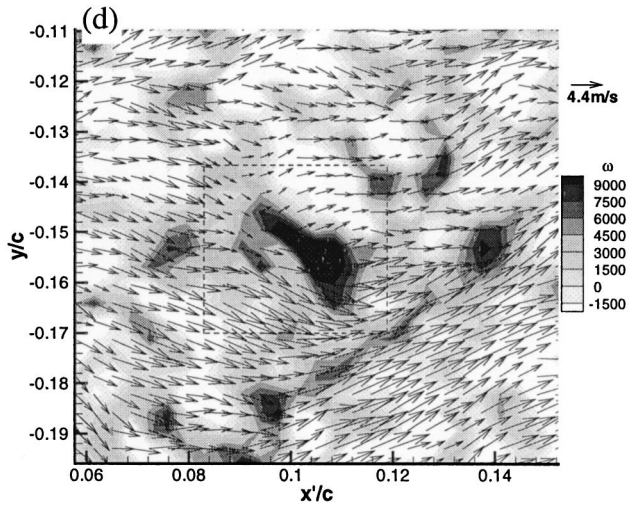

Fig. 12 (***continued***)

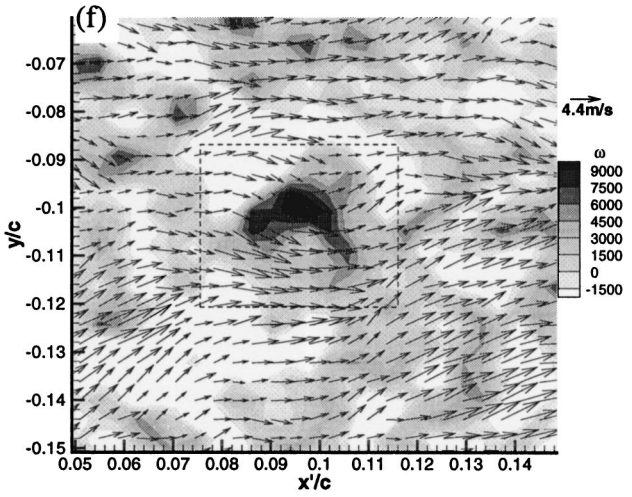

Fig. 12 (***continued***)

computed from $\Gamma=\Sigma\omega_i dA_i$, where ω is the vorticity in an elemental area $dA(=180\times180\ \mu m^2)$. The error in the circulation of the vortex based on a mean value is approximately 20%. Probability density histograms of the measured circulation normalized by the freestream velocity and chord length are presented in Fig. 13. It is evident that the characteristic vortex strength decreases as the gap size increases. Table 4 shows the mean and standard deviation of the tip vortex strength. The mean circulation around the foil deduced from Fig. 2 (an increment of 0.1 has been added to C_1 for 1 deg incidence) is $0.23Vc$, which is 3.3 to 5 times the mean vortex strengths for the 0.6–2.6 mm tip gaps, respectively.

Figure 13 also shows the estimated pressure coefficients ($C_{p\,\min}$) at the center of a Rankine vortex, $C_{p\,\min}=-2/\pi^2(\Gamma/Vd)^2$ where d is the diameter of the vortex core. The vorticity distributions show that d mostly varies between 3–4 vector spacings (i.e., 540–720 μm). No significant differences in the core sizes have been seen in the three gap sizes, although this statement is greatly affected by the ''coarse'' resolution. Consequently, we show the magnitudes of $C_{p\,\min}$ for $d=540\ \mu$m and 720 μm as a function of Γ. Values of $C_{p\,\min}$, for a core diameter of 540 μm, corresponding to the mean vortex circulation and up to an additional three standard deviation levels are presented in Table 4. As

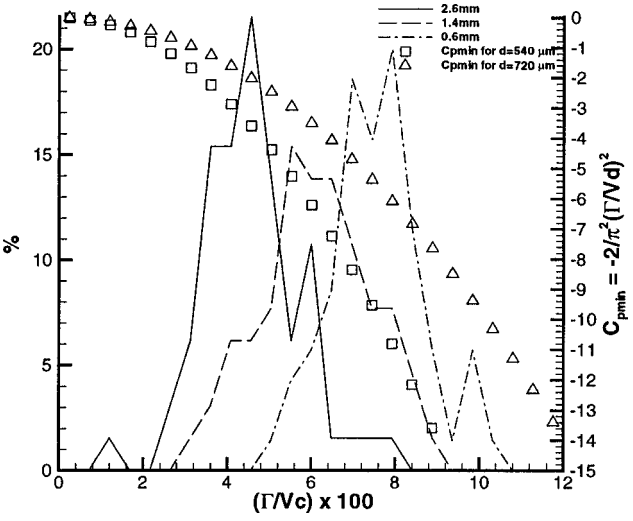

Fig. 13 Probability density histograms of circulation in the tip leakage vortex for the three gap sizes and corresponding minimum pressure coefficients.

Table 4

Gap Size, mm (λ)	0.6 (0.12)	1.4 (0.28)	2.6 (0.52)
Mean vortex strength, $(\Gamma/Vc)\times 100$, Γ_m	7.56	6.12	4.59
Standard deviation, Γ_s	1.12	1.33	1.175
$C_{p\ \min}$ for Γ_m, ($d=540\ \mu$m/720 μm)	−10/−5.5	−6.5/−3.7	−3/−1.8
$C_{p\ \min}$ for $\Gamma_m+\Gamma_s$, ($d=540\ \mu$m/720 μm)	−13/−7.3	−9.5/−5.5	−5.7/−3.2
$C_{p\ \min}$ for $\Gamma_m+2\Gamma_s$, ($d=540\ \mu$m/720 μm)	−16.5/−9.3	−13.2/−7.5	−8.3/−4.8
$C_{p\ \min}$ for $\Gamma_m+3\Gamma_s$, ($d=540\ \mu$m/720 μm)			−11.3/−6.3
Cavitation inception index from Fig. 6	11.5	10.1	9.0

is evident these $C_{p\ \min}$ estimates are consistent with the corresponding values of σ in Fig. 6. For the 2.6 mm gap, three standard deviation levels are required to match the inception level cavitation index that explains the steep slope of the curve in Fig. 6, compared to the trends in the smaller gaps.

The locations of the vortex cores in all the instantaneous realizations (points of maximum vorticity in the cross section of the vortex) are shown in Fig. 14(*a*)–(*c*) for the three clearances. All show substantial meandering over ranges that are much larger than the core size. The meandering increases with gap size. Even in the 0.6 mm case where it is confined to a region with diameter of 3.7 mm (in the $x'y$-plane), the meandering range is 7.4% of the chordlength. The vertical distance of the cores from the trailing edge decreases as the gap size increases. On an average, this distance is 9.3, 8.75, and 5 mm, i.e., 18.6%, 17.5%, and 10% of the chord length for the 0.6, 1.4, and 2.6 mm gap sizes, respectively. These results agree with the vortex traces in Fig. 11. Similar trends have been observed by Boulon et al. [12] who explain this trend using a potential flow model. A vortex near a wall has an ''image'' that causes an induced velocity directed from the pressure side to the suction side (downward in this case). With decreasing gaps the induced velocity increases, increasing as a result the *y*-distance of the vortex from the hydrofoil. The higher induced velocity also increases the effective incidence angle, which would in turn increase the lift.

5 Conclusion

Tip leakage cavitation is studied in detail on a fixed hydrofoil with three tip gap sizes of $\lambda = 0.12$, 0.28, and 0.52. The cavitation event rates decrease with increasing gap size. One of the main findings of this paper is the relationship between visual appearance of cavitation and the amplitude of the noise signals, i.e., what really causes high cavitation noise? High-amplitude cavitation noise is observed only when bubbles get highly distorted and fragmented. Much weaker signals (by an order of magnitude) are observed when the bubbles merely change shape or size. Cavitation noise is consistently observed in the 20–28 kHz and 5–8 kHz range. High-resolution PIV data are used for measuring the circulation and estimating the size and location of the tip leakage vortex. One needs even better resolution to identify the correct size of such vortex cores, but the results show a core size ranging from 540 μm–720 μm. The vortex strength decrease with increasing gap sizes. Minimum pressure coefficients calculated using a Rankine vortex model and the measured strengths and core diameters, lead to results that are consistent with the measured cavitation indices. The tip leakage vortex trajectory moves closer to the hydrofoil as the clearance is increased. Meandering of the vortex core is substantial in all cases and increases with increasing clearances.

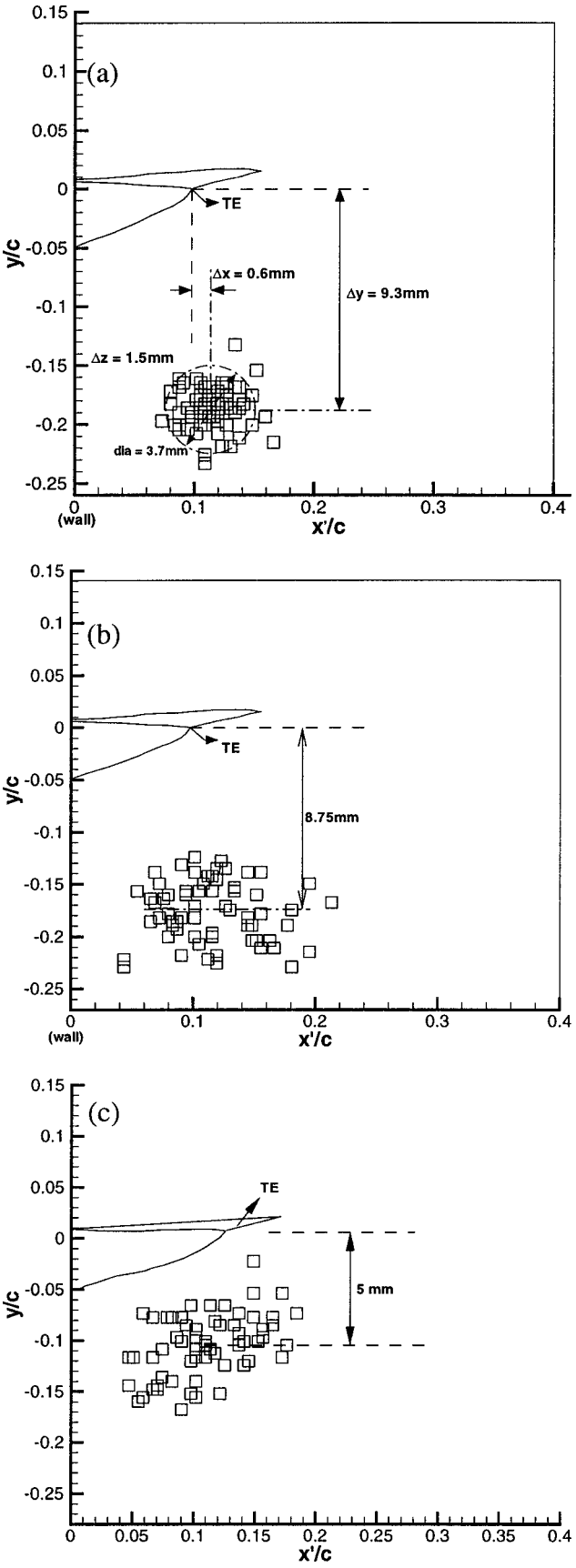

Fig. 14 Locations of the tip leakage vortex cores in the plane $x'y$ for gap sizes of (*a*) 0.6 mm (*b*) 1.4 mm and (*c*) 2.6 mm.

Acknowledgments

This project has been graciously supported by the Naval Surface Warfare Center–Carderock Division. The authors would like to thank Dr. B. Chen, Mr. Y. Ronzhes, Mr. Y. C. Chow, Mr. B. McFadden, Dr. E. Malkiel, and Dr. J. Karni for their contributions.

References

[1] Arndt, R. E. A., 1981, ''Cavitation in Fluid Machinery and Hydraulic Structures,'' Annu. Rev. Fluid Mech., **13**, pp. 273–328.
[2] Brennen, C. E., 1995, *Cavitation and Bubble Dynamics*, Oxford University Press, Oxford, UK.
[3] Katz, J., and O'hern, T. J., 1986, ''Cavitation in Large-Scale Shear Flows,'' ASME J. Fluids Eng., **108**, pp. 373–376.
[4] O'hern, T. J., 1990, ''An Experimental Investigation of Turbulent Shear Flow Cavitation,'' J. Fluid Mech., **215**, pp. 365–391.
[5] Ran, B., and Katz, J., 1991, ''The Response of Microscopic Bubbles to Sudden Changes in Ambient Pressure,'' J. Fluid Mech., **224**, pp. 91–115.
[6] Belahadji, B., Franc, J. P., and Michel, J. M., 1995, ''Cavitation in the Rotational Structures of a Turbulent Wake,'' J. Fluid Mech., **287**, pp. 383–403.
[7] Gopalan, S., Katz, J., and Knio, O., 1999, ''The Flow Structure in the Near Field of Jets and Its Effect on Cavitation Inception,'' J. Fluid Mech., **398**, pp. 1–43.
[8] Higuchi, H., Arndt, R. E. A., and Rogers, M. F., 1989, ''Characteristics of Tip Vortex Cavitation Noise,'' ASME J. Fluids Eng., **111**, pp. 495–501.
[9] Maines, B. H., and Arndt, R. E. A., 1997, ''Tip Vortex Formation and Cavitation,'' ASME J. Fluids Eng., **119**, pp. 413–419.
[10] Hsiao, C. T., and Pauley, L. L., 1998, ''Numerical Study of the Steady-State Tip Vortex Flow Over a Finite-Span Hydrofoil,'' ASME J. Fluids Eng., **120**, pp. 345–353.
[11] Farrell, K. J., and Billet, M. L., 1994, ''A Correlation of Leakage Vortex Cavitation in Axial-Flow Pumps,'' ASME J. Fluids Eng., **116**, pp. 551–557.
[12] Boulon, O., Callenaere, M., Franc, J. P., and Michel, J. M., 1999, ''An Experimental Insight Into the Effect of Confinement on Tip Vortex Cavitation of an Elliptical Hydrofoil,'' J. Fluid Mech., **390**, pp. 1–23.
[13] Chen, B., 2002 (NSWC-Carderock Division) private communication.
[14] Roth, G., Hart, D., and Katz, J., 1995, ''Feasibility of Using the L64720 Video Motion Estimation Processor (MEP) to Increase Efficiency of Velocity Map Generation for PIV,'' ASME/EALA Sixth International Symposium on Laser Anemometry, Hilton Head, SC.
[15] Roth, G., and Katz, J., 2001, ''Five Techniques for Increasing the Speed and Accuracy of PIV Interrogation,'' Meas. Sci. Technol., **12**, p. 238.
[16] Sridhar, G., and Katz, J., 1995, ''Lift and Drag Forces on Microscopic Bubbles Entrained by a Vortex,'' Phys. Fluids, **7**, pp. 389–399.
[17] Gopalan, S., and Katz, J., 2000, ''Flow Structure and Modeling Issues in the Closure Region of Attached Cavitation,'' Phys. Fluids, **12**, pp. 895–911.
[18] Huang, N. E., et al., 1998, ''The Empirical Mode Decomposition and the Hilbert Spectrum for Non-linear and Non-stationary Time Series Analysis,'' Proc. R. Soc. London, Ser. A, **454**, pp. 903–995.

Effect of Swirl on Rotordynamic Forces Caused by Front Shroud Pump Leakage

Yun Hsu
e-mail: yhsu@jaycor.com

Christopher E. Brennen
e-mail: brennen@caltech.edu

California Institute of Technology,
Mail Code 104-44,
Pasadena, CA 91125

Unsteady forces generated by fluid flow through the impeller shroud leakage path of a centrifugal pump were investigated. The effect of leakage path inlet swirl (pump discharge swirl) on the rotordynamic forces was re-examined. It was observed that increasing the inlet swirl is destabilizing both for normal and tangential rotordynamic forces. Attempts to reduce the swirl within the leakage path using ribs and grooves as swirl brakes showed benefits only at low leakage flow rate. [DOI: 10.1115/1.1511164]

1 Introduction

Previous experimental and analytical results have shown that discharge to suction leakage flows in the annulus surrounding a shrouded centrifugal pump contribute substantially to the fluid induced rotordynamic forces ([1,2]). Experiments conducted in the Rotor Force Test Facility (RFTF) at Caltech on an impeller undergoing a predetermined whirl motion have shown that the contributions to the normal and tangential forces from the leakage flows can be as much as 70% and 30% of the total, respectively ([3]). Other experiments ([4]) examining the consequences of leakage flows have shown that the rotordynamic forces are functions not only of whirl ratio, but also of the leakage flow rate and the impeller shroud to pump housing clearance. The magnitude of rotordynamic forces were found to be inversely proportional to the clearance. A region of forward subsynchronous whirl was found for which the average tangential force was destabilizing.

Guinzburg et al. [5] examined the difference in rotordynamic forces with and without a prescribed inlet swirl at entrance to the leakage path. The tangential force increased in the presence of inlet swirl, and hence the effect of inlet swirl was found to be destabilizing. Uy and Brennen [6] continued the work and did a parametric evaluation of the effect of inlet swirl. Later studies by Sivo et al. [7] examined the effectiveness of antiswirl brakes in reducing the destabilizing region of forward whirl.

Subsequent to the tests reported by Uy and Brennen, detailed comparison of the leakage path pressure profiles strongly suggested that the inlet swirl velocities were not consistent with the inclination of the inlet swirl vanes as assumed by Uy and Brennen. The present paper presents data in which the inlet swirl was measured; this requires a reassessment of the effect of inlet swirl on the rotordynamic coefficients. Also examined are the effects of antiswirl brakes as well as antiswirl grooves within the leakage pathway.

2 Rotordynamic Forces

Figure 1 shows a schematic of the hydrodynamic forces that act on a rotating impeller whirling in a circular orbit. The unsteady fluid forces (which are functions of rotor displacement) acting on the impeller due to the imposed whirl motion (eccentricity ε, whirl frequency Ω) are decomposed into a force normal to the direction of whirl motion, F_n, and a force in the direction of forward whirl motion, F_t. (Force moments would also occur from rotor displacement, see Tsujimoto et al. [8].) The normal and tangential forces are traditionally presented in dimensionless form as functions of the whirl frequency ratio, Ω/ω. Typical data for F_n and F_t from the present measurements is shown in Fig. 2.

It is convenient for rotordynamicists to fit F_n to a quadratic function of the whirl frequency ratio, Ω/ω, and to fit the dimensionless tangential force, F_t, to a linear function as shown in Fig. 2. The appropriate expressions are

$$F_n = M\left(\frac{\Omega}{\omega}\right)^2 - c\left(\frac{\Omega}{\omega}\right) - K; \quad F_t = -C\left(\frac{\Omega}{\omega}\right) + k \tag{1}$$

where the dimensionless coefficients are the direct added mass (M), direct damping (C), cross-coupled damping (c), direct stiffness (K), and the cross-coupled stiffness (k). It should be noted that the fluid-induced forces may not always conform to these simple functions of the whirl frequency ratio. However, this assumption is common in the rotordynamics literature. Brennen [9] and Jery [3] contain more detailed discussions of the derivation of Eqs. (1), and the process for experimentally measuring the forces. In the present work all five force coefficients were directly evaluated from the curve fits to the graphs of F_n and F_t.

For rotor stability, a positive normal force F_n will cause the eccentricity to increase and hence be destabilizing. From Eqs. (1), a large negative direct stiffness at zero whirl frequency ($\Omega/\omega = 0$) would correspond to such a case. When Ω/ω is positive, a positive tangential force F_t would also be destabilizing as this would drive the forward whirl motion.

A convenient measure of the rotordynamic stability is the ratio of cross-coupled stiffness to the direct damping (i.e., k/C) which is conventionally termed the whirl ratio. This defines the range of positive subsynchronous whirl frequency ratios, $0 < \Omega/\omega < k/C$, for which the tangential force is destabilizing.

3 Test Apparatus

The present experiments were conducted in the Rotor Force Test Facility (RFTF) at Caltech [3]. The leakage flow test section of the facility is schematically shown in Fig. 3. The intention is to isolate the leakage flow forces by using a solid rotor and to generate the flow through the leakage path by an auxiliary pump. The main components of the test section apparatus consist of the solid rotor, a stator (the stationary shroud), the rotating dynamometer (or internal force balance), an eccentric whirl mechanism and a leakage exit seal ring. The working fluid is water. An inlet guide vane is used for the tests with inlet swirl and is illustrated in Fig. 3.

The rotor is mounted directly to the rotating dynamometer, which in turn is connected to a data acquisition system that permits measurements of the rotordynamic force matrix components ([3]). The eccentric drive mechanism imposes a circular whirl orbit on the main shaft rotation. The radius of the whirl orbit (eccentricity) can be varied but this set of experiments used one

Contributed by the Fluids Engineering Division for publication in the JOURNAL OF FLUIDS ENGINEERING. Manuscript received by the Fluids Engineering Division August 17, 2001; revised manuscript received May 6, 2002. Associate Editor: Y. Tsujimoto.

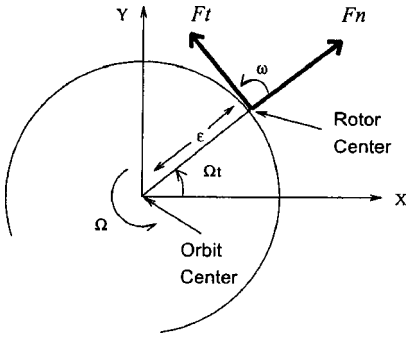

Fig. 1 Schematic of the fluid-induced forces acting on an impeller whirling in a circular orbit

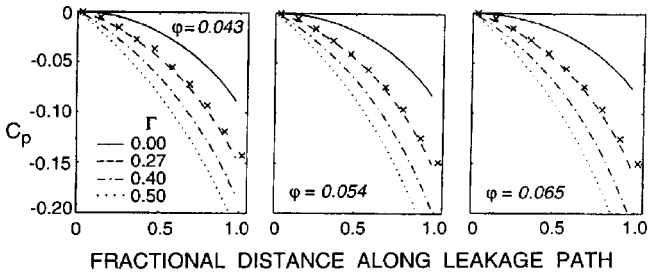

Fig. 4 Comparison of the experimental measurements (×) of the pressure coefficient (C_p) profiles in the leakage path for $\phi=0.043$, 0.054, and 0.065 with the calculated profiles for inlet swirl ratios of 0, 0.27, 0.4, and 0.5

eccentricity, $\varepsilon=0.025$ cm. The seal ring at the leakage exit models a wear ring. The clearance between the face seal and the impeller face is adjustable, but was set to 0.050 cm for these tests. The tested leakage flow rate ranged up to 1.15 l/s. The temperature drift of the dynamometer electronics is postulated to be the largest contributor to force measurement errors. The uncertainties were evaluated experimentally and in all reported rotordynamic force coefficients were 5% with the exception of the direct stiffness, K, for which the uncertainty was 8%. The uncertainty in the measurement of the flow rate was 1%.

The experimental configuration with the rotor and stator forming the leakage path is shown in Fig. 3. The two rotor/stator configurations referred to in this paper (the so-called conical and contoured rotor geometries) were described and used by Uy and Brennen [9]. The present tests used primarily the contoured rotor which has an eye-to-tip diameter ratio of 0.454, tip diameter of 18.73 cm, and an axial length of 4.29 cm. The rotor was designed using a third-order polynomial with the contour parallel to the centerline at the eye and perpendicular to the centerline at the tip. The matching stator was constructed to maintain a constant clearance, $H=0.30$ cm, normal to the surfaces. The conical rotor has a 45-deg leakage path and has the same tip radius and the same tip-to-eye diameter ratio as the contoured rotor. An axial clearance device that models a face seal on a centrifugal pump is used. The inner radius of the seal is 3.30 cm, and its clearance is set to 0.05 cm for all tests. The effect of inlet swirl was investigated by installing guide vanes at the leakage inlet to introduce pre-rotation in the direction of shaft rotation. Figure 3 shows a typical vane consisting of a logarithmic spiral channel with a turning angle of six deg. A series of vanes with angles $\alpha=1$ deg, 2 deg, and 6 deg were fabricated. The swirl ratio, Γ (the ratio of the leakage flow circumferential velocity to the impeller tip velocity at inlet to the leakage path) is varied by changing the inlet leakage flow rate and the turning angle. Another inlet guide plate with a set of 24 radial vanes designed to eliminate inlet swirl. The swirl ratio depends on the flow coefficient and turning angle, α, according to $\Gamma/\phi = H/B \tan\alpha$ where $B=0.318$ cm is the width of the logarithmic spiral channel. A derivation of this relation (which assumes all leakage flow is constrained to follow the vane) is found in Guinzburg et al. [5]. The relation was assumed by Uy and Brennen [6] in their presentation of the effects of inlet swirl on rotordynamic forces.

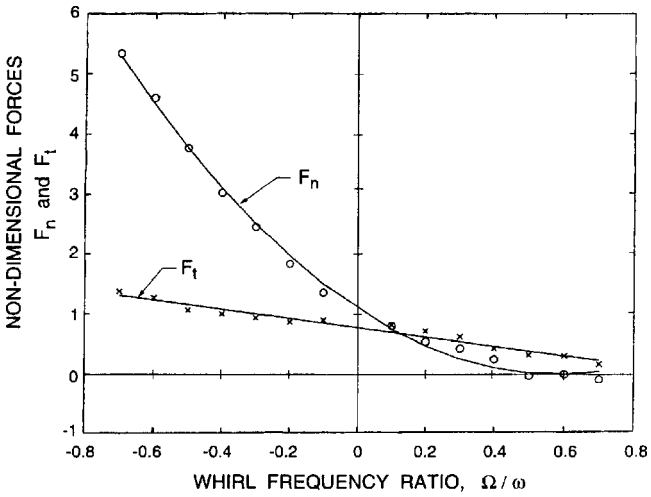

Fig. 2 Typical nondimensional data for F_n and F_t from the current experiments as functions of the whirl frequency ratio Ω/ω (data for contoured rotor with inlet swirl at $\phi=0.043$)

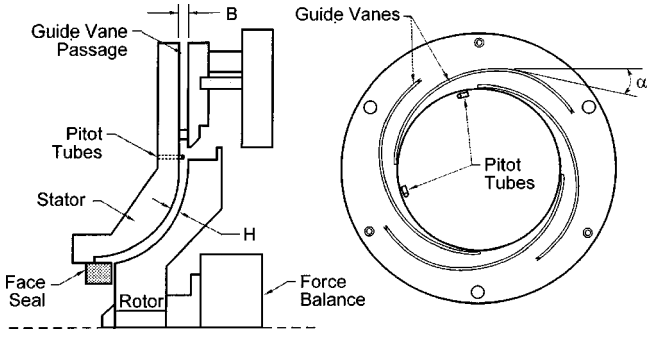

Fig. 3 Schematic of the experimental facility showing the rotor and stator assembly (left), the $\alpha=6$ deg inlet guide vanes (right) and the location of the Pitot tubes

However, during investigations of the leakage flow field, questions arose concerning the inlet velocities to the leakage path. One source of these questions were comparisons between experimentally measured leakage path pressure distributions and those calculated theoretically. We digress here to cover this issue.

4 Leakage Path Pressure Distributions

We present the pressure profile comparisons which led to the need for inlet swirl measurements (for full details see [10]). The pressure profiles inside the leakage path were examined both experimentally and computationally for the conical impeller fitted with the inlet guide vanes. The computations were done using the new vorticity method for solving the Childs' bulk flow equations ([10]). (Using the original Childs' perturbation method yields qualitatively similar results.) Pressure taps drilled through the stator of the conical impeller provided water manometer measurements for profiles of three different flows, $\phi=0.043$, 0.054, and 0.065, using the 6 deg inlet guide vane, which was designed to provide inlet swirl ratios of 0.4, 0.5, and 0.6, respectively, at each of those flow rates. Experiments were conducted with the rotor eccentric but not whirling ($\Omega/\omega=0$). The resulting pressure coefficient distributions are presented in Fig. 4; it can be seen that

the experimental pressure profiles, referenced to the pressure at inlet to the leakage path, are nearly identical for the three flows. Computationally the inlet swirl was the only parameter which affects the pressure profile significantly. As seen in Fig. 4, in all three flows the pressure profiles are best matched by setting the inlet swirl ratio in the computations to 0.25–0.27 of the rotor tip speed. This finding motivated the inlet swirl measurements and confirmed the suspicion that the inlet swirl was nearly the same for all of the inlet guide vanes regardless of the flow rate. Since there are only slight differences in the inlet structure of the conical and contoured rotors, the same conclusion applies to the contoured rotor.

5 Inlet Swirl Measurements

Motivated by the preceding results, Pitot tubes were installed to measure the flow velocities at inlet to the leakage path. Considerations were given to using five-hole Pitot tubes. This was not done, however, for several reasons. The flow velocities are likely to vary with distance from the walls. This would mean that several measurements at different distances from the walls would be needed to accurately assess the flow, a difficult feat considering the narrow spaces in the apparatus. In addition the flow is unsteady and highly disturbed, making the accuracy of the flow angle measurements a concern. Because of this, it was decided that a cruder measurement of the velocity in the tangential direction would suffice for the purposes of ascertaining the inlet flow conditions to the leakage path.

The stator had two holes drilled for insertion of the Pitot tubes, as shown in Fig. 3. The Pitot tubes were placed immediately after the exit of the inlet guide vanes and before the entrance to the leakage path, a gap of approximately 0.8 cm normal to the axis of rotation. Normally one would have the diameter of the Pitot tube be less than one quarter of the gap. The Pitot tubes were fabricated from 0.3 cm diameter stainless steel tubing. Their diameter is therefore comparable to the leakage path clearance and the width of the inlet guide vanes. The tubes were connected to the set of water manometer mentioned earlier for stagnation pressure readings. Existing pressure taps next to the Pitot tubes were used for static pressure measurements. The difference between the readings is the velocity head of the flow in the direction facing the Pitot tube.

In most of the tests only the swirl velocity was measured by setting the Pitot tubes tangent to the circumference. Changing their orientation to face the flow directly did not change the measurements, as the difference was within the uncertainties. Because of the large diameter of the Pitot tubes compared to the gap width, the measured velocities are likely to be some average value of the velocity in the circumferential direction near the inlet to the leakage path. Though the measurements of the swirl velocity may be imprecise, confidence in the results was bolstered by the agreement between the measured pressure profiles and those calculated using the measured inlet swirl ([10]).

Figure 5 shows that the inlet swirl vanes did not work as designed; they almost all provided about the same inlet swirl. On the other hand, the radial vanes *did* prevent inlet swirl at higher flow rates. These velocity measurements are consistent with theoretical predictions from the bulk flow model ([10]). It is postulated that inside the small clearance in the guide vane structure, viscous forces dominate and they act to slow the flow in the circumferential direction and expel the fluid in a more radial manner at the exit from the guide vanes. Also some mixing may occur inside the region between the end of the inlet guide vanes and the beginning of the leakage path and would reduce the effects of inlet swirl vanes.

Since the entrance regions of the contoured and the conical geometries are very similar, there is no reason to expect their inlet swirls would be different.

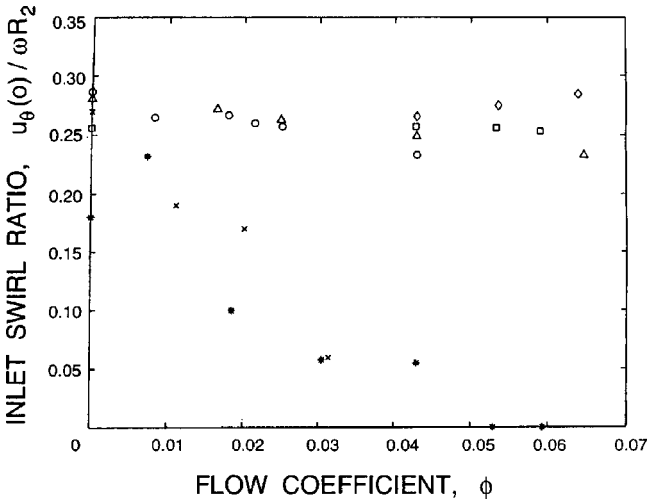

Fig. 5 Experimental inlet swirl ratio versus flow coefficient ϕ, with 6-deg inlet swirl vanes at 500 rpm(◇), 1000 rpm(□), with 2-deg swirl vanes at 500 rpm(△), 1000 rpm(○), and with radial vanes at 1400 rpm(×) and 1000 rpm(*)

6 Effects of Inlet Swirl

Uy and Brennen [6] performed a set of experiments to determine the effects of inlet swirl on the unsteady rotordynamic forces on the contoured impeller. Different inlet swirl angles were employed to alter the inlet swirl ratio, and a swirl vane with radial channels was used to generate data for zero inlet swirl. The flow coefficients ranged from $\phi = 0.01$ to 0.066 using flow rates from 0.17 to 1.15 l/s at 1000 rpm. The Reynolds numbers for $\phi = .055$ were $\mathrm{Re}_\omega = 27170$ and $\mathrm{Re}_{u_s} = 1494$. Uy and Brennen assumed the inlet swirl was consistent with the angles of the inlet guide vanes and therefore published Fig. 6, which showed that for nonzero inlet swirl, the magnitude of the inlet swirl, Γ, did not affect the rotordynamic forces.

However, the later comparison of pressure profiles led to questions concerning the accuracy of the assumed inlet swirl in the experiments ([10]). Subsequently, the Pitot tube measurements of inlet swirl velocities did show that the assumed swirl velocities were indeed incorrect. Figure 7 presents the corrected experimental data, showing only two inlet swirl ratios, evaluated using the correct, measured values of the swirl. It shows that the effect of swirl is destabilizing, as K becomes larger in negative magnitude and k/C increases. The coefficients representing the tangential forces, C and k, become larger with increasing swirl. At higher flow coefficients, $\phi > 0.03$, no discernible trends can be observed in the rotordynamic coefficients for constant swirl.

However, the general comments made by Uy and Brennen on the effect of swirl are still valid. For the coefficients which determine the normal force, M, c, and K, the added mass does not exhibit an appreciable difference in the cases with and without swirl. The magnitude of the direct stiffness is higher and the magnitude of the cross-coupled damping is smaller with no inlet swirl. In summary, the circumferential fluid velocity induced by inlet swirl affects the rotordynamic behavior significantly, especially the whirl ratio, which defines the range where tangential forces are destabilizing.

The combined effect of inlet swirl and leakage path geometry was also investigated. Figure 8 presents the rotordynamic force coefficients for both the contoured and conical leakage path geometry, updated with the measured inlet swirls. The coefficients of the normal force appear to be similar, but there are significant differences in the trends and magnitudes of the cross-coupled stiffness and direct damping, leading to substantial differences in

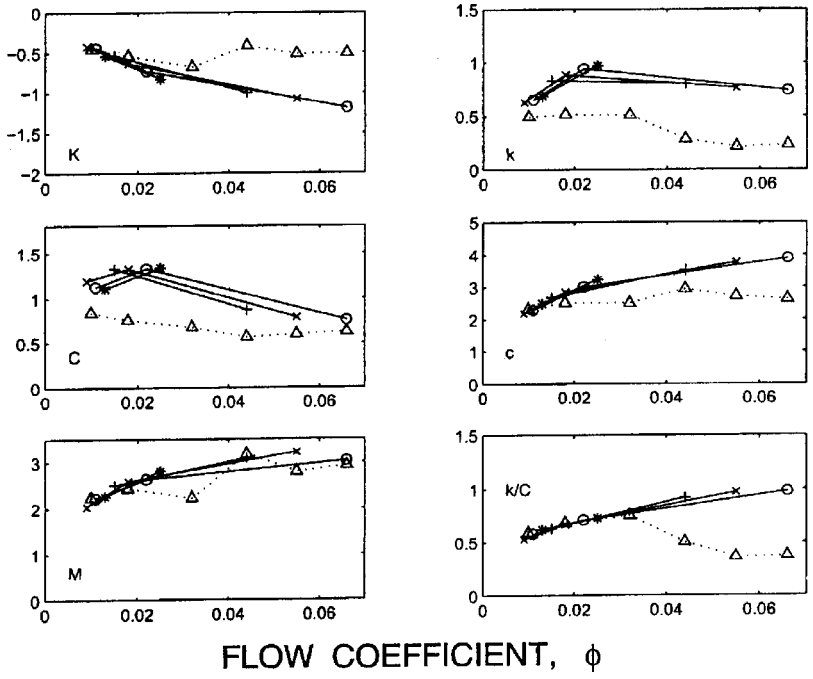

Fig. 6 Experimental rotordynamic coefficients for the contoured rotor plotted against flow coefficient, ϕ, for tests with inlet swirl, $\Gamma=0.0$ (△), 0.4 (+), 0.5 (×), 0.6 (○) and 0.7 (*) (presented by Uy and Brennen [6] and here shown to be inaccurate)

the whirl ratio. The contoured rotor exhibits an increasing whirl ratio with increasing flow rate, while the conical rotor exhibits the opposite trend.

7 Antiswirl Ribs and Grooves

We now shift attention from inlet swirl to swirl reduction in the leakage path by vanes installed within the passage. Previous investigations ([7]) demonstrated some benefits from fitting antiswirl ribs to the surface of the stator; they decreased the destabilizing forces. The inner surface of the conical stationary shroud was designed to accept meridional ribs or swirl brakes along the length of the leakage path. As shown in Fig. 9, four equally spaced ribs, 0.5 cm wide and 0.16 cm high, were installed for these tests. The effectiveness of cutting grooves on the stator sur-

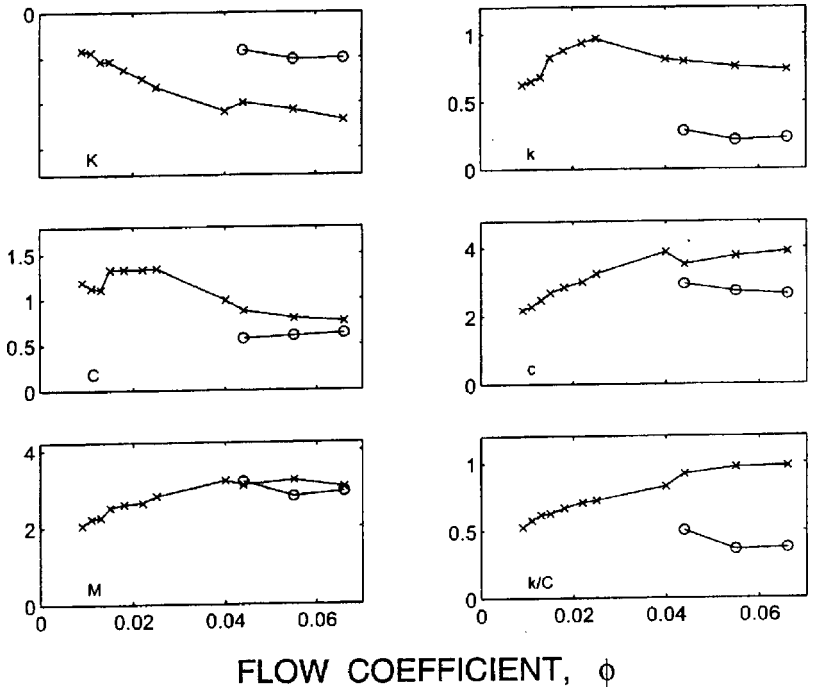

Fig. 7 Experimental rotordynamic coefficients for the contoured rotor plotted against flow coefficient, ϕ, for tests with inlet swirl, $\Gamma=0.0$, (○) and 0.26 (×)

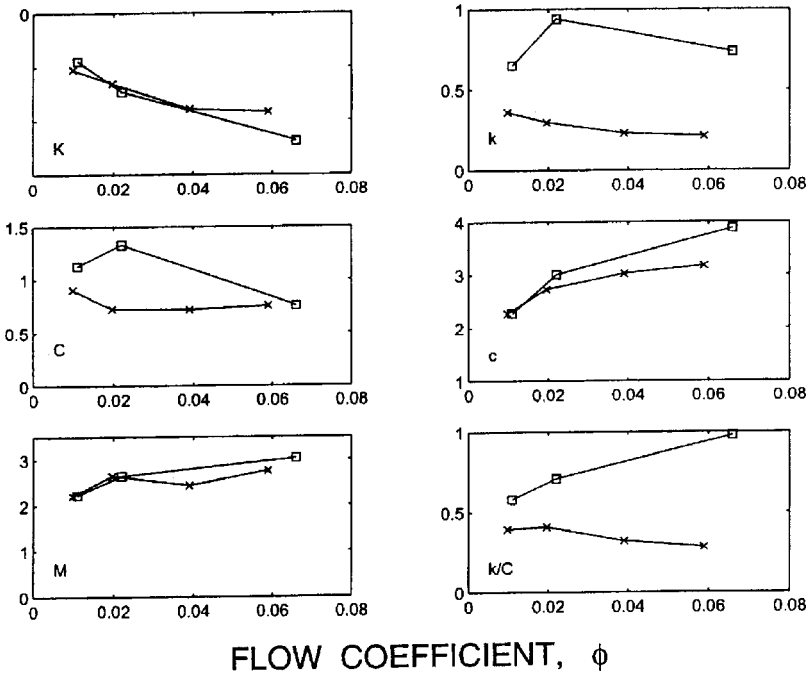

Fig. 8 Experimental rotordynamic coefficients plotted against flow coefficient ϕ for tests with inlet swirl with the contoured rotor ($\square, \Gamma = 0.27$) and the conical rotor ($\times, \Gamma = 0.27$)

face was also examined; the grooves duplicated the height and width of the brakes.

With a rotating impeller, fluid swirl is obviously generated in the leakage path, and the question arises as to how reducing this swirl will affect rotordynamic forces. Therefore, the effects of antiswirl ribs and grooves in the leakage path were investigated. Work by Sivo [7] identified some benefits to having antiswirl ribs in the leakage path, but only for very small flow coefficients.

Figure 10 shows the rotordynamic force coefficients as functions of the flow coefficient for the conical impeller and shroud. The tests were conducted with a 2-deg inlet swirl vane and compare the effects of antiswirl ribs and grooves.

Note that the magnitude of the direct stiffness K is smallest for the tests with no antiswirl devices. Thus in so far as the direct stiffness is concerned, the stability improves with grooves and even more with antiswirl ribs. However the cross-coupled damping coefficient does not show such changes, and the added mass remains about the same for all three cases.

The direct damping of the tangential forces has the same magnitude for all three cases, while the cross-coupled stiffness exhibits different trends. It decreases with flow coefficient with no swirl reduction devices, and increases in the presence of antiswirl ribs. With grooves, the cross-coupled stiffness first increases and then decreases with flow coefficient. This leads to improvements in the whirl ratio for antiswirl devices at low flow coefficients, but to a detrimental effect at higher flow rates. The whirl ratio for the case with antiswirl ribs is increasing with flow coefficient, in marked contrast to the decreasing trend when no antiswirl devices are present.

Thus it seems that antiswirl devices provide some benefit in reducing the destabilizing region in the tangential forces only for very small flow rates. They contribute to an increase in direct stiffness, helping the stability of normal forces.

8 Discussion

Experimental data show that as with annular seals, the rotordynamic forces from front shroud leakage flows in pumps are significantly affected by inlet swirl; an increase in the inlet swirl is destabilizing for both the normal and tangential forces. This observation agrees qualitatively with trends predicted from bulk flow computations. Reduction of inlet swirl provides significant benefits for rotordynamic stability.

As the effects of inlet swirl are destabilizing, reducing the swirl inside the leakage path might seem a beneficial strategy. The results, however, were mixed. At lower flow coefficients, swirl re-

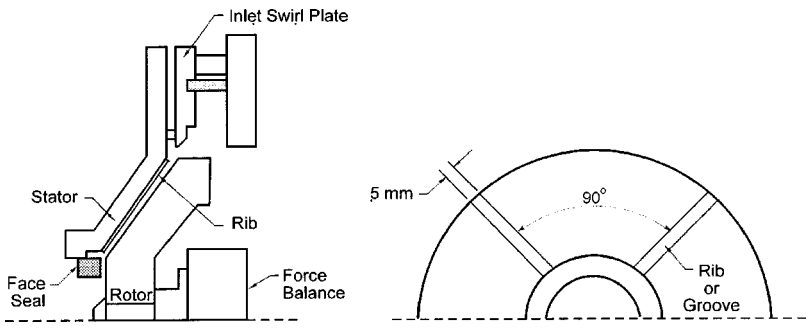

Fig. 9 Swirl reduction devices

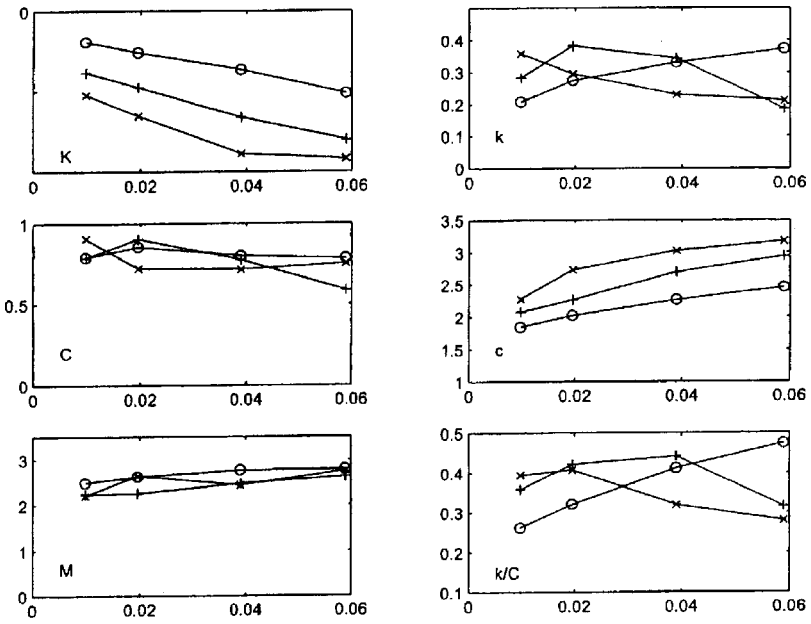

Fig. 10 Rotordynamic coefficients plotted against flow coefficient for experiments with inlet swirl: no antiswirl devices (×), four full-length antiswirl ribs (○), four full-length antiswirl grooves (+).

duction offered some benefit. However, at higher flow rates, the antiswirl devices reduced the unstable normal forces but increased the destabilizing tangential forces.

Nomenclature

B = width of inlet channel and swirl vane
C = direct damping normalized by $\rho\pi\omega R_2^2 L$
C_p = pressure coefficient, $\Delta p/\rho\omega^2 R_2^2$
c = cross-coupled damping normalized by $\rho\pi\omega R_2^2 L$
F_n = force normal to whirl orbit/$\rho\pi\omega^2 R_2^2 L\varepsilon$
F_t = force tangent to whirl orbit/$\rho\pi\omega^2 R_2^2 L\varepsilon$
H = clearance between impeller shroud and housing
K = direct stiffness normalized by $\rho\pi\omega^2 R_2^2 L$
k = cross-coupled stiffness normalized by $\rho\pi\omega^2 R_2^2 L$
k/C = whirl ratio
L = axial length of the leakage path
M = direct added mass normalized by $\rho\pi R_2^2 L$
Q = volumetric leakage flow rate
R_2 = radius of rotor and leakage path inlet, 9.366 cm
Re_ω = Reynolds number, $R_2\omega H/\nu$
Re_{u_s} = Reynolds number, $u_s H/\nu$
Re_{u_θ} = Reynolds number, $u_\theta H/\nu$
u_s = mean leakage throughflow velocity, $Q/2\pi R_2 H$
u_θ = mean swirl velocity at the leakage path inlet
α = angle of logarithmic spiral swirl vane
Δp = static pressure minus pressure at leakage inlet
Γ = leakage inlet swirl ratio, $u_\theta/\omega R_2$
ε = eccentricity of whirl orbit
ν = kinematic viscosity
ρ = fluid density
ϕ = leakage flow coefficient, $u_s/\omega R_2$
ω = main shaft radian frequency
Ω = whirl radian frequency
Ω/ω = whirl frequency ratio

References

[1] Adkins, D., and Brennen, C. E., 1988, "Analysis of Hydrodynamic Radial Forces on Centrifugal Pump Impellers," ASME J. Fluids Eng., **110**, pp. 20–28.
[2] Bolleter, U., Wyss, A., Welte, I., and Sturchler, R., 1987, "Measurement of Hydraulic Interaction Matrices of Boiler Feed Pump Impellers," ASME J. Vib., Acoust., Stress, Reliab. Des., **109**, pp. 144–151.
[3] Jery, B., 1986, "Experimental Study of Unsteady Hydrodynamic Force Matrices on Whirling Centrifugal Pump Impellers," Ph.D. thesis, California Institute of Technology, Pasadena, CA.
[4] Guinzburg, A., 1992, "Rotordynamic Forces Generated By Discharge-to-Suction Leakage Flows in Centrifugal Pumps," Ph.D. thesis, California Institute of Technology, Pasadena, CA.
[5] Guinzburg, A., Brennen, C. E., Acosta, A. J., and Caughey, T., 1993, "The Effect of Inlet Swirl on the Rotordynamic Shroud Forces in a Centrifugal Pump," ASME J. Eng. Gas Turbines Power, **115**, pp. 287–293.
[6] Uy, R., and Brennen, C. E., 1999, "Experimental Measurements of Rotordynamic Forces Caused by Front Shroud Pump Leakage," ASME J. Fluids Eng., **121**, pp. 633–637.
[7] Sivo, J., Acosta, A. J., Brennen, C. E., and Caughey, T. K., 1995, "The Influence of Swirl Brakes on the Rotordynamic Forces Generated by Discharge-to-Suction Leakage Flows in Centrifugal Pumps," ASME J. Fluids Eng., **117**, pp. 104–108.
[8] Tsujimoto, Y., Yoshida, Y., Ohashi, H., and Ishizaki, S., 1997, "Fluid Force Moment on a Centrifugal Impeller in Precessing Motion," ASME J. Fluids Eng., **119**, pp. 366–371.
[9] Brennen, C. E., 1994, *Hydrodynamics of Pumps*, Concepts ETI and Oxford University Press, Oxford, UK.
[10] Hsu, Y., 2001, "Rotordynamic Forces Generated by Annular Leakage Flows in Centrifugal Pumps," Ph.D. thesis, California Institute of Technology, Pasadena, CA.

U. Iben

F. Wrona

Robert Bosch GmbH,
Department FV/FLM,
P. Box 106050,
D-70059 Stuttgart,
Germany

C.-D. Munz

Institute for Aerodynamics and Gasdynamics,
Stuttgart University,
Pfaffenwaldring 21,
D-70550, Stuttgart,
Germany

M. Beck

Robert Bosch GmbH,
Department FV/FLM,
P. Box 106050,
D-70059 Stuttgart,
Germany

Cavitation in Hydraulic Tools Based on Thermodynamic Properties of Liquid and Gas

The simulation of cavitation phenomena plays an important role for development of modern hydraulic tools and injection systems. Cavitation leads to a reduction of mass flow and influences the wave motion in hydraulic components significantly. The article deals with the simulation of a homogeneous cavitation model based on thermodynamic properties of the liquid and steam to understand basic physical phenomena.
[DOI: 10.1115/1.1514200]

1 Introduction and Modeling Equations

The simulation of cavitated flows is necessary to prevent damages and to understand the time-dependent properties in the early development phase of hydraulic tools. Fast working valves induce strongly time-depending high and low pressure levels. The large range of temperature and the low pressure levels can lead to evaporation of the oil in the hydraulic pipelines and valves. The evaporation leads to a significant reduction of the speed of sound in the mixture, reduces the mass flow, and influences the working properties of valves. The condensation of the vapor bubbles can lead to noises and damages in the hydraulic components. In order to understand the complex physical processes and to protect technical tools from cavitation erosion, numerical simulations can be very helpful.

Many papers deal with these topics, see, for example [1–4]. In general, a combination of continuous and discrete models are used. The flow is described with the Euler or the Navier-Stokes equations which represent the continuous model. The cavitation is modeled by discrete bubble models where oscillations of single bubbles or bubble clouds are considered, [3–6]. The numerical handling of these approaches is very difficult for flows with high pressure gradients. Many model parameters which can hardly be obtained by experiments make a study of basic phenomena time consuming and uncertain. Oscillations of bubbles are based on the mechanical nonequilibrium, i.e., the pressure of the liquid phase differs from the pressure of the gas/steam phase which depends on the surface tension σ, viscosity ν, and the diameter of the bubbles. These approaches combine microscopic and macroscopic effects. To simulate flows in pipes which caused by shock or rarefraction waves, numerical schemes of high order are necessary to resolve the model based oscillations of the pressure which leads to enormous numerical costs, [3]. In this paper we are only interested in macroscopic effects combined with robust numerical schemes. Consequently, a homogenous two-phase model is used which is based on a thermodynamic and mechanic equilibrium model in the first step. The numerical studies show that the chosen model allows to analyze the wave motion in pipes with cavitation by robust numerical schemes.

Pioneering works on one-dimensional two-phase flow were published by Wallis [7] and Kolev [8]. Cavitating flows can be described by several models with different model levels. The first approach is to start with the conservation equations of the homogeneous mixture (barotropic model) which have been done in [1,9]. Here, the evaporation and condensation process is described by a thermodynamic equation of state. This approach can lead to stability problems due to the large variable range of mixture density and propagation speed. In Beck [10] a combination of an explicit and local implicit scheme is used to avoid the stability problems. The next step is to split the continuity equation for the gas and liquid phase and to couple it by a source term which was done in [11] for isotropic flow. The equation of energy was neglected. It can be shown analytically, that this approach is equivalent to the approach using the mixture equations, [12]. The next step is to consider the energy equation for the homogeneous mixture in connection with thermodynamic equilibrium or nonequilibrium models for the phase transient and additional heat flux. The homogeneous and inhomogeneous modeling equations adapted to the special problem of cavitated flow in pipes with a variable cross-sectional area were derived and partially investigated in [12].

The presented model was validated on an exact solution of a Riemann problem using the corresponding barotropic model, see Section 3.

Every natural liquid contains undissolved and dissolved air. The undissolved air appears as small bubbles in the fluid, which can be considered as cavitation nuclei. If the pressure decreases below the saturation pressure, the dissolved air releases. This so-called gas cavitation is a diffusion process which will not be considered here. We assume that the fluid contains a fixed mass of undissolved air which influences the properties, e.g., the speed of sound, of the liquid-gas mixture. Particularly, it comes apparent for small pressure values, see [7,12].

The notation used in the paper is the following: The index G

Contributed by the Fluids Engineering Division for publication in the JOURNAL OF FLUIDS ENGINEERING. Manuscript received by the Fluids Engineering Division July 10, 2001; revised manuscript received May 6, 2002. Associate Editor: Y. Tsujimoto.

denotes the gas and steam phase, the index L denotes the liquid phase. The physical values of the mixture are written without an index.

The velocity of fluid and gas/steam in a pipe is approximately the same, so a homogeneous mixture is considered, i.e., the velocity of the gas is equal to the velocity of the liquid. This assumption makes sense for acoustic cavitation. The cavitation appears as small bubbles or steam clouds. Further, we assume the steam to be equally distributed within the computational cells. Note, that due to the wave motion in a pipe, the fluid cannot evaporate completely. For this reason, the mass fraction of steam is strictly smaller than one. The mass fraction is defined by μ, the volume fraction is defined by ε, i.e.,

$$\mu = \frac{m_G}{m} \quad \text{and} \quad \varepsilon = \frac{V_G}{V}.$$

The mixture density is given by

$$\rho = \varepsilon\rho_G + (1-\varepsilon)\rho_L \quad \text{or} \quad \frac{1}{\rho} = \frac{\mu}{\rho_G} + \frac{1-\mu}{\rho_L}. \tag{1.1}$$

The modeling equations are derived in [11,12]. The homogeneous two-phase Euler equations in one space dimension consisting of the continuity equations for each phase, the momentum equation for the mixture, and disregarding the energy equation are

$$\begin{aligned} &\frac{\partial}{\partial t}(\varepsilon\rho_G) + \frac{\partial}{\partial z}(\varepsilon\rho_G v) = \Gamma, \\ &\frac{\partial}{\partial t}(1-\varepsilon)\rho_L + \frac{\partial}{\partial z}(1-\varepsilon)\rho_L v = -\Gamma, \\ &\frac{\partial}{\partial t}\rho v + \frac{\partial}{\partial z}(\rho v^2 + p) = \rho F \quad \text{with} \quad F = -\frac{\lambda_{in} v|v|}{2d}. \end{aligned} \tag{1.2}$$

The source term Γ describes the evaporation and condensation process of cavitation. The friction force is defined as a function of the shear stress on the wall, where the friction factor λ_{in} is a function of the Reynolds number, and the relative roughness of the pipe, [13]. It is assumed that the friction forces for the liquid and gas/steam are the same. The value d denotes the diameter of the pipe. We assume that the entropy is nearly constant. For a flow without a phase transient this assumption is satisfied. Only strong shocks of a pressure range larger than 3000 bar lead to a significant increase of entropy, see [12]. For small cavitation zones in pipes, the increase of entropy can be neglected as well.

Following [14], the number of partial differential equations used in existing one-dimensional models varies between three conservation equations for the mixture and five conservation equations for each phase separately. The splitting of the mass conservation equation in (1.2) was chosen to avoid stability problems if using the homogeneous mixture model and must be used for nonequilibrium models. The pressure is a function of density and temperature which is given just in an implicit formulation. This is a main difference to the modeling of problems from gas dynamics. A system of nonlinear equations has to be solved in each time-step in order to compute the primitive variables p and ε from the conservative variables

$$u_1 = \varepsilon\rho_G, \quad u_2 = (1-\varepsilon)\rho_L \quad \text{and} \quad u_3 = \rho v$$

which are used to solve the system (1.2) numerically.

A model for the source term Γ is not easily to derive, see [11,12,15]. If we consider just the gaseous phase in a one-dimensional flow, the mass conservation law can be written as follows:

$$\frac{\partial}{\partial t}(\varepsilon\rho_G) + \frac{\partial}{\partial z}(\varepsilon\rho_G v) = \rho\frac{d\mu}{dt} = \Gamma. \tag{1.3}$$

The value A denotes the cross-sectional area of the pipe which remains constant in our case, and Δz the length of each discretization. Note that the mass exchange on the right-hand side of Eq. (1.3) must be the substantial derivative of the gaseous mass because the mass exchange is strongly coupled to the fluid elements. A similar procedure leads to the continuity equation for the liquid phase

$$\frac{\partial}{\partial t}((1-\varepsilon)\rho_L) + \frac{\partial}{\partial x}((1-\varepsilon)\rho_L v) = -\rho\frac{d\mu}{dt}. \tag{1.4}$$

Note, that the summation of Eqs. (1.3) and (1.4) holds the continuity equation for the mixture. The system (1.2) will be abbreviated by (2.14)

$$\frac{\partial}{\partial t}\mathbf{u} + \frac{\partial}{\partial z}\mathbf{f}(\mathbf{u}) = \mathbf{g}(\mathbf{u}) \quad \text{with} \quad \mathbf{u} = (u_1, u_2, u_3)^T. \tag{1.5}$$

In order to use numerical schemes of high accuracy, the Jacobian of the flux function $\mathbf{f}$ has to be computed. Following [12,11], the eigenvalues are

$$\lambda_1 = v - c, \quad \lambda_2 = v, \quad \text{and} \quad \lambda_3 = v + c, \tag{1.6}$$

where c is the speed of sound for the homogeneous mixture. The eigenvalues λ_1 and λ_3 represent the characteristics of the system (1.2). The eigenvalue λ_2 represents the path. For fixed mass fraction μ the speed of sound can be computed by, [7],

$$\frac{1}{\rho c^2} = \frac{\varepsilon}{\rho_G c_G^2} + \frac{(1-\varepsilon)}{\rho_L c_L^2}. \tag{1.7}$$

The Eq. (1.7) first was conducted by Wallis, see [7]. To derive (1.7), we have used $p = p(u_1 + u_2)$ and additionally

$$\frac{\partial p}{\partial u_1} = \frac{\partial p}{\partial \rho}\frac{\partial \rho}{\partial u_1} = c^2, \quad \frac{\partial p}{\partial u_2} = \frac{\partial p}{\partial \rho}\frac{\partial p}{\partial u_2} = c^2.$$

The Eq. (1.7) can be derived in different ways, see [7] and [12]. The eigenvectors of $\mathbf{f}_u$ are

$$\mathbf{r}_1 = \begin{pmatrix} 1 \\ \dfrac{1-\mu}{\mu} \\ \dfrac{v-c}{\mu} \end{pmatrix}, \quad \mathbf{r}_2 = \begin{pmatrix} -1 \\ 1 \\ 0 \end{pmatrix}, \quad \text{and} \quad \mathbf{r}_3 = \begin{pmatrix} 1 \\ \dfrac{1-\mu}{\mu} \\ \dfrac{v+c}{\mu} \end{pmatrix}. \tag{1.8}$$

Note that we have to guarantee that $0 < \mu \leqslant 1$, otherwise the eigenvalues are degenerated. As mentioned in the Introduction, an initial mass fraction of undissolved air is given, so that the required assumption is satisfied. To solve (1.2) numerically, the first-order HLL scheme in connection with operator splitting is used. The computational domain $[-0.5, 0.5] \times [0, T]$ is equidistant spaced, i.e.,

$$-0.5 = z_0 < z_1 < \cdots < z_i < \cdots z_{N-1} < z_N = 0.5 \quad \text{with} \quad \Delta z = z_{i+1} - z_i$$

and

$$0 = t^0 < t^1 < \cdots < t^n < \cdots < T \quad \text{with} \quad \Delta t = t^{n+1} - t^n.$$

Further, we introduce the notation

$$\mathbf{u}_i^n = \begin{pmatrix} u_{1,i}^n \\ u_{2,i}^n \\ u_{3,i}^n \end{pmatrix} \quad \text{with} \quad u_{k,i}^n = u_k(z_i, t^n), \quad k = 1,2,3.$$

According to Toro [16], the homogeneous hyperbolic equation can be discretized as follows:

$$\mathbf{u}_i^{n+1} = \mathbf{u}_i^n + \frac{\Delta t}{\Delta z}(\mathbf{F}_{i-1/2}^{\text{HLL}} - \mathbf{F}_{i+1/2}^{\text{HLL}}). \tag{1.9}$$

The numerical flux functions $\mathbf{F}$ are defined by

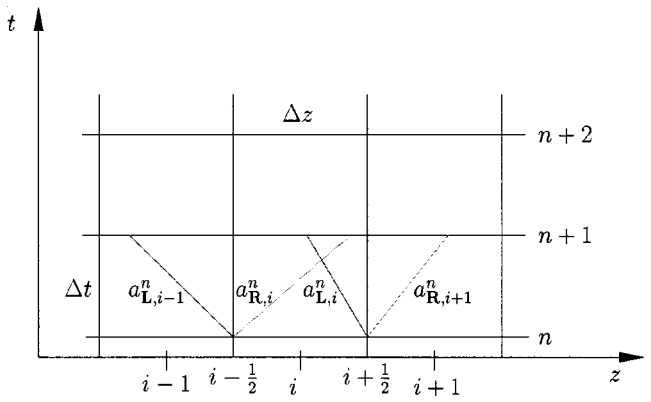

Fig. 1 Propagation speeds

$$\mathbf{F}^{\mathrm{HLL}}_{i+1/2}=\frac{a^n_{R,i+1}\mathbf{f}(\mathbf{u}^n_i)-a^n_{L,i}\mathbf{f}(\mathbf{u}^n_{i+1})+a^n_{L,i}a^n_{R,i+1}(\mathbf{u}^n_{i+1}-\mathbf{u}^n_i)}{a^n_{R,i+1}-a^n_{L,i}} \tag{1.10}$$

$$\mathbf{F}^{\mathrm{HLL}}_{i-1/2}=\frac{a^n_{R,i}\mathbf{f}(\mathbf{u}^n_{i-1})-a^n_{L,i-1}\mathbf{f}(\mathbf{u}^n_i)+a^n_{L,i-1}a^n_{R,i}(\mathbf{u}^n_i-\mathbf{u}^n_{i-1})}{a^n_{R,i}-a^n_{L,i-1}} \tag{1.11}$$

In this context, $a^n_{R,i}$ denotes of the greatest propagation speed and $a^n_{L,i}$ the smallest propagation speed in the computational cell i, and are set to λ_3, respectively, λ_1; see Fig. 1, as long as they are estimations of the propagation speeds. An underestimation of these values can lead to oscillations and occurs if the eigenvalues λ_i are less than the physical shock wave propagation speed. Especially at condensation processes, it turned out that oscillations in the numerical scheme often occurs, [9,11]. In order to avoid these numerical instabilities, at condensation processes the discrete propagation speed is locally set to the so-called grid speed $\Delta z/\Delta t$ with the correct sign of propagation.

This means that the estimated propagation speed is locally increased to the largest speed that is possible. The technique is often used for processes with strongly variable propagation speeds, see [17,18]. The value Δt is computed by

$$\Delta t=\lambda_{CFL}\frac{\Delta z}{\max_{k,i}|\lambda^n_{k,i}|},\quad k=1,2,3.$$

The value λ_{CFL} denotes the so-called CFL number. Finally, the ordinary differential equation

$$\mathbf{u}_t=\begin{pmatrix}\Gamma\\ -\Gamma\\ \rho F\end{pmatrix} \tag{1.12}$$

is solved to get a numerical solution for (1.2). Note that (1.12) has not to be solved for a flow with constant mass fraction μ and neglected friction $F=0$.

2 Thermodynamic Model for the Source Term

In order to receive results for the Eqs. (1.2) the system must be closed. Therefore one of the unknowns must be modeled and expressed in other physical properties. In this work we decided to model the mass fraction due to evaporation and condensation in a thermodynamic way. Following [12], the mass fraction can be computed by

$$\frac{d\mu}{dt}=\frac{1}{h''(p)-h'(p)}\left(\frac{dh''}{dp}-\frac{1}{\rho_L}+\mu\left(\frac{dh''}{dp}-\frac{1}{\rho_G}\right)-\mu\left(\frac{dh'}{dp}-\frac{1}{\rho_L}\right)\right)\frac{dp}{dt}. \tag{2.13}$$

For a small mass fraction μ, the following approximation

$$\mu(p)=\frac{h(p_{\mathrm{evap}})-h'(p)}{h''(p)-h'(p)} \tag{2.14}$$

can be used instead of (2.13) which is equivalent to $dh=0$, i.e., the evaporation and condensation processes are isenthalpic. Due to pressure losses or refraction waves, [9,11], the fluid reaches the vapor pressure p_{evap} and starts to evaporate on a path of constant enthalpy. The maximum amount of heat that can be received due the vaporization process is $\Delta h=h''(p)-h'(p)$. The local mass fraction μ of steam is directly coupled with the pressure distribution of the fluid-gas mixture by this approach. This is a consequence of the mechanical and thermodynamic equilibrium model considered here. The given model leads to the largest mass fraction of steam compared to the nonequilibrium cavitation models derived in [12,19]. The equilibrium model (2.14) does not consider surface tension σ, viscosity, or overheating effects which can be observed in real processes. The presented model can be used for studies of cavitation processes and basic phenomena of two-phase flows which will be described in the last section. To study more detailed effects of cavitation, the energy equation has to be considered.

Therefore the source term Γ used in the approach (1.2) can be transformed to

$$\Gamma=\rho\frac{d\mu}{dp}\left(\frac{\partial p}{\partial t}+v\frac{\partial p}{\partial z}\right).$$

This representation allows us to use the function $\mu(p)$ directly from (2.13) or (2.14). We have chosen the Eq. (2.14). The differences of mass fraction computed by (2.14) with respect to (2.13) are less than 10^{-5} for the processes considered in the next section.

For the thermodynamic equation of steam the ideal gas law is used, i.e., $p=\rho_G R_{\mathrm{H_2O}}T$. The equations of Van der Waals, Benedict, Weber, and Rubin, Redlich and Kwong, and Hirschfelder, Buehler, McGee, and Sutton, [20,21], could be used quite as for the steam phase. For the fluid, the properties of water $\rho_L=\rho_L(p,T)$, derived by Wagner et al. are used, [22]. These functions can also be used to compute the mass fraction of steam for a given pressure $p_{tr}<p\leqslant p_{\mathrm{evap}}$ and temperature T, where p_{tr} denotes the triple point of the fluid, [23]. For $p_{tr}<p\leqslant p_{\mathrm{evap}}$ the density of the fluid is fixed by constant because the density function of Wagner et al. represents the mixture density for this range.

The discretization of (1.12) is done in the following way:

$$\Gamma^n_i=\rho^{n+1/2}_i\left.\frac{d\mu}{dp}\right|^{n+1/2}_i\left(\frac{p^{n+1/2}_i-p^n_i}{\Delta t}+v^n_i\frac{p^{n+1/2}_{i+1}-p^{n+1/2}_{i-1}}{2\Delta z}\right), \tag{2.15}$$

where the derivative of the mass fraction by the pressure can be derived analytically by (2.14) for the full time-step Δt. The physical values denoted with $n+1/2$ are the result of the homogeneous hyperbolic problem (1.5) for $\mathbf{g}=\mathbf{0}$. On the boundaries of the computational domain there was no need to replace central discretization of the pressure gradient because we used dummy cells there.

The extension of the presented model to other fluids is quite simple. One has to measure the steam pressure p_{evap} as a function of the pressure p and temperature T. Further, the evaporation enthalpy has to be measured by experiments for the fluid.

3 Validation and Numerical Examples

As numerical examples we use Riemann problems as test cases. The Riemann problem consists of the hyperbolic system (1.2) and two constant states as initial data, which are separated by a discontinuity. It is a generalized shock tube problem. The solution of this problem has a relatively simple structure including shocks and rare faction waves. Because it can be calculated explicitly these problems are very useful for validation purposes, [16].

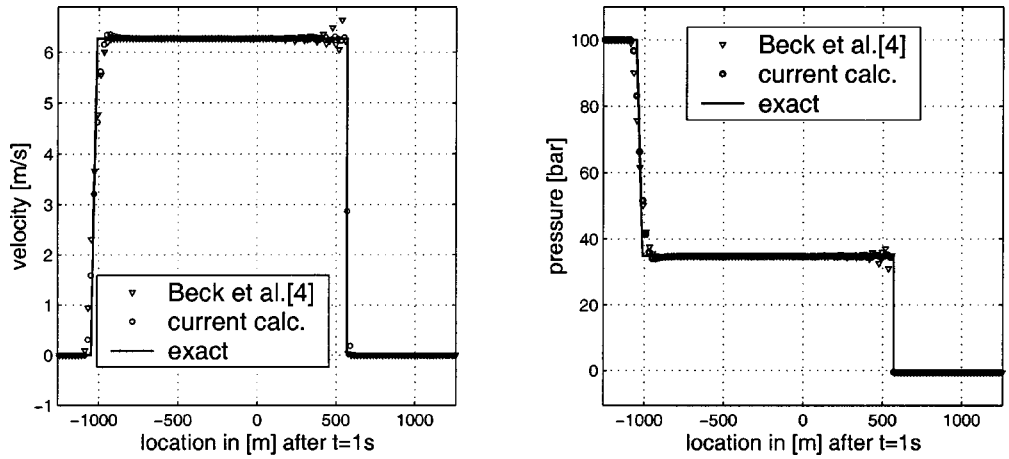

Fig. 2 Comparison of the pressure and velocity distribution for a Riemann problem with $p_L = 100$ bar and $p_R = -0.15$ bar at $t = 0$ s, with [9] and an exact solution

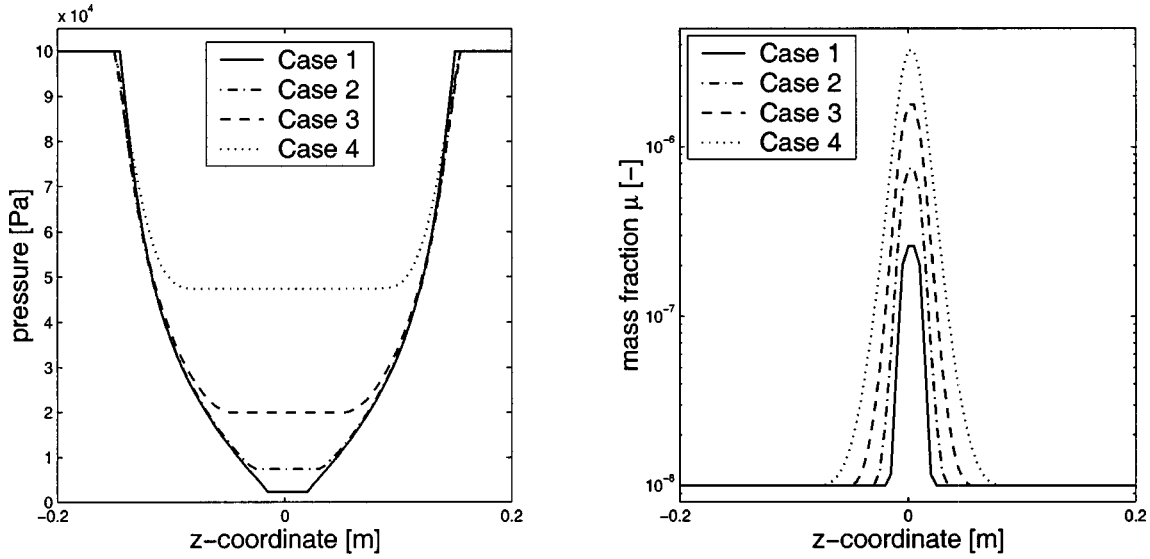

Fig. 3 Pressure distribution and mass fraction for different temperatures at $t = 100$ μs

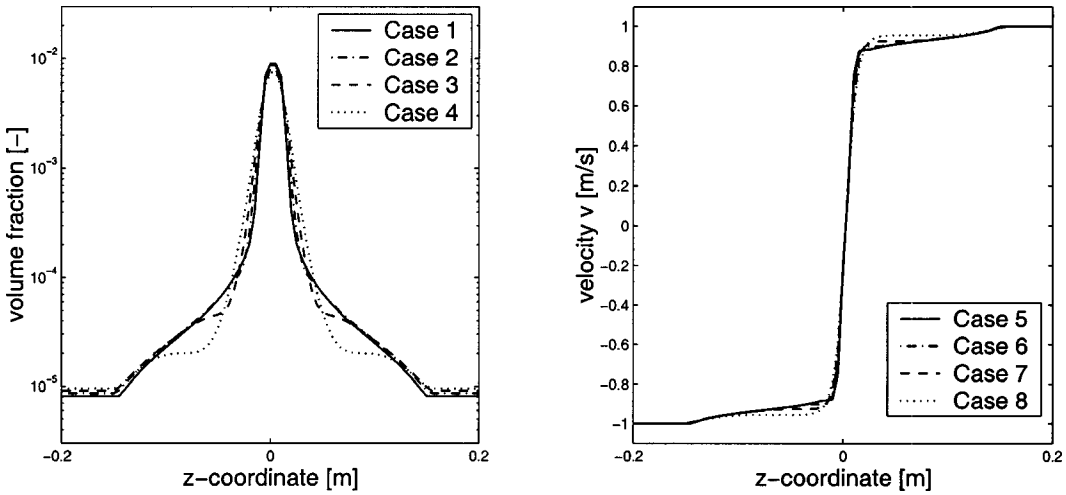

Fig. 4 Volume fraction and velocity distribution for four different temperatures at $t = 100$ μs

Table 1 Initial values for Riemann problems at $t=0$ s

	p_{left} [Pa]	v_{left} [m/s]	p_{right} [Pa]	v_{right} [m/s]	T [K]
Case 1	10^5	-1	10^5	1	293.15
Case 2	10^5	-1	10^5	1	313.15
Case 3	10^5	-1	10^5	1	333.15
Case 4	10^5	-1	10^5	1	353.15

Table 2 Initial data for Riemann problems at $t=0$ s

	p_{left} [Pa]	v_{left} [m/s]	p_{right} [Pa]	v_{right} [m/s]	T [K]
Case 5	10^7	0	10^5	0	313.15
Case 6	10^6	0	10^4	0	313.15
Case 7	10^5	0	10^3	0	313.15
Case 8	10^4	0	10^3	0	313.15

For the validation of the numerical scheme the equations of state from [9] are used. For this equation system one can obtain an analytic solution of the Riemann problem which is presented in Fig. 2. The values at the beginning of the calculation differs only in the pressure on the left and the right side of the Riemann problem, i.e., $p_L = 100$ bar and $p_R = -0.15$ bar. There is no physical inconsistency because the calculations was made with an pressure offset of 1.013 bar. With this values there is pure liquid on the left side and vapor on the right side at the start of calculation. The character of this solution is a right running shock wave and a left running expansion wave. Due to the small compressibility of the fluid the expansion fan is very thin compared to the ones occurring in a gas. The right running wave leads to a condensation of the vapor. The source term Γ describes the time-depending change of the mass fraction due to pressure increase. The evaporation process caused by pressure decrease is modeled by the same source term. Thus the source term works for the evaporation and as well as for the condensation correctly.

In Fig. 2 a very good agreement with the exact solution can be observed. Furthermore, although Beck et al. [9] used the same numerical scheme for their computations the solution oscillates behind the shock wave. In our current computations this phenomenon can be avoided just be splitting the equation of mass conservation.

We consider a pipe of one meter length with a constant cross-sectional area A for our own computations. For the first example,

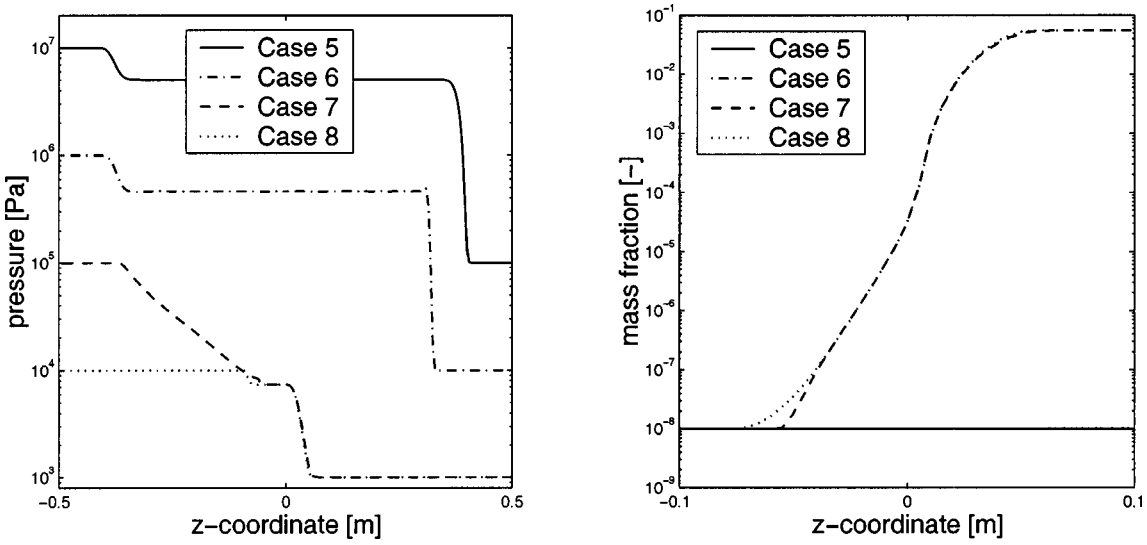

Fig. 5 Pressure distribution and mass fraction for different initial pressure at $t=250$ μs

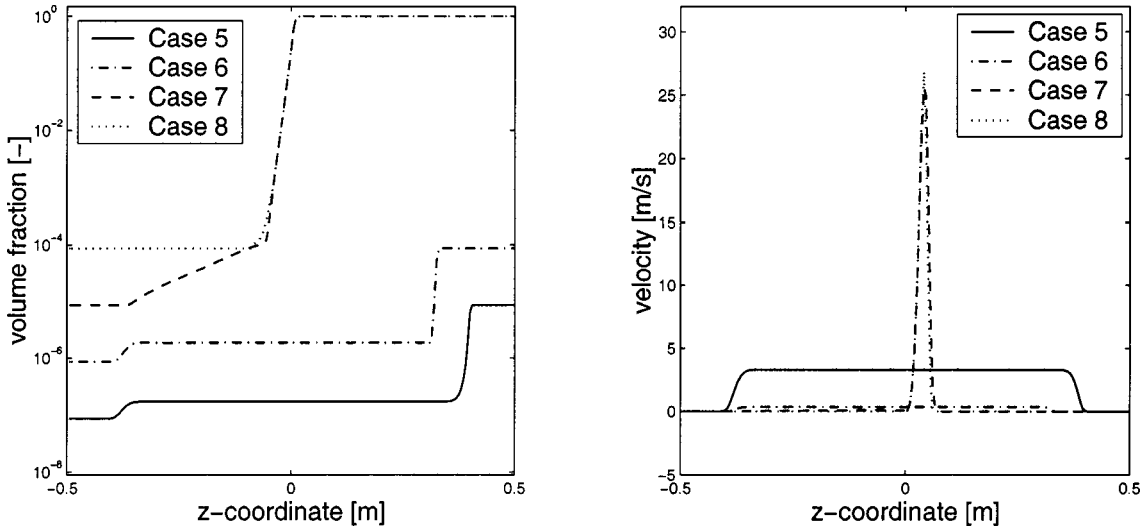

Fig. 6 Volume fraction and velocity distribution for different initial pressure at $t=250$ μs

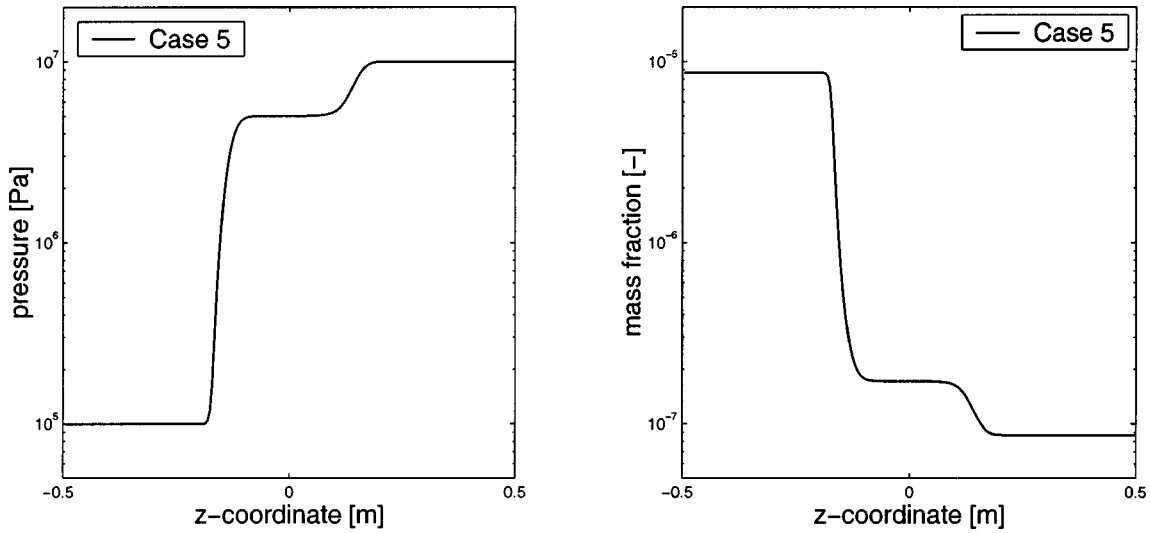

Fig. 7 Pressure and volume fraction distribution for the fifth case of Table 2 at $t=750\ \mu$s

the ends of the pipe are open, for the second example the ends are closed by rigid walls. The pipe is full filled with a liquid-gas mixture. The mixture is defined by the thermodynamic properties given in the previous section.

Example 1: The following table gives the values for $t=0$. We neglect the friction forces, i.e., $F=0$. The CFL number is fixed by 0.95 for each computational step and consequently Δt is computed in each time step again. The initial mass fraction of undissolved air is fixed by $\mu_0=10^{-8}$ which is constant for the complete simulation time. This assumption is also valid for the second case.

The first case can be interpreted as follows: the gas-liquid mixture flows with constant velocity in a pipe. Suddenly, one side of the pipe (at $z=0$) is completely closed which corresponds to an infinitely fast closing valve. Consequently, due to the inertia of the fluid, the pressure drops below the steam pressure. So, the fluid starts to evaporate. Because boundary conditions for closing valves are not implemented in the code, the initial conditions are chosen as presented. The point $z=0$ can be considered as a symmetry point in out example.

The Figs. 3 and 4 contain the plots of pressure p, volume fraction ε, mass fraction μ, and velocity v for the parameter set of Table 1.

Due to the initial conditions, the fluid starts to evaporate and the maximum of the mass fraction μ is quite different for each case. Further the pressure in the cavitated area drops hardly below the steam pressure. The steam pressure p_{evap} depends on the initial temperature T. On the other hand, the volume fraction ε is nearly equal distributed for the four cases. This effect has a great meaning for experimental investigations. The volume fraction is the physical property which is visible in experiments. One can only draw a conclusion from the volume fraction ε to the mass fraction μ by the knowledge of temperature T and pressure p at the corresponding place.

Example 2: For this example, the ends of the pipe are closed. As boundary conditions, reflection is assumed and implemented as suggested in Toro ([16] pp. 210–212). The Riemann problem is defined by different pressure values on the left and the right side of the assumed symmetry line at $z=0$. We are interested in the simulation of the wave motion starting with different initial data.

The temperature is constant for each data set. As shown in Fig. 5, the speed of sound and consequently the positions of shock waves strongly depend on the mass fraction of gas/steam.

The Figs. 5 and 6 contain the physical properties of the Riemann problem one of Table 2. They show their distributions after $t=250\ \mu$s before the waves have reached the walls. Figure 7 shows the pressure and the volume fraction of case 5 after the waves were reflected on the walls at $t=750\ \mu$s.

Conclusion

In this paper, a homogeneous cavitation model on the basis of the mechanical and thermodynamic equilibrium is introduced. The simulations of cavitating flow are connected to several difficulties which are the large range of mixture density and speed of sound. In connection with the described stabilization technique and the operator splitting method, cavitated flow can be simulated successfully. In contrast to [9] a continuity equation for each phase is used. This approach does not lead to oscillations behind the shock wave in contrast to the approach using one equation for the conservation of mass.

The next step is to add more physical properties of the cavitation process, i.e., to add the energy equation to the model (1.2) and to use more detailed source terms for the phase transition and momentum correlation as derived in [19,24].

References

[1] Hapke, T., and Iben, H.-K., 1998, "Kavitationsmodellierung bei eindimensional Str 'omungsvorg' angen," Motortech. Z.
[2] Huhn, J., and Wolf, J., 1975, *Zweiphasenströmung*, VEB Fachbuchverlag Leipzig.
[3] Nguyen-Schaefer, H., and Sprafke, H., 1998, "Numerical Study on Interaction Effects of Bubbles Induced by Air-Release and Cavitation in Hydraulic Systems," *Tenth Bath International Fluid Power Workshop*, Research Studies Press, John Wiley and Sons, New York.
[4] Sprafke, P., 1999, "Numerische und experimentelle Untersuchungen des dynamischen Verhaltens hydraulischer Systeme unter Berücksichtigung von Kavitation und Luftausgasung," Ph.D. thesis, University Karlsruhe.
[5] Baur, T., 1997, "Auswirkungen der Diffusion gelöster Gase auf das Wachstum von Kavitationsblasen," Ph.D. thesis, RWTH Aachen, Institut für Wasserbau und Wasserwirtschaft.
[6] Regner, G., 1999, "Blasendynamisches Kavitationsmodell für eine eindimensionale Strömungssimulation," Ph.D. thesis, Technical University Graz.
[7] Wallis, W., 1975, *One dimensional Two-Phase Flow*, McGraw-Hill, New York.
[8] Kolev, N. I., 1986, *Transiente Zweiphasen-Strömung*, Springer-Verlag, Berlin.
[9] Beck, M., Iben, U., Mittwollen, N., Iben, H.-K., and Munz, C.-D., 2001, "On Solution of Conservation Equations in Cavitated Hydraulic Pipelines," *3rd International Symposium on Computational Technologies for Fluid/Thermal/Chemical Systems with Industrial Applications*, July 22–26, Atlanta, GA.
[10] Beck, M., 2002, "Kavitation in Diesel-Einspritzsystemen," Ph.D. thesis, University Magdeburg and Robert Bosch GmbH, in preparation.
[11] Wrona, F., 2001, "Numerische Umsetzung von homogenen Kavitationsmodellen," Master's thesis, University Stuttgart.
[12] Iben, U., 2001, "Entwicklung und Untersuchung von Kavitationsmodellen im Zusammenhang mit transienten Leitungsströmungen," in preparation.

[13] Fox, R., and McDonalds, A., 1994, *Introduction to Fluid Mechanics*, John Wiley and Sons, New York.
[14] Lahey, T., and Wallis, G., 1975, ''Non-equilibrium Two-Phase Flow,'' Presented at the ASME Winter Annual Meeting, Nov. 30–Dec. 5, Houston, http://www.addall.com/Browse/Detail/0317080873.html.
[15] Hapke, I., 1995, ''Theoretische und Numerische Untersuchungen an Kavitationsmodellen,'' Master's thesis, Universität Magdeburg, ISUT.
[16] Toro, E. F., 1997, *Riemann Solvers and Numerical Methods for Fluid Dynamics*, Springer-Verlag, New York.
[17] Einfeldt, B., Munz, C.-D., Roe, P. L., and Sjögreen, B., 1991, ''On Godunov-Type Methods Near Low Densities,'' J. Comput. Phys., **92**, pp. 273–295.
[18] Harten, A., Lax, P., and van Leer, B., 1983, ''On Upstream Differencing and Godunov-Type Schemes for Hyperbolic Conservation Laws,'' SIAM Rev., **25**, pp. 35–62.
[19] Iben, U., 2000, ''Cavitation modeling,'' *Analysis, Modeling and Simulation*, Gordon and Breach, London.
[20] Iben, H.-K., and Schmidt, J., 1999, *Starthife Thermodynamik*, Teubner Verlag.
[21] Yorizane, M., and Masuoka, H., 1969, ''Equations of State at High Pressure From Standpoint of Gas-Liquid Equilibria,'' Int. Chem. Eng., **9**(3).
[22] Wagner, W., Span, S., and Bonsen, T., 1999, *Wasser und Wasserdampf*, Springer-Verlag, New York.
[23] Baehr, H. D., and Stephan, K., 1994, *Wärme- und Stoffübergang*, Springer-Verlag, New York.
[24] van Wijngaarden, L., 1976, ''Hydrodynamic Interaction Between Gas Bubbles in Liquid,'' J. Fluid Mech., pp. 27–44.

Motoaki Kimura
e-mail: kimura@mech.cst.nihon-u.ac.jp

Masahiro Takei

Department of Mechanical Engineering,
College of Science and Technology,
Nihon University,
8 Kanda Surugadai 1-Chome,
Chiyoda-ku
Tokyo 101-8308, Japan

Chih-Ming Ho
Mechanical and Aerospace Engineering
Department,
University of California,
Los Angeles, CA 90095

Yoshifuru Saito
Department of Electrical and Electronic
Engineering,
College of Technology,
Hosei University,
3-7-2 Kajino,
Koganei,
Tokyo 184-8584, Japan

Kiyoshi Horii
Shirayuri College,
1-25 Midorigaoka
Chiyoda-ku,
Tokyo 101-8308, Japan

Visualization of Shear Stress With Micro Imaging Chip and Discrete Wavelet Transform

The two-dimensional low-speed structure of a turbulent boundary layer has been clearly visualized by a combination of a shear stress sensor using micro electro mechanical systems and the discrete wavelet transform. The application of two-dimensional discrete wavelet transforms to the visualization of wall shear stress data obtained using the micro shear stress imaging chip is described. The experiment was carried out under various Reynolds number conditions. It is shown that it is possible to visualize the low-speed streak structure as contours of two-dimensional wavelet level corresponding to spanwise wave number as a function of Reynolds number. [DOI: 10.1115/1.1516599]

1 Introduction

The presence of near-wall shear stress streaks in turbulent boundary layers has been observed in flow visualization investigations, [1–5]. These streaks are typically very small at high Reynolds (Re) numbers and can not be properly resolved by traditional measurement techniques. Numerical simulations indicate that the streaks are associated with streamwise vortices in the viscous sublayer. The rotational motion of these vortices imposes high fluctuation surface shear stresses on the wall, [6]. Several techniques have been proposed for measuring shear stresses. The hot-film technique and its variants have been widely used in detailed investigations of fluctuating wall shear stress, [7,8]. The direction-sensitive laser Doppler anemometer is a technique that enables for the evaluation of both the magnitude and direction of the wall shear stress. The optical method proposed by Naquwi [9] is capable of measuring the wall shear stress at a high spatial resolution. However, an instrument with a fine spatial resolution, fast frequency response and high sensitivity for turbulent boundary layer research has not yet been developed.

The recent development of the micro electro mechanical systems (MEMS) manufacturing process has offered the possibility of sensing and controlling small near-wall streaks, [10]. A multidisciplinary research collaboration between UCLA and Caltech was initiated to design and fabricate a large-scale distributed control system with integrated micro-machined transducers and microelectronic circuits for surface shear stress control in turbulent boundary layers, [11,12].

However, the distribution of stripe structure with MEMS is an integral value composed of various frequency ingredients and can result in ambiguities in the stripe structure. Therefore, new techniques such as statistical and frequency analysis of the image data are necessary to perform detailed analysis. The stripe structure obtained with the micro-imaging chip is clearly visualized and analyzed using statistical methods, [13]. In terms of frequency analysis, the Fourier transform is a popular method but it removes the time-space information of the stripe structure.

Recent studies have investigated the use of the wavelet transform for time-space frequency analysis in mechanical engineering applications. The main advantage of wavelet analysis is its ability to analyze the frequency and not erase the time-space information. Wavelet transforms are classified as either continuous or discrete, [14]. Continuous wavelet transforms have been used for studies of time-frequency analysis in turbulent shear flow including self-similarity of a jet inner structure using one-dimensional continuous wavelets, [15], and scale transition in a mixing layer using two-dimensional continuous wavelets, [16]. In addition, most studies of time-frequency analysis use continuous wavelet transforms. Conversely, eddy motion in the atmospheric surface layer has been analyzed using the wavelet thresholding method, [17]. The analysis enables for an image to be decomposing and regenerated numerically according to the orthonormal transform. Saito [18] applied this principle to the analysis of electromagnetic waves.

Contributed by the Fluids Engineering Division for publication in the JOURNAL OF FLUIDS ENGINEERING. Manuscript received by the Fluids Engineering Division May 30, 2000; revised manuscript received May 29, 2002. Associate Editor: J. Bridges.

The purpose of this paper is to describe the application of two-dimensional discrete wavelet transforms to the visualization of wall shear stress data obtained using a micro shear stress imaging chip. The stripe structure of shear stresses in a turbulent boundary layer is extracted for various frequency levels.

2 Experiments

2.1 Micro Shear Stress Imaging Chip. A micro shear stress imaging chip, which is composed of multiple thermal type sensors, [19], is shown in Fig. 1. The chip has three rows of micro sensors, each of which contain an array of 25 sensors. Figure 2 shows plan and cross-sectional views of the micro shear stress sensor. Each micro sensor consists of a $150\times3\times0.45$ μm polysilicon resistor, and a $200\times200\times1.2$ μm silicon nitride diaphragm that seals a 2 μm deep vacuum cavity. The purpose of the cavity is to reduce heat transfer from the resistor to the substrate and to increase the sensitivity of the sensor, [20]. The sensors are connected to external constant temperature mode circuits, which are used in the hot-wire anemometer, to drive at an overheat ratio of 1.1 through gold bonding wires. Output from the anemometer circuits is digitized by a 64-channel Keithly Metrabyte ADC board in a Pentium-based PC. The sensitivity of the shear stress sensor is approximately 1.0 V/Pa at a gain of 10.

2.2 Shear Stress Sensor Calibration and Temperature Compensation. The heating power of a shear stress sensor operating in steady state conditions can be correlated with wall shear stress τ as follows, [8]:

$$i^2R^2=(T_f-T)(A+B\tau^{1/3}) \tag{1}$$

where T_f and T are the temperature of the heated sensor and the measured fluid, respectively, R is the resistance of the sensor, i is the heating current passing through the sensor, and A and B are calibration constants. Two theoretical methods are used to correlate the output voltage with the wall shear stress τ. In the first method, τ in fully developed turbulent flow is related to the streamwise pressure gradient by

$$dP_x/dx=-\tau/h \tag{2}$$

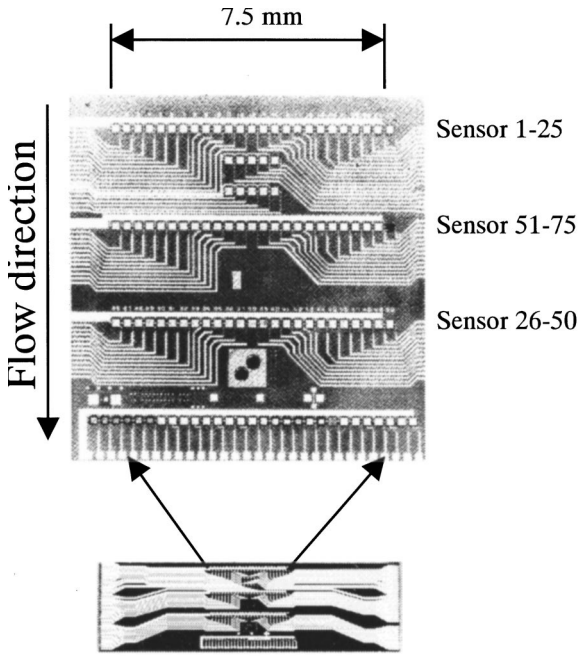

Fig. 1 Surface shear stress imaging chip

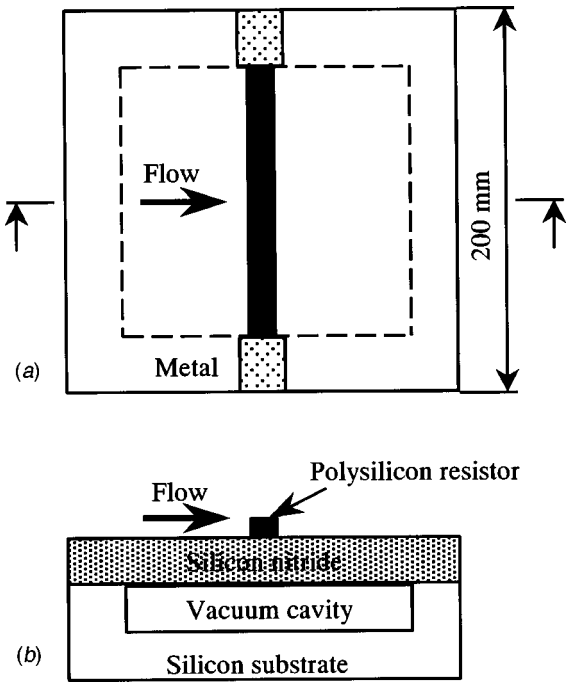

Fig. 2 Schematic plan (*a*) and cross-sectional (*b*) views of the micro shear stress sensor

where P_x is the local pressure, x is the streamwise coordinate, and h is the half-height of the wind channel. The pressure drop and output voltage of the sensor was measured at center velocities ranging from 8 to 20 m/s. If T is constant, the wall shear stress can be directly related to the output voltage E_o by a sixth-order polynomial as

$$\tau=a_0+a_1E_0+\ldots+a_6E_0^6 \tag{3}$$

where a_0a_1, a_2, $\ldots$ a_6 are calibration constants. These constants were calibrated in the channel flow in a downstream region in which turbulent flow was fully developed.

In the second method, an empirical relationship between Re and the wall shear stress in fully developed channel flow is obtained, [21], by using

$$u_\tau/u_\infty=0.1079\,\mathrm{Re}^{-0.089} \tag{4}$$

and

$$\tau=u_\tau^2\rho, \tag{5}$$

where u_τ is the friction velocity, u_∞ is the center velocity of the channel, Re ($=hu_\infty/\nu$, where h is the half-width of the channel and u_∞ is centerline velocity). The streamwise pressure gradient was measured and τ calculated using Eq. (2) and the second method given by Eqs. (4) and (5). Good agreement was observed between the two methods.

When T varies during the measurement process, a thermal correction should be applied. To determine the correction coefficient, previous micro shear stress sensor versus fine thermocouple simultaneous measurements have done in channel flow of 10 m/s at room temperatures ranging from 19.0 to 22.0°C. The slope of the sensor output/temperature curve was -310 mV/°C. Temperature compensation was achieved by collecting both ambient temperature and shear stress data and then performing an a posteriori correction using software.

2.3 Experimental Setup. This experiment was carried out in a turbulent channel flow facility. The channel, constructed of 13 mm Plexiglas, was 610 mm$\times$25.4 mm in cross section and 4880 mm long. A DC axial blower was used to generate the airflow.

Previous hot-wire measurements suggested that a centerline channel flow of 10 m/s consists of laminar entrance flow and fully developed turbulent flow at the downstream half channel. The micro shear stress imaging chip was flush mounted on the channel wall 4267 mm from the inlet. One array consisting of 25 micro shear-stress sensors covering a distance of 7.5 mm was used to measure the instantaneous spanwise distribution of turbulent surface shear stress, Re ranged from 6960 to 17,400.

2.4 Shear-Stress Distribution. Statistical values, which are root mean square, skewness factor, and flatness factor of wall shear stress measured using the imaging chip, are confirmed, [22], to be similar to the data obtained in previous experiments, [7,23], and by numerical computation, [6]. Figure 3 shows the distribution of two-dimensional shear stresses. The horizontal axis spans 7.5 mm (data number 25), and the vertical axis spans 51.2 ms (data number 512) for three different values of Re. Each shear stress value was normalized by

$$\overline{\tau} = \frac{\tau - \tau_m}{\tau_{\mathrm{rms}}} \tag{6}$$

using the mean shear stress $_m$ root mean square shear stress $_{\mathrm{rms}}$ for each Re number as shown in Figs. 3(*a*), (*b*), and (*c*). The high shear stress regions are marked in red while blue represents shear stress with 11 contour colors. Figure 3(*d*) shows the original data in the vertical direction at the point at which the maximum value was observed before normalization. The streaks were narrower, closer together, and appeared at shorter time intervals as Re increases. The shear stress fluctuation near to the wall increased rapidly, resulting in a significant peak in the turbulent boundary layer, because the velocity gradient increased rapidly due to the influence of eddies guided by bursting events. From Figs. 3(*a*) to (*c*), the red regions of Re=17,400 are insignificant and the blue region is larger than those for lower Re number conditions.

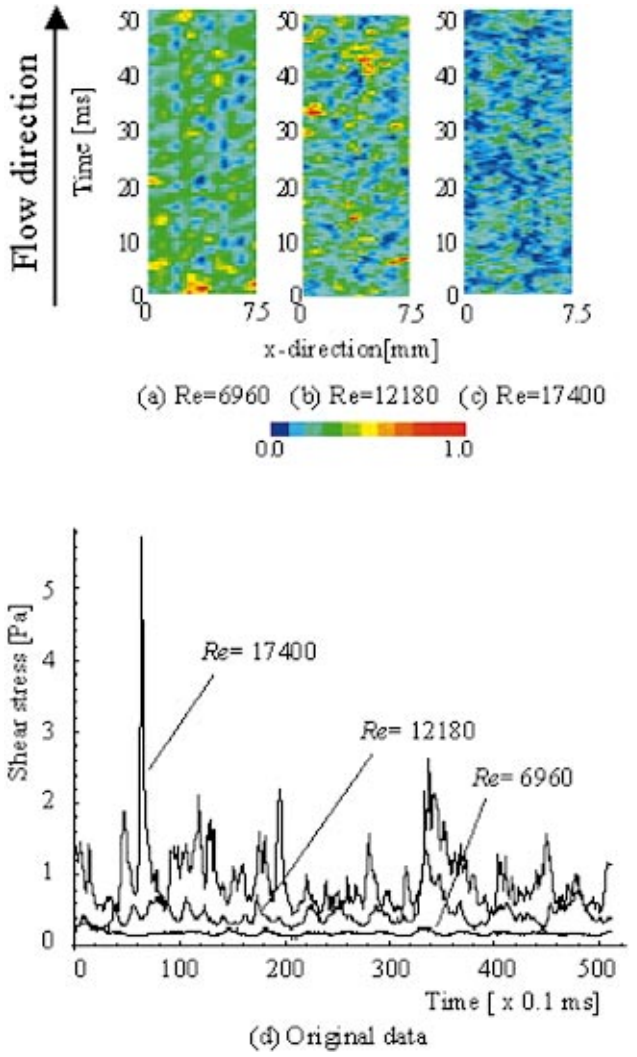

Fig. 3 Shear stress measured with the imaging chip; (*a*) Re =6960, (*b*) Re=12,180, (*c*) Re=17,400, (*d*) original data

3 Discussion

3.1 Spanwise Spacing of Low Speed Streaks. The characteristics of sublayer streaks are well documented. The streaks, which consist of low-speed fluid in the sublayer, appear randomly and are typically $1000\nu/u_\tau$ long in the streamwise direction, [24], with a mean spanwise spacing of $100\nu/u_\tau$, [5,25]. Here, ν and u_τ denote the kinematic viscosity and the wall shear velocity, respectively.

Next, the spanwise spacing of streaks was inspected by wave number spectrum with sensor data of 25 spanwise profiles as shown in Fig. 4. Low shear stress areas corresponding to low-speed streaks and high shear stress areas corresponding to kink parts of low-speed streaks were observed. Figure 5 shows an example of a spanwise wave number spectrum for the determination of the spanwise interval of streak structure. The figure shows the wave number spectrum for Re=6960. Local maxima at 200 and 300 [1/m] are not conspicuous peaks, but indicate a spanwise spacing interval of low speed streak. This result suggests that a spanwise spacing of low speed streaks is $99-150\nu/u_\tau$. Similar results were observed for a range of Re numbers. It is concluded that this value verifies the result of $100\nu/u_\tau$ obtained from visualization experiments.

3.2 Streamwise Wave Number Decomposition

3.2.1 Analysis Method and Results Using Two-Dimensional Discrete Wavelet Multiresolution Analysis. The original data was derived from 25 data points over 512 epochs. The 25 points were extrapolated to 32 points (4 on the right side and 3 on the left side) with Fourier series coefficients in order to afford the power of two for the discrete wavelet transform. The values of the original points, which are points 5 to 29 in the extrapolated coordinate system, were extracted after the calculation. The extrapolated length measured 9.6 mm ($300\,\mu\mathrm{m}\times 32$). In the case of the 16 input data and fourth-order Daubechies functions, multiresolution analysis outputs Level 0 to Level 3. The two-dimensional wavelet spectrum S was obtained from

$$S = W_n X W_m^T \tag{7}$$

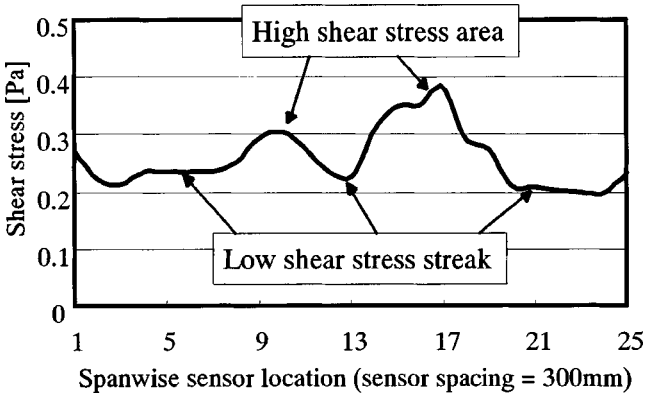

Fig. 4 Shear stress distribution in spanwise direction (Re =6960)

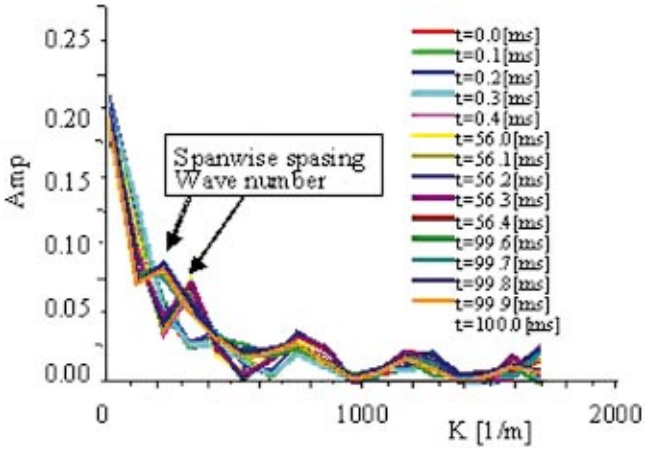

Fig. 5 Wave number spectrum of shear stress distribution in spanwise direction (Re=6960)

where W_m^T is a transpose of W_n. From Eq. (7), the discrete inverse wavelet transform is expressed by

$$X = W_n^T S W_m . \tag{8}$$

In this study, a 16th-order Daubechies function was used as the analyzing wavelet. A multiresolution analysis was performed using the inverse wavelet transform in Eq. (8), after the wavelet transform in Eq. (7) was operated to 25×512 shear stress distribution data in Fig. 3. In the case of the sixteenth-order Daubechies function and 512 ($=2^9$) time data (total measurement time $=51.2$ ms), the multiresolution analysis with respect to time classifies to seven levels as shown in

$$X = W_n^T S W_m = W_n^T S_0 W_m + W_n^T S_1 W_m + W_n^T S_2 W_m + W_n^T S_3 W_m + W_n^T S_4 W_m + W_n S_5 W_m + W_n^T S_6 W_m . \tag{9}$$

In Eq. (9), $W_n^T S_0 W_m$ is denoted Level 0, which indicates the lowest frequency, $W_n^T S_6 W_m$ is denoted Level 6, which indicates the highest frequency. In data point 32, the wavelet level of the multiresolution was decomposed from level 0 to level 3. The absolute values by Fourier transform and wavelets are shown in Fig. 6 and Fig. 7. Each level operates a form of band pass filter.

Figures 8, 9, and 10 show the multiresolution with nine contours for low Re number, middle Re number, and high Re number conditions, respectively. Low shear stresses are denoted blue and high shear stresses are denoted red. Minus values are produced because the values were normalized. Level 6 is not shown because noise was dominant. The patterns adding all levels from Level 0 to Level 6 enable the complete recovery of the original shear stress distributions in Fig. 3, because Daubechies analyzing wavelets are orthonormal functions. The relation between the representative frequency, which was calculated with the maximum P.S.D. in Figs. 6 and 7, and each wavelet level is shown in Table 1 and Fig. 11.

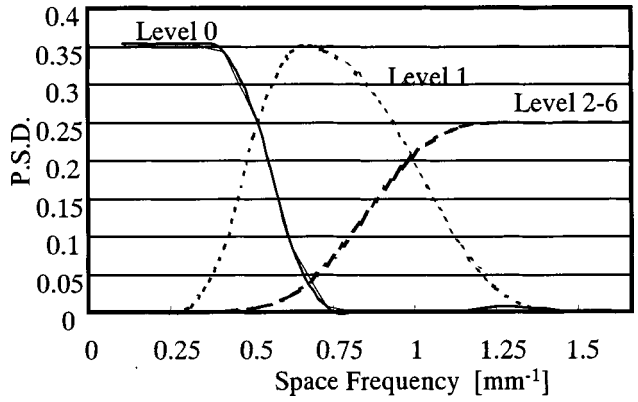

Fig. 6 Space frequency of 16th Daubechies

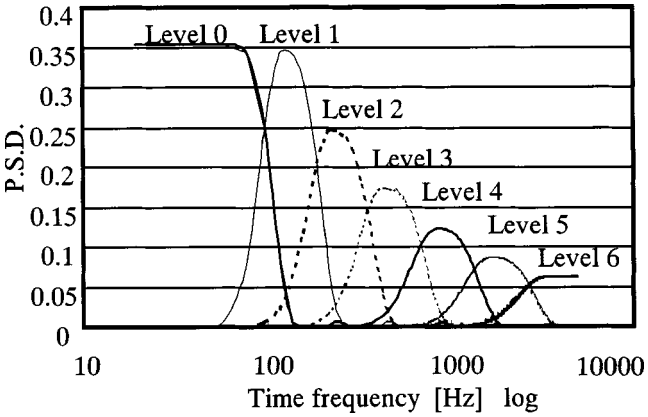

Fig. 7 Time frequency of 16th Daubechies

From these figures, the original input data were decomposed from the low-frequency component Level 0 to the high-frequency component Level 5. I have done the above section of spanwise spacing of low-speed streaks, if spanwise spacing is around 100 times of the wall unit, the spanwise wave number corresponding to Re=6960 and 17,400 becomes 0.24 mm^{-1} and 0.61 mm^{-1}, respectively. Level 0 shows a low-speed domain in Re=6960 and level 1 corresponds to Re=17,400. The stripe structures due to a series of bursting events in the low-speed shear stress area are visualized clearly for each frequency level without erasing the time and space information. In particular, red and green regions appear more clearly on Levels 0 and 1 for low Re numbers. The shear stress distribution appears until Level 3 and wave patterns are observed on Levels 4 and 5.

3.2.2 Discussion According to the Kolmogorov Turbulence Theory. The relation between wavelet level and wave number is discussed by application of the Kolmogorov turbulence theory to

Table 1 Relation between wavelets level and representative frequency

	Time frequency	Space frequency
Representative frequency on Level 0	2.0 ×10¹[Hz]	1.04 ×10⁻¹[mm⁻¹]
Representative frequency on Level 1	1.4 ×10²[Hz]	7.00 ×10⁻¹[mm⁻¹]
Representative frequency on Level 2	2.3 ×10²[Hz]	
Representative frequency on Level 3	4.5 ×10²[Hz]	
Representative frequency on Level 4	8.8 ×10²[Hz]	1.2 ×10⁰[mm⁻¹]
Representative frequency on Level 5	1.7 ×10³[Hz]	
Representative frequency on Level 6	4.7 ×10³[Hz]	
Maximum frequency on Level 6 f_{max}	4.7 ×10³[Hz]	1.6 ×10⁰[mm⁻¹]

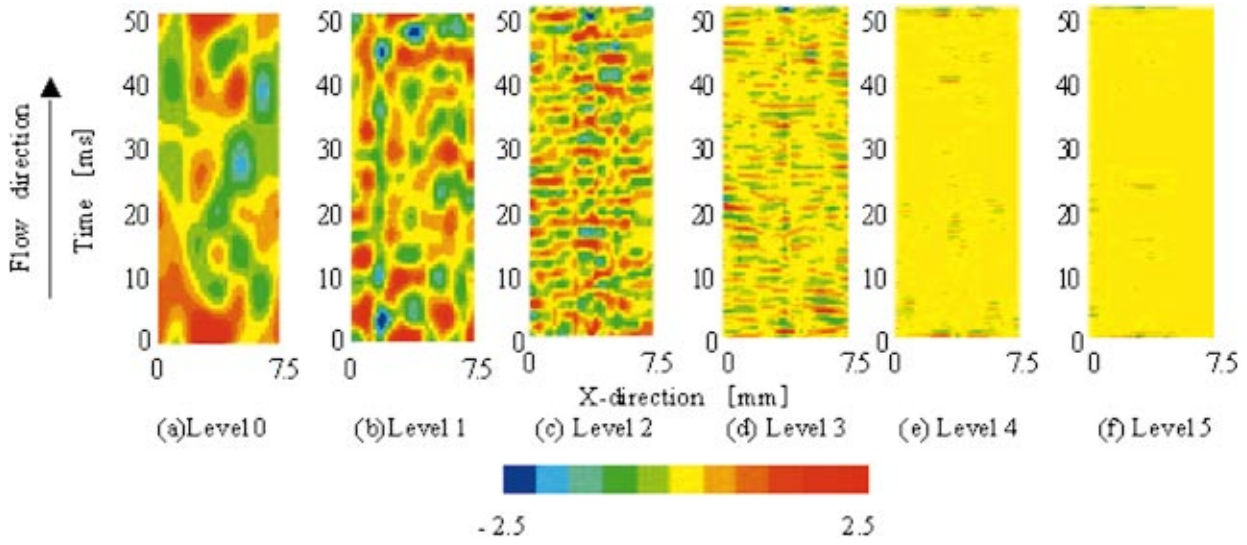

Fig. 8 Wavelets multiresolution in Re=6960

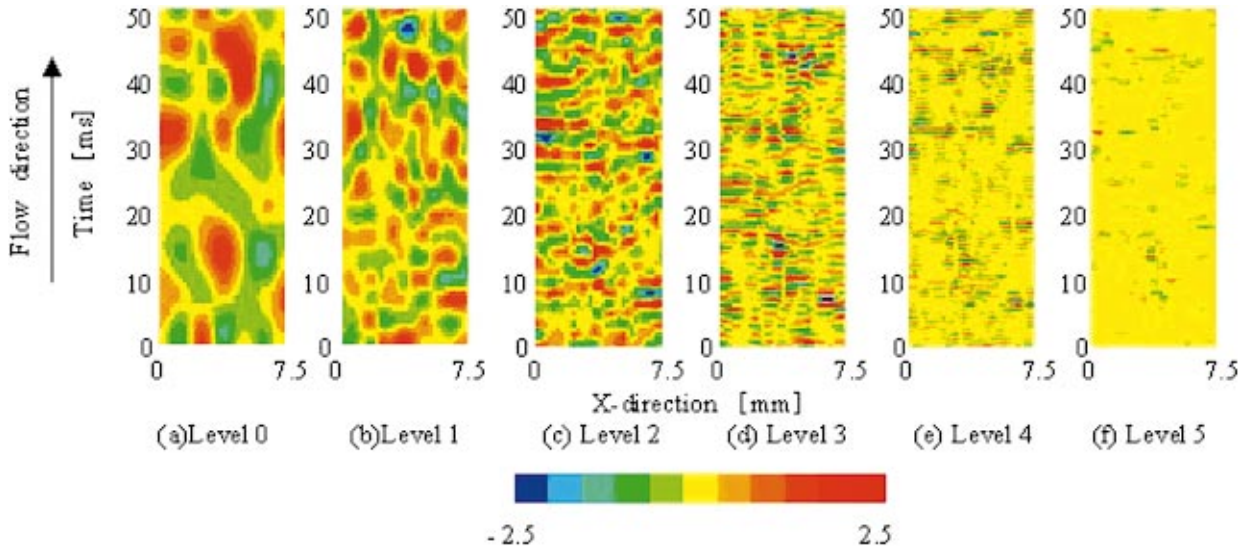

Fig. 9 Wavelets multiresolution in Re=12,180

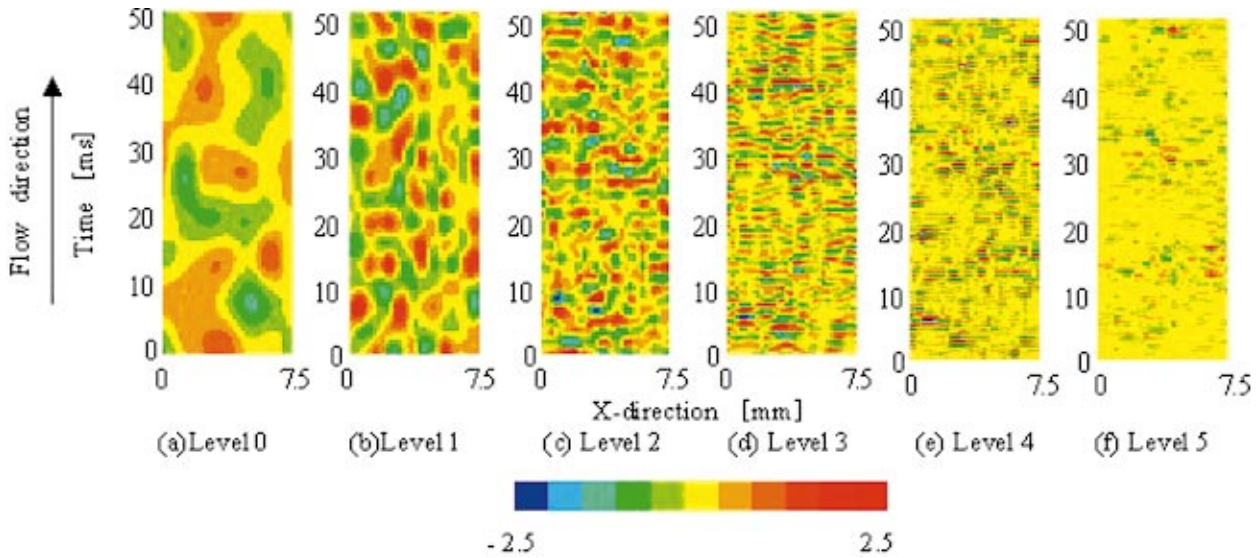

Fig. 10 Wavelets multiresolution in Re=17,400

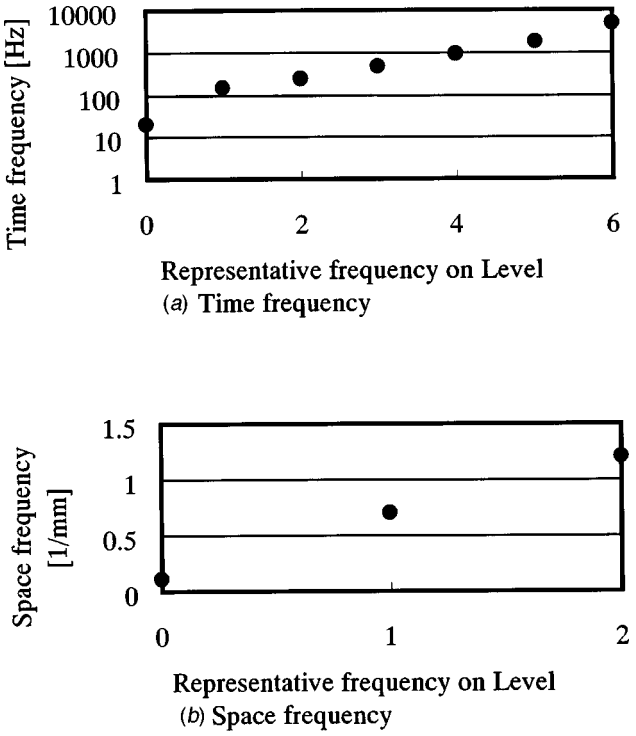

Fig. 11 Relation between wavelets level and representative frequency

the time axis of discrete wavelet multiresolved resolution. The Kolmogorov wave number k_k that indicates the highest viscous dispersion rate is expressed by

$$k_k = \left(\frac{\varepsilon}{\nu^3}\right)^{1/4} \tag{10}$$

where ν is the kinematic viscosity, ε is the energy transportation rate, that is

$$\varepsilon = A\frac{v_0^3}{l_0}$$
$$v_0 = 0.2\overline{v} \tag{11}$$

Table 2 Relation between wavelet level and representative wave number

	v=8m/s Re=6960	v=14m/s Re=12180	v=20m/s Re=17400
Representative wavenumber on Level 0	7.7 $\times 10^{-1}$[cm^{-1}]	4.4 $\times 10^{-1}$[cm^{-1}]	3.1 $\times 10^{-1}$[cm^{-1}]
Wavenumber in energy contain region k_0	8.0 $\times 10^{-1}$[cm^{-1}]	8.0 $\times 10^{-1}$[cm^{-1}]	8.0 $\times 10^{-1}$[cm^{-1}]
Representative wavenumber on Level 1	5.4 $\times 10^{0}$[cm^{-1}]	3.1 $\times 10^{0}$[cm^{-1}]	2.1 $\times 10^{0}$[cm^{-1}]
Representative wavenumber on Level 2	9.2 $\times 10^{0}$[cm^{-1}]	5.3 $\times 10^{0}$[cm^{-1}]	3.7 $\times 10^{0}$[cm^{-1}]
Representative wavenumber on Level 3	1.8 $\times 10^{1}$[cm^{-1}]	1.0 $\times 10^{1}$[cm^{-1}]	7.1 $\times 10^{1}$[cm^{-1}]
Representative wavenumber on Level 4	3.4 $\times 10^{1}$[cm^{-1}]	2.0 $\times 10^{1}$[cm^{-1}]	1.4 $\times 10^{1}$[cm^{-1}]
Representative wavenumber on Level 5	6.7 $\times 10^{1}$[cm^{-1}]	3.9 $\times 10^{1}$[cm^{-1}]	2.7 $\times 10^{1}$[cm^{-1}]
Representative wavenumber on Level 6	1.9 $\times 10^{2}$[cm^{-1}]	1.0 $\times 10^{2}$[cm^{-1}]	0.7 $\times 10^{2}$[cm^{-1}]
Maximum wavenumber on Level 6 k_{max}	1.96 $\times 10^{2}$[cm^{-1}]	1.12 $\times 10^{2}$[cm^{-1}]	0.79 $\times 10^{2}$[cm^{-1}]
Kolmogorov wavenumber k_k	3.49 $\times 10^{2}$[cm^{-1}]	2.67 $\times 10^{2}$[cm^{-1}]	1.76 $\times 10^{2}$[cm^{-1}]

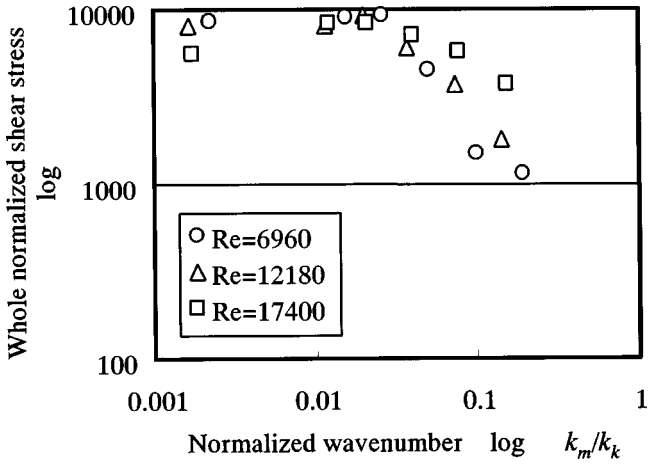

Fig. 12 Relation between whole normalized shear stress and wavenumber on the time space

where v_0 is a representative velocity fluctuation that is assumed to be 0.2 times the mean velocity $\overline{v}$, and l_0 is a length scale in the energy contain region that is assumed to be the radius of the pipeline. In this study, the constant A is assumed to be 1.0. The representative wave number on wavelet level m is obtained by

$$k_m = \frac{2\pi f_R}{v_0} \tag{12}$$

where f_R is a representative frequency, which is the maximum power spectrum density in Fig. 7. The relation between the wavelet level and the representative wave number is shown in Table 2. From this table, Level 0 indicates a wave number under the energy contain region, and Level 6 indicates the vicinity of k_k. The wavelet level covers from the energy contain region to the viscous dispersion region.

In the following section, all shear stresses on each wavelet level are defined by

$$\overline{\tau_{\text{all}}} = \sum_{j=1}^{512}\sum_{i=1}^{25}\sqrt{(\overline{\tau_{ij}})^2} \tag{13}$$

to consider the relation between the stress and Re. i is a position on the time axis, j is a position on the space axis. The results are shown in Fig. 12. The horizontal axis is the representative wavenumber in Table 1 normalized using k_k.

In this figure, the shear stress maintains an approximately constant value until wave number 0.02, which is equivalent to Level 2 irrespective of Re. This is because the wave number is near to the energy contain region from Table 2. However, at wave numbers greater than 0.02, the total shear stress decreases as the wave number increases. Moreover, the shear stress dramatically decreases for low values of Re. This is because the eddy dispersion is significantly influenced by the viscosity in low Re regions. The proposed visualization technique is therefore verified.

4 Conclusions

A micro shear-stress imaging chip was used to measure the instantaneous shear-stress distribution in a turbulent wall boundary layer in flow with Reynolds number ranging from 6960 to 17,400. The two-dimensional shear stress distributions were visualized with a two-dimensional discrete wavelet transform. The following conclusions are proposed:

1. The two-dimensional structure of wall shear stress can be decomposed and clearly visualized on each frequency level without erasing time-space information using two-dimensional wavelet multiresolution analysis.

2. It is possible to visualize the low speed streak structure on the wall as contours of two-dimensional wavelet level corresponding to spanwise wave number as a function of Re number.
3. The total shear stresses under Level 2 relevant to near energy contain region maintains the same value irrespective of Re number. However, the total shear stress over Level 3 in near viscous dispersion regions under low Re number conditions is lower than that under high Re number conditions. This is a reasonable observation because the structure is significantly influenced by viscosity under low Re number conditions.

Acknowledgments

The authors would like to thank Dr. F. Jiang and Dr. Y.-C. Tai from the California Institute of Technology for their help with this study.

References

[1] Kim, H. T., Kline, S. J., and Reynolds, W. C., 1971, ''The Production of Turbulence Near a Smooth Wall in a Turbulent Boundary Layer,'' J. Fluid Mech., **50**, Part 1, pp. 133–160.
[2] Falco, R., 1980, ''The Production of Turbulence Near a Wall,'' AIAA Paper No. 80-1356.
[3] Cantwell, B. J., 1981, ''Organized Motion in Turbulent Flow,'' Annu. Rev. Fluid Mech., **13**, pp. 457–515.
[4] Head, M. R., and Bandyopadhyay, P., 1981, ''New Aspects of Turbulent Boundary-Layer Structure,'' J. Fluid Mech., **107**, pp. 297–338.
[5] Smith, C. R., and Metzler, S. P., 1983, ''The Characteristics of Low-Speed Streaks in the Near-Wall Region of a Turbulent Boundary Layer,'' J. Fluid Mech., **129**, pp. 27–54.
[6] Kim, J., Moin, P., and Moser, R., 1987, ''Turbulent Statistics in Fully Developed Channel Flow at Low Reynolds Number,'' J. Fluid Mech., **177**, pp. 133–166.
[7] Alfredsson, P. H., Johansson, A. V., Haritonidis, J. H., and Eckelmann, H., 1988, ''The Fluctuating Wall-Shear Stress and the Velocity Field in the Viscous Sublayer,'' Phys. Fluids, **31**, pp. 1026–1033.
[8] Bruun, H. H., 1995, ''Hot-Wire Anemometry,'' Oxford University Press, Oxford, UK, pp. 272–286.
[9] Naqwi, A. A., and Reynolds, W. C., 1991, ''Measurement of Turbulent Wall Velocity Gradients Using Cylindrical Waves of Laser Light,'' Exp. Fluids, **10**, pp. 257–266.
[10] Ho, C. M., Tung, S., and Tai, Y. C., 1996, ''Interactive Control of Wall Structures by MEMS-Based Transducers,'' *Advances in Turbulence, Proceedings of the Sixth European Turbulence Conference*, Lausanne, Switzerland, July, p. 413.
[11] Tung, S., Hong, H., Huang, J. B., Ho, C. M., Liu, C., and Tai, Y. C., 1995, ''Control of a Streamwise Vortex by a Mechanical Actuator,'' *Proceedings of 10th Symposium on Turbulent Shear Flows*, **1**, Pennsylvania, Aug., pp. 1–19.
[12] Ho, C. M., Tung, S., Lee, G. B., Tai, Y. C., Jiang, F., and Tsao, T., 1997, ''MEMS-A Technology for Advancements in Aerospace Engineering,'' AIAA Paper No. 97-0545.
[13] Kimura, M., Tung, S., Ho, C. M., Jiang, F., and Tai, Y. C., 1997, ''MEMS for Aerodynamic Control,'' 28th AIAA Fluid Dynamics Conference, AIAA Paper No. 97-2118.
[14] Morlet, F., 1982, ''Wavelets Propagation and Sampling Theory,'' Geophysics, **47**, pp. 203–236.
[15] Everson, R., and Sirovich, L., 1990, ''Wavelets Analysis to the Turbulence Jet,'' Phys. Lett., **145**, pp. 314–322.
[16] Dallard, T., and Spedding, G. R., 1993, ''2-D Wavelet Transforms: Generalisation of the Hardy Space and Application to Experimental Studies,'' Eur. J. Mech. B/Fluids, **12**, pp. 107–134.
[17] Katul, G., and Vidakovic, B., 1998, ''Identification of Low-Dimensional Energy-Containing/Flux Transporting Eddy Motion in the Atmospheric Surface Layer Using Wavelet Thresholding Methods,'' J. Atmos. Sci., **55**, pp. 377–389.
[18] Saito, Y., 1996, ''Wavelets Analysis for Computational Electromagnetics, (in Japanese),'' Trans. Inst. Electr. Eng. Jpn., Part A, **116A**, pp. 833–839.
[19] Jiang, F., Tai, Y. C., Gupta, B., Goodman, R., Tung, S., Huang, J. B., and Ho, C. M., 1996, ''A Surface-Micromachined Shear Stress Imager,'' *Proceedings of the 9th International IEEE Workshop on MEMS*, San Diego, CA, p. 110.
[20] Huang, J. B., Tung, S., Ho, C. H., Liu, C., and Tai, Y. C., 1996, ''Improved Micro Thermal Shear-Stress Sensor,'' IEEE Trans. Instrum. Meas., **45**, pp. 570.
[21] Hussain, A. K. M. F., and Reynolds, W. C., 1970, ''The Mechanics of a Perturbation Wave in Turbulent Shear Flow,'' Air Force Office of Scientific Report, 70-1655TR, pp. 29–33.
[22] Kimura, M., Tung, S., Lew, J., Ho, C. M., Jiang, F., and Tai, Y. C., 1999, ''Measurements of Wall Shear Stress of a Turbulent Boundary Layer using a Micro-Shear-Stress Imaging Chip,'' Fluid Dyn. Res., **24**, pp. 329–342.
[23] Obi, S., Inoue, K., Furukawa, T., and Masuda, S., 1995, ''Experimental Study on the Statistics of Wall Shear Stress in Turbulent Channel Flows,'' *Proceedings of 10th Symposium on Turbulent Shear Flows*, **1**, pp. 5-19–5-24.
[24] Moin, P., and Kim, J., 1982, ''Numerical Investigation of Turbulent Channel Flow,'' J. Fluid Mech., **118**, pp. 341–377.
[25] Kline, S. J., Reynolds, W. C., Schraub, F. A., and Runstadler, P. W., 1967, ''The Structure of Turbulent Boundary Layers,'' J. Fluid Mech., **30**, pp. 741–773.

Per-Åge Krogstad
Department of Mechanics, Thermo and Fluid Dynamics,
The Norwegian University of Technology and Science,
N-7491 Trondheim, Norway
e-mail: Per.A.Krogstad@mtf.ntnu.no

Jon Harald Kaspersen
Senior Scientist,
Ultrasound Division,
Sintef Unimed,
N-7465 Trondheim, Norway
e-mail: Jon.H.Kaspersen@unimed.sintef.no

Structure Inclination Angle in a Turbulent Adverse Pressure Gradient Boundary Layer

The effect of a strong adverse pressure gradient on the turbulent structure in an equilibrium boundary layer was studied using two-point space-time correlations. The ρ_{uu} correlations from the adverse pressure gradient layer were found to be inclined at a considerably higher angle with respect to the wall in the inner region than in the corresponding zero pressure gradient reference case. A wavelet analysis of the correlation data showed that differences in the inclination angle exist at all length scales larger than the boundary layer thickness. The inclination angle for the conventionally averaged correlation contours was found to be in close agreement with the inclinations derived from the wavelet filtered contours corresponding to the most energetic wave numbers.
[DOI: 10.1115/1.1511161]

1 Introduction

In strong adverse pressure gradient (APG) boundary layers the main turbulent production term, $-\overline{uv}\partial U/\partial y$, has two maxima, one close to the surface and a second which moves towards the middle of the layer with increasing pressure gradient. This outer peak significantly affects the turbulence field, as may be observed from the various budgets for the turbulent quantities (e.g., Bradshaw [1], Spalart and Watmuff [2], Skåre and Krogstad [3]). As the outer production increases due to the pressure gradient, a significant turbulent diffusion away from this region develops. For strong adverse pressure gradient boundary layers, considerable diffusion towards the wall may therefore be present. Based on a quadrant analysis, Krogstad and Skåre [4], showed that the adverse pressure gradient significantly affects the time scales of the turbulent events, and also alters the contributions to $-\overline{uv}$ from the various quadrants. In contrast to the zero pressure gradient (ZPG) boundary layer, strong contributions from the first and fourth quadrant develop in the region between the outer production peak and the wall. Events in these quadrants are characterized by inrushing turbulent fluid which is reflected back from the wall. Hence, when an adverse pressure gradient is present, it appears that the turbulent flow in the outer layer may interact more efficiently with the inner flow than is normally the case for the zero pressure gradient layer.

The main aim of the present study is to investigate in more detail the effect this change in transport characteristics has on the large-scale turbulent motion.

2 Experimental Details

The APG boundary layer was generated in a closed return wind tunnel, fitted with a 6-m-long test section equipped with a flexible roof. This was carefully adjusted to produce equilibrium velocity profiles in the boundary layer. Equilibrium was achieved for a freestream velocity distribution given by $U_e \sim x^{-0.22}$. For $4.0 < x < 5.0$ m the mean velocity profiles, as well as the turbulent stresses were self similar, giving a strong velocity defect (Fig. 1) and a shear stress profile with a significant maximum in the outer layer (Fig. 2). As required for equilibrium layers, the length scales in the equilibrium region, such as boundary layer, displacement and momentum thicknesses, were found to increase linearly, and the skin friction coefficient and shape factor remained constant at $C_f \approx 6 \times 10^{-4}$ and $H = 2.0$, respectively. While the Reynolds number, Re_θ, was increasing from 39,000 to 51,000 in the equilibrium region, the nondimensional pressure gradient $\beta = (\delta^*/\tau_w) \times (dP_e/dx)$ was kept approximately constant at 20 in this region. Full details about the experiment are given in Skåre and Krogstad [3]. According to Krogstad and Skåre [4], the measurement uncertainty was estimated to be less than 2% in u and 5% in v.

In addition to previously reported single probe measurements, a number of measurements were obtained using arrays of eight equispaced X-wire probes (Fig. 3). These measurements were performed in the equilibrium region at $\mathrm{Re}_\theta = 42{,}000$. Three sets of arrays, each having a probe separation twice of the previous, were used to cover a large range of turbulent scales.

Similar data taken with an eight probe array with fixed probe spacing were kindly made available to us by Prof. R. A. Antonia at the University of Newcastle, Australia (see Antonia et al. [5] for

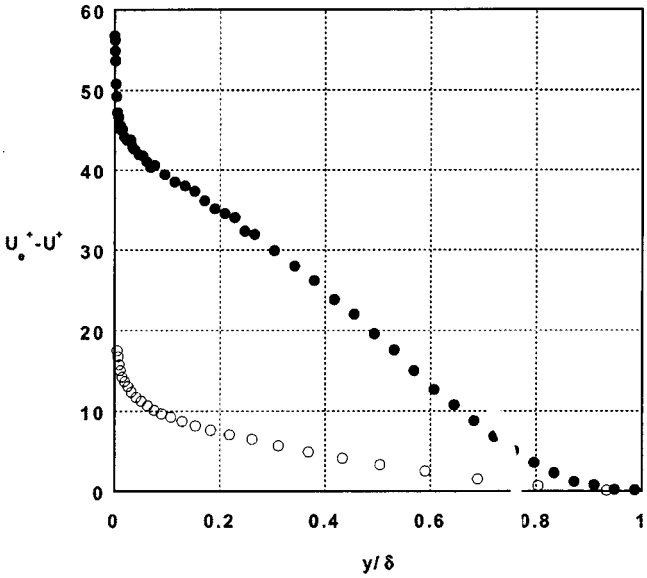

Fig. 1 Velocity defect data for the zero (○) and adverse (●) pressure gradient boundary layers

Contributed by the Fluids Engineering Division for publication in the JOURNAL OF FLUIDS ENGINEERING. Manuscript received by the Fluids Engineering Division May 30, 2000; revised manuscript received January 31, 2002. Associate Editor: P. W. Bearman.

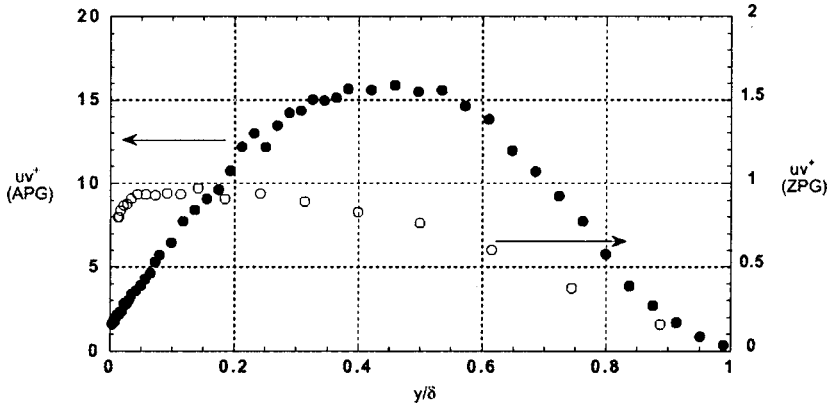

Fig. 2 Shear stresses. Symbols as in Fig. 1.

documentation). These data were taken in a zero pressure gradient layer (Re_θ=6030) generated in an open return wind tunnel, with a 5.4-m-long test section of 0.15×0.89 m^2 cross section. The same probe geometry and type of filters and amplifiers were used in both experiments, ensuring similar frequency response for the two cases. This allowed a direct comparison between the large-scale turbulent motions in the two flows to be made. The Reynolds numbers for both flows are well beyond the range where Reynolds number effects have been shown to be important ($\mathrm{Re}_\theta \leqslant 3000$). Although the Re in the APG case is almost an order of magnitude higher than for the ZPG flow, the range of length scales found in the two flows is assumed to be very similar. This follows from the ratio between the boundary layer thickness, δ, and the viscous length scale, ν/u_τ, which was $\delta^+=\delta u_\tau/\nu=4410$ and 4070 for the APG and ZPG boundary layers, respectively. (δ is taken to be the distance from the wall to the location where U is 99.5% of the freestream velocity, U_e.) Therefore Reynolds number effects are not expected to severely affect the comparison between the two flows.

Velocity defect and shear stress distributions for ZPG boundary layers are also shown in Figs. 1 and 2. (Note differences in scale.) The large peak in $-\overline{uv}$ for the APG layer produces significant differences in the budget for the turbulent kinetic energy, $k=\overline{u_iu_i}/2$, compared with a ZPG layer (budget may be found in Krogstad and Skåre [4]). A strong gain in turbulent energy near the wall due to the turbulent diffusion towards the wall, as well as high rates of turbulent production and dissipation near the middle of the layer, characterizes the APG budget compared to that of the ZPG layer.

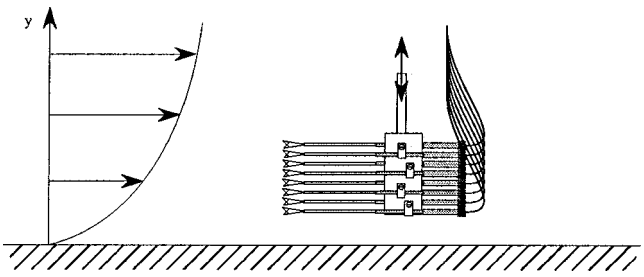

Fig. 3 Eight probe array

3 Two-Point Correlations

The two-point space-time correlations between two turbulent quantities p and q, defined as

$$\rho_{pq}(\mathbf{x}_0,\Delta\mathbf{x},\tau)=\frac{\overline{p(\mathbf{x}_0,t)q(\mathbf{x}_0+\Delta\mathbf{x},t+\tau)}}{(\overline{p^2q^2})^{1/2}} \tag{1}$$

were obtained using the arrays of eight X-wire probes. $\mathbf{x}$ is the position vector with components x, y, and z. The reference point is located at $\mathbf{x}_0$ and correlations are computed with respect to a second point, separated by a distance $\Delta\mathbf{x}$ from the reference.

While the array used in the ZPG layer spanned $\Delta y/\delta\approx0.54$, the arrays used in the APG layer covered $\Delta y/\delta\approx0.13$, 0.26, and 0.53. In order to convert measurements in the (y, t) domain into a pseudo (x, y) space plane, time was converted to distance using the Taylor hypothesis, i.e., $\Delta X^*=-U_c\Delta t/\delta$. In the plots presented, the convection velocity, U_c, was taken to be the same for all probes. The value chosen corresponded to the mean velocity of the reference probe. Using the same convection velocity for all probes may lead to some distortion of the correlation contours for the largest scales, as discussed by Krogstad and Skåre [4]. In the outer layer U varies only slowly with y in a ZPG boundary layer, so the assumption appears to be reasonable. Krogstad et al. [6] found that the convection velocity for scales larger than about $\Delta X^*=\Delta x/\delta\approx0.2$ is the same as the local mean velocity for $y^+\geqslant40$. For the APG layer the velocity increases virtually linearly with distance from the wall over the entire width of all the rakes used. For the correlations presented we will rely on the conclusion drawn by Spina and Smits [7], who observed that the structures contributing most to the correlations retain their shape and coherence for a considerable streamwise distance, producing virtually identical correlations for distances of more than one boundary layer thickness. This justifies the use of a single common convection velocity for two-point correlations.

Figure 4 shows iso-correlation contours of ρ_{uu} obtained in the two layers at different reference positions, $Y_0^*=y_0/\delta$. In the outer part of the layers, the inclination of the contours is close to 45 deg for both flows. This angle of inclination has previously been observed in boundary layers at zero pressure gradient conditions, e.g., in the flow visualizations by Head and Bandyopadhyay [8]. They used the concept of hairpin vortices to explain why the organized structures tend towards an inclination close to 45 deg. The vortex stretching due to the mean shear will cause a tilting of the structure towards the wall. This is resisted by the increase in induced velocity that each limb of the hairpin imposes on the other, which tends to tilt the structure back towards the wall perpendicular. Other investigators have assumed that the structures

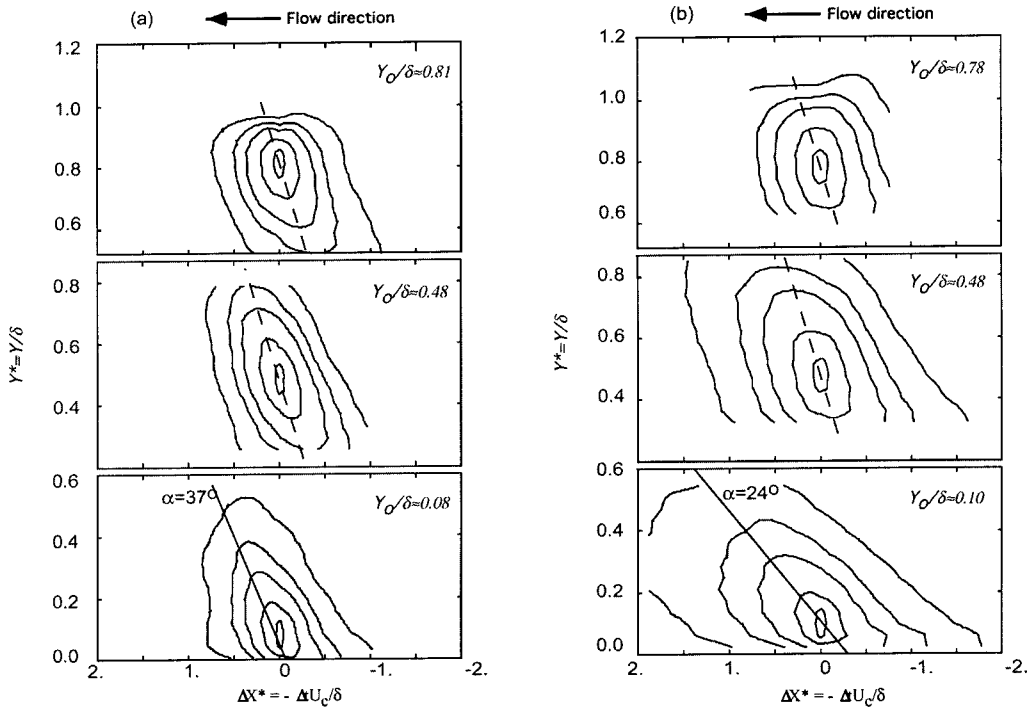

Fig. 4 Two-point velocity correlations, ρ_{uu}, in the (x,y)-plane. Contour levels: 0.1, 0.2, 0.3, 0.5, and 0.8. (*a*) Adverse pressure gradient, (*b*) Zero pressure gradient. Dashed lines: 45 deg inclination; Solid line: inclinations of the most energetic structures.

are aligned close to 45 deg because this is the direction of principal strain. This explanation is linked to an assumption of pure shear deformation, which may apply to incompressible laminar flows where the shear stresses τ_{xy} and τ_{yx} are identical and therefore their magnitude do not affect the direction of the principal stresses.

For two-dimensional turbulent boundary layers the stress tensor becomes

$$\tau_{ij}/\rho = -\overline{u_i u_j} = -\begin{pmatrix} \overline{u^2} & \overline{uv} & 0 \\ \overline{uv} & \overline{v^2} & 0 \\ 0 & 0 & \overline{w^2} \end{pmatrix} \tag{2}$$

and the normal stresses become important contributors to the direction of the principal stresses. In the (x, y)-plane the two principal stresses are found to be

$$-\sigma_{1,2} = \frac{\overline{u^2}+\overline{v^2} \pm ((\overline{u^2}-\overline{v^2})^2 + 4(\overline{uv})^2)^{1/2}}{2}. \tag{3}$$

That the pressure gradient has so little effect on the structure inclination in the outer layer is remarkable if this is a conventional stress-strain alignment mechanism, considering the large differences in magnitude and distribution of the turbulent stresses in this region. The distributions of the primary principal stresses for the two flows are shown in Fig. 5. In the outer layer the APG

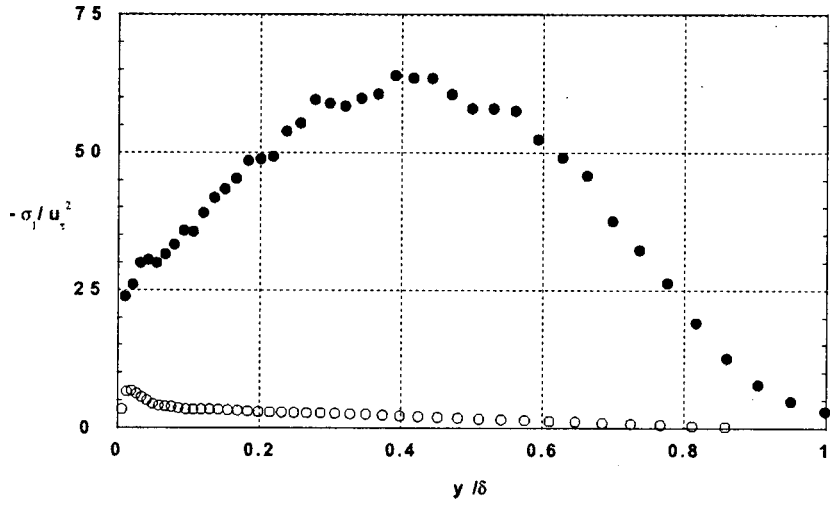

Fig. 5 Distributions of the largest principal stresses. Symbols as in Fig. 1.

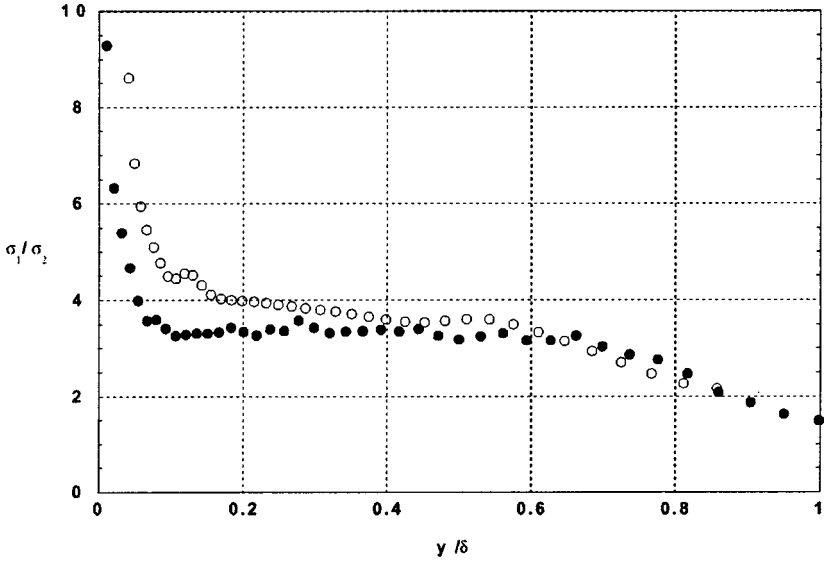

Fig. 6 Ratio between the first and second principal stresses. Symbols as in Fig. 1.

stresses are more than an order of magnitude higher than for the ZPG case, and the stress gradients are quite different. Although the principal stresses are quite different in magnitude, the ratio between the two principal stresses are virtually identical for $y/\delta > 0.4$ (Fig. 6). This indicates that if the deformation of the energetic structures is due to a simple stress-strain mechanism, the inclination angles for the two flows must indeed be very similar in this region (as demonstrated in Fig. 4). The differences between the stress ratios increase closer to the wall, where the largest structural differences between the two flows were found. In the bulk part of the layer the ratio is approximately constant at about $\sigma_1/\sigma_2 = 3-4$, which agrees with the data given by Champagne et al. [9].

The direction of the first principal stress is found at an angle of

$$\phi_1 = \frac{1}{2}\tan^{-1}\left(\frac{-2\overline{uv}}{\overline{v^2}-\overline{u^2}}\right) \tag{4}$$

with respect to the surface. Since $\overline{uv} < 0$ and $\overline{u^2} > \overline{v^2}$ for a conventional boundary layer, the direction of the principal stresses must lie in the range $\pi/4 \leqslant \phi_1 \leqslant \pi/2$. The direction of the second principal stress is $\phi_2 = \phi_1 + \pi/2$.[1] If all the turbulent stresses were linked to the strain tensor through an isotropic viscosity (as in the laminar case), ϕ_1 will represent the expected direction of deformation.

The distributions of ϕ_1 for the two flows, shown in Fig. 7, are virtually indistinguishable throughout the boundary layer. Thus both the directions of the principal stresses and the two-point velocity correlations tend to support the observations implied in the conclusions drawn by Head and Bandyopadhyay, that the organized structures are aligned according to a local mechanism which is independent of the magnitude of the stresses. Therefore a vortex model which is independent of the streamwise pressure gradient, as used by Perry and Marusic [11] to compute the turbulence characteristics of ZPG and APG boundary layers, appears to be justified. The considerable differences in the turbulent stresses for

[1]The direction of the first principal stress for the tensor $-\tau_{ij}/\rho = \overline{u_i u_j}$, as used by, e.g., Rogers and Moin [10], will be $\phi_1 - \pi/2$.

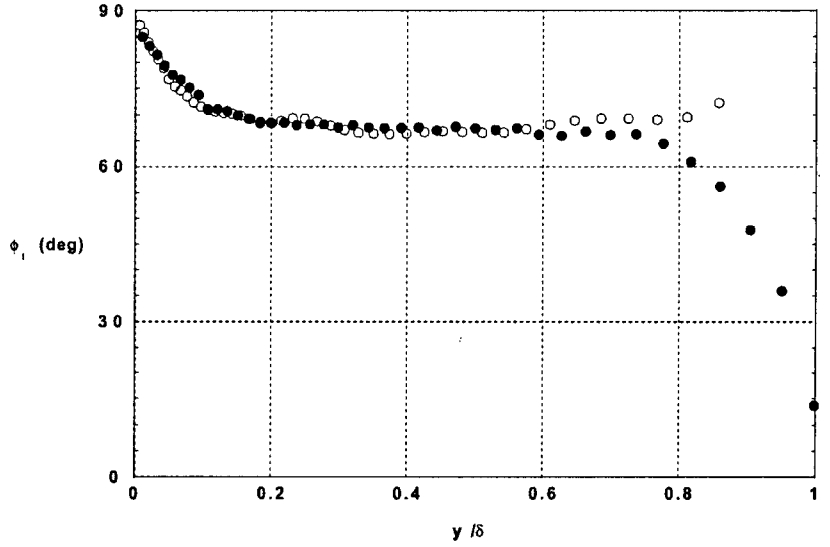

Fig. 7 Directions for the largest principal stresses. Symbols as in Fig. 1.

the two flows, reflect the differences in vortex stretching, rather than differences in the type of organized motion.

The main structural effects due to an APG are found close to the wall, where the angle of the two-point correlation is considerably steeper than for the ZPG layer. This effect is attributed to the strong vertical diffusion in the present APG flow, which tends to reduce the difference in flow structure between the inner and outer layer. Distinct differences in the length scales may also be observed. The APG strongly reduces the scales both in the streamwise and vertical direction. This is due to the strong negative mean velocity gradient, $\partial U/\partial x$.

4 Wavelet Analysis

To further explore the differences in inclination for the ρ_{uu} correlations, the array data sets were analyzed using one-dimensional wavelet transformations in t (see, e.g., Daubechies [12]). The u and v-signals from each probe were transformed into wavelet coefficients using the Mexican hat wavelet. 80 scales were used to analyze five batches of 2^{13} data from each probe. The wavelet power spectrum was in close agreement with the Fourier spectrum (Fig. 8, here shown for ZPG at $Y^*=0.10$). The range of wavelet length scales applied corresponded to $0.18 < \Delta X^* < 167$ for the ZPG flow, while in the APG case the scales were $0.03 < \Delta X^* < 28.1$. Since the largest differences between the two flows are found close to the surface, only the data corresponding to the lower graphs of Fig. 4 are presented here ($Y_0^*=0.10$ for the ZPG and 0.08 for the APG boundary layers, respectively).

A number of discrete scales were selected and these wavelet coefficients were transformed back to the velocity-time domain. Hence each of the original velocity signals were transformed into a set of signals, each corresponding to the motion of one particular scale. In this way a number of array data files could be constructed, for which only one dominant scale of turbulent motions would be present. Figure 9 shows a set of ρ_{uu} correlations as function of wavelet scales for the two flows using the data shown in Fig. 4. The correlations for the smallest scales are seen to be aligned perpendicular to the surface. (Note the differences in horizontal and vertical scales.) As the scale increases the correlations grow both in the vertical and streamwise directions. At the same time a distinct tilting towards the horizontal is evident. It is also apparent that for the two flows the difference in inclination angle increases with scale. For the smallest scales the correlations are organized roughly at the same angle, but for the largest scales the APG correlations are aligned more vertical than for the ZPG layer. It is also apparent that the APG correlations are higher and shorter than those of the ZPG boundary layer. This is in agreement with the reduced vortex stretching expected by the strong negative $\partial U/\partial x$ term in the APG flow.

It was verified that the results are not very sensitive to the type of wavelet used. Correlations were also computed using the Haar wavelet which is significantly different to the Mexican hat (Fig. 10). The positive correlations obtained for the two wavelets for scale $\Delta X^* \approx 4.8$ are shown in Fig. 11. The shapes are seen to be identical but a small difference in extent is evident, with the Haar wavelet correlations being slightly wider. This is partly due to the differences in characteristics of the two wavelets, but also due to the fact that with a finite number of 80 wavelet scales it was not possible to match the scales identically for the two cases.

All correlations alternate in the streamwise direction between regions of strong positive and negative values, showing that events triggered at one location induce strong opposing motions in the nearby region. (For the smallest scales, regions of negative correlations were also found above and below the reference point.) Since the location of these secondary correlation regions depends directly on the scales considered, they eventually cancel when the contributions from all scales are added up.

The inclination angles for the correlation contour $\rho_{uu}=0.3$ was extracted as function of the wavelet scales (Fig. 12). These angles were obtained from the line connecting the upper and lower extremal points on the curve. Bisset et al. [13] observed that for conventional two-point correlations, the contours of high correlations appear to be steeper than those of the lower values (see, e.g., Fig. 4). They suggested that since the small-scale turbulent motion must contribute mainly to the region of high correlations, the small-scale structures appear to be organized steeper with respect to the surface than the large-scale motion. This deduction is supported by Fig. 12 where the angle is seen to drop steadily from close to 90 deg at the smallest scales, to less than 20 deg in the ZPG case for the largest scales investigated here. This agrees well with the inclinations of the large scale motion which may be derived from the ZPG boundary layer measurements of Brown and Thomas [14] (about 17 deg at $Y_0^*=0.2$).

The dependence of the inclination with structure scale is seen to be similar for the two flows up to a scale of the order of the boundary layer thickness. At larger scales the angles tend towards an almost constant level. This large-scale inclination is significantly different for the two cases. With the pressure gradient present, the angle is of the order of 40 deg, more than twice the

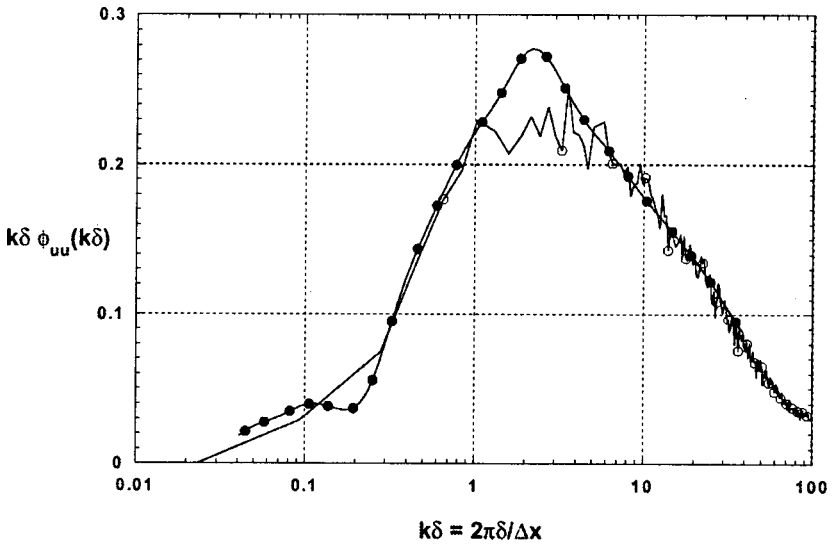

Fig. 8 Spectra for the zero pressure gradient layer at $y/\delta=0.10$. Wavelet spectrum: —●—; Fourier spectrum: —○—.

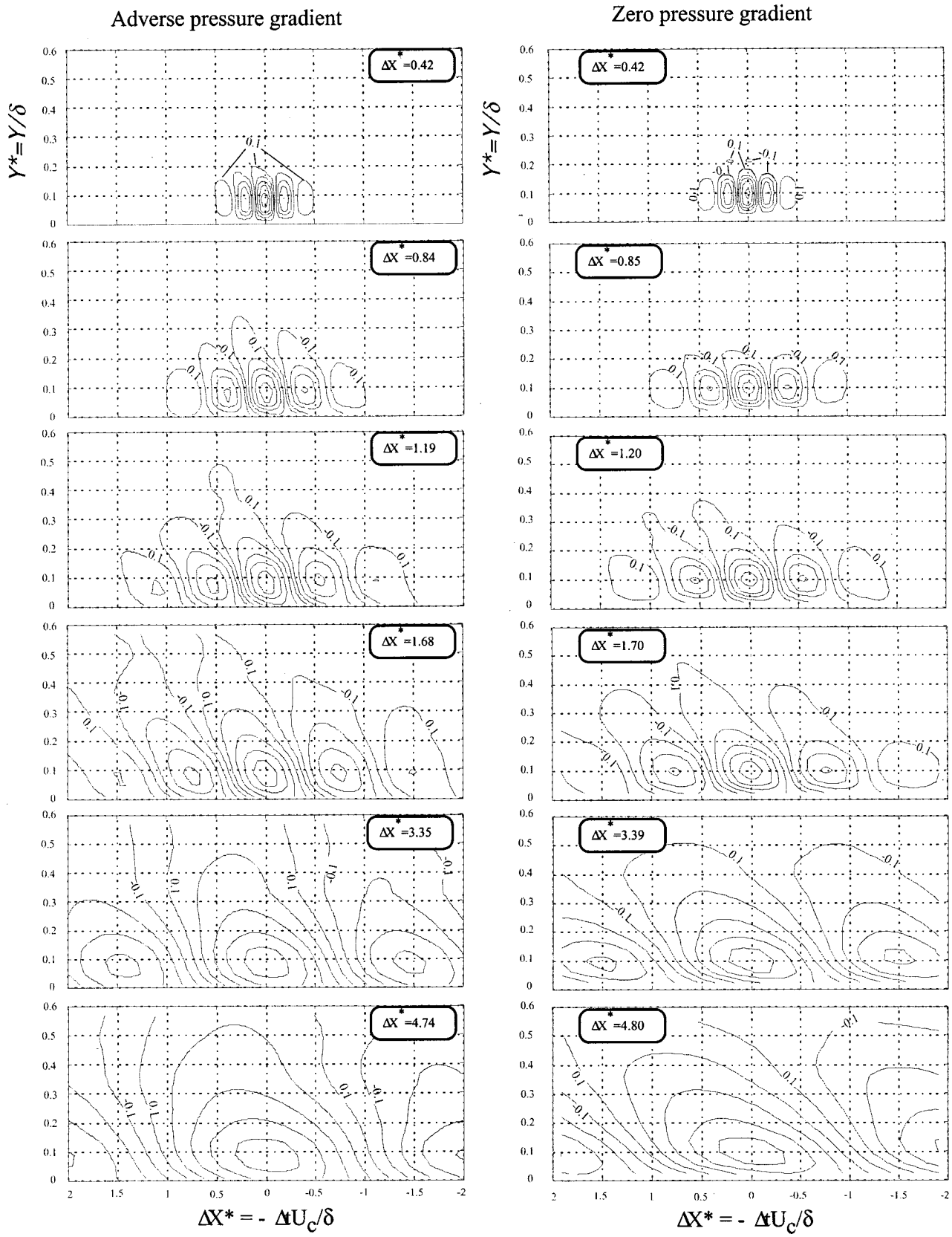

Fig. 9 Two-point velocity correlations, ρ_{uu}, in the (x,y)-plane as function of wavelet scale. Contour levels: −0.7 to 0.9 with 0.2 increments. Left: APG, Right: ZPG.

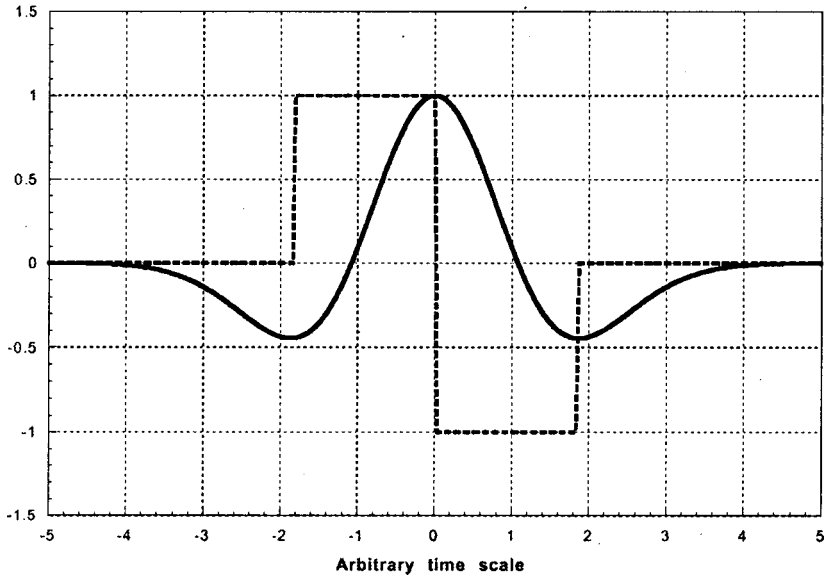

Fig. 10 Mexican hat (solid line) and Haar (dotted line) wavelets.

value for the ZPG case. Since the large scale motion is the main contributor to the conventional correlations, this confirms the differences observed in Fig. 4. From the Fourier or wavelet spectra the most energetic scales may be extracted. These were found to be $\Delta X^* \approx 3.4$ and 1.2 for the ZPG and APG layers, respectively. The inclinations found at these scales have been included in Fig. 4 and are seen to line up closely with the directions of the conventional two-point correlations.

Since the velocity distributions for the two cases are different, it may be argued that some of the differences observed in the inclination angles may be due to the use of a convection velocity which depends on the mean velocity at a fixed Y^* position. For the smallest scales the correlations do not extend very far away from the reference point, so the assumption appears to be justified. For the largest scales the correlation contour used to derive the inclination angle extends over a significant part of the layer and the velocity variation over the contour may be significant. We have therefore also included in Fig. 12 a set of angle estimates where the convection velocity used is the average mean velocity over the vertical extent of the $\rho_{uu} = 0.3$ contour. This implies that U_c increases with scale. For the ZPG case the increase is small since the profile is rather full, but for the APG layer U_c increased by about 40% from scale $\Delta X^* \approx 1$ to $\Delta X^* = 4.8$. As expected this causes a distinct reduction in the inclination angle for the largest scale, from about 40 to about 30 deg. The effect on the ZPG estimates is very small. However, despite the possible uncertainties in the choice of convection velocity, there appears to be no doubt that the large scale angles are different for the two flows.

Krogstad and Skåre [4] found that the conventional correlations for the wall normal velocity component, v, were very little affected by the pressure gradient. A set of scale-dependent correlations are shown in Fig. 13. Apart from the correlations for $\rho_{vv} = \pm 0.1$, which are more stretched in y in the APG case than for the ZPG layer, the correlations have roughly the same extent both in x and y in both cases. The strongest contributions to the conventional ρ_{vv} correlations are found at much higher wave numbers than for ρ_{uu}. Therefore the most important contributions are found for wavelet scales of the order $\Delta X^* = 1$ and smaller, where only a small amount of stretching in y for the APG case is apparent. This corroborates the findings of Krogstad and Skåre [4].

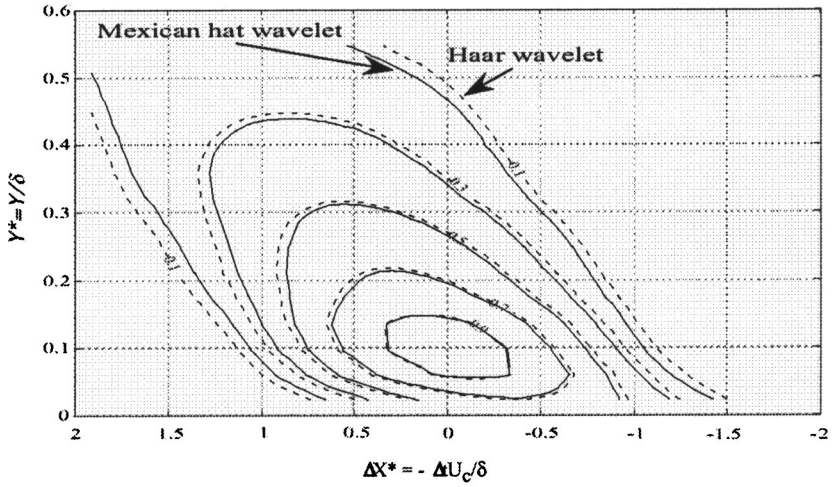

Fig. 11 Comparison between correlations obtained using the Mexican hat (solid line) and Haar (dotted line) wavelets. $\Delta X^* \approx 4.8$.

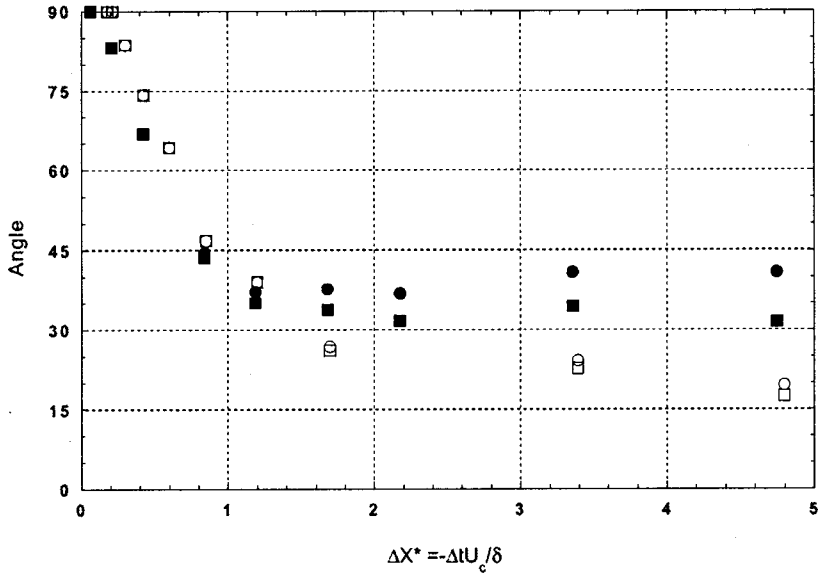

Fig. 12 Correlation inclination angle as function of wavelet scale, ΔX^*. Reference probe at $Y_0^* \approx 0.1$. Adverse pressure gradient: filled symbols, Zero pressure gradient: open symbols. ○: U_c taken as the mean velocity of the reference probe. □: U_c taken as the average mean velocity over the $\rho_{uu}=0.3$ contour.

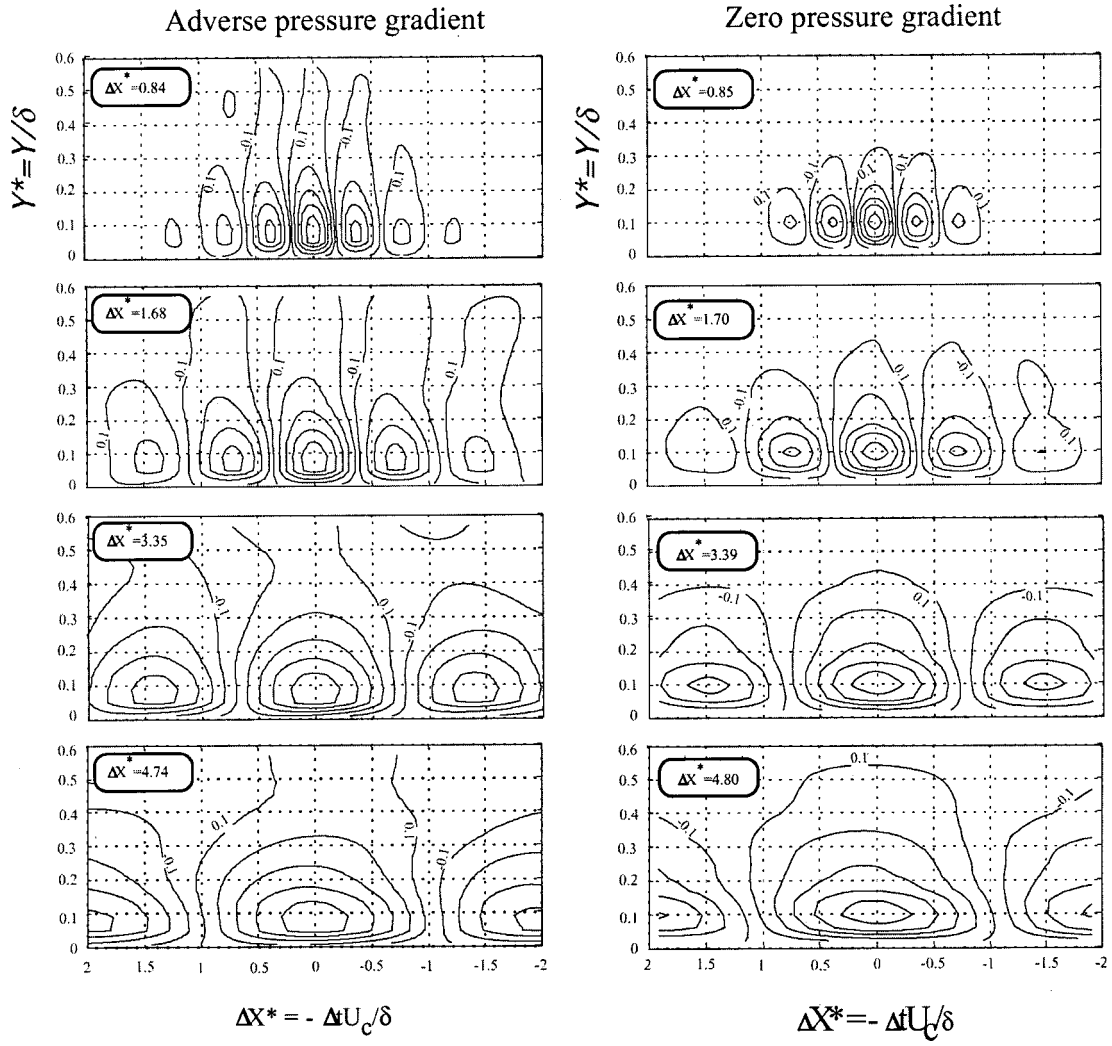

Fig. 13 Two-point velocity correlations, ρ_{vv}, in the (x,y)-plane as function of wavelet scale. Contour levels: −0.7 to 0.9 with 0.2 increments. Left: APG, Right: ZPG.

5 Conclusions

It has been documented by the use of two-point space-time correlations, that strong adverse pressure gradients effectively reduce the degree of anisotropy in a turbulent boundary layer. This effect is caused by the action of a negative $\partial U/\partial x$ which reduces the stretching of the coherent structures. The effect is most pronounced near the surface. A similar effect is caused by the strong turbulent diffusion towards the wall from the peak in turbulence production found in the outer layer. The inclination of the correlations in the outer layer was found to be insensitive to the pressure gradient, suggesting that the large-scale structures are aligned by a mechanism which is little sensitive to the characteristics of the mean flow. This was further supported by a study of the principal stresses of the turbulent stress tensor. Although the tensors for the ZPG and APG boundary layers are very different, the directions of the principal stresses with respect to the wall are virtually identical throughout the boundary layers.

Wavelet analysis was used to show that the inclination of the turbulent structures with respect to the wall depends strongly on the length scale associated with it. While small-scale motion is aligned virtually vertically, the angle becomes gradually smaller as the scale increases. When an adverse pressure gradient is applied, the dominant length scales in the streamwise direction are reduced, which causes the correlations at a particular scale to be tilted towards the wall normal. The inclination obtained from conventional two-point space-time correlations depends primarily on the scales of the most energetic structures.

Since the major contributions to $\overline{v^2}$ are found at much higher wave numbers than for $\overline{u^2}$, this explains why the ρ_{vv} correlations are found to be aligned almost vertically for all types of boundary layers. This was found to be the case for all wavelet scales investigated.

Nomenclature

APG = adverse pressure gradient
C_f = skin friction coefficient
Re = Reynolds number
U = mean velocity in streamwise direction (m/s)
X, Y, Z = length scales in x, y, and z-directions (m)
ZPG = zero pressure gradient
k = turbulent kinetic energy (m^2/s^2)
t = time (s)
u, v = fluctuating velocities in the x and y-directions (m/s)
u_τ = shear velocity (m/s)
x, y, z = coordinates in the streamwise, wall normal and lateral directions (m)
δ = boundary layer thickness (m)
θ = momentum thickness (m)
ρ = two-point space-time correlation function
ν = kinematic viscosity (m^2/s)
τ = shear stress (N/m^2)

Subscripts

e = freestream variable
i, j = general indices
o = reference position
w = wall variable

Superscripts

$+$ = variable normalized using u_τ and ν
$*$ = variable normalized with δ

References

[1] Bradshaw, P., 1967, "The Turbulent Structure of Equilibrium Turbulent Boundary Layers," J. Fluid Mech., **29**, pp. 625–645.
[2] Spalart, P. R., and Watmuff, J. H., 1993, "Experimental and Numerical Study of a Turbulent Boundary Layer With Pressure Gradients," J. Fluid Mech., **249**, pp. 337–371.
[3] Skåre, P. E., and Krogstad, P.-Å., 1994, "A Turbulent Boundary Layer Near Separation," J. Fluid Mech., **272**, pp. 319–348.
[4] Krogstad, P.-Å., and Skåre, P. E., 1995, "Influence of a Strong Pressure Gradient on the Turbulent Structure in a Boundary Layer," Phys. Fluids, **7**(8), pp. 2014–2024.
[5] Antonia, R. A., Browne, L. W. B., and Bisset, D. K., 1990, "Effect of Reynolds Number on the Organized Motion in a Turbulent Boundary Layer," *Near-Wall Turbulence*, S. J. Kline and N. H. Afgan, eds., Hemisphere, Washington, DC, pp. 488–506.
[6] Krogstad, P.-Å., Kaspersen, J. H., and Rimestad, S., 1998, "Convection Velocities in a Turbulent Boundary Layer," Phys. Fluids, **10**(4), pp. 949–957.
[7] Spina, E. F., and Smits, A. J., 1987, "Organized Structures in a Compressible, Turbulent Boundary Layer," J. Fluid Mech., **182**, pp. 85–109.
[8] Head, M. R., and Bandyopadhyay, P., 1981, "New Aspects of Turbulent Boundary-Layer Structure," J. Fluid Mech., **107**, pp. 297–338.
[9] Champagne, F. H., Harris, V. G., and Corrsin, S., 1970, "Experiments on Nearly Homogeneous Turbulent Shear Flow," J. Fluid Mech., **41**, pp. 81–139.
[10] Rogers, M. M., and Moin, P., 1987, "Structure of the Vorticity Field in Homogeneous Turbulent Flows," J. Fluid Mech., **176**, pp. 33–66.
[11] Perry, A. E., and Marusic, I., 1995, "A Wall-Wake Model for the Turbulence Structure of Boundary Layers. Part 1. Extension of the Attached Eddy Hypothesis," J. Fluid Mech., **298**, pp. 361–388.
[12] Daubechies, I., 1992, *Ten Lectures on Wavelets*, SIAM, USA.
[13] Bisset, D. K., Antonia, R. A., and Raupach, M. R., 1991, "Topology and Transport Properties of Large-Scale Organized Motion in a Slightly Heated Rough Wall Boundary Layer," Phys. Fluids A, **3**(9), pp. 2220–2228.
[14] Brown, G. L., and Thomas, S. W., 1977, "Large Structure in a Turbulent Boundary Layer," Phys. Fluids, **20**(10), pp. S243–S252.

Air Entrainment Effects on the Pressure Transients of Pumping Systems With Weir Discharge Chamber

T. S. Lee[1]
Associate Professor,
e-mail: mpeleets@nus.edu.sg

K. L. Ngoh

Mechanical Engineering Department,
National University of Singapore,
Singapore 119260, Singapore

This paper presents a new model for the study of air entrainment on the extreme pressure surges in pumping systems. For the present fluid system considered with a weir discharge chamber, numerical investigations showed that, with the proposed model of the air entrainment, reasonable predictions of transient pressures with proper phasing and attenuation of pressure peaks can be obtained. The results obtained are consistent with observations from field measurements made when the pumps were operating at low pump cutout levels where air entrainment due to attached surface vortex and falling jets from the inflow near the pump intake were present. Further studies were also made on the design characteristics of the weir discharge chamber on the extreme pressure transients for the unsteady flow in the pipeline system with various degrees of air entrainment. [DOI: 10.1115/1.1514204]

Introduction

A common flow arrangement in a pumping system for cooling water of thermal power plant or large air conditioning system in large building complex consists of a source of cooling water and a downstream discharge chamber discharging heated water into the sea. In between the source of cooling water and the sea, there are pumping stations installed with group of operating pumps and a pipeline system. The topography of the pipeline system used in the present study is shown in Fig. 1(*a*). Preliminary study on the pipeline system of Fig. 1(*a*) showed that the pressure along the pipeline would drop to subatmospheric pressure at the peak location B when the operating pumps are shut down or tripped. For the present applications with a pipeline system that can withstand high tensile (positive pressure) load but is very weak in receiving compressive (subatmospheric pressure) load, the pipeline may collapse (crash) if the duration of the extreme subatmospheric pressure is long. In the typical day to day operations of a cooling water pumping system, pipelines at high points will be frequently subjected to subatmospheric pressures. The pipelines may thus buckle if unprotected against long duration of negative pressure surges. One way to avoid this problem is to install air valves at the peak location at B. When the line pressure at the peak location drops below atmospheric pressure, the air valve opens to admit air. This prevents a further drop in the pressure in the pipeline. During a subsequent rise of the line pressure above the atmospheric pressure, the admitted air is allowed to escape under a controlled manner. However, the rapid expulsion of the air from an air valve may very often itself leads to the complete exhaustion of the air within a short duration. This will in turn result in dangerous pressure transients in the fluid system due to the severe flow deceleration that occurs when the water strikes the air valve while moving at the same rate as the exhausting air. In a series of studies undertaken at Colorado State University on extreme negative pressure occurring at the peak of a fluid system, [1], showed that if the duration of the extreme negative pressure did not exceed 60 seconds with no air valves installed, the use of very small air release valves with an appropriately sized weir discharge chamber could effectively reduce the extreme pressure transients in the fluid system. In the present study, the various design features of the weir discharge chamber were studied using a numerical approach without the air valves but included the effects of air content under transient condition. Numerical studies were conducted on various designs of the discharge chambers to investigate the duration of the negative pressure transients at point B with and without the air entrainment effects.

[1]To whom correspondence should be addressed.

Contributed by the Fluids Engineering Division for publication in the JOURNAL OF FLUIDS ENGINEERING. Manuscript received by the Fluids Engineering Division May 5, 2000, revised manuscript received May 3, 2002. Associate Editor: B. Schiavello.

Air Entrainment Model

Earlier investigations by Pearsall [2] showed that the presence of undissolved gas bubbles in a fluid reduces the wave speed. Through the present modeling, it can be shown that the effect of free air on wave speed is more significant under low-pressure conditions, when its volume is greater than under high-pressure conditions. The new model proposed here assumes the presence of an initial free entrained air of volumetric void fraction ε_o and dissolved gas content of relative volumetric void fraction ε_g in the liquid at atmospheric pressure and ambient temperature. Assumptions were also made that: (i) the gas-liquid mixture is homogeneous; (ii) the free gas bubbles in the liquid follow a polytropic compression law with $n=1.2-1.3$ (due to the occurrence of some heat transfer from the heated fluid in the pipeline to the surrounding soil); and (iii) the pressure and temperature within the air bubbles during the transient process is in equilibrium with the local fluid pressure and temperature. When the computed local transient pressure falls below the gas saturation pressure P_g, it is assumed that there is a release of dissolved gas of $\alpha_{gr}\varepsilon_g$. When the computed transient pressure recovers to a value above P_g, it is assumed that an equivalent amount of $\alpha_{ga}\varepsilon_g$ gas is absorbed into the fluid. For the present model, the value of ε has a lower limit determined by the vapor pressure P_v of the fluid. Whenever the transient pressure fall below P_v, it is assumed here that minimum pressure remained at P_v for the duration of this fluid transient. Hence, the values of the variable wave speed will have a lower bound, which is consistent with the field data observed.

Consider a control volume of gas-liquid mixture containing a fractional volume ε of gas in free bubble form. It can be shown that the effective bulk modulus K_T of the gas-liquid mixture is given by ([3])

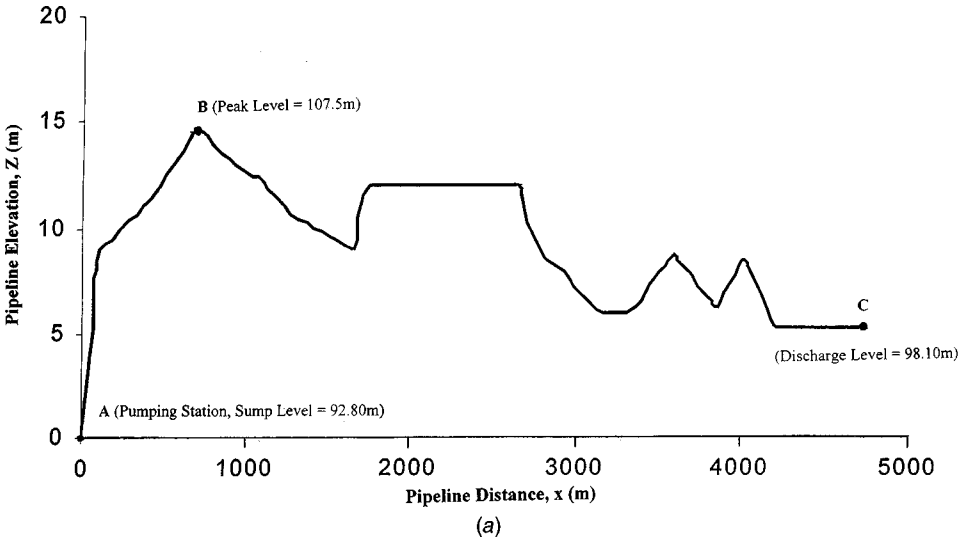

(*a*)

Fig. 1 (*a*) Pumping station pipeline profile, (*b*) Weir discharge chamber at location C

$$\frac{1}{K_T}=\frac{1}{K}+\frac{\varepsilon}{nP}+\frac{cD}{eE}. \tag{1}$$

At any instant of time $t=k\Delta t$ and at any location along the pipeline $x=i\Delta x$, the local wave speed a_i at an absolute pressure P_i and air volumetric void fraction of ε_i is given by

$$a_i^k=\left[\rho_w(1-\varepsilon_i^k)\left(\frac{1}{K}+\frac{\varepsilon_i^k}{nP_i^k}+\frac{cD}{eE}\right)\right]^{-1/2}. \tag{2}$$

For this model of variable wave speed the initial free air volumetric void fraction ε_o and dissolved gas relative volumetric void fraction ε_g at a reference absolute pressure Po and temperature To must be specified. The initial variable wave speed along a pipeline (at node points $i=0, 1,\ldots..., N$) is then computed through the absolute pressure distribution along the pipeline from Eq. (2) starting from $k=0$ (steady state).

The computation of the above transient local air volumetric void fraction in Eq. (3) along the pipeline is given by

$$\varepsilon_T^{k+1}=\left(\frac{P_i^k}{P_i^{k+1}}\right)^{1/n}\varepsilon_i^k \quad \text{and} \quad \varepsilon_o^{k+1}=\left(\frac{P_o}{P_i^{k+1}}\right)^{1/n}\varepsilon_o; \tag{3}$$

(a) for $P_i^{k+1}\geqslant P_g(T)$ and $\varepsilon_T^{k+1}\leqslant\varepsilon_o^{k+1}+\alpha_{gr}\varepsilon_g$: $\varepsilon_i^{k+1}=\varepsilon_T^{k+1}$ (3*a*)

(b) for $P_i^{k+1}\geqslant P_g(T)$ and $\varepsilon_T^{k+1}>\varepsilon_o^{k+1}+\alpha_{gr}\varepsilon_g$, with a time delay of $K_a\Delta t$:

$$\varepsilon_i^{k+1}=\left(\frac{P_i^k}{P_i^{k+1}}\right)^{1/n}(\varepsilon_i^k-\alpha_{ga}\varepsilon_g) \tag{3b}$$

(c) for $P_i^{k+1}<P_g(T)$ and at a time delay of $K_r\Delta t$:

$$\varepsilon_i^{k+1}=\left(\frac{p_i^k}{p_g}\right)^{1/n}(\varepsilon_i^k+\alpha_{gr}\varepsilon_g). \tag{3c}$$

The present study assumes the absorption of free gases and the release of dissolved gases with a time delay of $K_a\Delta t$ and $K_r\Delta t$, respectively, and an instant cavitation at P_v under transient conditions. In the present model, typical values used for K_a and K_r are 1.000. These K_a and K_r values are currently still under fine-tuning for the better prediction of the phasing in pressure transients analysis. However, when compared with the field data obtained so far, there are evidences in our studies to show that both K_a and K_r are slightly larger than 1.000 and that $K_a>K_r$. More field tests are currently performed to have a better estimation for the values of K_a and K_r (Lee and Cheong [4]). A typical free air content in the industrial water intake at atmospheric pressure is about 0.1% by volume and the free gas content evolved at gas release head is about 2.0% at atmospheric pressure head. The fractional parameter of gas absorption is $\alpha_{ga}\approx 0.3$ and the fractional parameter of gas release is $\alpha_{gr}\approx 0.6$ (Pearsall [2], Kranenburg [5], and Provoost [6]). For the comparative study of constant wave speed cases, the present study assumed $\varepsilon=0.000$ (fully deaerated water) in the fluid system even when the transient pressure falls below the P_g or P_v, i.e., the system is assumed completely free from the influence of entrapped air or water vapor.

The model expressions in Eq. (3) are very different from that given by Pearsall [2], Fox [3], Chaudhry, Bhallamudi, Martin, and Naghash [7], and Wylie, Streeter and Suo [8] where they do not take into considerations the evolution of dissolved gases and the re-absorption of released gases below and above P_g, respectively, in the transported fluid under transient flow conditions. The air entrainment models of Pearsall and Provoost assumed that the air volumetric void fraction (ε) is constant throughout the pipeline without local variation due to the transient pressure changes. Proper phasing of the transient pressure variation was difficult to obtain with the existing models especially when air entrainment in the fluid system exists. The present new model as described through the above Eq. (3) includes a computational procedure for the changes of local air volumetric void fraction (ε) due to local transient pressure variation. The evolution of dissolved gases and the re-absorption of released gases below and above P_g, respectively, in the transported fluid are also included in the present model (Lee and Pejovic [9]).

Method of Characteristics With Variable Wave Speed

The method of characteristics applied to the pressure transient problem with variable wave speed a_i as modeled above can be described (Fox [3]) by the respective C^+ and C^- characteristic equations

$$\frac{g}{a}\frac{dH}{dt}+\frac{dV}{dt}+\frac{g}{a}V\sin\phi+\frac{f_l}{2D}V|V|=0, \tag{4a}$$

$$dx/dt=V+a \tag{4b}$$

and

$$-\frac{g}{a}\frac{dH}{dt}+\frac{dV}{dt}+\frac{g}{a}V\sin\phi+\frac{f_l}{2D}V|V|=0, \tag{5a}$$

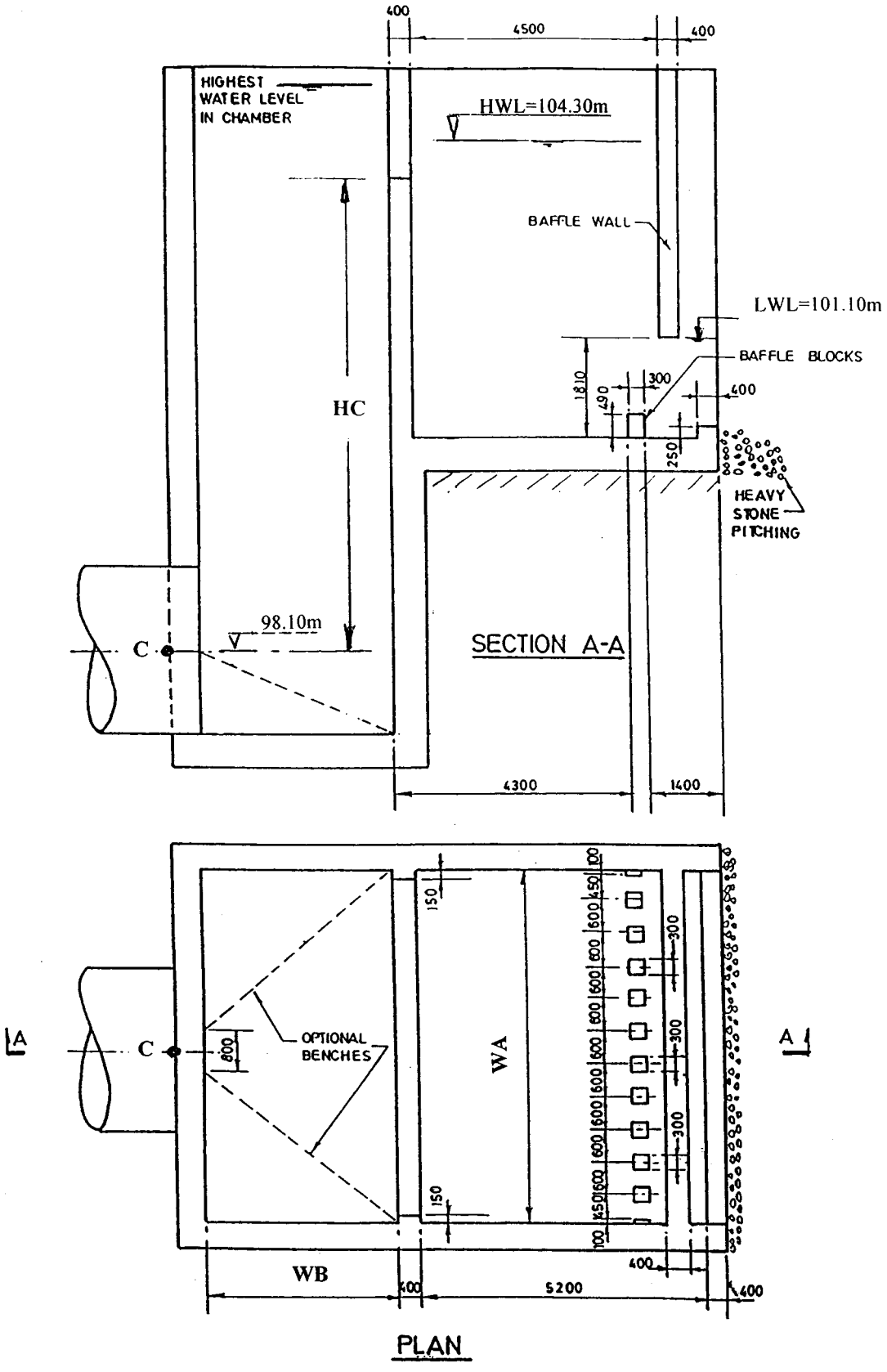

[Unless otherwise specified, all dimensions are in mm]

(*b*)

Fig. 1 (***continued***)

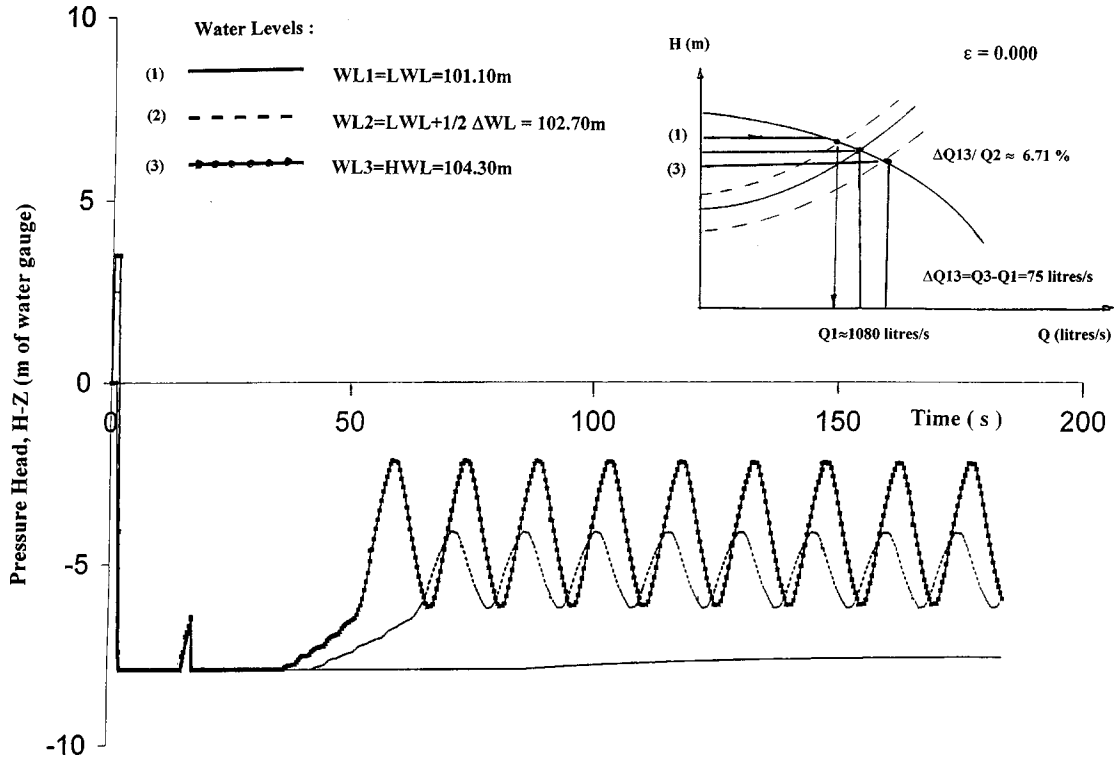

Fig. 2 Transient pressure at peak location B with HC at LWL

$$dx/dt = V - a. \tag{5b}$$

With air entrainment, the transient computation of ε_i along the pipeline depends on the local pressure and the state of the local air volume and is given by Eqs. (3), (4), and (5). The loss factor f_l used in conjunction with the method of characteristics in Eqs. (4) and (5) with air entrainment and gas release in a pipeline system is evaluated at the local point i using the characteristics of the flow at that point. The steady-state overall loss factor at the operating point of a system can be determined from the pump characteristic curve and the system curve. Irregular t-grid and regular x-grid were used in the present study. In the present work, i denotes the regular x-mesh point value at location $x=(i\Delta x)$ and k denotes the irregular time level corresponding to the time at $t^k=\Sigma(\Delta t^k)$. The value of the time-step Δt at each time level for a stable and accurate numerical solution is determined by the Courant-Friedrichs-Lewy (CFL) criterion (Roache [10])

$$\Delta t^k = \min[k_i \Delta x/(|V_i| + a_i)] \quad \text{for } i = 0,1,.....,N, \tag{6}$$

where k_i is a constant less than 1.0.

The characteristic equations specified by Eqs. (4)–(5) can thus be approximated by the finite difference expressions

$$\frac{g}{a_R}\frac{H_i^{k+1}-H_R}{\Delta t^k} + \frac{V_i^{k+1}-V_R}{\Delta t^k} + \frac{g}{a_R}V_R \sin\phi_i + \frac{f_{l_R}}{2D}V_R|V_R| = 0, \tag{7a}$$

$$\frac{x_i - x_R}{\Delta t^k} = V_R + a_R \tag{7b}$$

and

$$-\frac{g}{a_S}\frac{H_i^{k+1}-H_S}{\Delta t^k} + \frac{V_i^{k+1}-V_S}{\Delta t^k} + \frac{g}{a_S}V_S \sin\phi_i + \frac{f_{l_S}}{2D}V_S|V_S| = 0, \tag{8a}$$

$$\frac{x_i - x_S}{\Delta t^k} = V_S + a_S, \tag{8b}$$

where R is the point of interception of the C^+ characteristic line on the x-axis between node points $(i-1)$ and i at the kth time level and S is the point of interception of the C^- characteristic line on the x-axis between node points i and $i+1$. With conditions known at points $i-1$, i and $i+1$ at the kth time level, the conditions at R and S can be evaluated by a linear interpolation procedure. The conditions at R and S are then substituted into Eqs. (7)–(8) and the solutions at the $(k+1)$th time level at point i are obtained for $i=0,1,.....,N$. Grid point independent studies were made for $N=501$, 751, 1001, 1251, and 1501, for the length of the pipeline considered. An optimum mesh size of $N=1001$ was finally used for all the solutions presented in this work.

Operation and System Boundary Conditions

In order to safeguard the pipeline and its hydraulic components from over and/or under pressurization, it is important to determine extreme pressure loads under various operating conditions. Pump shutdown is an operational case that has to be investigated. This often gives rise to maximum and minimum pressures. The most severe case occurs when all the pumps in a station fail simultaneously owing to a power failure. In this case the flow in the pipeline rapidly diminishes to zero and then reverses. The pump also rapidly reduces its forward rotation and reverses shortly after the reversal of the flow. As the pump speed increases in the reverse direction, it causes great resistance to the back flow, which produces high pressure in the discharge line near the pump. To prevent reverse flow through the pump, a check valve is usually fitted immediately after each pump. When the flow reverses, the check valve is activated. A large pressure transient may occurs in the pipeline when the flow reverses and the check valves of the pumps are closing.

The equivalent pump transient characteristics in the pumping station during pump shutdown and pump run-down can be described by the homologous relationship for n_p pumps as

$$H_e^{k+1} = A_1(N^{k+1})^2 + (A_2/n_p)(N^{k+1})Q_0^{k+1} + (A_3/n_p^2)(Q_o^{k+1})^2 \tag{9a}$$

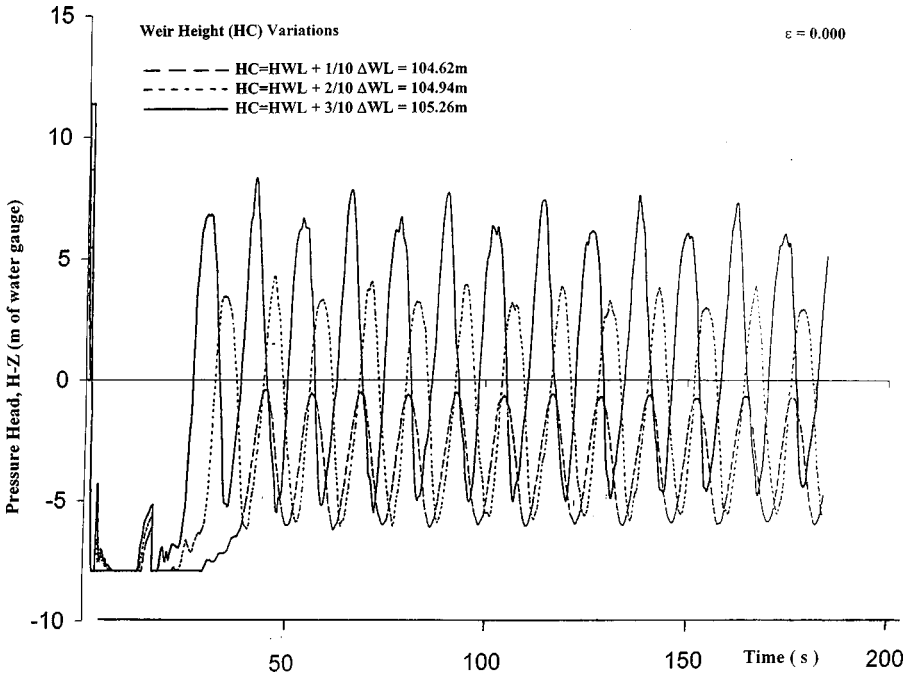

Fig. 3 Transient pressure at peak location B with HV above HWL

$$T_e^{k+1}=(B_1 n_p)(N^{k+1})^2+B_2(N^{k+1})Q_0^{k+1}+(B_3/n_p)(Q_o^{k+1})^2 \tag{9b}$$

$$\eta_e^{k+1}=C_1+(C_2/n_p)(Q_o^{k+1}/N^{k+1})+(C_3/n_p^2)(Q_o^{k+1}/N^{k+1})^2 \tag{9c}$$

$$T_e=-I_e d\omega/dt \tag{9d}$$

where $H_o^{k+1}=H_e^{k+1}$, $I_e=n_p I$, $\omega=2\pi N^k$ and H_e^k, Q_e^k, T_e^k, η_e^k, N^k are the instantaneous equivalent pump pressure head, volumetric flow rate, pump torque, pump efficiency and pump speed, respectively, n_p is the number of pumps, A_1, A_2, A_3, B_1, B_2, B_3, and C_1, C_2, C_3 are single-pump constants. The above pump characteristics are transient characteristics as the pump speeds N^k are different at different time levels after pump shutdown. The efficiency of the equivalent pump during pump run-down is assumed to be equal to the efficiency of the corresponding single-pump run-down efficiency. Equation (9*a*) is to be solved together with the C^- characteristic line described by Eqs. (7) and (8). A concept of equivalent pump was employed when there is more than one pump operating in a pumping station. The changes in pump speed during pump run-down for both normal and turbine modes are modeled (Fox [3]). The determination of the equivalent

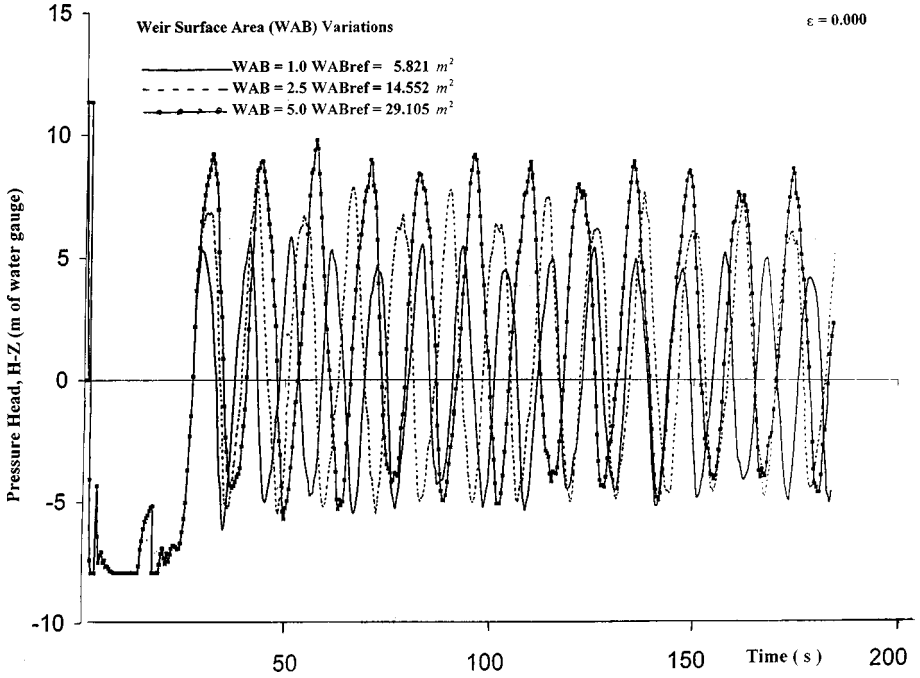

Fig. 4 Transient pressure at peak location B with HC=HWL+3/10 ΔWL=105.26 m

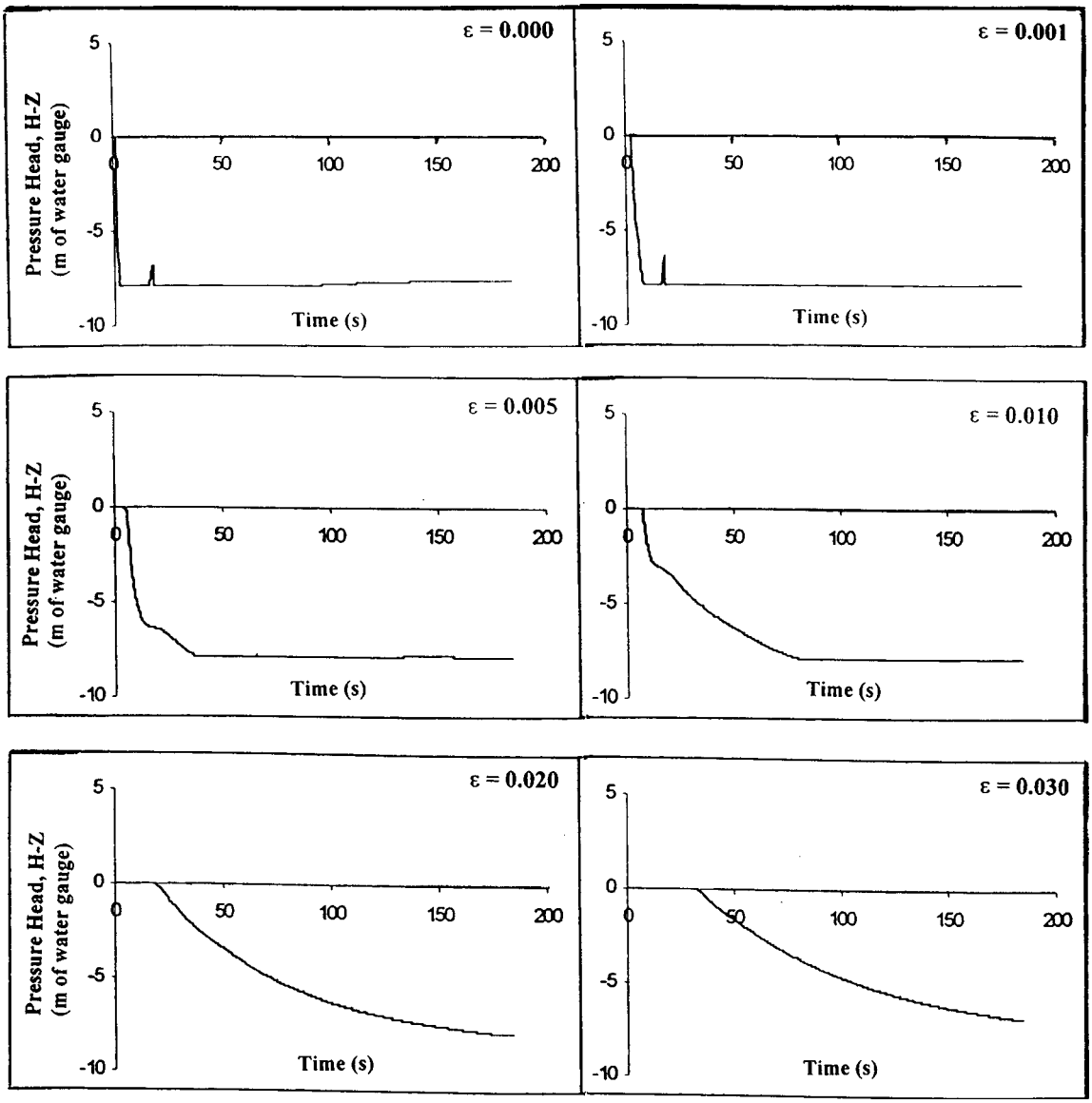

(*a*)

Fig. 5 (*a*) **Transient pressure at peak location B HC=LWL=101.10 m.** (*b*) **Transient pressure at peak location B HC=LWL +3/10 ΔWL=105.26 m.**

pump characteristics and computation of the run-down pump speed N^{k+1} is determined from Eqs. (9*b*)–(9*d*) by using the procedures of Wylie, Streeter, and Suo [8] and Fox [3], respectively. When a significant decrease in the flow rate is encountered in the pump, the check valve will be initiated to close. Downstream of the pipeline system at location C (Fig. 1(*a*)) is the weir discharge chamber (Fig. 1(*b*)).

Fluid Transient Responses in Weir Discharge Chamber

The discharge chamber (Fig. 1(*b*)) is located at node N at the end of the pipeline. The height of the water column inside the discharge chamber at steady state operation is known. Thus, during transient calculations at the $k+1$ time level of $t^{k+1}=t^k+\Delta t$, the C^+ Characteristics equation gives

$$H_N^{t+k}=H_{N-1}^{k+1}+BQ_{N-1}^{k+1}-RQ_{N-1}^{k+1}|Q_{N-1}^{k+1}|-BQ_N^{k+1}-CQ_{N-1}^{k+1} \tag{10a}$$

with $B=a/(gA_{\text{pipe}})$, $C=(\Delta t/A_{\text{pipe}})\sin\phi$, $R=(af_l\Delta t)/(2gDA_{\text{pipe}}^2)$ and $Q=$volumetric flow rate.

The estimation of the height of the water column HT_N^{k+1} inside the discharge chamber is given by the continuity requirement,

$$HT_N^{k+1}=HT_N^k+\frac{\Delta t((1-\varepsilon_N^{k+1})Q_N^{k+1}+(1-\varepsilon_N^k)Q_N^k)}{2A_{\tan k}}, \tag{10b}$$

where $A_{\tan k}=\text{WA}\times\text{WB}$ is the cross-sectional area of the discharge chamber as shown in Fig. 1(b). The piezometric pressure head at the junction (at an elevation of ZH_N) of the discharge chamber with the pipeline is related through

$$H_N^{k+1}=HT_N^{k+1}+ZH_N. \tag{10c}$$

Equations (10*a*)–(10*c*) give the solutions for the transient characteristics of the weir discharge chamber with the effects of air entrainment. As this is an open discharge chamber, overflow occurs if the volume of water inside the chamber exceeds its holding capacity. Thus, assuming that HC is the design height of the discharge weir chamber at location C (Fig. 1(*b*)):

$$HT_N^{k+1}=HC \quad \text{if} \quad HT_N^{k+1}\geqslant HC. \tag{11}$$

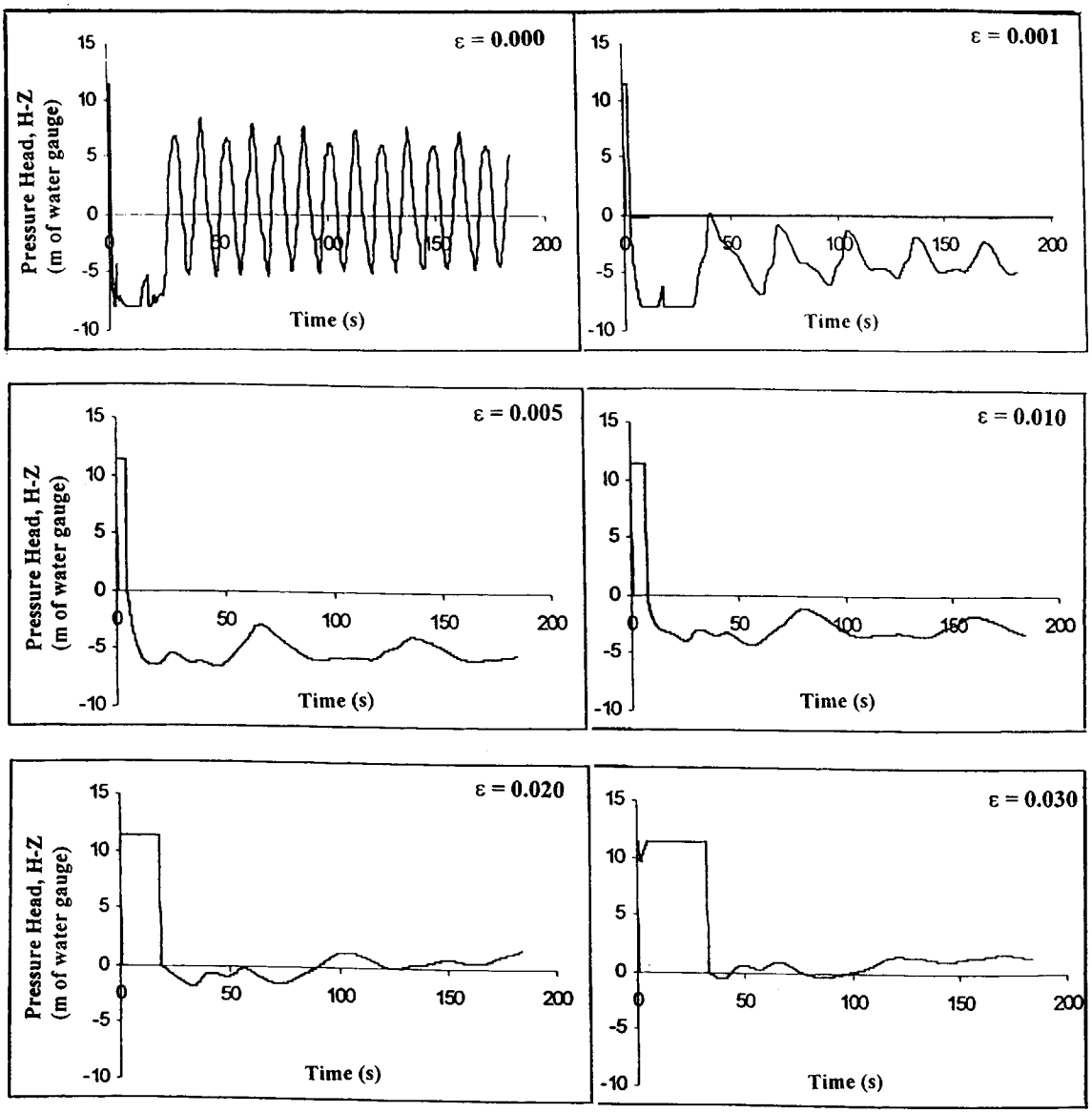

(*b*)

Fig. 5 (***continued***)

Results and Discussion

For the present studies, the pumping station uses three parallel centrifugal pumps of the same characteristics to supply a total of 1.08 m^3/s of cooling water from a holding reservoir at A through a 0.985 m diameter main of 4720 m length. The discharge weir chamber is installed at the end of the pipeline at C. The pressure transient characteristics with the discharge chamber were investigated for different design features of the chamber. The influence of the design variables (Fig. 1(*b*)), the chamber height (HC) and its cross-sectional area (WAB=WA×WB), on the pipeline pressure transient were investigated in this numerical study. A reference area WABref with WA, WB of 3 and 2 diameters of the pipe, respectively, was used. Typically, the peak level of the system at B (107.75 m) is higher than HC. However, HC is higher than LWL (101.10 m). The inertia (I) of the full pumpset (3 pumps) is 33.30 kgm^2. Each pump is also fitted with check valve at the immediate downstream end of the pump. For the cases considered with the heated water flowing through the fluid system, the water temperature was $T \approx 65°C$ with $P_v \approx -7.6$ m of water gauge. P_g was assumed approximately equal to P_v. The ε values investigated in this work was in the range of 0.000 to 0.030.

With no air entrainment ($\varepsilon = 0.000$), numerical studies were initially carried out for three different outlet tidal heights between the low water level (LWL) and high water level (HWL). With the weir height set at the low water level (HC=LWL). Figure 2 shows the transient pressure variations at the peak location B upon tripping all the pumps. For all the three cases studied, the pressure at the peak location B diminishes rapidly towards P_v (flat portion of the graph). With the outlet water level at WL1=LWL, the pressure at the peak location B remains at P_v for the duration (200s) of the numerical investigation. At higher water levels of WL2 and WL3, the results show an improvement of the pressure transients (become more positive). Thus, this study indicates that it is desirable to have a higher weir discharge level.

From the results of the above study, the weir height was next set at higher levels near the HWL. Investigations show that the duration of the transient pressure at P_v is significantly shorter with a higher HC. Although the period of pressure variation and the

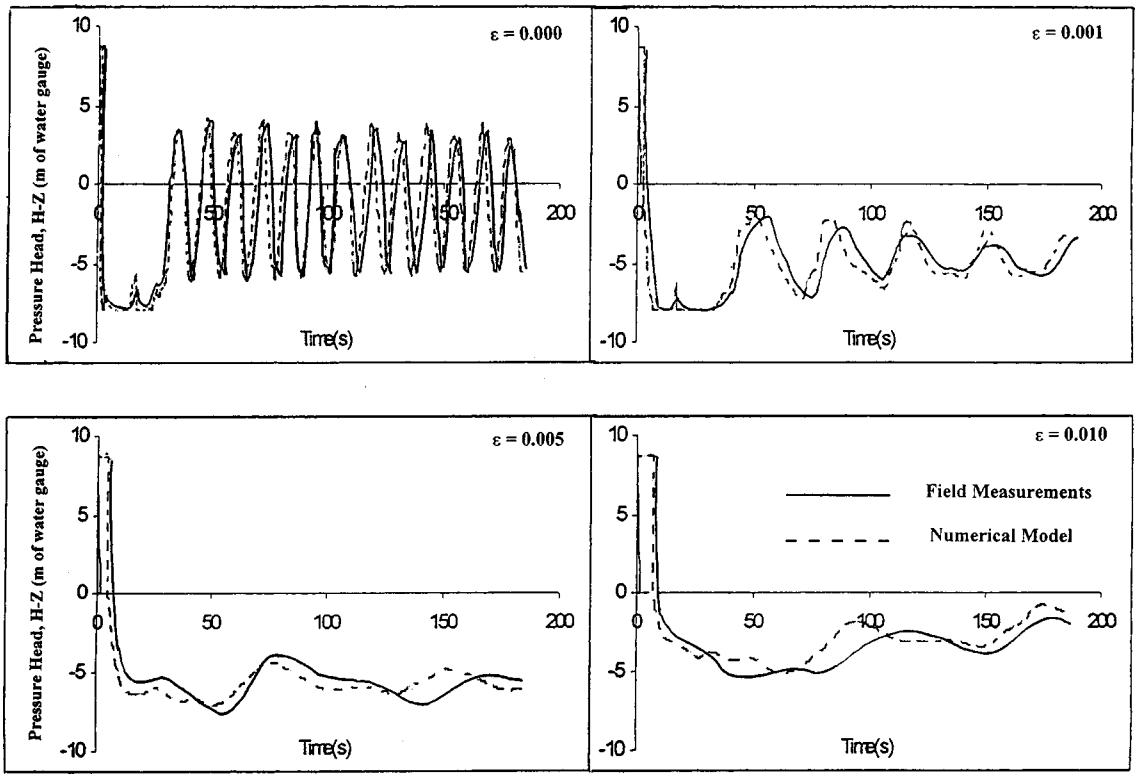

Fig. 6 Comparisons with field measurements transient pressure at peak location B with HC=HWL +2/10 ΔWL=104.94 m

lowest values of the transient pressure did not change significantly, the transient pressures for a higher weir discharge level show less negative peak-to-peak pressure variations. These results also indicate that higher discharge levels above the HWL are desirable. With weir heights well above the high water level, Fig. 3 shows that the transient characteristics at B further improves (i.e., less duration at gas release pressure). Positive transient pressures appear for HC>HWL+2/10 DWL. The variation of the static heads of the pumps operating point due to the changing tidal conditions and HC were also taken into considerations in the present study (Fig. 2).

Subsequently, three different cross-sectional areas of the weir discharge chamber were also investigated for HC above the HWL. Figure 4 shows the influences of different chamber cross-sectional areas at weir height HC=HWL+3/10 ΔWL. With a cross-sectional areas at 2.5 and 5.0 times greater than the reference cross-sectional area, the transient pressure at B has higher peak as compared to the standard cross-sectional area (WABref). However unlike the influence of different weir heights, there are little changes in the inception and duration time of the pressure surges at P_v for different cross-sectional areas investigated. The results obtained further confirm the previously obtained trends that at the higher weir height (HC=HWL+3/10ΔWL), there are more significant portions of the transient pressures which are above the atmospheric pressure when compared with the cases for the lower weir height.

The effects of the air entrainment (ε) on the transient pressures at B are shown in Figs. 5(*a*)–5(*b*) for weir heights of (*a*) HC =LWL and (*b*) HC=HWL+3/10 ΔWL, respectively. The cross-sectional area of the chamber is set at the standard reference value. The results show that the time taken for the pressure in the pipeline to drop to P_v after the pump trip is usually more gradual as the values of the air entrainment increases from 0.000 to 0.030. A study of many corresponding numerical cases using the above air entrainment model further shows four distinct characteristics of the pressure transient: (a) the pressure transients are irregular when compared with the air free cases and the period of pressure surges increase with increasing air entrainment; (b) the duration of the downsurge at gas release pressure decreases with increasing air entrainment levels; (c) with a higher weir discharge level, the duration of the pressure downsurge at gas release pressure decreases when compared with a lower weir discharge chamber; and (d) the pressure transients with air entrainment are nonsymmetrical with respect to the system static pressure head, while the pressure transients for the constant wave speed model were approximately symmetrical with respect to the system static pressure head (Jonsson [11]).

Comparison With Field Measurents

Field measurements (Lee and Cheong [10]) were carried out for one simulation case mentioned in this study in order to verify the validity of the numerical simulations. The transient pressures were measured at the location B (the peak location at the hill top) of the discharge pipe system as shown in Fig. 1(*a*) using piezoresistive absolute pressure transducers with the capability of monitoring subatmospheric pressures. Details of the accuracy of the instrumentation and measurement are described in Lee and Cheong [12]. Briefly, the pressure transducer when coupled to a piezoresistive amplifier produces a calibrated sensitivity of 50 mV/bar. With the calibration current set by fine adjustment through the piezoresistive amplifier and checked with a calibration plug, the overall measurement error of the pressure pulsations amplitude is of the order of 0.1%. The measurements were carried out by causing a simultaneous trip of the three pumps with the selected weir discharge chamber design of HC=HWL+2/10 ΔWL and with standard cross-sectional area. The corresponding transient pressures at a location B obtained from the numerical surge analysis are compared with the experimental values from pressure transducers in Fig. 6 for various air entrainment values. The air entrainment quantities were introduced into the pumping system through an air compressor by throttling the air supply and the

volumetric air supply was measured through an air flow meter. The measured data and the computed results with no air introduced $\varepsilon = 0.000$ and with air supply at $\varepsilon = 0.001$, 0.005, and 0.010 value were compared and are presented in Fig. 6. The numerical values compare very well with the corresponding field measurements except for the higher values of air entrainment. The computed pressure surges show basically same magnitude and phasing as the field measurements.

The accuracy of the air entrainment values introduced into the fluid system were also checked by looking at the resulting acoustic signatures of the flow through an electromagnetic flow meter. Previously the flowmeter was calibrated by correlating the acoustic signatures of the flow through the meter with known amount of air introduced into the system using an air compressor. For ease of comparison, all the air flow volumes were converted to air volume at standard conditions of one atmospheric pressure and 20°C. The full scale error of the air entrainment measurement is less than 3%. To improve the estimation accuracy of the air entrainment fraction, extreme care was also taken during the experimental measurements to minimize the surrounding electromagnetic interference of the overhead high power electrical appliances during the power shutoff and turnon. Also it should be noted here that, the field measurements were often made when the pumps were operating at low pump cutout water levels when air entrainment due to attached surface vortex and falling jets from the inflow near the pump intake might be present.

Conclusion

The effects of air entrainment on the pressure surges for unsteady flow in a pipeline system with a weir discharge chamber were investigated by using a new theoretical air entrainment model. Numerical studies show that entrained, entrapped or released gases in the transient fluid system tend to: (a) modify both the positive and the negative pressure peaks; (b) increase surge damping; and (c) produce nonsymmetrical pressure surges with respect to the system static pressure head. The pressure surges show irregular longer periods of downsurge and shorter periods of upsurge. The above transient characteristics are mainly due to the changing of local air fraction and local wave speed along the fluid system as a result of the transient variation of pressures and vice versa. The effectiveness of the weir discharge chamber with weir height above HWL is noted to be significant at higher values of entrained air volumetric void fraction ($\varepsilon \geqslant 0.02$). The numerical results on the transient pressure show same magnitude and phasing as the available field measurement data. This consistent analytical prediction of the pressure transient magnitude and phasing was previously not possible with the existing constant wave speed air entrainment models.

Acknowledgment

The author gratefully acknowledges the invaluable assistance of Prof. Steven J. Wright and Prof. Evan Benjamin Wylie in the arrangement of a Visiting Scholar position for the author at the College of Engineering, University of Michigan at Ann Arbor, MI, during his Sabbatical leave working on Fluid Transients in the U.S.A., 2001. The assistance of a research funding of Singapore dollars S$238,000.00 by the National University of Singapore for part of the above work under the research grant no. RP3972715 is also gratefully acknowledged.

Nomenclature

a = wave speed (m/s)
c = parameter for pipe constraint, Eq. (1)
D = pipeline mean diameter (m)
e = local pipe-wall thickness (m)
E = Young's modulus of elasticity (N/m^2)
f_l = loss factor
g = gravitational acceleration (m/s^2)
H = piezometric pressure head (m of water)
H_{atm} = atmospheric pressure (m of water)
HT = height of water column inside the discharge chamber (m)
HC = height of the discharge chamber (a design variable) (m)
HWL = high water level, HWL = 104.3 m
I = pump rotor moment of inertia including flywheel ($kg-m^2$)
k = time level at $t^k = \Sigma \Delta t^k$
K = bulk modulus of the liquid (N/m^2)
K_T = effective bulk modulus of the gas-liquid mixture (N/m^2)
K_a; K_r = empirical gas absorption and gas release coefficients
L = length of pipe (m)
LWL = low water level, LWL = 101.10 m
N^k = instantaneous pump speed (rpm)
N = number of node points
n = polytropic compression index
n_p = number of pumps operating
P = local pressure (N/m^2)
P_g = gas saturation pressure, $P_g = P_g(T)$
P_v = water vapor pressure, $P_v = P_v(T)$
Q = volumetric flow rate (liters/s)
t = instantaneous time in transient flow (s)
T = local water temperature (°C)
V = fluid velocity (m/s)
WA = weir chamber width (Fig. 1(*b*))
WB = weir chamber length (Fig. 1(*b*))
WAB = WA × WB
x = pipeline distance (m)
Z = pipeline elevation (m)
Δt^k = time-step at k-time level (s)
Δx = node point distance along pipeline
ΔWL = ΔWL = HWL − LWL = 3.20 m
α_{ga} = fraction of gas absorption
α_{gr} = fraction of gas release
ε = air volumetric void fraction in water
ε_T = total ε if no gas release or absorption
ε_g = dissolved air in liquid at H_{atm}
ε_o = an initial free entrained air
ρ_w = density of water
ϕ = slope of the pipeline

Subscripts

i = node point at $x = i\Delta x$
T = total

References

[1] Tullis, J. P., ed, 1971, *Control of Flow in Closed Conduits*, Colorado State University, Fort Collins, CO, pp. 315–340.
[2] Pearsall, I. S., 1965–1966, "The Velocity of Water Hammer Waves," Proc. Inst. Mech. Eng., **180**, Part.3E, pp. 12–20.
[3] Fox, J. A., 1984, *Hydraulic Analysis of Unsteady Flow In Pipe Network*, Macmillan Press, London.
[4] Lee, T. S., and Cheong, H. F., 2001, "Fluid Transient With Air Entrainment," Final Research Report No. R-265-000-021-112. Mechanical Engineering Department, National University of Singapore.
[5] Kranenburg, C., 1972, "The Effect of Free Gas on Cavitation in Pipelines Induced by Waterhammer," *Proc. Int. Conf. on Pressure Surges*, BHRA, Bath, U.K., pp. 65–80.
[6] Provoost, G. A., 1976, "Investigation Into Cavitation in a Prototype Pipeline Caused by Waterhammer," *Proc. 2nd Int. Conf. on Pressure Surges*, BHRA, Bedford, UK, pp. 35–43.
[7] Chaudhry, M. H., Bhallamudi, S. M., Martin, C. S., and Naghash, M., 1990, "Analysis of Transient Pressures in Bubbly, Homogeneous, Gas-Liquid Mixtures," ASME J. Fluids Eng., **112**, pp. 225–231.
[8] Wylie, E. B., Streeter, S. L., and Suo, L., 1993, *Fluid Transients in Systems*, McGraw-Hill, New York.

[9] Lee, T. S., and Pejovic, S., 1996, ''Air Influence on Similarity of Hydraulic Transients and Vibrations,'' ASME J. Fluids Eng., **118**, pp. 706–709.
[10] Roache, P. J., 1972, *Computational Fluid Dynamics*, Hermosa Publishers, Albuauerque, NM.
[11] Jonsson, L., 1985, ''Maximum Transient Pressures in a Conduit With Check Valve and Air Entrainment,'' *International Conference on the Hydraulics of Pumping Stations*, The University of Manchester Institute of Science and Technology (UMIST) & BHRA–The Fluid Engineering Center, England, pp. 55–76.
[12] Lee, T. S., and Cheong, H. F., 1998, ''Tanjong Rhu Pumping Station—Site Measurement and Analysis of Surge in Pumping Main,'' Ebara Engineering Singapore Pte Ltd., Singapore, Internal Report.

Turbulence Control With Particle Image Velocimetry in a Backward-Facing Step[1]

Mika Piirto
Research Scientist
e-mail: mika.piirto@tut.fi

Pentti Saarenrinne
Senior Researcher
e-mail: pentti.saarenrinne@tut.fi

Hannu Eloranta
Research Scientist
e-mail: hannu.eloranta@tut.fi

Tampere University of Technology,
Energy and Process Engineering,
P.O. Box 589,
33101 Tampere, Finland

A new concept of particle image velocimetry (PIV) for turbulence control is introduced. The PIV method is used to measure the flow and supply information on the turbulence quantities on-line for a control station connected to an actuator for flow manipulation. With this "closed-loop" system of PIV and PID controllers, it is possible to control increase or decrease turbulence quantities or length scales. Special techniques for the on-line measurement are developed. The mean velocity is computed with a moving time average operator and the Reynolds decomposition is applied for the calculation of the Reynolds stresses, velocity fluctuations, or other instantaneous turbulence quantities. The control concept is tested in a backward-facing step with a DC-motor based actuator for mixing of the near wall flow. A length-scale estimate similar to the integral scale and the Reynolds shear stress are calculated on-line. The results show it is possible to control the turbulence and for example to compensate the disturbance on the Reynolds shear stress caused by a manual change in flow velocity. The control frequency is quite slow (e.g., 0.1–100 Hz), limited primarily by the image-grabbing operations and the computation of the velocity vectors in the PIV station. For this reason the method is applicable for slow processes, e.g., to steer the mixing processes or more generally to manage the turbulence level or the length scales. [DOI: 10.1115/1.1516575]

1 Introduction

The control of turbulence and flow has always been an interesting topic in fluid dynamics. The management of the turbulence quantities, e.g., in order to decrease friction or to steer the mixing process, is an attractive idea. Most of the literature about turbulence control deals with cases in which drag reduction or flow separation prevention are used to (a) reduce skin friction, (b) control turbulence level, or (c) affect transition delay. Prandtl [1] pioneered flow control by using suction to delay boundary layer separation from the surface of a cylinder. There exists a number of publications on the matter: e.g., flow control is reviewed by Gad-el-Hak [2], control of turbulence in a boundary layer by Lumley and Blossey [3], and the control of combustion instabilities by McManus et al. [4].

The definitions for flow control or turbulence control are not straightforward. Flow control is understood to affect the flow field properties, such as mean velocities, or postpone flow separation. Turbulence control is usually considered to lower the turbulence level or to prevent transition to turbulence. In some cases turbulence is also produced consciously in the flow. In that case, if turbulence level is increased or decreased actively by a controller, the definition of turbulence control becomes expanded to cover not only the decreasing but also the increasing of turbulence, or keeping it constant.

The next question is what turbulence phenomenon or property should be monitored and what the goal of the control is. For the control of combustion instabilities the goal can quite simply be the suppression of large pressure fluctuations or large-scale vortices, [4]. But for many other industrial processes the goal of turbulence control is not always easy to set. The most intensive research is done to reduce skin friction on surfaces. Many turbulent flows display a combination of organized or coherent structures and apparently disorganized or incoherent structures. In the wall region or the turbulent boundary layer, coherent structures account for over 80% of the energy in turbulent fluctuations. The typical current published results indicate drag reduction gains of 5%–10% for boundary layer flows, [3]. However, theory indicates possible gains of 50%. Current knowledge rarely supports the practical use of boundary layer control and the penalty associated with the control device often exceeds the saving derived from its use, [5].

More profitable applications for turbulence control can be found in industrial devices. For example, in many mixing processes the properties of the fluid are time varying and adjusting of turbulence properties to a certain level is done by experience. Proper control of turbulence properties can easily enhance process efficiency considerably. Particle image velocimetry (PIV) opens a new perspective on the active control of turbulence in transparent fluids. Its clear advantage is that different velocity and length scales can be estimated directly from two-dimensional vector fields and also flow structures can be recognized. At the moment, the repetition rate of image grabbing and the computation time of vector fields restricts its use to processes needing slow control responses. Depending on the PIV system and the computation required, the control rate varies in the order of 0.1–100 Hz.

In order to test turbulence control possibilities with PIV, a test flow channel with a mixing equipment is built. A backward-facing step (BFS) is quite a typical test apparatus having a shear layer flow region which in this case is manipulated. Chun et al. [6] has studied an active spanwise-varying local forcing issuing from a thin slit near the separation line, and Lai et al. [7] has made research on the effect of oscillating a small foil in plunge on the reattachment of BFS flow. In this paper an on-line concept is used, and a DC motor with adjustable speed is connected to a rotating rod which is located on the wall before the step change. A control station is adjusting the speed of the motor.

The content of the paper is following: a ''closed-loop'' control system with PIV is introduced in Section 2. The experimental setup is explained in Section 3. A length scale similar to the inte-

[1]Presented at the Hydraulic Machinery and Systems—20th IAHR Symposium. Aug. 6–9, 2000, Charlotte, NC.

Contributed by the Fluids Engineering Division for publication in the JOURNAL OF FLUIDS ENGINEERING. Manuscript received by the Fluids Engineering Division, April 30, 2001; revised manuscript received May 31, 2002. Associate Editor: A. K. Prasad.

gral scale and Reynolds shear stress are derived for on-line control purposes and on-line control test runs are performed in Sections 4 and 5. Section 6 provides conclusions.

2 Turbulence Control With Particle Image Velocimetry (PIV)

2.1 Control Strategy. If time-average filtering for turbulence quantity is used, the filter operation of the measured turbulence quantity Ψ can be achieved in a short period of time, e.g., with a moving average operator Ψ_{ma}. The desired goal for a specific turbulence quantity is given by the set point Ψ_{sp}. According to the difference, which is called control error, $e(t) = \Psi_{sp} - \Psi_{ma}$, a controller connected to an actuator manipulate the measured flow. A PIV-based control schema is shown in Fig. 1. The ''closed-loop'' system consists of a PIV system, a control station, a process, and an actuator. In the conventional turbulence control context, a PIV station together with a camera is ''an intelligent sensor'' for characterizing turbulence. The process used as an example later in this paper is a backward-facing step (BFS) in a channel flow. The actuator is a DC motor connected to mixing equipment.

This kind of feedback control is useful in processes, in which it is necessary to change or manage turbulence according to the predefined knowledge of the process. Another possibility for using this kind of strategy is the necessity to maintain a certain turbulence quantity level when the physical conditions of the flow are changing. An example of this is a paper machine multiphase flow in which the pulp-suspension quality may change and the turbulence level should be kept constant in the BFSs of the inlet pipes before the head box.

2.2 Control Frequency. Depending on the required control frequency response, two different control approaches for PIV can be defined: (a) with control frequency higher than the dynamics of the turbulence phenomena and (b) with control frequency lower than the dynamics of the turbulence. Strategy (a) is very challenging and the PIV system connected to the controller and the actuator should be able to ''touch'' the flow structures in a similar way like in an example of a feed-forward control of a turbulent boundary layer in Rathnasingham and Breuer [8]. As a two-dimensional measurement system, turbulence structure information, e.g., in a boundary layer control case, would be beneficial even though the analysis of the structure would not be an easy task. From the control point of view the measurements may include too much noise. However, the main problem is definitely that the control frequency is far too low. This approach is difficult for rather high-speed sensing techniques like hot-wire arrays, especially when the detection of turbulence flow structures with these is even more difficult than with the PIV method.

When the dynamic of the control can be slow, it opens a new perspective on the control of turbulence with PIV. Using approach (b), the control frequency is not that critical and in many cases the measured turbulence quantities and the length scales can be even averaged or filtered over a short time period. The operation decreases noise and makes turbulence quantity estimation more reliable. As mentioned before, PIV as a two-dimensional measurement system offers valuable information about coherent structures which is available in each instantaneous vector field. By way of conclusion regarding PIV compared with the hot-wire array techniques, the advantage of the hot wire is the faster frequency response, whereas large instantaneous two-dimensional measurement fields are the strength of PIV.

2.3 Turbulence Quantity Estimation. There is a number of interesting turbulence quantities which can be estimated with PIV. Practically, a PIV velocity vector field can be considered as a matrix of sensors with instantaneous velocity information in each location. The quantity or the quantities chosen and used for the control of turbulence depend on the process and the defined control task. In many cases turbulence kinetic energy (TKE) may be one interesting quantity. Other possible quantities are u_{rms} and v_{rms} components individually. In an example of turbulent boundary layer control by Rathnasingham and Breuer [8], one goal is to decrease the u_{rms} component. More generally, coherent structures and their control play an important role in the dynamics of turbulent shear flows like in an example of active control of streamwise vortices and streaks in a boundary layer from Jacobson and Reynolds [9].

Several methods have been developed for the use of PIV in the analysis of coherent structures such as length-scale analysis with spatial correlations, [10], and structure scale analysis like Piirto et al. [11] and Eloranta et al. [12]. Also two-dimensional forms of spectral and length scale analysis, [11], can be useful in control. Examples of length scales measured with PIV in turbulent boundary layer are given by Tomkins and Adrian [13], Piirto et al. [11], and Yoda and Westerweel [14]. In the last-mentioned paper the effect of localized suction is examined. Later in this paper, length-scale estimation is used and an integral scale-type quantity is controlled.

Reynolds stress, especially Reynolds shear stress, is an important quantity in mixing processes of shear layers. Also, it is often used as an active turbulence control measure in wall-bounded flows, like in Jacobson and Reynolds [9] and Choi et al. [15]. To monitor time-dependence of Reynolds shear stress, instantaneous $u'v'$ is measured. For TKE, u_{rms}, v_{rms}, or more generally when Reynolds decomposition is needed, the mean flow has to be estimated. A method for estimating mean flow is explained later in this paper and Reynolds shear stress is used as another control example.

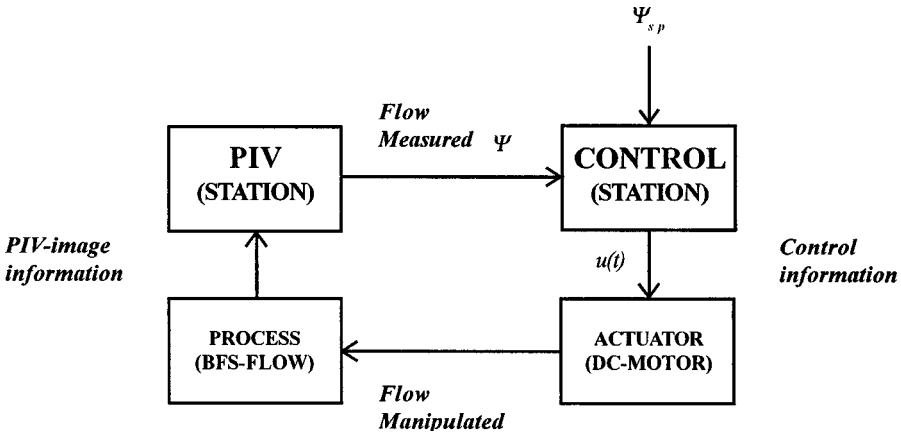

Fig. 1 PIV-based turbulence control system

Several other quantities which can be computed directly from velocity fields, such as kinetic energy, rotation, strain, or a pressure difference estimate, [16,17], can be other useful estimates. These quantities can be easily combined with control strategies because of their instantaneous nature, i.e., only one velocity field is needed for the calculation of an estimate. At the moment estimates for Taylor micro scales, [17], and dissipation, [18], are challenging for control purposes because of the spatial resolution limits of PIV.

3 Experimental Setup

The backward-facing step (BFS) concept or flow over a surface-mounted obstacle is investigated with particle image velocimetry (PIV), e.g., by Scarano and Riethmuller [19] and Sousa et al. [20]. The PIV measurement location of this BFS flow study is shown in Fig. 2. The step-height h ($h=10$ mm) based Reynolds number is $\mathrm{Re}\,h=U_0h/\nu\cong 10{,}000$. The height of the inlet channel is $2h$, the expansion ratio $ER=3/2$, and the width of the channel $4h$. The measurement window size is $3h\times 2h$. U and V are used for the streamwise (x) and for the spanwise (y) velocities, respectively. The rotating axle is located $1h$ before the step change.

3.1 PIV Measurements. The flow for the PIV measurements is seeded by hollow glass spheres with an average size of 5 μm. The PIV system consists of an Nd:YAG double-cavity laser with light sheet optics and a CCD camera of resolution 1280 $\times$1024 pixels. For the computation of the velocity vector fields the standard FFT-CC (cross-correlation algorithm) is utilized without overlapping for the on-line control tests and with overlapping of 50% for the off-line tests. The size of the interrogation area is 32$\times$32 pixel. In the off-line tests, before the final interrogation lap also integer displacement technique with the interrogation area of 64$\times$64 is applied and 300 vector fields are measured with each constant DC motor velocity. In these off-line tests, reasonably few (1–5) erroneous vectors ($<0.15\%$) exceeding the allowed velocity limit have been detected in each vector field of size 80$\times$44 vectors. The spurious vectors have been replaced by interpolation. The measurement random error for the standard FFT-CC and an integer displacement technique is in the order of 0.04 pixel, [21], and in this measurement case the increase in rms velocities is about 0.02 m/s. Also a test measurement set with a flow of zero velocity in the same measurement position leads to an increase or decrease of about the average 0.02 m/s in fluctuations. This minimum error is relevant for both the off-line and the control tests, and the increase of about 0.015–0.02 m/s in rms values can be found in all spatial locations of the measurement window. For the control tests the error is bigger because no precomputation for the integer displacement is performed. In that case the measurement error is in the order of 0.1 pixel, [21]. If the rms bias in the order of 0.04 pixels in all spatial locations is subtracted from this total measurement error of 0.1 pixel, the random measurement error in on-line tests is in the order of 0.06 pixel. The rms profiles can be considered more comparable with each other when the bias error at the base of the total error is identified.

3.2 Inflow Before the Axle. The water flow is pumped into a channel of length $70h$ before the BFS and the maximum mean streamwise velocity is about $U_0=1.0$ m/s before the sudden expansion in location $x/h=-2$. The inflow mean streamwise velocity distribution before the axle is measured with PIV in the same way with the off-line tests. The friction velocity is estimated using the universal turbulent boundary layer velocity profile of Spalding [22]. The laser sheet thickness is about 1 mm, and practically the shortest reliable measurement distance from the wall is about 1 mm. Because of this shortest reliable distance, the friction velocity could not be solved alone with PIV measurements but together with the boundary layer information of Spaldings velocity profile. The boundary layer properties of the location $x/h=-2$ are listed in Table 1 and the inflow mean streamwise velocity profile together with Spalding's profile are shown in Fig. 3. The boundary layer properties are calculated together with Spalding's profile. According to the shape factor $H=\delta^*/\theta\cong 1.47$, the inlet boundary layer flow seems to be close to the constant pressure equilibrium boundary layer.

Table 1 The boundary layer properties at location $x/h=-2$

$\delta\approx 6.4$ mm	$U_0\approx 1.0$ m/s	$\mathrm{Re}_\delta=U_0\delta/\nu\approx 6400$
$\delta^*\approx 0.94$ mm	$u_\tau\approx 0.051$ m/s	$\mathrm{Re}_{\delta^*}=U_0\delta^*/\nu\approx 940$
$\theta\approx 0.64$ mm	$\mathrm{Re}_\theta=U_0\theta/\nu\approx 640$	$\mathrm{Re}_\tau=u_\tau\delta/\nu\approx 326$

3.3 Rotating Axle. A DC motor is connected to a rotating rod. This cleaved axle is located upstream of the sudden expansion of the BFS, as shown in Fig. 4, and it is used as an actuator of this experimental set-up. The actuator located just before the tip of the step change on the wall affects the turbulence quantities in the shear layer. In Fig. 4 three different ways to affect the flow are shown. The positive speed of the motor is forward, i.e., in the flow direction (a), and the negative speed is against the flow (b). The axle can also be placed in the same plane with the surface of the wall (0 rpm) and thus it does not affect the flow (c). The distance of the left-side edge of the rotating half-axle from the BFS is 10 mm ($1h$) and the diameter of the rod is 2 mm of which, depending on the axle position, maximum half height ($0.1h$) is inside the flow. The actuator affects the flow in various ways: the rotating

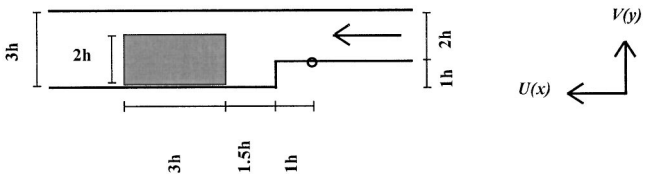

Fig. 2 Location of measurement window (gray area) in backward-facing step at $x/h=1.5\ldots 4.5$ from step change. Rotating rod is located $1h$ before the expansion.

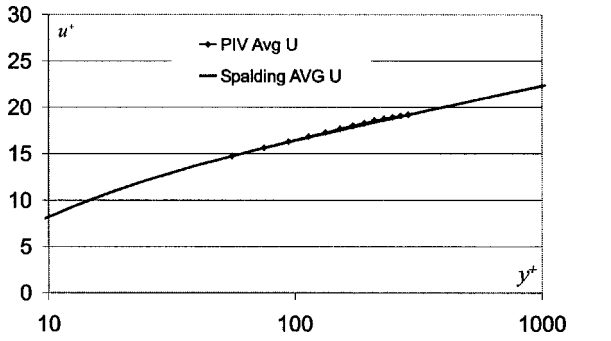

Fig. 3 The mean streamwise inflow velocity profile at the location $x/h=-2$ together with the Spalding's velocity profile for turbulent boundary layer

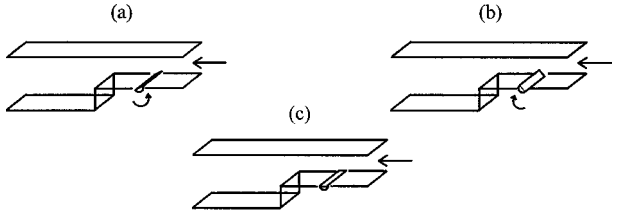

Fig. 4 Rotating axle in backward-facing step channel. The positive rotation of axle is forward, i.e., in the flow direction (*a*), and the negative against the flow direction (*b*). The axle can also be placed so as not to affect the flow (*c*).

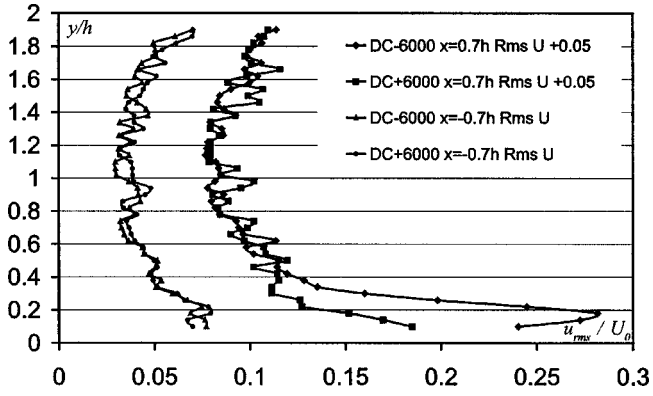

Fig. 5 Streamwise rms velocity profiles upstream and downstream from the axle with positive and negative maximum speeds of DC motor

rod (1) creates a passive barrier with changing height to the boundary layer, and (2) disturbs actively the boundary layer flow structures. In Fig. 5, streamwise r.m.s. velocity profiles are plotted $0.7h$ upstream and downstream of the rod. No significant differences in mean streamwise velocity or rms profiles with the DC motor maximum speeds -6000 and 6000 exist in the inflow side upstream of the rod ($x/h=-0.7h$). In the BFS side, at $x/h=0.7h$ downstream of the rod, the negative DC motor speed causes an enhanced shearing process on the top of the rod and freestream and thus increases turbulence level having the maximum streamwise r.m.s. velocity about 0.28 at $y/h=0.18$ from the bottom of the channel wall. The positive DC motor rotation causes increased turbulence intensity closer to the wall boundary layer region between $y/h=0.1-0.4$ than the negative DC motor speed does. This can be explained with the smaller velocity difference in the shearing between the freestream velocity and the tangential velocity of the rod. The rod tangential velocity is always smaller than the free stream velocity. When the motor positive velocity is increased, the velocity difference in the shearing diminishes and visa versa.

3.4 Control Station and PIV. The control station is linked together with a PIV station via RS-232. It receives the turbulence information and acts in a very similar way to the process control stations used in industry having features like on-line graphics, a user-interface for on-line parameter changes, the storing of the measured (or computed) quantities on the hard disk, and PID controllers.

A commercial PIV system is used and applications programmed with a C-language type code together with the Turbo-C DLLs (dynamic link library) to calculate the on-line turbulence estimates. Besides the computation of the turbulence characteristics, it intervals the measurements to the user-specified cycles. The tasks of the PIV station in one control cycle are as follows:

1. Wait for the right time after the previous cycle to grab dual-images to the memory.
2. Compute the velocity vector field.
3. Compute the on-line turbulence quantities.
4. Send the quantities to the control station via RS-232.

The control station receives the on-line turbulence information from the PIV system and further calculates the data. With the user interface, parameters for the PID controllers, control output limits, and the setpoints for the controlled turbulence quantity can be changed during the control tests. In the control tests of this paper, the PI controller without derivative part is used. In the increment form together with the filtering, it is

$$u(t)=u(t-1)+K_P[e(t)-e(t-1)]+K_I e(t) \tag{1}$$

$$e(t)=\psi_{sp}(t)-\psi_{ma}(t) \tag{2}$$

$$\psi_{ma}(t)=\frac{1}{N_{ma}}\sum_{k=0}^{N_{ma}-1}\psi(t-k) \tag{3}$$

in which $u(t)$ is the last calculated control output value and the new speed of the DC motor. K_P and K_I are the coefficients for the gain and the integration terms of the controller, respectively. The previous control cycle values are for the control output $u(t-1)$ and for the control error $e(t-1)$. The turbulence quantity, the instantaneous (on-line) value for the desired quantity, is marked with Ψ and indexed sp for the setpoint and ma for the moving average which is the average of the measurements of the last cycles N_{ma} in Eq. 3. The turbulence quantities in this test case are averaged over a period of 50 seconds when one control cycle is 2.5 s. This means that the moving average estimate is computed with the last 20 instantaneous samples.

Other controllers besides PID ones can be attached to the control station, like self-tuning controllers [23,24], and multiple input-multiple output (MIMO) controllers [24,25], depending on the turbulence control tasks. The control station software is written also with Turbo C++ like the DLLs of the PIV station.

4 Control of Integral Scale

The first turbulence quantity chosen to be controlled is based on the streamwise velocity correlation coefficient function (CCF) and thus the length scales in the flow. The integral length scales with the correlation curves are first tested in the off-line test for the time series of the velocity fields with the constant different speeds of the DC motor and then a control test is run. In the following tests it is assumed that the flow velocity is constant, i.e., there is no variations or changes in the main pump of the loop.

4.1 Off-Line Test. In the case of PIV, the length scale analysis is typically carried out with the spatial CCF instead of time-resolved CCF. The correlations and the spatially computed integral scales decrease when the positive speed of the DC motor is increased. The results measured in the whole measurement window are shown in Fig. 6. When the DC motor positive velocity is increased, the difference in the shearing between the freestream velocity and the tangential velocity of the rod diminishes and the length scales in the measurement region are reduced. However, the rod tangential velocity is always smaller than the freestream velocity. The normalized correlation is calculated for the streamwise velocity component in the streamwise direction. Limited to the maximum lag distance depending on the size of the vector field, the correlation function in discrete form is given in the following equations:

$$\hat{r}_u(\Delta i)=\frac{1}{(p-\Delta i)n}\sum_{i=1}^{p-\Delta i}\sum_{j=1}^{q}\sum_{\xi=1}^{n}\left(\frac{u'(i,j,\xi)\cdot u'(i+\Delta i,j,\xi)}{u_{\rm rms}(i,j)\cdot u_{\rm rms}(i+\Delta i,j)}\right) \tag{4}$$

$$u'(i,j,\xi)=U(i,j,\xi)-\overline{U}(i,j) \tag{5}$$

$$\overline{U}(i,j)=\frac{1}{n}\sum_{\xi=1}^{n}U(i,j,\xi) \tag{6}$$

$$u_{\rm rms}(i,j)=\sqrt{\frac{1}{n}\sum_{\xi=1}^{n}\langle u'(i,j,\xi)\rangle^2} \tag{7}$$

in which Δi is the spatial lag between the velocities, u' the fluctuation velocity, and $u(i,j,\xi)$ the instantaneous velocity in the position i,j of a particular vector field ξ.

In the computation of the normalized correlation, the time-average and the rms value should be known. The exact values for them are not available, because the control operations affect them continuously. In this flow case with the constant flow presumption, it is suggested to operate with the real velocities and the

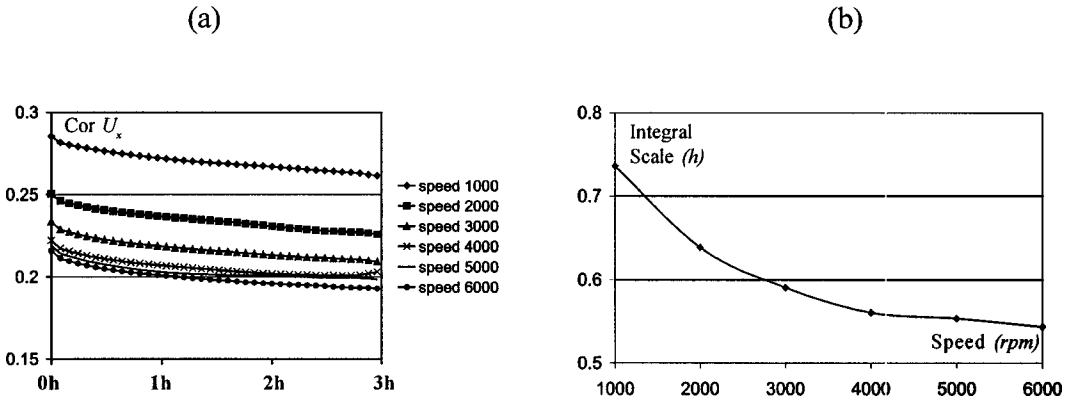

Fig. 6 Correlation curves for streamwise velocity in streamwise direction with different constant DC motor speeds (*a*) and their integral scales (*b*)

average of Eq. (6) is replaced with 0 and the rms value of Eq. (7) with 1, leading to a non-normalized correlation of one velocity vector field ($n=1$). Because the Reynolds decomposition and the scaling with the r.m.s. are not used, the on-line spatial correlations and the integral scale computed from them include information on the scales of the flow velocity structures besides the fluctuation velocity structures. Thus, with this calculation technique for CCF, it is important that the main flow velocity is kept constant. Also, the integral scale values are higher than the normalized ones would give. When the correlations are computed at the moment t, the estimate calculated with the Euler rule for an instantaneous integral scale is

$$\Lambda_{u_x}(t)=\sum_{\Delta i=0}^{p-1} r_u^{\wedge}(\Delta i,t)*dx \tag{8}$$

in which r represents the correlations of Eq. (4) at the moment t and dx is the distance between two adjacent velocity vectors ($=$ one lag distance) in the streamwise direction. The nonlinear effect of motor speed on the integral scale can be noticed in Fig. 6(*b*).

The interpretation of the integral scale is the longest connection of the velocities, [26], or the velocity structures in the flow field and it is considered to be a length scale of the large structures. The maximum distance is limited to the size of the measured window and therefore the correlations and the integral scales describe the flow structures and the correlations shorter than that. Furthermore, the non-normalized correlation curves do not reach zero. Because of these features, the integral scale solved here is relative and cannot be compared with the absolute values of integral scales for certain flows in which the maximum lag distance is not limited until the normalized correlation coefficients reach a stable zero.

4.2 Control Test. In the integral scale control test the main purpose is to keep the non-normalized integral scale or change it into the desired value (setpoint) given by the user. The PI control-

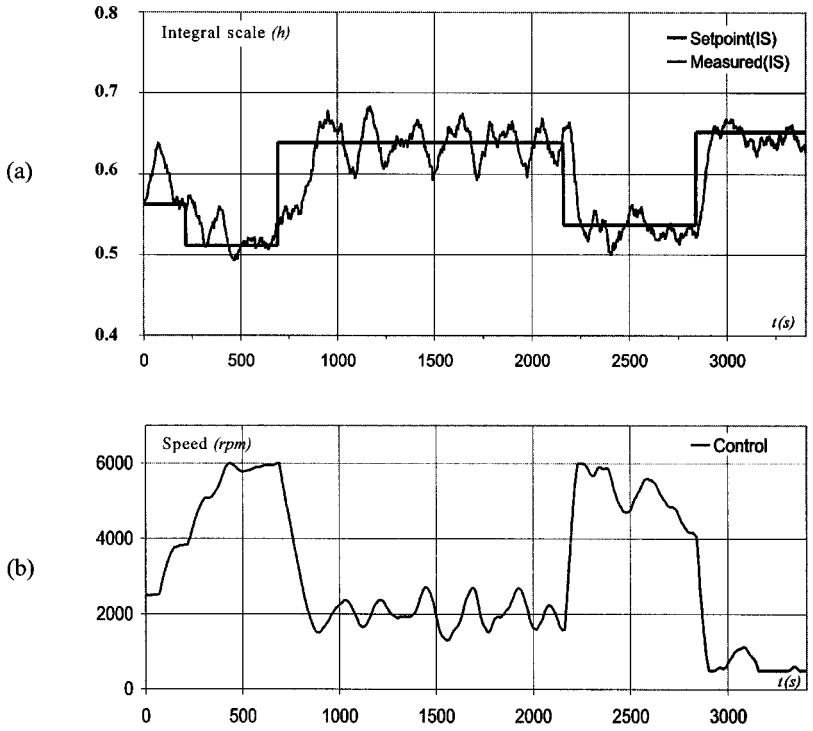

Fig. 7 Measured (MA filtered) and setpoint values for the integral scale (*a*) and the control output (*b*)

ler is experimentally tuned by some step changes and after that one test run is shown in Fig. 7(*a*) and (*b*). The higher the positive (forward) speed is, the shorter is the integral scale, which was also noticed in the integral scale of the off-line tests of Fig. 6. Another observation regarding the computation of the integral scale estimates is the existence of different length scales in different parts of the flow, [10]. In this case the main flow in the upper part of the channel has totally different flow structures and length scales compared with the recirculation zone. For this reason, the computational area should be chosen according to the flow structures to be measured. In this control case, the computational area is limited to the shear layer part and the recirculation zone. Note that the different computational area in on-line and off-line tests leads to different integral scales with the same DC motor speeds.

The control response of step changes varies, depending on the direction of the change. In this case, the effect of the manipulator alters with different DC motor speed ranges, which was also noticed in Fig. 6. The low frequency ($T=200$ s) in the measured integral scale of Fig. 7(*a*) could not be compensated by the tuning of the controller. The question remains whether the moving average operation in the control station made it difficult to tune the control parameters or whether it was caused by other reasons in the process. However, the results confirm it is possible to control a turbulence length scale.

5 Control of Reynolds Shear Stress

The second control test is based on the Reynolds stresses. In two-dimensional flow measurements different instantaneous values for $u'u'$, $u'v'$, and $v'v'$ can be computed. In this backward-facing step (BFS) case with two-dimensional measurements, probable the most interesting value to describe the turbulent mixing is the estimate for the shear stress. For n velocity vector fields Reynolds shear stress is

$$\overline{u'v'}(i,j)=\frac{1}{n}\sum_{\xi=1}^{n}u'(i,j,\xi)v'(i,j,\xi). \tag{9}$$

5.1 Off-Line Test. In the instantaneous estimate for $u'v'$ only one fluctuation field is used ($n=1$). A challenging part from this point of view is the computation of the fluctuations. One way to solve the estimate for fluctuations could be a method based on spatial fluctuation or LES-decomposed velocity fluctuation introduced by Adrian et al. [27] and implemented in special particle image velocimetry (PIV) vector analysis software by Piirto et al. [17]. The advantage of the spatial fluctuation operation is the possibility to estimate fluctuations and ''coherent structures'' in instantaneous velocity fields. However, in the actual definition of the Reynolds stresses, the velocity fluctuations are defined in the time-mean sense. Thus, the computation of the time-average is performed by another MA operation. The mean flow is computed with the circular stack of instantaneous vector fields in each control cycle. The minimum length for the MA filter is found with the error function of Fig. 8 in which MA field is compared to the average field computed off-line for 300 vector fields with the constant DC motor speed -1000. In this case the MA filter length $M_{ma}=20$ is chosen when the error with any constant motor speeds $-6000\ldots6000$ rpm is less than 2.5% when normalized by U_0. The MA filter length should not be too long either, because the mean flow estimates will become biased because of the on-line control operations. The moving average (Eq. (10)) and the fluctuation (Eq. (11)) for both the velocity components are computed first. For the streamwise component they are

$$\overline{U}(i,j,t)=\frac{1}{M_{ma}}\sum_{k=0}^{M_{ma}-1}U(i,j,t-k) \tag{10}$$

$$u'(i,j,t)=U(i,j,t)-\overline{U}(i,j,t). \tag{11}$$

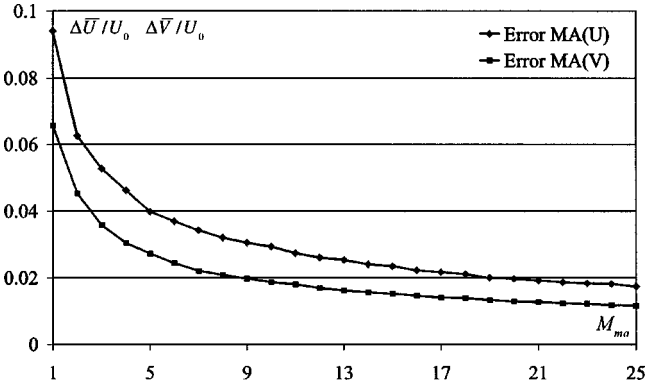

Fig. 8 Error of average values for streamwise (*U*) and spanwise (*V*) velocities in function of moving average filter length M_{ma}

Again, $U(i,j,t)$ is an instantaneous velocity in the position i,j of a particular vector field at the last sampled moment t and the index k defines the earlier sampled vector fields. The instantaneous Reynolds shear stress is solved at a moment t as

$$u'v'(i,j,t)=|u'(i,j,t)v'(i,j,t)|. \tag{12}$$

The absolute value in Eq. (12) is taken because of the spatial average operation. If the average of the Reynolds stresses in a certain spatial area is calculated without the absolute operator, the coherent structures causing the different signs for the Reynolds stresses can compensate each other. In the case of mixing, only the absolute values for the instantaneous stresses are of interest.

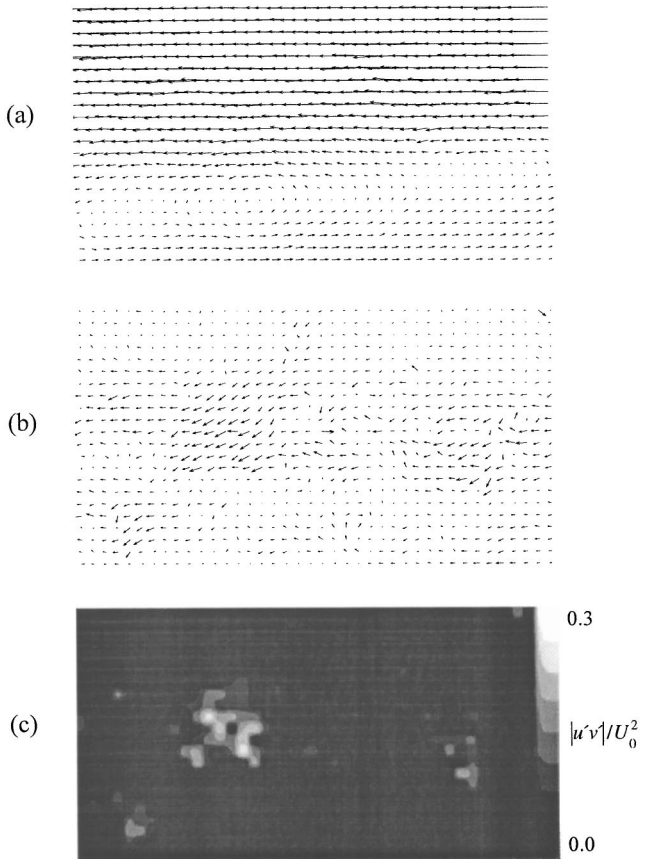

Fig. 9 Examples of MA velocity field (*a*), fluctuation field (*b*), and instantaneous Reynolds shear stress (*c*)

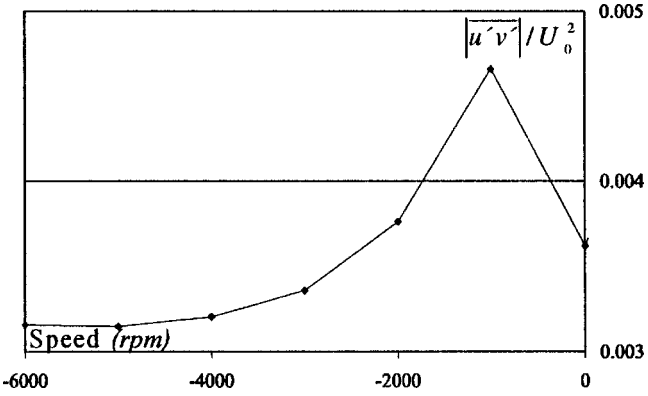

Fig. 10 Off-line test for absolute Reynolds shear stress. The samples are connected with lines.

So the estimate for the instantaneous Reynolds stress in a particular area of the flow is computed with the Eqs. (12) and (13). The spatial average operator for a specific area of the flow is

$$\psi(t)=\frac{1}{(N_{x2}-N_{x1}+1)(N_{y2}-N_{y1}+1)}\sum_{i=N_{x1}}^{N_{x2}}\sum_{j=N_{y1}}^{N_{y2}}\psi(i,j,t). \tag{13}$$

An example of the moving average vector field ($M_{ma}=20$) is shown in Fig. 9(*a*). An example of the fluctuation field and an instantaneous absolute value for Reynolds shear stress calculated from the fluctuation fields are shown in Figs 9(*b*) and (*c*), respectively. A certain user-defined spatial area is averaged in order to create one turbulence measurement value per control cycle. For this reason it is important to understand both the meaning of the chosen turbulence quantity and the effect of the spatial area in which the chosen quantity is controlled. In this BFS example the turbulence quantities, like the correlations, are totally different in the main stream (upper part of the channel) compared with the recirculation area. Therefore, the user-defined computational area in the control test is limited to the shear layer part of the BFS defined by the spatial parameters N_{x1}, N_{x2}, N_{y1}, N_{y2}. Before the on-line tests, an example of the absolute Reynolds shear stress with constant DC motor speeds for the whole measurement window is shown in Fig. 10. Slow rotation speed of the rod causes periodic disturbances leading to stronger coherent structures in Reynolds shear stress than high rotation speed does. Again note that in the on-line control runs, because there are more coherent structures in the shear layer part defined by the spatial parameters N_{x1}, N_{x2}, N_{y1}, N_{y2}, the values are higher than in this off-line example for the whole measurement window.

5.2 Control Test. In the Reynolds shear stress control both the setpoint change test and the disturbance test are carried out and the results shown in Figs. 11 and 12, respectively. The speed of the DC motor is negative against the flow, which means strong periodic disturbance especially with low-speed range. This is caused by the periodic barrier effect of the manipulator. The main source of the noise in measurement signal is that there are relatively few coherent structures in each fluctuation field, as already shown in Fig. 9(*b*), causing the statistical error. With the moving average filtering in the control station, the coherent structure information is increased and the measured signal becomes more acceptable for the control tests. The setpoint changes, depending on their directions, give very different control responses as can be noticed in Fig. 11. An interesting downward slope in the control signal from 2500 to 4500 s demonstrates the operation of the controller's integrating part to drift the error signal in to zero.

In the second test, shown in Fig. 12, two disturbances are generated by changing the velocity of the flow by changing the speed of the main pump of the test loop. This is done with the step change, first decreasing it by 20% and then increasing it by the same amount at the moments 9500 and 11150 s. The controller

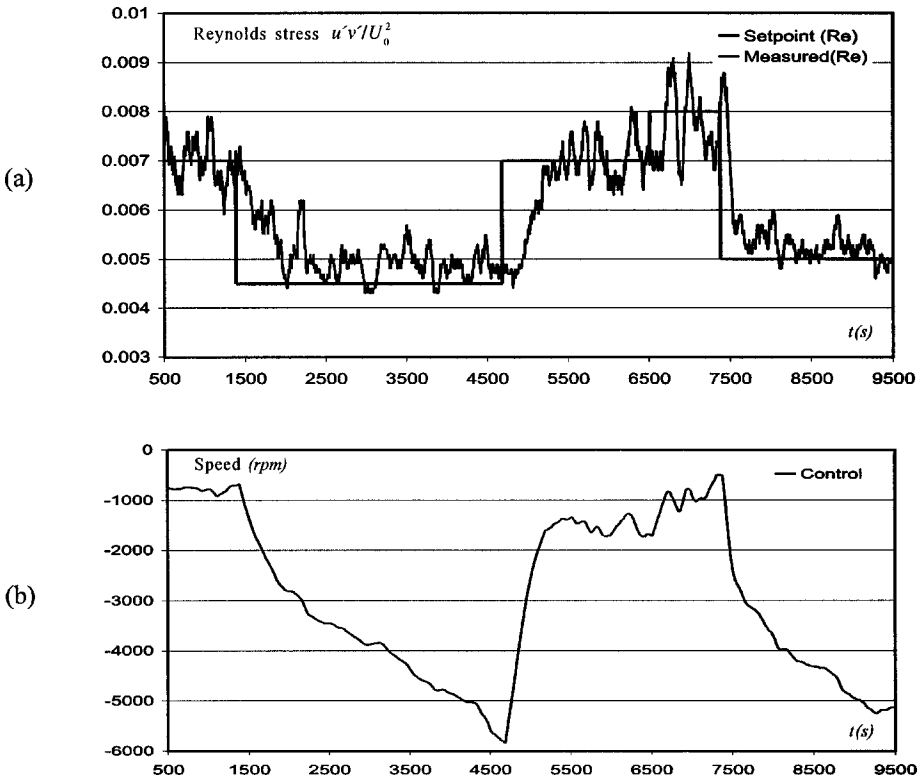

Fig. 11 Measured (MA filtered) and setpoint values for Reynolds shear stress (*a*) and control output (*b*)

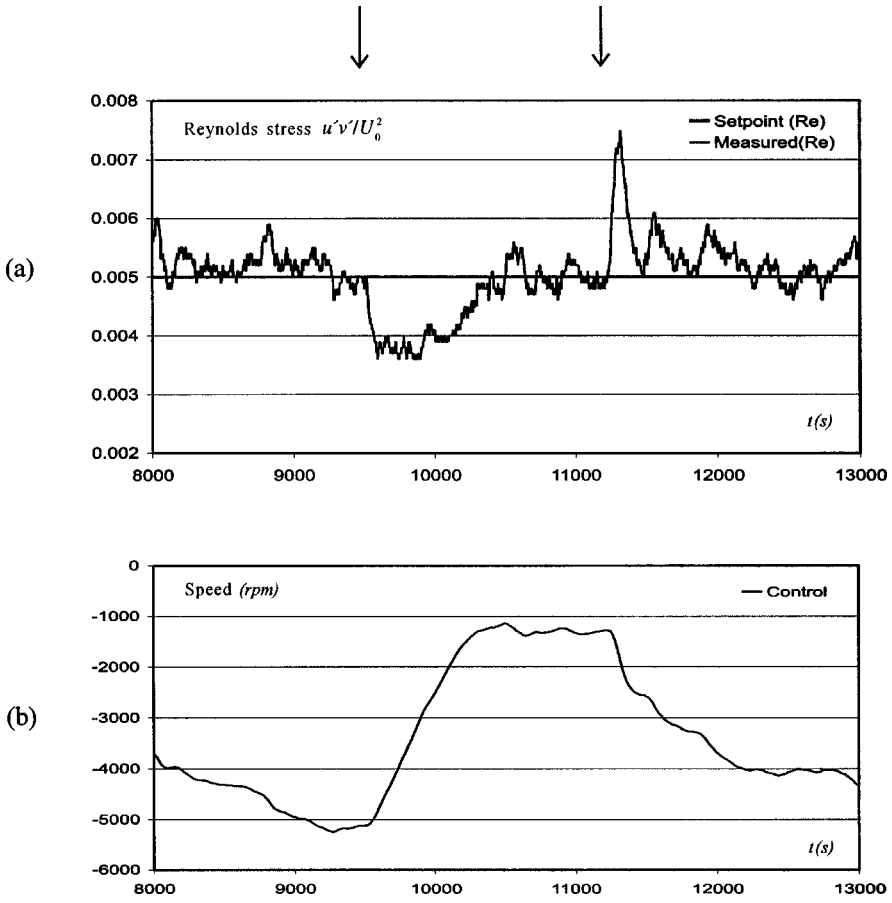

Fig. 12 Measured (MA filtered) and setpoint value (0.005) for Reynolds shear stress (*a*) and control output with two disturbances in flow speed at moments 9500 and 11150 s

can compensate the disturbance and the Reynolds shear stress receives the setpoint value. Also, this test shows the difference in the responses, depending on the direction of the Reynolds shear stress set point change.

6 Conclusions

A new concept of turbulence control with particle image velocimetry (PIV) is introduced. A PIV system can be considered as an intelligent sensor for turbulence analysis. The ''closed-loop'' PID controller with a PIV system, used as an example of the method, is the following: (1) A PIV station grabs images and computes them into velocity vector fields, (2) instantaneous turbulence quantities, correlations and length scales are estimated, (3) the estimates calculated in the PIV station are send to the control station, (4) the estimates are averaged over a relatively short time period (moving average) to decrease the noise, and (5) the difference between the moving averaged estimate and the desired setpoint (=control error) is used to manage the flow turbulence with controllers, and finally the control signals are sent to the actuator.

Special instantaneous turbulence quantities are developed for the control purpose. The integral scale is based on the limited spatial data and is computed from the non-normalized correlations, requiring time invariant mean flow velocity. The mean velocity can also be computed in the PIV station over a relatively short period of time. This mean velocity is used for the Reynolds decomposition and thus the instantaneous $u'v'$ can be calculated. Same scheme can be applied in the computation of turbulence kinetic energy or other quantities calculated from the velocity fluctuations.

The method is tested in a BFS. A DC motor based actuator is used to manipulate the flow on the wall just before the sudden expansion. Three different control tests are made which show it is possible to manage the turbulence and compensate the disturbances in the turbulence properties caused for example by the manual change of the flow velocity. At the moment, the restriction of the control system with PIV is a fairly low control frequency due to the time-consuming image processing, limiting its use to processes like mixing or shear layer control based on periodically formed turbulence quantities.

References

[1] Prandtl, L., 1904, ''Über Flüssigkeitsbewegung bei sehr kleiner Reibung,'' *Proc. Third Int. Math. Cong.*, Heidelberg, pp. 484–491.
[2] Gad-el-Hak, M., 1989, ''Flow Control,'' Appl. Mech. Rev., **42**(10), pp. 261–293.
[3] Lumley, J., and Blossey, P., 1998, ''Control of Turbulence,'' Annu. Rev. Fluid Mech., **30**, pp. 311–327.
[4] McManus, K., Poinsot, T., and Candel, S. M., 1993, ''A Review of Active Control of Combustion Instabilities,'' Prog. Energy Combust. Sci., **19**, pp. 1–29.
[5] Gad-el-Hak, M., 1994, ''Interactive Control of Turbulent Boundary Layers: A Futuristic Overview,'' AIAA J., **32**(9), pp. 1753–1765.
[6] Chun, S., Lee, I., and Sung, H. J., 1999, ''Effect of Spanwise-Varying Local Forcing on Turbulent Separated Flow Over a Backward-Facing Step,'' Exp. Fluids, **26**, pp. 437–440.
[7] Lai, J. C. S., Yue, M., and Platzer, F., 2002, ''Control of Backward-Facing Step Flow Using a Flapping Foil,'' Exp. Fluids, **32**, pp. 44–54.
[8] Rathnasingham, R., and Breuer, K. S., 1997, ''System Identification and Control of a Turbulent Boundary Layer,'' Phys. Fluids, **9**(7), pp. 1867–1869.
[9] Jacobson, S. A., and Reynolds, W. C., 1998, ''Active Control of Streamwise Vortices and Streaks in Boundary Layers,'' J. Fluid Mech., **360**, pp. 179–211.
[10] Piirto, M., and Saarenrinne, P., 1999, ''Turbulence Length Scale Estimation

With PIV,'' 8th International Conference on Laser Anemometry Advances and Applications, Rome.
[11] Piirto, M., Ihalainen, H., Eloranta, H., and Saarenrinne, P., 2001, ''2D Spectral and Turbulence Length Scale Estimation With PIV,'' J. of Visual., **4**(1) pp. 39–49.
[12] Eloranta, H., Saarenrinne P., and Piirto, M., 2000, ''Identification and Analysis of Coherent Structures in PIV-Data,'' Pivnet Task5, ERCOFTAC SIG 32 Workshop, Lisbon.
[13] Tomkins, C. D., and Adrian, R. J., 2000, ''Comparison of Energetic Spanwise Modes in a Boundary Layer and Channel,'' 10th Int. Symp. on Applications of Laser Techniques to Fluid Mechanics, Portugal.
[14] Yoda, M., and Westerweel, J., 2001, ''Particle Image Velocimetry Studies of a Boundary Layer Perturbed by Localized Suction,'' Exp. Fluids, **30**, pp. 239–245.
[15] Choi, H., Moin, P., and Kim, J., 1994, ''Active Turbulence Control for Drag Reduction in Wall-Bounded Flows,'' J. Fluid Mech., **262**, pp. 75–110.
[16] Baur, T., and Köngeter, J., 1999, ''PIV With High Temporal Resolution for the Determination of Local Pressure Reductions From Coherent Turbulence Phenomena,'' 3rd International Workshop on Particle Image Velocimetry, Santa Barbara, CA.
[17] Piirto, M., Eloranta, H., and Saarenrinne P., 2000, ''Interactive Software for Turbulence Analysis From PIV Vector Fields,'' 10th Int. Symp. on Applications of Laser Techniques to Fluid Mechanics, Lisbon.
[18] Saarenrinne, P., and Piirto, M., 2000, ''Turbulent Kinetic Energy Dissipation Rate Estimation From PIV Velocity Vector Fields,'' Exp. Fluids, **29**, pp. 300–307.
[19] Scarano, F., and Riethmuller, M. L., 1999, ''Iterative Multigrid Approach in PIV Image Processing With Discrete Window Offset,'' Exp. Fluids, **26**, pp. 513–523.
[20] Sousa, J. M. M., Freek, C., and Pereia, J. F. C., 1998, ''PIV Measurements of Turbulence Statistics in the Three-Dimensional Flow Over a Surface-Mounted Obstacle,'' Proc. of Ninth International Symposium on Applications of Laser Techniques to Fluid Mechanics, Portugal.
[21] Westerweel, J., 1997, ''Fundamentals of Digital Particle Image Velocimetry,'' Meas. Sci. Technol., **8**, pp. 1379–1392.
[22] Spalding, D. B., 1961, ''A Single Formula for the Law of the Wall,'' ASME J. Appl. Mech., **28**, pp. 455–457.
[23] Piirto, M., Koivo, H., and Virtanen P., 1989, ''Portable Data Acquisition and Control Station for Self-Tuning Control Applications,'' 1989 IEEE International Conference on Control and Applications, Jerusalem.
[24] Åström, K. J., and Wittenmark, B., 1995, *Adaptive Control*, 2nd Ed., Addison-Wesley, Reading, MA, p. 580.
[25] Piirto, M., Jussila, T., Koivo, H., and Virtanen P., 1989, ''Advanced Portable Control Station,'' IFAC Symposium on Low Cost Automation, Milan.
[26] Hinze, J. O., 1975, *Turbulence*, McGraw-Hill, New York, pp. 39–58.
[27] Adrian, R. J., Christensen, K. T., and Liu, Z. C., 2000, ''Analysis and Interpretation of Instantaneous Turbulent Velocity Fields,'' Exp. Fluids, **29**, pp. 275–290.

Journal of Fluids Engineering

Technical Brief

Pressure Drops of Water Flow Through Micromachined Particle Filters

Tzung K. Hsiai
Department of Biomedical Engineering and Division of Cardiovascular Medicine, School of Engineering and Keck School of Medicine, Los Angeles, CA 90089-1451. e-mail: hsiai@usc.edu

Sung Kwon Cho and Joon Mo Yang[1]
Mechanical and Aerospace Engineering Department, University of California, Los Angeles, CA 90095

Xing Yang and Yu-Chong Tai
Department of Electrical Engineering, California Institute of Technology, Pasadena, CA 91125

Chih-Ming Ho
Mechanical and Aerospace Engineering Department, University of California, Los Angeles, CA 90095

When the particle is in the order of microns, flow through the small opening produces a large velocity gradient, leading to high viscous dissipation. Understanding the flow field is critical in determining the power requirement. In this paper, we studied water flow through filters fabricated by micro-electro-mechanical system (MEMS) techniques. The pressure drop calculated by a three-dimensional numerical code of the Navier-Stokes equations is in a resonable agreement with the experimental data if the diameter and the side wall profile of the holes are measured with high accuracy. [DOI: 10.1115/1.1514209]

Introduction

Filtration through thin perforated plates (filters) is a common technique to collect solid particles suspended in fluids, [1]. With the advent of micro electro mechanical system (MEMS) technology, micromachined filters have been designed, [2–4], to isolate biological agents in the order of microns. The filter hole sizes must be less than or comparable to the sizes of target biological agents. Accordingly, the corresponding Reynolds numbers (Re_D) are less than 50, much lower than those of conventional filters. The Reynolds number is defined as $U_{in}D/\beta\nu$, where U_{in} is the inlet velocity, D the hole size, β the opening factor (ratio of area of holes to total area) of the filter, and ν the kinematic viscosity of the fluid. U_{in}/β represents the velocity of the fluid passing through the opening.

The empirical formulas established for the conventional filters, [5,6], cannot accurately predict the pressure drop through the microfilters, [4]. Dagan et al. [7] presented an infinite-series solution to the creeping viscous motion of flow through a single hole. Hasegawa et al. [8], who investigated liquid flow through very small orifices (8.8–1000 μm), demonstrated that the measured pressure drops deviated above those predicted by the Navier-Stokes numerical simulation as the hole size was decreased to micron order.

On the other hand, Yang et al. [9] presented a new design rule to predict the pressure drop of air flow through MEMS filters by embracing the Navier-Stokes numerical simulation with precise geometrical data of the filter. Likewise, we would anticipate good correlation with the Navier-Stokes numerical simulation for water flow through the MEMS filters. It is critical to precisely predict the pressure drop of fluid, which constitutes the basis of biomedical applications. In this context, we studied the pressure drop of water flow through the MEMS based microfilters, and compared the experimental data with the results from three-dimensional Navier-Stokes numerical simulation, [9].

MEMS Filters

The MEMS filters were fabricated by both surface and bulk micromachining technologies. For details in fabrication processes, please refer to Yang et al. [4], where they showed that the deposition of Parylene C polymer on the surface greatly improves the strength of the MEMS filters. Figure 1 illustrates the MEMS filters by photographs, geometric configuration and the sidewall profiles taken from a scanning electron microscope (SEM). The filtering region was an 8 mm $\times$ 8 mm membrane with a thickness of 3 μm, while the frame region was constructed from a 500-μm-thick silicon wafer. Two filters of different hole sizes (MEMS Filter I and MEMS Filter II, respectively) were fabricated and tested (Table 1).

As shown in Fig. 1(*c*), sidewalls were not perfectly perpendicular to the surface of the filters. Consequently, the diameters of the front and the back sides were different (Table 1). This variation inevitably occurred as a result of etching processes, [10–12]. Here, the opening factor (β) was calculated from the hole diameter (D) of back side and spacing between the holes (s). The precision in measuring the hole diameter of the MEMS filters influenced the accuracy of pressure prediction. A piezoelectrically driven optical interferometer type profiler (WYKO), which provides a lateral resolution of approximately 10 nm (0.01 μm), was used to profile the surfaces of filters (Fig. 2(*a*)). Three random locations on each MEMS filter were profiled. Since the hole geometry was not uniformly circular, the diameters were measured in both horizontal and vertical directions. A total of 57

[1]Currently at Nanogen, Inc., San Diego, CA 92121.

Contributed by the Fluids Engineering Division for publication in the JOURNAL OF FLUIDS ENGINEERING. Manuscript received by the Fluids Engineering Division October 19, 2000; revised manuscript received May 16, 2002. Associate Editor: Y. Matsumoto.

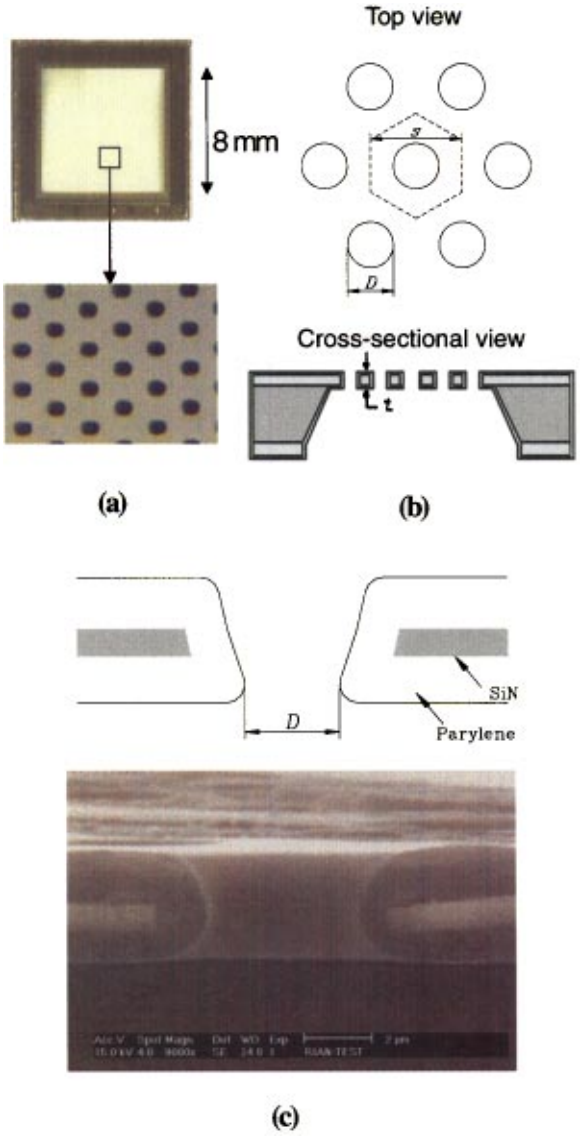

Fig. 1 Fabricated MEMS Filters with circular holes and thickness of 3 μm: (*a*) photographs of the MEMS Filter (*b*) geometric factors in the MEMS Filter (not to scale) (*c*) side-wall profiles and SEM pictures of the filtering hole

holes were sampled using the WYKO system, from which the probability density functions of the hole diameter and the mean diameters were obtained. Figure 2(*b*) shows the probability density function of MEMS Filter I. The sidewall geometry of the SEM picture was also profiled, modeled, and incorporated in the three-dimensional Navier-Stokes numerical simulation (see Fig. 1(*c*)). The measured dimensions of two MEMS filters tested in this experiment are shown in Table 1.

Table 1 Two MEMS filters (uncertainty in $D\pm1\%$ and in $\beta\pm2.8\%$)

Name	Hole Diameter (D, μm)	Opening Factor (β, %)	Filter Thickness (t, μm)
MEMS Filter I front side/back side	6.3/6.0	11.2/10.1	3.0
MEMS Filter II front side/back side	7.4/7.2	15.3/14.5	3.0

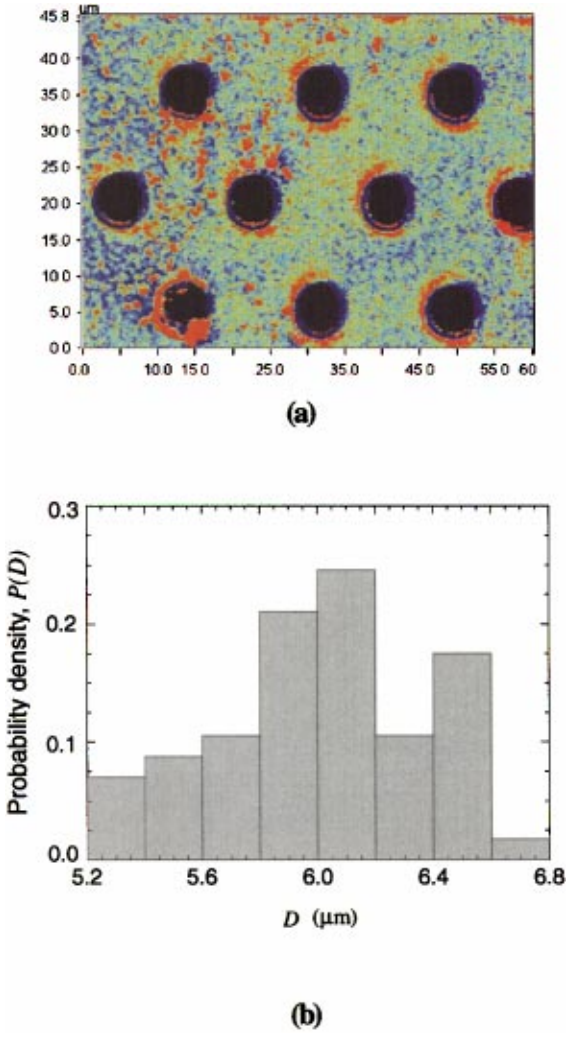

Fig. 2 (*a*) Image of the MEMS filtering holes by WYKO surface profiler and (*b*) probability density function of the hole size for MEMS Filter I (see Table 1)

Experimental Apparatus

A water channel was designed to measure the pressure drops through the MEMS filters. The water channel was built with an inlet, a settling chamber with sponge and wire mesh, a contraction chamber, and a test channel in which the MEMS filters were positioned. The test channel spanned 16 cm with a cross-section area of 8 mm$\times$8 mm to accommodate the filtering region of the MEMS filters. The contraction contour was derived from a fifth-order polynomial equation to yield an area ratio 3:1. A pressure transducer (Druck LPX 9381, range 0 to 5 psi) was used to measure the static pressure difference between upstream and downstream of the contraction within 0.1% accuracy. By the continuity equation and Bernoulli's principle, we derived the volumetric flow rate, [4,9]. The calculated flow rates validated those obtained from the electromagnetic flow meter (EMCD flow meter, type Mag 1100), which was installed downstream of the test channel. A second pressure transducer, which was connected to two pressure taps at 10 mm upstream and 10 mm downstream from the testing filter, measured the pressure drop through the MEMS filters. The uncertainty in both the pressure and inlet velocity measurement was $\pm1.5\%$. The propagated uncertainties in other physical quantities, which were estimated to be within the 95% confidence level according to Kline et al. [13] and Abernethy et al. [14], are included in the caption of Fig. 3.

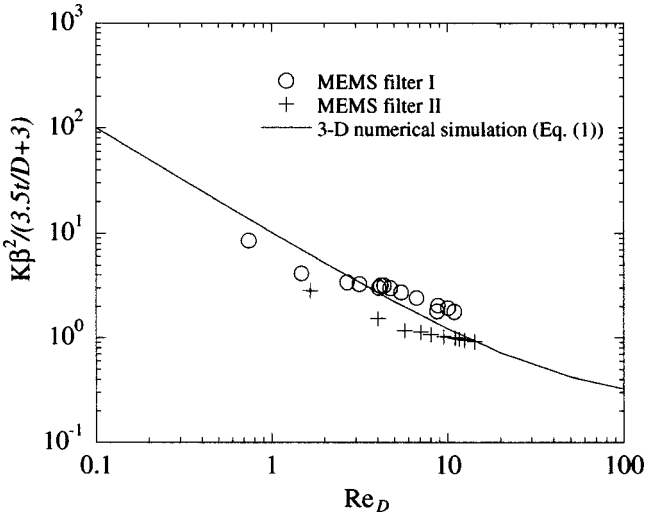

Fig. 3 The measured pressure drop of MEMS filters in comparison with nondimensionalized numerical formula (Eq. (1)). (Uncertainty in $K\beta^2/(3.5t/D+3)\pm 6.6\%$ and in $Re_D\pm 3.3\%$).

A constant hydrostatic pressure head was established using a water tank 1.5 meters above the flow channel. The test fluid used was distilled and deionized water (resistivity, >4 MΩ-cm). The water was delivered to the tank using a pump (Little Giant Pump Company, model A-430). Purification of the unwanted microparticles was established using two types of filters: (1) water was pumped through a capsule filter (Fisher Scientific, pore size 0.45 μm) for two hours prior to experiment and (2) during data collection, water was continuously pumped through a Millipore glass fiber filter (Fisher Scientific, pore size 0.8 μm). The flow rate was regulated by a ball valve (McMaster-Carr Supply CO., Nylon miniature ball valve) located upstream from the inlet.

Results and Discussions

To verify our experimental setup, we compared the pressure drop through conventional screens with Wieghardt's empirical formula, [5]. Our measured pressure drop fell within the acceptable scattering range observed by Wieghardt (not shown). To compare the pressure drops through the MEMS filters, a formula was established using the three-dimensional numerical simulations for laminar water flow at low Reynolds number:

$$K=\frac{\Delta P}{(1/2)\rho U_{in}^2}=\beta^{-2}\left[3.1\frac{t}{D}+3\right]\left[10.7\frac{v\beta}{U_{in}D}+0.22\right], \quad (1)$$

for $5\%<\beta<45\%$, $0.08<t/D<0.65$ and $1<U_{in}D/\beta\nu<100$, where K denotes the pressure drop coefficient, ΔP the pressure drop through the filters, and ρ the density of the fluid.

Each individual MEMS filter contained approximately half a million holes of varying sizes. The combination of complex hole geometry and a large number of holes made direct simulation of the entire flow field computationally challenging. Alternatively, we modeled and simulated the averaged geometry of hexagonal domain with a single hole out of the filters. This approach might have been inaccurate. The variation in the diameters of individual holes could have nonlinearly affected the pressure drop according to Eq. (1). Nevertheless, we confirmed that this effect was negligible (less than 2%) by estimating the nonlinear effect of the hole size distribution on the pressure drop using the probability density functions of the hole diameter and Eq. (1). The sidewall profiles, which also influenced the accuracy of the pressure drop prediction, was taken into account in the three dimensional Navier-Stokes numerical simulation. For details in numerical simulations, please refer to Yang et al. [9].

The three-dimensional simulation demonstrated that the pressure drop coefficient varied inversely with the opening factor (β) to the second power and proportionally with the Reynolds number to the first power. As shown in Fig. 3, the numerical simulation for MEMS filter I overestimated the pressure drop at $Re_D<2$, but underestimated at $Re_D>5$. For the MEMS filter II, the numerical simulation overestimated in the entire testing range of Re_D. The scattering of the pressure drop may be mainly related to the sensitivity of the numerical simulation to the hole diameter, D. Despite the installation of two purification filters, impurities could remain from the sponge and wire mesh used to regulate flow upstream. Moreover, the polymer, Parylene C, used to coat the surface of MEMS filters, is known to absorb water over prolonged period of immersion in water.

Nevertheless, the experimental data reasonably agreed with the conventional Navier-Stokes three-dimensional numerical simulation with a maximum of 40% deviation in the range of $2<Re_D<20$, suggesting that the Navier-Stokes equations in this range of Reynolds number could be applied to model the fluid flow at the micron scale. The characteristic flow scale (the hole size of MEMS filter) was larger than the molecular length scale characterizing the structure of the fluid. Thus, the surface force effect, which might have been dominant in the micron scale, seemed not critical.

Conclusions

Pressure drops across two MEMS filters with hole sizes of 6 μm and 7.2 μm, opening factors of 10.1% and 14.5%, and Reynolds numbers from 20 down to 0.7 were measured and compared with three-dimensional numerical simulation. Geometric factors including precise ratio of hole diameter to filter thickness, sidewall profile, opening factors, and Reynolds number, were taken into account for accurate prediction of the pressure drop. By incorporating the three-dimensional numerical simulation with accurate geometrical data, we were able to reasonably predict the pressure drop through the MEMS filters.

Acknowledgment

This work was supported by Defense Advanced Research Projects Agency (DARPA) MicroFlumes Program. T. K. H. was supported by National Institutes of Health, NRSA HL # 07895 and UCLA Cardiology Fellowship. The channel could not have become materialized without the technical assistance from John Seymour, Yi-Far Chen, and Eric Prophet. We would also like to thank Dean Ho for conducting the initial testing.

References

[1] Ho, C.-M., Huang, P.-H., Yang, J. M., Lee, G.-B., and Tai, Y.-C., 1998, "Active Flow Control by Micro Systems," *FLOWCON*, G. E. A. Meier and P. R. Viswanath, eds., International Union of Theoretical and Applied Mechanics (IUTAM) Symposium on Mechanics of Passive and Active Flow Control, Göttingen, Germany, Kluwer, Dordrecht, The Netherlands, pp. 18–19.

[2] Kittilsland, G. Steme, G., and Norden, B., 1990, "A Submicron Particle Filter in Silicon," Sens. Actuators, **23**, pp. 904–907.

[3] van Rijn, C. J. M., van der Wekken, M., Hijdam, W., and Elwenpoek, M. C., 1997, "Deflection and Maximum Load of Microfiltration Membrane Sieves Made With Silicon Micromachining," J. Microelectromech. Syst., **6**, pp. 48–54.

[4] Yang, X., Yang, J. M., Tai, Y. C., and Ho, C.-M., 1999, "Micromachined Membrane Particle Filters," Sens. Actuators, **73**(1–2), pp. 184–191.

[5] Wieghardt, K. E. G., 1953, "On the Resistance of Screens," Aeronaut. Q., **IV**, pp. 186–192.

[6] Derbunovich, G. I., Zemskaya, A. S., Repik, Ye. U., and Sosedko, Yu. P., 1984, "Hydraulic Drag of Perforated Plates," Fluid Mech.-Sov. Res., **13**(1), pp. 111–116.

[7] Dagan, Z., Weinbaum, S., and Pfeffer, R., 1982, "An Infinite-Series Solution for the Creeping Motion Through an Orifice of Finite Length," J. Fluid Mech., **115**, pp. 505–523.

[8] Hasegaw, T., Suganuma, M., and Watanabe, H., 1997, "Anomaly of Excess Pressure Drops of the Flow Through Very Small Orifices," Phys. Fluids, **9**, pp. 1–3.

[9] Yang, J. M., Yang, X., Ho, C. M., and Tai, Y. C., 2001, "Micromachined

Particle filter With Low Power Dissipation,'' ASME J. Fluids Eng., **123**, pp. 899–908.
[10] Pelka, J., Weiss, M., Hoppe, W., and Mewes, D., 1989, ''The Influence of Ion Scattering on Dry Etch Profiles,'' J. Vac. Sci. Technol. B, **7**, pp. 1483–1487.
[11] Daubenspeck, T. H. and Sukanek, P. C., 1990, ''Development of Chlorofluorocarbon/Oxygen Reactive Ion Etching Chemistry for Fine-Line Tungsten Patterning,'' J. Vac. Sci. Technol. B, **8**, pp. 586–595.
[12] May, P. W., Field, D., and Klempere, D. F., 1993, ''Simulation of Side-Wall Profiles in Reactive Ion Etching,'' Journal of Physics D: Applied physics, **26**, pp. 598–606.
[13] Kline, S. J. and McClintock, F. A., 1953, ''Describing Uncertainties in Single-Sample Experiments,'' Mech. Eng. (Am. Soc. Mech. Eng.), **75**, pp. 3–8.
[14] Abernethy, R. B., Benedict, R. P., and Dowdell, R. B., 1985, ''ASME Measurement Uncertainty,'' ASME J. Fluids Eng., **107**, pp. 161–164.